

Advances in Civil Engineering

Advanced Tunnelling Techniques and Information Modelling of Underground Infrastructure

Lead Guest Editor: Wen-Chieh Cheng

Guest Editors: Zhu-Shan Shao, Wen-Gang Zhang, and Dominic E. L. Ong





Advanced Tunnelling Techniques and Information Modelling of Underground Infrastructure

Advances in Civil Engineering

**Advanced Tunnelling Techniques and
Information Modelling of Underground
Infrastructure**

Lead Guest Editor: Wen-Chieh Cheng

Guest Editors: Zhu-Shan Shao, Wen-Gang Zhang,
and Dominic E. L. Ong



Copyright © 2021 Hindawi Limited. All rights reserved.

This is a special issue published in "Advances in Civil Engineering." All articles are open access articles distributed under the Creative Commons Attribution License, which permits unrestricted use, distribution, and reproduction in any medium, provided the original work is properly cited.






Chief Editor

Cumaraswamy Vipulanandan, USA










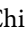



Associate Editors

Chiara Bedon , Italy
Constantin Chalioris , Greece
Ghassan Chehab , Lebanon
Ottavia Corbi, Italy
Mohamed ElGawady , USA
Husnain Haider , Saudi Arabia
Jian Ji , China
Jiang Jin , China
Shazim A. Memon , Kazakhstan
Hossein Moayedi , Vietnam
Sanjay Nimbalkar, Australia
Giuseppe Oliveto , Italy
Alessandro Palmeri , United Kingdom
Arnaud Perrot , France
Hugo Rodrigues , Portugal
Victor Yepes , Spain
Xianbo Zhao , Australia

Academic Editors

José A.F.O. Correia, Portugal
Glenda Abate, Italy
Khalid Abdel-Rahman , Germany
Ali Mardani Aghabaglou, Turkey
José Aguiar , Portugal
Afaq Ahmad , Pakistan
Muhammad Riaz Ahmad , Hong Kong
Hashim M.N. Al-Madani , Bahrain
Luigi Aldieri , Italy
Angelo Aloisio , Italy
Maria Cruz Alonso, Spain
Filipe Amarante dos Santos , Portugal
Serji N. Amirkhania, USA
Eleftherios K. Anastasiou , Greece
Panagiotis Ch. Anastasopoulos , USA
Mohamed Moafak Arbili , Iraq
Farhad Aslani , Australia
Siva Avudaiappan , Chile
Ozgur BASKAN , Turkey
Adewumi Babafemi, Nigeria
Morteza Bagherpour, Turkey
Qingsheng Bai , Germany
Nicola Baldo , Italy
Daniele Baraldi , Italy

Eva Barreira , Portugal
Emilio Bastidas-Arteaga , France
Rita Bento, Portugal
Rafael Bergillos , Spain
Han-bing Bian , China
Xia Bian , China
Huseyin Bilgin , Albania
Giovanni Biondi , Italy
Hugo C. Biscaia , Portugal
Rahul Biswas , India
Edén Bojórquez , Mexico
Giosuè Boscato , Italy
Melina Bosco , Italy
Jorge Branco , Portugal
Bruno Briseghella , China
Brian M. Broderick, Ireland
Emanuele Brunesi , Italy
Quoc-Bao Bui , Vietnam
Tan-Trung Bui , France
Nicola Buratti, Italy
Gaochuang Cai, France
Gladis Camarini , Brazil
Alberto Campisano , Italy
Qi Cao, China
Qixin Cao, China
Iacopo Carnacina , Italy
Alessio Cascardi, Italy
Paolo Castaldo , Italy
Nicola Cavalagli , Italy
Liborio Cavaleri , Italy
Anush Chandrappa , United Kingdom
Wen-Shao Chang , United Kingdom
Muhammad Tariq Amin Chaudhary, Kuwait
Po-Han Chen , Taiwan
Qian Chen , China
Wei Tong Chen , Taiwan
Qixiu Cheng, Hong Kong
Zhanbo Cheng, United Kingdom
Nicholas Chileshe, Australia
Prinya Chindaprasirt , Thailand
Corrado Chisari , United Kingdom
Se Jin Choi , Republic of Korea
Heap-Yih Chong , Australia
S.H. Chu , USA
Ting-Xiang Chu , China

Zhaofei Chu , China
Wonseok Chung , Republic of Korea
Donato Ciampa , Italy
Gian Paolo Cimellaro, Italy
Francesco Colangelo, Italy
Romulus Costache , Romania
Liviu-Adrian Cotfas , Romania
Antonio Maria D'Altri, Italy
Bruno Dal Lago , Italy
Amos Darko , Hong Kong
Arka Jyoti Das , India
Dario De Domenico , Italy
Gianmarco De Felice , Italy
Stefano De Miranda , Italy
Maria T. De Risi , Italy
Tayfun Dede, Turkey
Sadik O. Degertekin , Turkey
Camelia Delcea , Romania
Cristoforo Demartino, China
Giuseppe Di Filippo , Italy
Luigi Di Sarno, Italy
Fabio Di Trapani , Italy
Aboelkasim Diab , Egypt
Thi My Dung Do, Vietnam
Giulio Dondi , Italy
Jiangfeng Dong , China
Chao Dou , China
Mario D'Aniello , Italy
Jingtao Du , China
Ahmed Elghazouli, United Kingdom
Francesco Fabbrocino , Italy
Flora Faleschini , Italy
Dingqiang Fan, Hong Kong
Xueping Fan, China
Qian Fang , China
Salar Farahmand-Tabar , Iran
Ilenia Farina, Italy
Roberto Fedele, Italy
Guang-Liang Feng , China
Luigi Fenu , Italy
Tiago Ferreira , Portugal
Marco Filippo Ferrotto, Italy
Antonio Formisano , Italy
Guoyang Fu, Australia
Stefano Galassi , Italy

Junfeng Gao , China
Meng Gao , China
Giovanni Garcea , Italy
Enrique García-Macías, Spain
Emilio García-Taengua , United Kingdom
DongDong Ge , USA
Khaled Ghaedi, Malaysia
Khaled Ghaedi , Malaysia
Gian Felice Giaccu, Italy
Agathoklis Giaralis , United Kingdom
Ravindran Gobinath, India
Rodrigo Gonçalves, Portugal
Peilin Gong , China
Belén González-Fonteboa , Spain
Salvatore Grasso , Italy
Fan Gu, USA
Erhan Güneyisi , Turkey
Esra Mete Güneyisi, Turkey
Pingye Guo , China
Ankit Gupta , India
Federico Gusella , Italy
Kemal Hacıfendioglu, Turkey
Jianyong Han , China
Song Han , China
Asad Hanif , Macau
Hadi Hasanzadehshooiili , Canada
Mostafa Fahmi Hassanein, Egypt
Amir Ahmad Hedayat , Iran
Khandaker Hossain , Canada
Zahid Hossain , USA
Chao Hou, China
Biao Hu, China
Jiang Hu , China
Xiaodong Hu, China
Lei Huang , China
Cun Hui , China
Bon-Gang Hwang, Singapore
Jijo James , India
Abbas Fadhil Jasim , Iraq
Ahad Javanmardi , China
Krishnan Prabhakan Jaya, India
Dong-Sheng Jeng , Australia
Han-Yong Jeon, Republic of Korea
Pengjiao Jia, China
Shaohua Jiang , China

MOUSTAFA KASSEM , Malaysia
Mosbeh Kaloop , Egypt
Shankar Karuppanan , Ethiopia
John Kechagias , Greece
Mohammad Khajehzadeh , Iran
Afzal Husain Khan , Saudi Arabia
Mehran Khan , Hong Kong
Manoj Khandelwal, Australia
Jin Kook Kim , Republic of Korea
Woosuk Kim , Republic of Korea
Vaclav Koci , Czech Republic
Loke Kok Foong, Vietnam
Hailing Kong , China
Leonidas Alexandros Kouris , Greece
Kyriakos Kourousis , Ireland
Moacir Kripka , Brazil
Anupam Kumar, The Netherlands
Emma La Malfa Ribolla, Czech Republic
Ali Lakirouhani , Iran
Angus C. C. Lam, China
Thanh Quang Khai Lam , Vietnam
Luciano Lamberti, Italy
Andreas Lampropoulos , United Kingdom
Raffaele Landolfo, Italy
Massimo Latour , Italy
Bang Yeon Lee , Republic of Korea
Eul-Bum Lee , Republic of Korea
Zhen Lei , Canada
Leonardo Leonetti , Italy
Chun-Qing Li , Australia
Dongsheng Li , China
Gen Li, China
Jiale Li , China
Minghui Li, China
Qingchao Li , China
Shuang Yang Li , China
Sunwei Li , Hong Kong
Yajun Li , China
Shun Liang , China
Francesco Liguori , Italy
Jae-Han Lim , Republic of Korea
Jia-Rui Lin , China
Kun Lin , China
Shibin Lin, China

Tzu-Kang Lin , Taiwan
Yu-Cheng Lin , Taiwan
Hexu Liu, USA
Jian Lin Liu , China
Xiaoli Liu , China
Xuemei Liu , Australia
Zaobao Liu , China
Zhuang-Zhuang Liu, China
Diego Lopez-Garcia , Chile
Cristiano Loss , Canada
Lyan-Ywan Lu , Taiwan
Jin Luo , USA
Yanbin Luo , China
Jianjun Ma , China
Junwei Ma , China
Tian-Shou Ma, China
Zhongguo John Ma , USA
Maria Macchiaroli, Italy
Domenico Magisano, Italy
Reza Mahinroosta, Australia
Yann Malecot , France
Prabhat Kumar Mandal , India
John Mander, USA
Iman Mansouri, Iran
André Dias Martins, Portugal
Domagoj Matesan , Croatia
Jose Matos, Portugal
Vasant Matsagar , India
Claudio Mazzotti , Italy
Ahmed Mebarki , France
Gang Mei , China
Kasim Mermerdas, Turkey
Giovanni Minafò , Italy
Masoomah Mirrashid , Iran
Abbas Mohajerani , Australia
Fadzli Mohamed Nazri , Malaysia
Fabrizio Mollaioli , Italy
Rosario Montuori , Italy
H. Naderpour , Iran
Hassan Nasir , Pakistan
Hossein Nassiraei , Iran
Satheeskumar Navaratnam , Australia
Ignacio J. Navarro , Spain
Ashish Kumar Nayak , India
Behzad Nematollahi , Australia

Chayut Ngamkhanong , Thailand
Trung Ngo, Australia
Tengfei Nian, China
Mehdi Nikoo , Canada
Youjun Ning , China
Olugbenga Timo Oladinrin , United Kingdom
Oladimeji Benedict Olalusi, South Africa
Timothy O. Olawumi , Hong Kong
Alejandro Orfila , Spain
Maurizio Orlando , Italy
Siti Aminah Osman, Malaysia
Walid Oueslati , Tunisia
SUVASH PAUL , Bangladesh
John-Paris Pantouvakis , Greece
Fabrizio Paolacci , Italy
Giuseppina Pappalardo , Italy
Fulvio Parisi , Italy
Dimitrios G. Pavlou , Norway
Daniele Pellegrini , Italy
Gatheeshgar Perampalam , United Kingdom
Daniele Perrone , Italy
Giuseppe Piccardo , Italy
Vagelis Plevris , Qatar
Andrea Pranno , Italy
Adolfo Preciado , Mexico
Chongchong Qi , China
Yu Qian, USA
Ying Qin , China
Giuseppe Quaranta , Italy
Krishanu ROY , New Zealand
Vlastimir Radonjanin, Serbia
Carlo Rainieri , Italy
Rahul V. Ralegaonkar, India
Raizal Saifulnaz Muhammad Rashid, Malaysia
Alessandro Rasulo , Italy
Chonghong Ren , China
Qing-Xin Ren, China
Dimitris Rizos , USA
Geoffrey W. Rodgers , New Zealand
Pier Paolo Rossi, Italy
Nicola Ruggieri , Italy
JUNLONG SHANG, Singapore

Nikhil Saboo, India
Anna Saetta, Italy
Juan Sagaseta , United Kingdom
Timo Saksala, Finland
Mostafa Salari, Canada
Ginevra Salerno , Italy
Evangelos J. Sapountzakis , Greece
Vassilis Sarhosis , United Kingdom
Navaratnarajah Sathiparan , Sri Lanka
Fabrizio Scozzese , Italy
Halil Sezen , USA
Payam Shafigh , Malaysia
M. Shahria Alam, Canada
Yi Shan, China
Hussein Sharaf, Iraq
Mostafa Sharifzadeh, Australia
Sanjay Kumar Shukla, Australia
Amir Si Larbi , France
Okan Sirin , Qatar
Piotr Smarzewski , Poland
Francesca Sollecito , Italy
Rui Song , China
Tian-Yi Song, Australia
Flavio Stochino , Italy
Mayank Sukhija , USA
Piti Sukontasukkul , Thailand
Jianping Sun, Singapore
Xiao Sun , China
T. Tafsirojjan , Australia
Fujiao Tang , China
Patrick W.C. Tang , Australia
Zhi Cheng Tang , China
Weerachart Tangchirapat , Thailand
Xiabin Tao, China
Piergiorgio Tataranni , Italy
Elisabete Teixeira , Portugal
Jorge Iván Tobón , Colombia
Jing-Zhong Tong, China
Francesco Trentadue , Italy
Antonello Troncone, Italy
Majbah Uddin , USA
Tariq Umar , United Kingdom
Muahmmad Usman, United Kingdom
Muhammad Usman , Pakistan
Mucteba Uysal , Turkey

Ilaria Venanzi , Italy
Castorina S. Vieira , Portugal
Valeria Vignali , Italy
Claudia Vitone , Italy
Liwei WEN , China
Chunfeng Wan , China
Hua-Ping Wan, China
Roman Wan-Wendner , Austria
Chaohui Wang , China
Hao Wang , USA
Shiming Wang , China
Wayne Yu Wang , United Kingdom
Wen-Da Wang, China
Xing Wang , China
Xiuling Wang , China
Zhenjun Wang , China
Xin-Jiang Wei , China
Tao Wen , China
Weiping Wen , China
Lei Weng , China
Chao Wu , United Kingdom
Jiangyu Wu, China
Wangjie Wu , China
Wenbing Wu , China
Zhixing Xiao, China
Gang Xu, China
Jian Xu , China
Panpan , China
Rongchao Xu , China
HE YONGLIANG, China
Michael Yam, Hong Kong
Hailu Yang , China
Xu-Xu Yang , China
Hui Yao , China
Xinyu Ye , China
Zhoujing Ye, China
Gürol Yildirim , Turkey
Dawei Yin , China
Doo-Yeol Yoo , Republic of Korea
Zhanping You , USA
Afshar A. Yousefi , Iran
Xinbao Yu , USA
Dongdong Yuan , China
Geun Y. Yun , Republic of Korea


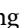
Hyun-Do Yun , Republic of Korea
Cemal YİĞİT , Turkey
Paolo Zampieri, Italy
Giulio Zani , Italy
Mariano Angelo Zanini , Italy
Zhixiong Zeng , Hong Kong
Mustafa Zeybek, Turkey
Henglong Zhang , China
Jiupeng Zhang, China
Tingting Zhang , China
Zengping Zhang, China
Zetian Zhang , China
Zhigang Zhang , China
Zhipeng Zhao , Japan
Jun Zhao , China
Annan Zhou , Australia
Jia-wen Zhou , China
Hai-Tao Zhu , China
Peng Zhu , China
QuanJie Zhu , China
Wenjun Zhu , China
Marco Zucca, Italy
Haoran Zuo, Australia
Junqing Zuo , China
Robert Černý , Czech Republic
Süleyman İpek , Turkey

Contents






Research on Tunnel Surrounding Rock Failure and Energy Dissipation Based on Cyclic Impact and Shear Loading

Yu Ding, Zhuoying Tan , Shuguang Li , Runke Huo , Ziliang Liu, and Yong Ma
Research Article (15 pages), Article ID 8838695, Volume 2021 (2021)


Three-Dimensional Reconstruction of Tunnel Face Based on Multiple Images

Wenge Qiu, Liao Jian , Yunjian Cheng , and Hengbin Bai
Research Article (11 pages), Article ID 8837309, Volume 2021 (2021)




The Ground Settlement and the Existing Pipeline Response Induced by the Nonsynchronous Construction of a Twin-Tunnel

Shicheng Sun , Chuanxin Rong , Houliang Wang , Linzhao Cui , and Xin Shi 
Research Article (12 pages), Article ID 8815304, Volume 2021 (2021)



Evacuation Experiment Study in Up and Down Escape Staircase of Underground Road

Da-jun Yuan, Hui Jin , Zhi-cong Chen, and Sheng-nan Liu
Research Article (10 pages), Article ID 8834180, Volume 2021 (2021)



Application of 3D Laser Scanning in Underground Station Cavity Clusters

Li Pinpin , Qiu Wenge , Cheng Yunjian, and Lu Feng 
Research Article (12 pages), Article ID 8896363, Volume 2021 (2021)



Development of Data Integration and Sharing for Geotechnical Engineering Information Modeling Based on IFC

Jiaming Wu , Jian Chen , Guoliang Chen, Zhe Wu, Yu Zhong, Bin Chen, Wenhui Ke, and Juehao Huang
Research Article (15 pages), Article ID 8884864, Volume 2021 (2021)







Field Investigation of Blasting-Induced Vibration in Concrete Linings during Expansion of Old Highway Tunnel

Ya-Qiong Wang , Lin-Jin Gong, Nan-Nan An, Xing-Bin Peng, Wei Wang, and Zhi-Feng Wang 
Research Article (11 pages), Article ID 8820544, Volume 2021 (2021)


Study on the Water-Physical Properties of the Cement-Plaster Bonded Rock-Like Materials

Yong Zhang , Zhiguo Cao, and Xiaomeng Shi 
Research Article (7 pages), Article ID 8863064, Volume 2021 (2021)






Strength Recovery Model of Clay during Thixotropy

Bin Tang , Biaohe Zhou , Liang Xie , Jianfeng Yin , Shengnan Zhao , and Zhibing Wang 
Research Article (11 pages), Article ID 8825107, Volume 2021 (2021)


Bending Capacity of Concrete-Encased Underground Electrical Duct Banks under Monotonic Loading: An Experimental Study

Ting-jin Liu , Liang-yi Cai, Qiang Liao, and Yu-bing Yang
Research Article (17 pages), Article ID 8836232, Volume 2021 (2021)



Construction Sequence Optimization and Settlement Control Countermeasures of Metro Tunnels Underpassing Expressway

Chengzhong Zhang , Qiang Zhang , Ziming Pei , Zhanping Song , and Junbao Wang 
Research Article (17 pages), Article ID 8834368, Volume 2021 (2021)

Stability and Countermeasures for a Deposit Slope with Artificial Scarp: Numerical Analysis and Field Monitoring

Yong Hong, Zhushan Shao , Guangbin Shi, and Jiabao Liu
Research Article (13 pages), Article ID 8822080, Volume 2020 (2020)


Analytical Solution of a Circular Opening considering Nonuniform Pressure and Its Engineering Application

Peng Wu, Yanlong Chen , Liang Chen, Xianbiao Mao, and Wei Zhang 
Research Article (13 pages), Article ID 8828917, Volume 2020 (2020)



Experimental Study on the Soil Conditioning Materials for EPB Shield Tunneling in Silty Sand

Chi-Hao Cheng , Shao-Ming Liao , Xiao-Bo Huo , and Li-Sheng Chen 
Research Article (21 pages), Article ID 8856569, Volume 2020 (2020)


Effect of the Double-Line Spiral Tunnel Curvature on the Tunnel Construction Stability

Chao Zhang, Chao Wang, Xibin Niu, Shaoqiang Zhang, and Huiling Zhao 
Research Article (9 pages), Article ID 8827806, Volume 2020 (2020)


Experimental Study on the Transverse Effective Bending Rigidity of Segmental Lining Structures

Yong-feng Tang, Han-cheng Chen, Zhen-wei Ye, Ting-jin Liu , and Yu-bing Yang 
Research Article (20 pages), Article ID 8836505, Volume 2020 (2020)


The Effects of Multipropped Deep Excavation-Induced Ground Movements on Adjacent High-Rise Building Founded on Piled Raft in Sand

Mukhtiar Ali Soomro , Naeem Mangi, Wen-Chieh Cheng, and Dildar Ali Mangnejo
Research Article (12 pages), Article ID 8897507, Volume 2020 (2020)


Research and Application of Support Resistant Limiting Dampers in the Deep-Buried Large-Section Loess Tunnel

Yong Deng, Jiangsheng Xie, and Shuguang Li 
Research Article (12 pages), Article ID 8841703, Volume 2020 (2020)

The Influence of Physical and Chemical Reactions on Water Leakage in a Multiarch Tunnel







Jian-Xun Shi , Zhao-Hui Li, Yong-Qiang He, Guo-Ming Zhang, and Ming-Qiang Wei
Research Article (8 pages), Article ID 8830739, Volume 2020 (2020)

Evaluation of Ground Displacements Caused by Installing Jet Grouted Columns Using Machine Learning Methods

Zhi-Feng Wang , Xing-Bin Peng, Yong Liu, Wen-Chieh Cheng, Ya-Qiong Wang, and Chao-Jun Wu
Research Article (11 pages), Article ID 8857293, Volume 2020 (2020)


Contents

Analysis and Monitoring of Small-Scale Rock Fracture Zone Deformation and Shaft Failure in a Metal Mine

Rong Lu , Fengshan Ma , Jie Zhao , Jianbo Wang , Guilin Li , and Bing Dai 

Research Article (14 pages), Article ID 8879258, Volume 2020 (2020)

Study on the Large Deformation Characteristics and Disaster Mechanism of a Thin-Layer Soft-Rock Tunnel

Xiulian Zhang, Manchao He, Fengnian Wang, Gan Li, Shengxin Xu, and Zhigang Tao 


Research Article (15 pages), Article ID 8826337, Volume 2020 (2020)

Observed Performance of Highway Embankment over Soft Marine Clay: A Case Study in Wenzhou, China

Xia Bian, Jin-Kai Yan , and Wei Zhang

Research Article (13 pages), Article ID 8813832, Volume 2020 (2020)

The Influence of Complex Subway Station Construction on High Retaining Walls and Appropriate Countermeasures

Kai Wang, Zhaoping Li , Xuezhao Xu, Leilei Shi, and Fanbo Zhang

Research Article (12 pages), Article ID 8853001, Volume 2020 (2020)

Research Article

Research on Tunnel Surrounding Rock Failure and Energy Dissipation Based on Cyclic Impact and Shear Loading

Yu Ding,^{1,2,3} Zhuoying Tan ^{1,2,3}, Shuguang Li ^{4,5}, Runke Huo ⁵, Ziliang Liu,^{1,2,3}
and Yong Ma^{1,2,3}

¹School of Civil and Resource Engineering, University of Science and Technology Beijing, Beijing 100083, China

²Beijing Key Laboratory of Urban Underground Space Engineering, University of Science and Technology Beijing, Beijing 100083, China

³State Key Laboratory of High-Efficient Mining and Safety of Metal Mines, University of Science and Technology Beijing, Beijing 100083, China

⁴Post-doctoral Research Workstation, China Railway 20th Bureau Group Co., Ltd., Xi'an 710016, China

⁵School of Civil Engineering, Xi'an University of Architecture and Technology, Xi'an 710055, China

Correspondence should be addressed to Zhuoying Tan; markzhy_tan@163.com and Shuguang Li; lssgg2015@163.com

Received 24 September 2020; Revised 18 January 2021; Accepted 15 June 2021; Published 23 June 2021

Academic Editor: Jian Ji

Copyright © 2021 Yu Ding et al. This is an open access article distributed under the Creative Commons Attribution License, which permits unrestricted use, distribution, and reproduction in any medium, provided the original work is properly cited.

Aiming at the cyclic impact deformation and failure of tunnel surrounding rock under shear stress, a self-developed rotation-impact simulation test platform was used to determine the number of failures, stress-strain curves, and energy in the process of cyclic impact failure. The failure process of rock under different impact velocities and shear stresses has been systematically studied. Results show that, under the same impact speed, the shear stress will increase with the increase in the rotation speed, but an upper limit will exist. When the rotation speed reaches this upper limit, the shear stress will no longer increase. The presence of shear stress will reduce the number of impacts required for rock failure. When the impact speed is 7.2 m/s, the number of impacts at the maximum rotation speed is 60% of the static state. When the impact velocity is 16.8 m/s, this value is only 33.3%. At the same impact velocity, the stress-strain curves under different rotation speeds do not change significantly, but with the increase in the rotation speed, the slope of the elastic stage of the stress-strain curve gradually decreases, and the corresponding stress of the rock sample decreases when the maximum strain is reached. With the increase in shear stress, the crushing specific energy required for rock failure gradually decreases. The greater the impact velocity, the more obvious the impact of shear stress on energy dissipation. In the tunnel process, when the surrounding rock is subjected to impact loads from different directions, only the axial strain analysis will have certain safety hazards, and timely support and reinforcement work are required.

1. Introduction

With the development of various types of large-scale geotechnical engineering, tunnel engineering is being increasingly applied in different fields, such as in large-section railways, underground transportation systems, highway tunnel construction, and mining transportation tunnels. However, due to blasting excavation disturbance, safety issues such as tunnel deformation, instability, and surrounding rock damage caused by high ground stress have always been a hot spot in tunnel engineering research [1–4].

Blasting is widely used in tunnels and other geotechnical engineering projects because it is economical, efficient, and fast. Part of the energy generated by explosives during blasting excavation is used to strip the rock mass to achieve the purpose of engineering excavation. Another part of the energy is transferred to the surrounding rock mass in the form of blasting shock wave, causing a certain degree of damage and destruction to the surrounding rock mass, thereby causing safety hazards to the tunnel surrounding the rock engineering project [5, 6]. For the middle and far areas away from the blasting source, although the stress wave

generated by one blasting is not strong enough to cause direct damage to the rock mass, it will cause the natural cracks in the rock to propagate and extend. Under the repeated action of the stress wave, the number and length of the internal cracks in the rock continue to increase, gradually connecting, penetrating, and forming the main crack. The internal damage of the rock evolves and develops in a nonlinear cumulative manner and eventually leads to loosening and slippage of the structural surface. Many engineering examples have proved that even buildings far away from the blasting operation point will also experience collapse, deformation, and instability [7, 8]. Rock is a brittle material with multiple internal cracks, which have obvious anisotropy. Different loading methods and directions will lead to different failure modes. For example, in a natural environment, when the in situ stress and other static loads are low, the original cracks inside the rock will close, and the development of cracks will be restricted when damaged by impact loads. The rock has a strong ability to resist damage. But when the static load exceeds a certain range, the crack inside the rock is almost at the stage of breaking through, and the rock's antidestructive ability is weak. Research shows that, under the action of the same stress wave, different incident angles at the crack will result in different reflected waves and failure laws, which will affect the failure laws of rocks and the transfer of stress wave energy [9]. Given the perturbation and damage of tunnels and another geotechnical engineering under cyclic loading during blasting and excavation and during normal use, many scholars have conducted in-depth studies on the mechanical properties, failure laws, and damage evolution of rocks under static cyclic loading. For the research of tunnel deformation and tunnel safety, numerical simulation is a convenient, profitable, and quick method; many scholars have conducted very comprehensive studies [10–13]. Combining with the engineering site, Ağbay and Topal [14] found that the ground settlement caused by double tunnel engineering mainly depends on the deformation modulus of surrounding rock and soil through field monitoring and numerical simulation methods, and a new formula for predicting ground deformation caused by double tunnel engineering is proposed. Singh [15] aimed at the impact and vibration damage of nearby open-pit blasting to underground coal mines; the borehole extensometers and strain and stress sensors arranged on the roof and pillars were used to monitor the vibration and deformation of the ground before and after the blasting. Sharma et al. [16] studied the effect of large-scale excavation on the deformation of adjacent rapid transit tunnels through various monitoring methods, and the results showed that the stiffness of the tunnel lining has a greater impact on the deformation and damage of the tunnel caused by the adjacent excavation. The research on the characteristics of tunnel surrounding rock is mainly carried out through the indoor impact test. Li et al. [17] studied the dynamic mechanics of the noncontinuous jointed rock model under cyclic dynamic loading and found that the deformation modulus of the jointed rock mass increases with the increase of the loading frequency, and the irreversible deformation increases with the number of cycles.

It increases and decreases as the loading frequency increases. Experimental research by Bagde and Petro [18] showed that the dynamic fatigue strength, dynamic axial stiffness, and dynamic modulus of rock are related to the frequency and amplitude of the load. Liu and He [19] used the MTS-815 testing machine to conduct cyclic test research on sandstone specimens under different confining pressures. The results showed that confining pressure has a greater impact on the mechanical properties of rocks under cyclic loading; axial strain and irreversible volume strain increase when the rock fatigue damages with the increase of pressure. Li and Ma [20] used two cylindrical granite cores to make the incident rod and the transmission rod, respectively, sandwiched between the two soil layers of different thickness and water content to simulate the filling in the joint and used a pendulum to impact the incident rod. They provided stress wave, used stress wave separation technology to obtain the stress-strain curve in the impact process, and studied the influence of fillings on the dynamic mechanical properties of joints. The fatigue deformation and strength degradation of rock under cyclic loading are mainly reflected in the incubation, propagation, and penetration of internal microcracks. To evaluate the development of rock damage, it is necessary to define its damage variables reasonably. According to the observed size, the damage variables can be determined from the microscopic, mesoscopic, and macroscopic perspectives. The microangle is mainly carried out from the material's atomic or molecular point of view. At present, it is difficult to observe the exchange process of atoms and molecules under cyclic loading. Therefore, rock damage is mainly defined by mesoscopic and macroscopic perspectives [21]. Many scholars have tried to define rock damage variables in the mesoperspective and macroperspective. At present, the more mature methods mainly include CT scanning method [22], acoustic wave velocity method [23], acoustic emission method [24], resistivity method [25], and energy method [26].

For the dynamic response of tunnel surrounding rock subjected to impact load, many scholars at home and abroad have studied it from the perspective of theoretical analysis, test, and numerical simulation. As early as 1984, Dowding [27] studied the problem of tunnel rock damage through the blasting test and found that the compressive wave strain caused by the explosion can be equivalent transformed into seismic shear strain and surface wave strain, and the tunnel rock strain can be used as a basic index to judge tunnel damage. Since then, more and more attention has been paid to the tunnel safety problems caused by the explosion, and the research on tunnel vibration monitoring and deformation control has gradually formed a discipline [28]. Zhao et al. [29] carried out a rock dynamics study on the excavation of an ammunition depot cavern in Singapore and systematically studied the dynamic characteristics of rocks with different materials, the dynamic shear characteristics of rock joints, and the influence mechanism of the rock structure on the dynamic response, which provided the necessary basis for the design and construction of the cavern project. Chen et al. [30] used the discrete element software UDEC to simulate the propagation process of the explosion

stress wave in the underground rock mass, and compared with the empirical formula calculation and field test results, it was found that UDEC can simulate the propagation process of the explosion shock wave in rock, and the results have high reliability. Hao et al. [31] studied the influence of rock joints on stress wave propagation by adjusting the angle between rock joints and rock surface and gave the peak attenuation, frequency spectrum, and spatial variation law of the stress wave. Zhou and Jenssen [32], from the perspective of explosive storage safety distance, studied the damage law of the adjacent cabin in case of an accidental explosion and proposed the separation principle of underground storage facilities according to the investigation report and test results of tunnel damage. Deng et al. [33] and Zhao et al. [34] used a numerical simulation method to analyze the damage of the tunnel under the action of the explosion shock wave. The results show that rock joints have a great influence on tunnel damage, while the initial stress of the rock mass has little effect. Through bolt support, particle velocity can be changed to improve tunnel stability. Zhu et al. [35] analyzed the failure law of rock under the action of the explosion shock wave by the finite element analysis method. The results show that the peak particle velocity (PPV) increases with the increase of explosive density and with the decrease of distance from the explosion source. With the increase of the rock joint dip angle, PPV first decreases and then increases sharply. With the increase of joint spacing, PPV first increases and then keeps stable. The research results are of great significance to engineering design and support.

The foregoing analysis shows that there have been many studies on tunnel deformation and fatigue damage of tunnel surrounding rock masses under cyclic loading. There are three main methods for these studies. The first method is to guide tunnel projects under construction based on the experience and results of previous project site analysis. For example, urban underground projects such as subways and underground pipe networks have many reference cases [36–38]. The second method is to use the method of simulation test in the laboratory to study the damage, failure process, and related laws of the rock under different load conditions through various rock mechanics testing machines or design experiments. This is also the current research result. It is one of the most common methods, but the disadvantage of this method is that it loses the constraints of the natural environment, and its results have certain limitations. The third method is through a variety of computer simulation software. This method is a new method that has emerged with the development of computer technology in recent years. It has the advantages of a good economy, wide application range, and visualization of the analysis process. The above research methods are mainly devoted to solving two problems in underground geotechnical engineering. The first is the impact of blasting impact and nearby engineering excavation on existing engineering such as underground tunnels and caverns. The main factors affecting the deformation and failure of tunnel surrounding rock and their occurrence mechanism are determined through the aforementioned research methods. The second is to carry out corresponding support and stability studies for the failure

mechanism of surrounding rocks to solve the safety problems encountered in the project. In laboratory tests aimed at this direction, scholars mainly simulate the failure mechanism of rocks in different environments by changing the conditions of rock loading, such as applying external loads such as axial pressure and confining pressure to the rock mass to be tested or changing the temperature and water content. This article is also carried out based on this research idea. In actual engineering, the impact of blasting generated in different directions will cause the rock mass to be superimposed on impact loads of different angles, which will cause shear strain in the rock and make the failure process of the rock more complicated. Under the rotation-impact cyclic load, no relevant research results are available as to what kind of failure law the rock will show and how the stress-strain relationship, damage variable, energy absorption, impact force, and rotation speed are related. Because of the above problems, this paper will use the self-developed impact dynamics simulation test bench to systematically study the rock failure process under the action of cyclic rotating impact.

2. Introduction of Rotation-Impact Experiment Scheme

2.1. Rotation-Impact Simulation Test Bench. As the most widely used test device in geotechnical engineering impact tests, the Hopkinson bar was invented by Bertram Hopkinson in 1914, to measure the transmission effect of stress waves in metal bars. At present, the widely used device in the stress wave impact test is the split Hopkinson pressure bar (SHPB) designed by Kolsky in 1949, which can impose an impact load with a certain strain rate on the specimen. The device is mainly composed of a launch system, test rod system (including incident rod and reflector rod), and data monitoring system. By pasting high-sensitivity strain gauges on the incident rod and the reflecting rod, the stress waves on the incident rod and the transmission rod can be obtained, and the dynamic stress, strain, and strain of the specimen clamped between the two pressure rods can be obtained by indirect methods. Through this method, the difficulty and uncertainty of data capture encountered in indirect measurement can be effectively avoided [39]. The device is simple to operate, ingenious in testing methods, and can be modified for different research needs.

The dynamic simulation test bed used in this article is a rotation-impact simulation device jointly designed and developed by the University of Science and Technology Beijing and the University of Toronto based on the split Hopkinson pressure bar. The test bed is mainly composed of high-precision test platform, test rod system, launch system, rotation system, and data acquisition system. The schematic diagram and physical diagram of the test bed are shown in Figures 1 and 2. The working process of the test bed is as follows: the cylinder in the launch system is set to a certain air pressure value so that the impact rod will rush out of the launch pipe under the action of gas and hit the tail of the drill pipe in the test rod system at a certain speed. At this time, the drill pipe will gain a certain speed, and then, the drill bit at

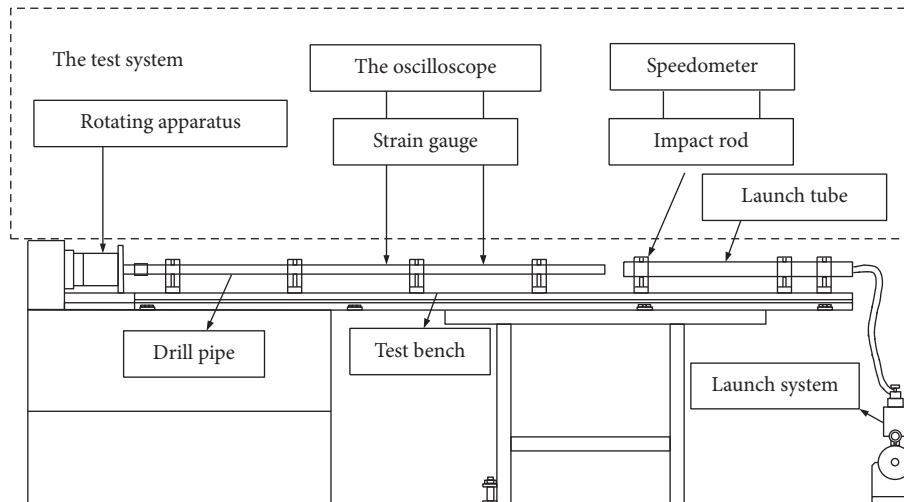


FIGURE 1: Schematic diagram of the rotation-impact simulation system.



FIGURE 2: Physical drawing of the rotation-impact simulation system.

the end of the drill pipe impacts the rotating rock sample under the control of the rotating system, thus completing a complete rotating impact process.

Compared with the split Hopkinson rod, this test bed retains the launch system, the test rod system (only the incident rod, that is, the drill rod), the data monitoring system, and the new rotation system. The modified test bench can keep the rock mass to be tested constantly at the preset rotation speed. When the drill pipe contacts the rock to be tested, a set of shear stress waves will be generated, and the shear stress waves can pass through the contact surface. The drill pipe (measured by the shear strain gauge installed on the drill pipe) and the internal transmission of the rock, the shear stress wave transmitted to the rock part, and the incident wave will cause damage to the rock together. While retaining the advantages of the separated Hopkinson pressure bar, such as convenient operation, the test bench also adds a shear stress wave with a controllable value. By controlling the equipment to superimpose the shear stress wave and the conventional incident stress wave, it is possible to explore the cyclic impact failure law of the rock under the action of shear stress. However, because the

rock to be tested is rotating, the test rig lacks the transmission rod part, and the size of the transmitted wave cannot be directly measured, and a reasonable conversion is required in the energy calculation process. In this paper, the stress homogenization assumption will be used for calculation, that is, the stress generated at the two ends of the rock sample during the impact is equal, and the transmitted wave can be derived from the reflected wave [40–43].

The impact rod and drill pipe of the test bed are made of high-strength steel, with a density of 7850 kg/m^3 , the elastic modulus of 210 GPa, and shear modulus of 90 GPa. The diameter of both rods is 25 mm, the length of the impact rod is 200 mm, and the length of the drill pipe is 1800 mm. PDC bit is selected for this test, with an inner diameter of 25 mm and the outer diameter of 35 mm.

2.2. Test Equipment and Principle. During the test, the data acquisition instruments mainly include CS-1D dynamic resistance strain gauge, DPO2014B mixed signal oscilloscope, MTTU microsecond time detector, and digital electromagnetic tachometer. The actual device diagram is shown in Figure 3. The CS-1D dynamic resistance strain gauge adopts electronic automatic balance technology. It is an ultradynamic high-performance automatic balance strain gauge (frequency range is 0–1 MHz). It is equipped with different types of strain gauges and strain gauge sensors. It can realize the measurement of stress, tensile pressure, speed, acceleration, displacement, torque, and other physical quantities. The DPO2014B digital oscilloscope provides 100 MHz bandwidth and 1 GS/s sampling rate. Waveform capture frequency is 5000 per second. The variable low-pass filter is used to stop unnecessary noise and still display high-frequency events. Using infrared detection technology, the MTTU microsecond time detector can accurately measure the microsecond level of high-speed motion process. The impact speed of the drill pipe can be calculated by calibrating the distance between two infrared laser beams. In the drop weight, SHPB, and

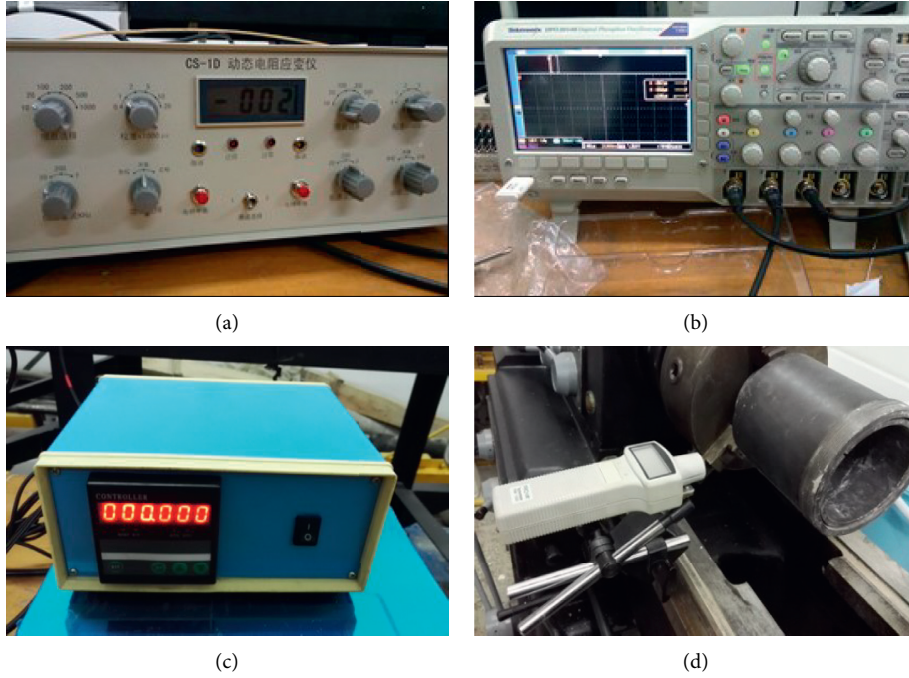


FIGURE 3: Physical drawing of test equipment. (a) Dynamic resistance strain gauge. (b) Oscilloscope. (c) Microsecond chronograph. (d) Electromagnetic tachometer.

other tests, the final speed can be used as a controllable parameter in the impact test after the final speed is measured. The digital electromagnetic tachometer can measure accurately without contacting the rotating system, and the range of speed measurement is from 2 rpm to 9999 rpm.

2.3. Stress Wave Propagation Process of the Test Platform.

In the deformable solid medium, the disturbance to the mechanical equilibrium state is manifested in the change in the particle velocity and the corresponding change of the stress and strain state. The disturbance caused by stress and strain propagates in solid at a certain speed in the form of a wave, which is called a stress wave. Before the start of the test, a reserved width d should be set between the drill pipe and the rock sample to be tested. When the impact rod collides with the drill pipe, the incident stress wave will be generated inside the drill pipe, and then, the incident wave will reflect on the contact surface of the drill pipe and the rock sample to form a tensile wave. When the incident wave is completely reflected, the reserved width is closed. Therefore, the reserved width is the displacement of the impact end of the impact rod when the impact rod impacts the knot. The velocity of the stress wave generated in the impact of the equal diameter rod is related to the inherent characteristics of the rod material (elastic modulus and density) but not to the length of the drill pipe. Therefore, when the impact rod of length L_0 collides symmetrically with the drill pipe at the impact velocity V_0 , the particle velocity in the drill pipe after the wave is $v = V_0/2$, and the incident wave width is $\tau = 2L_0/c_0$. Therefore, the calculation formula for the reserved width d and wave speed c_0 is

$$\begin{aligned}
 d &= vt, \\
 &= \frac{L_0 V_0}{c_0}, \\
 c_0 &= \sqrt{\frac{E_0}{\rho_0}},
 \end{aligned} \tag{1}$$

where c_0 is the stress wave velocity, E_0 is the elastic modulus of the drill pipe, and ρ_0 is the drill pipe density.

The first reflected wave ε_{r1} is reflected at the loading end to form a secondary impact loading ε_{i2} . When the secondary loading stress wave reaches the drill bit, the drill bit and the sample only touch. At this time, because the rock sample is rotating at high speed, the compression wave generated by the impact is reflected to form compression wave ε_{r2} and shear wave γ . The system wave diagram is shown in Figure 4.

2.4. Calculation and Analysis of Related Parameters in Impact Process.

The stress wave of the rotation-impact system is monitored by a strain gauge attached to the drill pipe. When the stress wave passes through the drill pipe, the strain caused will cause a voltage change. The strain value can be calculated through the principle of the Wheatstone bridge, and then, the material stress-strain relationship can calculate the stress value at different moments.

According to the Wheatstone bridge principle and oscilloscope parameter setting, the calculation formulas of axial strain $\varepsilon(t)$, shear strain $\gamma(t)$, and display voltage are as follows:

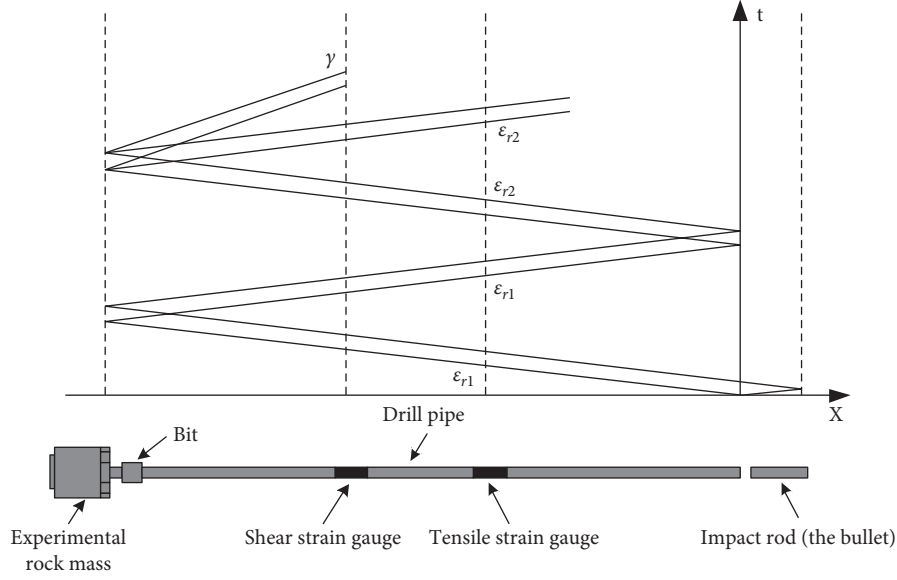


FIGURE 4: Experimental device and wave system.

$$\begin{aligned}\varepsilon(t) &= \frac{1}{2} \frac{2}{U_0} \frac{2.0}{k_1} \frac{U_{x1}}{K_2}, \\ &= \frac{2U_{x1}}{U_0 K_1 K_2},\end{aligned}\quad (2)$$

$$\begin{aligned}\gamma(t) &= \frac{1}{2} \frac{2}{U_0} \frac{2.0}{k_1} \frac{U_{x2}}{K_2}, \\ &= \frac{2U_{x2}}{U_0 K_1 K_2},\end{aligned}\quad (3)$$

where U_0 is the bridge voltage (take 4 V), U_x is the voltage displayed by the oscilloscope (U_{x1} and U_{x2} are the voltage changes caused by tension and compression strain and shear strain, respectively), K_1 is the strain gauge sensitivity coefficient (take 2.00), and K_2 is the gain value on the strain gauge, that is, the magnification factor (take 500).

Based on the strain value obtained by the above formula, combined with the stress-strain relationship, the axial stress $\sigma(t)$ and shear stress in the drill pipe can be obtained, namely,

$$\begin{aligned}\sigma(t) &= E_0 \varepsilon(t), \\ &= \frac{2E_0 U_x}{U_0 K_1 K_2},\end{aligned}\quad (4)$$

$$\begin{aligned}\tau(t) &= G_0 \varepsilon(t), \\ &= \frac{2G_0 U_x}{U_0 K_1 K_2},\end{aligned}\quad (5)$$

where G_0 is the shear modulus of the drill pipe.

According to the stress wave propagation law and the one-dimensional stress theory, the calculation formulas for the internal axial stress $\sigma_a(t)$, axial strain $\varepsilon_a(t)$, and strain rate $\dot{\varepsilon}$ of the rock specimen during the impact process are as follows [40]:

$$\sigma_a(t) = \frac{E_0 A_0}{2A_s} [\varepsilon_i(t) + \varepsilon_r(t) + \varepsilon_t(t)], \quad (6)$$

$$\varepsilon_a(t) = \frac{c_0}{l_s} \int_0^t [\varepsilon_i(t) - \varepsilon_r(t) - \varepsilon_t(t)] dt, \quad (7)$$

$$\dot{\varepsilon} = \frac{c_0}{l_s} [\dot{\varepsilon}_i(t) - \dot{\varepsilon}_r(t) - \dot{\varepsilon}_t(t)]. \quad (8)$$

According to the assumption of stress homogenization [41, 42], assuming that the strains at both ends of the sample are equal, that is, $\sigma_i(t) + \sigma_r(t) = \sigma_t(t)$, then equations (5)–(7) can be transformed into

$$\sigma_a(t) = \frac{E_0 A_0}{A_s} [\sigma_i(t) + \sigma_r(t)], \quad (9)$$

$$\varepsilon_a(t) = \frac{c_0}{l_s} \int_0^t \varepsilon_r(t) dt,$$

$$\dot{\varepsilon} = \frac{c_0}{l_s} \dot{\varepsilon}_r(t), \quad (10)$$

where A_0 is the cross-sectional area of the drill pipe, A_s is the cross-sectional area of the rock sample, $\varepsilon_i(t)$ is the incident wave strain, $\varepsilon_r(t)$ is the reflected wave strain, and $\varepsilon_t(t)$ is the transmitted wave strain.

The formula for calculating incident wave energy E_i and reflected wave energy E_r in the drill pipe is [42, 43]

$$\begin{cases} E_i = \frac{Ac_0}{E_0} \int_0^{t_p} \sigma_i^2 dt, \\ E_r = \frac{Ac_0}{E_0} \int_0^{t_p} \sigma_r^2 dt, \end{cases} \quad (11)$$

where t_p is the duration of the stress wave, which is determined by the experiment.

3. Test Process and Analysis

3.1. Rock Sample Preparation. In this test, the rock sample was taken from the site of an underground highway tunnel in Chongqing. The buried depth of the tunnel is about 15 m, the tunnel face is 25 m wide, and the height is 10 m. The project requires drilling and blasting activities in and around the tunnel. Therefore, the surrounding rock of the tunnel will be subjected to impact loads in different directions. The tunnel site and blasting layout site are shown in Figure 5.

The rock samples in this test are taken from the excavation site of the underground tunnel. The rock samples were cut and then transported to the laboratory. Preliminary analysis shows that the rock samples are typical granite with fine grain size, solid texture, and massive structure. A coring machine takes out the core with good integrity and homogeneity, and then, the core is cut by a rock cutter. According to the size of the rotating rock bin in the test platform and the test recommendations of the International Society for Rock Mechanics, the rocks were processed into cylindrical samples with a diameter of 50 mm and a height of 100 mm, and the samples were ground to make the surface unevenness less than 0.02 mm. The physical map of the sample is shown in Figure 6. The density, uniaxial compressive strength, elastic modulus, longitudinal wave velocity, and Poisson's ratio of the granite samples are obtained by physical and mechanical tests in the laboratory. The statistical results are shown in Table 1.

3.2. Relationship between Air Pressure, Impact Velocity, and Stress. In the impact simulation test, the kinetic energy required for the drill rod to impact the rock sample is obtained after the impact rod impacts, and the impact rod end velocity is determined by the air pressure value of the cylinder of the launch system. Therefore, before the start of the test, it is necessary to calibrate the quantitative relationship between the end velocity of the impact rod and the air pressure value of the cylinder. The specific operation method is to adjust the air pressure value of the cylinder so that the impact rod can obtain an initial speed to rush out of the pipe at a certain launch pressure. At the same time, a microsecond timer (see Figure 3(c)) is used to measure the time for the impact rod to pass a fixed distance. In this way, only a simple conversion relationship is needed to obtain the initial velocity of the striker. In the first test, the air pressure value of the cylinder is set to 2 psi, increasing by 1 psi each time until the air pressure value is 20 psi. Perform 3 tests under each pressure value, and take the average of the 3 test results and record. By testing the end velocity of the impact rod under different air pressures, draw a scatter diagram of the cylinder air pressure P (psi) and the impact end velocity V_0 (m/s) of the impact rod, as shown in Figure 7. The fitting formula is

$$\begin{aligned} V_0 &= 0.39062P + 5.98364, \\ R^2 &= 0.99. \end{aligned} \quad (12)$$

It can be seen from the figure that the air pressure impact end velocity of the cylinder is very correlated, and the impact end velocity can be calibrated by adjusting the air pressure. In the following text, different impact end velocities can be used for analysis. The oscilloscope displays different voltages under different working conditions, as shown in Figure 8. Figure 8(a) is the output image of the oscilloscope when the impact speed is 7.2 m/s and the rotation speed is 225 rpm. Figure 8(b) is the output image of the oscilloscope when the impact speed is 11.2 m/s and the rotation speed is 66 rpm. In the figure, channel 1 is the voltage change caused by the shear strain gauge, channel 2 is the voltage change caused by the tension and compression strain, and channel 3 is the sound level monitoring during the impact. By adjusting the air pressure value, the impact velocity is 7.2, 9.4, 11.2, 13.6, and 16.8 m/s. Then, according to the output voltage value of the oscilloscope, using formulas (2) and (4) to convert, you can obtain the tensile and compressive stress wave waveforms at different impact speeds, as shown in Figure 9.

The waveform of the stress wave depends on the shape and length of the impact rod. In this experiment, the impact rod is an equal-diameter cylinder, so the incident stress wave and the reflected stress wave in the tension and compression stress wave are both approximately rectangular. This is consistent with the previous research on the waveform. It can be seen from Figure 9 that, as the impact velocity increases, the amplitude of the incident wave and the reflected wave gradually increase. According to multiple test results, a fitting is performed between the incident wave amplitude and the reflected wave amplitude and the impact velocity, and the result is shown in Figure 10. The analysis indicates that the incident stress wave has a strong correlation with the impact velocity, while the reflected stress wave is related to the rock wave impedance, the degree of closure of internal fissures, and the energy absorption of the rock, so the degree of correlation with the impact velocity is slightly lower than that of the incident wave. The impact speed can be used as a reference for the amplitude of tension and compression stress waves.

The shear force on the drill pipe is obtained at the moment of impact contact between the drill pipe and the high-speed rotating rock sample. The rotation speed of the rock sample is fixed at 66 rpm by adjusting the rotating system, and the impact test is carried out at 5 different impact speeds. According to the output voltage of the oscilloscope and combining (3) and (5), the calculated scatter plot is shown in Figure 11. It can be seen from the figure that when the rotation speed is constant, the amplitude of the shear stress in the drill pipe increases with the increase of the impact speed, which is positively correlated, but the increase rate gradually slows down. The shape of the shear stress wave is slightly different from the tensile-compression stress wave. This is because the reason and method of the formation of the shear stress wave are different from the tensile-compression stress wave. Because the drill pipe and the rock

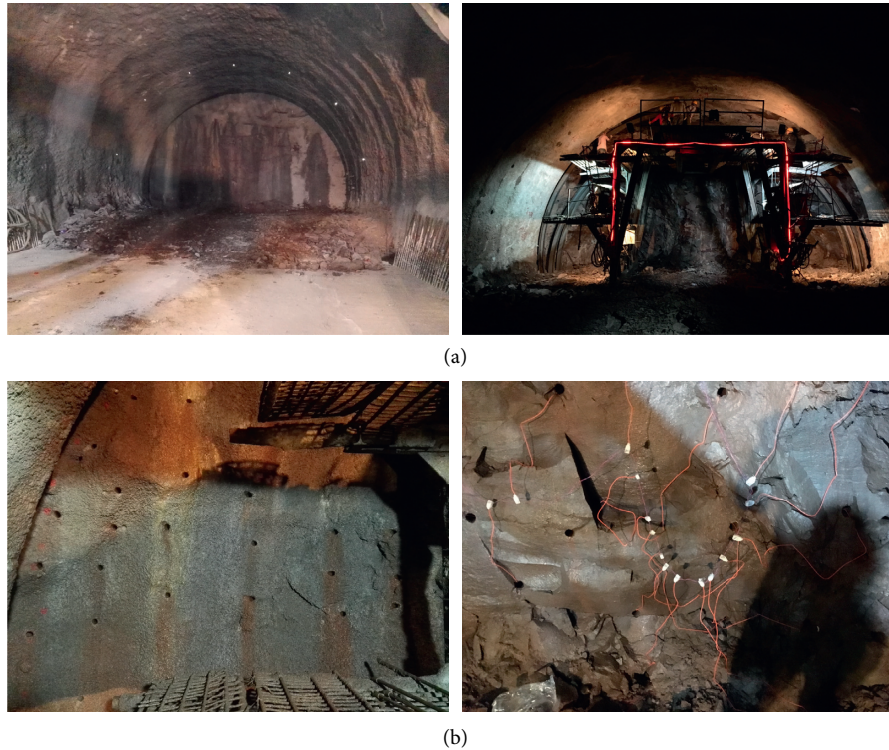


FIGURE 5: Tunnel excavation. (a) Tunnel face. (b) Blasting layout site.



FIGURE 6: Part of the rock sample.

sample have a shorter contact time, the shear stress wave duration (wavelength) is less than the tension and compression stress wave.

To further determine the relationship and law of the shear stress, impact velocity, and rotation velocity, the effect of impact velocity on shear stress amplitude under various speeds was examined. The test results are shown in Figure 12. As shown in the figure, the shear stress increases with the increase in the impact speed at the same rotation speed. At the same impact speed, the shear stress also increases with the increase in the rotational speed, and the increasing trend of the shear stress is more obvious with the increase in the impact speed. When the impact speed is low, taking 7.2 and 9.4 m/s as examples, the shear stress will increase with the increase in the rotational speed before the rotational speed reaches 120 rpm. However, when the speed exceeds 120 rpm,

the shear stress almost does not increase with the increase in the rotational speed. When the impact speed is 11.2 and 13.6 m/s, the shear stress exhibits an obvious linear growth trend before the rotation speed reaches 120 rpm. When the rotation speed continues to increase, the increase in the shear stress is significantly reduced and almost stops when the speed reaches 225 rpm. When the impact velocity is 16.8 m/s, with the increase in the rotation speed, the shear stress always has a significant increasing trend, and the increase rate is only slightly reduced in the final stage. The above analysis shows that, under a fixed impact velocity, the shear stress has a corresponding upper limit of the rotation speed. When the rotation speed is lower than this upper limit, the shear stress will increase with the increase in the rotation speed and present an approximately linear relationship in the initial stage. Then, the growth rate will gradually decrease. When the rotation speed continues to increase until it is higher than this upper limit, the shear stress will no longer increase with the increase in the rotation speed.

3.3. Impact Times Required for Specimen Failure under Cyclic Loading. The previous test results indicate that the impact velocity has a strong correlation with tensile and compressive stresses and shear stresses. When the rock is subjected to pressure that exceeds its resistance strength or the damage reaches a certain value under the action of cyclic loading, failure will occur. In this part, the cyclic impact failure law of the specimen under different impact speeds and rotation speeds is studied. The rotating speed is set at 0,

TABLE 1: Physical and mechanical parameters of the rock sample.

Rock types	Density (kg/m ³)	Compressive strength (MPa)	Elastic modulus (GPa)	P-wave velocity (m/s)	Poisson's ratio
Granite	2560	208	18.39	4400	0.09

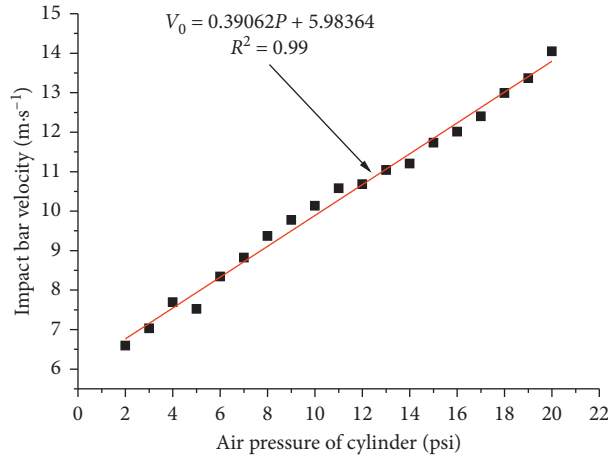


FIGURE 7: Relationship between cylinder air pressure and impact end velocity.

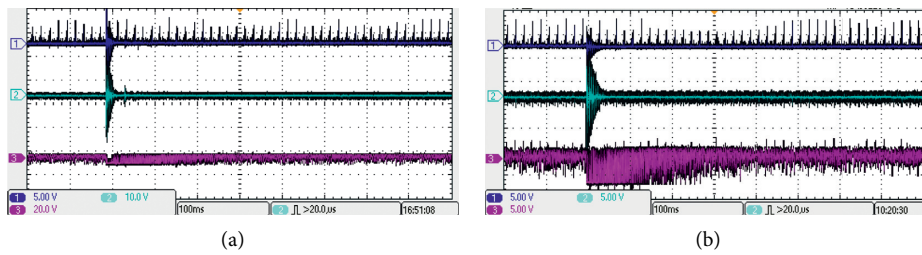


FIGURE 8: Schematic diagram of the oscilloscope interface under different working conditions. (a) Impact speed 7.2 m/s; rotation speed 225 rpm. (b) Impact speed 11.2 m/s; rotation speed 66 rpm.

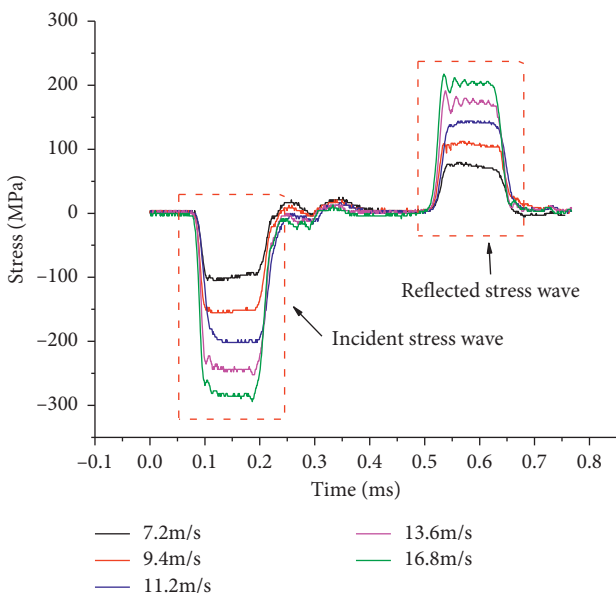


FIGURE 9: Tension and compression stress wave waveform.

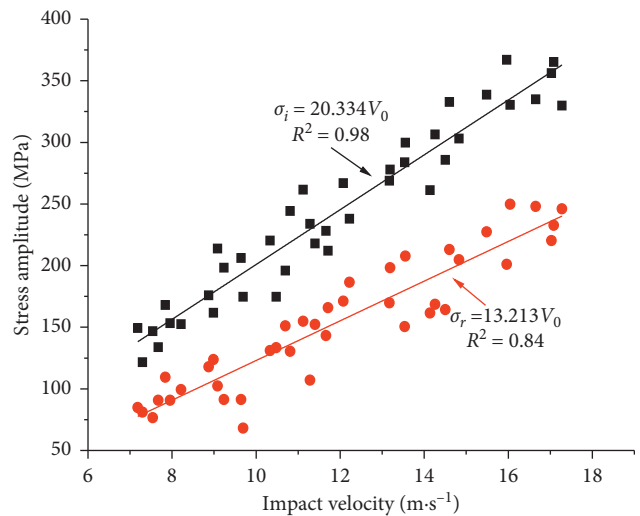


FIGURE 10: Relationship between tensile and compression stress wave amplitude and impact velocity.

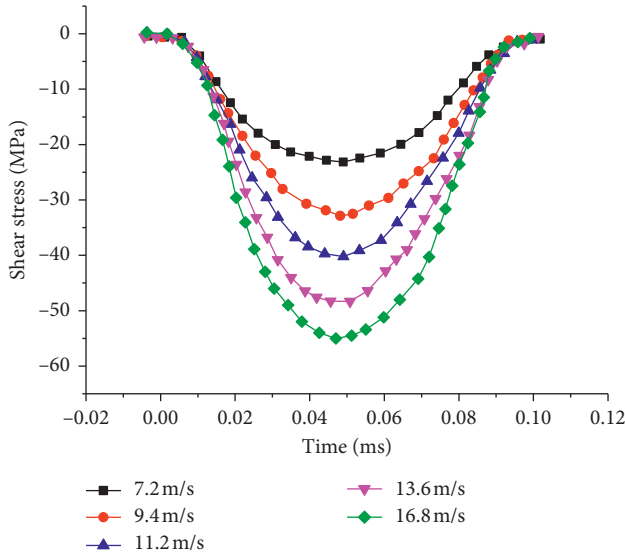


FIGURE 11: Shear stress waveform.

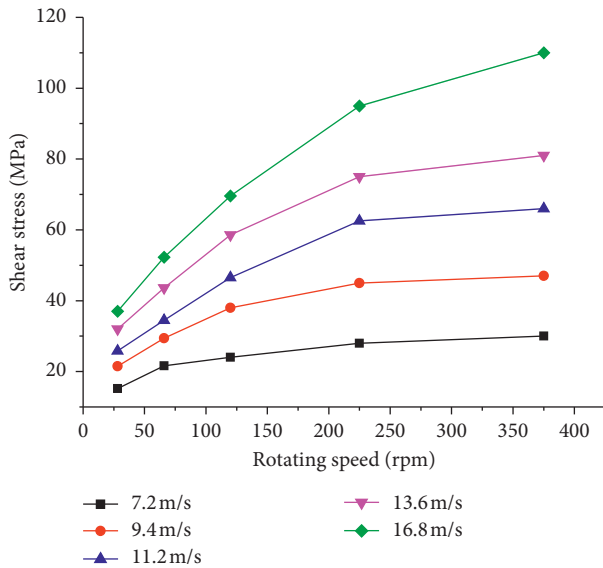


FIGURE 12: Shear stress under different conditions.

28, 66, 120, 225, and 375 rpm, and the samples are subjected to cyclic impact with five different impact speeds until macroscopic failure occurs. Table 2 lists the number of impacts when the specimen is damaged at different speeds and draws a scatter chart, as shown in Figure 13. The figure shows that, at the same impact speed, a great rotation speed corresponds to fewer impacts required for failure, indicating that the rock is more prone to fatigue failure under the combined action of impact load and shear.

3.4. Stress-Strain Curve of the Sample under Cyclic Load.

The stress-strain curve is an important basis for judging rock failure under cyclic loading. Figure 12(a) shows the stress-strain curve of a typical rock when macroscopic failure has not occurred. The total sample is in an elastic and

TABLE 2: Impact times under different rotation speeds and impact speeds.

Rotation speed (rpm)	Impact speed (m/s)				
	7.2	9.4	11.2	13.6	16.8
0	45	37	22	12	6
28	43	36	19	11	6
66	39	33	17	10	5
120	35	26	14	6	4
255	30	24	12	5	2
375	27	23	11	4	2

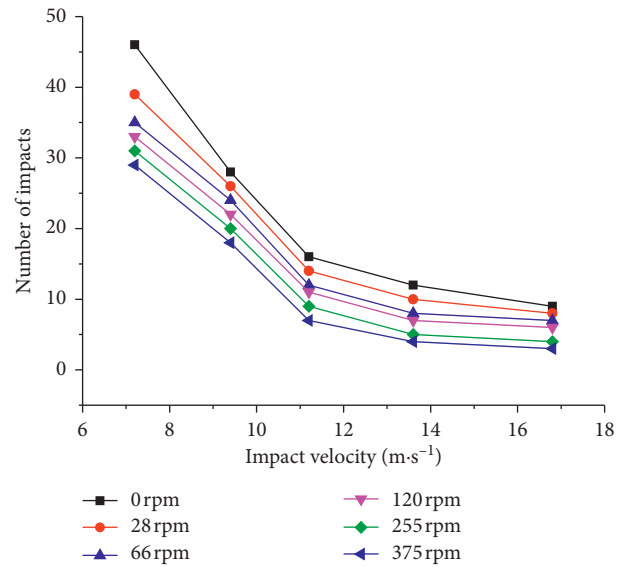


FIGURE 13: Relationship between impact times and impact speed at different speeds.

elastoplastic state during the entire process. The stress-strain curve can be roughly divided into four stages according to the development process: compaction phase (AB), elastic phase (BC), crack development phase (CD), and unloading phase (DE). The compaction phase is the process of closing the internal fissures of the rock. The elastic stage is the elastic deformation (recoverable) of the rock sample after compaction. In these two processes, the rock is not damaged, either macroscopically or microscopically. The crack development stage is the stable development stage of the internal cracks in the rock. At this time, the rock does not undergo macroscopic damage, and only part of the damage is accumulated in the microscopic view. The unloading stage is a process in which the strain of the rock gradually decreases as the stress decreases. When the specimen undergoes macroscopic failure, the curve in the unloading phase in the stress-strain curve changes most significantly. Even if the stress no longer increases, the stress still increases, and the rock is in a state of plastic yield.

The following is an analysis of the stress-strain curve of the sample under the same impact speed and different rotation speeds. Under the condition of the impact velocity of 13.6 m/s, the stress-strain curve of the specimen at different rotation speeds is drawn, as shown in Figure 14. The figure

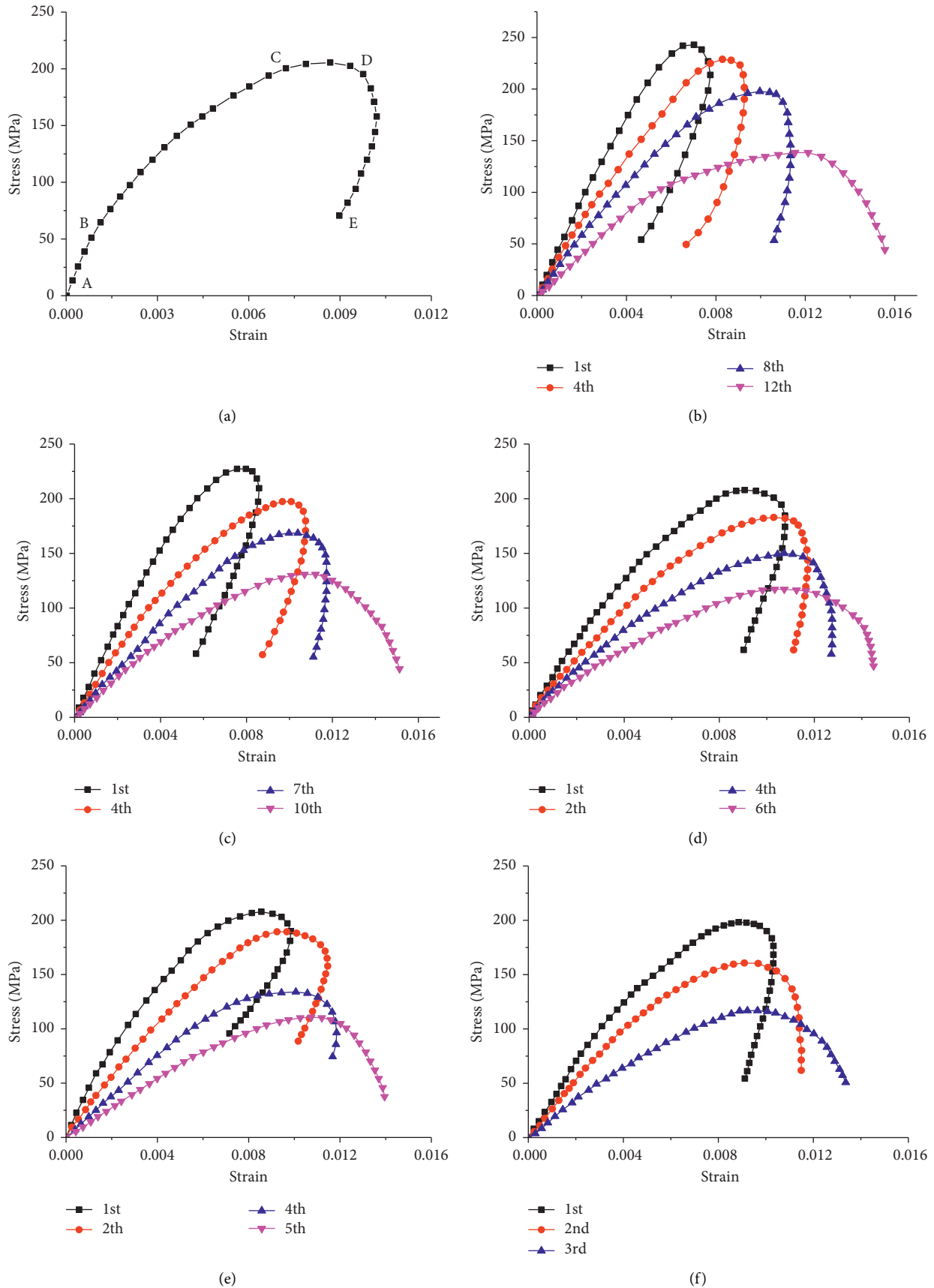


FIGURE 14: Stress-strain curve with the impact velocity of 13.6 m/s. (a) Typical stress-strain curve. (b) Rotation speed is 0 rpm. (c) Rotation speed is 66 rpm. (d) Rotation speed is 120 rpm. (e) Rotation speed is 255 rpm. (f) Rotation speed is 375 rpm.

shows that when the impact velocity is the same, the shape and development process of the stress-strain curve of the specimen at different rotational speeds are consistent with that of the static sample, indicating that the existence of shear stress does not affect the overall change trend of the axial compression stress-strain curve of the specimen. Figure 12 shows that, under the premise of keeping the impact velocity constant, the number of failures of the rock sample gradually decreases as the rotation speed increases. At the same time, under the same number of impacts, the slope of the elastic phase (BC phase) of the stress-strain curve gradually decreases with the increase in speed, which means that when the rock reaches the same strain, the required stress value is smaller. A comparison of the stress-strain curve under the first impact at different rotation speeds shows that the corresponding stress at the peak of the curve gradually decreases with the increase in the rotation speed, which indicates that the increase in the rotation speed will reduce the rock sample to the deformation failure stage (CD stage) stress value, that is, the failure stage of the internal crack propagation of the rock sample under lower stress.

3.5. Energy Dissipation Law under Different Conditions. It can be seen from the previous analysis that increasing shear stress under cyclic impact load can accelerate rock failure. The disturbance caused by stress and strain propagates in the solid at a certain speed in the form of a wave, which is called a stress wave. The energy absorption of rock failure is mainly used for the kinetic energy required for the closure, development, penetration, and failure of internal fissures. The more the energy absorption, the faster the development of rock failure, so the energy dissipation rate can be used as the basis for the degree of rock damage.

The stress wave energy can be calculated by (11). It can be seen from the formula that the stress wave energy is related to the drill pipe cross-sectional area, elastic modulus (shear modulus), wave velocity, stress value, and time. Among them, the cross-sectional area, elastic modulus, and wave velocity of the drill pipe are only related to the material of the drill pipe. The stress wave stress value and time can be obtained from the waveform diagram. According to the waveform data obtained by the oscilloscope, the stress wave energy can be calculated by combining (11).

To discuss the energy dissipation of stress waves and the law of rock absorption under cyclic loading, the fracture specific energy δ is defined as the cumulative energy absorbed per unit volume of the rock specimen in the process of cyclic impact failure. The calculation formula is as follows:

$$\begin{aligned} \delta &= \sum_{k=1}^n E_{V_k}, \\ &= \sum_{k=1}^n \left(\frac{E_{ik} - E_{rk}}{V_s} \right), \end{aligned} \quad (13)$$

where δ is the specific energy of crushing, E_{V_k} is the absorbed energy per unit volume generated by the k th impact of the sample, V_s is the volume of the rock sample, n is the number of the cyclic effects, E_{ik} is the incident wave energy of the k th impact, and E_{rk} is the energy of the k th impact reflected wave.

From the test results and equations (11) and (13), the required δ in the rock breaking process can be obtained. The calculation result is shown in Figure 15.

The figure shows that when no rotating load is applied to the rock sample, the impact velocity with the smallest crushing specific energy is 11.2 m/s, which can also be considered as the optimal damage impact velocity for this kind of rock. With the increase in speed, the crushing ratio required for the destruction of the sample gradually decreases, but the decrease is related to the speed. When the rotation speed is in the range of 0–120 rpm, the specific energy curves of unit volume under different impact speeds show a trend of first decreasing and then increasing. The optimal failure impact speed is 9.4 m/s when the rotation speed is 66 rpm, and the optimal failure impact speed of other rotation speeds (0, 32, and 120 rpm) is 11.2 m/s. For a certain kind of rock, the crushing specific energy is different at different impact speeds. For the tested rock in this experiment, when there is no shear stress (that is, when the rotation speed is 0 rpm), the optimal damage impact velocity is 11.2 m/s. It can be seen from the figure that when the rotation speed is increased to 28 rpm, although 11.2 m/s is still the optimal damage impact velocity, compared with other impact velocities, the gap in crushing specific energy is significantly reduced. When the rotation speed is 66 rpm, the optimal impact speed becomes 9.4 m/s. The reason is analyzed because the shear stress generated by 0 rpm and 28 rpm is small, and the impact on the impact damage is also small. When the speed increased to 66 rpm, the influence of shear stress began to increase, and the optimal impact speed was effectively reduced. It can be considered that, for the type of rock used in this experiment, the shear stress when the rotation speed reaches 66 rpm is an effective intervention point.

With the continuous increase in the rotation speed, the optimal impact velocity also gradually increases. When the speed reaches 375 rpm, the crushing specific energy of 16.8 m/s impact speed is significantly lower than that of other impact speeds, and its value is only 30% of the crushing specific energy when the impact speed is 7.2 m/s. From the above analysis, it is not difficult to find that when there is no shear stress (rotation speed is 0 rpm), the rock sample used in this test has the lowest impact speed of 11.2 m/s. When the rotation speed gradually increased to 66 rpm, the shear stress effectively reduced the optimal impact velocity, making the optimal impact velocity 9.4 m/s. As the shear stress continues to increase, the optimal damage impact velocity also increases. In summary, as the shear stress increases, the optimal damage impact velocity has experienced the first drop, and in the process of rising, there is an inflection point. The impact velocity of 7.2 m/s does not become the optimal impact velocity at different rotation speeds because a large

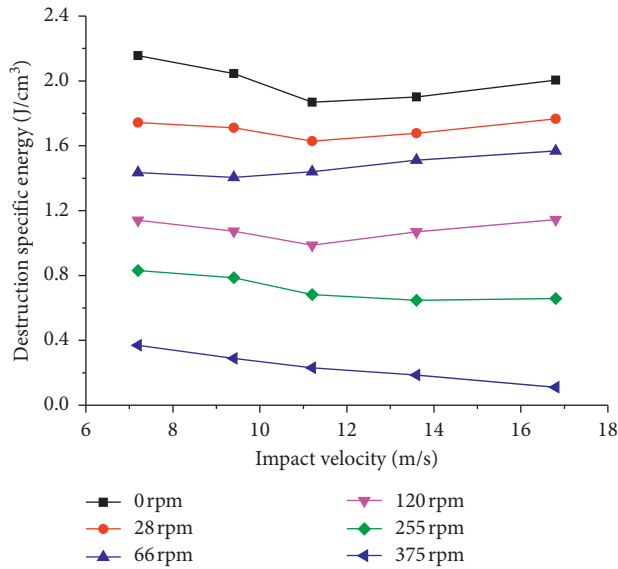


FIGURE 15: Specific crushing energy under different working conditions.

part of the stress wave energy is used in the compression and elastic stages of rock deformation at low speed. In contrast, the energy used for macrofailure processes, such as crack development of rock failure, is relatively small. The above analysis process indicates that the reasonable selection of impact speed and rotation speed will have a great influence on the rock-breaking efficiency for a specific rock type.

4. Discussion

Explosive stress wave reflection tensile theory states that when the rock is broken, the tensile stress inside the rock is greater than its tensile strength due to the effect of the tensile wave after the stress wave is reflected on the free surface. Under the action of cyclic loading, the internal cracks of the rock continue to develop, which also reduces the tensile strength of the rock, causing the rock to be destroyed even under the action of a lower stress wave. The surrounding rock of the tunnel is in a complex geological environment. Under the action of in situ stress, the surrounding rock of the tunnel is subjected not only to multidirectional static loads and blasting impact loads but also to shear loads, such as the superposition of stress waves in different directions, shield construction, and other rotation drilling works. Rock is a material whose shear strength is less than its compressive strength. When subjected to shear, it will inevitably lead to a lower threshold for failure.

When the impact velocity remains the same, the number of impacts required for rock failure decreases with the increase in the rotation speed, indicating that the increase in the rotation speed and the shear force promotes the failure of the rock. Fissures are more likely to be torn; they are easier to penetrate compared with a simple compression process. We can easily see that the increase in rotation speed does not lead to an obvious change of the curve, which indicates that the shear force does not directly participate in the change in the axial

deformation of rock. Independent analysis can be performed in the axial compression and calculation. From the perspective of energy analysis, when the shear stress increases, the crushing ratio energy required for rock failure gradually decreases. The energy needed for rock failure is a fixed value; thus, we can determine that the work performed by the shear stress gradually increases during the failure process, but this part of the energy is not reflected in the axial compression deformation. Therefore, in actual tunnel engineering, the stress-strain analysis under the simple impact of the surrounding rock may lead to inaccurate predictions of damage, resulting in accidents. Therefore, when the surrounding rock of the tunnel is subjected to superimposed effects of blasting impacts in different directions or rotation impact load, construction personnel must pay special attention to the corresponding support and reinforcement measures of the surrounding rock.

5. Conclusions

- (1) In this paper, the dynamic impact simulation test bench developed by the authors is used to study the law of rock damage under rotating cyclic impact load. The research results show that compared with the traditional cyclic impact test, the appearance of shear force will accelerate the process of rock failure and reduce the number of impacts required for rock failure. A great impact speed corresponds to a great change brought about by the increase in rotation speed. When the impact speed is 7.2 m/s, the number of impacts at the maximum speed is 60% of the static state; when the impact speed is 16.8 m/s, this value is only 33.3%.
- (2) When the rotation speed is constant, the increase in the impact speed will lead to an increase in the shear force, but this increase will gradually decrease. When the impact velocity is constant, the increase in the rotation speed of the rock sample will lead to an increase in the shear stress, but an upper limit exists. When this upper limit is exceeded, the shear stress no longer increases with the increase in the rotation speed. This situation can provide an idea for the failure process of rock drilling, reduce energy loss, and improve drilling efficiency.
- (3) Under different shear stress, the stress-strain curve of rock under impact has no obvious change, but the slope of the elastic stage in the curve decreases, that is, the stress value required for strain in rock decreases. This finding shows that the crack development and penetration speed are faster under shear stress, which is also the main reason the rock is more easily damaged under shear stress. In tunnel engineering, judging safety based on only the axial deformation of the surrounding rock mass or the stress-strain curve is risky. When the surrounding rock is subjected to impact loads from different directions or rotating impact damage, special attention should be paid to the safety situation, and

timely support and reinforcement measures should be taken.

- (4) An analysis of the specific energy of rock fragmentation under different working conditions indicates that the increase in shear stress will cause particular fragmentation energy to decrease. The rotating sample provides the shear stress wave in this test. Therefore, for the time being, only the energy of the tensile and compressive stress wave is calculated and analyzed. Future research will focus on the energy dissipation of the shear stress wave.
- (5) The drill bit used in this article is a three-wing PDC drill bit. There are many different types and sizes of drill bits in actual engineering. The influence of different drill bits on the mechanism of failure is a direction that needs to be studied in the future. At the same time, the shear stresses in this paper are all instantaneous stresses, and whether the failure mechanism of rock is different when the shear stress is constant is also the content that needs to be studied in the follow-up work.

Data Availability

The data included in this study are available from the corresponding author upon request.

Conflicts of Interest

The authors declare that they have no conflicts of interest.

Acknowledgments

The authors would like to thank the National Natural Science Foundation of China (no. 51574015), National Key R&D Program of China (2018YFC0808701), and China Postdoctoral Science Foundation (2020M673525) for their sponsorship.

References

- [1] Q. Sun, D. Dias, L. R. E. Sousa, and W. Liu, "Soft soil layer-tunnel interaction under seismic loading," *Tunnelling and Underground Space Technology*, vol. 98, Article ID 103329, 2020.
- [2] W. Yu, W. Wang, X. Chen, and S. Du, "Field investigations of high stress soft surrounding rocks and deformation control," *Journal of Rock Mechanics and Geotechnical Engineering*, vol. 7, no. 4, pp. 421–433, 2015.
- [3] S. Wang, C. Li, Z. Liu, and J. Fang, "Optimization of construction scheme and supporting technology for HJS soft rock tunnel," *International Journal of Mining Science and Technology*, vol. 24, no. 6, pp. 847–852, 2014.
- [4] P. X. Li, X. T. Feng, G. L. Feng, Y. X. Xiao, and B. R. Chen, "Rockburst and microseismic characteristics around lithological interfaces under different excavation directions in deep tunnels," *Engineering Geology*, vol. 260, pp. 105–209, 2019.
- [5] M. Ramulu, A. K. Chakraborty, and T. G. Sitharam, "Damage assessment of basaltic rock mass due to repeated blasting in a railway tunnelling project—a case study," *Tunnelling and Underground Space Technology*, vol. 24, no. 2, pp. 208–221, 2009.
- [6] K. Dey and V. M. S. R. Murthy, "Prediction of blast-induced overbreak from uncontrolled burn-cut blasting in tunnels driven through medium rock class," *Tunnelling and Underground Space Technology incorporating Trenchless Technology Research*, vol. 28, pp. 49–56, 2012.
- [7] J. H. Shin, H. G. Moon, and S. E. Chae, "Effect of blast-induced vibration on existing tunnels in soft rocks," *Tunnelling and Underground Space Technology Incorporating Trenchless Technology Research*, vol. 26, no. 1, pp. 51–61, 2011.
- [8] A. Ansell, "In situ testing of young shotcrete subjected to vibrations from blasting," *Tunnelling and Underground Space Technology Incorporating Trenchless Technology Research*, vol. 19, no. 6, pp. 587–596, 2004.
- [9] J. Zhao and J. G. Cai, "Transmission of elastic P-waves across single fractures with a nonlinear normal deformational behavior," *Rock Mechanics and Rock Engineering*, vol. 41, no. 1, pp. 3–22, 2001.
- [10] C. O. Aksoy, K. Ogul, I. Topal, S. C. Ozer, V. Ozacar, and E. Posluk, "Numerical modeling of non-deformable support in swelling and squeezing rock," *International Journal of Rock Mechanics and Mining Sciences*, vol. 52, pp. 61–70, 2012.
- [11] M. Ramoni and G. Anagnostou, "The interaction between shield, ground and tunnel support in TBM tunnelling through squeezing ground," *Rock Mechanics and Rock Engineering*, vol. 44, no. 1, pp. 37–61, 2011.
- [12] D. P. Do, N. T. Tran, V. T. Mai, D. Hoxha, and M. N. Vu, "Time-dependent reliability analysis of deep tunnel in the viscoelastic burger rock with sequential installation of liners," *Rock Mechanics and Rock Engineering*, vol. 53, no. 3, pp. 1–27, 2020.
- [13] G. Barla, M. Bonini, and M. Semeraro, "Analysis of the behaviour of a yield-control support system in squeezing rock," *Tunnelling and Underground Space Technology*, vol. 26, no. 1, pp. 146–154, 2011.
- [14] E. T. Ağbay and T. Topal, "Evaluation of twin tunnel-induced surface ground deformation by empirical and numerical analyses (NATM part of Eurasia tunnel, turkey)," *Computers and Geotechnics*, vol. 119, Article ID 103367, 2020.
- [15] P. K. Singh, "Blast vibration damage to underground coal mines from adjacent open-pit blasting," *International Journal of Rock Mechanics and Mining Sciences*, vol. 39, no. 8, pp. 959–973, 2002.
- [16] J. S. Sharma, A. M. Hefny, J. Zhao, and C. W. Chan, "Effect of large excavation on deformation of adjacent MRT tunnels," *Tunnelling and Underground Space Technology Incorporating Trenchless Technology Research*, vol. 16, no. 2, pp. 93–98, 2001.
- [17] N. Li, W. Chen, P. Zhang, and G. Swoboda, "The mechanical properties and a fatigue-damage model for jointed rock masses subjected to dynamic cyclical loading," *International Journal of Rock Mechanics and Mining Sciences*, vol. 38, no. 7, pp. 1071–1079, 2001.
- [18] M. N. Bagde and V. Petro, "Fatigue and dynamic energy behaviour of rock subjected to cyclical loading," *International Journal of Rock Mechanics & Mining Sciences*, vol. 46, no. 1, pp. 200–209, 2009.
- [19] E. Liu and S. He, "Effects of cyclic dynamic loading on the mechanical properties of intact rock samples under confining pressure conditions," *Engineering Geology*, vol. 125, no. 27, pp. 82–91, 2012.
- [20] J. C. Li and G. W. Ma, "Experimental study of stress wave propagation across a filled rock joint," *International Journal of*

- Rock Mechanics and Mining Sciences*, vol. 46, no. 3, pp. 375–380, 2009.
- [21] Y. L. Lu, D. Elsworth, and L. G. Wang, “Microcrack-based coupled damage and flow modeling of fracturing evolution in permeable brittle rocks,” *Computers and Geotechnics*, vol. 49, no. 4, pp. 226–244, 2013.
- [22] J. Y. Fang, F. N. Dang, Y. T. Xiao, W. H. Ding, and J. X. Fang, “Quantitative study on the CT test process of siltstone under triaxial compression,” *Chinese Journal of Rock Mechanics and Engineering*, vol. 34, no. 10, pp. 1976–1984, 2015.
- [23] J. H. Chen, J. S. Zhang, and X. P. Li, “Model of rock blasting-induced damage considering integrity of rock mass and its application,” *Chinese Journal of Geotechnical Engineering*, vol. 38, no. 5, pp. 857–866, 2016.
- [24] L. Zhang, D. Yang, and Z. Chen, “Deformation and failure characteristics of weathered granite under uniaxial compression,” *AIP Advances*, vol. 9, no. 7, pp. 205–222, 2019.
- [25] Y. H. Wang, Y. F. Liu, and H. T. Ma, “Changing regularity of rock damage variable and resistivity under loading condition,” *Safety Science*, vol. 50, no. 4, pp. 718–722, 2012.
- [26] Z. Y. Li, G. Wu, T. Z. Huang, and Y. Liu, “Variation of energy and criteria for strength failure of shale under triaxial cyclic loading,” *Chinese Journal of Rock Mechanics and Engineering*, vol. 37, no. 3, pp. 662–670, 2018.
- [27] C. H. Dowding, “Estimating earthquake damage from explosion testing of full-scale tunnels,” *Advances in Tunnelling Technology and Subsurface Use*, vol. 4, no. 3, pp. 113–119, 1984.
- [28] C. H. Dowding, “Blast vibration monitoring and control,” *Mining Science and Technology*, vol. 2, no. 4, pp. 308–309, 1985.
- [29] J. Zhao, Y. X. Zhou, A. M. Hefny et al., “Rock dynamics research related to cavern development for ammunition storage,” *Tunnelling and Underground Space Technology*, vol. 14, no. 4, pp. 513–526, 1999.
- [30] S. G. Chen, J. G. Cai, J. Zhao, and Y. X. Zhou, “Discrete element modelling of an underground explosion in a jointed rock mass,” *Geotechnical & Geological Engineering*, vol. 18, no. 2, pp. 59–78, 2000.
- [31] H. Hao, Y. Wu, G. Ma, and Y. Zhou, “Characteristics of surface ground motions induced by blasts in jointed rock mass,” *Soil Dynamics and Earthquake Engineering*, vol. 21, no. 2, pp. 85–98, 2001.
- [32] Y. Zhou and A. Jenssen, “Internal separation distances for underground explosives storage in hard rock,” *Tunnelling and Underground Space Technology Incorporating Trenchless Technology Research*, vol. 24, no. 2, pp. 119–125, 2009.
- [33] X. F. Deng, J. B. Zhu, S. G. Chen, Z. Y. Zhao, Y. X. Zhou, and J. Zhao, “Numerical study on tunnel damage subject to blast-induced shock wave in jointed rock masses,” *Tunnelling and Underground Space Technology*, vol. 43, no. 6, pp. 88–100, 2014.
- [34] Z. Y. Zhao, S. G. Chen, J. B. Zhu, X. F. Deng, Y. X. Zhou, and J. Zhao, “UDEC-AUTODYN hybrid modeling of a large-scale underground explosion test,” *Rock Mechanics and Rock Engineering*, vol. 48, no. 2, pp. 737–747, 2015.
- [35] J. B. Zhu, Y. S. Li, S. Y. Wu, R. Zhang, and L. Ren, “Decoupled explosion in an underground opening and dynamic responses of surrounding rock masses and structures and induced ground motions: a FEM-DEM numerical study,” *Tunnelling and Underground Space Technology incorporating Trenchless Technology Research*, vol. 82, no. 12, pp. 442–454, 2018.
- [36] W. C. Cheng, J. C. Ni, A. Arulrajah, and H. W. Huang, “A simple approach for characterising tunnel bore conditions based upon pipe-jacking data,” *Tunnelling and Underground Space Technology*, vol. 71, no. 1, pp. 494–504, 2018.
- [37] W. C. Cheng, L. Wang, Z. F. Xue, J. C. Ni, M. M. Rahman, and A. Arulrajah, “Lubrication performance of pipejacking in soft alluvial deposits,” *Tunnelling and Underground Space Technology*, vol. 91, Article ID 102991, 2019.
- [38] W. C. Cheng, G. Li, N. Liu, J. Xu, and S. Horpibulsuk, “Recent massive incidents for subway construction in soft alluvial deposits of Taiwan: a review,” *Tunnelling and Underground Space Technology*, vol. 96, Article ID 103178, 2020.
- [39] H. Kolsky, “An investigation of the mechanical properties of materials at very high rates of loading,” *Proceedings of the Physical Society B*, vol. 62, no. 11, p. 676, 1949.
- [40] Q. Ping, X. Luo, Q. Y. Ma, and P. Yuan, “Broken energy dissipation characteristics of sandstone specimens under impact loads,” *Chinese Journal of Rock Mechanics and Engineering*, vol. 34, no. 9, pp. 4197–4203, 2015.
- [41] L. Song and S. S. Hu, “Two-wave and three-wave method in SHPB data processing,” *Explosion and Shock Waves*, vol. 25, no. 4, pp. 368–373, 2005.
- [42] C. J. Xia, H. P. Xie, Y. Ju, and H. W. Zhou, “Experimental study of energy dissipation of porous rock under impact loading,” *Engineering Mechanics*, vol. 23, no. 9, pp. 1–5, 2006.
- [43] H. Kolsky, “Stress waves in solids,” *Journal of Sound and Vibration*, vol. 1, no. 1, pp. 88–110, 1964.

Research Article

Three-Dimensional Reconstruction of Tunnel Face Based on Multiple Images

Wenge Qiu,^{1,2} Liao Jian ,¹ Yunjian Cheng ,³ and Hengbin Bai²

¹Key Laboratory of Transportation Tunnel Engineering, Ministry of Education, School of Civil Engineering, Southwest Jiaotong University, Chengdu 610031, China

²Chengdu Tianyou Tunnelkey Co., Ltd., Chengdu 610031, China

³School of Civil Engineering and Geomatics, Southwest Petroleum University, Chengdu 610031, China

Correspondence should be addressed to Liao Jian; 2017320070@my.swjtu.edu.cn

Received 23 September 2020; Revised 27 March 2021; Accepted 3 April 2021; Published 19 April 2021

Academic Editor: Wen-Chieh Cheng

Copyright © 2021 Wenge Qiu et al. This is an open access article distributed under the Creative Commons Attribution License, which permits unrestricted use, distribution, and reproduction in any medium, provided the original work is properly cited.

The current geological sketch in tunnel engineering is mainly based on sketches of workers. However, geological sketch drawn by workers always offers fundamental data purely due to its drawing mode. A novel drawing method for geological sketch has been introduced using multiview photos in this process. The images of tunnel faces are taken from multiple angles, and every two pictures have overlaps. By measuring the distance between the camera and the tunnel face using a laser range finder, the photographic scale of each photo can be confirmed. SpeededUp Robust Features (SURF) is a good practice for detecting feature points, and the sparse point cloud is reconstructed from multiview photos by structure from motion (SFM). However, the sparse point cloud is not suitable for analysis for structural planes due to its sparsity. Therefore, patch-based multiview stereo (PMVS) is used to reconstruct dense point cloud from the sparse point cloud. After 3D reconstruction, the details of the tunnel face are recorded. The proposed technique was applied to multiview photos acquired in the Xiaosanxia railway tunnel and Fengjie tunnel in Chongqing, China. In order to record the geological conditions of the tunnel face quickly and accurately, Chengdu Tianyou Tunnelkey has developed a set of software and hardware integration system called CameraPad. Besides, CameraPad was used to collect the multiview photos of the tunnel face in the No. 1 Xinan railway tunnel in Jilin, China. By comparing with traditional and existing methods, the proposed method offers a more reductive model for geological conditions of the tunnel face.

1. Introduction

Tunnel engineering is concealed engineering, which is often affected by a variety of adverse geological conditions. As the geological conditions of the area that the tunnel traverses are becoming more and more complex, tunnel engineering has also become extremely challenging. And geological prospecting is becoming more and more critical. However, relying merely on the geological prospecting of the previous period is an utterly inadequate method in dealing with a difficult situation for the complex geological conditions. Therefore, the geological prospecting during the tunnel construction period will be more meaningful for tunnel engineering. The stratum lithology, geological structure, and structural plane occurrence in the tunnel construction period need to be recorded to provide raw data, which are used

for the interpretation and analysis of geotectonic movement and the prediction of long-term stability of rock mass. At the same time, it also provides an essential geological foundation to optimize tunnel excavation and strengthening methods.

Traditionally, the geological sketch of the tunnel face is often used to record the geological conditions during the tunnel construction period. The geological conditions of the tunnel face are often very complicated, and it is difficult to completely record the geological conditions in the traditional geological sketch.

It is difficult to observe the tunnel face directly when the TBM and shield method are used in recent years, so many scholars have proposed many new techniques for collecting the geological conditions of the tunnel face. Yamamoto et al. developed the TBM Excavation Control System to acquire the accurate prediction of the geological conditions ahead of

and surrounding the tunnel face in tunnel excavation by Tunnel Boring Machine (TBM). When using the TBM method, it is difficult to observe the tunnel face during the tunnelling process. Besides, it is difficult to obtain the geological conditions during the construction period, so such a method is proposed [1]. Li et al. used a digital optical borehole camera to directly observe the gaps in the rock mass through predrilled holes [2]. This method has been applied to the prediction of advanced geological conditions, which can make an excellent assessment of the geological conditions in front of the tunnel face.

The equipment for the data collection of 3D reconstruction has also become lighter and more portable. Izadi et al. used a Kinect camera that can be held and moved freely to quickly perform 3D reconstruction of indoor scenes [3]. Track the position and posture of the sensor through the depth data using Kinect camera to reconstruct the 3D scene in time. This method has shown how to utilize low-cost equipment for rapid 3D reconstruction. At the same time, terrestrial laser scanning (TLS) technology is also used for the construction of the three-dimensional model of the tunnel face. Wang et al. proposed a new method for tunnel digital geological mapping and recording using 3D terrestrial laser scanning (TLS) [4]. The point cloud obtained from TLS was used to generate the most suitable structural plane on the tunnel face, and then the direction of the structural plane was calculated. The result has shown the digital geological sketch based on the unfolded image of the tunnel face, including the traces and directions of the fissures, classification of rock types, and water leakage. Cacciari and Futai proposed a method of using a terrestrial laser scanner (TLS) to generate discrete fracture networks (DFNs) of geological mapping [5]. The proposed method has effectively established the fractured rock masses of tunnel faces. Cacciari and Futai attempted to evaluate the current methods of geometrical discontinuity characterization by terrestrial laser scanning (TLS) in tunnel engineering [6]. By comparison, the mean trace lengths obtained from rectangular sampling windows are more suitable for estimating different geological surface orientations. Cheng et al. developed a general technique to automatically identify the different types of components using TLS [7]. Li et al. proposed deformation monitoring using TLS in Underground Station Cavity Clusters [8].

Traditional geological prospecting methods also have incorporated many new technologies to predict geological conditions in front of the tunnel. McCrae and Cook proposed a geological mapping for tunnels at relatively shallow depths (<250 m) in strong discontinuous rocks, focusing on a means of locating possible instabilities and selecting support requirements on the basis of rock mass characterization. Therefore, characterizing the behaviour of discontinuities has become the major requirements in the geological mapping process [9]. Zarei et al. used geological mapping to evaluate high local groundwater inflow to a rock tunnel [10]. Due to the given hydrogeological assumptions and the simplification of heterogeneous media, the use of analytical and numerical tools to predict possible groundwater inflows from these characteristics often failed.

Therefore, through detailed geological features, reliable groundwater inflow can be predicted. Xiong et al. proposed a regional scale 3D geological model for assessing tunnel engineering, based on regional field surveys of geological boundary and attitude [11]. Afterwards, according to the construction process, geological information was obtained from the tunnel face. This method dynamically adjusts the three-dimensional geological model according to the information obtained at different stages, providing a reference for tunnel engineering. Soldo et al. proposed the importance of site investigation of geological conditions for tunnel engineering. All the collected data must be interpreted inside a robust conceptual framework and primarily came from field surveys in geology, enhanced by new methods and technologies for investigating and modelling [12].

As a result, the geological conditions of the tunnel face play an important role in the tunnel construction period. The tunnel design needs to be compatible with the actual geological conditions in front of the tunnel, achieving a safer and more economical construction.

In order to preserve the geological data and present them in a three-dimensional visualization form, a method was proposed for the establishment of a three-dimensional geological model. A novel image preprocessing scheme can accurately and quickly take out the tunnel face area as the raw data for 3D modelling. Since it takes a long time to perform high-precision modelling of the tunnel face, the proposed image preprocessing scheme can effectively reduce the amount of calculation in the reconstruction process. The process of 3D reconstruction of the tunnel face is faster than before. At the same time, the photographing effect is poor due to the jitter in the handheld shooting. Besides, it is obviously problematic that the camera site is too close or too far to the tunnel face. The authors also designed a device named CameraPad to automatically take clear pictures of the tunnel face. The device can rotate the camera in three axes automatically to collect tunnel face photos after being placed in front of the tunnel as required. Due to the built-in gyroscope, the relative position of each photo can be obtained after rotating in three axes, and the camera exterior parameters can also be obtained. Compared with the traditional method of estimating exterior parameters through algorithms, it is more accurate.

To sum up, this article can offer research objectives as follows: ① a novel method of rapid 3D reconstruction of the tunnel faces automatically; ② a new device to collect data for fast 3D reconstruction of the tunnel faces; ③ application of the proposed method.

2. Background and Related Work

In today's tunnel engineering, geological conditions play an increasingly important role, affecting the days and cost of tunnel construction. Therefore, the record of geological conditions during construction has also been paid more and more attention. In order to record the geological conditions of the tunnel face quickly and accurately, Chengdu Tianyou Tunnelkey has developed a set of software and hardware

integration system called CameraPad. As shown in Figure 1, the main components of the CameraPad are divided into four parts: ① camera module; ② distance measuring module; ③ gyroscope module; and ④ pan/tilt/zoom (PTZ) module. Among them, the camera module is used to obtain multiview photos, and the distance measuring module composed of the laser range finder is used to measure the distance from the shooting position to the tunnel face to determine the photographing scale. Besides, the PTZ module is mainly used to measure and adjust attitude parameters, and the gyroscope is used to record the orientation of the lens while taking photos.

First of all, put CameraPad in a suitable position in front of the tunnel face. Besides, roughly align the lens to the centerline of the tunnel face. The device is turned on, and the laser range finder will be used as an aid to select a suitable position. Place two geological boards on the tunnel face in advance to convert the reconstructed model from the camera coordinate system to the geodetic coordinate system [7]. Take down the photosource equipped with the CameraPad and place it in a suitable position so that the tunnel face can be photographed clearly. After a one-button start, CameraPad will use the PTZ to adjust the posture to collect the image of the tunnel face.

Then, CameraPad can be wirelessly connected and the data can be exported in the hotspot mode, and then the 3D reconstruction is performed.

Finally, mark structural planes, joints, fissures, and lithology in the 3D reconstructed model.

The algorithm flow of the software associated with CameraPad is shown in Figure 2.

3. Image Preprocessing

As shown in Figure 3, multiple pictures from the tunnel face in Xiaosanxia railway tunnel in Chongqing were regarded as input in this process. Since multiple photos are used to reconstruct the 3D geological model of the tunnel face, the surrounding primary lining will be captured while taking pictures. In order to speed up the reconstruction process, the area of the captured tunnel face is used as the reconstructed image. Besides, the area of primary lining is taken as a non-reconstructed image area. Therefore, the 3D geological reconstruction of the tunnel face can speed up and reduce the amount of calculation. We extract the area of the tunnel face and use it as the basic data for 3D reconstruction, as shown in Figure 4(e).

First, the Gaussian filtering operation is performed on the picture of the tunnel face taken by the camera shown in Figure 4(a). Bergholm proposed a Gaussian filter for noise reduction and edge detection [13]. As shown in Figure 5, in the 3×3 pixels' area of the photograph, the pixel at the center point is the weighted average of all nine-pixel values, and the value of each pixel is calculated as follows:

$$G(x, y) = \frac{1}{2\pi\sigma^2} e^{-((x^2+y^2)/2\sigma^2)}, \quad (1)$$

where $\sigma = 6$ is selected after multiple sets of data verification and x, y represent the position relative to the center of the

area shown in Figure 5, with the origin at the center. The X-axis is horizontal to the right, and the Y-axis is vertically upward.

Gaussian filter is a linear smoothing filter, which is widely used in the noise reduction process of image processing. In essence, Gaussian filtering is the process of weighted averaging the entire image. The value of each pixel is obtained by the weighted mean of itself and other pixel values in the neighborhood. The specific operation of Gaussian filtering is to scan each pixel in the image with a template, and the weighted average intensity of the pixels in the neighborhood determined by the template was used to replace the intensity of the center pixel of the template.

As shown in Figure 4(b), after the Gaussian filtering operation, the noise in the image is removed to facilitate subsequent image processing. The region growing algorithm is used to remove the areas that meet the preset threshold [14, 15], as shown in Figure 4(c). In this way, the area of primary lining in the picture can be roughly determined, as shown in Figure 4(d). Thus, the area of the tunnel face in the picture is further defined, as shown in Figure 4(e). We combined Gaussian filter with region growing algorithm to extract the tunnel face area in the images.

4. The Extraction and Matching of Feature Points

4.1. The Extraction of Feature Points. Feature points are used to describe the corresponding relationship that can be used to match two photos. Feature points should have apparent characteristics that are clearly different from nonfeature points and can be repeatedly detected in different photos. Feature points are essential for seeking the homonymy points in other images, and a lot of research studies have been done in the field of computer vision. In view of the inconvenience of taking photos at the construction site, the feature point extraction with scale invariance and rotation invariance is adopted.

SURF (SpeededUp Robust Features) is an accelerated version based on the Scale Invariant Feature Transformation (SIFT) algorithm [16]. The SURF operator is much faster than the SIFT operator in detecting feature points of the image [17, 18]. In the case of multiple pictures in the same scene, the extracted feature points have better stability.

Feature point detection based on Hessian matrix is the core of SURF:

$$\det(H(\mathbf{x}, \sigma)) = \begin{vmatrix} L_{xx}(\mathbf{x}, \sigma) & L_{xy}(\mathbf{x}, \sigma) \\ L_{xy}(\mathbf{x}, \sigma) & L_{yy}(\mathbf{x}, \sigma) \end{vmatrix} \quad (2)$$

$$= L_{xx}(\mathbf{x}, \sigma)L_{yy}(\mathbf{x}, \sigma) - (L_{xy}(\mathbf{x}, \sigma))^2.$$

Among them, $L_{xx}(\mathbf{x}, \sigma)$ represents the convolution of the Gaussian second-order derivative $\partial^2 g(\sigma)/\partial x^2$ of the image at the position of the pixel $\mathbf{x} = (x, y)$ with a scale of σ ; $L_{yy}(\mathbf{x}, \sigma)$ represents the convolution of the Gaussian second-order derivative $\partial^2 g(\sigma)/\partial y^2$ of the image at the position of the pixel $\mathbf{x} = (x, y)$ with the scale of σ ; and $L_{xy}(\mathbf{x}, \sigma)$ represents the convolution of the Gaussian second-order

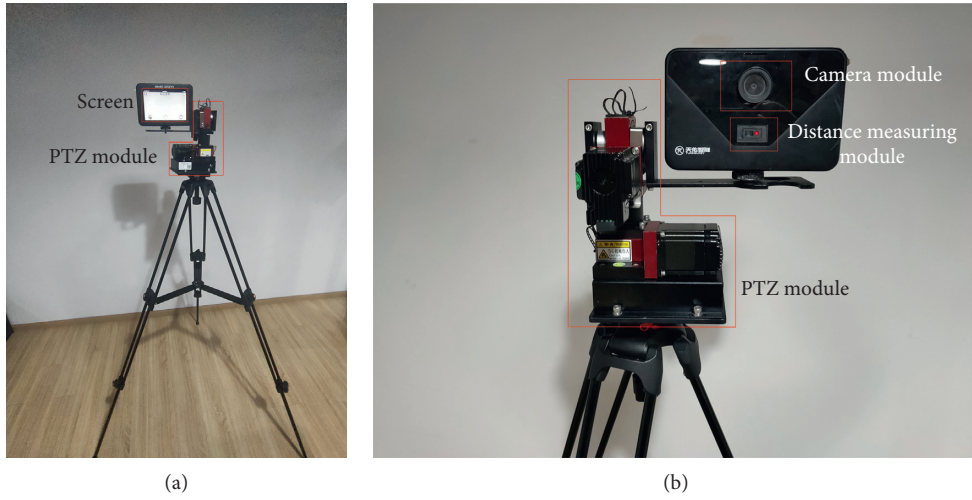


FIGURE 1: Module composition and usage scenarios of CameraPad.

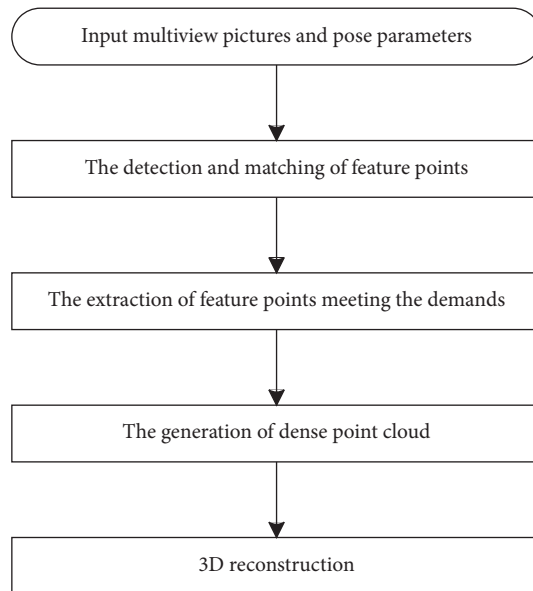


FIGURE 2: The algorithm flow of the software associated with CameraPad.

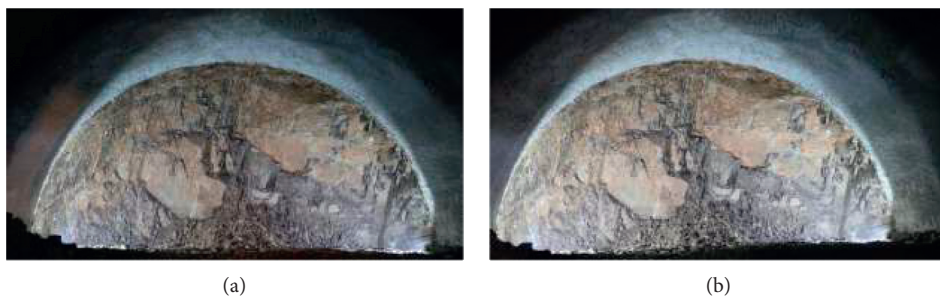


FIGURE 3: Continued.

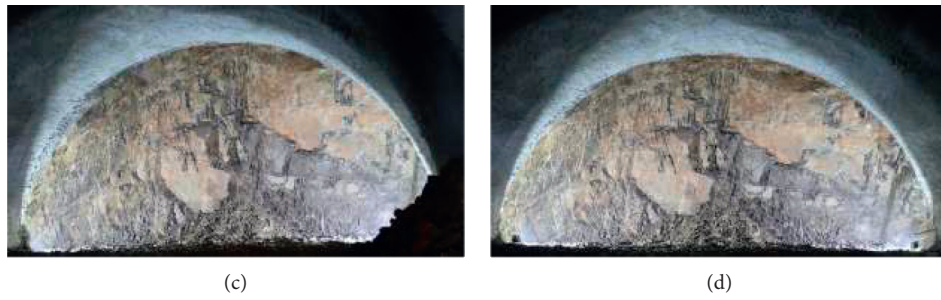


FIGURE 3: The images of the tunnel face obtained from the Xiaosanxia railway tunnel in Chongqing, China.

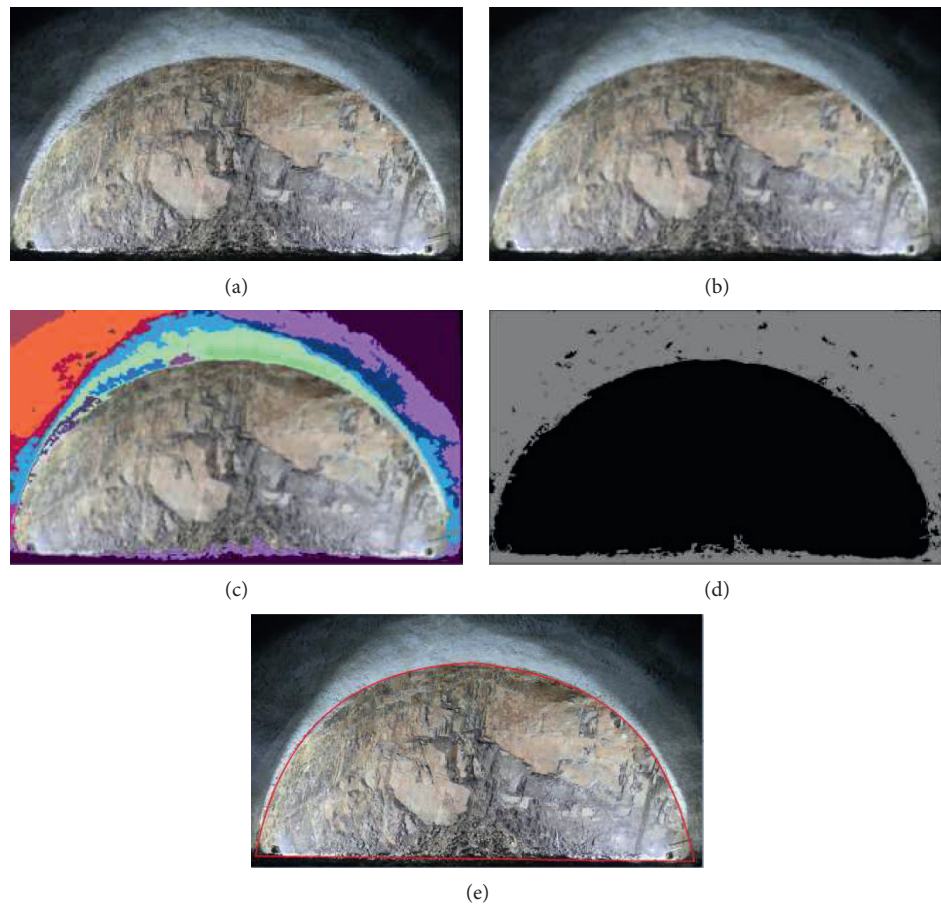


FIGURE 4: Extraction of tunnel face area from the image. (a) The original image of tunnel face. (b) The image after Gaussian filtering. (c) The image after region growth processing. (d) The area of tunnel face extracted. (e) The result after image preprocessing.

$(-1, 1)$	$(0, 1)$	$(1, 1)$
$(-1, 0)$	$(0, 0)$	$(1, 0)$
$(-1, -1)$	$(0, -1)$	$(1, -1)$

FIGURE 5: Gaussian filter.

derivative $\partial^2 g(\sigma)/\partial x \partial y$ of the image at the position of the pixel $\mathbf{x} = (x, y)$ with the scale of σ .

The SURF algorithm makes full use of the fast integration algorithm of the rectangular area to accelerate the convolution calculation of the Box Matrix and the source graph. Besides, the analysis of the Haar wavelet used in the feature vector extraction is also speeded up. Therefore, the SURF algorithm can be used in computer vision object recognition and 3D reconstruction.

The initialization of Box Matrix is as follows:

- (1) Given an image of size $M \times N$, set a red rectangular box with a size of $m \times n$, as shown in Figure 6.
- (2) Create a new one-dimensional array of size M to store intermediate variables in the calculation process, represented by red pixels. The values of the red pixels are the sum of each column of pixels.
- (3) Assuming that the coordinate $(0, 0)$ on the top left corner of the red rectangular box is regarded as the center of the movement, slide the rectangular box from $(0, 0)$ to $(M-m, 0)$ pixel by pixel in the right. Whenever the red rectangular box is moved to a new position, calculate the sum of the pixels in the red rectangular box. After moving to the next row, push the red rectangular box to $(0, 1)$ and slide the red rectangular box from $(0, 1)$ to $(M-m, 1)$ pixel by pixel in the right. Repeat this until the red rectangular box slides from $(0, N-n)$ to the right pixel by pixel to $(M-m, N-n)$.
- (4) The calculation of the sum of pixels in the red rectangular box, first sum each column of pixels in the orange rectangular box, place the result in the red pixel and then sum the red pixels in the corresponding green rectangular box. Therefore, the result is the sum of the red rectangular box.

The SURF (SpeededUp Robust Features) further simplifies the second derivative of the Gaussian function, using 9×9 Box Matrix instead of Gaussian second-order derivatives with $\sigma = 1.2$, as shown in Figure 6. H_{approx} is denoted by D_{xx} , D_{yy} , and D_{xy} . The relative weights in Hessian matrix need to be further balanced with $(|L_{xy}(1.2)|_F |D_{xx}(9)|_F) / (|L_{xx}(1.2)|_F |D_{xy}(9)|_F) = 0.912 \approx 0.9$ for computational efficiency, where $|D_{xx}(9)|_F$ is the Frobenius norm of D_{xx} [17].

After simplification, take the value of the Hessian matrix as follows:

$$\det(H_{\text{approx}}) = D_{xx}D_{yy} - (0.9D_{xy})^2. \quad (3)$$

The SURF feature point detection is also called Fast Hessian Detector. The Hessian matrix is the core of the entire SURF algorithm and is a second-order matrix composed of the second partial derivative of a real-valued function whose independent variable is a vector. The results of feature point matching are shown in Figure 7.

4.2. Distribution and Matching of Feature Points in Main Direction. As shown in Figure 8, the SURF algorithm counts

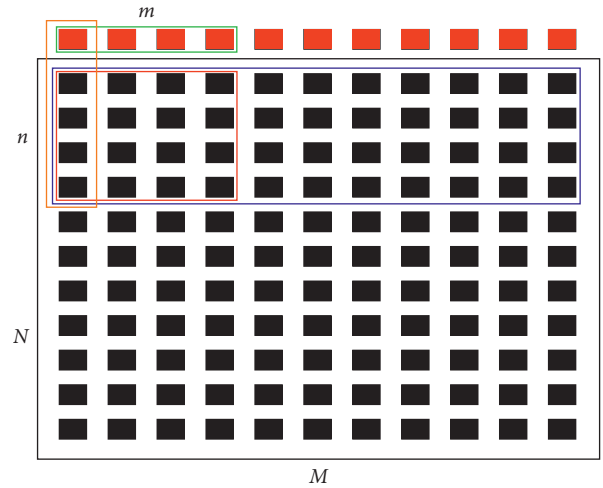


FIGURE 6: The principle of Box Filter.

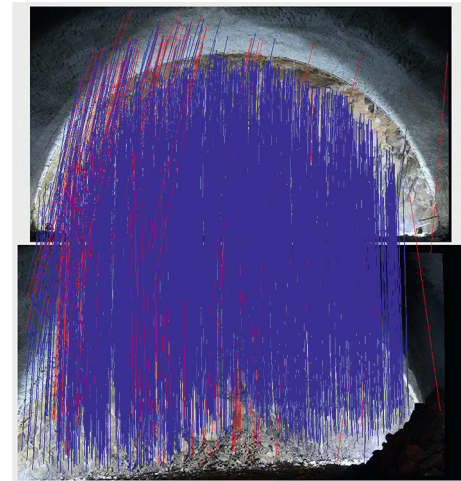


FIGURE 7: Feature point matching results. The blue lines in the figure are the matches that meet the preset threshold condition, and the red lines are the matches that do not meet the preset threshold condition.

the Harr wavelet features of the circular neighborhood of feature points. A 60° fan-shaped area is used in the circular neighborhood of the feature points, and the sums of the horizontal and vertical Harr wavelet features of all points in the 60° fan-shaped area are counted. And the fan-shaped area is rotated 60° around the feature point in turn, so as to traversal the six 60° fan-shaped regions of the circular neighborhood. Therefore, the Harr wavelet values in the six fan-shaped regions are summed to obtain six vector directions, and the vector direction with the largest modulus is the main direction of the feature point.

4.3. The Generation of Feature Point Descriptors. After determining the main direction of the feature points, rotate the coordinate axis in the main direction. Select a $20\sigma \times 20\sigma$ area surrounding a feature point and divide it into 4×4 small rectangular area, as shown in Figure 9. Then, calculate the 25 Haar wavelet values of size $\sigma \times \sigma$ in each small rectangular

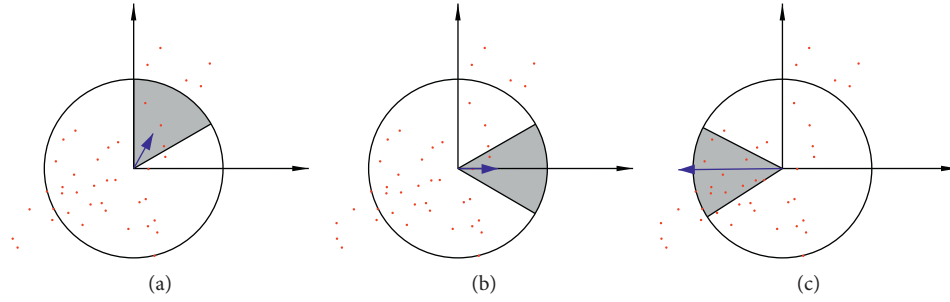


FIGURE 8: Determination of the main direction of feature points.

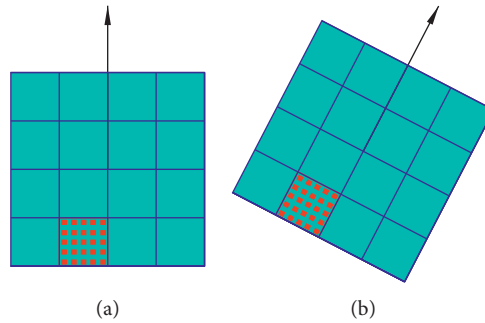


FIGURE 9: The generation of feature point descriptors.

area. According to the principle of separation of positive and negative, calculate the sum of wavelet values in the x -direction and y -direction in the area: Σdx , $\Sigma |dx|$, Σdx , $\Sigma |dy|$. With eight gradient directions in each small rectangular area, a $4 \times 4 \times 8 = 128$ -dimensional real number vector is obtained [17]. After the feature points are extracted, the Euler distance of the two feature vectors can be calculated in the vector space of the feature points. This paper adopts Nearest Neighbor Distance Ratio (NNDR) for matching:

$$\text{NNDR} = \frac{D_{\text{Closest Point}}}{D_{\text{Next nearest point}}}, \quad (4)$$

where D_{Closest} is the Euler distance between the feature point description vector and the closest feature point description vector and $D_{\text{Next nearest point}}$ is the Euler distance between the feature point description vector and the next nearest feature point description vector.

When NNDR is less than the preset threshold, the match is accepted.

5. Three-Dimensional Reconstruction Based on Improved Structure-from-Motion (SFM) and Patch-Based Multiview Stereo (PMVS) Software

5.1. Improved Structure from Motion (SFM). The structure-from-motion (SFM) algorithm is an algorithm for sparse point cloud based on collected disordered pictures, that is, to recover the three-dimensional structure of an object from motion (images taken at different times) [19]. In this process, it is necessary to estimate the exterior parameters involved

with position parameters and attitude parameters when taking pictures and reconstruct the sparse point cloud with the intrinsic parameters of the camera.

For the initial matching results of the feature vectors obtained above, a random sample consensus (RANSAC) is used to remove the invalid feature vectors [20]. Through accurate matching results, the homonymy points in multiple photos are also determined, as shown in Figure 10. Then, according to the principle of pinhole imaging [21], a series of projection equations are established. The difference values between the estimated projecting position and the actual projecting position of points are calculated through the projection equation set. These difference values are accumulated to construct the objective function [22]:

$$f(\mathbf{K}^i, \mathbf{D}^i, \mathbf{R}^i, \mathbf{t}^i, \mathbf{X}_j) = \min_{\mathbf{K}^i, \mathbf{D}^i, \mathbf{R}^i, \mathbf{t}^i, \mathbf{X}_j} \sum_{i,j} \|\mathbf{x}_j^i - \tilde{\mathbf{x}}_j^i\|^2, \quad (5)$$

where i represents the input order of photos; \mathbf{K}^i represents the intrinsic parameter matrix of the camera that took the i photo; \mathbf{D}^i represents the radial distortion parameter; $(\mathbf{R}^i | \mathbf{T}^i)$ represents the exterior parameter matrix of the camera taking the i photo (where \mathbf{R}^i represents the rotation matrix and \mathbf{t}^i represents the translation matrix); and $\mathbf{X}_j = [x_j \ y_j \ z_j]$ represents the spatial point.

The spatial information of the feature points is obtained by solving the above formula, and the intrinsic parameters are obtained by using calibration boards [23]. The exterior parameters, intrinsic parameters, and spatial information of the traditional SFM algorithm are all estimated by the algorithm, while the exterior parameters and intrinsic parameters of the proposed method are obtained externally. Only the spatial information is estimated by the algorithm, which will obviously

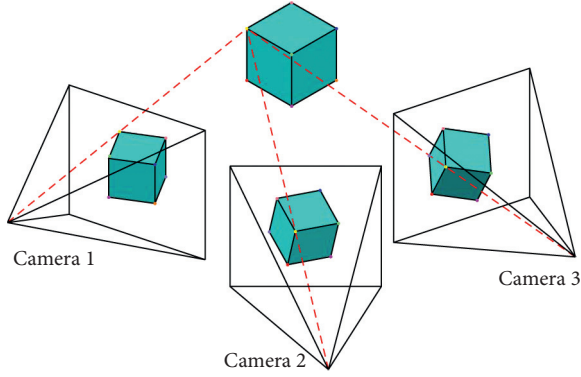


FIGURE 10: Schematic diagram of the three-dimensional reconstruction of SFM.

greatly improve the accuracy and speed of 3D visualization. The extracted point cloud is shown in Figure 11 [24].

5.2. Patch-Based Multiview Stereo (PMVS). PMVS is a patch-based multiview stereo algorithm proposed by Furukawa in 2007 [25]. Due to its high accuracy and wide application scenarios, it is popularized on a large scale. The point cloud in Figure 11 is so sparse that the output result of the previous step is used as input for the dense reconstruction of the sparse point cloud.

Each feature point that was successfully matched in the previous step is defined as a seed patch, which contains the following attributes:

$$\begin{aligned} \mathbf{c}(p) &\leftarrow \{\text{Triangulation from } f \text{ and } f'\}, \\ \mathbf{n}(p) &\leftarrow \frac{\overrightarrow{\mathbf{c}(p)O(I_i)}}{\left| \overrightarrow{\mathbf{c}(p)O(I_i)} \right|}, \\ R(p) &\leftarrow I_i. \end{aligned} \quad (6)$$

Among them, $\mathbf{c}(p)$ represents the center of the patch p ; $\mathbf{n}(p)$ represents the normal vector of the patch p ; $R(p)$ represents the reference picture of the patch p ; f and f' represent the detected feature points that match successfully; and $O(I_i)$ represents the camera optical center corresponding to the picture I_i .

The photometric discrepancy function $g(p)$ is defined as

$$g(p) = \frac{1}{|V(p)/R(p)|} \sum_{I \in V(p)/R(p)} h(p, I, R(p)), \quad (7)$$

where $V(p)$ denotes a set of images in which p is visible and $h(p, I, R(p))$ is defined to be a pairwise photometric discrepancy function between picture I and the reference picture $R(p)$ of patch p .

$g(p)$ is used to select the best one from the set of matching feature points of patch p as the final patch. Next, the patch p is expanded, and the neighbor patch p' is initialized with the information of patch p . When all the patch sets are expanded, the patches with weak grayscale consistency and geometric consistency are removed.

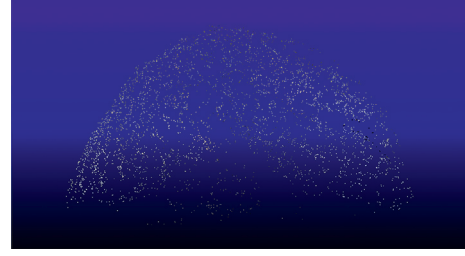


FIGURE 11: The point cloud extracted after SFM.

Therefore, the feature point f is obtained by improved structure from motion (SFM). Assuming that the corresponding patch is p , $\mathbf{c}(p)$ and $\mathbf{n}(p)$ are obtained as variables through the above formula. The photometric discrepancy energy is evaluated many times in the energy minimization procedure performed by a conjugate gradient method to find the optimal patch as the final patch p . Given a patch p , we initialize p' as a neighbor of p . Through a more complex optimization process to optimize $\mathbf{c}(p')$ and $\mathbf{n}(p')$, the new patches are expanded. After the expansion, a filtering operation will be performed to remove the patches of weaker visibility consistency.

Compared with Multiphoto Geometrically Constrained Matching (MPGC) and Maximization of the Posterior Marginal (MPM), the PMVS algorithm is more straightforward and faster in terms of the amount of calculation. Besides, the input parameters of PMVS are required less. The intrinsic parameter matrix and exterior parameter matrix of the image output by SFM can be used for dense reconstruction of the point cloud based on multiple images. Therefore, the method proposed in this paper uses PMVS for the dense reconstruction of the point cloud. The dense reconstruction of the point cloud based on PMVS is shown in Figure 12. The final 3D reconstruction effect based on PMVS is shown in Figure 13.

6. Application

The Xiaosanxia railway tunnel is located in Chongqing, China. In this tunnel, the CameraPad system developed by Chengdu Tianyou Tunnelkey was used to collect data. As shown in Figure 13, the images of the tunnel face were mainly gathered to perform the three-dimensional geological reconstruction along the tunnel excavation line. As shown in Figure 13, the high-definition three-dimensional reconstruction model and the built-in gyroscope of CameraPad are very helpful for the identification of structural planes and the drawing of joints and fissures in the future. Not only that, but the 3D geological model in the geodetic coordinate system can also provide a basis for measuring the dip direction.

The definition of the 3D geological model obtained by the proposed method can be adjusted by replacing the camera module of the CameraPad. The high-definition camera module can provide better results for identifying joint and fissures in the future. It can be seen that the high-definition camera module plays an essential role in recognition of the tunnel face with the crushed surrounding rock.



FIGURE 12: The point cloud extracted after dense reconstruction.

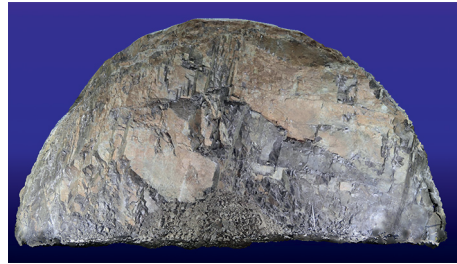


FIGURE 13: The final result after 3D reconstruction.

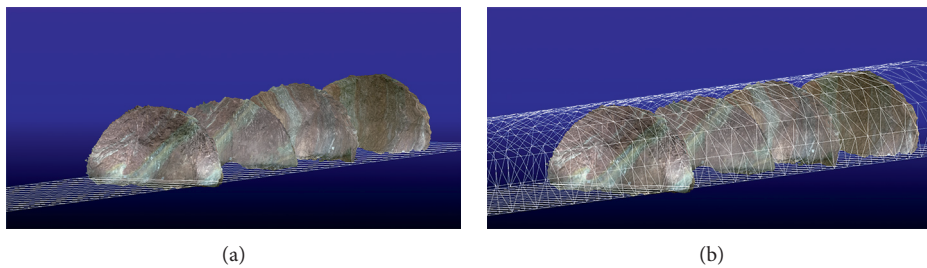


FIGURE 14: (a) The results of 3D reconstruction in Fengjie railway tunnel in Chongqing. (b) 3D geological model arranged according to the design of the rail line.

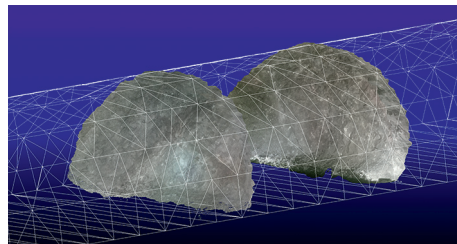


FIGURE 15: The results of 3D reconstruction in No. 1 Xinan railway tunnel in Jilin.

Compared to 3D reconstruction from video flowing, CameraPad is also more suitable for use in tunnel engineering. The video flowing at 25 frames per second is used for 3D reconstruction [26], which is very convenient for some scenes that require online 3D reconstruction. Since online demand usually severely limits the available resolution of vidicon, this method also has the disadvantage of relatively low resolution.

CameraPad developed by Chengdu Tianyou Tunnelkey was used to collect data in Fengjie railway tunnel in Chongqing, China. As shown in Figure 14, the images of the tunnel face were mainly gathered to perform the 3D geological reconstruction along the tunnel excavation line.

The proposed method placed these 3D geological models according to the tunnel design data and the mileage of the tunnel face, as shown in Figure 14. In this way, the geological conditions during tunnel construction can be better represented and used as geological data storage. Compared with the traditional geological sketch, the proposed method not only is more intuitive but also can provide geological data for construction design more effectively. Through the geological conditions of the tunnel face, we can also make a prediction for the following geological conditions.

CameraPad developed by Chengdu Tianyou Tunnelkey was used to collect data in No. 1 Xinan railway tunnel in Jilin, China. As shown in Figure 15, the images of the tunnel face

were mainly gathered to perform the 3D geological reconstruction along the tunnel excavation line.

The proposed method placed these 3D geological models according to the tunnel design data and the mileage of the tunnel face, as shown in Figure 15.

7. Conclusions and Future Work

In this paper, the SURF algorithm was used to extract and match the feature points from the multiple photos of the tunnel face. Next, SFM is used to extract the sparse point cloud, and then the dense reconstruction of the point cloud is performed based on the patch-based multiview stereo algorithm. So far, the picture is pasted to the corresponding patch, and the three-dimensional reconstruction is completed. In order to speed up the process of 3D reconstruction, the proposed method preprocessed the multiple photos and extracted part of the tunnel face for reconstruction. The 3D geological model reconstructed in this way has the characteristics of full color and a high degree of precision. Compared with the traditional hand-drawn geological sketch, the method proposed in this paper is more efficient, and the geological conditions of the tunnel face can be entirely recorded by assigning values to the patches. Compared with the three-dimensional geological model obtained by the TLS method, the method proposed in this paper has the characteristics of full color, which makes it easier to identify the seepage and the stratum lithology. The proposed method can also be combined with BIM technology to build a BIM model during the construction period so that the record has a better manifestation.

In this paper, the proposed method has the advantages of 3D visualization and high precision compared with traditional geological data preservation methods. A novel image preprocessing scheme can accurately and quickly take out the tunnel face area as the raw data for 3D modelling. Due to the built-in gyroscope, the relative position of each photo can be obtained after rotating in three axes, and the camera exterior parameters can also be obtained. Compared with the traditional method of estimating exterior parameters through algorithms, it is more accurate.

There are still many problems to be solved. For example, the automatic identification of the attitude of rock formation and the structural plane of the three-dimensional geological model of the tunnel face are well down. The automatic identification of joints, fissures, and water leakage is also in future work. Of course, it is also hoped that in the future, automatic identification of rock formations and lithology will be achieved to complete the automatic 3D geological sketch.

Data Availability

The experimental data used in this study were obtained from Xiaosanxia railway tunnel and Fengjie railway tunnel in Shanxi Province, China. Besides, data were also obtained from No. 1 Xinan railway tunnel in Jilin, China. The data used to support the results of this study can be obtained from the corresponding author.

Conflicts of Interest

The authors declare that they have no conflicts of interest.

Authors' Contributions

Jian Liao contributed to conceptualization, methodology, writing, and formal analysis. Cheng Yunjian was responsible for the investigation, data curation, and algorithm. Qiu Wenge supervised the study.

Acknowledgments

This research was made possible through the National Natural Science Foundation of China (grant nos. 51991395 and u1434206) and supported by the Sichuan Science and Technology Program (2021YFSY0043).






References

- [1] T. Yamamoto, S. Shirasagi, S. Yamamoto et al., "Evaluation of the geological condition ahead of the tunnel face by geostatistical techniques using TBM driving data," *Tunnelling and Underground Space Technology*, vol. 18, no. 2-3, pp. 213–221, 2003.
- [2] S. J. Li, X.-T. Feng, C. Y. Wang, and J. A. Hudson, "ISRM suggested method for rock fractures observations using a borehole digital optical televiewer," *Rock Mechanics and Rock Engineering*, vol. 46, no. 3, pp. 635–644, 2013.
- [3] S. Izadi, D. Kim, O. Hilliges et al., "KinectFusion: real-time 3D reconstruction and interaction using a moving depth camera," in *Proceedings of the 24th Annual ACM Symposium on User Interface Software and Technology*, pp. 559–568, New York, NY, USA, October 2011.
- [4] G. Wang, Q. Feng, and K. Roshoff, "A new approach to tunnel digital geological mapping using 3D terrestrial laser scanning technique," in *ISRM International Symposium on Rock Mechanics-SINOROCK 2009* International Society for Rock Mechanics and Rock Engineering, Lisbon, Portugal, 2009.
- [5] P. P. Cacciari and M. M. Futai, "Modeling a shallow rock tunnel using terrestrial laser scanning and discrete fracture networks," *Rock Mechanics and Rock Engineering*, vol. 50, no. 5, pp. 1217–1242, 2017.
- [6] P. P. Cacciari and M. M. Futai, "Mapping and characterization of rock discontinuities in a tunnel using 3D terrestrial laser scanning," *Bulletin of Engineering Geology and the Environment*, vol. 75, no. 1, pp. 223–237, 2016.
- [7] Y.-J. Cheng, W.-G. Qiu, and D.-Y. Duan, "Automatic creation of as-is building information model from single-track railway tunnel point clouds," *Automation in Construction*, vol. 106, p. 102911, 2019.
- [8] P. Li, W. Qiu, Y. Cheng et al., "Application of 3D laser scanning in underground station cavity clusters," *Advances in Civil Engineering*, vol. 2021, no. z2, 12 pages, Article ID 8896363, 2021.
- [9] R. McCrae and R. Cook, "Tunnel mapping in strong discontinuous rocks," *International Journal of Mining Engineering*, vol. 3, no. 1, pp. 79–89, 1985.
- [10] H. R. Zarei, A. Uromeihy, M. Sharifzadeh et al., "Evaluation of high local groundwater inflow to a rock tunnel by characterization of geological features," *Tunnelling and Underground Space Technology*, vol. 26, no. 2, pp. 364–373, 2011.

- [11] Z. Xiong, J. Guo, Y. Xia, H. Lu, M. Wang, and S. Shi, "A 3D multi-scale geology modeling method for tunnel engineering risk assessment," *Tunnelling and Underground Space Technology*, vol. 73, pp. 71–81, 2018.
- [12] L. Soldo, M. Vendramini, A. Eusebio et al., "Tunnels design and geological studies," *Tunnelling and Underground Space Technology*, vol. 84, pp. 82–98, 2019.
- [13] F. Bergholm, "Edge focusing," *IEEE Transactions on Pattern Analysis and Machine Intelligence*, vol. 9, 1987.
- [14] S. A. Hojjatoleslami and J. Kittler, "Region growing: a new approach," *IEEE Transactions on Image Processing*, vol. 7, no. 7, p. 1079, 1998.
- [15] R. Adams and L. Bishof, "Seeded region growing," *IEEE Transactions on Pattern Analysis and Machine Intelligence*, vol. 16, 1994.
- [16] D. G. Lowe, "Object recognition from local scale-invariant features," in *Proceedings of the Seventh IEEE International Conference on Computer Vision*, pp. 1150–1157, IEEE, Corfu, Greece, September 1999.
- [17] H. Bay, T. Tuytelaars, and L. Van Gool, "Surf: speeded up robust features," in *Proceedings of the European Conference on Computer Vision*, pp. 404–417, Springer, Graz, Austria, May 2006.
- [18] D. G. Lowe, "Distinctive image features from scale-invariant keypoints," *International Journal of Computer Vision*, vol. 60, no. 2, pp. 91–110, 2004.
- [19] N. Snavely, S. M. Seitz, and R. Szeliski, "Photo tourism: exploring photo collections in 3D," in *ACM Siggraph 2006 Papers*, pp. 835–846, Springer, Berlin, Germany, 2006.
- [20] R. Hartley and A. Zisserman, *Multiple View Geometry in Computer Vision*, Cambridge University Press, Cambridge, UK, 2003.
- [21] C.-F. Wu, *Mathematical Methods in Computer Vision*, Science Press, Beijing, China, 2008.
- [22] R. Szeliski, *Computer Vision: Algorithms and Applications*, Springer Science & Business Media, Berlin, Germany, 2010.
- [23] M. Lemmens, *Photogrammetry: Geometric Data from Imagery*, Springer, Berlin, Germany, 2011.
- [24] P. Clini, N. Frapiccini, M. Mengoni et al., "SFM technique and focus stacking for digital documentation of archaeological artifacts," *Radiology*, vol. 41, 2016.
- [25] Y. Furukawa and J. Ponce, "Accurate, dense, and robust multi-view stereopsis (PMVS)," in *Proceedings of the IEEE Computer Society Conference on Computer Vision and Pattern Recognition*, Minneapolis, MN, USA, June 2007.
- [26] A. Geiger, J. Ziegler, and C. Stiller, "Stereoscan: dense 3d reconstruction in real-time," in *Proceedings of the 2011 IEEE Intelligent Vehicles Symposium (IV)*, pp. 963–968, IEEE, Baden-Baden, Germany, June 2011.

Research Article

The Ground Settlement and the Existing Pipeline Response Induced by the Nonsynchronous Construction of a Twin-Tunnel

Shicheng Sun ^{1,2}, Chuanxin Rong ^{1,2}, Houliang Wang ³, Linzhao Cui ³,
and Xin Shi ²

¹State Key Laboratory of Mining Response and Disaster Prevention and Control in Deep Coal Mine,
Anhui University of Science and Technology, Huainan 232001, China

²School of Civil Engineering and Architecture, Anhui University of Science and Technology, Huainan 232001, China

³Anhui Water Resources Development Co., Ltd., Bengbu 233000, China

Correspondence should be addressed to Chuanxin Rong; rongcx@ustc.edu

Received 4 September 2020; Revised 4 March 2021; Accepted 17 March 2021; Published 31 March 2021

Academic Editor: Wen-Chieh Cheng

Copyright © 2021 Shicheng Sun et al. This is an open access article distributed under the Creative Commons Attribution License, which permits unrestricted use, distribution, and reproduction in any medium, provided the original work is properly cited.

Shielding tunnel construction always has negative impacts on the surrounding buildings. Because of repeated disturbances caused by the construction, more attention should be paid to the impacts of the nonsynchronous construction of a twin-tunnel. In this research, a three-dimensional model was established to simulate the construction process of a twin-tunnel in a section of the Hefei No. 4 metro line, and the calculation results were validated with the measured settlement data. Based on the model, the ground settlement and the existing pipeline responses were studied in detail. The results showed that, after the first tunnel (FT) construction, the settlement curves conformed to a Gaussian distribution. Additionally, after the second tunnel (ST) construction, the final settlement curves were no longer completely symmetrical. The influences of the twin-tunnel space and the pipeline-soil relative stiffness on the settlements were further studied. The results showed that the final settlement curves of the ground surface and the pipeline were mainly W-shaped, U-shaped, and V-shaped. As the twin-tunnel space increased and the pipeline-soil relative stiffness decreased, the settlement curve gradually changed from V-shaped to W-shaped. C was defined as the ratio of two maximum settlements in the W-shaped settlement curve. As the space increased, C started to decrease from 1 and then increased to 1.

1. Introduction

The construction of a tunnel is a complex engineering problem involving many aspects. Taking into account the uncertainty of the geological lithology and the complexity of the construction environment, more consideration should be given to the soil-structure interaction during tunnel construction, and efforts should be made to reduce the adverse impacts of tunnel construction [1–3]. In particular, in urban areas, because of the interaction between the soil and the structure, the disturbance caused by shielding construction may reduce the safety of roads and pipelines [4, 5]. When a tunnel crosses pipelines at close range, it can easily cause ground settlement and deformation or even the destruction of the pipelines [6, 7], which will seriously affect the production and life of the surrounding residents and

result in negative economic and social impacts. Considering this situation, it is necessary to conduct an in-depth study of the settlement behaviors caused by twin-tunnel construction.

Many scholars have achieved research results related to the influence mechanisms of tunnel construction and the prediction method of settlements. The Peck formula is the most widely used by engineers and researchers. Based on this, many scholars have conducted in-depth research studies [9–11]. The analytical method has been used to obtain the settlements of the ground and pipelines through the pipeline-soil interaction. Attewell et al. [12] and Wei et al. [13–15] established an analytical solution for soil deformation. Based on the Winkler foundation model, Huang et al. [16] and Shi et al. [17, 18] considered the interaction of a tunnel-soil-pipeline. A series of finite element simulations

were also used for relevant research studies. Wang et al. [19] and Shi et al. [20, 21] analyzed the sensitivity of each parameter to the settlement of the ground and a pipeline based on numerical simulation. In addition, the effects of different pipeline orientations on tunneling were studied via a centrifugal test. Ma et al. [22] carried out a three-dimensional centrifugal model test and a numerical simulation to study the influence of double-stack tunnel construction on existing pipelines with different construction sequences. Previous research has made predictions, primarily about the final settlement of the ground and a pipeline after tunnel construction, but little attention has been paid to the development of the settlement with the second construction disturbance.

In this research, the settlements of the ground surface and the response of a pipeline during nonsynchronous twin-tunnel construction were studied. The in-depth analysis of the characteristics of the settlement development was introduced during the FT and ST construction. At the same time, to determine the final settlement characteristics of the ground surface and pipeline, we further studied the influences of the pipeline-soil relative stiffness and the twin-tunnel space on the final settlements.

2. Analysis of the Ground Settlements and the Pipeline Response

The phenomenon of ground movement and the pipeline deformation caused by tunnel shielding is a three-dimensional problem that can be explained by the interaction of a tunnel-soil-pipeline [21]. According to Shi et al. [20], it can be known that, from the vertical direction, this phenomenon mainly includes the stress relief caused by the excavation of the construction plane, the pressure imbalance caused by the grouting, and the consolidation settlement caused by the change of the water level. During the construction process, the formation loss is transmitted upward to cause the deformation of the surface and buried pipelines. In this process, the pressure of the overlying soil of the pipeline and the emptying of the underlying soil cause the deformation and overall displacement of the pipeline [23]. At the same time, the existence of the pipeline as a “beam” in the soil also reduces the settlement of the ground surface. The interaction is coordinated, and eventually the interaction will be stabilized.

Generally speaking, the impact of a tunnel vertically undercrossing the ground and a pipeline is the largest [24]. For the case of a single-line vertically undercrossing the pipeline, assuming that the pipeline and soil are continuous and elastic, the Peck formula is widely used [8]:

$$S = S_{\max} \exp\left[-\frac{x^2}{2i^2}\right], \quad (1)$$

$$S_{\max} = \frac{V_{\text{loss}}}{i\sqrt{2\pi}}, \quad (2)$$

where S is the settlement at the distance x from the centerline of the tunnel on the cross-section, S_{\max} is the maximum

ground surface settlement, and the settlement of the ground surface is described by the settlement tank width i and the formation loss rate V_{loss} . At the same time, equations (1) and (2) can be used to describe the settlement of a pipeline. Under certain conditions, the settlement of the ground surface can be used to estimate the settlement of a pipeline [25]. The interaction of pipeline-soil is relatively clear during single-tunnel construction. According to the previous analysis, when the parameters are easier to obtain, the analytical method can provide relatively simple and accurate results. It is necessary to consider the interaction of the tunnels when studying the settlement during twin-tunnel construction, especially when the tunnels are constructed in turn. At this time, either the analytical method is difficult to solve or the solution is more complicated. Therefore, it was planned to conduct research in conjunction with the Peck formula and pay more attention to the final settlement.

The calculation of the impact of twin-tunnel construction is more complicated and it needs to be discussed according to the situation. Specifically, based on the results of existing settlements [26, 27], the final settlement can be divided into three categories. If there is a maximum settlement and the settlement curve is symmetrical, then the settlement is called a V-shaped settlement. If there are two maximum settlements (the two maximum settlements can be different), the settlement curve is W-shaped. Additionally, the U-shaped settlement (with a wider settlement center) is between the V-shaped and the W-shaped settlements. The final settlement of the ground surface and a pipeline is affected by many factors. For a V-shaped settlement, because of the overlap of the affected area of the excavation planes, an equivalent method can be used and the Peck formula can be applied. For a W-shaped settlement, the Peck formula can be extended from a single-tunnel to a twin-tunnel [28]. When the right tunnel is constructed first, the final settlement curve can be calculated using the following equation:

$$S = S_{\max s} \exp\left[-\frac{(x - 0.5L)^2}{2i_s^2}\right] + S_{\max f} \exp\left[-\frac{(x + 0.5L)^2}{2i_f^2}\right] \quad (3)$$

where S is the settlement at the distance x from the centerline of the twin-tunnel on the cross-section, $S_{\max f}$ and $S_{\max s}$ are the maximum settlements corresponding to the twin-tunnel, i_f and i_s are the settlement tank widths caused by the construction of FT and ST, respectively, and L is the twin-tunnel space. In equation (3), the formation loss rate V_{loss} and the settlement tank width i are used to calculate the settlement regardless of whether there is a pipeline, so the equation is still applicable to the existence of pipelines in the soil. When considering the impact of the FT construction on the ST, the values of V_{loss} and i corresponding to the twin-tunnel are different, and the maximum settlements $S_{\max f}$ and $S_{\max s}$ at the two locations are different.

3. Project Overview

This project was located between the High-speed Railway South Station and Chengkan Road Station in the Hefei No. 4

metro line. The length of the shielding construction was 1060 m. The twin-tunnel in this section contained two parallel circular tunnels with a centerline space L of 15 m, and the outer diameter D of the tunnels was 6 m. The shielding segments were 0.3 m thick and 1.5 m long. They were made of C50 concrete. The buried depth of the top of the twin-tunnel was about 8.9 m. The twin-tunnel vertically undercrossed a rainwater pipeline with a diameter of 1.5 m. The rainwater pipeline was made of reinforced concrete with a wall thickness of 0.1 m. The upper surface of the pipeline was 4.5 m below the ground surface. The closest distance between the tunnels and the pipeline was 2.9 m. The relative positional relationship between the tunnels and the pipeline is shown in Figure 1.

According to the geological survey report for the High-speed Railway South Station and Chengkan Road Station, there were three main types of soil, as shown in Figure 1, including fill, clay, and silty clay. The tunnels and the pipeline were all located in the clay layer. The basic mechanical parameters related to the soil layer and the tunnels are shown in Table 1. The amount of water in the survey depth was poor, and the impact of groundwater was small, so the groundwater could be ignored in the simulation analysis.

4. Three-Dimensional Numerical Model

4.1. FEM Model. A three-dimensional numerical model was established with GTS/NX software, which has often been used in the excavation simulation [29, 30]. The model of the shielding tunnels undercrossing the pipeline was established to simulate the whole process of the construction, and the sizes of the tunnels and the pipeline in the model were consistent with the actual sizes. Considering the boundary effect, the model was centered on the pipeline and twin-tunnel, and the size of the model was $80\text{ m} \times 75\text{ m} \times 40\text{ m}$. Automatic boundary conditions were selected. The upper surface was a free surface. The horizontal displacements on all sides were constrained, and the fixed constraint was applied at the bottom. The model size, the grid division, and the simulation of the shield driving are shown in Figure 2.

Before the twin-tunnel was excavated, the pipeline was first constructed and then the initial stress was cleared. During the simulation of the construction, the construction length of each step was the width of two segments, that is, 3.0 m. The construction of a single tunnel contained 25 such steps. In each simulating step, the shield shell was placed first. Then, the segments were installed, and the grouting was synchronized. During the simulating, the digging pressure was applied perpendicularly to the excavation plane, the jacking force was applied parallel to the segments, and the grouting pressure was applied perpendicularly to the segment. In the simulating step, activation instructions were used to simulate construction, passivation instructions were used to simulate excavation, and change properties instructions were used to simulate grouting. According to the construction organization design of the section, the directions of the twin-tunnel shielding were the same during construction. After the construction of the right tunnel was completed, the construction of the left tunnel began.

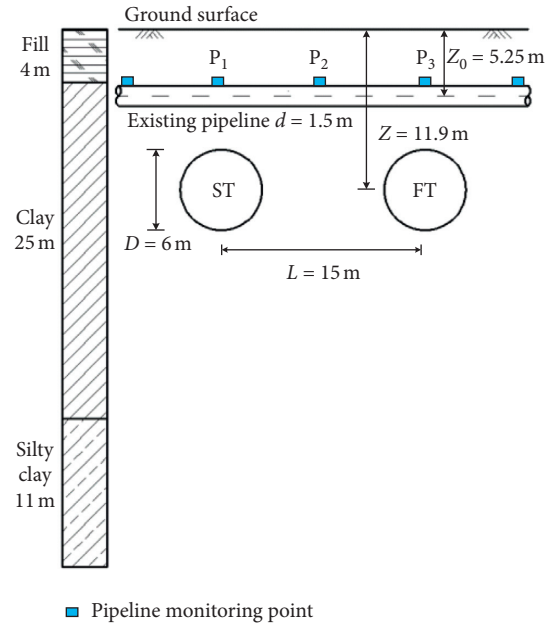


FIGURE 1: Profile of twin-tunnel crossing existing pipeline.

4.2. Material Model and Parameters. The basic mechanical parameters related to the soil layer and the shielding are shown in Table 1. For the three soil layers involved in the model, the modified Mohr–Coulomb yield criterion was used as the constitutive model, that is, the actual hardened soil model. The hardened soil model is widely used in the numerical analysis of excavation engineering because it can better reflect the stress-strain relationship when soil is unloaded [31, 32]. The constitutive relationship involved some parameters including the triaxial test secant stiffness E_{50}^{ref} , the tangent stiffness of the main compression loading test $E_{\text{oed}}^{\text{ref}}$, the unloading Elastic modulus $E_{\text{ur}}^{\text{ref}}$, the failure rate λ , and the reference pressure P^{ref} . The basic mechanical parameters of the soil were provided in the geological report. The parameters we needed mainly referred to the study of Shi et al. [30]. In [30], the data was obtained from experiments and verified with the field measured data. The partial parameters of the soil are given in Table 2.

All of the materials in the model except for the soil were isotropic linear elastic materials. The soil was simulated with the solid element. The shield shell, segments, and the pipeline were simulated with the plate element. For a more accurate simulation result, the model considered the digging pressure of the excavation plane, the horizontal jacking force, and the grouting pressure on the previous segments. The values of the three were the average values of the actual construction parameters. The digging pressure was 120 MPa, the jacking force was 100 MPa, and the grouting pressure was 0.2 MPa.

4.3. Verification of the Numerical Model. During the construction process, the settlements of the ground surface and the pipeline were measured and recorded. The measured settlements and the calculated settlements were compared and analyzed. Figure 3 shows the measured settlements and

TABLE 1: Basic mechanical parameters related to the soil layer and the shielding.

Material type	Thickness (m)	Density ($\text{kN}\cdot\text{m}^{-3}$)	Elastic modulus (MPa)	Cohesion (kPa)	Friction angle ($^\circ$)	Poisson ratio
Fill	4	17.5	9	10	8	0.39
Clay	25	19.8	16.1	55	15	0.29
Silty clay	11	19.6	23	36	18	0.28
Shield shell	0.05	78	2.5×10^5	—	—	0.2
Segment	0.3	25	3.8×10^3	—	—	0.2
Grouting layer	0.05	20	5.0×10^2	—	—	0.3
Concrete pipeline	0.1	25	2.5×10^4	—	—	0.2

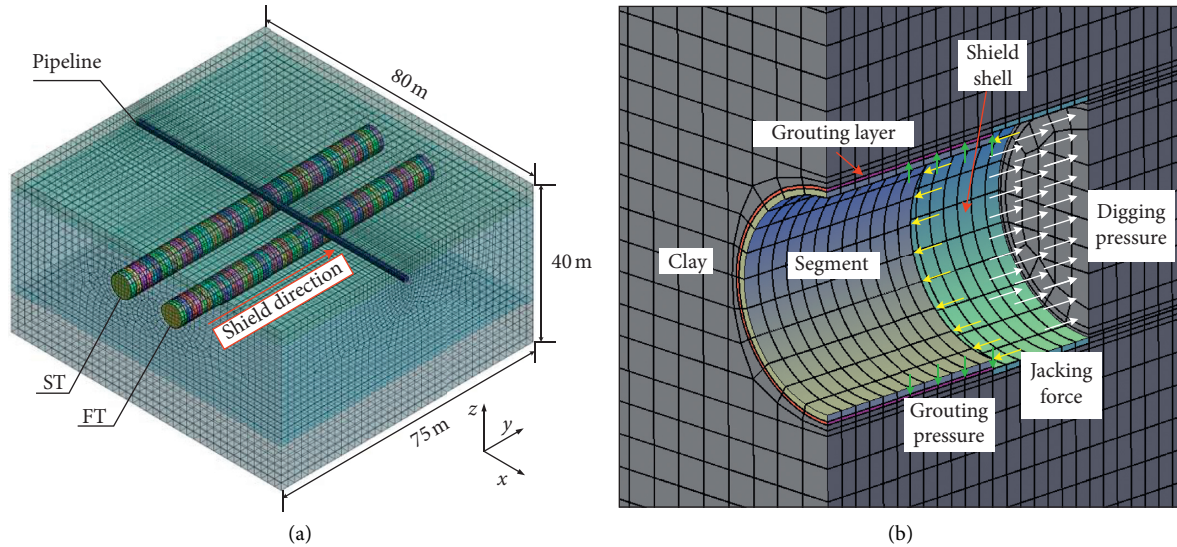


FIGURE 2: The finite-element model. (a) The mesh. (b) Simulation of shield driving.

TABLE 2: Mechanical parameters of the HS model of the soil layer.

Soil layer	E_{50}^{ref} (kN/m^2)	$E_{\text{oed}}^{\text{ref}}$ (kN/m^2)	$E_{\text{ur}}^{\text{ref}}$ (kN/m^2)	k_0^{NC}	λ	p^{ref} (kN/m^2)	n	φ ($^\circ$)
Fill	8054	8054	24162	0.65	0.9	100	0.8	8
Clay	12167	12167	36501	0.39	0.9	100	0.7	10
Silty clay	13286	13286	39858	0.38	0.9	100	0.6	17

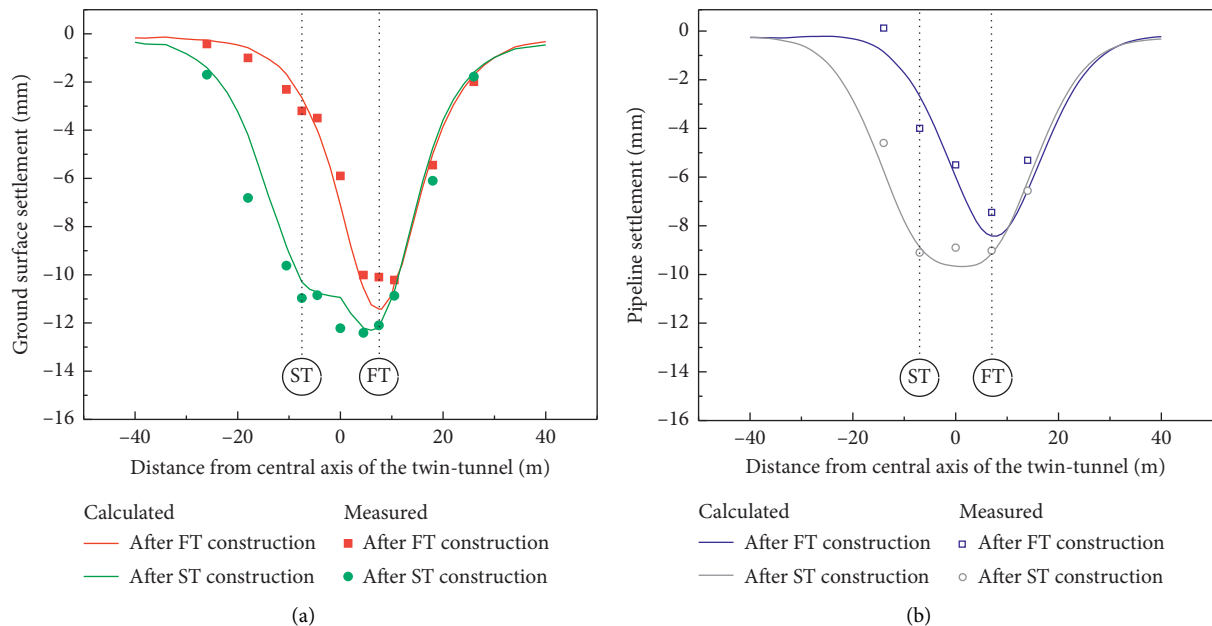


FIGURE 3: Comparison of calculated and measured settlement development. (a) Ground surface settlement. (b) Pipeline settlement.

the simulated calculation settlements after the FT construction and ST construction. According to Figure 3(a), after the FT construction was completed, the differences between the measured and calculated results of ground surface settlement were in the range of 0.1 mm–1.3 mm. The measured maximum settlement was -10.2 mm, the calculated maximum settlement was -11.4 mm, and the difference between the two was 11%. It can be seen from Figure 3(a) that the distribution of the two results was consistent. With consideration of the error of the measured result, it was believed that the calculated measured result was consistent with the measured result. After the ST construction was completed, the measured settlement and the calculated settlement were further developed. The final maximum measured settlement and the calculated settlement of the ground surface were -12.4 mm and -12.2 mm, respectively. The two were basically the same with a 2% difference, and the positions of maximum settlements were consistent. Through the above analysis, we found that the measured settlement and the calculated settlement curve had the same shape, but the measured result had a larger settlement range. This might have been due to external disturbance factors such as the vehicle dynamic loads and the construction loads above the ground. Figure 3(b) shows the comparison of the measured settlements and the calculated settlements of the pipeline. This comparison showed that after the FT construction and after the ST construction, although there were some differences between the measured settlements and the calculated settlements, the settlement distributions of the two were consistent. It was assumed in the model that the pipeline was continuous, but in practice it was not, and this was one of the reasons for the differences. The analysis of the measured and simulated settlement values showed that the calculation results of the model were credible. Therefore, further analysis could be made based on the results of this model.

5. Analysis of Results

5.1. Ground Surface Settlement. Based on the calculated results of the above model, a detailed analysis of the settlement of the ground surface was necessary. In the subsequent analysis, “-” indicated that the excavation plane had not yet reached the pipeline, “0 m” indicated that the excavation plane was directly below the pipeline, and “+” indicated that the excavation plane had undercrossed the pipeline. The direction of the pipeline extension was recorded as the x -axis, and the direction of the shielding tunnel was recorded as the y -axis. The FT centerline was at $x = 7.5$ m, and the ST centerline was at $x = -7.5$ m.

Figure 4 shows the settlement curve of the ground surface above the pipeline during the FT construction. When the excavation plane had not yet reached the pipeline and it was a long distance from the pipeline, the ground above the pipeline was not affected. When the excavation plane continued to approach, the ground surface began to settle. Figure 4 shows that when the excavation plane was 15 m away from the pipeline ($y = -15$ m), significant settlement began to appear on the ground above the FT centerline. As

the construction continued, the FT excavation plane gradually approached the pipeline, the settlement of the ground surface gradually increased, and the settlement was symmetrically distributed. When the excavation plane was directly below the pipeline ($y = 0$ m), the maximum settlement of the ground surface reached 4.9 mm. When the excavation plane had undercrossed the pipeline and was 15 m away from the pipeline ($y = +15$ m), the ground surface settlement was essentially stable. The maximum settlement of the ground surface was 11.4 mm after the completion of the FT construction. The maximum settlement occurred on the FT centerline ($x = -7.5$ m). During the FT construction, the rate of ground surface settlement development gradually increased in the beginning and then gradually decreased after undercrossing the pipeline. Finally, the settlement did not increase. The settlement developed the fastest in the range of -6 m to 6 m. The settlement generated in this range accounted for 52% of the total settlement during the FT construction. Therefore, more attention had to be paid to the excavation around the pipeline.

After the FT construction was completed, the settlement of the ground surface continued to be analyzed during the ST construction. Figure 5 shows the settlement curve during the ST construction. As the figure shows, during the ST construction, the developments of ground surface settlements on both sides of the ST centerline were inconsistent. The settlement range and the settlement value on the left side were larger. Furthermore, the settlement on the right side of the FT tunnel ($x > 7.5$ m) remained basically unchanged during the ST construction. This could be explained by the construction disturbance. The ground surface on the right side of the FT tunnel has been greatly disturbed during the FT construction. During the ST construction, because of the long distance and small disturbance, the secondary disturbance did not cause further development of the settlement. The ground surface inside the twin-tunnel area was affected by two disturbances. The effects of the two disturbances were different. It can be seen from the figure that the second disturbance caused by the ST construction had less influence. The ground surface settlement around the ST also remained unchanged at the beginning, and the settlement did not increase until the excavation plane was 9 m away from the pipeline ($y = -9$ m). Subsequently, the ground surface settlement gradually increased with the progress of the ST construction, and the location of the maximum settlement slowly approached the ST. After the excavation plane had undercrossed the pipeline and was 9 m away from the pipeline ($y = +9$ m), the settlement was essentially stable. After the ST construction was completed, that is, when the entire twin-tunnel was completed, the maximum settlement of the ground surface was 12.3 mm, and the maximum settlement was located inside the twin-tunnel area ($x = 5$ m).

After comparing and analyzing the development of the ground surface settlement during the FT and ST construction, it was evident that the FT construction had a greater impact on the settlement of the ground surface. The influence range was wider and the settlement developed more quickly. For the three points on the ground surface on $x = -7.5$ m, 0 m, and 7.5 m from left to right, the settlement

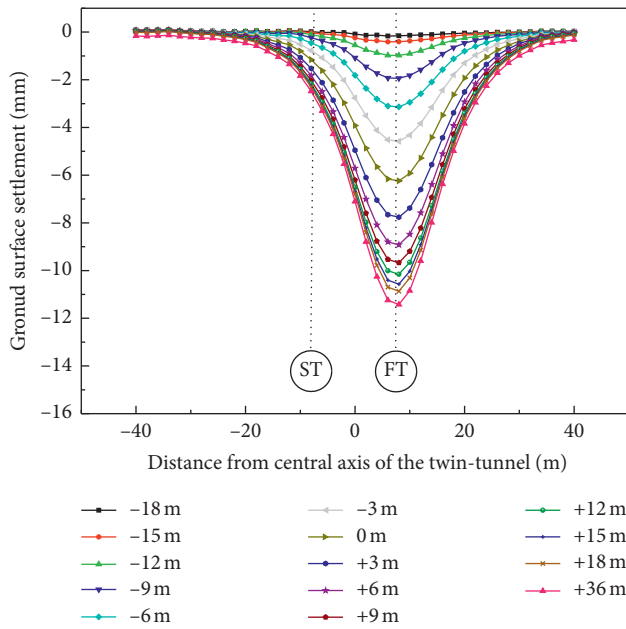


FIGURE 4: The ground surface settlement directly above the pipeline during the FT construction.

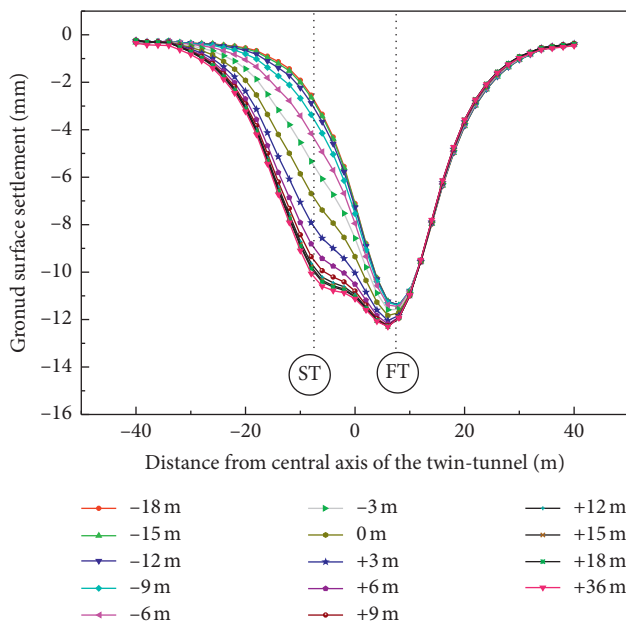


FIGURE 5: The ground surface settlement directly above the pipeline during the ST construction.

caused by the FT construction accounted for 28%, 64%, and 94% of the total settlement, respectively. The ST construction could only increase the ground surface settlement directly above the ST, and it had almost no influence on the ground surface above the FT.

5.2. Pipeline Settlement. Figure 6 shows the settlement of the pipeline during the FT construction and the ST construction. As the figure shows, the settlement development of the pipeline was consistent with the settlement development of

the ground surface. During the FT construction, the settlement of the pipeline was centered on the FT centerline, and as the construction progressed, the settlement of the pipeline continued to increase. After the completion of the FT construction, the settlement curve was symmetrically distributed. The maximum settlement was 8.4 mm, which occurred on the FT centerline. Similar to the development of the ground surface settlement, the pipeline settlement continued to develop during the ST construction. The settlement center slowly approached the ST. After the ST construction was completed, the maximum settlement of the ground surface was 9.7 mm and the maximum settlement was located inside the twin-tunnel area ($x=1$ m). At the same time, there were some differences between the settlements of the ground surface and the pipeline. The final settlement curve of the ground surface was no longer symmetrical, but the final settlement curve of the pipeline remained essentially symmetrical. This difference in settlement curves between the ground surface and the pipeline was due to the difference in the stiffness. The stiffness of the pipeline was greater and the pipeline had a greater ability to resist construction disturbance. The effect of the difference of the stiffnesses on the settlements is discussed later in Section 6.

Three points P_1 , P_2 , and P_3 (as shown in Figure 1) on the pipeline were selected. Figure 7 shows the settlement developments of the three points during the twin-tunnel construction. As shown in the figure, during the FT construction, the settlement on the pipeline developed in three stages: stage I: when the excavation plane had not reached $y=15$ m (-36 to -15 m), the settlement was stable and unchanged; stage II: in the range of -15 m to $+18$ m, the settlement increased linearly; and stage III: the settlement developed slowly until it stabilized after the excavation plane was 18 m away from the pipeline ($+18$ m to $+36$ m). The settlement of the pipeline was produced mainly in stage II. In stage II, the settlement increased linearly with different rates at different locations. The closer the location was to the excavation plane, the faster the settlement development was. During the ST construction, the settlement developments of the three points on the pipeline were the same as those of the FT construction. Compared with the FT construction, in stage II', the time became shorter and the settlement developments were less. The settlement of P_1 developed the fastest and increased the most. After the ST construction, the final settlement differences between three points were reduced, and the settlements were all approximately 9 mm. The settlement above the centerline of the twin-tunnel (P_2) was the largest, and the settlement above the FT centerline (P_1) was the smallest.

6. Study of the Influence of the Twin-Tunnel Undercrossing the Pipeline

Currently, the design and the construction of city tunnels mostly involve two parallel tunnels. To avoid excessive disturbance, the construction scheme of a twin-tunnel with the same shielding directions and different shielding time is widely adopted [33]. The excavation planes of the two

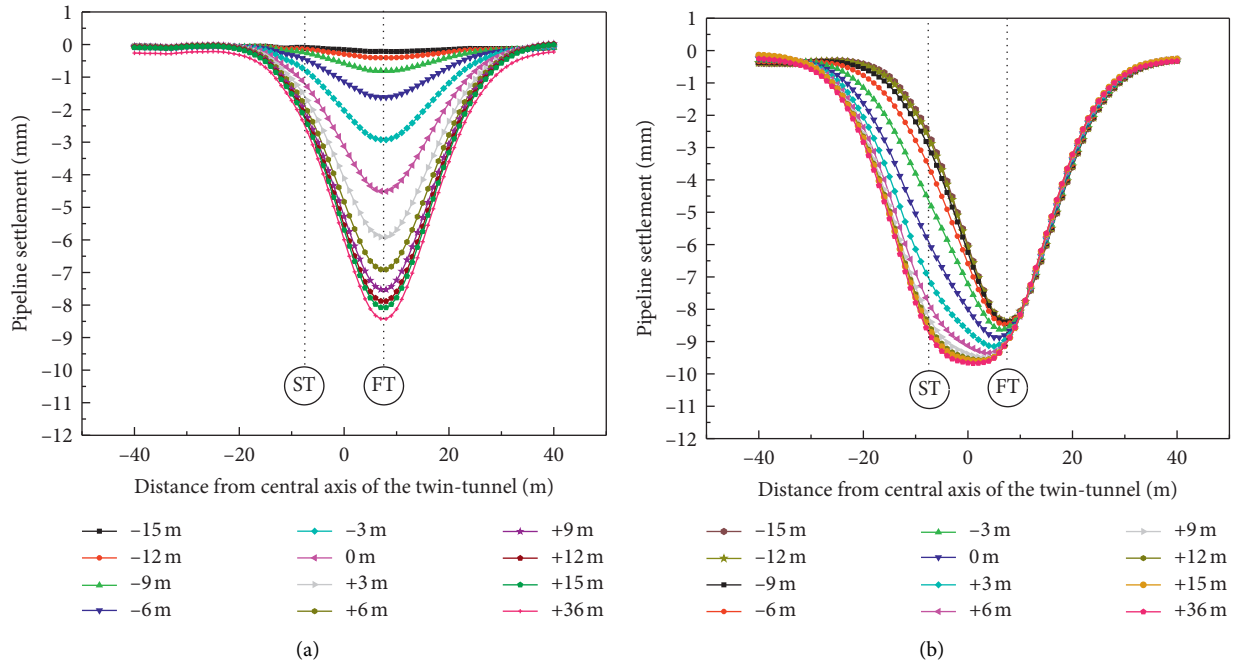


FIGURE 6: Settlement of the pipeline during construction. (a) FT construction. (b) ST construction.

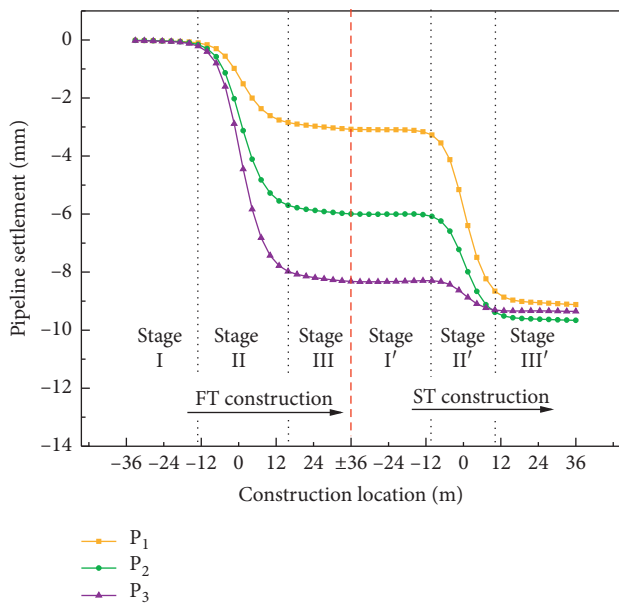


FIGURE 7: Settlement change of three points on the pipeline during the twin-tunnel construction.

tunnels always maintain a certain distance during construction. From the above analysis, it was evident that the ST construction caused a second disturbance to the stabilized soil and pipeline. The Earth pressure was redistributed and the settlement changed accordingly. At that time, the influence of the twin-tunnel construction on the ground surface and the pipeline was more complicated.

Many factors determined the settlement of the ground surface and the pipeline. These factors could be divided into two types. One type of factor involved tunnel parameters

such as the tunnel depth, the twin-tunnel space, and the construction method. The other type involved the pipeline parameters, such as the size and the stiffness of the pipeline, the pipeline-soil distance, and the pipeline-soil relative stiffness. These parameters determined the formation loss rate V_{loss} and the settlement tank width i (V_{loss} determined the depth and i determined the width [34]). Considering the noted factors, the key parameters including the twin-tunnel space L and the pipeline-soil relative stiffness K were selected for further study.

6.1. Influence of the Twin-Tunnel Space L on the Settlements. Considering the actual project, the twin-tunnel space L was taken as 9 m ($1.5 D$), 12 m ($2 D$), 15 m ($2.5 D$), 18 m ($3 D$), and 21 m ($3.5 D$) for calculation and analysis. The other variables remained constant during the calculation.

Figure 8 shows the settlement curves of the ground surface and the pipeline at different spaces in the twin-tunnel. For different spaces, the settlement developments during the FT construction were the same, and the final maximum settlement values were the same. The spaces in the twin-tunnel were different, the impact of the ST construction was significantly different, and the final settlements after ST construction were significantly different. Figure 8(a) shows the final settlement curves of the ground surface after the ST construction. From the figure, it could be seen that the larger the twin-tunnel space was, the larger the range of the ground surface settlement was. All of the maximum settlements of the ground surface occurred in the range of $-1/2L-1/2L$. Additionally, as the space increased, the location of the maximum settlement became closer to the FT centerline. Out the range of $-L-L$, the greater the space was, the greater the settlement of each point on the ground surface was.

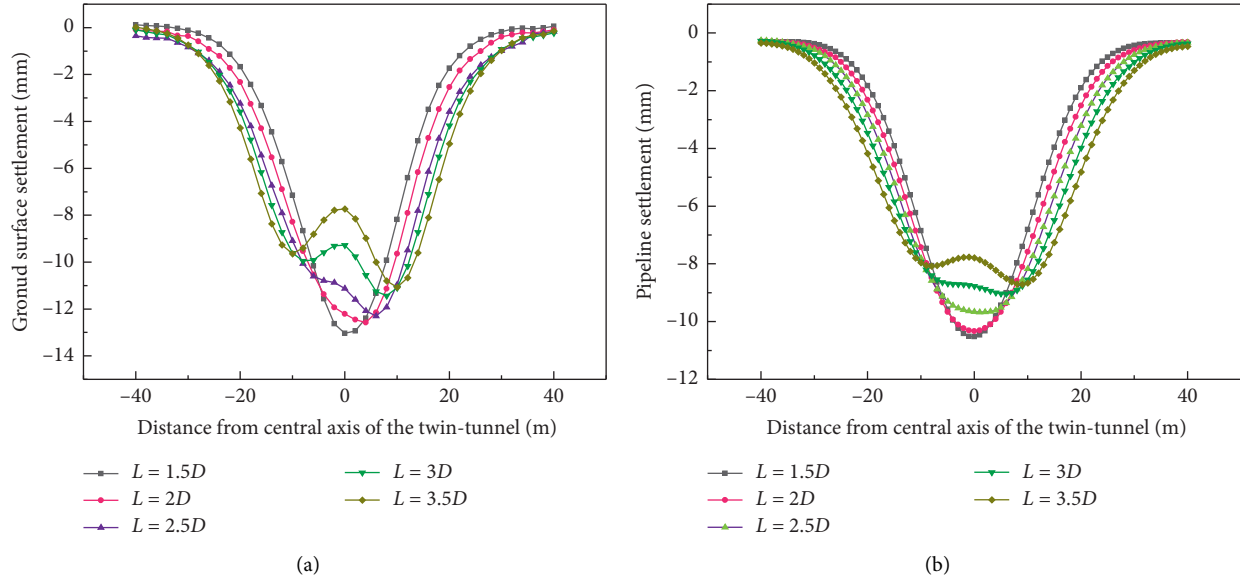


FIGURE 8: The settlement during ST construction with different spaces. (a) Ground surface settlement. (b) Pipeline construction.

Between $-L-L$, as the space increased, the settlement of the ground surface gradually decreased, and the settlement curve had a significant difference. According to the study of Xu [9], we could judge whether the curve conformed to the Gaussian distribution through the linear relationship of $\ln(S/S_{\max}) \sim x^2$ and judge whether the curve was symmetric through the slope. Through the above analysis, it could be found when $L = 1.5D$, the settlement curve conformed to a Gaussian distribution, which could be calculated with the Peck formula. When $L = 2D$, the settlement curve was no longer symmetrical. When $L = 2.5D$, the settlement curve approached the W-shape. When the tunnel space continued to increase to $3D$, the ground surface settlement curve was obviously W-shaped. The figure shows that the twin-tunnel space continued to increase, and the difference between the two maximum settlements of the W-shaped settlement curve gradually decreased. It could be speculated that when the twin-tunnel space was sufficiently large, the two maximum settlements would be the same, and the settlement curve of the ground surface would be a standard W-shape. In that case, the construction of the two tunnels would not affect each other, and the twin-tunnel construction could be calculated separately and superimposed.

The settlements of the pipeline at different spaces are shown in Figure 8(b). Similarly, out the range of $-L-L$, as the space L increased, the settlement of the corresponding point on the pipeline increased and the settlement range increased. In the range of $-L-L$, the settlement of the pipeline decreased with the increase of the space, and the shape of the settlement curve was different. When $L = 1.5D, 2D, 2.5D$, the settlement curve of the pipeline was V-shaped. When $L = 3D$, the settlement curve of the pipeline could be regarded as U-shaped, and when the space continued to increase to $3.5D$, the settlement curve appeared to have two settlement centers above the twin-tunnel, corresponding to the two different maximum settlements. The settlement curve was obviously W-shaped.

Table 3 provides the statistics of the settlement characteristics of the ground surface and the pipeline for different twin-tunnel spaces. By comparing the settlement of the ground surface with the settlement of the pipeline, it could be found that the settlement range and the settlement value of the pipeline were smaller than the settlement of the ground surface for each space. Additionally, the location of the maximum settlement of the ground surface was closer to the FT centerline. For the same space, when the pipeline settlement curve was W-shaped, the ground surface settlement curve was definitely W-shaped. Furthermore, when the ground surface settlement curve was not W-shaped, the pipeline settlement was definitely not W-shaped. That is, the ground surface was more prone to have a W-shaped settlement curve than the pipeline was. When the settlement curve was W-shaped, the difference between the two maximum settlements of the pipeline was smaller than that of the ground surface. The settlement difference between the ground surface and the pipeline in the above analysis was due to the difference in the stiffness.

6.2. Influence of the Stiffness of the Pipeline and Soil on the Settlements. When considering the impact of the stiffness on the settlement, many factors such as the elastic modulus of the soil, the cross-sectional shape, area, and elastic modulus of the pipeline had to be considered. To facilitate the research, the parameter K was defined as the pipeline-soil relative rigidity stiffness according to the study of Vorster et al. [35]:

$$K = \frac{EI}{i_f^3 r_0 E_s}, \quad (4)$$

where EI is the stiffness of the pipeline, i_f is the settlement tank width caused by the FT construction, r_0 is the outer radius of the pipeline, and E_s is the elastic modulus of the

TABLE 3: Settlements of the ground surface and the pipeline with different spaces.

L	Settlement range width (m)		Maximum settlement (mm)		Maximum settlement location (m)		Settlement curve shape	
	Surface	Pipeline	Surface	Pipeline	Surface	Pipeline	Surface	Pipeline
1.5 D	60	52	-13.0	-10.5	$x = 0$	$x = 0$	V	V
2 D	65	54	-12.6	-10.3	$x = 4$	$x = 0$	U	V
2.5 D	68	58	-12.3	-9.7	$x = 6$	$x = 1$	U	U
3 D	72	62	-11.4(-9.9)	-9.0	$x = 8(-8)$	$x = 6$	W	U
3.5 D	73	66	-11.1(-9.6)	-8.7 (-8.1)	$x = 10(-10)$	$x = 8(-8)$	W	W

Note: there were two maximum settlements in the W-shape, and the other maximum settlement was in the bracket.

soil. Combined with the research of Zhao et al. [25], i_f is the width of the ground surface settlement tank.

In actual engineering, pipelines for different purposes have different sizes and materials. In general, common pipelines include polyvinyl chloride (PVC) pipelines (elastic modulus of 2.5 GPa), concrete pipelines (elastic modulus of 25 GPa), cast iron pipelines (elastic modulus of 150 GPa), and steel pipelines (elastic modulus of 200 GPa). When the twin-tunnel space was maintained at 15 m, the four relative stiffnesses were used for calculation. The settlement curves after the completion of the FT construction and the ST construction are shown in Figure 9.

During the FT construction, the larger the stiffness of the pipeline was, the smaller the settlement of the pipeline was. The width of the settlement area was between 10 D and 16 D . The settlement characteristics of the ground surface were similar to those of the pipeline. The characteristics of the ground surface settlement for different stiffnesses were different, and the settlement tank width i_f was different. The values of i_f for different stiffness conditions are shown in Table 4. The settlements of the ground surface after the ST construction are shown in Figure 9(a). When the pipeline-soil relative stiffness K was small, the settlement of the ground surface was W-shaped and the settlement was large. As the pipeline-soil relative rigidity stiffness increased, the settlement curve gradually developed toward a U-shape. Because of the small stiffness of the soil, it was difficult for the ground surface to have a V-shaped settlement. The settlement curves of the pipeline after the ST construction with different pipeline-soil relative stiffnesses are shown in Figure 9(b). When K was small, the settlement curve of the pipeline was the same as the settlement of the ground surface. To some extent, the settlement of the pipeline could be replaced by the ground surface settlement. When K increased to 1.9, the pipeline settlement was U-shaped. When K continued to increase, the pipeline settlement was V-shaped. The settlement characteristics of the ground surface and the pipeline are given in Table 4.

6.3. Judgment of the Shape of the Settlement Curve. Based on this analysis, it was obvious that the settlement curves of the ground surface and the pipeline had different characteristics at different spaces and stiffnesses. To better understand the settlement characteristics of the ground surface and the pipeline, 20 sets of models with different spaces ($L = 1.5 D, 2 D, 2.5 D, 3 D, 3.5 D$) and different pipeline-soil relative stiffnesses ($K = 0.4, 1.9, 6.6, 8.8$) were

calculated. The shapes of the settlement curves of the ground surface and the pipeline after the ST construction are summarized in Table 5. As shown in Table 5, as the space increased and the relative stiffness decreased, the settlement curves of the ground surface and the pipeline developed from V-shaped to W-shaped. When $L \leq 1.5 D$, the ground settlement was V-shaped for the four kinds of stiffnesses, and the construction disturbance of the twin-tunnel could be equivalently calculated. When the space increased, the settlements of the ground surface and the pipeline began to differ. When $L \geq 3 D$, the settlement of the surface was W-shaped for each stiffness. When the space L was between 1.5 D and 3 D , the shape of the settlement curve depended on the relative stiffness. For the settlement of the pipeline, when $L \leq 2 D$ or $K \geq 6.6$, the settlement curve was V-shaped or U-shaped. The settlement of the pipeline was W-shaped only when the space was large, and the relative stiffness was small. Table 5 also shows that, for the two factors of the twin-tunnel space and the pipeline-soil relative rigidity, the twin-tunnel space had a greater impact on the settlement. Additionally, when the change of the relative stiffness was small, the effect on the settlement was negligible.

6.4. Further Study of the W-shaped Settlement. Based on this research, it was found that the settlement curves of the ground surface and the pipeline could be divided into W-shaped, U-shaped, and V-shaped settlement curves because of their different spaces and stiffnesses. The V-shaped and U-shaped settlements only had one maximum settlement, but the W-shaped settlement had two maximum settlements. More attention was paid to the maximum settlements. Through the previous analysis, it could be known that when the W-shaped settlement occurred, the two maximum settlements appeared on the centerlines of the twin-tunnel. Because of the greater stiffness of the pipeline, it was difficult for W-shaped settlement to occur in the actual project. Therefore, only the W-shaped settlement of the ground surface was discussed. The W-shaped settlement meant that the settlement curve had two maximum settlements, namely, $S_{\max f}$ and $S_{\max s}$ in equation (3). Defining $C = S_{\max s}/S_{\max f}$, C reflected the impacts of the FT construction and the ST construction.

6.4.1. Influence of the Twin-Tunnel Space on the W-Shaped Settlement. Table 5 shows that when the pipe-soil relative stiffness K was 0.4 and the space L was 2 $D, 2.5 D, 3 D$, or

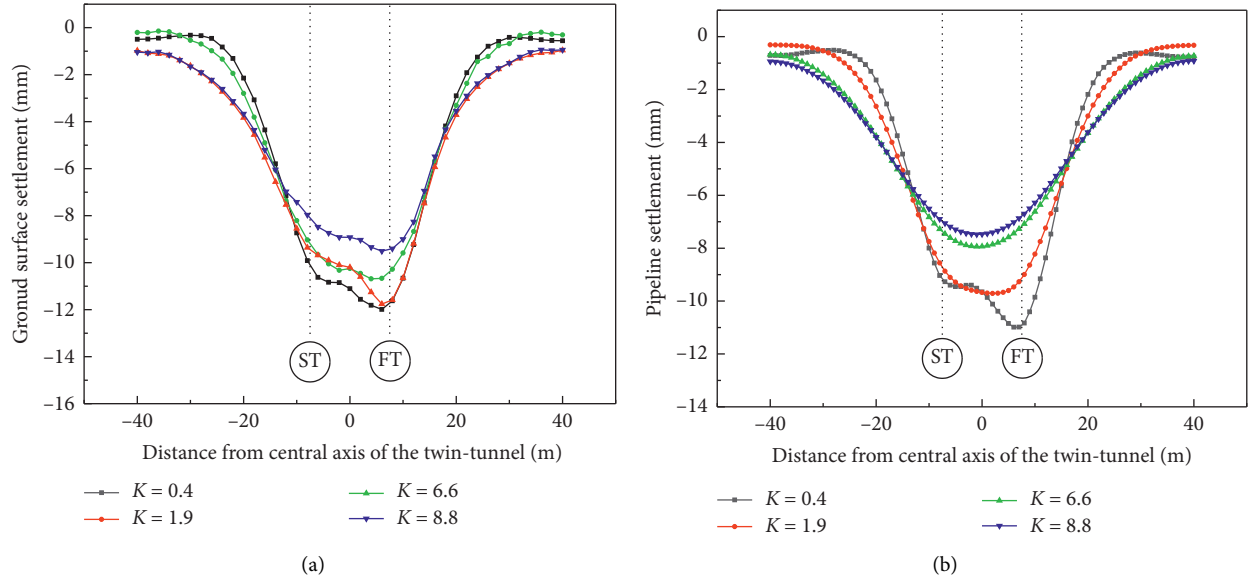


FIGURE 9: The settlement during the ST construction with different relative stiffnesses. (a) Ground surface settlement. (b) Pipeline construction.

TABLE 4: Settlements of ground surface and the pipeline with different rigidities.

Material	E (GPa)	i_f (m)	K	Surface settlement	Pipeline settlement
PVC	2.5	8	0.4	W	W
Concrete	25	9	1.9	W	U
Cast iron	150	11	6.6	W	V
Steel	200	12	8.8	U	V

TABLE 5: Settlement curve shapes for the ground surface and the pipeline.

K	L				
	$1.5 D$	$2 D$	$2.5 D$	$3 D$	$3.5 D$
0.4	V(V)	W(U)	W(U)	W(W)	W(W)
1.9	V(V)	U(V)	U(U)	W(U)	W(W)
6.6	V(V)	V(V)	U(V)	W(U)	W(U)
8.8	V(V)	V(V)	U(V)	W(V)	W(U)

Note: the curve shape of the pipeline settlement is in the bracket.

$3.5 D$, the ground surface settlements were W-shaped. This set of data was further analyzed. The statistics of the maximum settlements of the ground surface for the same stiffness and different spaces are shown in Figure 10. After the FT construction, the maximum settlement ($S_{\max f}$) of the ground surface was 11.5 mm. After the ST construction, $S_{\max f}$ increased further, and another maximum settlement $S_{\max s}$ was formed. From Figure 10, it could be inferred that when $L < 2 D$, the two maximum settlements were almost equal; that is, $C = 1$. In fact, the settlement might be U-shaped, and this was consistent with the U-shaped settlement characteristics. Figure 10 shows that as the space increased, $S_{\max f}$ and $S_{\max s}$ both decreased. At the same time, for the spaces of $2 D$, $2.5 D$, $3 D$, and $3.5 D$, C was 0.98, 0.89, 0.85, and 0.85, respectively. Within a certain range, as

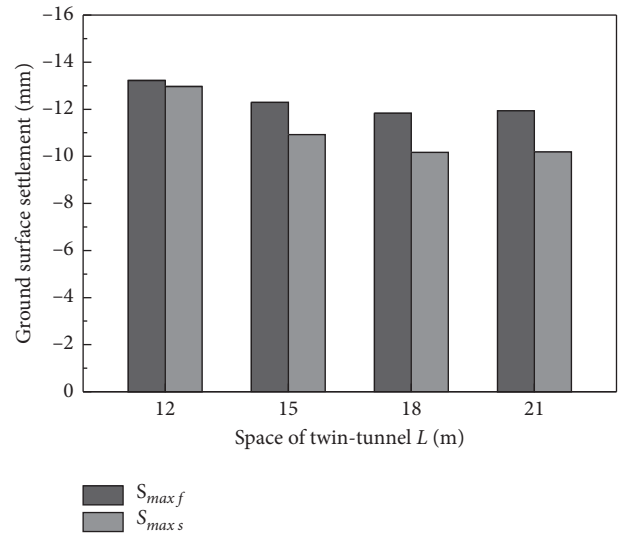


FIGURE 10: $S_{\max f}$ and $S_{\max s}$ for different spaces.

the space increased, the difference between the two maximum settlements became smaller and smaller. When the twin-tunnel space was large enough, the FT and ST construction did not affect each other, the shape of the settlement curve was a standard symmetric W-shaped, and the value of C was also 1. This showed that as the space changed from small to large, both $S_{\max f}$ and $S_{\max s}$ decreased, but the magnitude of the reduction was different, and the two maximum settlements changed from being the same ($C = 1$) to having different values. Based on the statistical results, C was the smallest when the space was 21 m. Then, C increased, and the two maximum settlements were eventually the same ($C = 1$). That is, in the process of L increasing from small to large, C began to decrease from 1, then started to increase at around 0.85, and finally increased to 1. The minimum value

TABLE 6: $S_{\max f}$ and $S_{\max s}$ for different relative stiffnesses.

K	$S_{\max f}$ (mm)	$S_{\max s}$ (mm)	C
0.4	-11.9	-10.2	0.85
1.9	-11.7	-10.1	0.86
6.6	-11.5	-9.9	0.86
8.8	-11.4	-9.8	0.86

of C was around 0.85, and at that time, the difference between the two maximum settlements was 1.74 mm.

6.4.2. *Influence of the Pipeline-Soil Relative Stiffness on the W-Shaped Settlement.* Table 5 shows that when the space was $L = 3D$ and $3.5D$, the settlement curve of the ground surface for the four stiffnesses was W-shaped. Taking $L = 3.5D$ as an example, the relationship between C and the relative stiffness was as shown in Table 6. Table 6 shows that the greater the pipeline-soil relative stiffness was, the smaller the $S_{\max f}$ and $S_{\max s}$ were. However, C was essentially unchanged and stable at about 0.86, indicating that when the W-shaped settlement occurred on the ground, the pipeline-soil relative stiffness had basically no effect on C .

7. Conclusions

In this research, a three-dimensional finite element model was established and verified according to the engineering background of a section of the Hefei No. 4 metro line. Based on the numerical model, the settlement characteristics of the surface and the pipeline were studied. According to the calculated results, the following conclusions could be drawn:

- (1) The settlement development characteristics of the ground surface and the pipeline were consistent. As the tunnel construction progressed, the settlement developed at different rates. The closer the tunnel construction surface was to the pipeline, the faster the settlement developed. After the FT construction, the settlement curves of the ground surface and the pipeline conformed to a Gaussian distribution. Additionally, after the ST construction, the settlements continued to develop, and the final settlement curves were no longer completely symmetrical.
- (2) Compared with the ST construction, the FT construction had a greater impact on the settlements of the ground surface and the pipeline. During the ST construction, the settlement continued to develop on the basis of the impact of the FT construction. In addition, the position of maximum settlement continued to move toward the ST centerline. The position maximum settlement was eventually located between the FT centerline and the ST centerline.
- (3) Many factors affected the final settlement curve shapes of the ground surface and the pipeline. The settlement curve with different factors might be V-shaped, U-shaped, or W-shaped. The twin-tunnel space L and the pipeline-soil relative stiffness K had a greater influence. As the twin-tunnel space increased

and the pipeline-soil relative stiffness decreased, the settlement curve gradually changed from being V-shaped to being W-shaped. Additionally, L had a greater influence on the final settlement curve. The ground was more likely to have a W-shaped settlement.

- (4) For the W-shaped ground surface settlement, C was defined as the ratio of two maximum settlement values. As the space L increased, the ratio C began to decrease from 1 to 0.85 and then gradually increased to 1. The relative stiffness K had essentially no effect on C , and C was stable at approximately 0.86.

It should be noted that, in this research, all the analysis was based on a project of the Hefei no. 4 metro line, irrespective of other construction schemes/projects. An in-depth analysis concerning different tunnel depths and pipeline-tunnel spacing is deemed necessary to better study the tunnel construction-induced disturbance. The results would be discussed in another paper.

Data Availability

The data used to support the findings of this study are available from the corresponding author upon request.

Conflicts of Interest

The authors declare that there are no conflicts of interest regarding the publication of this paper.

Acknowledgments

This work was supported by the National Natural Science Foundation of China (grant no. 51878005).

References

- [1] W.-C. Cheng, L. Wang, Z.-F. Xue, J. C. Ni, M. M. Rahman, and A. Arulrajah, "Lubrication performance of pipejacking in soft alluvial deposits," *Tunnelling and Underground Space Technology*, vol. 91, Article ID 102991, 2019.
- [2] Y. Liang, X. Y. Chen, J. S. Yang, and L. C. Huang, "Risk analysis and control measures for slurry shield tunneling diagonally under an urban river embankment," *Advances in Civil Engineering*, vol. 2020, Article ID 8875800, 11 pages, 2020.
- [3] W.-C. Cheng, J. C. Ni, A. Arulrajah, and H.-W. Huang, "A simple approach for characterising tunnel bore conditions based upon pipe-jacking data," *Tunnelling and Underground Space Technology*, vol. 71, pp. 494–504, 2018.
- [4] Y. Miao, Y. Zhong, B. Ruan, K. Cheng, and G. Wang, "Seismic response of a subway station in soft soil considering the structure-soil-structure interaction," *Tunnelling and Underground Space Technology*, vol. 106, Article ID 103629, 2020.
- [5] M. I. Peerun, D. E. L. Ong, C. S. Choo, and W. C. Cheng, "Effect of interparticle behavior on the development of soil arching in soil-structure interaction," *Tunnelling and Underground Space Technology*, vol. 106, Article ID 103610, 2020.
- [6] J. Shi, Y. Wang, J. Yu, and C. W. W. Ng, "Buried pipeline responses to ground displacements induced by adjacent static

- pipe bursting,” *Canadian Geotechnical Journal*, vol. 86, pp. 89–99, 2019.
- [7] X. R. Tan, H. Zhang, G. Zhang, Y. M. Zhu, and P. Tu, “An improved method for predicting the greenfield stratum movements caused by shield tunnel construction,” *Applied Sciences*, vol. 9, no. 21, p. 4522, 2019.
 - [8] R. B. Peck, “Deep excavations and tunneling in soft ground,” in *Proceedings of the 7th International Conference on Soil Mechanics and Foundation Engineering*, pp. 225–290, Mexico City, Mexico, 1969.
 - [9] X. M. Xu, “Applicability analysis of Peck formula in Hefei area and study on the ground subsidence of shield construction near the deep foundation,” Master thesis, Hefei University of Technology, 2016, in Chinese.
 - [10] H. Yang, F. Liu, and S. Lin, “Investigation on the 3D ground settlement induced by shallow tunneling considering the effects of buildings,” *KSCE Journal of Civil Engineering*, vol. 24, no. 2, pp. 365–376, 2020.
 - [11] Z. P. Song, X. X. Tian, Y. W. Zhang, Y. Shao, and Y. Feng, “A new modified Peck formula for predicting the surface settlement based on stochastic medium theory,” *Advances in Civil Engineering*, vol. 2019, Article ID 7328190, 14 pages, 2019.
 - [12] P. B. Attewell, J. Yeates, and A. R. Selby, *Soil Movements Induced by Tunneling and Their Effects on Pipelines and Structures*, Chapman & Hall, New York, NY, USA, 1986.
 - [13] G. Wei, “Establishment of uniform ground movement model for shield tunnels,” *Chinese Journal of Geotechnical Engineering*, vol. 29, pp. 554–559, 2007, in Chinese.
 - [14] G. Wei, “Prediction of ground deformation induced by shield,” *Chinese Journal of Rock Mechanics and Engineering*, vol. 28, pp. 418–424, 2009, in Chinese.
 - [15] G. Wei, S. Y. Pang, and S. M. Zhang, “Prediction of ground deformation induced by double parallel shield tunneling,” *Disaster Advances*, vol. 6, pp. 91–98, 2013.
 - [16] M. Huang, X. Zhou, J. Yu, C. F. Leung, and J. Q. W. Tan, “Estimating the effects of tunnelling on existing jointed pipelines based on Winkler model effects of tunneling on existing jointed pipelines based on Winkler model,” *Tunnelling and Underground Space Technology*, vol. 86, pp. 89–99, 2019.
 - [17] X. Shi, C. X. Rong, H. Cheng, L. Z. Cui, and J. Kong, “An energy solution for predicting buried pipeline response induced by tunneling based on a uniform ground movement model,” *Mathematical Problems in Engineering*, vol. 2020, Article ID 7905750, 12 pages, 2020.
 - [18] X. Shi, C. X. Rong, H. L. Wang, L. Z. Cui, H. B. Cai, and B. Wang, “Analytical study of soil displacement induced by twin shield tunneling in semi-infinite viscoelastic ground,” *Advances in Civil Engineering*, vol. 2020, Article ID 8839010, 20 pages, 2020.
 - [19] Y. Wang, J. Shi, and C. W. W. Ng, “Numerical modeling of tunneling effect on buried pipelines,” *Canadian Geotechnical Journal*, vol. 48, no. 7, pp. 1125–1137, 2011.
 - [20] J. Shi, X. Zhang, L. Chen, and L. Chen, “Numerical investigation of pipeline responses to tunneling-induced ground settlements in clay,” *Soil Mechanics and Foundation Engineering*, vol. 54, no. 5, pp. 303–309, 2017.
 - [21] J. W. Shi, W. Yu, and C. W. W. Ng, “Three-dimensional centrifuge modeling of ground and pipeline response to tunnel excavation,” *Journal of Geotechnical and Geoenvironmental Engineering*, vol. 142, no. 11, Article ID 04016054, 2016.
 - [22] S. Ma, Y. Liu, X. Lv, Y. Shao, and Y. Feng, “Settlement and load transfer mechanism of pipeline due to twin stacked tunneling with different construction sequences,” *KSCE Journal of Civil Engineering*, vol. 22, no. 10, pp. 3810–3817, 2018.
 - [23] X. G. Li, T. Wang, and Y. Yang, “An investigation into the tunnel-soil-pipeline interaction by in situ measured settlements of the pipelines,” *Advances in Civil Engineering*, vol. 2020, Article ID 8850380, 18 pages, 2020.
 - [24] A. P. S. Selvadurai, *Elastic Analysis of Soil-Foundation Interaction*, Scientific Publishing Company, New York, NY, USA, 1979.
 - [25] Z. T. Zhao, J. Liu, T. Wang, and J. Y. Liu, “Relationship between the surface subsidence and the pipeline displacement induced by metro tunnel construction,” *Rock and Soil Mechanics*, vol. 36, pp. 1159–1166, 2015, in Chinese.
 - [26] Z. G. Zhang, M. S. Huang, C. P. Zhang, K. M. Jiang, Z. W. Wang, and X. G. Xi, “Complex variable solution for twin tunneling-induced ground movements considering nonuniform convergence pattern,” *International Journal of Geomechanics*, vol. 20, no. 6, p. 18, Article ID 704020060, 2020.
 - [27] X. L. Yang and J. M. Wang, “Ground movement prediction for tunnels using simplified procedure,” *Tunnelling and Underground Space Technology*, vol. 26, no. 3, pp. 462–471, 2011.
 - [28] S.-L. Chen, M.-W. Gui, and M.-C. Yang, “Applicability of the principle of superposition in estimating ground surface settlement of twin- and quadruple-tube tunnels,” *Tunnelling and Underground Space Technology*, vol. 28, pp. 135–149, 2012.
 - [29] A. S. N. Alagha and D. N. Chapman, “Numerical modelling of tunnel face stability in homogeneous and layered soft ground,” *Tunnelling and Underground Space Technology*, vol. 94, Article ID 103096, 2019.
 - [30] X. Shi, C. X. Rong, H. Cheng, L. Z. Cui, B. Wang, and S. C. Sun, “Analysis on deformation and stress characteristics of a Multibraced pit-in-pit excavation in a subway transfer station,” *Advances in Civil Engineering*, vol. 2020, Article ID 8844461, 19 pages, 2020.
 - [31] Y. B. Fu, S. Y. He, S. Z. Zhang, and Y. Yang, “Parameter analysis on hardening soil model of soft soil for foundation pits based on shear rates in Shenzhen Bay, China,” *Advances in Materials Science and Engineering*, vol. 2020, Article ID 7810918, 11 pages, 2020.
 - [32] Y. W. Zhang, “Study on the influence of shallow excavation on municipal underground pipeline,” Master thesis, Wuhan University of Technology, 2015, in Chinese.
 - [33] S. Li, P. Li, M. Zhang, and Y. Liu, “Influence of approaching excavation on adjacent segments for twin tunnels influence of approaching excavation on adjacent segments for twin tunnels,” *Applied Sciences*, vol. 10, no. 1, p. 98, 2020.
 - [34] F. B. Wu, H. Jin, Y. J. Shang, and Y. Q. Liu, “Study of building/structure settlement prediction method surrounding urban rail transit tunnel engineering,” *Chinese Journal of Rock Mechanics and Engineering*, vol. 32, pp. 3535–3544, 2013, in Chinese.
 - [35] T. E. Vorster, A. Klar, K. Soga, and R. J. Mair, “Estimating the effects of tunneling on existing pipelines,” *Journal of Geotechnical and Geoenvironmental Engineering*, vol. 131, no. 11, pp. 1399–1410, 2005.

Research Article

Evacuation Experiment Study in Up and Down Escape Staircase of Underground Road

Da-jun Yuan,¹ Hui Jin ,¹ Zhi-cong Chen,² and Sheng-nan Liu¹

¹School of Civil Engineering, Beijing Jiaotong University, Beijing 100044, China

²Xiamen Rail Transit Group Limited Corporation, Xiamen 361004, China

Correspondence should be addressed to Hui Jin; 17115308@bjtu.edu.cn

Received 13 June 2020; Revised 20 February 2021; Accepted 8 March 2021; Published 19 March 2021

Academic Editor: Wen-Chieh Cheng

Copyright © 2021 Da-jun Yuan et al. This is an open access article distributed under the Creative Commons Attribution License, which permits unrestricted use, distribution, and reproduction in any medium, provided the original work is properly cited.

To measure evacuation basic parameters, reveal evacuation performance, and study reasonable staircase spacing of up and down escape staircase in case of fire, an evacuation experiment, which was based on the most unfavorable evacuation scenario, was conducted. The experiment took personnel and vehicles of actual underground road traffic into account, and evacuation process image data were extracted and analyzed by artificial statistics. Experimental results indicate that the personnel plane evacuation speed is between 1.43 and 1.95 m/s, and the upstairs evacuation speed that is less affected by gender and age is mainly between 0.5 and 1.1 m/s; under the escape stairs width of 0.8 m, the average capacity of escape staircase is 0.7 P/s, and the entrance of the staircase is evacuation bottleneck and queuing phenomenon occurs. Based on the experiment, a calculation model of three-phase personnel net evacuation time was established. By simplifying the evacuation model, a calculation formula of the reasonable escape stair spacing considering the influence of multiple factors was proposed. And the proposed theoretical model was verified by project cases of up and down escape staircase. With 2 min emergency broadcasting time and 6 min Available Safety Evacuation Time of medium-sized fire as the Personnel Safety Evacuation Rule's reference, the recommended value of escape staircase spacing of single pipe double-deck two-way four-lane (double pipes double-deck two-way eight-lane) underground roads is 64.3 m.

1. Introduction

As the greatest security threat during the operation period, tunnel fire causes incalculable loss of life and property and also brings about a great negative social impact. Urban underground roads usually have the characteristics of dense traffic, large human loads, numerous entrances, and exits, and so on, which are different from ordinary road tunnels. Reasonable and effective evacuation escape channel arrangement is a prerequisite for the personnel's autonomous rescue and a necessary condition for professional firefighting rescue in the underground road fire.

Evacuation in the up and down escape staircase of the tunnel is a new evacuation pattern introduced with the emergence of the double-deck shield tunnel. At present, the traffic tunnel fire protection technology specification has not yet provided provision for escape stairs function requirements, which means that the standardized design of escape staircases

lacks a unified basis. Although the Shanghai Municipal Provincial Standard "Road Tunnel Design Code"(2008) [1] recommends that the escape stairs spacing should be controlled within 120 m, the width of stairs is not less than 0.8 m, and the maximum capacity of personnel is 1.0 P/s, but there is still no supporting theoretical and actual verification.

Reasonable escape stairs spacing was mainly studied by numerical simulation and on-site evacuation test. Some scholars established specific fire evacuation model scenarios through the joint simulation of fire field numerical simulation software such as FDS and personnel evacuation simulation software such as STEPS, Simulex, and EVAC-NET, and according to the specific engineering background, the prediction of the safety evacuation time, the safety check calculation of the escape channel spacing, and the optimization of the personnel evacuation strategy were carried out. Researches showed that the recommended escape stairs spacing is between 80 and 100 m [2–5].

Numerical simulation cannot reflect the real evacuation behavior and evacuation characteristics. Therefore, some scholars have carried out some on-site evacuation simulation tests to make up for the defects and deficiencies of computer numerical simulation. The attention was firstly paid to the personnel's behavior evacuation characteristics, evacuation signs, and other facilities on the choice of personnel escape exits under fire conditions [6, 7]. In recent years, some scholars investigated the characteristics of road walking speed in a full-scale tunnel filled with smoke [8–10], and Zhang et al. [11] conducted evacuation experiments to examine the movement speed and evacuation capacity in an underwater shield road tunnel with different vertical exits. In addition, some scholars focused on evacuation characteristics of escape slides [12, 13] and horizontal corridors outdoor trials [14, 15]. But most of the existing physical personnel evacuation tests focused on the characteristics of personnel evacuation behavior, the escape exit selection, and the effectiveness of escape exit signs. However, the relationship between evacuation characteristics and escape stairway spacing has not been systematically studied, and there is still no theoretical design basis for the reasonable escape staircase spacing.

To solve these problems, an evacuation experiment based on the most unfavorable evacuation scenario was conducted. A calculation model of three-phase personnel net evacuation time was established. Finally, a calculation formula of the reasonable escape stair spacing considering the influence of multiple factors was proposed. Results will contribute to providing scientific guidance for the design of up and down escape stairs.

2. Personnel Safety Evacuation Rule

ASET (Available Safety Evacuation Time) and RSET (Required Safety Evacuation Time) are two key indicators for assessing whether people can evacuate safely in a fire incident. ASET is defined as the time for a fire to develop into a direct threat to a person, and RSET is defined as the time that a person flees to the safe area. Engineering disaster prevention system and requirements for safe evacuation require that all personnel in the tunnel can evacuate to the safe area before the fire reaches a dangerous state, i.e., $ASET > RSET$ [2]. Personnel Safety Evacuation Rule is shown in Figure 1.

According to the analysis of foreign tunnel data and fire accident cases, if the ventilation, firefighting, emergency lighting system, and other systems in the tunnel are working normally, the safe evacuation time is generally within 15 minutes, while a medium-scale fire (20 MW) occurs during the normal operation phase. "Road Tunnel Design Code" recommends that personnel safety evacuation time RSET should be less than 15 min. In the evacuation simulation study of the Shanghai Yangtze River Tunnel using STEPS, Cao and Shen [16] found that smoke can not be controlled assumingly beyond 6 minutes under a medium-scale fire. In the optimization analysis of the highway tunnel escape stair spacing under the lane plate, Zhang et al. [3] used 6 minutes as ASET referring to the "Metro Design Code," and "Beijing

East Second Ring Underground Road Disaster Prevention Design Standard" also stipulates that ASET is 6 minutes.

As shown in Figure 2 the evacuation process is divided into the following three main time nodes according to the measurability of evacuation time.

2.1. Alarm Time t_1 . Alarm Time t_1 refers to the time that personnel was informed of fire intelligence. PIARC research report showed that the alarm time for general-level manual control tunnels is 2 to 5 minutes, and the city's underground road safety level is usually much higher. Therefore the alarm issued time is shorter than the average manual control tunnels. For example, the alarm program designed by the Shanghai Yangtze River Fire Alarm System can be confirmed and started within 2 minutes [15].

2.2. Hesitation and Reaction Time t_2 . The time required for a person to respond to an emergency broadcast until they get off transport is t_2 . This part of the time can be divided into two parts. According to the observation data of Noren and Winer [17], after the release of the emergency broadcast, the hesitation time of the personnel in the vehicle, which is as the first part, is usually within 1.5 minutes and the individual differences are large. The time that the people hear the clear alarm and decide to get off the transportation is the second part, and the relevant scholars found that the second part of t_2 is 15 s after conducting a field test as the time required to personnel respond to emergency broadcasts until they get off, t_2 can be determined to be 105 s.

2.3. Net Evacuation Time t_3 . The time that personnel flees to a nonfire tunnel or traffic layer is t_3 , and it refers to the time required for the last stayer to arrive at the exit of the evacuation passage. The net evacuation time of the crowd is affected by factors such as the distance of the tunnel escape stairs, the characteristics of crowd evacuation, and individuals.

The estimated value of the complete evacuation time of the underground road after a fire is given by equation (1). It can be judged whether there is a security threat to evacuation by comparing the complete evacuation time with ASET.

$$T = t_1 + t_2 + t_3 \leq ASET, \quad (1)$$

where T is the required safety evacuation time, which consists of t_1 , t_2 , and t_3 and is requested $T \leq ASET$ [2].

To guide the design of the tunnel disaster prevention system, the relationship between the net evacuation time and the distance between the tunnel escape stairs and the capacity of the stairs must be established.

3. Personnel Evacuation Test

3.1. Evacuation Test Platform for Escape Staircase. A personnel evacuation test was carried out in the underground traffic connection channel of a double-hole tunnel in Tongzhou New Town, Beijing. The double-hole tunnel with a length of 1.2 km contains six straight-through escape stairs.

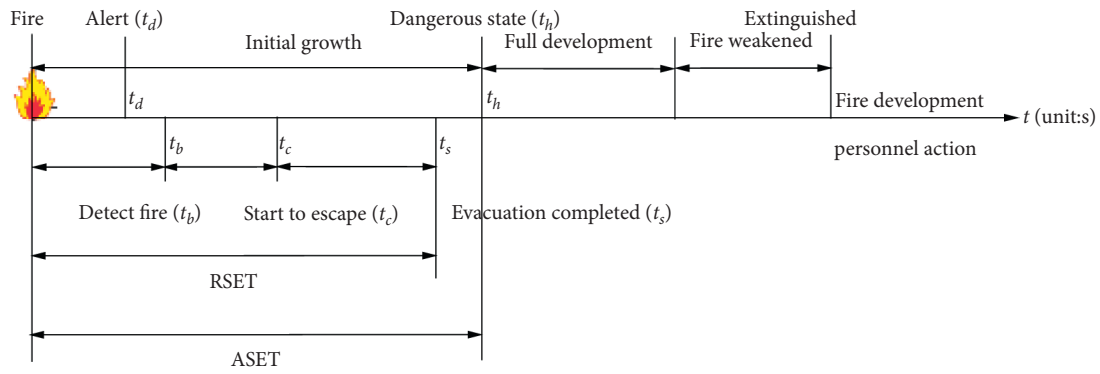


FIGURE 1: Personnel safety evacuation rule [2].

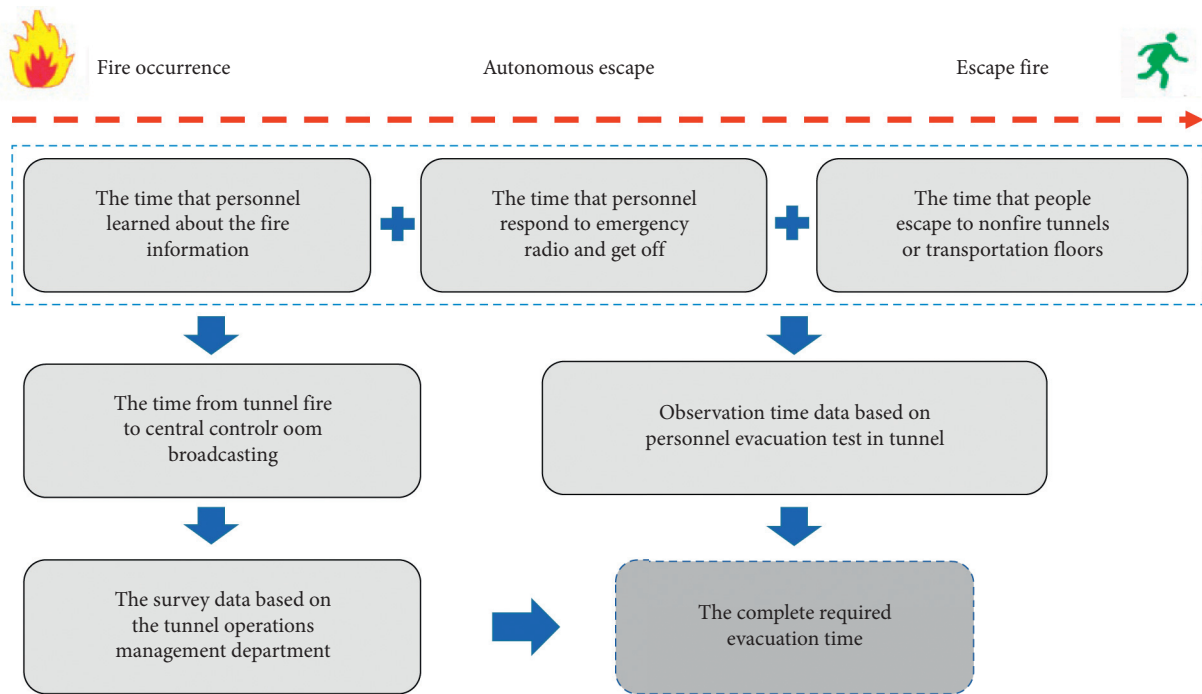


FIGURE 2: Resolution of personnel evacuation node time.

The test section of the tunnel is 400 m long, starts at K1+500, and ends at K1+100. The escape staircase at K1+450 was selected as the evacuation exit.

A test scene was set up with enclosures in the first two escape stairs and in the middle platform, as shown in Figure 3. Stair enclosures were constructed by splicing a 1.8 m high retaining wall. According to “Road Tunnel Design Code,” evacuation indicators were placed on the wall at the corner of the escape staircase. The construction of the test escape staircase and the typical double-deck escape staircase was shown in Table 1.

The test section simulates the traffic conditions of two lanes for cars with a width of 3.5 m, and the vehicle parking distance is 1.5 m. As shown in Figure 4, at the exit of the near escape (K1+400 to K1+450), 10 physical vehicles entering and 6 simulated vehicles were parked at a set interval of 1.5 m, and the rest of the road (K1+300 to K1+400, K1+450 to K1+500) was equipped with simulated vehicles

at the same interval of 1.5 m. The size of the simulation vehicle is 4.5 m × 1.8, and the physical vehicles include 2 minivans, 5 small cars, 1 SUV, and 2 commercial vehicles. The fullness factor cars were selected as 0.5~1 (Full number is 4).

3.2. *Testing Personnel.* Participants were required to be in a good physical condition and have no experience of driving on underground roads, fire evacuation drills in tunnels, and being firefighters or fire engineers. To avoid the influence of “Learning Effect” and ensure test results were satisfactory, specific details, such as the site environment, tunnel layout, emergency exit location, test content, and process, etc., were not informed to participants.

The number of experimenters was determined by the number of vehicles deployed within a 50 m escape distance and the fullness factor. In this experiment, 40 people (32

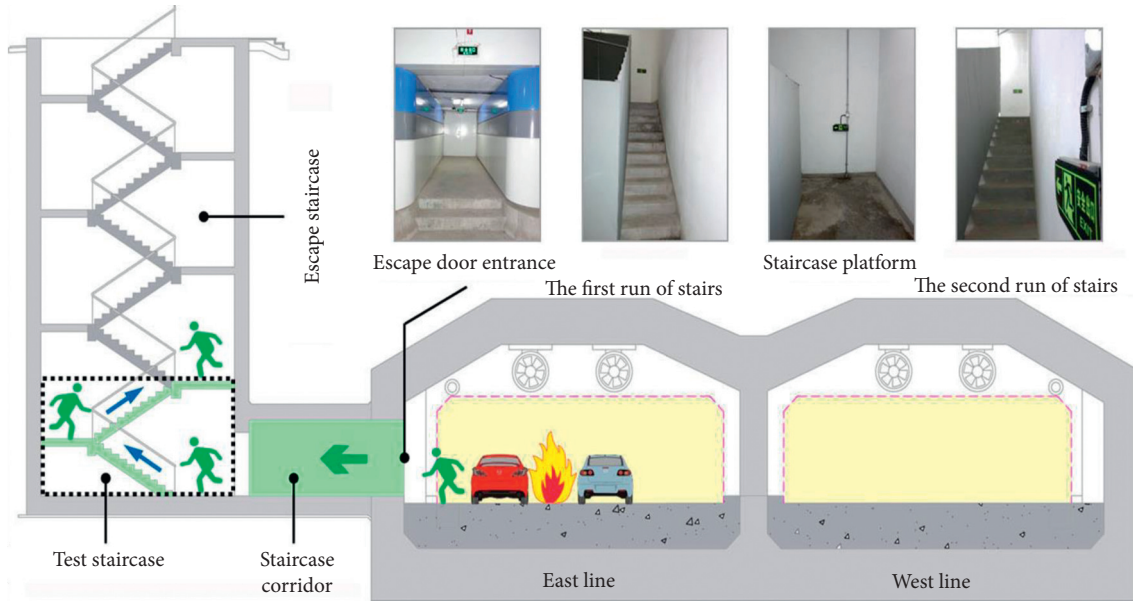


FIGURE 3: Form of escape staircase in the experiment.

TABLE 1: Comparison between experiment escape staircase and the Nanjing Weisan Road Tunnel's.

Project	Stair width (m)	Stair angle	Stairs stepping ($W \times H$)	Staircase formation
Test stairs	0.8	30°	170 mm × 280 mm	(10 + 10) steps + 2.0 m middle platform
Typical stairs	0.8	30°	151 mm × 267 mm	(9 + 17) steps + 1.2 m middle platform

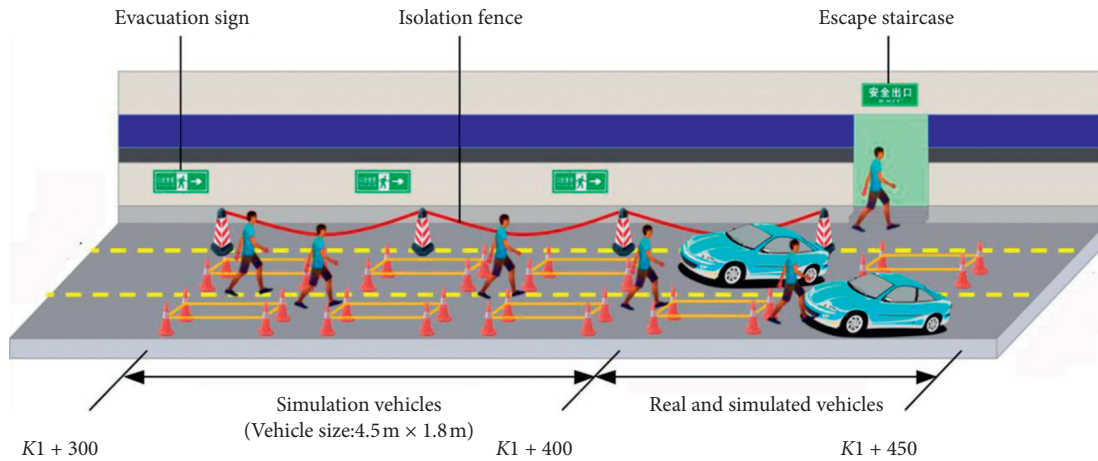


FIGURE 4: Evacuation scenario arrangement of the tunnel.

men and 8 women) participated in the evacuation test, as shown in Table 2 and Table 3. Some of the people brought bags into the venue to get closer to the real evacuation scenarios.

3.3. *Image Acquisition.* Video capture guns numbered C1 to C4 were arranged in the tunnel test section at an interval of 50 m. In addition, two hemispherical cameras numbered C5 and C6 were, respectively, arranged in the front room of escape stairs and the exit of the escape section to record the time for the staff to go upstairs.

TABLE 2: Form of experiment participants' source.

Source	Number	In total
College students	13	40
People work in designing institute	12	
Security personnel	15	

3.4. *Test Conditions and Progress.* The most unfavorable evacuation situation under normal traffic conditions is as follows: the ignition point was located at an entrance of an escape staircase, which made the exit unusable and vehicles behind the fire stop. Therefore, all personnel within the

TABLE 3: Form of experiment participants' type.

Age	Male ratio (%)	Female ratio (%)
17~29	25	10
30~50	32	5
>50	23	5

range from the ignition point to the upstream nearby available escape stairs (defined as the first range of escape spacing) evacuated to that stair exit available, as shown in Figure 5. Based on this most unfavorable evacuation situation, the evacuation of personnel was studied at the escape spacing of three groups of 50 m, 100 m, and 150 m.

During the test, as shown in Figure 4 and 5, 40 test personnel were randomly distributed on both sides of the door of physical vehicles or model vehicles in the corresponding working area, and the commander held the loudspeaker and continuously issued an evacuation broadcasting instruction of "A fire broke out in the front tunnel, please get off and evacuate imminently!" At the same time, traffic lights in the tunnel were switched to "no traffic". In addition, both the main tunnel and the escape stairwell were fully illuminated, and all people were evacuated in accordance with evacuation signs on sidewalls to the rear escape exit. To simplify the movement trajectory of the personnel and facilitate the extraction of the movement parameters of the people, the clustering behavior in the natural evacuation was not considered [7]. It assumed that the people in the same car were independent of each other and then escaped to the evacuation exit immediately after getting off, which would not form a family evacuation group. The net evacuation time was defined as the elapsed time from the issuance of the evacuation broadcast to the last stayer who went through the exit of the escape stair landing. Test screen images at different locations are shown in Figure 6.

4. Observation Results of Evacuation Test

4.1. Evacuation Speed of Personnel under Emergency. Figure 7 is a box distribution diagram of evacuation speed for different types of personnel on the pavement in the case of an escape interval of 50 m. The coordinate axes M1 to M3 and W1 to W3 represent the male and female personnel in the age of 17~29, 30~50, and 51~80, respectively. The measured value of the evacuation speed when the crowd walked on the road was between 1.43 and 1.95 m/s. The evacuation speed decreases with age for same gender testers; for the same age group, the evacuation speed of males was higher than that of females, except for participants aged 51~80 years old. The main reason is that there were only 2 females in this age group while 9 in men. Therefore, the observation data are scattered.

4.2. Evacuation Speed of People Going Upstairs in an Emergency. Figure 8 shows the change of evacuation speed of personnel going upstairs in an escape stairway. It can be seen from Figure 8 that the first few testers who entered the escape stairway have a faster speed of up to 1.1 m/s. At this

time, congestion before the entrance of the stairs has not yet been formed and the traffic is smooth. When the number of people rushing into the entrance of escape stairs in unit time exceeds the actual capacity of the stairs, the failure to disperse the crowd timely will lead to crowds and large areas of backlog, and the staff will be close to each other and difficult to walk (i.e., crowd queuing), etc. Furthermore, the speed of personnel going upstairs drops dramatically, and the fluctuation is stable around 0.6 m/s. At this time, the upstairs speed tends to be the same, and there is little difference in the upstairs speed between different types of individuals.

4.3. Traffic Capacity of Escape Stairs. The relationship between the stair passing time and the number of people passing through the exit when the escape stair spacing is 50 m is shown in Figure 9. The time between when the first tester enters the escape stairway entrance and the last tester leaves the escape staircase exit is 61 s in total, which is called stair passing time. In addition, there is a significant linear correlation between the number of people passing and the passage time, which reflects that the evacuation speed of the pedestrians on the stairs is relatively constant and the interval between the individuals is uniform. Before the congestion at the stairs entrance occurs, the observed value of the average time occupied by personnel on the escape stairs is 7.0 s. After the crowd queuing phenomenon appears, the average time is 12.5 s, which shows that the degree of blockage of the population has a significant impact on the length of the passage time.

Taking the continuous, uninterrupted flow of people at the exit of escape stairs as the research object, the observed value of the escape rate of escape stairs with a clear width of 0.8 m is about 0.7 P/s, which is used to describe the escape capacity of stairs, and in this scenario, the personnel can only wait in line and go through the stairs exit one by one. In front of the entrance of the stairs, there is an evolutionary characteristic of people arriving, crowd backlogs, congestion alleviating and dissipating, and people evacuating to the target exit show a strong sense of competition, as shown in Figure 10. Therefore, how to optimize the escape stair spacing, reduce the queue waiting time and ensure the evacuation of the crowd in a safe time is critical to the optimizing of the tunnel design.

4.4. Net Evacuation Time. The net evacuation time of the three groups of different escape stair spacing and their composition were plotted as Figure 11. It can be seen from Figure 11 that the net evacuation time increases linearly as the escape stairs spacing increases, and the walking time on pavement and waiting time in line account for a large proportion. Furthermore, the waiting time for queuing decreases linearly with the increases of the escape stairs spacing, and the passage time on stairs is independent of the escape stair spacing. Therefore, increasing the escape stairs spacing reduces the waiting time so that the road travel time and the waiting time in the line achieve the optimal combination, which can increase the effective escape time and realize the optimized design of the tunnel.

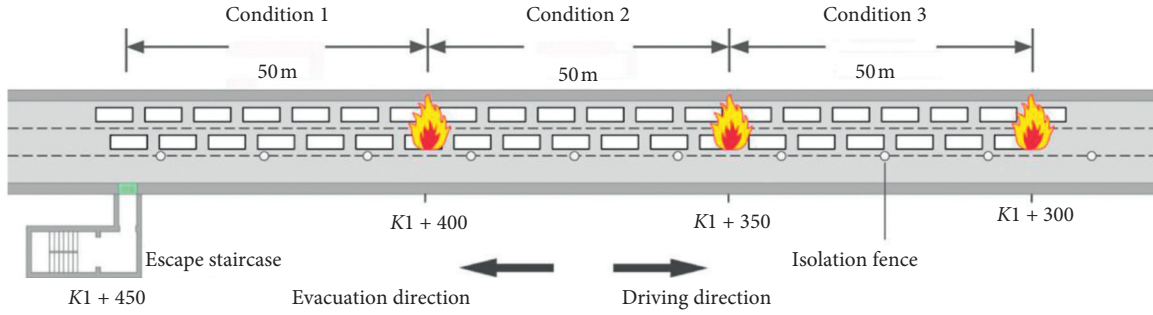


FIGURE 5: Evacuation experiment scenarios under different spacing of escape staircase.



FIGURE 6: Imagery pictures of evacuation.

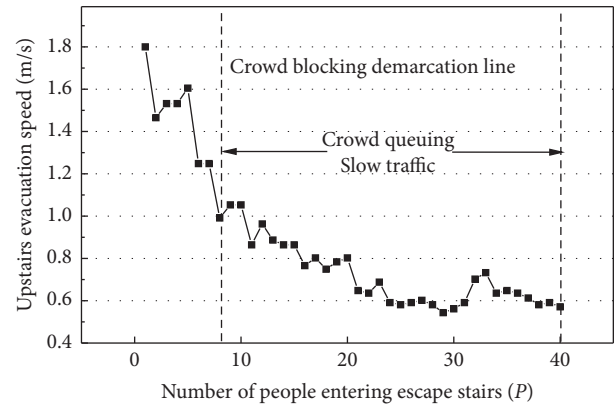


FIGURE 8: Curve of personnel upstairs speed.

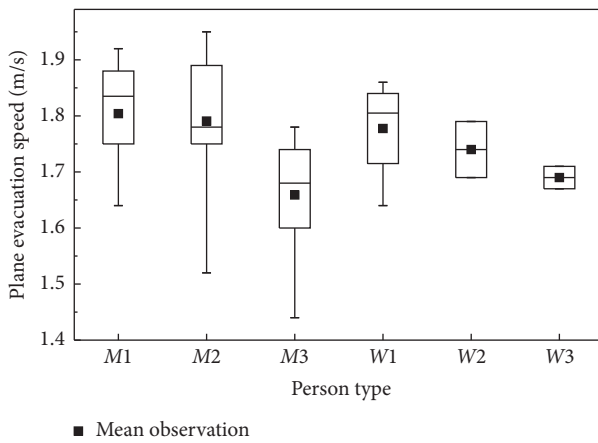


FIGURE 7: Box figure of plane evacuation speed.

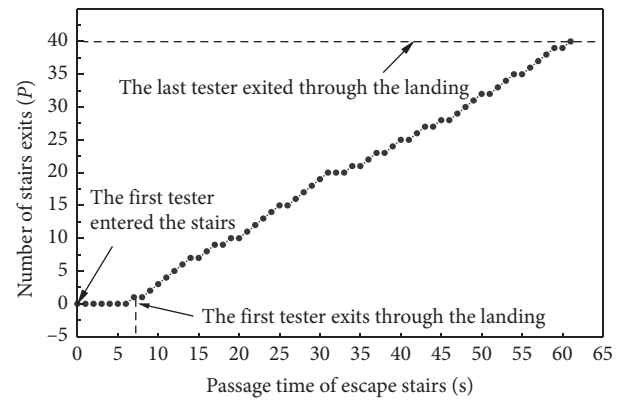


FIGURE 9: Curve of staircase passing time with the exit passing number (under 50 m staircases spacing).

5. Design Method of Escape Stair Spacing

5.1. Calculation Model of Net Evacuation Time of the Personnel. Observing the last stayer, the progress of evacuation is divided into three stages: road evacuation, waiting in line, and staircase evacuation. The corresponding evacuation time is t_r (the road evacuation time), t_w (the waiting time in line), t_s (the staircase evacuation

time). With the assumption that the observed is the farthest from the escape stairs entrance and the man reaches the stair entrance at the speed of a road evacuation, the calculation model of the 3-stage net evacuation time t_3 ignoring the length of the queued crowd is expressed as follows:

$$t_3 = t_r + t_w + t_s. \tag{2}$$

In the equation,

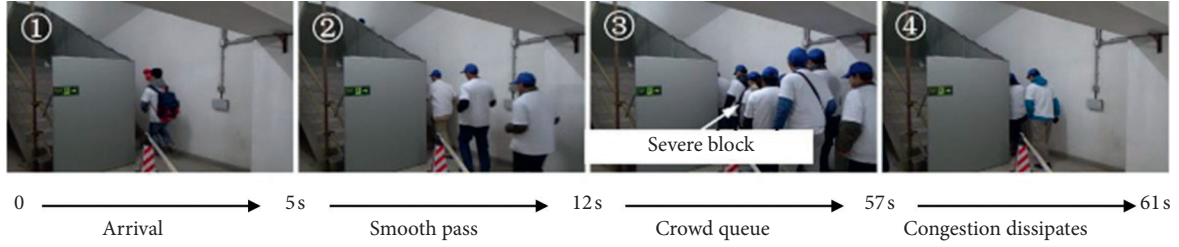


FIGURE 10: Changing process of crowd flow in front of escape staircase.

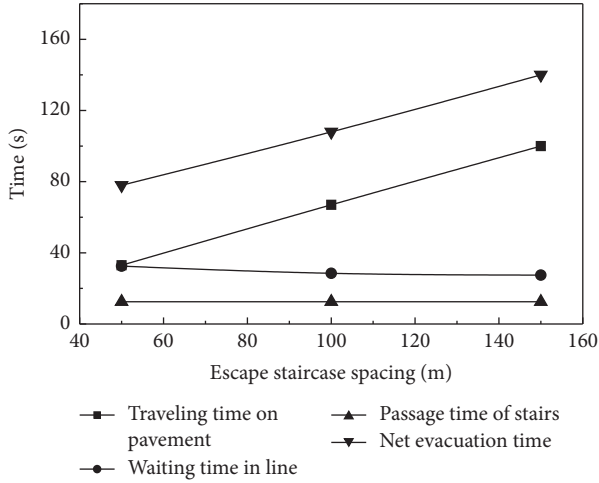


FIGURE 11: Relationship between various evacuation times and escape stair spacing.

$$\begin{aligned}
 t_r &= \frac{S}{v_p}, \\
 t_w &= \frac{\alpha N}{Q}, \\
 t_s &= \frac{L}{v_c},
 \end{aligned} \quad (3)$$

where S is the escape stairs spacing (m); v_p is the pavement evacuation speed (m/s); α is the coefficient of the queuing crowd, which is the ratio of the number of people waiting in line when the observed arrives at the escape stairway entrance to the total number of people (N) and affected by the escape capacity of stairs (Q) and the length of the escape stair spacing; L is the distance required to go upstairs (m); v_c is the speed of going upstairs during the evacuation in line (m/s).

In fact, the number of people in the fire-affected area is not independent of the escape stair spacing. Assuming that the number of lanes in the one-way road is n ; the parking spacing is s (m); the length of the vehicle is 4.5 m; the average number of passengers on vehicles is q (P), the number of people in the fire-affected area can be estimated by the following equation:

$$N = \frac{nSq}{s + 4.5} \quad (4)$$

Net evacuation time of personnel can be expressed as follows:

$$t_3 = \frac{S}{v_p} + \frac{\alpha nSq}{(s + 4.5)Q} + \frac{L}{v_c} \quad (5)$$

According to the guidelines, Equation (1), t_3 needs to meet the following formula:

$$t_3 \leq [t_3] = ASET - t_1 - t_2 = 135 \text{ s}, \quad (6)$$

where $[t_3]$ is the allowable value of net evacuation time; according to section 2, $ASET = 6$ min, $t_1 = 2$ min, $t_2 = 105$.

5.2. Calculation Model of Escape Stair Spacing. Based on test results, when the stairway capacity is constant, the shorter the queue waiting time of the observed is, the longer the effective evacuation time is. To minimize queuing people, it is required that the time taken for people passing through the stairs is equal to the traveling time passing through per parking spacing:

$$\frac{nq_0}{Q} = \frac{s + 4.5}{v_p}, \quad (7)$$

where q_0 is the number of passengers in the vehicle with no one waiting in line when the parking spacing is certain. When the actual number of passengers in the vehicle q is more than q_0 , the crowd will gather at the entrance of the stairs. The number of people in front of the observed will accumulate constantly with the increase of escape stair spacing and can be expressed approximately by the following equation:

$$N_\alpha = n(q - q_0) \frac{S}{s + 4.5} \quad (8)$$

Dividing equation (8) by Equation (4) gives the following:

$$\alpha = 1 - \frac{(s + 4.5)Q}{nqv_p} \quad (9)$$

The formula for calculating the escape stair spacing is obtained by equations (5), (6), (9):

$$S = \frac{Q(s + 4.5)([t_3] - L/v_c)}{nq} \quad (10)$$

TABLE 4: Evacuation note time and cumulative evacuation time under different escape staircase spacing.

Escape staircase spacing (m)	50	100	150
Calculated value of walking time on pavement (s)	33	67	100
Calculated value of the time while waiting in line (s)	0~61	0~128	0~185
Calculated value of the time taken for getting through stairs (s)	12.5	12.5	12.5
Calculated value of the net evacuation time of personnel t_3 (s)	36~107.5	60~203	84~298
Trial value of net evacuation time of personnel t_3 (s)	78	108	140

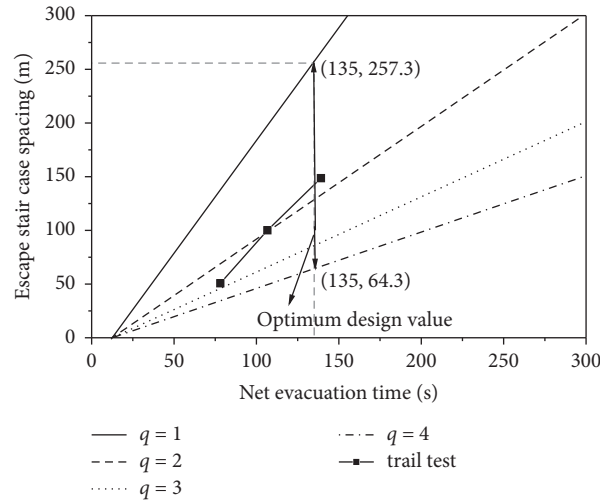


FIGURE 12: Escape stair spacing design curve.

TABLE 5: Project cases of up and down escape staircase [18, 19].

Name of the tunnel	Diameter of the tunnel (m)	Number of lanes	Structure of escape stairs
Nanjing Weisan road tunnel	14.5	Double pipes, double layer eight traffic lanes	Set a group of escape stairs every 64 m, the width of the step of the stair is 0.8 m
Anghai Jungong road tunnel	14.5	Double pipes, double layer eight traffic lanes	Set a group of escape stairs every 80 m, the width of the step of the stair is 0.8 m
Hanghai Shangzhong road tunnel	14.5	Double pipes, double layer eight traffic lanes	Set a group of escape stairs every 100 m, the width of the step of the stair is 0.8 m
Yangzhou slender west lake tunnel	14.5	Single pipe, double layer eight traffic lanes	Set a group of escape stairs every 100 m
Shanghai bund tunnel	13.9	Single pipe, double layer six traffic lanes	Set a group of escape stairs every 100 m

5.3. *Comparison and Verification between Theory and Experiment.* According to the simulated test, evacuation parameters such as $v_p = 1.5$ m/s, $Q = 0.7 P/s$, $t_s = 12.5$ s were obtained. In addition, considering test parameters $s = 1.5$ m, $n = 2$, and $q = (1\sim 4) P$, calculated values of the traveling time on pavement, the waiting time in line, the passage time of stairs, and the net evacuation time were calculated based on the above-mentioned theory. As shown in Table 4, all test values of net evacuation times are within the calculated value range.

Based on the proposed method and experiment results, design curves of the escape stair spacing with different q were obtained. As shown in Figure 12, the test value gradually shifts to a curve of $q = 1$ as the escape stair spacing increases. The possible reason is the number of people remains

unchanged when the escape staircase spacing is 100 and 150 m, the equivalent number of people on a car decreases, so the net evacuation time decreases and falls outside the curve of $q = 2$, especially for the escape staircase spacing of 150 m. The escape stair spacing with respect to the allowed net evacuation time under this test scenario was calculated to be 64.3~257.3 m, and considering the most unfavorable situation, the optimal escape stair spacing should be set to 64.3 m. Compared with the project cases of up and down escape staircase, as shown in Table 5, the escape stair spacing of Nanjing Weisan Road Tunnel is basically consistent with the theoretical value, but the escape stair spacing of other tunnels is generally larger, which means that there is a security risk to some degree.

6. Conclusions

To relate evacuation basic parameters and reasonable staircase spacing of up and down escape staircase in case of fire, an evacuation experiment, which was based on the most unfavorable evacuation scenario, was conducted. Based on the experiment, a calculation model of three-phase personnel net evacuation time was established. By simplifying the evacuation model, a calculation formula of the reasonable escape stair spacing considering the influence of multiple factors was proposed. And the theoretical model was applied to project cases of up and down escape staircase and verified. But this study did not quantify the impact of psychological panic and randomness of evacuees on evacuation behavior, so further research will be carried out in the future. The main findings of the studies are as follows:

- (1) In the emergency state, the observed value of evacuation speed of the crowd walking in the tunnels is between 1.43 and 1.95 m/s, which is greatly affected by gender and age. Specifically, the evacuation speed of males is higher than that of females, and the evacuation speed of the young and middle-aged population is faster. The observed value of evacuation speed of the crowd going upstairs is between 0.5 and 1.1 m/s. After the phenomenon of queuing in the staircase appears, there will be a continuous stream of people, and the individual characteristics will become weak. There is not much difference in the speed of going upstairs between different types of people as well.
- (2) The mean of the observed value of traffic capacity of escape stairs with 0.8 m net width is 0.7 P/s, and the stream of people can only move forward in a single-stranded way. The entrance of the stairs is the bottleneck in the process of the evacuation of the entire stairs. The crowds there are extremely prone to be overstocking, contributing to cluster accidents due to the blockage of people. Therefore, it is necessary to strengthen the orderly guidance to the people at the entrance of stairs through broadcasting. The net evacuation time of the crowd increases linearly with the increasing escape stair spacing, and the walking time on pavement and waiting in line take a relatively major proportion.
- (3) A three-stage calculation model of net evacuation time was established. The theoretical calculation equation of the net evacuation time on the escape stair spacing, traffic capacity of stairs, and the number of evacuees was proposed as well. Based on this, by simplifying the crowd evacuation model, further considering the queuing effect, the number of people on the pavement, the parking space, and the capacity of the escape stairs, a reasonable formula for calculating the escape staircase spacing was proposed.
- (4) The results of theoretical calculation and experimental observation were compared and analyzed,

and the optimal escape stair spacing under this test scenario is calculated to be 64.3 m considering the worst case of $q = 4P$, which is generally smaller than the set value of escape stair spacing of existing double layer tunnels except for Nanjing Weisan Road Tunnel.

Data Availability

All the data, models, and codes generated or used during the study are included in the manuscript.

Conflicts of Interest

The authors declare that they have no conflicts of interest.

Acknowledgments

This work was supported by National Natural Science Foundation "Joint Fund Project" (No. U1834208).

References

- [1] DG-TJ08-2033-2008, *Rode Tunnel Design Code*, DG-TJ08-2033-2008, Shanghai, China, 2008, in Chinese.
- [2] W. S. Liu, "Personnel evacuation simulation analysis and safety assessment of Shanghai Yangtze tunnel." (in Chinese)," *Underground Engineering and Tunnels*, no. 2, pp. 6–9+17+56, 2011.
- [3] P. H. Zhang, M. C. Yu, and J. Song, "Optimizing analysis on escape stair spacing for downward longitudinal evacuation in road tunnel," *Shenyang Jianzhu University (Natural Science)*, vol. 30, no. 4, pp. 688–694, 2014, in Chinese.
- [4] J. A. Capote, D. Alvear, O. Abreu, A. Cuesta, and V. Alonso, "A real-time stochastic evacuation model for road tunnels," *Safety Science*, vol. 52, pp. 73–80, 2013.
- [5] M. Seike, N. Kawabata, and M. Hasegawa, "Evacuation speed in full-scale darkened tunnel filled with smoke," *Fire Safety Journal*, vol. 91, pp. 901–907, 2017.
- [6] L. C. Boer, D. W. Veldhuijzen, and V. Zanten, *Behaviour on Tunnel Fire*, pp. 91–98, Springer, Berlin, Germany, 2007.
- [7] D. Nilsson, M. Johansson, and H. Frantzich, "Evacuation experiment in a road tunnel: a study of human behaviour and technical installations," *Fire Safety Journal*, vol. 44, no. 4, pp. 458–468, 2009.
- [8] K. Fridolf, K. Andrée, D. Nilsson, and H. Frantzich, "The impact of smoke on walking speed," *Fire and Materials*, vol. 38, no. 7, pp. 744–759, 2013.
- [9] M. Seike, N. Kawabata, and M. Hasegawa, "Quantitative assessment method for road tunnel fire safety: development of an evacuation simulation method using cfd-derived smoke behavior," *Safety Science*, vol. 94, pp. 116–127, 2017.
- [10] E. Ronchi, K. Fridolf, H. Frantzich et al., "A tunnel evacuation experiment on movement speed and exit choice in smoke," *Fire Safety Journal*, vol. 97, pp. 126–136, 2017.
- [11] Y.-c. Zhang, A. Zhou, Y. Xiang et al., "Evacuation experiments in vertical exit passages in an underwater road shield tunnel," *Physica A: Statistical Mechanics and Its Applications*, vol. 512, pp. 1140–1151, 2018.
- [12] Z. Fang, J. P. Yuan, and Z. Zhang, "Evacuation pattern of city underwater tunnel and result analysis of evacuation drill. (in Chinese)," *Fire Science and Technology*, vol. 27, no. 10, pp. 746–749, 2008.

- [13] B. Xie, S. Zhang, Z. Xu, L. He, B. Xi, and M. Wang, “Experimental study on vertical evacuation capacity of evacuation slide in road shield tunnel,” *Tunnelling and Underground Space Technology*, vol. 97, p. 103250, 2020.
- [14] Y. C. Zhang, Y. Xiang, C. He, D. Zhang, and Y. Tang, “Experimental study on pedestrian behavior and traffic capacity of cross passage in highway tunnel.” (in Chinese),” *Journal of Southwest Jiaotong University*, vol. 51, no. 04, pp. 615–620, 2016.
- [15] Q. Zhou, H. B. Xu, and C. X. Xing, “Experimental study on the pass rate of cross aisle of highway tunnel.” (in Chinese),” *Fire Science and Technology*, vol. 35, no. 7, pp. 939–941, 2016.
- [16] W. H. Cao and Q. Shen W, *Design of Extra-diameter and Overlength Shield Tunnel—The Shanghai Yangtze River Tunnel*, China Building Industry Press, Beijing, China, 2010, in Chinese.
- [17] A. Noren and J. Winer, *Modelling Crowd Evacuation from Road and Train Tunnels—Data and Design for Faster Evacuations*, Lund University, Lund, Sweden, 2003.
- [18] Y. Z. Hu, “On an innovation of tunnel cross section design of double-deck & double-direction shield method.” (in Chinese),” *China Municipal Engineering*, vol. 149, pp. 1–3, 2010.
- [19] C. J. Qiao, X. H. Guo, and X. H. Ke, “Design of nanjing weisan road tunnel,” *Wuhan Investigation & Design*, no. 6, pp. 53–57+46, 2011.

Research Article

Application of 3D Laser Scanning in Underground Station Cavity Clusters

Li Pinpin ¹, Qiu Wenge ^{1,2}, Cheng Yunjian,³ and Lu Feng ⁴

¹Key Laboratory of Transportation Tunnel Engineering, Ministry of Education, Southwest Jiaotong University, Chengdu 610031, China

²Chengdu Tianyou Tunnelkey Co., Ltd., Chengdu 610031, China

³School of Civil Engineering and Geomatics, Southwest Petroleum University, Chengdu 610500, China

⁴School of Emergency Science, Xihua University, Chengdu 610039, China

Correspondence should be addressed to Qiu Wenge; qiuwen_qw@163.com

Received 6 September 2020; Revised 15 January 2021; Accepted 27 January 2021; Published 17 February 2021

Academic Editor: Wen-Chieh Cheng

Copyright © 2021 Li Pinpin et al. This is an open access article distributed under the Creative Commons Attribution License, which permits unrestricted use, distribution, and reproduction in any medium, provided the original work is properly cited.

Given the shortcomings of the tunnel overbreak and underbreak control and primary support sectional area detection such as the single means, large workload, low efficiency, and poor accuracy, the use of three-dimensional laser technology can solve the above problems. Based on the Badaling Tunnel Great Wall underground station of the Beijing-Zhangjiakou Railway, the 3D laser scanning technology is used to analyze the distribution of the tunnel overbreak and underbreak and the sectional area of the primary support, compared with the total station measurement results. The results showed that the layout of the scanning measurement station should consider the requirements of scanning accuracy, control the station length and scanning incidence angle, and minimize the scanning station length to reduce the scanning error. The majority of the tunnel section was in overbreak, with the overbreak area ranging from 6.22 m² to 13.17 m² and the overbreak rate ranging from 0.283 to 0.598, and the area of underbreak was relatively small; no overexceeded headroom was found in the primary support, and the tunnel vault was not overbreak. The primary support clearance value of the vault is 0~15 mm, the clearance value of the sidewall is 35 mm~40 mm, and the sidewall needs to be secondary shotcrete. The difference value between the 3D laser scanning measurement data and the total station measurement data is within 3 mm, which is within the error range, indicating the validity and reliability of the 3D laser measurement result.

1. Introduction

The overbreak and underbreak are inevitable in the tunnel construction with drilling and blasting method and influence the tunnel construction quality and tunnel economy. Overbreak will lead to tunnel slag quantity and the shotcrete increase in construction; the tunnel underbreak leads to inadequate tunnel headroom and the need for secondary excavation and may again lead to overexcavation, both of which would delay the progress of construction and increase the cost of construction [1]. At the same time, in case of the tunnel overbreak and underbreak being severe, it will have an impact on the stress of the surrounding rocks and the reliability of the tunnel structure [2]. Tunnel primary support clearance monitoring is an important part of lining

quality control. The primary support clearance invading the secondary lining limits leads to reducing the thickness of the secondary lining, resulting in the lack of tunnel strength [3]; the primary support invasion limit needs to carry out temporary support reinforcement, radial grouting reinforcement, and even changing the arch, seriously affecting the tunnel construction progress and increasing construction costs [4]. The too large primary support clearance results in secondary lining thickening, increasing lining rigidity and self-gravity and reducing the bending resistance of the lining [5].

The traditional methods for detecting the tunnel overbreak and underbreak and tunnel clearances include close-up photography, total station position measurement, and manual observation [6]. The method of close-

up photography has to set up a survey station in the tunnel, lay out the survey line, shoot the palm surface with three angles, respectively, to obtain a three-dimensional image, and then compare it with the design excavation section to obtain the tunnel undercut [7]. The total station measures the profile of the section by measuring several points on the same section, and individual data were obtained to estimate the tunnel overbreak and underbreak condition of the newly excavated section. The traditional method has shortcomings such as a large measuring workload, a small number of points, low accuracy, and poor efficiency. Artificial observation is a supplementary method to the above methods, which is more subjective and requires more experience in tunnel construction. The comparison between 3D laser scanning technology and traditional tunnel measurement methods is shown in Table 1 [8, 9].

3D laser scanning is increasingly used in tunnel engineering [10, 11], but less research has been done in underground station construction, and application research in underground station cavity groups in high-speed rail tunnels has not been involved, and this paper has great engineering reference significance. This paper uses the FARO Focus 3D S120 3D scanner system.

2. Engineering Background

The new Beijing–Zhangjiakou Railway is a key construction project planned and implemented by the state with a total length of 173.964 km, which is the eastern section of the Beijing–Lanzhou channel, one of the eight longitudinal and eight transverse channels. Badaling Great Wall Station is located in the new Badaling tunnel of the JZSG-3 section of the railway. The geographical location of Badaling Great Wall Station is shown in Figure 1.

The total length of the station is 470 m, the underground construction area is 36,000 m², and the total length of the equipment cave group is 7190 m. The transition between station and tunnel is realized through the large-span transition section from double line to four lines at both ends of Badaling Great Wall Station. The length of the transition section of the station is 163 m; the maximum cross-sectional area of the station and tunnel is 494.4 m² with a maximum span of 32.7 m and height of 19.5 m. The distribution of cave chamber groups in Badaling Great Wall Station is shown in Figure 2. The large-span transition section has poor surrounding rocks, which makes the construction extremely difficult.

3. 3D Laser Application Solutions

In this paper, Faro Focus 3D 120 3D laser scanner is used, which has an external velocity of 20 meters every 3 minutes, and the laser emission density has 976000 points per second. The measurement time per station is 2 to 5 minutes with an accuracy of 2 mm (10% reflectance) and an accuracy of 0.6 mm (90% reflectance) when the angle of incidence is zero at 25 m. The scanning radius range is 0.6 m~150 m. However, the farther the distance and the more sparse the

scanning point cloud, the lower the accuracy is. The scanning frequency is 122–976 Hz, and the laser parameters are 905 nm, 20 MW, 3R class. The specific parameters of the scanner are shown in Table 2.

The 3D laser scanning system includes (see Figure 3) a 3D laser scanner (a), a special tripod (b), two ball prisms (c), and four splicing spheres (d). 3D laser scanner system through the total station is used to measure the ball prisms target, to achieve the positioning of the global 3D scanning data, with 3D coordinate positioning, to facilitate the later point cloud data to splice accurately, and compare with cross-sectional data. The splicing spheres are used as the positioning reference point, and the positioning accuracy is 0.1 mm.

3.1. 3D Laser Scanning Programs

3.1.1. 3D Laser Scanning Application Process. The laser point cloud data of the underground station outline were collected, locating the absolute coordinates of target 1 with the total station. The distance between the scanning stations is 40 m, and the scanning time is 2~5 min. Importing of absolute coordinates of position targets, stitching multisite tunnel point cloud data initializing, and compressing the underground station point cloud data were carried out. Processing point cloud data, generating tunnel overbreak and underbreak cloud map and tunnel headroom detection cloud map, generating reports automatically were carried out.

TK-PCAS is a tunnel laser scanning information system developed by Chengdu Tianyou Tunnelkey Co., Ltd., which has been successfully applied to many railway tunnel projects, including the Badaling Tunnel of the Beijing–Zhangjiakou High-Speed Railway and the Yujingshan Tunnel of the Chengdu–Guizhou Railway. The application process of 3D laser scanning in underground station tunnels is shown in Figure 4.

3.1.2. 3D Laser Scanning Field Measurements. The schematic diagram of the 3D scanner scanning station is shown in Figure 5. The real coordinates of the reference point are known, and the absolute coordinates of the positioning target are determined through the total station release to the positioning target 1. The purpose of the positioning target is to provide absolute coordinates for the laser point cloud; while the positioning sphere is for the point cloud data collected by the adjacent scanning station to be quickly and accurately spliced, the positioning target 1 should be within the measuring range of the scanning station 1 and scanning station 2, and the new positioning target 2 should be arranged after the scanning station 2; through the point cloud of the scanning station 2, the relative position relationship between the target 1 and the target 2 can be determined, to determine the absolute coordinates of the positioning target 2 coordinates.

The detailed steps of 3D laser scanning field measurement are as follows:

TABLE 1: Comparison of 3D laser and conventional measurement methods.

Method	Measurement efficiency	Measurement accuracy	Data format	Working intensity	Lighting conditions
3D laser	Millions of point clouds in seconds	Millimeter class, high accuracy	3D point cloud	Lower	Not demanding
Close-up photography	Requires control point layout, more efficient	Less accurate	High-definition pictures	Relatively low	Demanding
Total station	Slow measurement speed, needs to lay out measurement points	The large spacing of sample points, low interval accuracy	Measured point coordinates data	Relatively high	Not demanding
Manual observation	Varying from person to person	Varying from person to person, with poor accuracy	None	Relatively low	Demanding

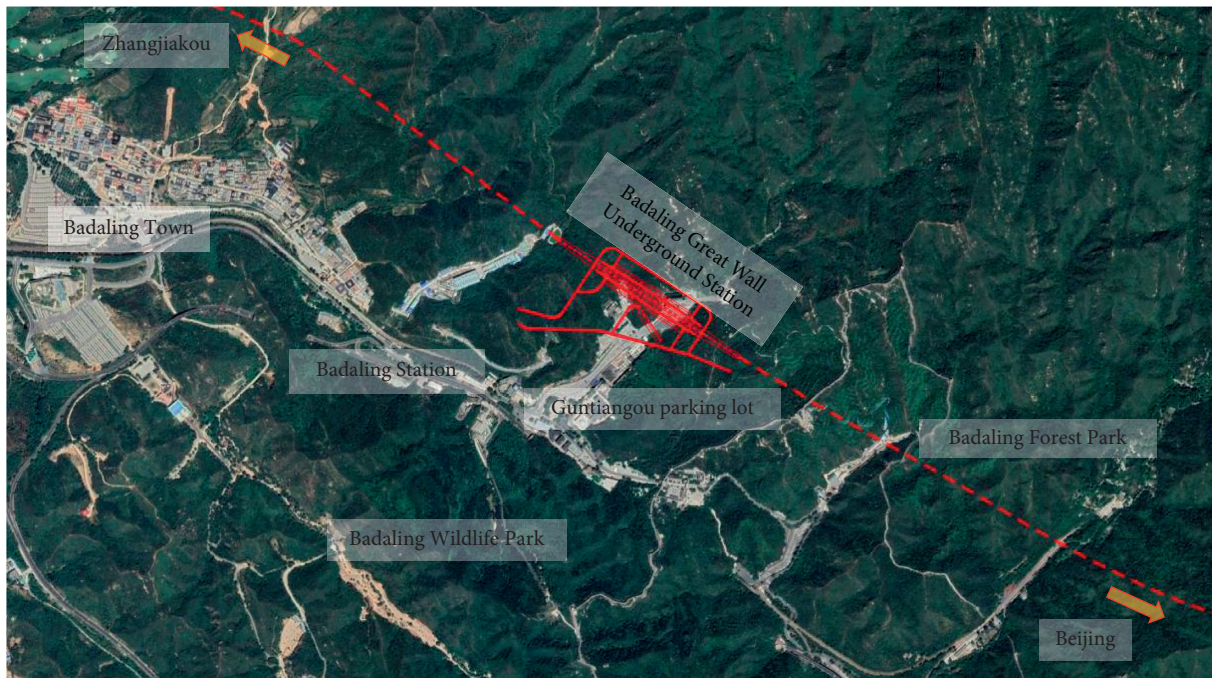


FIGURE 1: Location of Badaling Great Wall Station.

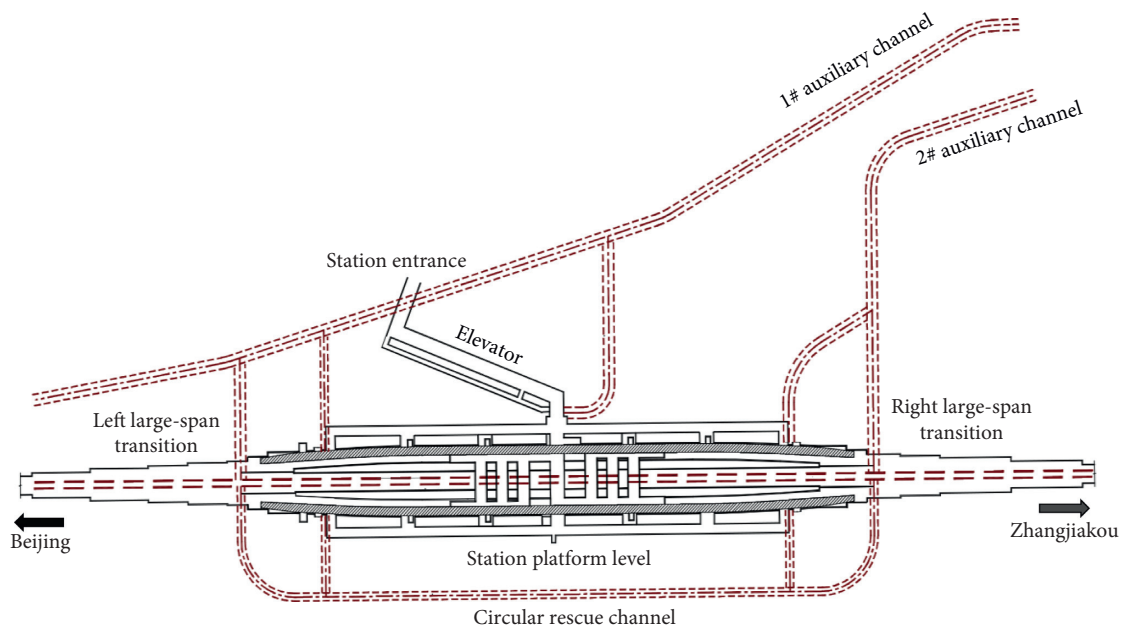


FIGURE 2: Distribution of caverns at the great wall station.

TABLE 2: FARO Focus 3D parameter indicators.

Items	Accuracy (25 m)	Scan frequency	Horizontal field	Vertical field	Scan time
Value	2 mm	500 Hz	360°	305°	2~5 min

Note. There is a positive correlation between scanning accuracy and 3D laser dot density: the larger the 3D laser dot density, the higher the scanning accuracy, and the lower the scanning speed. The parameters in this paper only represent the applicable parameters of the project.

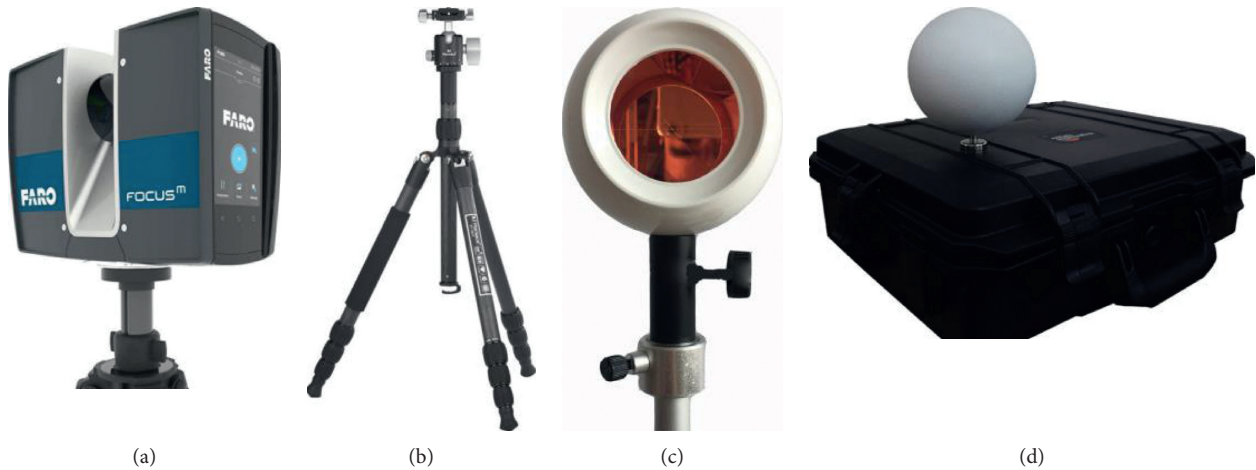


FIGURE 3: 3D laser scanning system instrumentation.

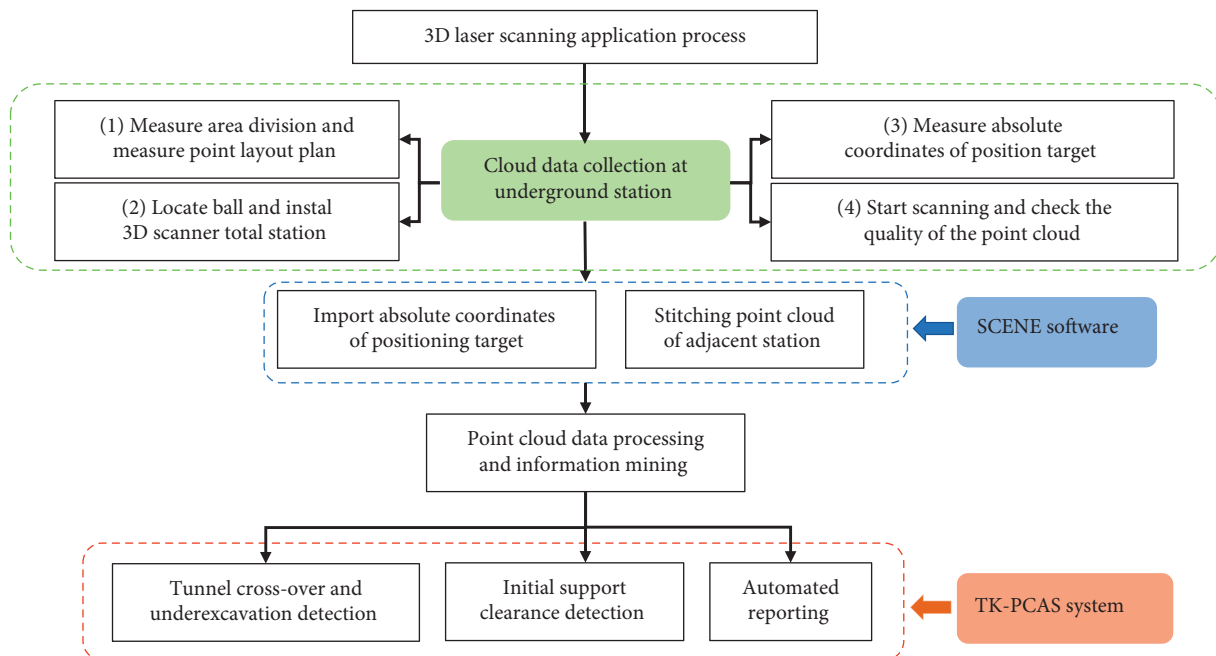


FIGURE 4: 3D scanner scanning application flow.

Step 1. Place the positioning target 1 at the hole of the station to be measured, draw a survey line from the coordinate reference point outside the station to be measured to target 1, and determine the absolute coordinates of target 1.

Step 2. Set up the scanning survey station 1 at 20 m in the measuring direction of the hole and set up the FARO Focus 3D 120; the positioning balls 1 and 2 are placed on

both sides at 40 m in the measuring direction of the hole; to make the later identification convenient, there should be a certain height difference between the two balls.

Step 3. Turn on the laser scanner and start to measure, and after the laser beam is scanned 360 degrees horizontally, the measurement is completed; save the 3D point cloud data and check the station point cloud map on the display.

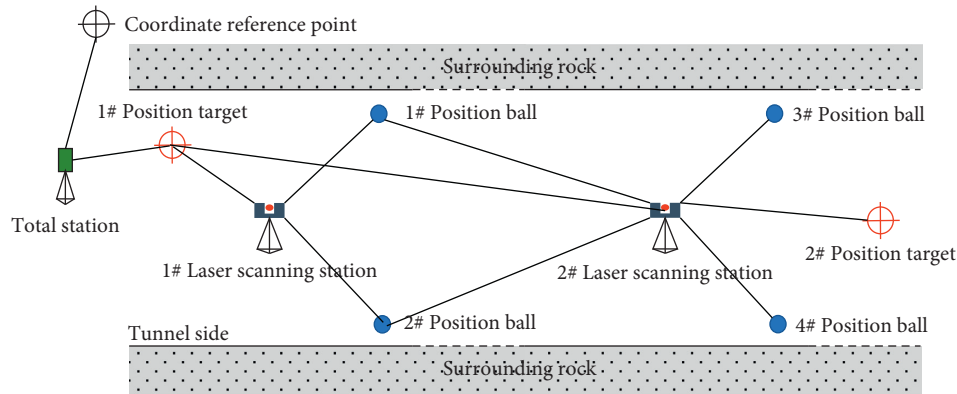


FIGURE 5: Schematic diagram of the 3D scanner scanning station.

Step 4. Measure station 1 after the completion of the scan, the laser scanner along the scanning forward direction to move 40 m; set to scan the measuring station 2, in the measurement direction to continue to advance 20 m on both sides placed positioning ball 3 and positioning ball 4, positioning ball 1 and positioning ball 2 to remain in place.

Step 5. Continue the measurement, save the 3D point cloud data, and check the station point cloud map again.

Step 6. Repeat the above steps until the interior contours of the station are completely scanned.

3.1.3. 3D Laser Scanning Station Distribution. Since a tunnel is a narrow, closed space structure, the use of a 3D laser scanner for tunnel section scanning should fully consider the uneven distribution of tunnel point clouds. Reasonable station planning can reduce its impact on point accuracy. At the same time, factors such as operation cost should also be considered.

Based on the design drawing of the Great Wall Station and the layout of the cavern clusters, and considering the factors influencing the scanning accuracy, the underground station is divided into 20 measurement zones and arranged 38 measurement stations (the scanning range of the scanning measurement stations within the same mileage is the scanning measurement zone). The scanner station is located in the center of the measurement area. Figure 6 shows the distribution of scanning zones in the Great Wall Station of Badaling Tunnel.

When the 3D scanner adopts high-resolution mode, the measurement accuracy at a distance of 20 m is 2 mm, the measuring zone length L takes 40 m, and the width H is obtained according to the width of the tunnel section projection, wherein the tunnel section projection width of measuring zone 1 is 15 m, and the tunnel section projection width of measuring zone 6 is 8 m. Through calculation, the minimum accuracy of measuring station 1 is 2 mm, which meets the design requirement of minimum accuracy; the width of each of the station layers is 2 mm. Zone layout is the

same; the accuracy of each survey area is also basically known; to survey area 6 for example, after the calculation of its minimum accuracy of 3 mm, it fully meets the tunnel construction accuracy requirements.

3.2. 3D Laser Data Processing Optimization. Through the software TK-PCAS tunnel laser scanning information system large quantities of 3D point cloud measurement data automatically process at a speed of fewer than 20 minutes per station, generate laser scanning images, and provide accurate quantitative analysis reports.

3.2.1. Measurement Accuracy Optimization. Scanning station distribution needs to consider the minimum requirements for scanning point accuracy, select the appropriate resolution, station location, and control the scan time in a reasonable range.

The scanning accuracy of a laser scanner is determined by three factors:

- (1) Angular resolution φ : the angular resolution determines the density of the laser point cloud, in the same measurement distance, the higher the angular resolution, the higher the density of the laser point cloud and the greater the measurement accuracy.
- (2) Measurement area size A : the measurement area size includes the length L and width H of the measurement area, which leads to the angle of incidence α and measurement distance S from the scanner to the corner measurement point.
- (3) Laser footprint D : the diameter of the laser footprint D will diverge as the measurement distance increases; the farther the measurement distance, the larger the diameter of the laser footprint, and the smaller the measurement accuracy.

The scanner station is located in the center of the measurement area (as shown in Figure 7), and the scanning measurement accuracy of the four corners is the worst. The error in the point occurs with the change of angle following a

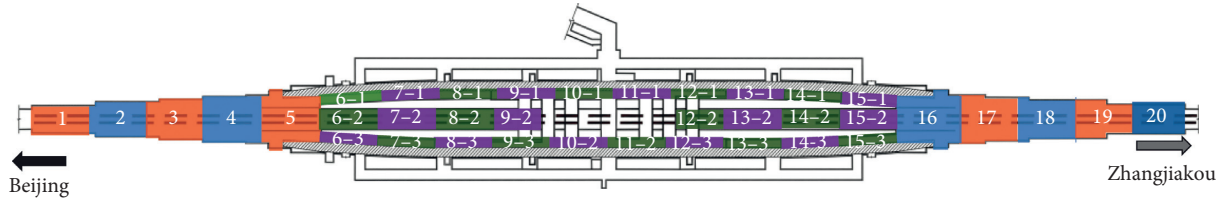


FIGURE 6: Scan survey area delineation at the Great Wall Station.

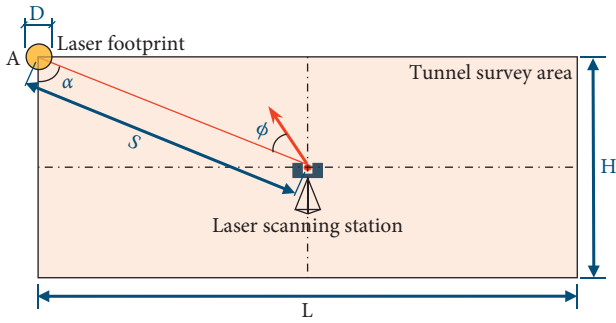


FIGURE 7: Schematic diagram of scanner measurement accuracy.

certain law, and the error variation has a certain limit value; When the angle of incidence is fixed, the error in the point cloud grows linearly with the growth of the measurement distance [12]. When the incidence distance is fixed and the effect of the incidence angle on the measurement accuracy is considered, the error in the point cloud is

$$\bar{\sigma}_p = \frac{\sigma_p}{\cos\alpha}, \quad (1)$$

where α is the scan angle of incidence; $\bar{\sigma}_p$ is the error in the point cloud at an incidence angle of α ; and σ_p is the error in the point cloud at an incidence angle of 0.

Assuming that the tunnel contour is a rectangular in-ground projection as shown in the figure, the FARO laser scanner is located at the intersection point of the tunnel center axis, and the measurement point with the largest angle of incidence is located at corner point A. The maximum scanning angle of incidence within the measurement station range is

$$\alpha_{\max} = \arctan\left(\frac{L}{H}\right), \quad (2)$$

where α_{\max} is the maximum angle of scan incidence within the range of this station; L is the length of the tunnel profile projection, called the station length; and H is the width of the tunnel profile projection. The higher the laser reflectance, the greater the laser accuracy. The following figure shows the accuracy of tunnel measurement when the laser reflectance is 10% and 90%, respectively.

Figure 8(a) shows the three-dimensional view of point cloud scanned by laser obtained by Javier Roca-Pardiñas [13]. Figure 8(b) shows the expansion of the laser-scanned point cloud along the midline of the tunnel. The tunnel is a circular section with a radius of 5 cm, and the 3D laser scanner is located in the middle line of the tunnel. The

figures reveal that within the range of 20 m scanning station, the distribution of point cloud density is not uniform. The point cloud density at the section where the scanner is located is the largest, and the density of the four angular point clouds farthest from the scanner is the smallest.

Delaloye [14] suggested the station spacing $L = H$, and according to equation (2), $\alpha = 45^\circ$. From Figure 9(a), it can be seen that the tunnel should be within 25 m of the laser measurement distance under unfavorable conditions (10% reflectivity) to meet the scanning accuracy requirements. It is known from equation (2) and Figure 9(b) that the error only starts to rise sharply when the angle of incidence is greater than 65° . When $\alpha = 65^\circ$, $L = 2.1 D$. Due to the actual tunnel construction site conditions, the laser scanner may not be set up exactly at the center axis of the tunnel, so the station spacing is recommended to take $L = (1 \sim 2)D$.

3.2.2. Point Cloud Noise Optimization. Due to the poor air quality, high dust density, large particles in the tunnel, and the presence of construction personnel and construction machinery, there are natural noise points in the laser scan. Measuring instruments will produce a series of errors in the process of collecting data, and the 3D laser scanner is no exception; its collected point cloud data contains unwanted redundant points and noise points mixed with the effective point cloud. The redundant points and noise will not only multiply the amount of point cloud data but also affect the application of point cloud data. Therefore, for the characteristics of underground station cavities, the optimization research of point cloud denoising is carried out based on KD-Tree topology and neighborhood search technology.

(1) KD-Tree Topology and Neighborhood Search. At present, there are two main methods for constructing point cloud neighborhoods: constructing Euclidean neighborhoods by Euclidean distance and constructing k -neighborhoods by finding k -nearest neighboring points [15]. The point cloud neighborhood search method is only suitable for point clouds with more uniform distribution; the k -neighborhood construction by finding k -nearest neighbors is suitable for tunneling longitudinal point clouds with uneven density.

The basic principle of k -neighborhood search is to calculate the distance from one point to all other points separately and then sort the points in ascending order according to the distance, and finally take the top k points as the k -nearest neighbor points of the point. Using KD-Tree to partition the whole point cloud scene makes it more efficient to search the neighboring points in the process of finding the k -neighborhood [16].

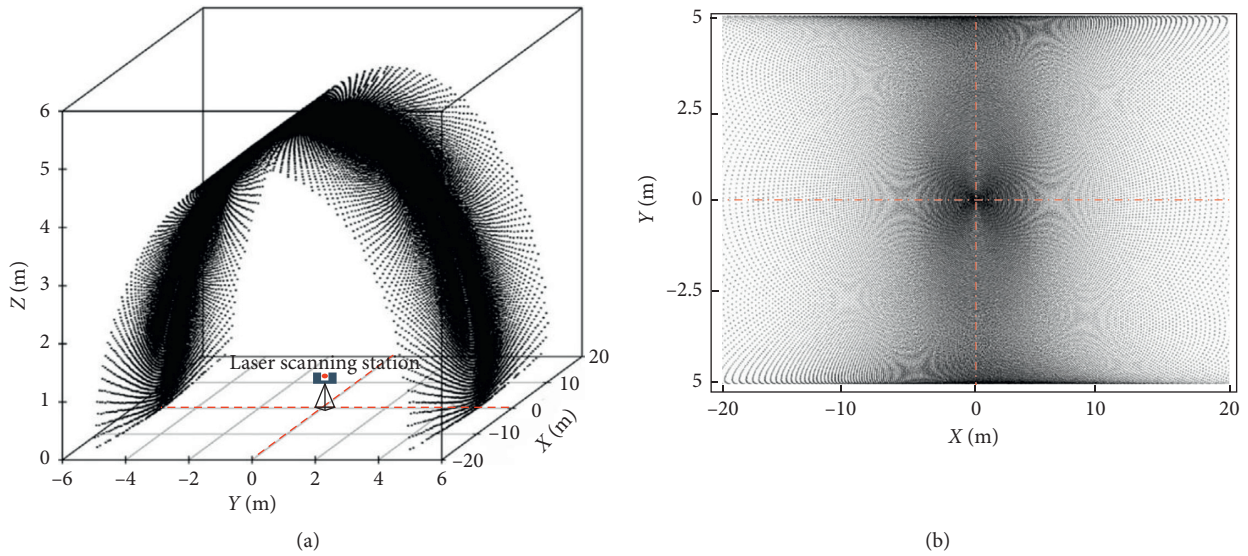


FIGURE 8: Laser scanning point cloud distribution. (a) Three-dimensional view. (b) Expanded view.

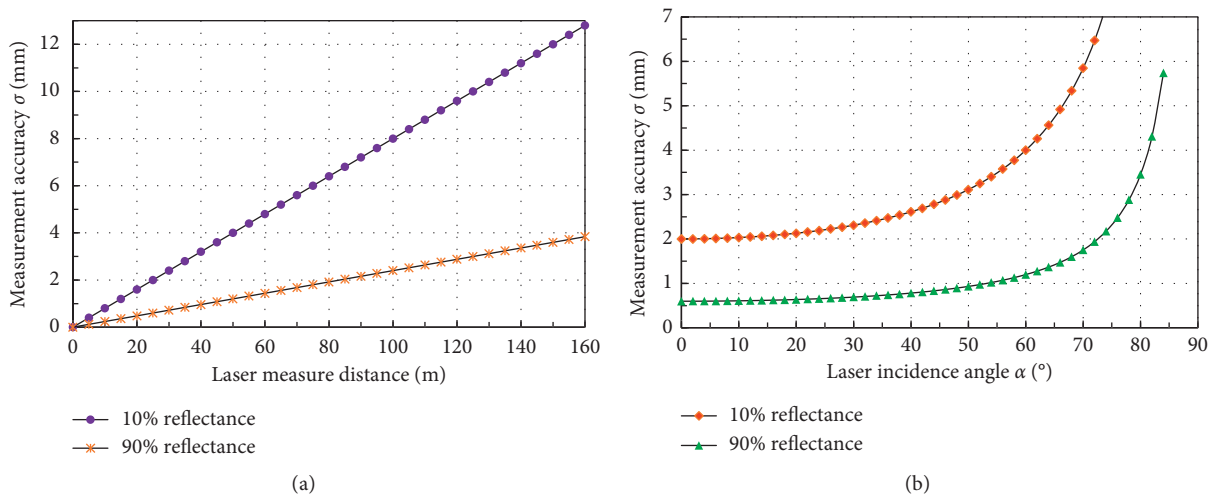


FIGURE 9: Variation of measurement accuracy with measurement distance and angle of incidence. (a) Measurement accuracy at different measurement distances. (b) Measurement accuracy at different laser incidence angles.

KD-Tree is a generalized form of searching from binary trees to multidimensional data. k denotes the spatial dimension, so KD-Tree is also called K -dimensional search tree. The quickest way to construct a KD-Tree is to use the splitting method like fast classification by placing the values of the specified dimension on the root node and dividing the remaining points with smaller values than the previous node in this dimension in the left subtree and those with larger values than the previous node in the right subtree. Then, the process is repeated on the left and right subtrees until the last tree of the classification contains only one element.

(2) *Laser Cloud Map Noise Reduction Method.* The steps of isolated noise filtering in laser point cloud based on KD-tree include organizing the laser point cloud based on KD-tree, finding out the k -nearest neighbors, and secondly, filtering

out the isolated noise based on the statistical properties of the distance between the isolated noise point and its several k -nearest neighbors.

Assuming that the median of the distances of the k -nearest neighbors of the laser points approximately satisfies the normal distribution, then 99.73% of the points will fall in this region (shown in Figure 10), and the points within this range will be regarded as valid points, and only a very few points that do not meet the conditions will fall outside the range, and these points will be regarded as noise points to be removed. By setting the threshold value in this way, the threshold value can be calculated automatically according to the data size, without manual repetition of setting, which improves efficiency and speed.

If the average of the distances of the k -nearest neighbors of any laser point i is D , then

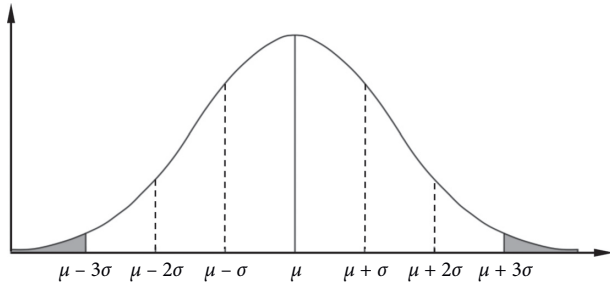


FIGURE 10: Normal distribution curve schematic diagram.

$$\mu = \sum_{i=1}^n D_i \quad (3)$$

The standard deviation s is

$$s = \sqrt{\frac{\sum_{i=1}^n (D_i - \mu)^2}{n}} \quad (4)$$

When $|\mu - 3\sigma| \leq D_i \leq |\mu + 3\sigma|$, it is a valid laser point; otherwise, it is an isolated noise point and is automatically filtered out.

(3) *Effect of Noise Reduction Optimization.* Figure 11 shows the 3D point cloud image of the tunnel during the operation period. Figure 11(a) shows the 3D scanned raw cloud image, and Figure 11(b) shows the point cloud after the noise reduction process. The noise in the cloud image is mainly construction crew residuals, protruding objects inside the lining, noise on the lining profile section, and other particulate matter that affects the laser imaging. The comparison of the figures before and after filtering shows that all the noise on the tunnel contour disappears, the construction personnel clutter noise also disappears, and the noise in the part connected to the track near the bottom plate also basically disappears, while the effective points on the tunnel contour section are not significantly mistakenly deleted and do not affect the subsequent processing.

4. 3D Laser Scanning Results and Analysis

4.1. *The Tunnel Overbreak and Underbreak Detection.* The 3D laser scanning technology evaluated the tunnel overbreak and underbreak, and the accuracy of the tunnel overbreak and underbreak and calculations (including excavation volume, overexcavation volume, the tunnel overbreak and underbreak volume, and effective excavation volume) can reach the millimeter level [6]. Accurate tunnel overbreak and underbreak statistics can provide a reference for the next cycle of drilling and blasting, thus achieving the purpose of controlling overexcavation and avoiding underexcavation.

Data collection frequently constructed tunnels can be limited by several site factors [10]. Laser scanning in dusty tunnels significantly reduces the point cloud quality and the scanner is subject to dust and moisture that affects its service life, so as far as possible, the tunnel excavation profile

sections are scanned according to the excavation progress, after blasting, mechanical slagging, and manual cleaning.

In this paper, the 3D laser point cloud data is compared with the excavation design section based on the TK-PCAS system to analyze the over-the-tunnel overbreak and underbreak condition of the tunnel. The actual excavation section is called overexcavation and the tunnel overbreak and underbreak if the contour of the designed tunnel is outside the datum line and inside the datum line. The contours of the design section are known according to the tunnel design documents, and the actual excavation contours are analyzed by the 3D laser scanning point cloud.

Figure 12 is a scanning cloud map of the excavation profile for the mileage range DK68 + 455 to DK68 + 459. Positive values (blue) indicate overbreak and negative values (red) indicate underbreak. Figure 13 shows that the tunnel overbreak and underbreak exists around the excavation contour, with the maximum depth of the tunnel overbreak and underbreak reaching 150 mm; a small area of the overbreak and underbreak exists in the center of the vault, with the depth of about 50 mm; most of the tunnel excavation contour is in the state of the overbreak, with the maximum depth of overexcavation reaching 200 mm.

Table 3 shows the tunnel overbreak and underbreak size statistics for sections DK68 + 455 to DK68 + 459.

The results from Table 3 show that the tunnel cross section is generally in overbreak, with the overbreak area ranging from 6.22 m² to 13.17 m² and the overbreak rate ranging from 0.283 to 0.598. The area of the tunnel underbreak is small, with the tunnel underbreak area ranging from 0.15 m² to 0.43 m² and the underbreak rate was between 0.007 and 0.019.

4.2. *Primary Support Clearance Monitoring.* After the primary support is constructed for a certain distance (generally 40 m), the clearance of the tunnel can be scanned and inspected. After the scanning point cloud data is processed, the primary support surface contour cloud map is obtained. Through comparatively analyzing the point cloud contour surface and the design section of the primary support (including reserved deformation amount), the primary support clearance cloud map is obtained. Positive clearance values indicate that the point cloud profile is inside the design section of the primary support and has not reached the design limit. Negative clearance values indicate that the point cloud profile is outside the design section of the primary support.

Figure 14 shows the 3D scan data of the primary support clearances in the cross section of the mileage range DK68 + 409 ~ 449. The 3D laser scan point cloud is shown in Figure 14(a) below, and the primary support clearances are shown in Figure 14(b). Figure 15 shows the expanded view of primary support clearances' scanning cloud map.

As we can see in Figure 15, the point cloud profile is inside the design section of the primary support (clearance is positive), the sectional area value is 0 ~ 15 mm in the vault, and the clearance value is larger in the sidewall of primary support, which is 35 ~ 40 mm, and the secondary shotcrete is needed in the sidewall. The ground part is out of the scope of analysis.

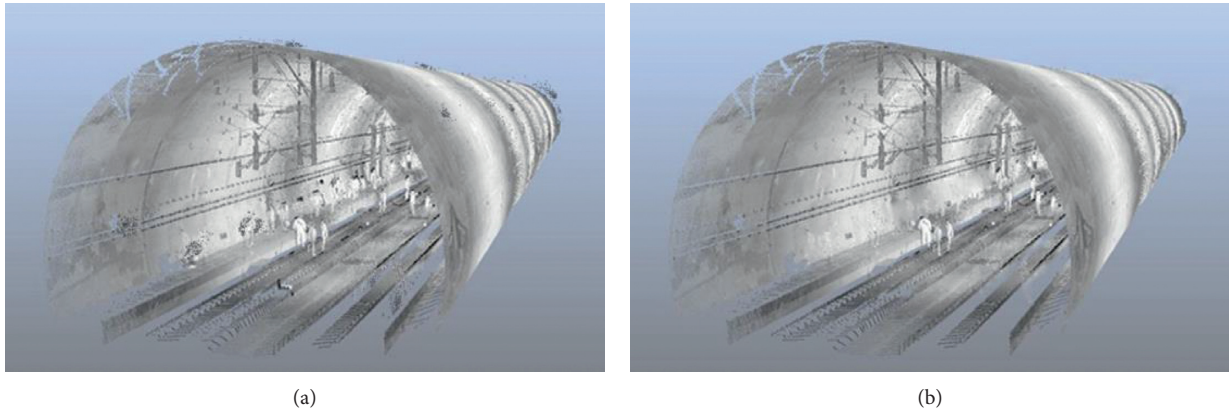


FIGURE 11: Noise reduction processing effect. (a) Original cloud map. (b) Noise reduction cloud map.

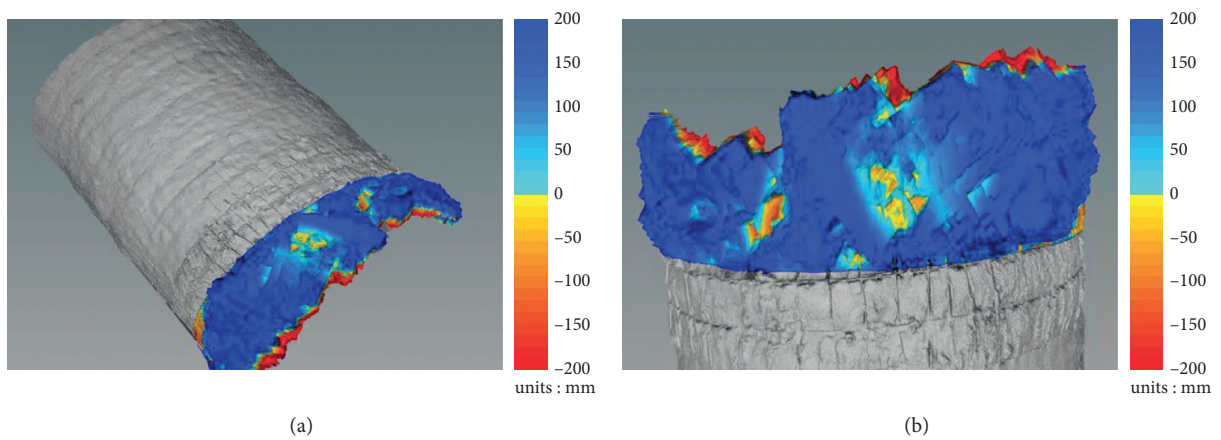


FIGURE 12: The tunnel overbreak and underbreak scanning. (a) Side view. (b) Front view.

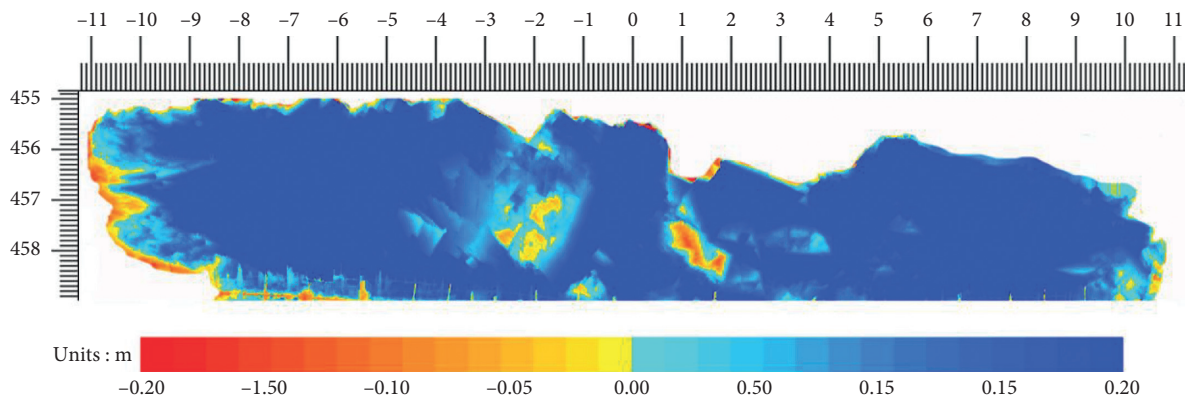


FIGURE 13: Expanded image of the tunnel overbreak and underbreak scanning.

According to the construction site conditions, a monitoring section is arranged at an interval of 10 m at the surface of the primary support of the tunnel, and 5 measurement points are arranged symmetrically at each monitoring section, which is located at the top of the arch, left arch foot, right arch foot, left wall, and right wall. The measurement results of the mileage range of DK68 + 410 ~ DK68 + 449 are shown in Figure 16. 3D laser scanning can

obtain the complete cross section of the outline of the sectional area, while the total station is only measuring a limited number of points, the tunnel clearance values are positive; that is, the tunnel overall outline did not intrude into the secondary lining design section. The clearance value in the vault is smaller, followed by the arch foot on both sides, and the primary support at the side walls has the largest clearance value.

TABLE 3: Statistical table of the tunnel overbreak and underbreak dimensions.

Mileage range	Design area (m ²)	Overbreak area (m ²)	Overbreak		Underbreak		Underbreak rate
			Overbreak volume (m ³)	Overbreak rate	Underbreak area (m ²)	Underbreak volume (m ³)	
DK455~DK456	22	6.22	0.51	0.283	0.15	0.08	0.007
DK456~DK457	22	8.56	0.75	0.389	0.28	0.11	0.013
DK457~DK458	22	11.25	0.64	0.511	0.43	0.16	0.019
DK458~DK459	22	13.17	0.71	0.598	0.39	0.14	0.017

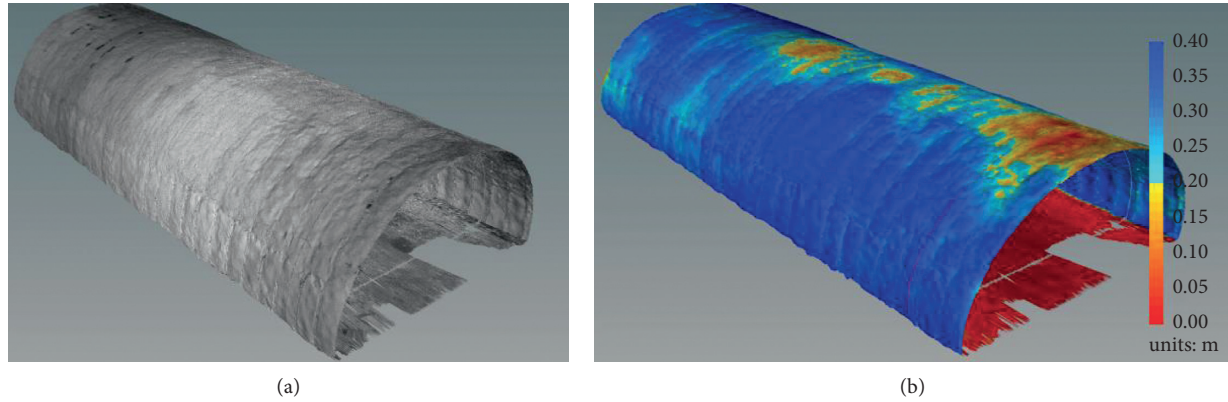


FIGURE 14: Primary support clearances' scanning cloud map of the tunnel. (a) 3D laser scanning point cloud. (b) Primary support clearances' scanning map.

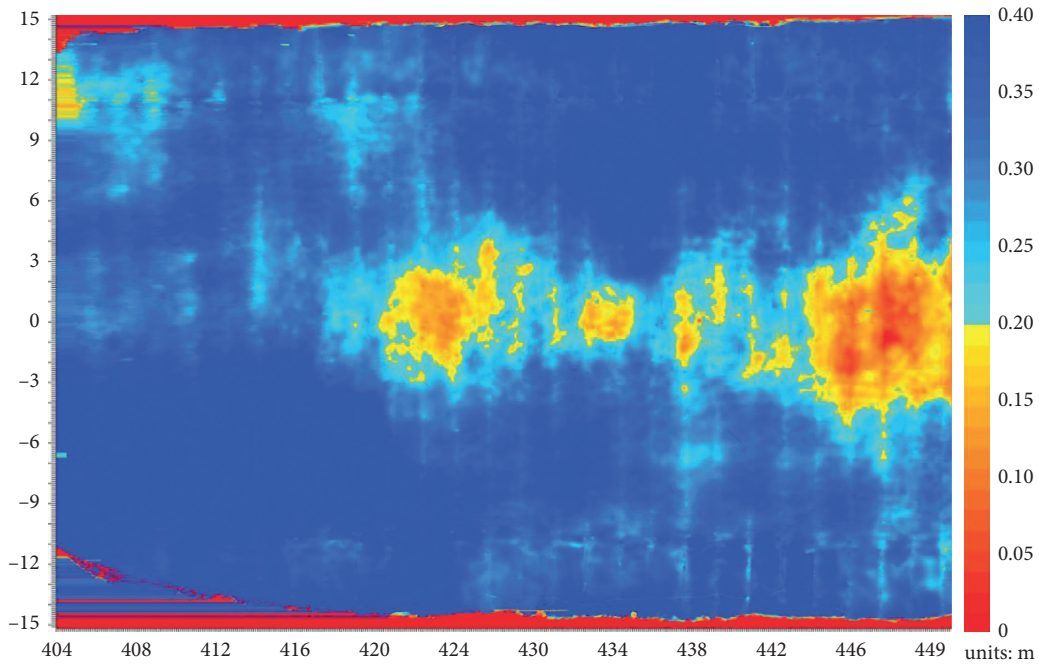


FIGURE 15: Expanded view of primary support clearances' scanning cloud map.

As we can see from Table 4, the difference value of 3D laser scanning clearance and the total station measurement data is within 3 mm, which is the largest error location in the left wall, the absolute value of the difference is 2.6 mm, which is the smallest error location in

the left arch foot, the absolute value of the difference is 0.4, and 3D laser scanning of the clearance value is generally greater than the total station measurement data, because of the difference with the measurement time, The difference reflects the initial deformation of the tunnel,

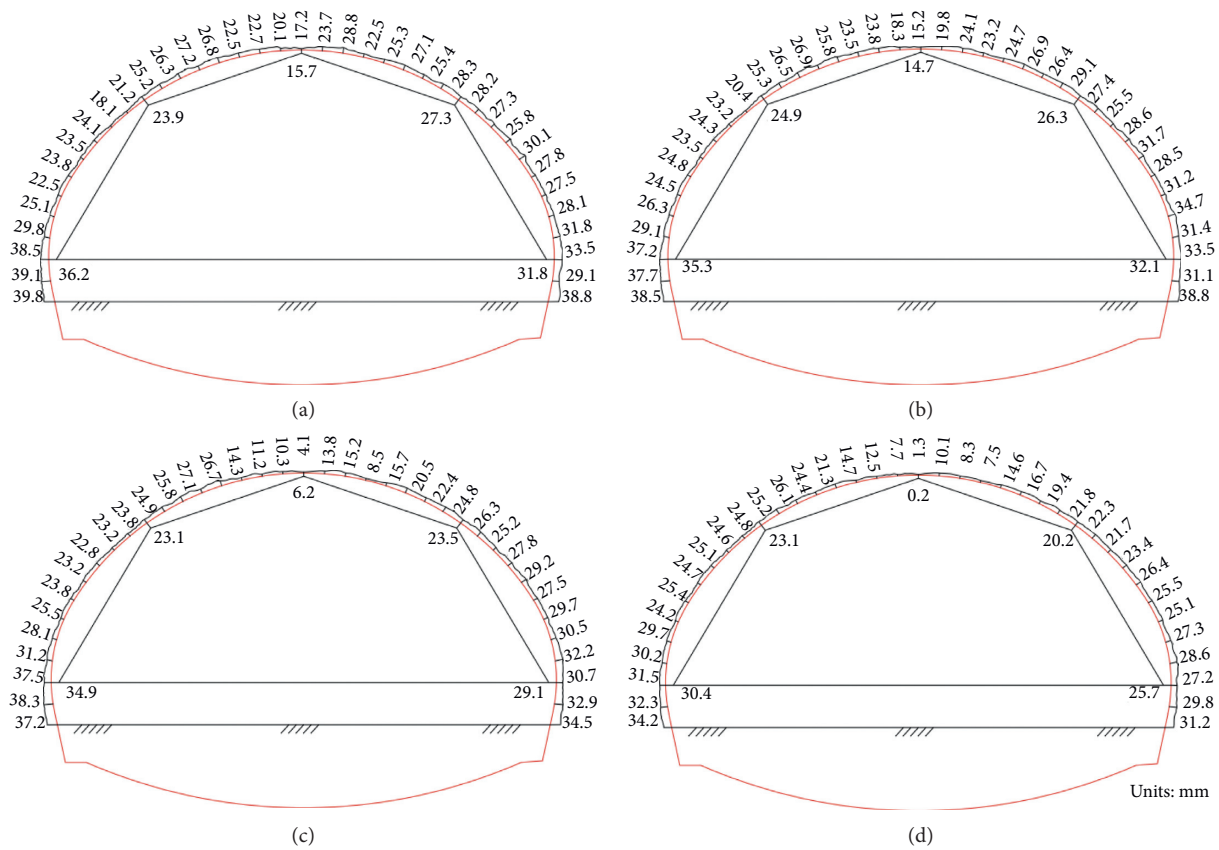


FIGURE 16: 3D laser scanning and total station section measurement data comparison. (a) DK68 + 415. (b) DK68 + 425. (c) DK68 + 435. (d) DK68 + 445.

TABLE 4: Statistical table of primary support clearances of tunnel.

Mileage	Tunnel clearance (mm)								
	Vault			Left arch			Left wall		
	3D laser	Total station	Difference value	3D laser	Total station	Difference value	3D laser	Total station	Difference value
DK68 + 415	17.2	15.7	1.5	25.2	23.9	1.3	38.5	36.2	2.3
DK68 + 425	15.2	14.7	0.5	25.3	24.9	0.4	37.2	35.3	1.9
DK68 + 435	4.1	6.2	-2.1	24.9	23.1	1.8	37.5	34.9	2.6
DK68 + 445	1.3	0.2	1.1	25.2	24.1	1.1	31.5	30.4	1.1

which was measured by the total station later than the 3D laser scan.

5. Conclusions

In this paper, 3D laser scanning technology is investigated as a method for monitoring the tunnel overbreak and underbreak and primary support clearance in the construction of underground station tunnel clusters, and the main conclusions are as follows.

The tunnel structure is a thin and long line structure; scanning station layout considering the specific requirements of scanning accuracy needs to control the station length and scanning incidence angle. To reduce the scanning error, the scanning station length should be reduced; the distance between the two stations is about 40 m, with a station scanning radius of 20 m. There are 4 corners of each

measurement area; the worst scanning measurement accuracy, after calculation and analysis of the minimum accuracy of station 1, is 2 mm. The minimum accuracy of the measuring zone 6 mm is 3 mm, which fully meets the requirements of tunnel construction accuracy. The station spacing is recommended to take $L = (1 \sim 2)D$.

Based on the TK-PACS system, the tunnel overbreak and underbreak profile can be obtained by comparing the 3D scan data with the design cross section, and the results show that the tunnel cross section is generally in overbreak, with the overbreak area ranging from 6.22 m² to 13.17 m², and the area of the tunnel underbreak is small.

By scanning the tunnel primary support sectional area, we obtained the primary support surface contour cloud map, and the tunnel clearance detection cloud map was obtained. The results showed that the tunnel primary support did not exceed the design section, the clearance value of the vault

part was 0~15 mm, and the clearance value of the sidewall was larger, the clearance value was 35~40 mm, and the sidewall needed to be shotcrete twice.

By the comparison of 3D laser scanning clearance and the total station measurement date, the difference value is within 3 mm, which is within the error margin. The position with the largest error is the left wall with a value of 2.6 mm, and the position with the smallest error is the left arch foot with a value of 0.4 mm.

Data Availability

The 3D laser data collected and used for analysis will be available from the corresponding author upon request.

Conflicts of Interest

The authors declare that there are no conflicts of interest regarding the publication of this article.

Acknowledgments

This work was supported by the Science and Technology Research and Development Project of China Railway Corporation (2017G007-A), National Key R&D Program of China (2017YFC0806000), and Big Data-Driven Structural Disasters Prediction and Maintenance in Hazardous Geological Regions of Subsea Tunnels (51991395).

References

- [1] D. Liu, W. Gao, and M. Liu, "The cause of excessive or insufficient excavation in tunnel construction and its control," *Chinese Journal of Underground Space and Engineering*, vol. 3, no. 2, pp. 1468–1471, 2007.
- [2] M. Wang and B. Guan, "The statistical rule of tunnel overbreak and its influence on tunnel reliability," *Chinese Journal of Geotechnical Engineering*, vol. 1, pp. 85–90, 1997.
- [3] W. Bo, L. Tianbin, H. Chuan et al., "Model test of effect of lining thinning on tunnel structure bearing capacity," *Journal of the China Railway Society*, vol. 35, no. 2, pp. 106–114, 2013.
- [4] Z. Qin and H. Liang, "The method and significance of cross-section clearance detection before tunnel arch wall lining," *Journal of China and Foreign Highway*, vol. 1, pp. 125–128, 2007.
- [5] F. Jimeng and Q. Wenge, "Model test on the effect of tunnel lining stiffness to structure durability," *Journal of Central South University (Science and Technology)*, vol. 44, no. 9, pp. 3884–3890, 2013.
- [6] L. Tao, Q. Wenge, C. Yunjian et al., "Study on tunnel support evaluation system based on holographic deformation monitoring," *Chinese Journal of Underground Space and Engineering*, vol. 16, no. 2, pp. 583–590, 2020.
- [7] T. Shengli, G. Xiurun, and T. Zhijun, "Testing study on digital close-range photogrammetry measuring deformations of tunnel and underground space," *Chinese Journal of Rock Mechanics and Engineering*, vol. 7, pp. 1309–1315, 2006.
- [8] J. Li, Y. Wan, and X. Gao, "A new approach for subway tunnel deformation monitoring: high-resolution terrestrial laser scanning," *ISPRS-International Archives of the Photogrammetry, Remote Sensing and Spatial Information Sciences*, vol. XXXIX-B5, pp. 223–228, 2012.
- [9] K. R. Shoff, "A new approach to tunnel digital geological mapping using 3D terrestrial laser scanning technique paper No.315," *Isrm-sponsored International Symposium on Rock Mechanics: "Rock Characterisation Modelling and Engineering Design Methods"*, International Society for Rock Mechanics & University of Hong Kong, Hong Kong, China, 2009.
- [10] S. Fekete, M. Diederichs, and M. Lato, "Geotechnical and operational applications for 3-dimensional laser scanning in drill and blast tunnels," *Tunnelling and Underground Space Technology Incorporating Trenchless Technology Research*, vol. 25, no. 5, 2010.
- [11] J.-Y. Han, J. Guo, Y.-S. Jiang et al., "Monitoring tunnel deformations by means of multi-epoch dispersed 3D LiDAR point clouds: an improved approach," *Tunnelling and Underground Space Technology*, vol. 38, pp. 385–389, 2013.
- [12] S. Li, *Tunnel Continuous Cross-Section Extraction and Deformation Analysis Using Terrestrial Scanning* Chang'an University, Xi'an, China, 2015.
- [13] D. Delaloye, "Development of a new methodology for measuring deformation in tunnels and shafts with terrestrial laser scanning (LiDAR) using elliptical fitting algorithms," Msc Thesis, Queen's University, Kingston, Canada, 2012.
- [14] J. Roca-Pardiñas, R. Argüelles-Fraga, F. de Asís López, and C. Ordóñez, "Analysis of the influence of range and angle of incidence of terrestrial laser scanning measurements on tunnel inspection," *Tunnelling and Underground Space Technology*, vol. 43, pp. 133–139, 2014.
- [15] F. F. Zhang, Y. B. Liang, and J. Wang, "The nearest neighbor search filtering of point cloud data based on noise isolation," *Engineering of Surveying and Mapping*, vol. 27, no.1, pp. 29–33, 2018.
- [16] M. F. Song, D. Z. Jia, J. W. Guo et al., "A point cloud compression algorithm based on k neighborhood cuboid," *Science of Surveying and Mapping*, vol. 44, no. 10, pp. 93–100, 2019.

Research Article

Development of Data Integration and Sharing for Geotechnical Engineering Information Modeling Based on IFC

Jiaming Wu ^{1,2}, Jian Chen ^{1,2,3,4,5}, Guoliang Chen,^{1,2,3,4} Zhe Wu,⁶ Yu Zhong,⁷ Bin Chen,⁴ Wenhui Ke,⁸ and Juehao Huang^{1,2,3,4}

¹State Key Laboratory of Geomechanics and Geotechnical Engineering, Institute of Rock and Soil Mechanics, Chinese Academy of Sciences, Wuhan 430071, China

²School of Engineering Science, University of Chinese Academy of Sciences, Beijing 100049, China

³Hubei Key Laboratory of Geo-Environmental Engineering, Wuhan 430071, China

⁴The Soft Soil Research Center in Ningbo University of Technology,

State Key Laboratory of Geomechanics and Geotechnical Engineering, Ningbo 315211, China

⁵China-Pakistan Joint Research Center on Earth Sciences, Islamabad, Pakistan

⁶China State Construction International Holdings Limited, Hong Kong 999077, China

⁷Wuhan Metro Group Co., Ltd., Wuhan 430071, China

⁸Wuhan Municipal Construction Group Co., Ltd., Wuhan 430071, China

Correspondence should be addressed to Jian Chen; chenjian@whrsm.ac.cn

Received 10 September 2020; Revised 30 December 2020; Accepted 1 February 2021; Published 13 February 2021

Academic Editor: Wen-Chieh Cheng

Copyright © 2021 Jiaming Wu et al. This is an open access article distributed under the Creative Commons Attribution License, which permits unrestricted use, distribution, and reproduction in any medium, provided the original work is properly cited.

With the rapid development of infrastructure construction, geotechnical engineering has always been worthy of attention due to its complexity and diversity. Accelerating the informatization of geotechnical engineering will contribute to the project management, but the information contained in geotechnical engineering cannot be well integrated because of the lack of unified data standards. Building Information Modeling (BIM) has been considered as an effective technology to manage information, and Industry Foundation Classes (IFC) in BIM serves as a neutral and open standard for the exchange of information. However, it was found that BIM cannot express the information of some structure objects and geological objects well during the construction process of geotechnical engineering. Combined with the characteristics of geotechnical engineering, taking advantage of the good extensibility of IFC, this paper proposes a “Built-In Generation Schema” for geotechnical structure models and a “Plug-In Extension Schema” for three-dimensional (3D) geological models, ultimately forming the basic data system of geotechnical engineering information models based on IFC. Applying extended IFC to the modeling process, the BIM-based modeling method of geotechnical models is proposed. In addition, an IFC-based platform is developed to integrate geological models and structure models for further displaying and analyzing of geotechnical engineering models. The work in this paper provides a feasible way and technical support for promoting the integration and sharing of geotechnical engineering information and enhancing the multiprofessional collaborative work.

1. Introduction

With the acceleration of social urbanization, the demand for urban infrastructure continues to thrive. Geotechnical engineering is a crucial component of infrastructure construction, and its complexity and diversity have always been worthy of attention [1, 2]. Geotechnical engineering is closely related to geological engineering, structure engineering, and other

disciplines. In the process of construction, it often needs multidisciplinary coordination, which will bring challenges to project management [3]. In the whole life of geotechnical engineering, different kinds of information and data need to be acquired timely, which requires rapid processing and integration, real-time feedback, and guidance for construction [4].

Building Information Modeling (BIM) [5], as an innovative concept and method intended to improve

interoperability in the process of modeling, has swept the global engineering construction industry since the beginning of this century. It is believed that BIM has triggered the second digital revolution in the field of engineering design and construction and promoted the transformation and upgrading of construction-related industries [6, 7]. BIM technology exchanges various types of information of construction projects through an internationally used open data standard Industry Foundation Classes (IFC), which has been gradually considered as the most extensive data standard of BIM since its publication [8]. Due to its good scalability, IFC is an intermediary aimed at realizing cross-domain, cross-specialty, cross-stage, and cross-platform data interaction and sharing, and it is also the key to improve the collaborative operation of BIM system [9].

When viewing from the poor data-exchange performance and information island problem faced by the informatization of geotechnical engineering, the successful experience of BIM technology brings us thinking and enlightenment: can BIM be applied to geotechnical engineering informatization? Can BIM effectively result in better information management for geotechnical engineering? To answer these questions and solve the problem of data information islanding in geotechnical engineering, IFC will be the key due to its good scalability. Hence, in this paper, the first and foremost priority is to apply and extend IFC into geotechnical engineering for data integration and sharing.

Due to the short of the uniform data standard for geotechnical models, it is necessary to extend IFC standard for geotechnical structure and geological model. An IFC-based strategy is established to extend the definition of multisource data in geotechnical engineering into BIM environment. For the IFC-based integrated model, it is intended not only to be used for visually displaying, but also to be extended for numerical calculation and analysis.

2. Literature Review

2.1. 3D Geological Model. The construction of geotechnical engineering is inseparable from the mastery and utilization of geological conditions. Researchers from different perspectives proposed many theories and technologies for three-dimensional (3D) geological modeling [10–12]. In order to simulate the complex geological structure, related modeling software has been developed (ArcGIS [13], GoCAD [14], Surpac [15], etc.). These models usually have specific data formats, such as GeoSciML [16] and 3D-GEM [17]. However, these developed data standards are mainly oriented in the 3D Geographic Information System (GIS) field.

In addition, in geotechnical engineering, some computing software is used to build geological models to analyze and evaluate the safety and stability of engineering geological bodies [18]. These geological models are built based on survey data, and many of the strata are simplified, making them relatively simple [19, 20]. Moreover, when the structural model needs to be considered, most of the calculation add simplified structural units as needed.

To sum up, geological models are mainly considered in traditional geotechnical engineering. Either structure models are not considered, or simplified structure units are considered, but the integration between geological models and structure models is not really realized. Moreover, data exchange and information fusion are not satisfactory, and it is difficult to form a collaborative system that can be integrated and shared. This makes it tough to transfer and share information in the process of geotechnical engineering construction, and it is prone to generate information island problems, which will lead to time delay, cost increase and even safety accidents. The main reason is the lack of unified data standards between the geological model and structure model which cannot be effectively integrated, and information cannot be shared and exchanged.

2.2. Extending the Information Models Based on IFC.

With the in-depth research and application of IFC, researchers held the view that the information description of IFC in some professional fields was not complete, and various options for extending the IFC model had emerged accordingly [21]. Extensive efforts were undertaken by Yabuki and Li [22] to implement IFC for infrastructure. For bridge engineering, they extended quite a few IFC entities and created an IFC-bridge information model. For shield tunneling, Yabuki et al. [23] developed an IFC-based product model and applied it to a shield tunnel project to manage some information. Zhou et al. [24] also contributed to extending the application of IFC standard in shield tunnels, making IFC accommodate the segment assembly process. In response to the lack of IFC standards in road engineering, Lee and Kim [25] described the spatial and physical structure elements for the road structure to create the road information model. Lee et al. [26] also proposed the extension mechanism for the NATM tunnel, a data schema aimed at implementing a description of various components based on IFC. More than that, many organizations are also actively promoting the application of IFC in infrastructure engineering, such as the European research project V-Con and French working group MINnD Concepts [27]. Their works have deepened the application of IFC in infrastructure engineering, but so far the scope of these BIM projects is mainly on structure objects. Geology, as the prerequisite and foundation of engineering construction projects, is not fully reflected in IFC framework.

Zhou et al. [28] proposed a metro protection information model (MPIM) based on IFC, which extended the simple geological model and external building model as the foundation for MPIM. Providakis et al. [29] proposed a methodology that the buildings were modeled together with the ground, the subsurface geology, and the tunnel, in which IFC is employed to act as a conversion medium between the BIM data and other analysis tools.

Some preliminary study on geological models based on IFC has been carried out, but its proposed models were mainly used for visualization. There still exists a big gap between current modeling methods and growing demands for integrating geological objects and geotechnical structures

in a uniform standard and extending the integrated model to carry out geotechnical design and numerical analysis.

On the whole, in order to solve the problem imposed by short of the uniform data standard for geotechnical models, an IFC-based schema is proposed in this paper to better integrate the geological model and structure model. And the extended integrated model fully considers the characteristics of geotechnical engineering, which can not only be visualized but also meet the requirements of geotechnical design and numerical analysis.

3. Geotechnical Engineering Informatization

Different from traditional building engineering, geotechnical engineering is both building engineering and geological engineering. The two core elements in geotechnical engineering are the geological body and engineering structure, which interact with and influence each other. The geological body is not only the carrier of geotechnical engineering structure, but also the object of construction and reconstruction. In addition, the geological body is strengthened and protected by the engineering structure. The structure is in general man-made, while the ground is nature-generated. That is, the man-made structures and natural geological settings comprise the backbone of geotechnical modeling, but they have totally different features.

There are many kinds of structures used in geotechnical engineering, such as underground diaphragm wall, bored pile, reinforced concrete support, steel support, anchor rod, steel arch, and shield segment. Geotechnical structures have the same features as those defined in BIM models, as they are all man-made or designed by our engineers. Geotechnical structures and general building structures are in the same line in essence, and it is relatively straightforward to reach a consensus on the model implementation mechanism and specific expression form. Therefore, it is natural for geotechnical structures to adopt IFC and BIM technology for modeling.

However, the big difference exists between the geological models and the BIM models. The geological model is made by engineering designers according to the speculation of discrete geological survey points, while the BIM structure model is created by designers. Not only that, but 3D geological modeling is mostly applied in visualization but has not been deeply applied in the practical application of geotechnical engineering, just like the “good-looking but useless” evaluation by many engineering implementers, which reduces the utilization value of information.

Considering the growing demand for big data integration and sharing in geotechnical engineering, the application of BIM technology is expected to realize the collaborative systemization of geotechnical engineering software. The big obstacle is that the data standard is not unified between geological models and BIM models, and they need to reach a consensus. For geotechnical structure, it is natural to utilize the existing entities in current IFC standard due to the similar features as those defined in BIM models. However, for geological model, IFC standard will be used as the intermediate bridge of data conversion to accommodate the

demands of geological modeling in BIM environment. It could be an efficient method to solve the problem of inconsistency of current data standards.

In order to generate geotechnical structure information in the BIM domain, we will build corresponding components in terms of entity and relationship using the inherent components in IFC classes. So we can call this “Built-In Generation Schema,” while, for geological data, it has not been considered in IFC framework before. We need to create new IFC entities for them by extending IFC data structure. Also, there will be some new entities and relationships established in IFC framework. The data model for geological data will be included into IFC framework using its extension mechanism. Compared to the geotechnical structure, we then call this “Plug-In Extension Schema” for geological modeling. And then, an integrated BIM model for geotechnical engineering is formed by the two based on IFC. Based on the proposed data generation mechanism under IFC framework, the integrated BIM model helps us overcome the lack of unified data standard between the geological model and structure model. On this basis, we use the integrated model to serve the geotechnical design.

4. Data Integration and Sharing Mechanism Based on IFC

4.1. IFC Data Schema. The most indispensable concept in IFC is the entity, a class of objects defined with common properties. It is produced in an object-oriented manner, expressing information by means of defining attributes and attaching constraints to attributes. IFC framework has a distinctive hierarchy and modular characteristics, the data schema architecture of which is split into four layers, namely, domain layer, interoperability layer, core layer, and resource layer. The core layer includes kernel schema and core extension schema, which serves to ensure the sustainability of the model and assist the entity update. IFC standard provides three extension mechanisms: entity extension, *IfcProxy*-based entity definition, and extended property set [27].

As the most crucial entity in the core layer, *IfcRoot* is the root entity that implements other entities in the core layer, the interaction layer, and the domain layer. As Figure 1 shows, *IfcObjectDefinition*, *IfcRelationship*, and *IfcPropertyDefinition* are three considerable subclasses of *IfcRoot*. *IfcObjectDefinition* is a definition form of IFC objects, and *IfcObject* derived from it defines the object entities in the IFC standard [26]. *IfcProduct*, as a subtype derived from *IfcObject*, can be used to represent the tangible or objective entities involved in the construction process. And it explicitly defines the spatial structure entity *IfcSpatialStructurElement* and physical entity *IfcElement* that constitute the project object. *IfcRelationship*, defining the relationship between all objects derived from *IfcObject*, through its various subtypes, can integrate the newly added entities into the IFC framework. *IfcPropertyDefinition* is a property definition entity, which represents a generalization of the properties of a specific object. Its subtype *IfcPropertySetDefintion* defines a property set.

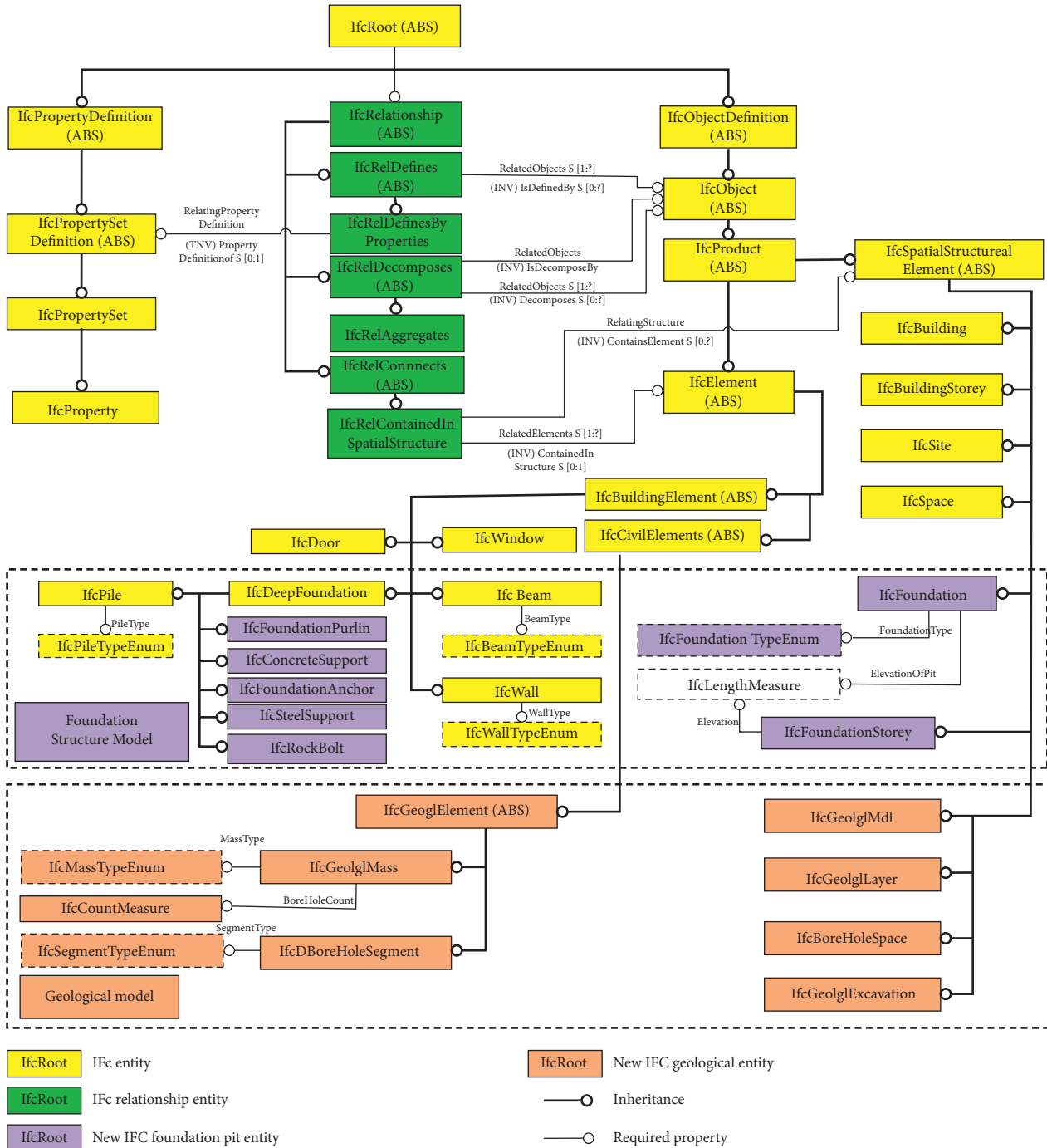


FIGURE 1: IFC extended EXPRESS-G diagram of the geotechnical information model.

To extend geotechnical engineering information in accordance with IFC standards, taking geotechnical engineering characteristics and model requirements into account is indispensable. For a specific object in geotechnical engineering, we select a subtype derived from *IfcObject* as its supertype and assigning properties to it. As for the relationship types between objects, we associate one corresponding subtype of *IfcRelationship* and define the property of the relationship entity. According to specific requirements of the project, the entity dynamic properties are extended

through *IfcPropertySet*. Moreover, *IfcPropertySet* is associated with the subclass entity of the main entity *IfcObject* through the relationship entity *IfcRelDefinedByProperties*, which makes abstract objects concrete.

4.2. “Built-In Generation Schema” for Geotechnical Structure. Geotechnical engineering structures have common characteristics with general building structures. For this reason, the entity description of the geotechnical engineering

structure can inherit and reference the building structure entity in the existing IFC data schema. In the IFC framework, `IfcBuildingElement` is used to define and represent some common building components in the building field. For extending the geotechnical structure entities, an abstract entity representing the physical element of geotechnical structure is added under the `IfcBuildingElement`. Some of the components in the newly added subtype can call existing entities, and some need to be newly defined and described. This is what we call “Built-In Generation Schema.”

Foundation structures, acting as a typical representative in geotechnical engineering, are herein used to describe this extension mechanism. When it comes to the current edition, the deep foundation entity `IfcDeepFoundation` has been included as a subtype of `IfcBuildingElement`. In consequence, the foundation structure object can inherit and call `IfcDeepFoundation`. And some of the foundation components that have not yet been included can be defined directly under the `IfcFoundation`, which is shown in Figure 1.

4.2.1. Representation of the IFC-Based Physical Element. Taking the retaining structure system of fender pile and internal support as an example, the main components are cast-in-place pile, crown beam, concrete support, steel support, steel purlin, and anchor cable (pole). To be specific, the crown beam entity inherits directly from the `IfcBeam`, which is derived from `IfcBuildingElement`, utilizing its enumeration type to represent the crown beam category, as shown in Table 1. As for the cast-in-place pile entity, it calls `IfcPile`, which is a subtype of `IfcDeepFoundation`, and uses its enumeration type for category description. Other components are defined as subtypes of `IfcDeepFoundation`, and information is extended by the means of defining entity type, including `IfcConcreteSupport`, `IfcSteelSupport`, `IfcRockBolt`, and `IfcFoundationPurlin`.

4.2.2. Representation of the IFC-Based Spatial Structure Element. `IfcSpatialStructureElement` is the supertype of all spatial structures in IFC, decomposing the project model into various suitable subsets according to the spatial layout. Although spatial description types such as `IfcBuilding`, `IfcBuildingStory`, `IfcSite`, and `IfcSpace` already exist in IFC, they are all designed for building engineering. Accordingly, `IfcFoundation` and `IfcFoundationStorey` are added as the spatial structure entity to specifically describe the foundation structure.

With the effect of providing characteristic data of foundation structure, `IfcFoundation` involves location, spatial geometry, depth, and some other information. The basic characteristics of the structure system type and relative elevation are expressed by `FoundationType` and `ElevationOfFoundation`. The enumeration type `OffoundationType` is `IfcFoundationTypeEnum`, which is defined as follows:

```
TYPE IfcFoundationTypeEnum = ENUMERATION
OF (ROW_PILE, DIAPHRAGM_WALL, SHEET_
PILE, SMW, USERDEFINED, NOTDEFINED);
END_TYPE;
```

As the spatial part corresponding to each layer of foundation, `IfcFoundationStorey` describes the spatial location, spatial geometry, and other information of each layer of foundation structure in view of the support location of each layer. The relation entity `IfcReggregates` is the indispensable bridge connecting the hierarchical relations among the spatial structure elements of the foundation. The vertical hierarchical relationship of the foundation spatial structure element is shown in Figure 2. The `IfcSite` is located in the global coordinate system of `IfcProject`, where `IfcFoundation` is located in `IfcSite`, `IfcFoundationStorey` may include multiple adjacent layered spaces as a complex to form a complex type, or it may only contain a single-layered space to form an element type.

4.3. “Plug-In Extension Schema” for the Geological Model. As mentioned above, in view of the common characteristics of foundation structure and BIM structure, we proposed the “Built-In Generation Schema.” The current IFC framework is mainly for building structures. However, conspicuous differences between 3D geological model data and BIM structural data that have been identified have impeded the adoption of geological model data into IFC framework. In order for geological model data to be integrated into IFC, it is urgently needed to create new entities, describe new relationship characteristics, and extend new information types. In consideration of the fact that `IfcCivilElement` has been added in IFC4 to describe entities of civil engineering objects, we can directly add `IfcGeolglElement` under `IfcCivilElement` to express the geological model. All components of `IfcGeolglElement` need to be newly added. Accordingly, we put forward the IFC-based “Plug-In Extension Schema” for the geological model.

A typical 3D geological model consists of geological objects such as strata, strata block, obstacles, underground cavities, and so on. In this paper, the blocks, obstacles, and underground cavities are classified into a class of objects, collectively referred to as geological mass, through the types of which actual objects can be distinguished. The ultimate goal of creating the geological model is to define the IFC elements of these geological objects, the relationships between them, and the property information of the geological objects. Its overall framework is shown in Figure 3. The newly added geological IFC objects include geological physical elements and geological spatial structure elements. It is the relationship entity `IfcRelContainedInSpatialStructure` that connects geological physical elements with geological spatial structure elements, while the relationships between geological spatial structure elements are established through `IfcRelAggregate`. The layered characteristics of rock

TABLE 1: Representation of foundation components.

Element	Crown beam	IFC entity	IfcBeam
Type	TYPE IfcBeamTypeEnum = ENUMERATION OF (FIXED_SECTION, VARIABLE_SECTION, USERDEFINED, NOTDEFINED); END_TYPE;		
Shape	IfcExtrudedAreaSolid	Section Contour	IfcParameterizedProfileDef
PropertySet	Pset_Beam		
Element	Fender pile	IFC entity	IfFoundationPile
Type	TYPE IfcPileTypeEnum = ENUMERATION OF (CAST-IN-PLACE, IMPACT-CONE, DIGGING, USERDEFINED, NOTDEFINED); END_TYPE;		
Shape	IfcSectionedSpine	Section Contour	IfcParameterizedProfileDef
PropertySet	Pset_Pile		
Element	Steel support	IFC entity	IfcSteelSupport
Type	TYPE IfcSteelSupportTypeEnum = ENUMERATION OF (STEEL_TUBE, FASHIONED_IRON, USERDEFINED, NOTDEFINED); END_TYPE;		
Shape	IfcExtrudedAreaSolid	Section Contour	IfcParameterizedProfileDef
PropertySet	Pset_SteelSupport		
Element	Concrete support	IFC entity	IfcConcreteSupport
Type	TYPE IfcConcreteSupportTypeEnum = ENUMERATION OF (STRAIGHT_LINE, CURVE, USERDEFINED, NOTDEFINED); END_TYPE;		
Shape	IfcExtrudedAreaSolid	Section Contour	IfcParameterizedProfileDef
PropertySet	Pset_ConcreteSupport		
Element	Foundation purlin	IFC entity	IfcFoundationPurlin
Type	TYPE IfcFoundationPurlinTypeEnum = ENUMERATION OF (USERDEFINED, NOTDEFINED); END_TYPE;		
Shape	IfcExtrudedAreaSolid	Section Contour	IfcParameterizedProfileDef
PropertySet	Pset_FoundationPurlin		

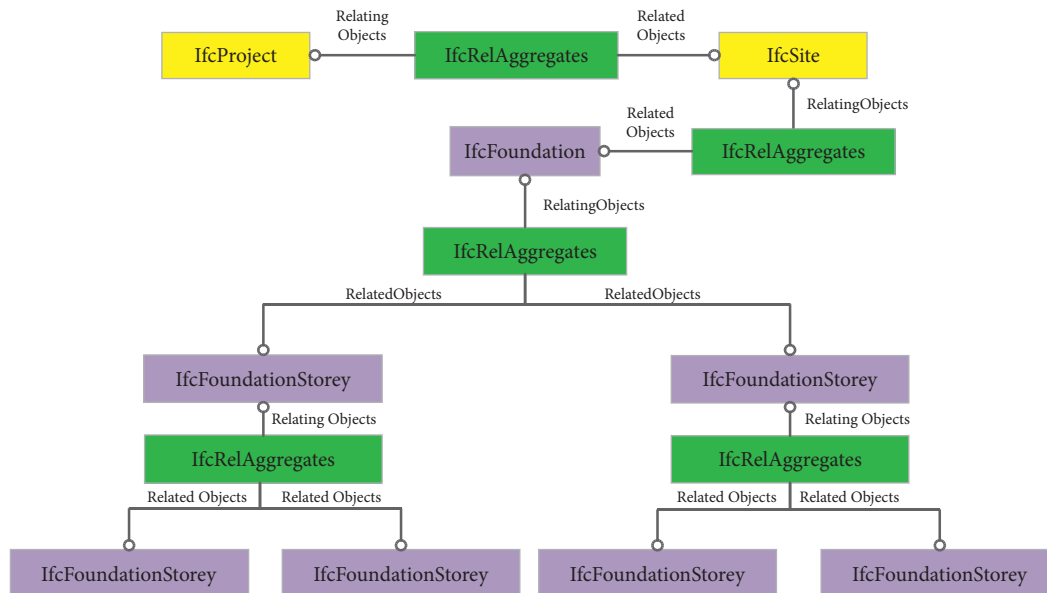


FIGURE 2: Hierarchical relationship of structure model spatial structure elements.

and soil, as well as physical, chemical, mechanical property, and other property information of the new entity, are realized by extending IfcProperty and the property set IfcPropertySet.

4.3.1. *Representation of the IFC-Based Physical Element.* Taking the representation characteristics and modeling requirements of geological model data into account, while referring to the structure model description and extension

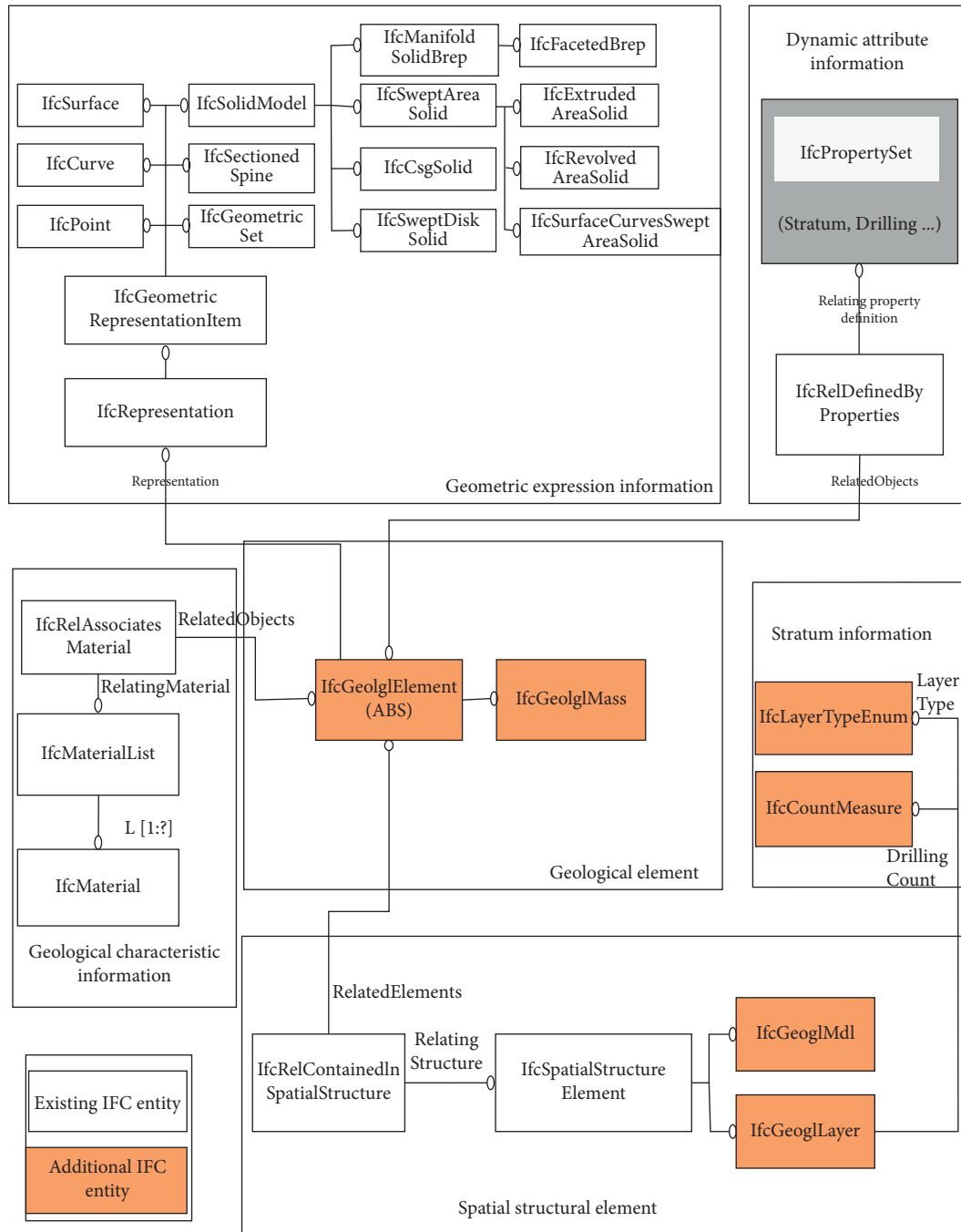


FIGURE 3: The EXPRESS-G diagram of the geological information model based on extended IFC.

mechanism in IFC, we choose to add a geological entity *IfcGeogIElement* as an abstract subtype derived from *IfcCivilElement* to describe geological objects. The geological block entity *IfcGeogIMass* is derived from *IfcGeogIElement*, and the same stratum is composed of one or more *IfcGeogIMass*. The hierarchical relationship is shown in Figure 3. In addition, to distinguish ordinary stratigraphic blocks from boulders or cavities, *IfcGeogIMassEnum* is defined for representation, and its express specification is as follows:

```

TYPE IfcGeogIMassEnum = ENUMERATION OF
(STATUM, BOULDER, CAVITY, NOT_DEFINED);
END_TYPE;
    
```

4.3.2. Representation of the IFC-Based Spatial Structure Element. As new entities derived from the abstract super-type *IfcSpatialStructureElement*, the geological model entity *IfcGeogIMdl* and the stratum entity *IfcGeogILayer* are defined to describe various spatial conceptual entities in the

geological model, as shown in Figure 4. More specifically, `IfcGeogMdl` describes the space occupied by the underground geological body, while `IfcGeogLayer` is a spatial entity composed of geological blocks with the same properties in the geological space.

4.3.3. Relationship between Entities. The relationship between entities includes the relationship between spatial entities and the relationship between spatial entities and physical entities. Figure 4 demonstrates the relationship between spatial entities, where `IfcRelAggregates` plays an essential role in connecting the relationship between `IfcGeogMdl` and `IfcGeogLayer`. One `IfcGeogMdl` is aggregated from one or more `IfcGeogLayer`. Meanwhile, one `IfcGeogLayer` can also contain multiple `IfcGeogLayer`. For example, age stratification consists of multiple lithologic strata. Figure 5 gives a specific representation of the relationship between spatial entities and physical entities. The relationship between `IfcGeogLayer` and `IfcGeogMass` is expressed by `IfcRelContainedInSpatialStructure`, and one `IfcGeogLayer` could further contain one or more `IfcGeogMass`.

4.3.4. Property. Stratigraphic property information mainly contains two types: one is the layered characteristics of rock and soil, including relevant information such as strata age, lithology, state, and thickness of the stratum; the other is the geophysical and mechanical property, which refers to the relevant physical and mechanical parameter information and geotechnical characteristics by the method of experiments. For expressing these two types of property information, we extend `IfcPropertySet` and `IfcProperty`. The definitions of stratum property and property set created in this paper are shown in Tables 2 and 3.

5. Modeling Method for Geotechnical Engineering Based on IFC Standard

According to the proposed IFC-based strategy, and “Built-In Generation Schema” for geotechnical structure and “Plug-In Generation Schema” for the geological model, in this section, we will develop corresponding methods to build a geotechnical engineering information model that can accurately describe and display the various information based on IFC using C++ language.

5.1. Modeling Foundation Structures. By compiling the extended IFC standard, the parameters required to describe each type of component of the foundation retaining structure are obtained, which are generally the identification number, name, description, geometric shape expression, category, associated element, property set, and so on. When creating component models, we use the modeling software API to read these parameters, and then call the IFC analysis module to create the IFC type of the corresponding component instance and associate these parameters. In this way, the components in the IFC information model output by the

foundation structure model can be organized according to the data standard extended in this paper, so as to realize the information sharing based on IFC.

There are a number of foundation structure types. The modeling method changes depending on the types of the structure components. In order to reduce the modeling workload, as well as shorten the modeling cycle, this paper presents a method of creating a “foundation structure model library.” To be specific, a parametric modeling technology is adopted to create a BIM template library for different components for the structure system, thus forming a general structure model library. The main modeling process is illustrated in Figure 6.

Based on the Visual Studio platform, secondary development is employed to implement the foundation structure modeling module based on IFC standard and BIM technology. In consideration of the modeling process, referring to the “Built-In Generation Schema” for geotechnical structure, the organizational framework of the procedure in this paper is established. Figure 7 demonstrates a specific description of the implementation process. The module mainly includes component modeling parameter information, structure element, property definition, and IFC entity read-write submodule. On the consideration of the requirements of the IFC data model, modeling parameter information management part is mainly to set the input component parameters to establish a special data management class, so as to be convenient to call. In the structure element modeling part, based on the “Built-In Generation Schema,” all component classes (pile, support, crown beam, etc.) are derived from the `FoundationElement` class, and all of them can call the corresponding data management class. Additionally, the method functions for component models are created in this part, and relationships between components are established through `RelConnectsElement` class. Making use of the `RelDefinesByProperties` class, the definition of the dynamic properties of the foundation component is implemented. Last but not least, the IFC entity read-write submodule has two functions. The first function is to read the IFC file and analyze the parameters needed for component modeling to form a component model. The second objective, on the grounds of the parameters required to describe the IFC entity of each component, is to convert each component class to the IFC entity to form an IFC file.

5.2. Building a 3D Geological Model. We rely on `GeoFrame`, a self-developed 3D geological modeling platform, to build a 3D geological model. In this platform, a 3D solid model and its properties are combined to form 3D elements, among which a 3D solid model is composed of the body (simple and complex), surface (simple and complex), ring, triangle, edge, node, and point conceptual models. The 3D vector spatial data model is oriented to geological entities as a whole and has a clear hierarchical structure inside the entity. It can perform spatial analysis inside the entity, which is convenient for maintenance operations such as model updating and modification. The geological data model abstracts geological entity into four basic elements of 3D space, point,

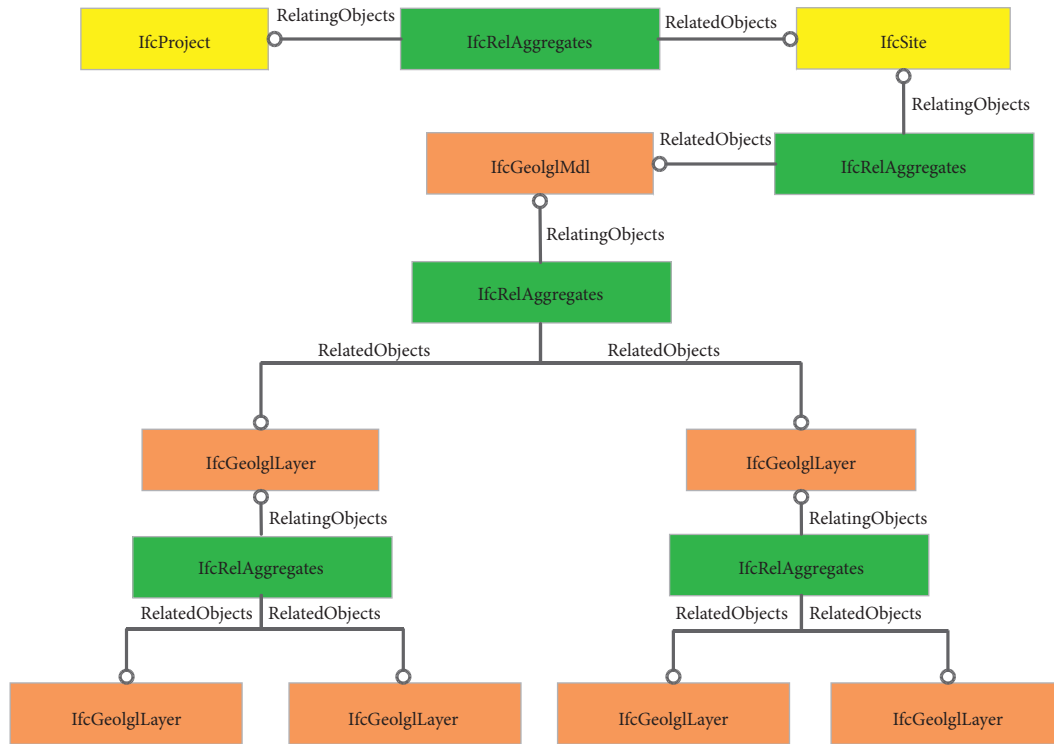


FIGURE 4: Hierarchical relationships of geological model spatial structure elements.

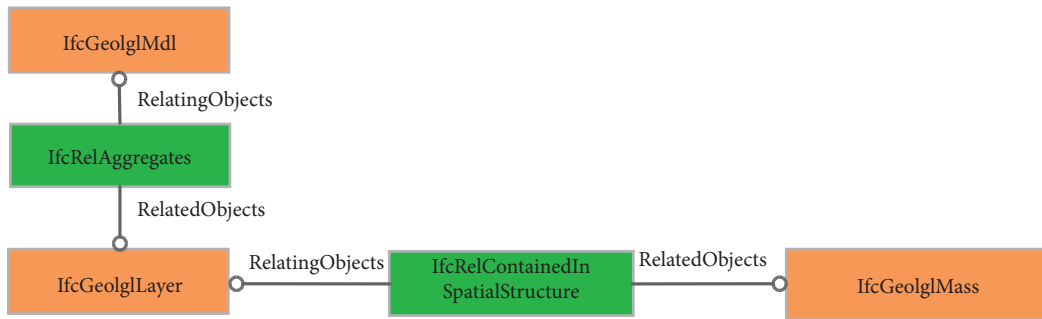


FIGURE 5: Relationships between the physical elements and spatial elements.

TABLE 2: Stratum public IFC property definition.

PropertySet name: Pset_GeoglmLayerCommon		
Applicable entities: IfcGeoglmLayer		
Property name	Property type	Property data type
StratumCode	IfcPropertySingleValue	IfcLabel
GeologicalAge	IfcPropertySingleValue	IfcLabel
Geologicalithology	IfcPropertySingleValue	IfcLabel
State	IfcPropertySingleValue	IfcLabel
FeatureDescription	IfcPropertySingleValue	IfcLabel
TopDepth	IfcPropertySingleValue	IfcLabel
BottomDepth	IfcPropertySingleValue	IfcLabel
LayerThickness	IfcPropertySingleValue	IfcLabel
DistributionCharacteristics	IfcPropertySingleValue	IfcLabel

TABLE 3: Stratum physical IFC property definition.

PropertySet Name: Pset_GeolglLayerPhysical			
Applicable entities: IfcGeolglLayer			
Property name	Property type	Property data type	
Density	IfcPropertySingleValue	IfcNumericMeasure	
WaterContent	IfcPropertySingleValue	IfcNormalizedRatioMeasure	
VoidRatio	IfcPropertySingleValue	IfcNumericMeasure	
ElasticityModulus	IfcPropertySingleValue	IfcNumericMeasure	
TensileStrength	IfcPropertySingleValue	IfcNumericMeasure	
CompressiveStrength	IfcPropertySingleValue	IfcNumericMeasure	
ShearStrength	IfcPropertySingleValue	IfcNumericMeasure	
Saturability	IfcPropertySingleValue	IfcNormalizedRatioMeasure	
Permeability	IfcPropertySingleValue	IfcNumericMeasure	
PoissonRatio	IfcPropertySingleValue	IfcNumericMeasure	
Engineering geological characteristics	IfcPropertySingleValue	IfcLabel	

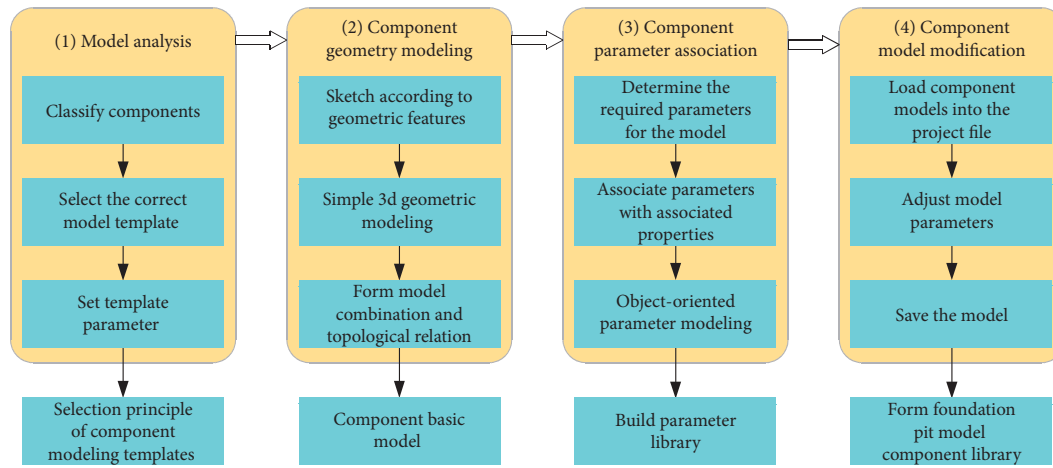


FIGURE 6: Modeling steps of structure components.

line, surface, and body, and explicitly constructs more complex objects with the geometry of these basic elements.

By virtue of the fact that both the geological model object and IFC model object belong to semantic model, geometric analysis, information extraction, and data conversion can be adopted for the geological model object to realize the conversion of information. Furthermore, by the means of reconstructing the data, based on the “Plug-In Extension Schema” for the geological model, the transformation between the geological model and the IFC model is realized. In order to guarantee the integrity of geometry information in the process of data transformation, IFC geological model is also subdivided into point, line, and surface elements, and mapping relationship is established with the elements of the geological model. The mapping relationship of model elements is shown in Figure 8.

In terms of geometric expression, due to the irregular geometry of the geological body, boundary representation is adopted to describe geological model objects. Likewise, the IFC model can make use of boundary representation to describe and form a geometric entity through the combination of multiple boundary surface patches. In IFC standard, the abstract base class of geometric entities based on

boundary representation is `IfcManifoldSolidBrep`. Its subtype `IfcAdvancedBrep` corresponds to the boundary enclosed by the spline surface. `IfcFacetedBrep`, also as its subtype, can describe the entity represented by the boundary surrounded by polygons. In our 3D geological model based on the “Plug-In Extension Schema,” `IfcFacetedBrep` is applied to express the geometric information of `IfcGeolglMass` with uniform internal characteristics. For `IfcGeolglMass` containing boulders or cavities inside, `IfcFacetedBrepWithVoids`, a subtype of `IfcFacetedBrep`, is extended to describe.

Based on the above comparative analysis of the geological model and IFC model, a special IFC output plug-in is developed with C++ language. By analyzing the 3D geological model established in GeoFrame and taking advantage of the “Plug-In Extension Schema,” the IFC entities and related properties are created, and the information flow in the form of a string is generated according to the definition of the IFC standard and output into a standard STEP format file. As a consequence, the output of physical files of the geological model based on the “Plug-In Extension Schema” is realized, which lays a solid foundation for the integration of the geological model and structure model.

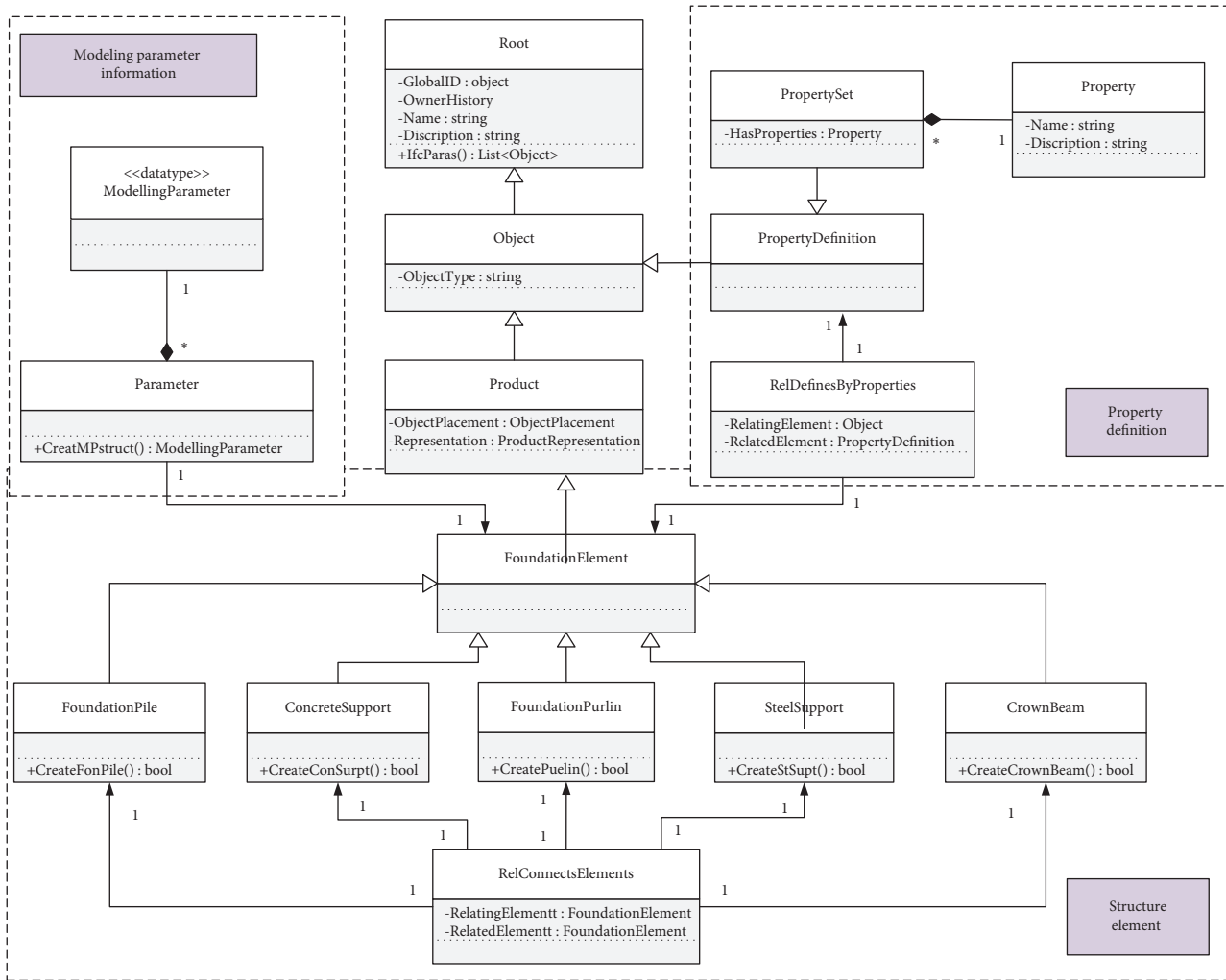


FIGURE 7: Logical structure of IFC-based foundation structure modeling.

6. Example

In this section, we will take a metro station in a city as an example to verify the validity of the basic data system and modeling methodology of the geotechnical engineering information model proposed in this paper. In the example, we will build the foundation structure model and 3D geological model based on the extended IFC standard and integrate them on the basis of IFC standard.

The metro station is a two-level underground island-type station with a closed frame structure, which adopts an open-cut method. The support structure system of fender pile and internal support is intended for the construction of the foundation. The first layer of lateral support is reinforced concrete, while the second and third layers of lateral support are steel tubes. The connection between steel supports and fender piles are the purlins, which are sustained by angle steel supports. In particular, in order to ensure the stability of the end well, it is prerequisite to set up concrete diagonal bracing and steel tube diagonal bracing. Making use of the

“Built-In Generation Schema,” the basic models and the overall model built by parametric modeling are displayed in Figures 9 and 10. By analyzing the 25 geological boreholes obtained in the previous investigation in this area, it is revealed that the stratum mainly consists of 13 lithologic soil layers such as plain fill, residual soil, and granite. Figure 11 presents a geological model built in GeoFrame using borehole survey data. According to the geological objects defined previously based on the “Plug-In Extension Schema,” the geological model is exported to the STEP format file.

By the lights of IFC++ open-source tools, using C++ language for secondary development, an IFC integration platform was developed. By analyzing the implementation mode of IFC standard and adopting the method of Early Binding, the data structure based on EXPRESS under IFC core module was implemented as the corresponding C++ class, and finally the C++ class library of IFC standard was formed. We then developed a module for reading and writing IFC files specifically for Express expression, which

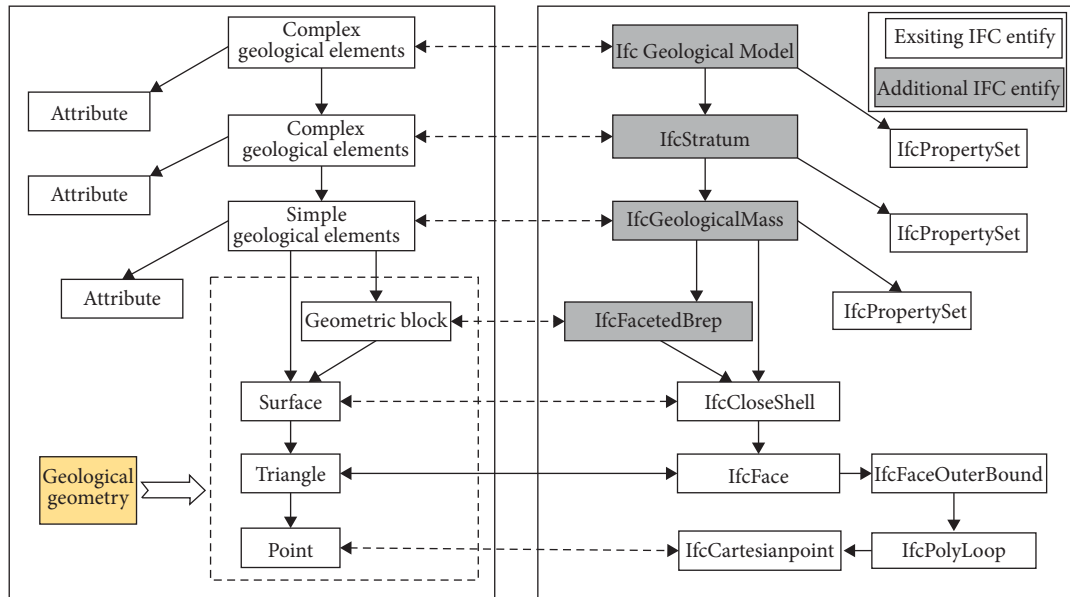


FIGURE 8: Map of the geological model and IFC model elements.

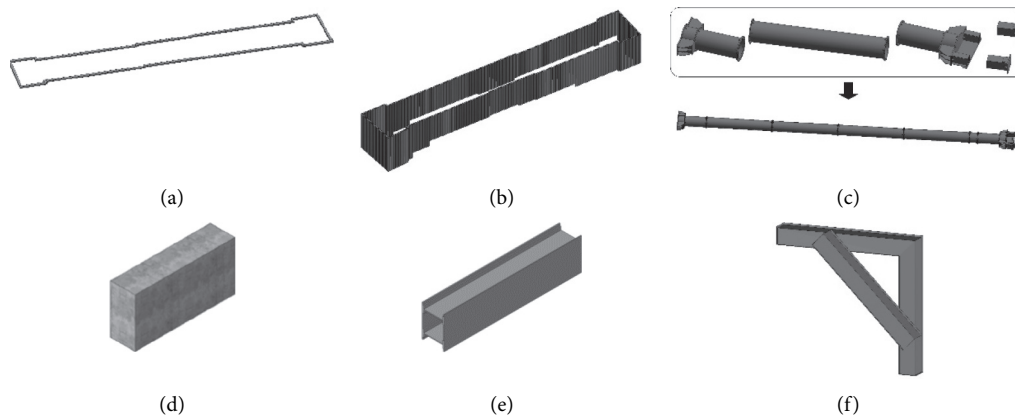


FIGURE 9: Models of main structure components. (a) Crown beam. (b) Fender pile. (c) Steel support. (d) Concrete support. (e) Steel purlin. (f) Steel bracket.

was used to transform IFC physical files and the corresponding IFC core classes. Moreover, based on OSG 3D display engine, 3D model display function was developed, used to display the IFC geometric entities. In order to facilitate data creation, viewing, and deletion, the IFC structure tree expression pattern was built according to the IFC data structure hierarchy. This platform realized the functions of viewing 3D geometric model, transforming multiple IFC files, and integrating different professional model files. It is also scalable to be able to connect many professional software.

The STEP file of 3D geological model based on the output of the “Plug-In Extension Schema” is imported into the platform for display, and the structure model in the form of IFC files is synchronously imported into the platform, so

as to implement the integration of geotechnical engineering models in Figure 12. Fully considering the characteristics of geotechnical engineering, the integrated BIM model is interactively processed. The integrated BIM model is extended to generate numerical meshes for geotechnical computations and then can be carried out geotechnical design and numerical analysis, as shown in Figure 13.

According to the proposed IFC-based schema, geological models and geotechnical structure models are integrated as shown in Figure 12, which helps us overcome the lack of unified data standard between the geological model and structure model and makes it easy for us to manage data and information. Our integrated model could be further used in mesh generation and numerical calculation, as shown in Figure 13. So the integrated model not only can be used for

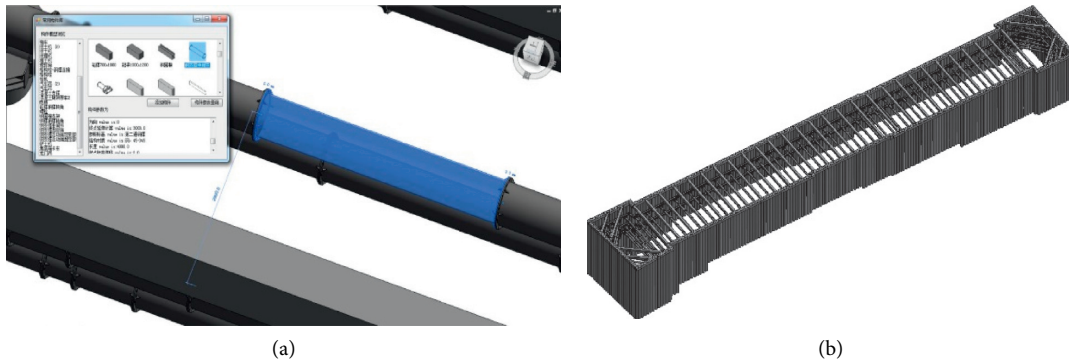


FIGURE 10: BIM model of foundation structure. (a) Call component library and search information. (b) Assembled BIM model.

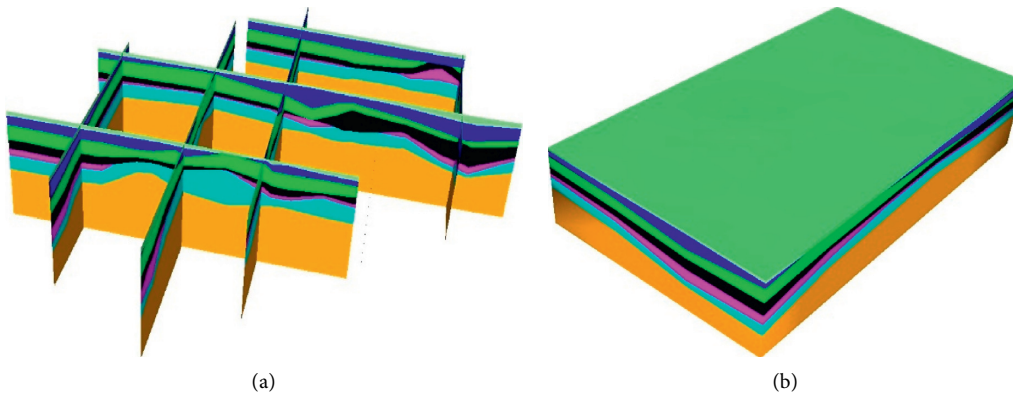


FIGURE 11: A geological model. (a) The profile of a geological model. (b) 3D geological model.

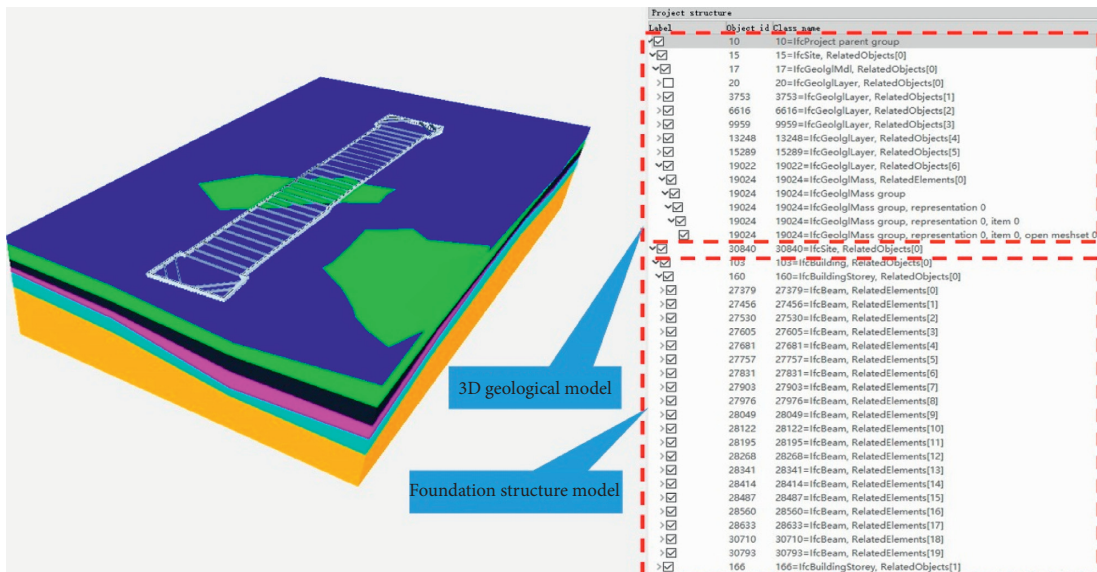


FIGURE 12: The integrated display of the geological model and the structure model.

visualization but also has the ability to be extended to generate numerical meshes for geotechnical computations. The integrated model of geotechnical engineering based on

BIM technology can serve the geotechnical design and effectively results in better information management for geotechnical engineering.

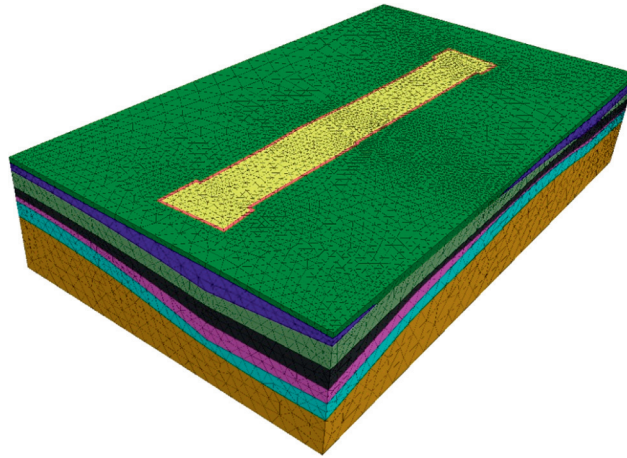


FIGURE 13: A numerical mesh model transformed from integrated BIM model.

7. Conclusion

In the process of geotechnical engineering construction, the information contained in geotechnical engineering cannot be well integrated because of the lack of unified data standards. According to the characteristics of geotechnical engineering objects, based on the existing IFC standard description mechanism, this paper adopts the method of extending IFC entity to describe geotechnical engineering objects such as geological model and geological structure model. Considering the fact that the geological structure model and building model have a lot in common, some geological structures can directly inherit and reference existing IFC entities, and the others that have not yet been included need to be newly added, so we have put forward a “Built-In Generation Schema” for geotechnical structure model. In view of the lack of definition of geological models in IFC, corresponding IFC entities and relationships need to be constructed from scratch, and hence a “Plug-In Extension Schema” for the geological model has been developed. On the basis of the realization of the data expression of geotechnical engineering information based on IFC standard, the basic data system of geotechnical engineering information model based on BIM technology has been formed to overcome the shortage of multisource data fusion.

Taking the diversity of foundation structure models into account, a “foundation structure model library” has been presented to store various basic components. Through parametric modeling, we have contributed to the modeling process and modeling method of the foundation structure model based on BIM technology. Additionally, the IFC extension for the geological model has been employed to the one-to-one mapping between the geological model and IFC model, thus realizing the output of the geological model based on the extended IFC standard. An integration platform, aimed to realize the integration and sharing of the geological model and geotechnical structure model based on the extended IFC standard, has been preliminarily developed. Based on proposed data generation mechanism under IFC framework, geological models and geotechnical structure models are integrated, so as to solve the problem of

inconsistency of current data standards. Combined with the characteristics of geotechnical engineering, our integrated model is both “good-looking and useful,” which not only can be visualized display but also can be utilized to generate numerical meshes for geotechnical computations.

The research in this paper lays a solid foundation for promoting the application of BIM technology in the geotechnical engineering field and also provides a feasible way and technical support for promoting the integration and sharing of geotechnical engineering information and carrying out geotechnical design and numerical analysis. It also will be dedicated to serving the digital twin model of geotechnical engineering.

In the future, researches on the integrated data model in the field of geotechnical engineering based on BIM technology will continue. In order to further realize the design and calculation of geotechnical engineering, there is a need to further study the interconversion between the integrated BIM model and finite element analysis model.

Data Availability

The data generated in this research are available from the corresponding author on request.

Conflicts of Interest

The authors declare that they have no conflicts of interest.

Acknowledgments

The research was supported by National Natural Science Foundation of China (Grants no. 52079135 and no. 51909259), the International Partnership Program of Chinese Academy of Sciences (Grant no. 131551KYSB20180042), the Science and Technology R&D Project of China State Construction International Holdings Limited (Grant no. CSCI-2020-Z-21), and Ningbo Public Welfare Science and Technology Planning Project (Grant no. 2019C50012). A special acknowledgement should be expressed to China-Pakistan

Joint Research Center on Earth Sciences that supported the implementation of this study.

References

- [1] M. H. Faber and M. G. Stewart, "Risk assessment for civil engineering facilities: critical overview and discussion," *Reliability Engineering & System Safety*, vol. 80, no. 2, pp. 173–184, 2003.
- [2] I. C. Cárdenas, S. S. H. Al-jibouri, J. I. M. Halman, and F. A. van Tol, "Capturing and integrating knowledge for managing risks in tunnel works," *Risk Analysis*, vol. 33, no. 1, pp. 92–108, 2013.
- [3] Q. Z. Yu, L. Y. Ding, C. Zhou, and H. B. Luo, "Analysis of factors influencing safety management for metro construction in China," *Accident Analysis & Prevention*, vol. 68, pp. 131–138, 2014.
- [4] Y. Zhou, L. Y. Ding, and L. J. Chen, "Application of 4D visualization technology for safety management in metro construction," *Automation in Construction*, vol. 34, pp. 25–36, 2013.
- [5] T. Vilutiene, D. Kalibatiene, M. R. Hosseini, E. Pellicer, and E. K. Zavadskas, "Building information modeling (BIM) for structural engineering: a bibliometric analysis of the literature," *Advances in Civil Engineering*, vol. 2019, Article ID 5290690, 19 pages, 2019.
- [6] B. Becerik-Gerber, F. Jazizadeh, N. Li, and G. Calis, "Application areas and data requirements for BIM-enabled facilities management," *Journal of Construction Engineering and Management*, vol. 138, no. 3, pp. 431–442, 2012.
- [7] L. Y. Ding, Y. Zhou, H. B. Luo, and X. G. Wu, "Using nD technology to develop an integrated construction management system for city rail transit construction," *Automation in Construction*, vol. 21, pp. 64–73, 2012.
- [8] J. Shi, J. Dao, L. Jiang, and Z. Pan, "Research on IFC- and FDS-based information sharing for building fire safety analysis," *Advances in Civil Engineering*, vol. 2019, Article ID 3604369, 18 pages, 2019.
- [9] T. Cerovsek, "A review and outlook for a 'Building Information Model' (BIM): a multi-standpoint framework for technological development," *Advanced Engineering Informatics*, vol. 25, no. 2, pp. 224–244, 2011.
- [10] P. Calcagno, J. P. Chilès, G. Courrioux, and A. Guillen, "Geological modelling from field data and geological knowledge," *Physics of the Earth and Planetary Interiors*, vol. 171, no. 3, pp. 147–157, 2008.
- [11] P. B. Scharling, E. S. Rasmussen, T. O. Sonnenborg, P. Engesgaard, and K. Hinsby, "Three-dimensional regional-scale hydrostratigraphic modeling based on sequence stratigraphic methods: a case study of the Miocene succession in Denmark," *Hydrogeology Journal*, vol. 17, no. 8, pp. 1913–1933, 2009.
- [12] O. Kaufmann and T. Martin, "3D geological modelling from boreholes, cross-sections and geological maps, application over former natural gas storages in coal mines," *Computers & Geosciences*, vol. 34, no. 3, pp. 278–290, 2008.
- [13] R. Song, X. Qin, Y. Tao et al., "A semi-automatic method for 3D modeling and visualizing complex geological bodies," *Bulletin of Engineering Geology and the Environment*, vol. 78, no. 3, pp. 1371–1383, 2019.
- [14] A. Zanchi, S. Francesca, Z. Stefano, S. Simone, and G. Graziano, "3D reconstruction of complex geological bodies: examples from the Alps," *Computers & Geosciences*, vol. 35, no. 1, pp. 49–69, 2009.
- [15] Z.-q. Luo, C.-y. Xie, J.-m. Zhou, N. Jia, X.-m. Liu, and H. Xu, "Numerical analysis of stability for mined-out area in multi-field coupling," *Journal of Central South University*, vol. 22, no. 2, pp. 669–675, 2015.
- [16] M. Sen and T. Duffy, "GeoSciML: development of a generic GeoScience markup language," *Computers & Geosciences*, vol. 31, no. 9, pp. 1095–1103, 2005.
- [17] W. Tegtmeier, S. Zlatanova, P. J. M. van Oosterom, and H. R. G. K. Hack, "3D-GEM: geo-technical extension towards an integrated 3D information model for infrastructural development," *Computers & Geosciences*, vol. 64, pp. 126–135, 2014.
- [18] H. Cheng, J. Chen, R. Chen, G. Chen, and Y. Zhong, "Risk assessment of slope failure considering the variability in soil properties," *Computers and Geotechnics*, vol. 103, pp. 61–72, 2018.
- [19] G. Zheng, X. Yang, H. Zhou, Y. Du, J. Sun, and X. Yu, "A simplified prediction method for evaluating tunnel displacement induced by laterally adjacent excavations," *Computers and Geotechnics*, vol. 95, pp. 119–128, 2018.
- [20] H. Cheng, J. Chen, and G. Chen, "Analysis of ground surface settlement induced by a large EPB shield tunnelling: a case study in Beijing, China," *Environmental Earth Sciences*, vol. 78, 2019.
- [21] T. Ganbat, H. Chong, P. Liao, and Y. Wu, "A bibliometric review on risk management and building information modeling for international construction," *Advances in Civil Engineering*, vol. 2018, Article ID 8351679, 13 pages, 2018.
- [22] N. Yabuki and Z. Li, *Development of New IFC-BRIDGE Data Model and a Concrete Bridge Design System Using Multi-Agents*, Springer, Berlin, Germany, 2006.
- [23] N. Yabuki, H. Machinaka, and Z. Li, *A Cooperative Engineering Environment Using Virtual Reality with Sensory User Interfaces for Steel Bridge Erection*, Springer, Berlin, Germany, 2006.
- [24] Y. Zhou, Y. Wang, L. Ding, and P. E. D. Love, "Utilizing IFC for shield segment assembly in underground tunneling," *Automation in Construction*, vol. 93, pp. 178–191, 2018.
- [25] S.-H. Lee and B.-G. Kim, "IFC extension for road structures and digital modeling," *Procedia Engineering*, vol. 14, no. 2, pp. 1037–1042, 2011.
- [26] S.-H. Lee, S. I. Park, and J. Park, "Development of an IFC-based data schema for the design information representation of the NATM tunnel," *KSCE Journal of Civil Engineering*, vol. 20, no. 6, pp. 2112–2123, 2016.
- [27] A. Costin, A. Adibfar, H. Hu, and S. S. Chen, "Building Information Modeling (BIM) for transportation infrastructure - literature review, applications, challenges, and recommendations," *Automation in Construction*, vol. 94, pp. 257–281, 2018.
- [28] Y. Zhou, Z. Hu, and W. Zhang, "Development and application of an industry foundation classes-based metro protection information model," *Mathematical Problems in Engineering*, vol. 2018, Article ID 1820631, 20 pages, 2018.
- [29] S. Providakis, C. D. F. Rogers, and D. N. Chapman, "Predictions of settlement risk induced by tunnelling using BIM and 3D visualization tools," *Tunnelling and Underground Space Technology*, vol. 92, p. 103049, 2019.

Research Article

Field Investigation of Blasting-Induced Vibration in Concrete Linings during Expansion of Old Highway Tunnel

Ya-Qiong Wang ¹, Lin-Jin Gong,² Nan-Nan An,² Xing-Bin Peng,² Wei Wang,^{1,3}
and Zhi-Feng Wang ¹

¹School of Highway, Chang'an University and Shaanxi Provincial Major Laboratory for Highway Bridge & Tunnel, Xi'an 710064, China

²School of Highway, Chang'an University, Xi'an 710064, China

³CCCC Second Harbour Engineering Co., Ltd., Wuhan, Hubei 430040, China

Correspondence should be addressed to Zhi-Feng Wang; zhifeng.wang@chd.edu.cn

Received 23 June 2020; Revised 6 August 2020; Accepted 30 January 2021; Published 10 February 2021

Academic Editor: Hugo Rodrigues

Copyright © 2021 Ya-Qiong Wang et al. This is an open access article distributed under the Creative Commons Attribution License, which permits unrestricted use, distribution, and reproduction in any medium, provided the original work is properly cited.

Numerous mountain highway tunnels in China do not satisfy the current traffic design standards and therefore need to be rebuilt or expanded. The drilling-blasting method is the primary method employed in China for expanding mountain highway tunnels, and it is crucial to monitor the vibrations caused by blasting. This study conducted a field investigation of the vibrations caused by blasting during the expansion of Yujiaya tunnel, which was built in 1999. The blasting-induced vibrations in the new and old concrete linings were monitored and analyzed during the expansion. The measured values of the peak particle velocity (PPV) varied within the range of 0.097–8.246 cm/s. The attenuation law of the PPV was determined via a regression analysis using Sadovsky's empirical formula. The relationship between the main vibration frequency and the distance from the blasting source was expressed as a power function. Finally, the safety distances of the concrete linings subject to blasting vibrations were analyzed and discussed.

1. Introduction

In China, numerous old mountain highway tunnels have undergone local collapse, water leakage, and lining cracking, among other issues [1–5]. These highway tunnels are in a subhealth state, have entered the “high maintenance” management period, and do not satisfy current traffic design standards; thus, they must be rebuilt or expanded [6]. The drilling-blasting method is the primary method employed in China for the construction of mountain tunnels [7–9], where blasting control is the key issue faced during the process of expanding old tunnels [10–13]. During tunnel expansion and the construction processes involved, blasting vibrations of different strengths inevitably cause macroscopic damage or microscopic cumulative damage to underground structures or adjacent buildings [14–18]. If the blasting control is not reasonable, it may cause a continuous collapse of the old

concrete lining, introducing considerable difficulty to the expansion of tunnels [19–22]. Therefore, it is important to monitor blasting-induced vibration during the process of expanding old tunnels for ensuring safety [23–26]. Several studies have investigated the effects of underground engineering blasting on adjacent structures (in terms of the critical limit, dynamic response caused by blasting, etc.) via field tests, numerical simulations, and model tests [27–31]; however, most of them focused on the linings of existing tunnels, adjacent buildings, airport runways, and hydro-power stations [32–36]. In the case of a wireless sensor network, Lai et al. [37] investigated the effects of blasting-induced vibrations on the structure of the existing tunnel. Feldgun et al. [14] proposed a comprehensive approach to simulate an explosion occurring inside a buried axisymmetric lined cavity. However, there have been few studies on the effects of blasting vibrations caused by *in situ* expansion of highway tunnels, which require close attention.

This study aimed to perform a field test to investigate the vibrations caused by blasting during the *in situ* expansion of the Yujiaya tunnel, which was built in 1999; it is the first *in situ* expansion project conducted in the Shaanxi Province. In this study, the vibration velocity and the main vibration frequency in the new and old concrete linings were measured. The attenuation law of the peak particle velocity (PPV) for the new and old concrete linings was analyzed. The relationship between the main vibration frequency and the distance to the blasting source was examined. Additionally, the safety distances of concrete linings subject to blasting vibrations were investigated.

2. Project Background

Yujiaya tunnel is a single-hole tunnel located on the S309 line of the highway from Lueyang County to Kang County, Shaanxi province, as shown in Figure 1. After complete construction, it was opened to traffic on June 15, 1999. On July 14, 2015, because the top lining concrete of the tunnel partially collapsed, the tunnel was analyzed and tested in detail to verify its quality status. As shown in Figure 2, the test results indicated that Yujiaya tunnel had the following damage: a partial collapse of the lining, cracks in the lining and water leakage, an insufficient lining thickness and defects, an insufficient lining strength, drainage system failure, no lighting, no fire protection, safety facilities, and so forth. Figure 3 presents cross-sectional views of the Yujiaya tunnel before and after expansion. As shown, the height and width of the old Yujiaya tunnel were 7.8 and 8.5 m, respectively. To improve the traffic conditions, they were increased to 8.75 and 10.0 m, respectively, in the new Yujiaya tunnel. Figure 4 presents a longitudinal view of the Yujiaya tunnel and the geological conditions. As shown, the Yujiaya tunnel was approximately 518 m long (medium-long tunnel) with mileage piles of K101 + 850 – K102 + 368. The geological conditions for the Yujiaya tunnel are also presented in Figure 4. As shown, the strata in the tunnel area were mainly composed of phyllite rock, and the Yujiaya tunnel crossed three fault fracture zones and limestone strata. The unconfined compressive strength of the phyllite rock ranged from 12.8 to 39.6 MPa.

The *in situ* expansion process of the tunnel is mainly divided into two phases: demolition of the old lining structure and excavation of local surrounding rock. The old lining is demolished mainly via the cutting method along with low-magnitude vibration and loose, weak blasting. Moreover, the excavation of the surrounding rock is mainly conducted via weak blasting, and mechanical machines can be used for this process. In the *in situ* expansion, two and three rows of boreholes are arranged around the rock in the upper and lower steps, respectively, which are perimeter holes and auxiliary holes from the outside to the inside, as shown in Figure 5. The perimeter holes are spaced and uncoupled charge structures, whereas the auxiliary holes are continuous uncoupled charge structures. A slight delay in blasting is applied between each row of holes (different-colored holes use different detonator segments). The detonator

segments correspond to $\bar{1}$, $\bar{2}$, and $\bar{3}$, and the delay between adjacent detonator segments is 100 ms (determined according to the blasting engineer's experience). Thus, layer-by-layer detonation is performed from the adjacent free face to the outside, eliminating the stress wave superposition effect caused by the explosion.

3. Field Monitoring Program

3.1. Monitoring Principle Using TC-4850. The blasting vibration testing system was primarily composed of a signal sensor (picker) and a data recorder. A three-vector vibration sensor and a TC-4850 self-recording instrument (Chengdu Zhongke Instrument Co., Ltd.) were used during the monitoring process. The sensor converted the blasting vibration signals to electrical signals, which were then converted to digital signals through analog-to-digital conversion via the self-recording instrument. Finally, the data recorder was connected to the computer through a special data line after the test, and the vibration signals were extracted, stored, processed, and analyzed using the Blasting Vibration Analysis software [38]. The test process is depicted in Figure 6. In the field test, the PPV and main vibration frequency were monitored. The PPV and the main vibration frequency were in the ranges of 0–35 cm/s and 0–10 kHz, respectively, and their test accuracies were 0.0001 cm/s and 0.1 Hz, respectively.

3.2. Monitoring Scheme and Layout of Test Points. The layout of the monitoring points adhered to the following principles: (1) the location and direction monitoring of the maximum PPV; (2) real-time monitoring of the blasting vibrations; and (3) observation of the attenuation law of the blasting vibrations. According to the foregoing monitoring principles and the propagation law of blast stress waves, the monitoring sections were arranged on both sidewalls of the new and old sections of the Yujiaya tunnel. Two monitoring points were set in each section. The monitoring points were determined to be at the same height as that of the side walls: approximately 1.5 m above road level, at which it was convenient to perform measurements. As shown in Figure 7, four monitoring points were arranged for each blasting process denoted as C1, C2, C3, and C4.

The distances between the monitoring points on each side and the blasting source were R_1 , R_2 , R_3 , and R_4 . A three-vector sensor was installed at each monitoring point to measure three vibration velocities: the horizontal radial velocity V_x , horizontal tangential velocity V_y , and vertical velocity V_z . Because the terrain at each monitoring point was relatively flat and the height difference between adjacent monitoring points was small, the influence of the height difference on the propagation of the blasting stress wave could be neglected in the field test.

4. Results and Discussion

4.1. PPV. In the field test, the vibration velocities in different directions were measured. Figure 8 presents typical curves of the measured vibration velocities (V_x , V_y , and V_z) in the

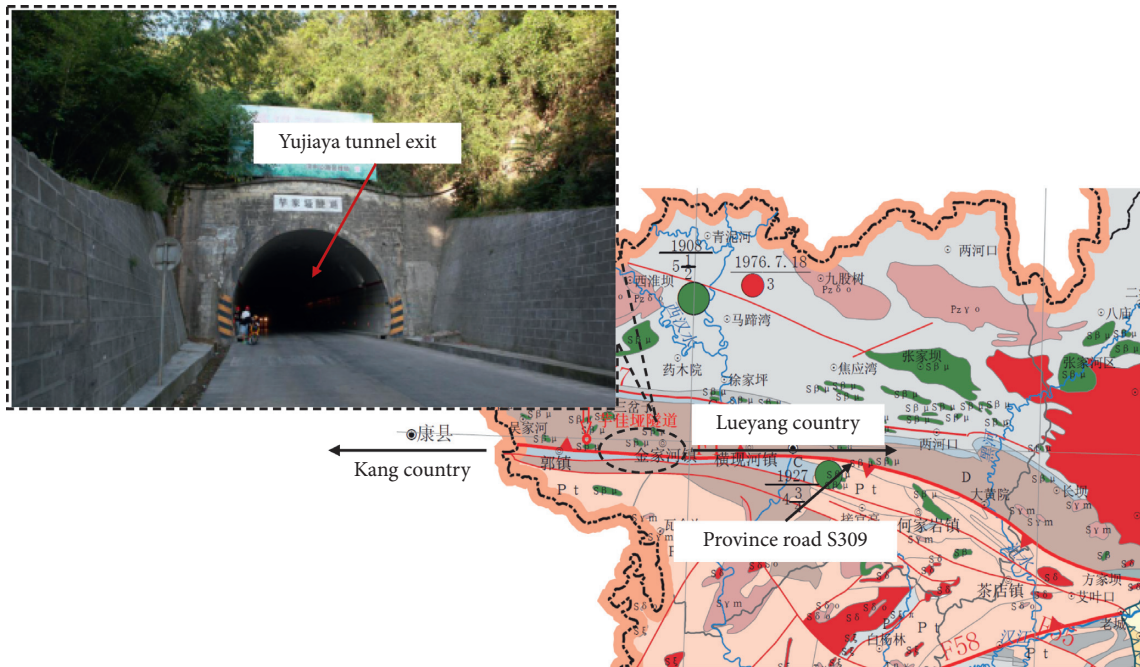


FIGURE 1: Plan view of the location of Yujiaya tunnel.

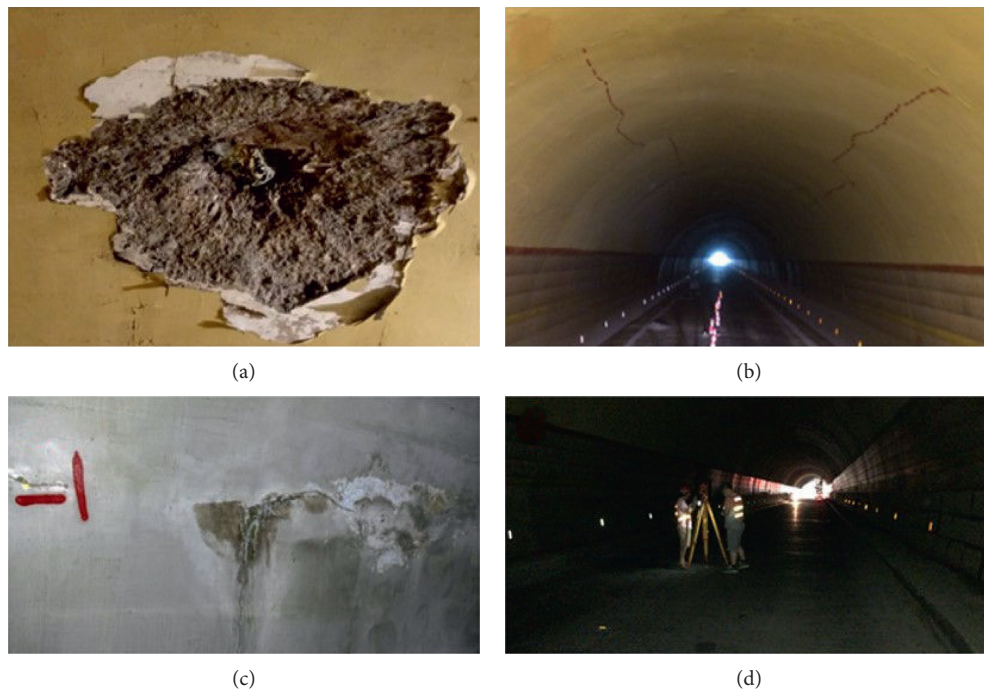


FIGURE 2: Damage to Yujiaya tunnel: (a) partial collapse of the lining; (b) cracks in the lining; (c) leakage; (d) poor traffic conditions.

new concrete lining for one test. As shown, the peak vibration velocities (PPVs) in the three directions were 0.197, 0.280, and 0.384 cm/s, respectively. To further study the attenuation law of the peak vibration velocities caused by blasting in the expansion of the Yujiaya tunnel, 10 field tests were conducted during the construction process, and a large amount of PPV data was collected, as shown in Table 1. Many researchers have proposed prediction formulas for

blasting vibration, which are generally based on Sadovsky's empirical formula, and the parameters are revised and perfected in actual blasting engineering. Additionally, formulas for predicting the relationship among the PPV, trinitrotoluene (TNT) weight, and safe distance were also proposed in China and were incorporated into the Safety regulations for blasting in China [39]. The PPV can be predicted as follows:

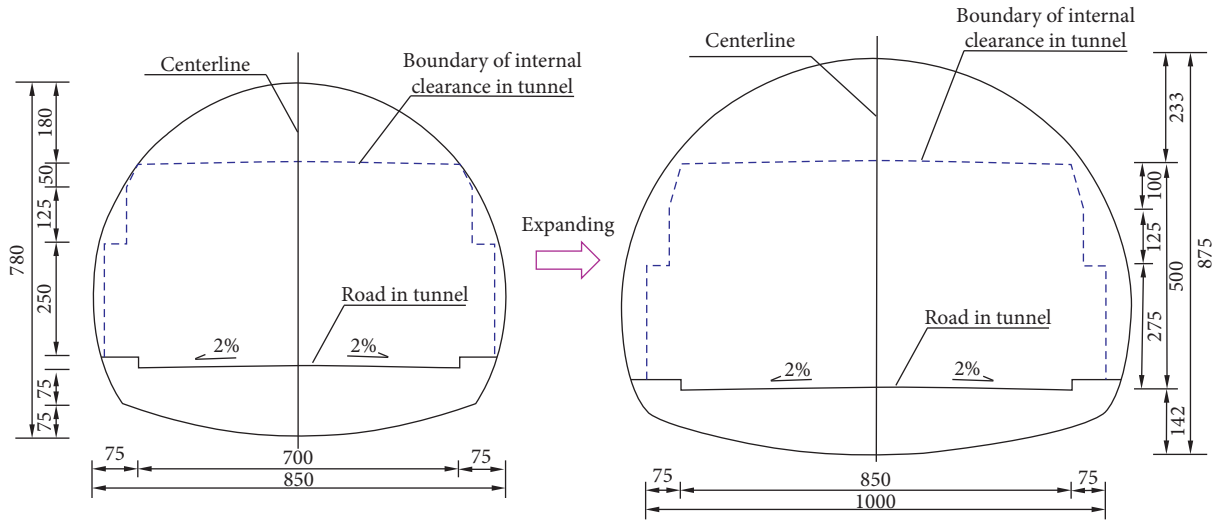


FIGURE 3: Cross-sectional views of Yujiaya tunnel before and after expansion.

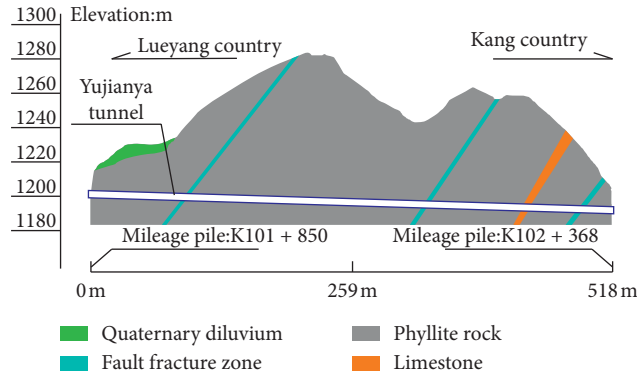


FIGURE 4: Longitudinal view of Yujiaya tunnel and the geological conditions.

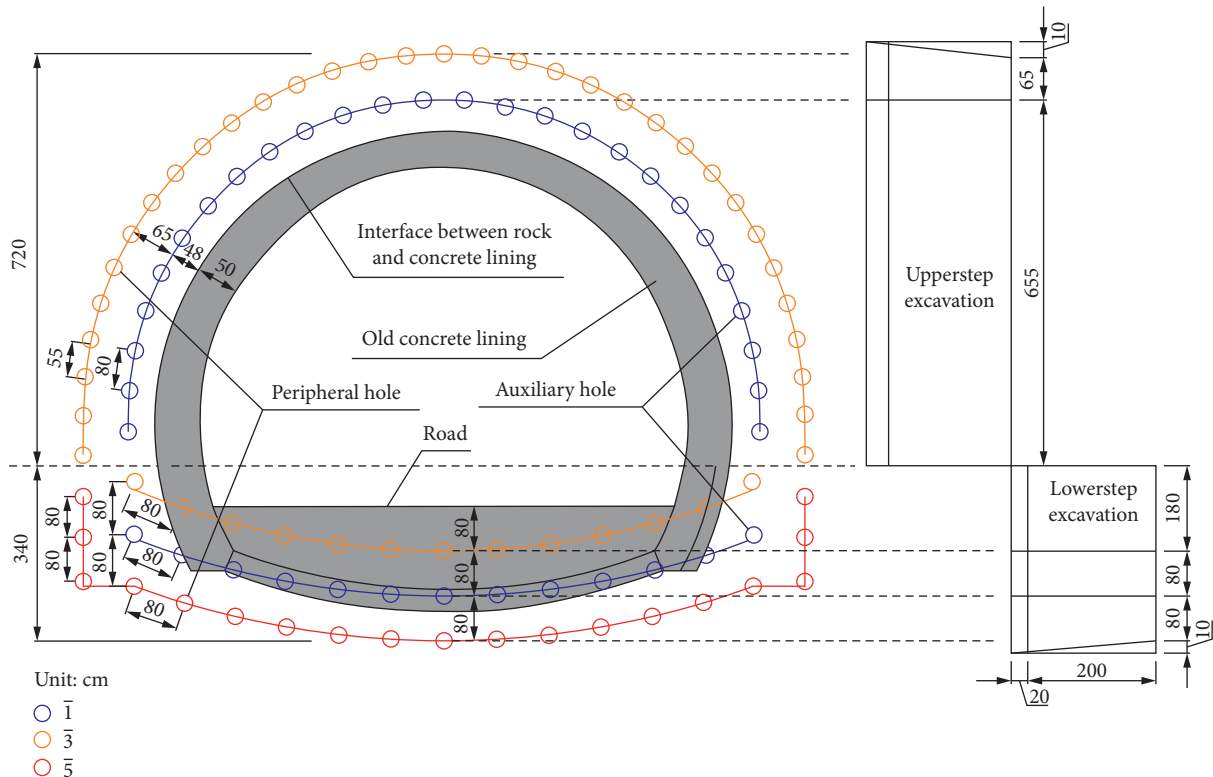


FIGURE 5: Layout of blasting holes during the construction for expanding Yujiaya tunnel.

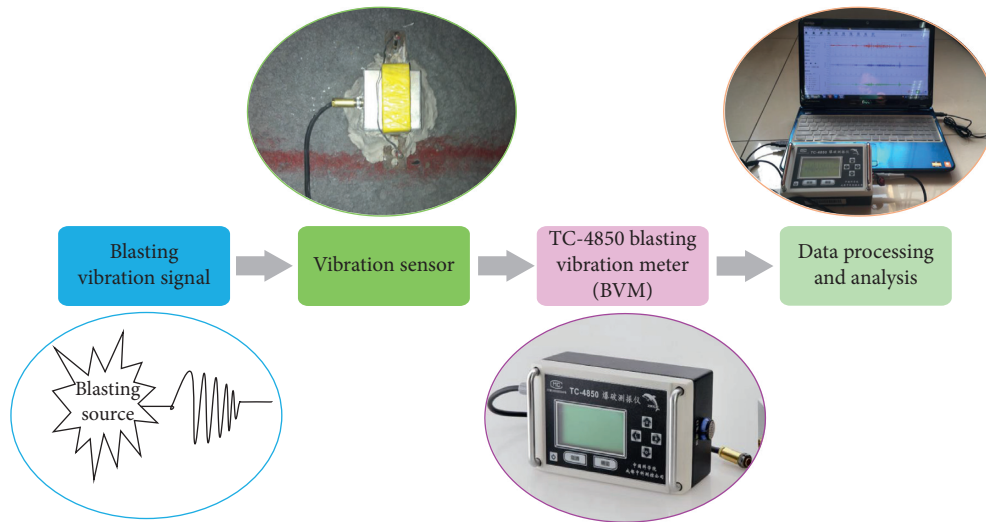


FIGURE 6: Principle for testing the blasting-induced vibrations.

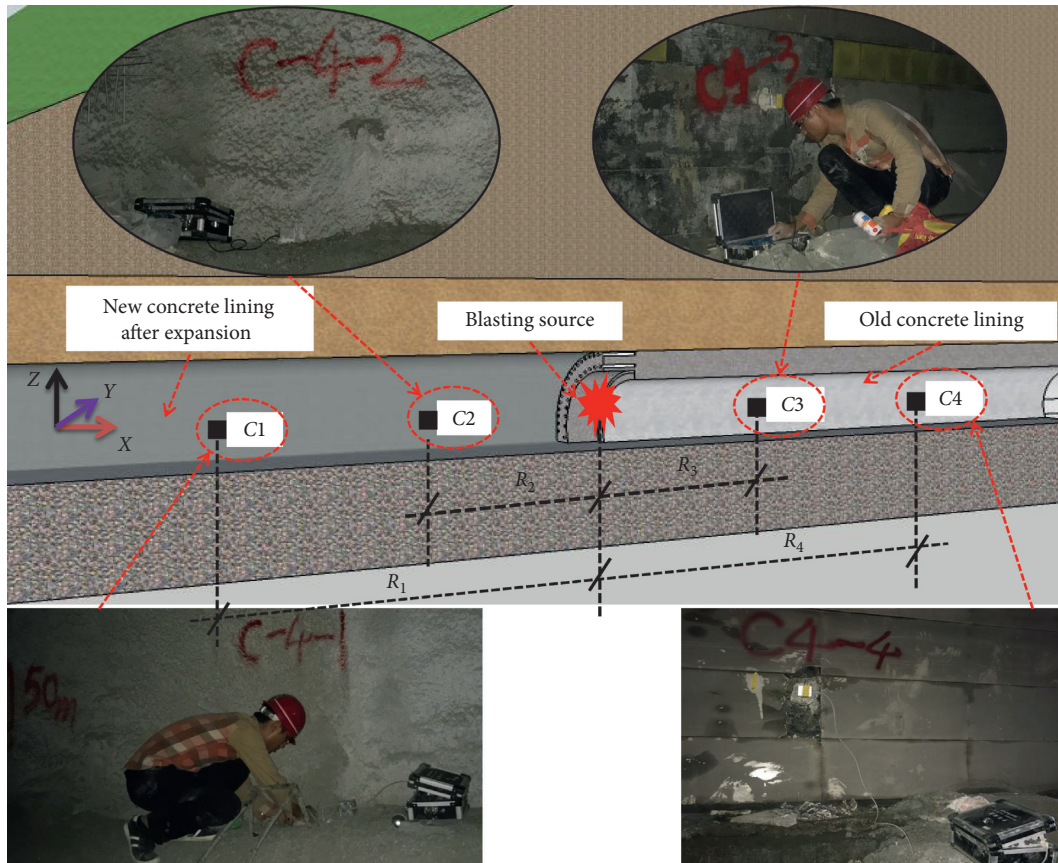


FIGURE 7: Layout of the monitoring points in the tunnel lining.

$$PPV = K \left(\frac{Q^{1/3}}{R} \right)^\alpha = K [PD]^{-\alpha}, \quad (1)$$

$$[PD] = \left(\frac{R}{Q^{1/3}} \right), \quad (2)$$

where PPV represents the PPV (in cm/s); Q represents the TNT weight (kg); R represents the linear distance from the blasting source to monitoring points (m); K and α are parameters related to the blasting vibrations, which are influenced by the rock characteristics, site conditions, blasting methods, and so forth; and $[PD]$ represents the proportional distance ($m/kg^{1/3}$).

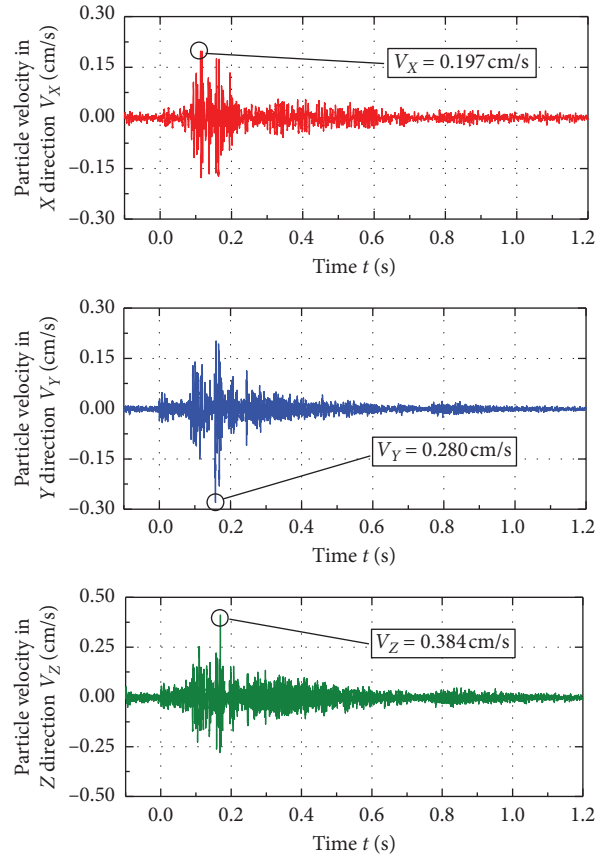


FIGURE 8: Typical curve of measured vibration velocities (V_X , V_Y , and V_Z) for the new concrete lining (in test 1, $R_4=110.8$).

TABLE 1: Measured PPVs in this case history.

Test number	TNT weight per delay (kg)	Distance to blasting source (m)	PPV of new concrete lining (cm/s)			Distance to blasting source (m)	PPV of the old concrete lining (cm/s)		
			V_X	V_Y	V_Z		V_X	V_Y	V_Z
1	50.4	$R_2 = 20.3$	7.258	6.501	6.647	$R_3 = 29.6$	4.572	6.875	5.006
		$R_1 = 42.7$	2.904	2.206	1.324	$R_4 = 110.8$	0.197	0.280	0.384
2	27.3	$R_2 = 19.7$	6.465	5.535	4.943	$R_3 = 20.0$	5.701	8.246	5.476
		$R_1 = 52.6$	1.346	0.640	1.674	$R_4 = 74.2$	0.375	1.165	1.211
3	31.2	$R_2 = 22.7$	4.121	3.194	3.030	$R_3 = 40.4$	3.307	3.641	2.741
		$R_1 = 44.0$	1.122	1.067	1.846	$R_4 = 95.7$	0.445	1.265	0.915
4	27.3	$R_2 = 31.6$	2.100	2.911	2.120	$R_3 = 50.8$	1.865	2.273	1.978
		$R_1 = 98.0$	0.505	0.194	0.178	$R_4 = 70.9$	1.996	1.997	1.044
5	31.2	$R_2 = 48.9$	1.474	1.826	0.807	$R_3 = 37.2$	3.653	4.919	2.007
		$R_1 = 109.5$	0.170	0.170	0.242	$R_4 = 70.8$	0.403	1.824	1.189
6	27.3	$R_2 = 29.9$	3.617	2.654	1.637	$R_3 = 42.4$	1.279	2.289	1.686
		$R_1 = 117.2$	0.180	0.137	0.378	$R_4 = 101.5$	0.359	0.804	0.840
7	31.2	$R_2 = 26.5$	4.181	2.209	3.261	$R_3 = 55.3$	1.666	2.851	1.798
		$R_1 = 71.3$	0.790	0.289	0.256	$R_4 = 135.2$	0.406	0.488	0.703
8	27.3	$R_2 = 36.2$	1.272	2.167	2.122	$R_3 = 44.8$	0.910	2.541	1.345
		$R_1 = 79.2$	0.649	0.292	0.323	$R_4 = 156.6$	0.422	0.658	0.256
9	31.2	$R_2 = 28.4$	1.840	2.492	1.715	$R_3 = 87.0$	0.840	0.988	1.697
		$R_1 = 78.6$	0.294	0.693	0.867	$R_4 = 114.2$	0.206	0.740	0.193
10	27.3	$R_2 = 42.9$	1.673	2.195	0.730	$R_3 = 98.1$	0.686	0.216	0.363
		$R_1 = 140.4$	0.159	0.097	0.409	$R_4 = 120.4$	0.545	0.452	0.938

According to the field test data for the blasting vibrations in Table 1, the variations of the PPV with respect to the proportional distance ([PD]) for the new and old concrete linings were analyzed via regression analysis. Figures 9 and 10 present the variation of the PPV with respect to [PD] for the new concrete lining and the old concrete lining, respectively. As shown, the measured PPVs in the new and old concrete linings of the Yujiaya tunnel decreased with an increase in the proportional distance, indicating that the PPV was higher for a larger TNT weight and lower for a longer distance to the blasting source. Because the surrounding rock structure of the new tunnel differed from that of the old tunnel lining, the incident and reflection modes of the stress wave were different, resulting in significant differences in the PPV between the new and old concrete linings. According to the regression analysis using equations (1) and (2), the corresponding attenuation parameters K and α of stress wave propagation were determined, and then the empirical formula for the attenuation of the PPV in each direction was obtained, as follows (as shown in Figures 9 and 10):

New concrete lining:

$$\begin{cases} V_X = 170.15 [PD]^{-1.810}, & R^2 = 0.82, \\ V_Y = 206.92 [PD]^{-1.965}, & R^2 = 0.79, \\ V_Z = 68.69 [PD]^{-1.523}, & R^2 = 0.73. \end{cases} \quad (3)$$

Old concrete lining:

$$\begin{cases} V_X = 124.41 [PD]^{-1.599}, & R^2 = 0.78, \\ V_Y = 216.59 [PD]^{-1.632}, & R^2 = 0.84, \\ V_Z = 74.32 [PD]^{-1.359}, & R^2 = 0.70. \end{cases} \quad (4)$$

Comparing the fitted curves in Figures 9 and 10 reveals that the K value of the new concrete linings varied between 68 and 206 and that α varied greatly, ranging from 1.523 to 1.965. However, the K value of the old concrete linings varied widely (between 74 and 216), and α varied from 1.359 to 1.623. Therefore, the PPV caused by blasting was attenuated faster in the new concrete lining than in the old concrete lining. In the case of the new concrete lining, when the stress wave encounters a free surface, joint fissure, or fault during the propagation process, it may be reflected and refracted, which can result in energy loss of the stress wave and rapid attenuation of the PPV. Additionally, because the new tunnel excavation forms a circular cutting groove, similar to the artificial damping belt, the blasting stress wave cannot directly act on the primary support structure; rather, it affects the primary support structure through the tunnel floor and the vault diffraction at the monitoring points of the new concrete linings. It was mainly affected by the stress in the X and Y directions; thus, the PPV in the Z direction was lower than that in the other directions for the new concrete linings. Additionally, the correlation coefficients of the fitting curves (R^2) were relatively small, ranging from 0.70 to 0.84. This is explained as follows: the geological surrounding rock conditions in the tunnel were complex, the blasting

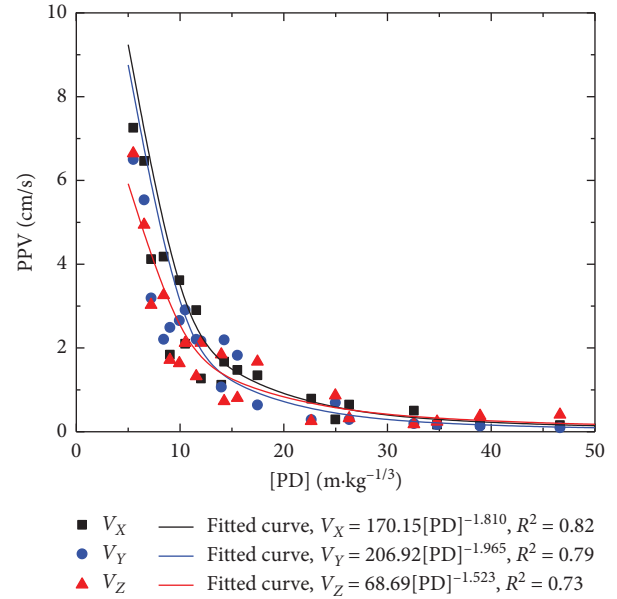


FIGURE 9: Variation of the PPV with respect to [PD] for the new concrete lining.

conditions and environmental factors changed significantly, and the difference between the installation position and the height of the instrument may have led to an error in the measurement of the PPV. However, overall, the attenuation law of the PPV was consistent with Sadovsky's empirical formula.

4.2. Main Vibration Frequency. In many countries, the influence of the main vibration frequency of the blasting stress wave is considered during the formulation of the Blasting Safety Regulations. Previous studies indicated that the main vibration frequency of blasting vibrations affects the damage to buildings and structures [40–42]. The main vibration frequency closer to the natural frequency of the buildings results in greater damage to the buildings. A large amount of data for the main vibration frequency induced by blasting in this case history was collected, as shown in Table 2. Additionally, the distribution of the measured main vibration frequency was analyzed for the new and old concrete linings. As shown in Figures 11 and 12, the measured main vibration frequency was divided into five intervals: 0–30, 30–60, 60–90, 90–120, and >120 Hz. The main vibration frequency in this case history was mainly distributed in the range of 0–90 Hz (approximately 85% of the data). Figure 13 presents the variation of the main vibration frequency with respect to the distance to the blasting source. As shown, the main vibration frequency measured in the blasting was higher (between 11.72 and 147.45 Hz), but with the increasing distance to the blasting source, the main vibration frequency decreased, similar to the investigation results for the frequency variation reported by Singh et al. [36, 43]. This confirms the accuracy of the test results. Additionally, because the natural frequencies of most ground structures are relatively low, it is more difficult for high-frequency vibration to resonate with adjacent structures, and the vibration does not damage buildings or structures. To quantitatively evaluate the relationship between the main

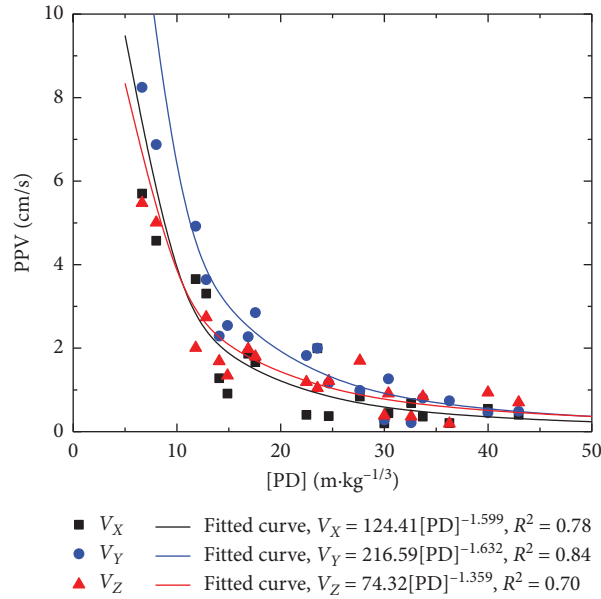


FIGURE 10: Variation of the PPV with respect to [PD] for the old concrete lining.

TABLE 2: Observed main vibration frequency for the examined case history.

Test number	TNT weight per delay (kg)	Distance to blasting source (m)	Main vibration frequency of new concrete lining (Hz)			Distance to blasting source (m)	Main vibration frequency of old concrete lining (Hz)		
			F_X	F_Y	F_Z		F_X	F_Y	F_Z
1	50.4	$R_2 = 20.3$	45.62	117.14	89.65	$R_3 = 29.6$ $R_4 = 110.8$	123.25	93.95	113.28
		$R_1 = 42.7$	40.25	23.53	18.90		11.72	23.43	23.45
2	27.3	$R_2 = 19.7$	119.61	127.97	64.52	$R_3 = 20.0$ $R_4 = 74.2$	118.60	83.32	108.76
		$R_1 = 52.6$	27.35	35.87	54.60		37.45	27.62	18.55
3	31.2	$R_2 = 22.7$	62.55	112.36	108.42	$R_3 = 40.4$ $R_4 = 95.7$	28.98	127.65	105.26
		$R_1 = 44.0$	44.68	50.29	72.68		22.92	69.30	20.15
4	27.3	$R_2 = 31.6$	75.69	67.45	25.68	$R_3 = 50.8$ $R_4 = 70.9$	87.82	65.05	49.60
		$R_1 = 98.0$	35.89	20.58	26.50		17.87	35.65	28.37
5	31.2	$R_2 = 48.9$	56.67	69.85	29.62	$R_3 = 37.2$ $R_4 = 70.8$	122.05	78.62	60.25
		$R_1 = 109.5$	29.68	25.46	19.60		35.80	42.68	39.07
6	27.3	$R_2 = 29.9$	39.83	67.79	130.34	$R_3 = 42.4$ $R_4 = 101.5$	55.54	65.06	46.58
		$R_1 = 117.2$	19.62	15.67	22.18		22.15	32.58	28.40
7	31.2	$R_2 = 26.5$	127.65	86.20	147.45	$R_3 = 55.3$ $R_4 = 135.2$	78.52	65.43	45.09
		$R_1 = 71.3$	38.66	42.18	19.57		12.56	24.11	19.50
8	27.3	$R_2 = 36.2$	83.34	69.22	74.05	$R_3 = 44.8$ $R_4 = 156.6$	85.62	76.53	55.45
		$R_1 = 79.2$	23.80	56.49	79.52		13.68	17.98	26.80
9	31.2	$R_2 = 28.4$	112.36	56.26	78.32	$R_3 = 87.0$ $R_4 = 114.2$	25.68	102.60	39.86
		$R_1 = 78.6$	42.32	65.24	25.60		25.64	22.30	32.05
10	27.3	$R_2 = 42.9$	57.29	61.07	87.00	$R_3 = 98.1$ $R_4 = 120.4$	72.58	45.62	19.82
		$R_1 = 140.4$	17.85	24.68	20.55		42.26	22.80	21.09

vibration frequency and the distance to the blasting source, a regression analysis of the observed data was performed, which indicated that a power function ($y = 2018x^{-0.93}$, $R^2 = 0.77$) may be reasonable, as shown in Figure 13.

4.3. Discussion on Safety Distance of Concrete Linings. In this study, the PPVs at different distances from the blasting

source were determined via the field test. However, the PPVs close to the blasting source could not be monitored, owing to safety considerations. Therefore, the PPVs at different distances from the blasting source were calculated using equation (4). Figure 14 presents the variation of the PPV in different directions with respect to the distance from the blasting source for the concrete lining. The PPV curve is based on equation (4). As shown, for the TNT weight of

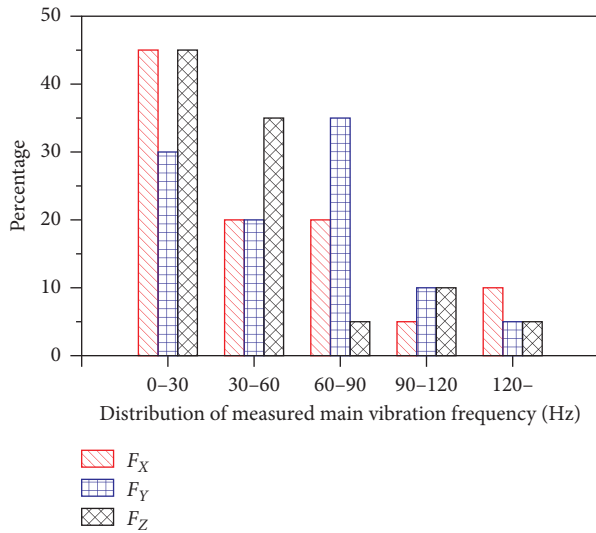


FIGURE 11: Distribution of the measured main vibration frequency for the old concrete lining.

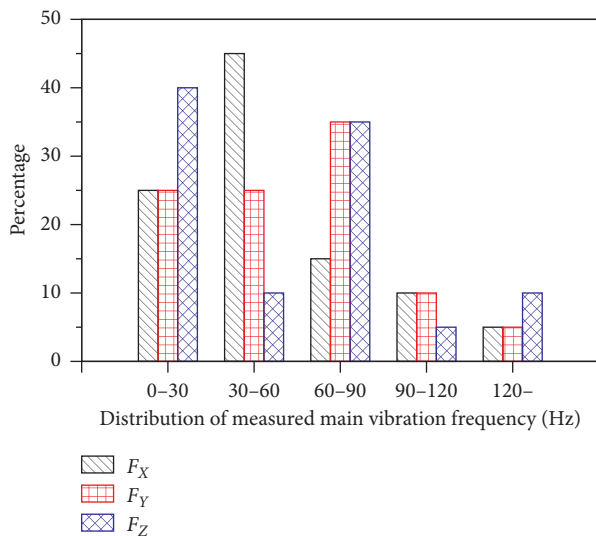


FIGURE 12: Distribution of the measured main vibration frequency for the new concrete lining.

$Q_{max} = 50.4$ kg, if the PPV is > 20 cm/s, damage may be induced to the concrete lining, and the safety distance for the case of $10 \leq V_X \leq 20$ cm/s is 16–24 m. The safety distances for the cases of $10 \leq V_Y \leq 20$ cm/s and $10 \leq V_Z \leq 20$ cm/s are 12–18 and 10–17 m, respectively. The obtained safety distances are valuable references for similar tunnel construction projects.

5. Conclusions

At present, several old mountain highway tunnels in China need to be rebuilt or expanded because of the declining health of concrete linings and the growing traffic demands. It is important to monitor the vibrations caused by blasting to avoid the continuous collapse of the old concrete lining during the expansion of old mountain highway tunnels. In

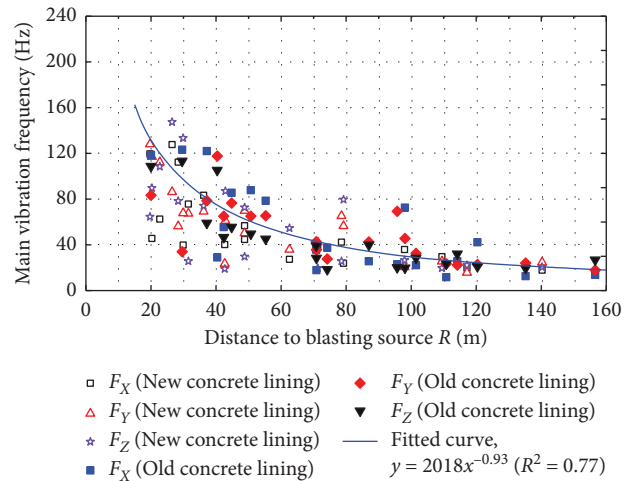


FIGURE 13: Variation of the main vibration frequency with respect to the distance to the blasting source.

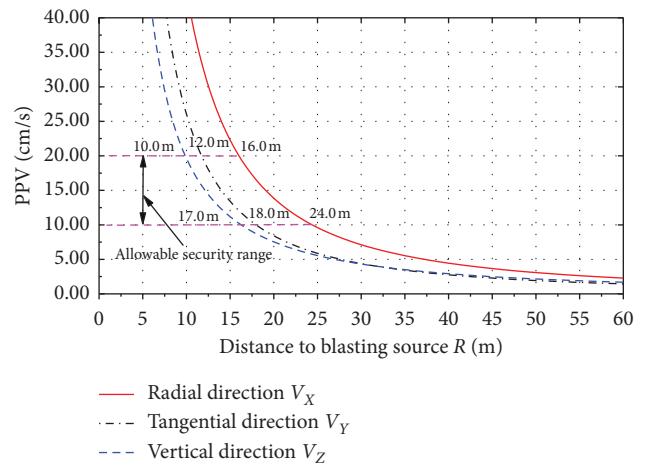


FIGURE 14: Variation of the PPV with respect to the distance from the blasting source for the concrete lining.

this study, a case history of the expansion of the Yujiaya tunnel, located in Shaanxi Province and constructed in 1999, was analyzed. During the expansion process, the blasting-induced vibrations in the new and old concrete linings were monitored. The results indicated that the measured values of the PPV varied within the range of 0.097–8.246 cm/s. By performing a regression analysis with Sadovsky’s empirical formula, the attenuation law of the PPV was determined. A power function was established to quantitatively evaluate the relationship between the main vibration frequency and the distance to the blasting source. The results indicated that the safety distance of concrete linings for the case of $10 \leq V_X \leq 20$ cm/s is 16–24 m, and the safety distances for the two cases of $10 \leq V_Y \leq 20$ cm/s and $10 \leq V_Z \leq 20$ cm/s are 12–18 and 10–17 m, respectively.

Data Availability

The data used to support the findings of this research work are included within the article.

Conflicts of Interest

The authors declare no conflicts of interest.

Acknowledgments

This work was funded by the National Key R&D Program of China (Grant no. 2017YFC0805306), the project supported by the Natural Science Basic Research Plan in Shaanxi Province of China (Grant no. 2019JQ-114), the National Nature Science Foundation of China (NSFC) (Grant nos. 41702287 and 51978059), and the Fundamental Research Funds for the Central Universities (Grant no. 300102218517). The financial support received is gratefully acknowledged.

References

- [1] W. C. Cheng, J. C. Ni, and S. L. Shen, "Experimental and analytical modeling of shield segment under cyclic loading," *International Journal of Geomechanics*, vol. 17, no. 6, Article ID 04016146, 2016.
- [2] W.-C. Cheng, G. Li, N. Liu, J. Xu, and S. Horpibulsuk, "Recent massive incidents for subway construction in soft alluvial deposits of Taiwan: a review," *Tunnelling and Underground Space Technology*, vol. 96, Article ID 103178, 2020.
- [3] J. Lai, X. Wang, J. Qiu et al., "A state-of-the-art review of sustainable energy based freeze proof technology for cold-region tunnels in China," *Renewable and Sustainable Energy Reviews*, vol. 82, no. 3, pp. 3554–3569, 2018.
- [4] Y.-Q. Wang, Z.-F. Wang, and W.-C. Cheng, "A review on land subsidence caused by groundwater withdrawal in Xi'an, China," *Bulletin of Engineering Geology and the Environment*, vol. 78, no. 4, pp. 2851–2863, 2019a.
- [5] Z.-F. Wang, S.-L. Shen, and G. Modoni, "Enhancing discharge of spoil to mitigate disturbance induced by horizontal jet grouting in clayey soil: theoretical model and application," *Computers and Geotechnics*, vol. 111, pp. 222–228, 2019b.
- [6] Y.-q. Wang, S. Xu, R. Ren, S. Zhang, and Z. Ren, "Application of the twin-tube complementary ventilation system in large-sloping road tunnels in China," *International Journal of Ventilation*, vol. 19, no. 1, pp. 63–82, 2020a.
- [7] P. Li, Y. Zhao, and X. Zhou, "Displacement characteristics of high-speed railway tunnel construction in loess ground by using multi-step excavation method," *Tunnelling and Underground Space Technology*, vol. 51, pp. 41–55, 2016.
- [8] S. Lu, C. Zhou, N. Jiang, and X. Xu, "Effect of excavation blasting in an under-cross tunnel on airport runway," *Geotechnical and Geological Engineering*, vol. 33, no. 4, pp. 973–981, 2015.
- [9] R. Ren, S. Xu, Z. Ren et al., "Numerical investigation of particle concentration distribution characteristics in twin-tunnel complementary ventilation system," *Mathematical Problems in Engineering*, vol. 2018, Article ID 1329187, 13 pages, 2018.
- [10] W.-C. Cheng, J. C. Ni, H.-W. Huang, J. S. Shen, and J. S. Shen, "The use of tunnelling parameters and spoil characteristics to assess soil types: a case study from alluvial deposits at a pipejacking project site," *Bulletin of Engineering Geology and the Environment*, vol. 78, no. 4, pp. 2933–2942, 2019a.
- [11] P. Li and Y. Zhao, "Performance of a multi-face tunnel excavated in loess ground based on field monitoring and numerical modeling," *Arabian Journal of Geosciences*, vol. 9, no. 14, 640 pages, 2016.
- [12] J. Qiu, H. Liu, J. Lai, H. Lai, J. Chen, and K. Wang, "Investigating the long-term settlement of a tunnel built over improved loessial foundation soil using jet grouting technique," *Journal of Performance of Constructed Facilities*, vol. 32, no. 5, Article ID 04018066, 2018.
- [13] J. Qiu, Y. Xie, H. Fan, Z. Wang, and Y. Zhang, "Centrifuge modelling of twin-tunnelling induced ground movements in loess strata," *Arabian Journal of Geosciences*, vol. 10, no. 22, 493 pages, 2017.
- [14] V. R. Feldgun, A. V. Kochetkov, Y. S. Karinski, and D. Z. Yankelevsky, "Internal blast loading in a buried lined tunnel," *International Journal of Impact Engineering*, vol. 35, no. 3, pp. 172–183, 2008.
- [15] W. He, J.-y. Chen, and J. Guo, "Dynamic analysis of subway station subjected to internal blast loading," *Journal of Central South University*, vol. 18, no. 3, pp. 917–924, 2011.
- [16] N. Jiang and C. Zhou, "Blasting vibration safety criterion for a tunnel liner structure," *Tunnelling and Underground Space Technology*, vol. 32, pp. 52–57, 2012.
- [17] H. Liu, "Dynamic analysis of subway structures under blast loading," *Geotechnical and Geological Engineering*, vol. 27, no. 6, p. 699, 2009.
- [18] Z.-F. Wang, S.-L. Shen, G. Modoni, and A. Zhou, "Excess pore water pressure caused by the installation of jet grouting columns in clay," *Computers and Geotechnics*, vol. 125, Article ID 103667, 2020b.
- [19] W.-C. Cheng, J. C. Ni, A. Arulrajah, and H.-W. Huang, "A simple approach for characterising tunnel bore conditions based upon pipe-jacking data," *Tunnelling and Underground Space Technology*, vol. 71, pp. 494–504, 2018.
- [20] Y. Wei, X. Gao, and S. Liang, "A combined SPM/NI/EDS method to quantify properties of inner and outer C-S-H in OPC and slag-blended cement pastes," *Cement and Concrete Composites*, vol. 85, pp. 56–66, 2018.
- [21] Y. Wei, X. Gao, F. Wang, and Y. Zhong, "Nonlinear strain distribution in a field-instrumented concrete pavement slab in response to environmental effects," *Road Materials and Pavement Design*, vol. 20, no. 2, pp. 367–380, 2019.
- [22] Y. Wei, S. Liang, W. Guo, and W. Hansen, "Stress prediction in very early-age concrete subject to restraint under varying temperature histories," *Cement and Concrete Composites*, vol. 83, pp. 45–56, 2017.
- [23] M. Chen, W. B. Lu, P. Yan, and Y. G. Hu, "Blasting excavation induced damage of surrounding rock masses in deep-buried tunnels," *KSCE Journal of Civil Engineering*, vol. 20, no. 2, pp. 933–942, 2016.
- [24] W.-C. Cheng, L. Wang, Z.-F. Xue, J. C. Ni, M. M. Rahman, and A. Arulrajah, "Lubrication performance of pipejacking in soft alluvial deposits," *Tunnelling and Underground Space Technology*, vol. 91, p. 102991, 2019b.
- [25] R. Kumar, D. Choudhury, and K. Bhargava, "Determination of blast-induced ground vibration equations for rocks using mechanical and geological properties," *Journal of Rock Mechanics and Geotechnical Engineering*, vol. 8, no. 3, pp. 341–349, 2016.
- [26] K.-I. Song, T.-M. Oh, and G.-C. Cho, "Precutting of tunnel perimeter for reducing blasting-induced vibration and damaged zone - numerical analysis," *KSCE Journal of Civil Engineering*, vol. 18, no. 4, pp. 1165–1175, 2014.
- [27] L. Ahmed and A. Ansell, "Structural dynamic and stress wave models for the analysis of shotcrete on rock exposed to blasting," *Engineering structures*, vol. 35, pp. 11–17, 2012.

- [28] L. Ahmed and A. Ansell, "Vibration vulnerability of shotcrete on tunnel walls during construction blasting," *Tunnelling and Underground Space Technology*, vol. 42, pp. 105–111, 2014.
- [29] M. Monjezi, M. Ghafurikalajahi, and A. Bahrami, "Prediction of blast-induced ground vibration using artificial neural networks," *Tunnelling and Underground Space Technology*, vol. 26, no. 1, pp. 46–50, 2011.
- [30] Q. M. Xie, Y. Y. Xia, and X. P. Li, "Study on blasting vibration control of creep mass slope of longtan hydropower station," *Journal of Rock Mechanics and Engineering*, vol. 22, no. 11, pp. 1929–1932, 2003, in Chinese.
- [31] H. Yu, Y. Yuan, G. Yu, and X. Liu, "Evaluation of influence of vibrations generated by blasting construction on an existing tunnel in soft soils," *Tunnelling and Underground Space Technology*, vol. 43, pp. 59–66, 2014.
- [32] J. S. Lee, S. K. Ahn, and M. Sagong, "Attenuation of blast vibration in tunneling using a pre-cut discontinuity," *Tunnelling and Underground Space Technology*, vol. 52, pp. 30–37, 2016.
- [33] A. Parida and M. K. Mishra, "Blast vibration analysis by different predictor approaches—a comparison," *Procedia Earth and Planetary Science*, vol. 11, pp. 337–345, 2015.
- [34] Z.-F. Wang, J. S. Shen, and W.-C. Cheng, "Simple method to predict ground displacements caused by installing horizontal jet-grouting columns," *Mathematical Problems in Engineering*, vol. 2018, Article ID 1897394, 11 pages, 2018a.
- [35] Z.-F. Wang, W.-C. Cheng, and Y.-Q. Wang, "Investigation into geohazards during urbanization process of Xi'an, China," *Natural Hazards*, vol. 92, no. 3, pp. 1937–1953, 2018b.
- [36] J. H. Yang, W. B. Lu, Q. H. Jiang, C. Yao, and C. B. Zhou, "Frequency comparison of blast-induced vibration per delay for the full-face millisecond delay blasting in underground opening excavation," *Tunnelling and Underground Space Technology*, vol. 51, pp. 189–201, 2016.
- [37] J. Lai, H. Fan, J. Chen, J. Qiu, and K. Wang, "Blasting vibration monitoring of undercrossing railway tunnel using wireless sensor network," *International Journal of Distributed Sensor Networks*, vol. 11, no. 6, Article ID 703980, 2015.
- [38] J. H. Yang, W. B. Lu, Z. G. Zhao, P. Yan, and M. Chen, "Safety distance for secondary shotcrete subjected to blasting vibration in jinping-II deep-buried tunnels," *Tunnelling and Underground Space Technology*, vol. 43, pp. 123–132, 2014.
- [39] SRFB, *Safety Regulations for Blasting: National Standards Editorial Committee of the People's Republic of China*, China Standards Press, Beijing, China, 2014, in Chinese.
- [40] X.M. Guan, X.C. Wang, Z. Zhu, L. Zhang, and H.X. Fu, "Ground vibration test and dynamic response of horseshoe-shaped pipeline during tunnel blasting excavation in pebbly sandy soil," *Geotechnical and Geological Engineering*, vol. 38, pp. 3725–3736, 2020.
- [41] X. Guan, C. Zhang, F. Zhao, B. Mou, and Y. Ge, "Stress response and damage characteristics of local members of a structure due to tunnel blasting vibrations based on the high-order local modal analysis," *Shock and Vibration*, vol. 2019, Article ID 7075024, 18 pages, 2019.
- [42] C. Shi, Q. Zhao, M. Lei, and M. Peng, "Vibration velocity control standard of buried pipeline under blast loading of adjacent tunnel," *Soils and Foundations*, vol. 59, no. 6, pp. 2195–2205, 2019.
- [43] P. K. Singh, M. P. Roy, R. K. Paswan, R. K. Dubey, and C. Drebenstedt, "Blast vibration effects in an underground mine caused by open-pit mining," *International Journal of Rock Mechanics and Mining Sciences*, vol. 80, pp. 79–88, 2015.

Research Article

Study on the Water-Physical Properties of the Cement-Plaster Bonded Rock-Like Materials

Yong Zhang ¹, Zhiguo Cao,¹ and Xiaomeng Shi ²

¹State Key Laboratory of Water Resources Protection and Utilization in Coal Mining, Beijing 100011, China

²School of Civil Engineering, Beijing Jiaotong University, Beijing 100044, China

Correspondence should be addressed to Xiaomeng Shi; shixm@bjtu.edu.cn

Received 24 September 2020; Revised 14 January 2021; Accepted 25 January 2021; Published 8 February 2021

Academic Editor: Wen-Chieh Cheng

Copyright © 2021 Yong Zhang et al. This is an open access article distributed under the Creative Commons Attribution License, which permits unrestricted use, distribution, and reproduction in any medium, provided the original work is properly cited.

The cement-plaster bonded rock-like material is one of the most commonly used materials to simulate different rocks in physical model tests. However, the applicability of this material in solid-fluid coupling model tests is not clear because there are few research studies on the water-physical properties of this material and its similarity to the actual rock is uncertain. This paper presents a systemic experimental study on the water-physical properties of the cement-plaster bonded rock-like materials. The parameters of rock-like materials, including water absorption, softening coefficient, and permeability coefficient, were compared with those of actual rocks to analyse the applicability of such material. Then, the influence of proportion on the water-physical properties of this material was discussed. By multiple regression analysis of the test results, empirical equations between the water-physical parameters and proportions were proposed. The equations can be used to estimate the water-physical properties of cement-plaster bonded rock-like materials with specific proportion and thus to select suitable materials in the solid-fluid coupling physical model tests.

1. Introduction

The physical model test is a common method to research geotechnical problems in the domains of mining engineering and civil engineering [1–5]. It tries to replicate the geologic body and the structure with an equal or small scale in the laboratory, which could provide a reference for the actual engineering. However, there are still some problems with this approach, one of which is how to make an applicable artificial material to conduct the solid-fluid coupling physical model test [6]. More specifically, it is difficult to select the material with proper water-physical parameters to meet the similarity requirements.

Most of the research studies on solid-fluid coupling materials focus on the nonhydrophilic organic ingredients. Jacoby and Schmeling [7] used glycerol and molten paraffin to simulate mantle convection and plate motion. Kincaid and Olson [8] used paraffin, mineral oil, plaster, and other semiplastic mixed materials as lithosphere to simulate the dynamic process of plate motion. Gong et al. [9] used sand

and talcum powder as aggregates and paraffin oil as a cementing agent to simulate the plastically destructive rock mass with low strength and large deformation. Li et al. [10] developed a new type of solid-coupling similar material (PSTO) composed of paraffin, sand, and talcum powder, according to the solid-fluid coupling similarity theory. Huang et al. [11] used quartz sand and bentonite as aggregates and silicone oil and vaseline as bonding materials to develop an artificial material to simulate a water-resisting layer in a solid-fluid coupling physical model test. Ge and Xu [12] proposed a method for making a transparent hard rock-like material made of a mixture of rosin saturated solution (RSS), epoxy resin (ER), and curing agent (CA). Although the above materials could meet partial similarity requirements in water-physical properties, the basic mechanical parameters, such as strength and elastic modulus, are significantly different from the actual rocks due to the existence of these organic ingredients. So, this kind of rock-like material is far from an ideal solid-fluid coupling material.

The cement-plaster bonded material is the most commonly used rock-like material because its mechanical behaviors are consistent with actual rocks, and the raw materials are common, cheap, and nontoxic. For this material, the basic properties have been well studied, and there are many application cases [13–15]. However, few studies on the water-physical properties of this material have been reported, and its applicability in the solid-fluid coupling physical model test is uncertain.

In this paper, the water-physical properties of the cement-plaster bonded rock-like material are systematically studied through orthogonal experiments. The applicability of this material is discussed by comparing the water-physical properties of the rock-like material with actual rocks. The multifactors' regression analysis on the test data reveals the relationships between the water-physical properties of the rock-like materials and the proportions of the raw materials. This paper can provide a theoretical basis and reference for the application of such materials in solid-fluid coupling physical model tests.

2. Similitude Criterion for Water-Physical Parameters

The water-physical properties of rocks mainly include water content, water absorption, permeability, softening, and frost resistance [16]. Among these parameters, the natural moisture content can be controlled through the curing conditions, and the frost resistance was rarely involved in the physical modelling. Therefore, this study only focuses on three water-physical parameters: water absorption w_a , permeability coefficient k , and softening coefficient η_c .

For most physical modelling tests, the model is always reduced to scale with the prototype. The ratios of the parameters between the prototype and the model are defined as the similitude scales.

Water absorption w_a is the proportion of water which can be absorbed by rock under specific immersion conditions. It can be calculated as follows:

$$w_a = \frac{m_o - m_{dr}}{m_{dr}} \times 100\%, \quad (1)$$

where m_o is the saturated quality and m_{dr} is the dried quality.

The water absorption w_a is dimensionless, so the similitude scale is $C_w = 1$, which means the water absorption w_a of the rock-like material should be equal to that of actual rock.

Permeability is the property of rocks that is an indication of the ability for fluids to flow through rocks. According to the similarity theory [1], the similitude scale of permeability coefficient k is as follows:

$$C_k = \frac{\sqrt{C_l}}{C_\gamma}, \quad (2)$$

where C_l and C_γ are similitude scales of geometry and weight, which are given parameters in the tests.

The softening coefficient η_c is the ratio of the compressive strength of the rock in the saturated state σ_{cw} to that in the dried state σ_c :

$$\eta_c = \frac{\sigma_{cw}}{\sigma_c}. \quad (3)$$

Since the softening coefficient is dimensionless, the similitude scale is $C_\eta = 1$.

In the following experiments, these similitude scales are an important basis for discussing the similarity of such materials to the actual rocks.

3. Orthogonal Experiment on the Water-Physical Properties of Rock-Like Materials

3.1. Raw Component Materials. The rock-like materials are composed of cement, plaster, and quartz sand and mixed by water. The cement and plaster are the bonding materials, and the quartz sand is the aggregate. Table 1 lists the characteristics of the raw materials.

3.2. Experiment Design and Process. The orthogonal experimental design method has been widely used in the experimental design, especially in multifactor experiments. This method has obvious advantages compared with other methods in proportioning tests and is commonly used in the research on the ratio of rock-like artificial materials [17, 18].

In this experiment, A/B (the ratio of the aggregate to bonding materials), C/B (the percentage of cement in bonding materials), and GS (the grain size of the quartz sand) are defined as the three critical factors in this orthogonal experiment, and each factor has four levels. The orthogonal experimental scheme is shown in Table 2.

According to the orthogonal experimental design method [17], the detailed proportions of rock-like materials for all the test conditions are shown in Table 3.

Making the specimens of the rock-like material is the first step of this experiment. Figure 1 shows the mould of the specimen with the inside dimension $\Phi 50 \times 100$ mm. There are seven specimens for each proportion, numbered $i-1 \sim i-7$, where i is the test number, as shown in Table 3. Figure 2 shows the specimens of cement-plaster bonded rock-like materials.

The uniaxial compressive test was carried out on no. $i-1$ to $i-3$ specimens to obtain the compressive strength in naturally air-dried state σ_c . The specimens numbered $i-4$ to $i-6$ were dried and then weighed to get the drying quality m_{dr} . Then, the permeability coefficient k of the specimens $i-4$ to $i-6$ was measured by penetration tests. The saturated specimens were weighed to obtain saturated quality m_o . At last, the uniaxial compressive tests were carried out again on the saturated specimens $i-4$ to $i-6$ to obtain the compressive strength in the saturated state σ_{cw} . According to equations (1) and (3), the water absorption w_a and softening coefficient η_c of the specimen are calculated. The test results are shown in Table 4.

TABLE 1: Characteristics of raw component materials.

Raw materials	Components and types
Quartz sand	SiO ₂ > 95%
Cement	Ordinary Portland cement
Plaster	Calcined building plaster powder

TABLE 2: Factors and levels in the orthogonal experiment.

Level	A/B	C/B (%)	GS (mm)
1	2:1	0	0.25 ~ 0.50
2	4:1	33	0.5 ~ 1
3	6:1	66	1 ~ 2
4	8:1	100	2 ~ 4

TABLE 3: Orthogonal experiment schemes.

Number <i>i</i>	A/B	C/B (%)	GS (mm)
1	2:1	0	0.25 ~ 0.50
2	2:1	33	0.5 ~ 1
3	2:1	66	1 ~ 2
4	2:1	100	2 ~ 4
5	4:1	0	0.5 ~ 1
6	4:1	33	0.25 ~ 0.50
7	4:1	66	2 ~ 4
8	4:1	100	1 ~ 2
9	6:1	0	1 ~ 2
10	6:1	33	2 ~ 4
11	6:1	66	0.25 ~ 0.50
12	6:1	100	0.5 ~ 1
13	8:1	0	2 ~ 4
14	8:1	33	1 ~ 2
15	8:1	66	0.5 ~ 1
16	8:1	100	0.25 ~ 0.50

4. Similarity Analysis between the Rock-Like Materials and Actual Rocks

Figure 3 shows the failure pattern of the cement-plaster bonded rock-like material in the saturated state, which is similar to that of the actual rocks. By comparing the water-physical properties of rock-like materials, as shown in Table 4, with the properties of actual rocks, as shown in Table 5 [16], the similarity could be analysed. The variation range of water absorption w_a is 13.5% ~ 30.3%, softening coefficient η_c is 0.421 ~ 0.713, and permeability coefficient k is $1.62 \times 10^{-6} \sim 4.66 \times 10^{-4}$ cm/s.

The water absorptions of actual rocks do not exceed 10%. Obviously, the rock-like materials absorbed much more water than the actual rocks. So, this kind of material cannot meet the requirement of similarity of water absorption. In other words, the cement-plaster bonded rock-like material could not be used in a physical modelling, if the water absorption was defined as a key influencing factor or an important research subject.

The softening coefficient of rock-like materials is similar with that of the actual rocks, especially for the medium-hard rock and soft rock. But, for the hard rocks with a softening

coefficient more than 0.7, the rock-like material could not simulate well.

The permeability coefficient of the rock varies over a wide range. By comparing the data, the rock-like material can be used to simulate limestone and sandstone with more cracks and pores. For the dense rock, the permeability coefficient is too small to be simulated by such material.

In general, the softening and permeability coefficients of this material are relatively similar to those of actual rocks, and this material is suitable for the simulation of soft or medium-hard rocks with cracks or pores. However, in the physical modelling tests where water absorption is a key influencing factor or an important research subject, the use of this material is not recommended because of the difference in water absorption.

5. Influence of Proportions on the Water-Physical Properties

5.1. Water Absorption. According to the orthogonal experiment theory, the mean values and the variation ranges of the water absorption for each factor at each level are calculated, and the results are shown in Table 6. The intuitive analysis diagram is shown in Figure 4. It can be seen that the change of each factor could lead to the variation of water absorption. *GS* is the most sensitive factor. The water absorption increases with the increase of the *A/B*, decreases with the rise of *C/B*, and increases significantly with the increase of *GS*.

5.2. Softening Coefficient. The mean values and the variation ranges of the softening coefficient for each factor at each level are calculated, and the results are shown in Table 7. The intuitive analysis diagram is shown in Figure 5. Apparently, the softening coefficient increases significantly with the rise of *C/B*, while *A/B* and *GS* have little effect on it. The reason is that the strength of the gypsum in the bonding material is very much affected by water. This leads to a smaller softening coefficient for materials with a higher gypsum content.

5.3. Permeability Coefficient. The mean values and the variation ranges of the permeability coefficient for each factor at each level are calculated, and the results are shown in Table 8. The intuitive analysis diagram is shown in Figure 6. The effect of *GS* on the permeability coefficient is the most obvious, and the permeability coefficient increases significantly with the increase of *GS*. The *A/B* and *C/B* also have some influence on the permeability coefficient. It increases with the rise of *A/B* and decreases with the increase of *C/B*.

6. Multifactors Regression Analysis

The above intuitive analysis diagrams show that, except for the exponential relationship between the permeability coefficient and the *GS*, all other factors and the water-physical parameters can be described by the linear relationship. Define *A/B* as X_1 , *C/B* as X_2 , and the mean values of *GS* as X_3 .

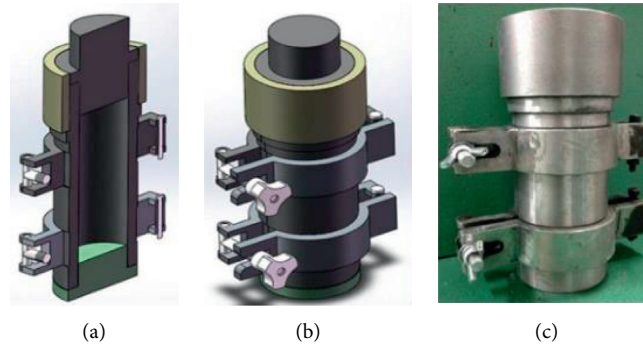


FIGURE 1: The specimen mould.



FIGURE 2: The maintained specimen.

TABLE 4: Orthogonal experiment results of the similar material ratio.

Number	Water absorption w_a (%)				Softening coefficient η_c				Permeability coefficient k (10^{-5} cm/s)			
	I	II	III	Mean	I	II	III	Mean	I	II	III	Mean
1	15.1	16.2	16.1	15.8	0.477	0.482	0.469	0.476	0.098	0.256	0.132	0.162
2	17.6	17.8	18.6	18.0	0.505	0.498	0.503	0.502	0.355	0.398	0.453	0.402
3	18.8	19.6	19.2	19.2	0.633	0.641	0.64	0.638	4.068	4.003	3.824	3.965
4	21.1	20.8	19.6	20.5	0.708	0.701	0.703	0.704	10.085	8.987	8.624	9.232
5	21.5	20.2	21.3	21.0	0.506	0.503	0.494	0.501	0.878	0.968	0.926	0.924
6	13.2	14.5	13.1	13.6	0.589	0.581	0.579	0.583	0.312	0.485	0.391	0.396
7	22.2	21.8	22.9	22.3	0.601	0.605	0.600	0.602	28.069	29.622	31.268	29.653
8	19.8	20.8	19.7	20.1	0.622	0.618	0.629	0.623	8.658	7.652	7.285	7.865
9	26.1	27.1	26.3	26.5	0.441	0.451	0.446	0.446	9.712	10.989	9.134	9.945
10	30.5	30.1	30.3	30.3	0.481	0.485	0.498	0.488	38.956	39.861	41.339	40.052
11	13.0	14.1	13.4	13.5	0.628	0.633	0.635	0.632	0.751	0.621	0.584	0.652
12	16.8	16.9	17.9	17.2	0.712	0.725	0.702	0.713	1.389	1.847	1.687	1.641
13	30.0	31.0	29.9	30.3	0.415	0.42	0.428	0.421	49.698	41.295	48.846	46.613
14	26.5	26.8	27.7	27.0	0.556	0.543	0.551	0.550	13.369	12.087	12.803	12.753
15	20.1	21.1	20.9	20.7	0.561	0.568	0.557	0.562	2.611	2.148	2.945	2.568
16	16.6	16.5	15.8	16.3	0.687	0.692	0.691	0.690	0.772	0.821	0.948	0.847

Define water absorption w_a as Y_1 , softening coefficient η_c as Y_2 , and permeability coefficient k as Y_3 . Multifactors' regression analysis was carried out on the orthogonal test data of all 16 groups of rock-like materials in Table 3, and the results are shown as follows:

$$\left. \begin{aligned} Y_1 &= 0.126 + 0.010X_1 - 0.045X_2 + 0.039X_3 \\ Y_2 &= 0.498 - 0.004X_1 + 0.220X_2 - 0.011X_3 \\ Y_3 &= -16.762 + 2.115X_1 - 7.898X_2 + 7.874e^{0.548X_3} \end{aligned} \right\} \quad (4)$$



FIGURE 3: Failure of a saturated specimen.

TABLE 5: Water-physical properties of common rocks.

Rock type	Water absorption w_a (%)	Softening coefficient η_c	Cracks and pores	Permeability coefficient (cm/s)
Granite	0.1 ~ 0.4	0.80 ~ 0.98	Dense and microcracks	$1.1 \times 10^{-12} \sim 9.5 \times 10^{-11}$
			Microcracks	$1.1 \times 10^{-11} \sim 2.5 \times 10^{-11}$
			Coarse cracks	$2.8 \times 10^{-9} \sim 7 \times 10^{-8}$
Limestone	0.1 ~ 4.5	0.68 ~ 0.94	Dense	$3 \times 10^{-12} \sim 6 \times 10^{-10}$
			Microcracks and micropore	$2 \times 10^{-9} \sim 3 \times 10^{-6}$
			Porous	$9 \times 10^{-5} \sim 3 \times 10^{-4}$
Sandstone	0.2 ~ 9.0	0.60 ~ 0.97	Dense	$10^{-13} \sim 2.5 \times 10^{-12}$
			Porous	5.5×10^{-6}
Shale	0.5 ~ 3.2	0.55 ~ 0.70	Micropore	$2 \times 10^{-10} \sim 8 \times 10^{-9}$

TABLE 6: Extremum difference analysis of water absorption.

Factor	Water absorption w_a (%)				Range
	Level 1	Level 2	Level 3	Level 4	
A/B	18.4	19.3	21.9	23.6	5.2
C/B	23.4	22.2	18.9	18.5	4.9
GS	14.8	19.2	23.2	25.9	11.1

For these three regression equations, the correlation coefficients are 0.812, 0.855, and 0.832, respectively. The relationship between the proportion of materials and the

water-physical properties can be described quantitatively by the above regression equations, which can be used to estimate the water-physical properties of cement-plaster

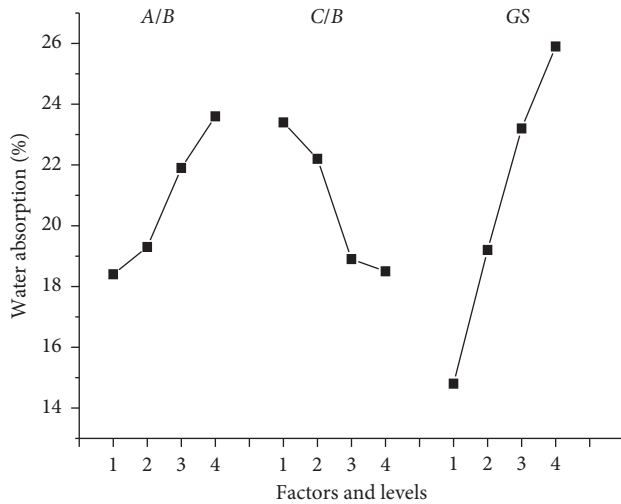


FIGURE 4: Sensitivity analysis of water absorption.

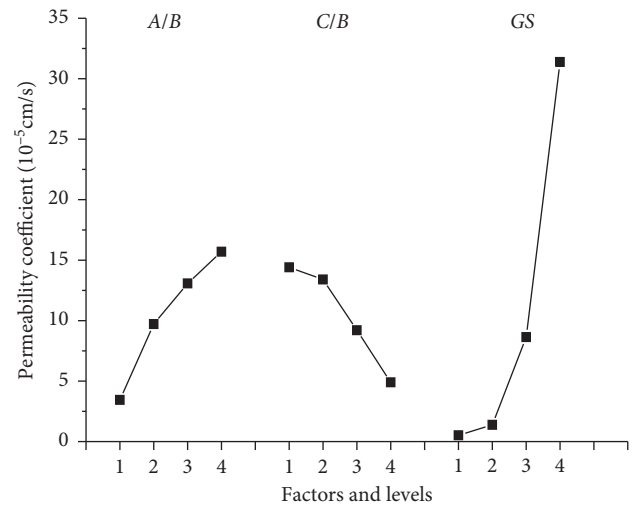


FIGURE 6: Sensitivity analysis of the permeability coefficient.

TABLE 7: Extremum difference analysis of the softening coefficient.

Factor	Softening coefficient η_c				Range
	Level 1	Level 2	Level 3	Level 4	
A/B	0.580	0.577	0.570	0.556	0.024
C/B	0.461	0.531	0.609	0.682	0.221
GS	0.595	0.570	0.564	0.554	0.041

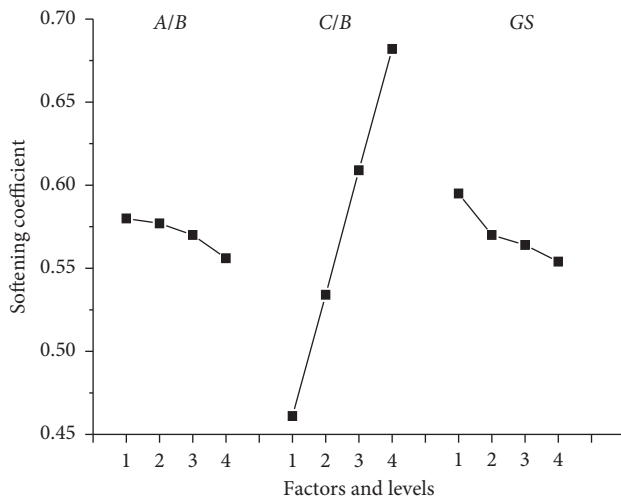


FIGURE 5: Sensitivity analysis of the softening coefficient.

TABLE 8: Extremum difference analysis of the permeability coefficient.

Factor	Permeability coefficient k (10^{-5} cm/s)				Range
	Level 1	Level 2	Level 3	Level 4	
A/B	3.440	9.710	13.072	15.695	12.255
C/B	14.411	13.401	9.209	4.896	9.515
GS	0.514	1.384	8.632	31.387	30.873

bonded rock-like materials with specific proportion and thus to select suitable materials in the solid-fluid coupling physical model tests.

7. Conclusions

- (1) The failure pattern of the cement-plaster bonded rock-like material in the saturated state is similar to that of the actual rocks. For this material, the variation range of water absorption w_a is 13.5% ~ 30.3%, softening coefficient η_c is 0.421 ~ 0.713, and permeability coefficient k is $1.62 \times 10^{-6} \sim 4.66 \times 10^{-4}$ cm/s.
- (2) The softening and permeability coefficients of this material are relatively similar to those of actual rocks, and this material is suitable for the simulation of soft or medium-hard rocks with cracks or pores. However, in the physical modelling tests where water absorption is a key influencing factor or an important research subject, the use of this material is not recommended because of the difference in water absorption.
- (3) The water absorption increases with the increase of the A/B, decreases with the rise of C/B, and increases significantly with the increase of GS. The softening coefficient increases significantly with the rise of C/B, while A/B and GS have little effect on it. The permeability coefficient increases significantly with the increase of GS, increases with the rise of A/B, and decreases with the increase of C/B.
- (4) The relationship between the proportion of materials and the water-physical properties can be described quantitatively by the regression equations based on the orthogonal test results. The equations can be used to estimate the water-physical properties of cement-plaster bonded rock-like materials with specific proportion and thus to select suitable materials in the solid-fluid coupling physical model tests.

Data Availability

The data used to support the findings of this study are available from the corresponding author upon request.

Conflicts of Interest

The authors declare that they have no conflicts of interest regarding the publication of this paper.

Acknowledgments

This work was supported by the Open Fund of State Key Laboratory of Water Resource Protection and Utilization in Coal Mining (Grant no. GJNY-18-73.2) and Science and Technology Innovation Project of China Energy Investment Corporation (SHJT-16-26).

References

- [1] D. Z. Gu, *Similar Materials and Similar Models*, China University of Mining and Technology Press, Xuzhou, China, 1995.
- [2] Y. M. Lin, *Experimental Rock Mechanics – Physical Modelling*, China Coal Industry Publishing House, Beijing, China, 1984.
- [3] M. C. He, W. L. Gong, H. M. Zhai, and H. P. Zhang, “Physical modeling of deep ground excavation in geologically horizontal strata based on infrared thermography,” *Tunnelling and Underground Space Technology*, vol. 25, no. 4, pp. 366–376, 2010.
- [4] J. Liu, X.-T. Feng, X.-L. Ding, J. Zhang, and D.-M. Yue, “Stability assessment of the Three-Gorges Dam foundation, China, using physical and numerical modeling-Part I: physical model tests,” *International Journal of Rock Mechanics and Mining Sciences*, vol. 40, no. 5, pp. 609–631, 2003.
- [5] Z. K. Li, Q. J. Xu, G. F. Luo et al., “3D geo-mechanical model test for large scaled underground hydropower station,” *Journal of Hydraulic Engineering*, vol. 33, no. 5, pp. 31–36, 2002.
- [6] J. Zhang and Z. J. Hou, “Experimental study on simulation materials for solid-liquid coupling,” *Chinese Journal of Rock Mechanics and Engineering*, vol. 23, no. 18, pp. 3157–3161, 2004.
- [7] W. R. Jacoby and H. Schmeling, “Convection experiments and the driving mechanism,” *Geologische Rundschau*, vol. 70, no. 1, pp. 207–230, 1981.
- [8] C. Kincaid and P. Olson, “An experimental study of subduction and slab migration,” *Journal of Geophysical Research: Solid Earth*, vol. 92, no. B13, pp. 13832–13840, 1987.
- [9] Z. X. Gong, C. M. Guo, and D. S. Gao, “The experiment studies of the geomechanical model material,” *Journal of Yangtze River Scientific Research Institute*, vol. 10, no. 1, pp. 32–46, 1984.
- [10] S. C. Li, X. D. Feng, S. C. Li et al., “Research and development of a new similar material for solid-fluid coupling and its application,” *Chinese Journal of Rock Mechanics and Engineering*, vol. 29, no. 2, pp. 281–288, 2010.
- [11] Q. X. Huang, W. Z. Zhang, and Z. C. Hou, “Study of simulation materials of aquifuge for solid-liquid coupling,” *Chinese Journal of Rock Mechanics and Engineering*, vol. 29, no. S1, pp. 2813–2818, 2010.
- [12] J. Ge and Y. Xu, “A method for making transparent hard rock-like material and its application,” *Advances in Materials Science and Engineering*, vol. 2019, pp. 1–14, Article ID 1274171, 2019.
- [13] X. M. Shi, B. G. Liu, Y. Y. Xiang, and Y. Qi, “A method for selecting similar materials for rocks in scaled physical modeling tests,” *Journal of Mining Science*, vol. 54, no. 6, pp. 938–948, 2018.
- [14] X. M. Shi, B. G. Liu, and J. Xiao, “A method for determining the ratio of similar materials with cement and plaster as bonding agents,” *Rock and Soil Mechanics*, vol. 36, no. 5, pp. 1357–1362, 2015.
- [15] P. P. Luo, S. R. Wang, P. Hagan et al., “Mechanical performances of cement-gypsum composite material containing a weak interlayer with different angles,” *DYNA*, vol. 94, no. 4, pp. 447–454, 2019.
- [16] M. F. Cai, *Rock Mechanics and Rock Engineering*, Science Press, Beijing, China, 2002.
- [17] J. Y. Dong, J. H. Yang, G. X. Yang et al., “Research on similar material proportioning test of model test based on orthogonal design,” *Journal of China Coal Society*, vol. 37, no. 1, pp. 44–79, 2012.
- [18] H. C. Zhu and M. W. Xie, “The way using orthogonal experiment to make up a prescription of similar materials,” *Journal of Wuhan University of Hydraulic and Electric Engineering*, vol. 23, no. 4, pp. 103–109, 1990.

Research Article

Strength Recovery Model of Clay during Thixotropy

Bin Tang ¹, **Biaohe Zhou** ², **Liang Xie** ^{2,3}, **Jianfeng Yin** ⁴, **Shengnan Zhao** ²,
and **Zhibing Wang** ²

¹Guangxi Key Laboratory of Geotechnical Mechanics and Engineering, Guilin University of Technology, Guilin 541004, China

²Institute of Civil and Architectural Engineering, Guilin University of Technology, Guilin 541004, China

³Geotechnical Engineering Company, Wuhan Surveying-Geotechnical Research Institute Co., Ltd., MCC Group, Wuhan 430080, China

⁴Hunan Nonferrous Institute of Engineering Prospecting Co., Ltd. Changsha, Hunan 410129, China

Correspondence should be addressed to Bin Tang; tangbin@glut.edu.cn

Received 30 August 2020; Revised 24 December 2020; Accepted 23 January 2021; Published 3 February 2021

Academic Editor: Wen-Chieh Cheng

Copyright © 2021 Bin Tang et al. This is an open access article distributed under the Creative Commons Attribution License, which permits unrestricted use, distribution, and reproduction in any medium, provided the original work is properly cited.

Thixotropy is a hot topic in the field of rheology of dispersed systems. Many researchers have proposed different models and hypotheses to explain the thixotropy of clay. In this paper, the strength recovery model of Zhanjiang Formation clay in the process of thixotropy is studied. Firstly, through unconfined compressive strength test, the influence of soil sensitivity, moisture content, and density on the strength growth of remolded soil was studied. The results show great influence of sensitivity, moisture content, and density on the thixotropic strength of the Zhanjiang Formation clay: the higher the sensitivity and the density, the stronger the thixotropy of soil; the higher the moisture content, the weaker the thixotropy of soil. Based on the test results, a strength recovery model of Zhanjiang Formation clay in the process of thixotropy was established. The model was verified by the validation test data and the data obtained from the existing literature. The results suggest that the model prediction is in good agreement with the verification test data and data from existing literature, which proves the confidence of the model in predicting the degree of strength recovery in the process of thixotropy of Zhanjiang Formation clay. The model provides basis for stability calculation of surrounding soil after construction disturbance of underground structures in this stratum.

1. Introduction

With the rapid development of urban construction in China, there are more and more underground structures that exploit and utilize underground space. During the construction of underground structures, the surrounding soil is disturbed and its strength reduced [1]. After completion of construction, the strength of soil will gradually recover due to thixotropy. Thixotropy is one of the complex rheological properties. The thixotropy of soil refers to the phenomenon that the structural strength of soil decreases sharply or even flows under the action of external forces, and the structure and strength gradually recover with the lapse of time after the external force stops [2]. In 1949, Boswell [3] made a thixotropic study on a large number of sedimentary aggregates and found that all materials except clean sand showed thixotropic characteristics. Díaz-Rodríguez and

Santamarina [4], Xiuli et al. [5], and Li et al. [6], respectively, studied the thixotropy of Mexican soil, Yellow River Delta silt, and Cuihu wetland soft soil. These results show that the influence of thixotropy can increase the strength of remolded soil to 100% or even higher. The study of thixotropy is of great guiding significance to deeply understand the mechanical mechanism of soil, solve the problem of engineering foundation stability, and prevent geological disasters. Some researchers have studied this from different aspects.

In terms of influencing factors of thixotropy, the moisture content of soil has an important influence on the thixotropy of soil [7–11]. Mitchell [12] pointed out that, compared with chemical factors, the moisture content of soil has an important influence on changing the intergranular force, then affecting the thixotropy of soil. Wang et al. [13] studied the thixotropy of dredged silt from Taihu Lake and

Baima Lake with different moisture content and found that the smaller the moisture content, the greater the thixotropy. Thixotropic agents can change the thixotropy of materials to a great extent, and the thixotropy is related to the density of materials [14–16]. Quanji et al. [17] found that adding a small amount of nanoclay can significantly promote the reflocculation or structural reconstruction of particles and effectively improve the thixotropy of cement paste. Qian and De Schutter [18] used nanoclay and moisture reducing agent to change the thixotropy of cement paste at the same time, and these two additives greatly accelerate the microparticle agglomeration of cement paste. Appellants' researches on the influencing factors of thixotropy are mostly qualitative and lack quantitative description.

In terms of thixotropy mechanism, thixotropy is the result of the interaction between microscopic particles [19–22]. Li et al. [23] analyzed the change law of interparticle force and particle network structure with measurement time, measurement rate in paste yield process in mesolevel, and explained the thixotropy mechanism of whole tailings paste. Zhang et al. [24] used scanning electron microscope and mercury intrusion experiment to study the change law of microstructure and pores with time after clay remodeling in Zhanjiang Formation and attributed the strength increase to the adaptive adjustment of microstructure caused by the change of force field. Huo et al. [25] think that clay is an energy dissipation system. Upon shearing, one part of the energy input from the outside makes the particles slightly adjusted, rubbed, and then dissipated, while the other part is transferred to heat energy, which intensifies the thermal movement of particles. After curing for a period of time, the energy dissipates, and the particles converge again until a new balance is reached. These researchers have discussed the thixotropy mechanism from the aspects of microstructure, self-adaptive adjustment of microstructure, and energy dissipation, but the understanding of the mechanism of soil thixotropy still stays in the stage of incomplete qualitative explanation, lacking reliable test data support, and it is difficult to explain the nature of the occurrence and development of soil thixotropy in the root.

In terms of constitutive models, many researchers have proposed empirical models or semiempirical and semi-theoretical constitutive models to describe the thixotropy of materials based on experiments or existing constitutive models of materials [26–33]. Mendes [34] put forward a constitutive model of structural fluid, which can well predict the thixotropy, viscoelasticity, and yield behavior of materials. Wei et al. [35] extended the previous pure scalar thixotropic “multilambda” model and combined it with the isotropic motion hardening (IKH) model, which reflected well the complex transient rheological behavior of the thixotropic viscoelastic plastic (TEVP) fluid. These models are more or less contradictory between the number of model parameters and the calculation accuracy, which makes it difficult to obtain general analytical solutions and accurate numerical solutions. Moreover, most of these models are

proposed for some specific fluids, and it is difficult to apply them to engineering practice.

The above work has promoted the research progress of thixotropy of soil, but there are still some drawbacks in previous studies. First of all, there are a great many of the complex factors affecting thixotropy, and the current research has not studied the influence degree of these factors from a quantitative point of view. In addition, the existence of soil thixotropy has a great influence on the engineering practice [36–39]. For example, the construction processes such as pipe jacking and pile sinking will disturb the surrounding soil and reduce its strength. After completion of construction, the strength of the soil will gradually recover, showing timeliness [40–42]. The clay of Zhanjiang Formation features strong constitutive property [43], high plasticity [44], micropermeability [45], strong acidity produced by oxidation hydrolysis [46], spatial distribution difference [47], creep property [48], thixotropy [24], etc., and it is an extremely abnormal soil with special properties, resulting in its rare engineering characteristics. But the problems about the strength recovery law of structural clay in Zhanjiang Formation during thixotropy are still unclear, and a model which can accurately reflect the soil thixotropic strength recovery has not yet been established to guide the engineering practice. To find the thixotropic recovery model of clay strength, this paper studies the growth law of soil strength with curing time based on the unconfined compressive strength test of remolded soil of Zhanjiang Formation clay, discusses the influence of soil sensitivity, moisture content, and density on thixotropy, and puts forward a model to predict the strength growth of remolded soil during thixotropy. The parameters of the model are few and easy to obtain, which simplifies the previous model calculation and is convenient for engineering applications.

2. Basic Physical Property Tests

Through existing regional geological data and engineering geological surveys, typical strata are selected for investigation, drilling, and sampling. Three groups of undisturbed soil samples 1, 2, and 3 of Zhanjiang Formation clay were taken from Baosteel Zhanjiang Iron and Steel Base in Donghai Island, Zhanjiang City, Guangdong Province, China. The depth for soil sampling for sample groups 1, 2, and 3 is 33.25–34.05 m, 53.25–54.05 m, and 65.25–66.05 m, respectively. Sampling was carried out by using a stainless steel open thin-walled sampler with an inner diameter of 100 mm, a wall thickness of 2 mm, a cutting edge angle of 60°, and a length of 300 mm. The upper end of the sampler was connected with a drill stem by screws and was provided with an exhaust (drain) hole and a spherical valve, to release air and water pressure during sampling, prevent water from reentering, and maintain a vacuum above the soil sample during lifting. The drying method, ring knife method, pycnometer method, and liquid-plastic limit combined method were used to test the basic physical properties such

as natural moisture content, natural density, specific gravity, liquid limit, and plastic limit of the Zhanjiang Formation clay. For the test methods, refer to the relevant provisions of Articles 5.2, 6.2, and 7.2 of Standard for Geotechnical Test Methods (GB/T50123-2019), and the test results are shown in Table 1.

As shown in Table 1, the physical properties of structural clay in Zhanjiang Formation are inferior, with the characteristics of high water content and high plasticity.

3. Influence of Sensitivity on Thixotropy

Thixotropic property is caused by the restoration of soil structure with the lapse of standing time after the internal structure of the soil is destroyed. To study the influence of soil sensitivity S_t on strength recovery, three groups of undisturbed soil samples 1, 2, and 3 with different sensitivity were remolded and the internal structure was destroyed to obtain remolded samples. The remoulding pattern is a homogeneous soil simulating the shape of undisturbed soil, which is obtained by drying and crushing the undisturbed soil, and then remoulding it according to the density and moisture content of the undisturbed soil. For the sample preparation method, refer to the relevant provisions of Articles 4.3.1 and 4.4.2 of Standard for Geotechnical Test Methods (GB/T50123-2019). Wrap the sample in preservative film, place it in PVC tubes, put on the lids, and seal with wax; store it in an airtight moisturizing jar for curing and control the room temperature at $25 \pm 2^\circ\text{C}$. As shown in the researches that the soil strength recovery is fast at the initial stage and slow at the later stage [4, 5], we set the curing times at 0 d, 1 d, 7 d, 30 d, and 60 d. Unconfined compressive strength tests were carried out on three groups of Zhanjiang Formation clay with different sensitivity at different curing times, and the unconfined compressive strength values of undisturbed soil and remolded soil samples of different curing times were obtained. For the unconfined compressive strength test method, refer to the relevant provisions of Article 20 of Standard for Geotechnical Test Methods (GB/T50123-2019), and the test results are shown in Table 2.

Table 2 suggests that the structural clay of Zhanjiang Formation has high strength, but the strength decreases greatly after remolding. With lapse of curing time, the strength increases obviously, and it has strong constitutive property and thixotropy. The structural clay of Zhanjiang Formation has inferior physical properties and superior mechanical properties, which makes rare engineering characteristics for the clay in Zhanjiang Formation.

To study the strength recovery law of Zhanjiang Formation clay during thixotropy, the relation between the unconfined compressive strength of remolded soil samples and the logarithm of curing time $q'_u(t) - \log t$ was established, whereas $\log t$ is meaningless at 0 d, and Table 2 shows that the values of $q'_u(0)$ and $q'_u(1)$ of the three groups of soil samples have little change and the error between them can be ignored. Therefore, the data with curing times of 1 d, 7 d, 30 d, and 60 d in Table 2 are selected to fit the curve of the relation between unconfined compressive strength of

remolded soil samples and logarithm of curing time $q'_u(t) - \log t$, and the results are shown in Figure 1.

As can be seen from Figure 1, $q'_u(t)$ grows with $\log t$. The reason the strength of soil increases with the increase of curing time is the remolding input energy to the soil, part of which destroys the internal structure of the soil, and the other part of which is converted into heat energy, which intensifies the thermal movement of particles, and the particles are separated from each other, thus reducing the acting force between particles. After curing for a period of time, the energy dissipates, and the particles converge again until a new balance is reached, and the strength increases accordingly [25]. And there is a linear relation between $q'_u(t)$ and $\log t$:

$$q'_u(t) = A \log t + B, \quad (1)$$

where B is the intercept of the straight line $q'_u(t) - \log t$, namely, $B = q'_u(1)$, in kPa . Because $q'_u(1) \approx q'_u(0)$ in Table 2, we can approximately assume that

$$B = q'_u(1) = q'_u(0) = \frac{q_u}{S_t}. \quad (2)$$

A is the slope of the straight line $q'_u(t) - \log t$, in kPa , which is related to the rate of strength recovery in the thixotropic process. Let $A = q_u a$, where q_u is the unconfined compressive strength of undisturbed soil, in kPa . a is the coefficient related to the slope of a straight line $q'_u(t) - \log t$, dimensionless. When $t = 0$, it is true that

$$A = q_u a = q'_u(0) S_t a. \quad (3)$$

The sizes of A and a reflect the thixotropy intensity degree of soil. The greater the A and a , the stronger the thixotropy, whereas the weaker the thixotropy. According to the ratio of q_u and $q'_u(0)$ in Table 2, the sensitivity S_t of the three groups of samples is 4.07, 5.53, and 4.39, respectively. It can be seen from Figure 1 that the greater the sensitivity is, the greater the A and the stronger the thixotropy of the soil is, which is consistent with the hypothetical results of (3).

To determine the coefficient a , the next section will discuss the influence of the basic physical properties of soil on the coefficient a .

4. Influence of Moisture Content on Thixotropy

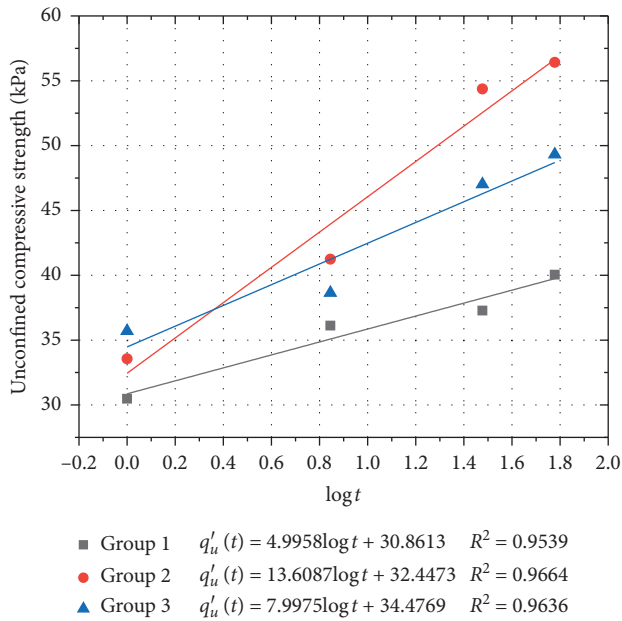
Taking another group of Zhanjiang Formation clay from the field to study the influence of moisture content on thixotropy, the sampling method is the same as that in Section 2. The undisturbed soil has an unconfined compressive strength of $q_u = 138.28 \text{ kPa}$, a moisture content of 45%, and a density of 1.71 g/cm^3 . The undisturbed soil was remolded to prepare remolded soil samples with the same density (1.71 g/cm^3) but different moisture content (40%, 45%, and 50%). The sample preparation method was the same as in Section 3. After curing the remolded soil samples for 1 d, 7 d, 30 d, and 60 d, the unconfined compressive strength was measured, respectively, and the test method was the same as in Section 3. The test results are shown in Table 3. Establish the $q'_u(t) - \log t$ relation curves of remolded soil samples

TABLE 1: Test results of physical properties of Zhanjiang Formation clay.

Group	Moisture content ω (%)	Natural density ρ (g/cm ³)	Specific gravity G_s	Liquid limit w_L (%)	Plastic limit w_p (%)
1	48.79	1.75	2.67	63.06	32.70
2	38.01	1.76	2.71	52.10	31.23
3	46.59	1.77	2.68	58.30	32.40

TABLE 2: Unconfined compressive strength test results of samples with different sensitivity at different curing times.

Group	Undisturbed soil sample q_u (kPa)	Remolded soil sample curing for	Remolded soil sample curing for	Remolded soil sample curing for	Remolded soil sample curing for	Remolded soil sample curing for
		0 d $q'_u(0)$ (kPa)	1 d $q'_u(1)$ (kPa)	7 d $q'_u(7)$ (kPa)	30 d $q'_u(30)$ (kPa)	60 d $q'_u(60)$ (kPa)
1	122.88	30.19	30.48	36.12	37.28	40.05
2	183.65	33.21	33.56	41.24	54.37	56.42
3	154.91	35.26	35.71	38.65	47.02	49.32

FIGURE 1: The $q'_u(t) - \log t$ relation curve of samples with different sensitivity.

with different moisture content according to Table 3, as shown in Figure 2.

It can be seen from Figure 2 that the slope A of the straight line $q'_u(t) - \log t$ decreases with the increase of moisture content, indicating that the thixotropy of Zhanjiang Formation clay decreases with the increase of moisture content [13]. The reason is that the original cementation between particles is destroyed by remodeling. As a solvent, moisture will dissolve some cementation substances, and the concentration in samples with low moisture content is higher than that in samples with high moisture content. Therefore, after curing, the connection between particles of samples with lower moisture content is more obvious than that of samples with higher moisture content. It can be seen from formula (3) that, $A = q_u a$, the value of a can be calculated by formula $a = A/q_u$ according to Figure 2, and

$q_u = 138.28$ kPa, and the $a - w$ relation can be fitted linearly, as shown in Figure 3.

It can be seen from Figure 3 that a decreases with the increase of w and there is a linear relation between them:

$$a = \alpha w + \beta, \quad (4)$$

where α is the slope of the $a - w$ relation curve, dimensionless; β is the intercept of the $a - w$ relation curve, dimensionless; the moisture content w is in decimal form.

5. Influence of Density on Thixotropy

Taking a group of Zhanjiang Formation clay from the field to study the influence of density on thixotropy, the sampling method is the same as that in Section 2. The undisturbed soil has an unconfined compressive strength of $q_u = 154.91$ kPa, a moisture content of 46.59%, and a density of 1.85 g/cm³. The unaltered soil was remolded to prepare remolded soil samples with the same moisture content (46.59%) but different densities (1.89 g/cm³, 1.85 g/cm³, and 1.77 g/cm³). The sample preparation method was the same as in Section 3. After curing the remolded soil samples for 1 d, 7 d, 30 d, and 60 d, the unconfined compressive strength was measured, respectively, and the test method was the same as in Section 3. The test results are shown in Table 4. Establish the $q'_u(t) - \log t$ relation curves of remolded soil samples with different densities according to Table 4, as shown in Figure 4.

It can be seen from Figure 4 that the slope A of the straight line $q'_u(t) - \log t$ increases with the increase of density ρ , indicating that the thixotropy of Zhanjiang Formation clay increases with the increase of density. The smaller the pore ratio of soil, the greater the thixotropy of soil [11], and the smaller the pore ratio of soil, the higher its density, the smaller the spacing between soil particles, and the larger the contact area. After curing, the connection between particles is more obvious than that of less dense soil, so the thixotropy of dense soil is stronger. Therefore, the thixotropy of soil with high density is stronger. It can be seen from formula (3) that, $A = q_u a$, the values of a can be calculated by $a = A/q_u$ according to Figure 4 and

TABLE 3: Unconfined compressive strength of remolded samples with different moisture contents at different curing times.

Moisture content (%)	Remolded soil sample curing for 1 d $q_u'(1)$ (kPa)	Remolded soil sample curing for 7 d $q_u'(7)$ (kPa)	Remolded soil sample curing for 30 d $q_u'(30)$ (kPa)	Remolded soil sample curing for 60 d $q_u'(60)$ (kPa)
40	28.51	33.22	40.68	41.85
45	18.17	21.34	26.67	30.17
50	8.54	10.64	13.17	15.75

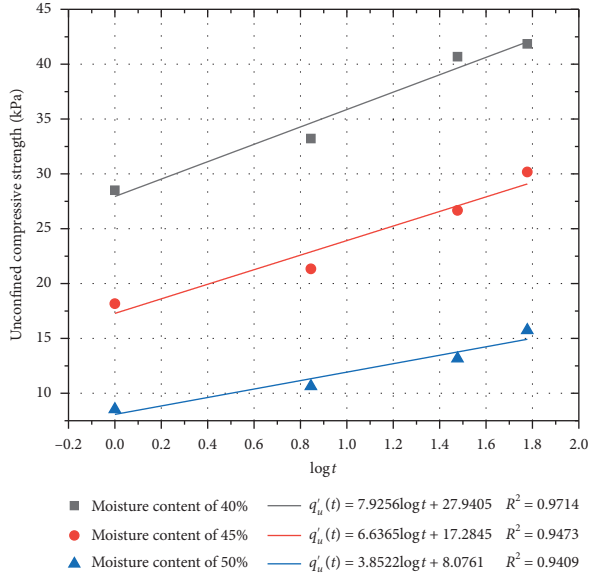


FIGURE 2: Relation curve $q_u'(t) - \log t$ of samples with different moisture content.

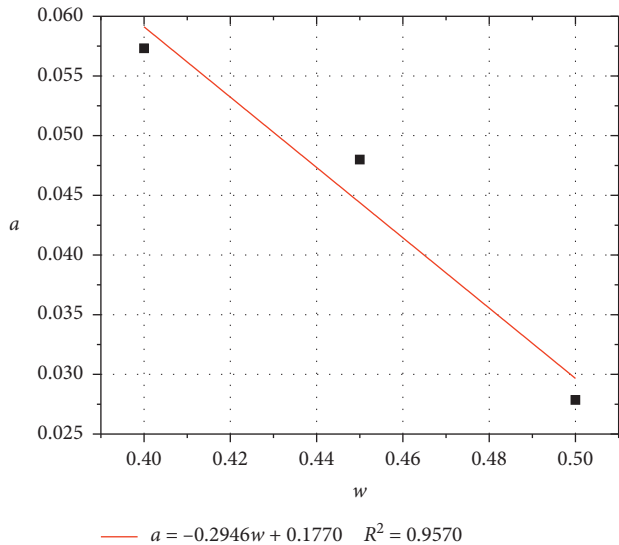


FIGURE 3: Relation curve $a - w$.

$q_u = 154.91$ kPa, and the $a - \rho$ relation can be fitted linearly, as shown in Figure 5.

As can be seen from Figure 5, a increases with the increase of ρ , demonstrating a linear relation between them:

$$a = \gamma\rho + \eta, \quad (5)$$

where γ is the slope of the $a - \rho$ relation curve, dimensionless; η is the intercept of the $a - \rho$ relation curve, dimensionless; for ρ , the value with dimension removed is taken.

Figures 3 and 4 show a linear relation between a and moisture content w , density ρ within a certain range, and the corresponding values of w , ρ , and a in Figures 3 and 4 shown in Table 5.

On the ground that both moisture content w and density ρ have a linear relation with a within a certain range, we can use a binary linear regression method to carry out regression analysis and determine their quantitative relation, assuming that the quantitative relation among them is

$$a = k_0 + k_1w + k_2\rho, \quad (6)$$

where k_0 , k_1 , and k_2 are regression parameters, dimensionless.

The results of regression analysis are shown in Tables 6 and 7.

According to Table 6, the linear regression coefficient multiple $R = 0.8995$, indicating that w , ρ , and a are correlated. The value of significance F is 0.0834, showing a significant regression effect. As shown in Table 7, the values of k_0 , k_1 , and k_2 in (6) are -0.1777 , -0.3291 , and 0.2143 , respectively; then,

$$a = -0.1777 - 0.3291w + 0.2143\rho. \quad (7)$$

6. Thixotropic Strength Recovery Model

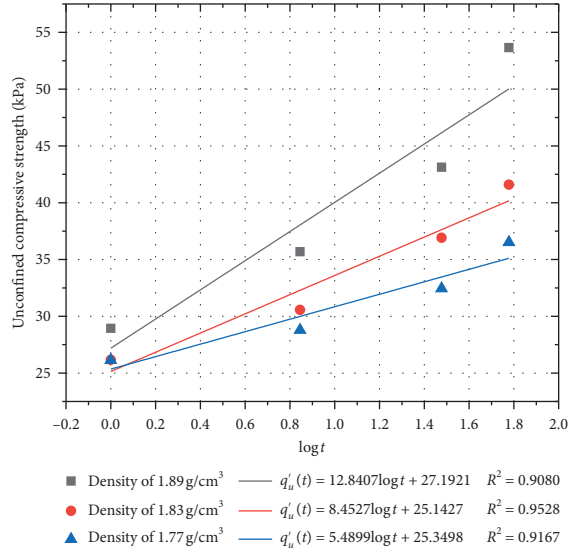
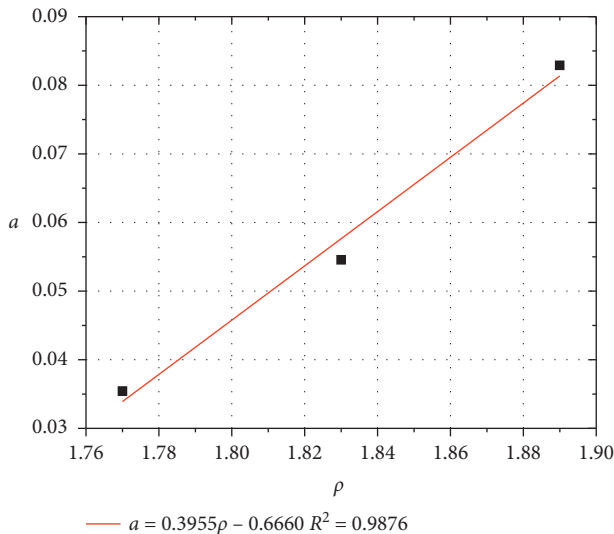
In terms of prediction model, Zhang Xianwei studied the strength growth law of different curing times after clay remolding through unconfined compressive strength test and penetration test and put forward the empirical formula of strength recovery as a power function form [24].

$$q_u'(t) = Ct^D. \quad (8)$$

Because the parameter meaning of the power function is not clear, the logarithm of the power function is used to make the parameter meaning clear. In this paper, the empirical formula in logarithmic form (1) is obtained by data fitting. According to the above analysis, sensitivity, moisture content, and density have obvious influences on thixotropic recovery. Substituting (2), (3), and (6) into (1), the thixotropic strength recovery model of Zhanjiang Formation clay can be obtained:

TABLE 4: Unconfined compressive strength of remolded samples with different densities at different curing times.

Density (g/m ³)	Remolded soil sample curing for 1 d $q'_u(1)$ (kPa)	Remolded soil sample curing for 7 d $q'_u(7)$ (kPa)	Remolded soil sample curing for 30 d $q'_u(30)$ (kPa)	Remolded soil sample curing for 60 d $q'_u(60)$ (kPa)
1.89	28.94	35.69	43.13	53.66
1.83	26.17	30.56	36.91	41.59
1.77	26.15	28.79	32.45	36.52

FIGURE 4: Relation curve $q'_u(t) - \log t$ of samples with different densities.FIGURE 5: Relation curve $a - \rho$.

$$q'_u(t) = q'_u(0)S_t(k_0 + k_1w + k_2\rho)\log t + \frac{q_u}{S_t}, \quad (9)$$

where $q'_u(t)$ is the unconfined compressive strength corresponding to the curing time t , in kPa; $q'_u(0)$ is the unconfined

TABLE 5: The test values of w , ρ , and a .

Indicators	Values					
w	0.4	0.45	0.4659	0.4659	0.4659	0.5
ρ	1.71	1.71	1.77	1.83	1.89	1.71
a	0.0573	0.0480	0.0354	0.0546	0.0829	0.0279

TABLE 6: Regression statistics.

Regression parameters	Values
Multiple R	0.8995
R square	0.8091
Adjusted R square	0.6818
Standard error	0.0109
Significance F	0.0834
Observed value	6

TABLE 7: Regression parameters.

Coefficients	Values
Intercept	-0.1777
w variable 1	-0.3291
ρ variable 2	0.2143

compressive strength corresponding to the curing time at 0 d, in kPa; q_u is the unconfined compressive strength of undisturbed soil, in kPa; w takes its decimal form; ρ takes the value with dimension removed; k_0 , k_1 , and k_2 are model parameters, dimensionless, determined by referring to the determination method in Section 4.

Substituting the values of k_0 , k_1 , and k_2 into (9), we get

$$q'_u(t) = q'_u(0)S_t(-0.1777 - 0.3291w + 0.2143\rho)\log t + \frac{q_u}{S_t}. \quad (10)$$

It can be seen from formula (10) that the model considers the influence of moisture content, density, and sensitivity on thixotropy, where the coefficient of moisture content is negative, and the greater the moisture content, the smaller the soil strength growth, and vice versa. The coefficient of sensitivity and density is positive, and the greater the sensitivity and density, the more obvious the soil strength growth. Deriving t from (9), we get

$$\frac{dq'_u(t)}{dt} = \frac{q'_u(0)S_t(k_0 + k_1w + k_2\rho)}{t \ln 10}. \quad (11)$$

By substituting the test data of groups 1, 2, and 3 into formula (11) according to Table 1, the curves of thixotropic

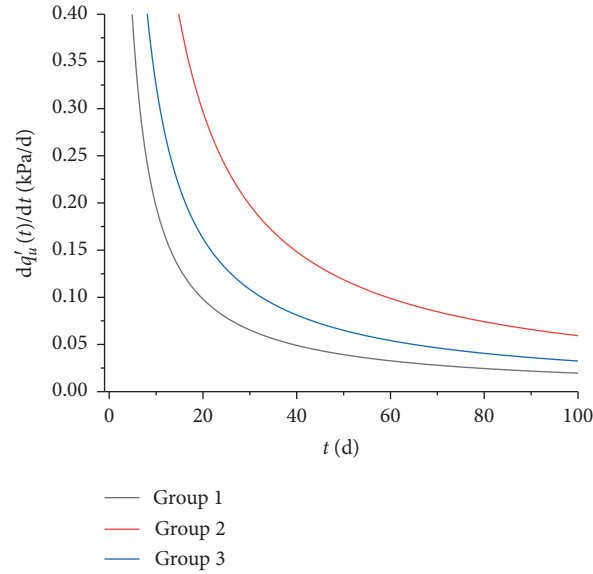


FIGURE 6: The relation curve of thixotropic strength recovery rate and curing time.

recovery rates of the three groups soil samples changing with time can be obtained, as shown in Figure 6.

It can be seen from Figure 6 that the thixotropic recovery rate of the three groups of soil samples decreases with the increase of curing time. Specifically, it decreases rapidly within 0 to 60 days and, after 60 days, tends to be stable and keeps stable at a smaller value, indicating that the thixotropic recovery is very slow after 60 days of curing time, and the strength of the soil cannot be restored to the strength of the original soil in a short time after the structure of the soil is destroyed.

7. Model Verification

To verify the rationality of the model, three different groups of undisturbed soil 4, 5, and 6 of Zhanjiang Formation clay were taken for verification test. The depth of soil sampling for specimens 4, 5, and 6 is 2.00–3.00 m, 6.00–9.00 m, and 19.25–20.05 m, respectively. The basic physical properties such as natural moisture content, natural density, and specific gravity of the soil samples taken for the verification test were measured. Sampling and testing methods are the same as those in Section 2, and the results are shown in Table 8.

Unconfined compressive strength tests were carried out on undisturbed soil samples and remolded soil samples with different curing times (0 d, 1 d, 5 d, 10 d, 15 d, 30 d, and 60 d) for the three groups 4, 5, and 6 of Zhanjiang Formation clay, and the unconfined compressive strength values of undisturbed soil and remolded soil samples with different curing times were obtained. The testing method is the same as that in Section 3, as shown in Table 9.

Using formula (10) to predict the intensity recovery of groups 4, 5, and 6, substituting the initial conditions of soil groups 4, 5, and 6 into formula (10) according to Tables 8 and 9, we get the strength recovery prediction curves for groups 4, 5, and 6 as follows:

$$q'_u(t) = 0.1951 \log t + 5.11, \quad (12)$$

$$q'_u(t) = 4.8554 \log t + 27.02, \quad (13)$$

$$q'_u(t) = 10.6613 \log t + 49.68. \quad (14)$$

The test data in Table 9 are compared with the prediction results of formulas (12)–(14), and the results are shown in Figure 7.

To further verify the rationality of the model, the test data of the literature [24] is quoted to verify the model, and the data of the literature [24] are shown in Tables 10 and 11.

Substituting the physical and mechanical indexes into formula (10) according to Tables 10 and 11, the strength recovery prediction curve is as follows:

$$q'_u(t) = 2.65 \log t + 25, \quad (15)$$

$$q'_u(t) = 7.96 \log t + 20.68, \quad (16)$$

$$q'_u(t) = 51.31 \log t + 94.15. \quad (17)$$

Comparing the test data in Table 11 with the prediction result of formulas (15)–(17), the result is shown in Figure 8.

It can be seen from Figures 7 and 8 that the test data are in good agreement with the predicted results of the model, and the theoretical curve calculated by this model can reflect

TABLE 8: The test results of physical properties of Zhanjiang Formation clay.

Group	Moisture content ω (%)	Natural density ρ (g/cm ³)	Specific gravity G_s
4	55.38	1.71	2.67
5	45.79	1.72	2.71
6	42.26	1.71	2.72

TABLE 9: Unconfined compressive strength test results of samples at different curing times.

Group	q_u (kPa)	$q'_u(0)$ (kPa)	$q'_u(1)$ (kPa)	$q'_u(5)$ (kPa)	$q'_u(10)$ (kPa)	$q'_u(15)$ (kPa)	$q'_u(30)$ (kPa)	$q'_u(60)$ (kPa)
4	30.02	5.11	5.11	5.35	5.41	5.54	5.60	5.73
5	120.78	27.02	27.54	28.42	32.88	34.74	35.20	35.66
6	214.62	49.68	50.62	53.46	58.79	62.64	67.38	69.75

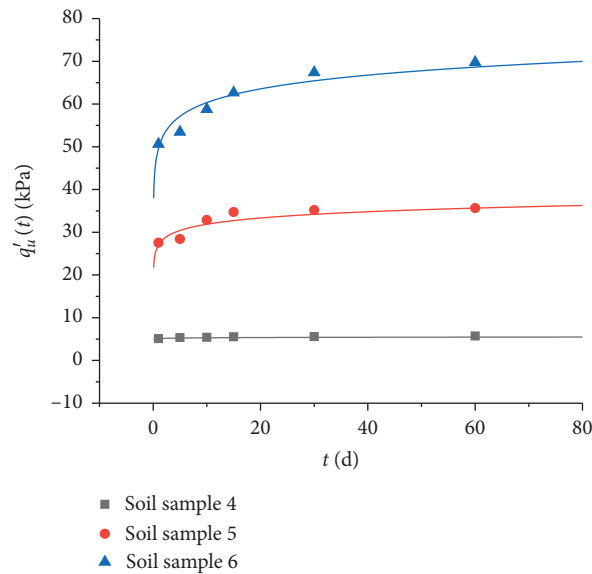


FIGURE 7: Comparison of test data and model prediction.

TABLE 10: The physical and mechanical indexes of clay of the literature [24].

Group	Moisture content ω (%)	Natural density ρ (g/cm ³)	Sensitivity S_t
7	50.00	1.67	7
8	40.13	1.70	7
9	35.00	1.73	7

TABLE 11: Strength at different curing times of clay of the literature [24].

Group	$q'_u(0)$ (kPa)	$q'_u(5)$ (kPa)	$q'_u(10)$ (kPa)	$q'_u(15)$ (kPa)	$q'_u(30)$ (kPa)	$q'_u(60)$ (kPa)
7	25.00	27.17	28.46	29.31	31.02	33.14
8	20.68	27.12	29.03	30.05	33.01	35.32
9	94.15	129.52	143.25	156.37	168.90	187.26

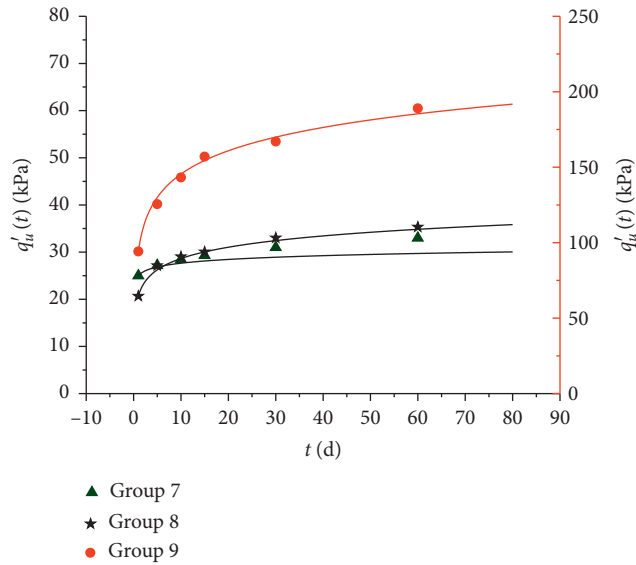


FIGURE 8: Comparison of the data of the literature [24] and model prediction.

the law of strength recovery of structural clay in Zhanjiang Formation during thixotropy.

8. Conclusion

In this paper, Zhanjiang Formation clay of undisturbed soil and remolded soil at different curing times is taken as research object. Through a series of unconfined compressive strength tests, the relation between thixotropic strength growth and curing time and the relation of sensitivity, moisture content, density of soil, and its thixotropy are studied, and the strength recovery model considering the influence of sensitivity, moisture content, and density on thixotropy is established.

- (1) Curing for 60 days after remolding, the strength of Zhanjiang Formation clay increased by 30% of its initial strength, showing obvious thixotropy. The relation between the logarithm of curing time and strength is fitted, and the fitting parameters R^2 are all greater than 0.95. The logarithmic form can reflect the law of strength growth.
- (2) Sensitivity, moisture content, and density have great influence on the thixotropic strength of the Zhanjiang Formation clay, and the higher the sensitivity and density are, the stronger the thixotropy of soil is. The higher the moisture content is, the weaker the thixotropy of soil is.
- (3) Based on the test results, considering the effects of sensitivity, moisture content, and density on thixotropy, a strength recovery model of remolded soil in Zhanjiang Formation was established: $q'_u(t) = q'_u(0)S_t(k_0 + k_1w + k_2\rho)\log t + q_u/S_t$. The model could be used to predict the degree of strength recovery in the process of thixotropy of Zhanjiang Formation clay.

- (4) The model is validated by the validation test data and the existing literature data, and the model prediction data is in good agreement with the validation test data and the existing literature data.

Data Availability

The experimental data used to support the findings of this study are provided in the article.

Conflicts of Interest

The authors declare that there are no conflicts of interest.

Acknowledgments

This work was supported by the National Natural Science Foundation of China (41867035), the Project of Guangxi Key Laboratory of Geotechnical Mechanics and Engineering (2016-A-01), Guangxi Key Laboratory of Geomechanics and Geotechnical Engineering of China (no. 13-KF-05), and Guangxi Natural Science Foundation under Grant no. 2017GXNSFAA198092. The authors gratefully acknowledge the financial support.

References


- [1] W.-C. Cheng, L. Ge, N. Liu, J. Xu, and S. Horpibulsuk, "Recent massive incidents for subway construction in soft alluvial deposits of Taiwan: a review," *Tunnelling and Underground Space Technology incorporating Trenchless Technology Research*, vol. 96, 2020.
- [2] J. C. Ruge, F. Molina-Gómez, and J. P. Rojas, "Thixotropic behaviour study of clayey soils from the lacustrine deposits of Bogotá high plateau," in *Proceedings of the 5th International Meeting for Researchers in Materials and Plasma Technology (5th IMRMPT)*, vol. 1386, San José de Cúcuta, Colombia, May 2019.
- [3] P. G. H. Boswell, "A preliminary examination of the thixotropy of some sedimentary rocks," *Quarterly Journal of Geological Science*, vol. 104, p. 499, 1949.
- [4] J. A. Díaz-Rodríguez and J. C. Santamarina, "Thixotropy: the case of Mexico city soils," in *Proceedings of the XI Pan-American Conference on Soils Mechanics and Geotechnical Engineering*, pp. 441–448, Curitiba, Brazil, 1999.
- [5] F. Xiuli, S. Zhou, and L. Lin, "Study on thixotropy of silt in modern Yellow River delta and its application," *Ocean University of China Acta Sinica*, vol. 36, no. 6, pp. 1053–1056, 2004.
- [6] L. Li, L. Chen, and S. Gao, "Experimental study on thixotropy of soft soil in Cuihu Wetland," *Rock and Soil Mechanics*, vol. 31, no. 3, pp. 765–768, 2010.
- [7] S. Sochan and H. Tanaka, "Properties of very soft clays: a study of thixotropic hardening and behavior under low consolidation pressure," *Soils and Foundations*, vol. 52, no. 2, 2012.
- [8] K. H. Andersen and S. Yang, "Thixotropy of marine clays," *Geotechnical Testing Journal*, vol. 39, no. 2, 2015.
- [9] A. Rafat Shahriar, M. Zoyunl Abedin, and R. Jadid, "Thixotropic aging and its effect on 1-D compression behavior of soft reconstituted clays," *Applied Clay Science*, vol. 153, 2018.
- [10] A. Rafat Shahriar and R. Jadid, "An experimental investigation on the effect of thixotropic aging on primary and

- secondary compression of reconstituted dredged clays," *Applied Clay Science*, vol. 162, 2018.
- [11] M. Zhang, J. Yin, and W. Wang, "Influence of physical and mechanical properties of structural clay of Zhanjiang formation on its thixotropy," *Journal of Engineering Geology*, pp. 1–9, 2020.
- [12] J. K. Mitchell, "Fundamental aspects of thixotropy in soils," *Journal of the Soil Mechanics and Foundations Division*, vol. 86, no. 3, pp. 803–836, 1960.
- [13] L. Wang, L. Cao, and Li Lei, "Study on thixotropic characteristics of dredged silt in Taihu Lake and Baima Lake," *Journal of Engineering Geology*, vol. 23, no. 3, pp. 548–553, 2015.
- [14] Y. Wang, S. Xu, and G. Wang, "Experiment and characteristics of thixotropic cement slurry materials proportioning," *Coal Mine Safety*, vol. 50, no. 3, pp. 35–37, 2019.
- [15] B. Liang, W. Ji, and Z. Qin, "Study on preparation and properties of highly thixotropic tailings filling materials," *Nonmetallic Minerals*, vol. 43, no. 3, pp. 50–52, 2020.
- [16] Yu Liu, M. Li, and P. Yan, "Effect of mineral admixtures on rheological property and thixotropy of cementitious materials slurry," *Journal of Silicate*, vol. 47, no. 5, pp. 594–601, 2019.
- [17] Z. Quanji, G. R. Lomboy, and K. Wang, "Influence of nano-sized highly purified magnesium alumino silicate clay on thixotropic behavior of fresh cement pastes," *Construction and Building Materials*, vol. 69, 2014.
- [18] Y. Qian and G. De Schutter, "Enhancing thixotropy of fresh cement pastes with nanoclay in presence of polycarboxylate ether superplasticizer (PCE)," *Cement and Concrete Research*, vol. 111, 2018.
- [19] A. Jacobsson and P. Roland, "Thixotropic action in remoulded quick clay," *Bulletin of the International Association of Engineering Geology*, vol. 5, no. 1, 1972.
- [20] C. Martin, P. Frédéric, P. Jean-Michel, M. Albert, L. Peter, and C. Bernard, "Dissociation of thixotropic clay gels," *Physical Review. E, Statistical, Nonlinear, and Soft Matter Physics*, vol. 66, no. 2, 2002.
- [21] X. W. Zhang, L. W. Kong, A. W. Yang, and H. M. Sayem, "Thixotropic mechanism of clay: a microstructural investigation," *Soils and Foundations*, vol. 57, no. 1, 2017.
- [22] G. Landrou, C. Brumaud, M. L. Plötze, W. Frank, and G. Habert, "A fresh look at dense clay paste: deflocculation and thixotropy mechanisms," *Colloids and Surfaces A: Physicochemical and Engineering Aspects*, vol. 539, 2018.
- [23] C. Li, B. Yan, S. Wang, H. Hou, and G. Chen, "Yield stress variability behavior of full tailings paste under time-rate double factors," *Chinese Journal of Engineering*, vol. 42, no. 10, pp. 1308–1317, 2020.
- [24] X. Zhang, L. Kong, and J. Li, "Microscopic mechanism of strength recovery during thixotropy of clay," *Chinese Journal of Geotechnical Engineering*, vol. 36, no. 8, pp. 1407–1411, 2014.
- [25] H. Huo, L. Qi, and H. Lei, "Thinking and experimental study on thixotropy of Tianjin soft clay," *Chinese Journal of Rock Mechanics and Engineering Newspaper*, vol. 35, no. 3, pp. 631–637, 2016.
- [26] K. Dullaert and J. Mewis, "A structural kinetics model for thixotropy," *Journal of Non Newtonian Fluid Mechanics*, vol. 139, no. 1-2, pp. 21–30, 2006.
- [27] H. A. Barnes, "Thixotropy-a review," *Journal of Non-newtonian Fluid Mechanics*, vol. 70, no. 1-2, pp. 1–33, 1997.
- [28] G. Q. Guo, "Some constitutive models of thixotropic fluids," *Mechanics and Practice*, vol. 2, no. 6, pp. 20–22, 2000.
- [29] D. Konraad and M. Jan, "A structural kinetics model for thixotropy," *Journal of Non-newtonian Fluid Mechanics*, vol. 139, no. 1, pp. 21–30, 2006.
- [30] Y. Xu, H. Xu, and N. Wu, "Numerical simulation of thixotropy of highly sensitive soft soil," in *Proceedings of the First National Seminar on Geotechnical Constitutive Theory*, pp. 240–245, Beijing, China, 2008.
- [31] Y. Zhang, D. Gan, and X. Chen, "Shear thixotropy experiment of tailings cemented filling slurry and its thixotropy prediction model based on dimensional analysis," *Chinese Journal of Nonferrous Metals*, vol. 30, no. 4, pp. 951–959, 2020.
- [32] Z. Wang, C. Lu, and Z. Xu, "The thixotropy of saturated sand under cyclic loading," *Chinese Journal of Geotechnical Engineering*, vol. 36, no. 10, pp. 1831–1837, 2014.
- [33] J. Li, W. Wang, Y. Zhu, H. Xu, and X. Xie, "An elastic-viscoplastic model for time-dependent behavior of soft clay and its application on rheological consolidation," *Mathematical Problems in Engineering*, vol. 2014, Article ID 587412, 14 pages, 2014.
- [34] P. R. D. Mendes, "Thixotropic elasto-viscoplastic model for structured fluids," *Soft Matter*, vol. 7, p. 2471, 2011.
- [35] Y. Wei, M. J. Solomon, and R. G. Larson, "A multimode structural kinetics constitutive equation for the transient rheology of thixotropic elasto-viscoplastic fluids," *Journal of Rheology*, vol. 62, no. 1, pp. 321–342, 2018.
- [36] G. B. Kul'Chitskii, "Thixotropy of soils of the Middle Ob region and its consideration when constructing pile foundations," *Soil Mechanics and Foundation Engineering*, vol. 12, no. 3, pp. 168–170, 1975.
- [37] Y. Xu, C. Wang, and M. Huang, "Study on thixotropy of saturated soft soil in wet-sprayed pile construction," *Chinese Journal of Geotechnical Engineering*, vol. 35, no. 10, pp. 1784–1789, 2013.
- [38] A.J. Lutenecker, "Aged undrained shear strength of remolded clays," in *Proceedings of the 8th International Conference Offshore Site Investigation Geotechnics*, no. 6, pp. 378–383, London, UK, September 2017.
- [39] H. A. Al-Janabi and C. P. Aubeny, "Experimental measurement of thixotropy and sensitivity in gulf of Mexico clay," in *Proceedings of the 29th International Ocean and Polar Engineering Conference*, pp. 16–21, Honolulu, HI, USA, June 2019.
- [40] Li Lin, J. Li, D. Sun, and F. Rui, "Time-effect study on bearing capacity of static pressure pile on natural saturated clay foundation," *Rock and Soil Mechanics*, vol. 38, no. 9, pp. 2515–2522, 2017.
- [41] W.-C. Cheng, J. C. Ni, A. Arulrajah, and H.-W. Huang, "A simple approach for characterising tunnel bore conditions based upon pipe-jacking data," *Tunnelling and Underground Space Technology*, vol. 71, pp. 494–504, 2018.
- [42] W.-C. Cheng, L. Wang, Z.-F. Xue, J. C. Ni, M. M. Rahman, and A. Arulrajah, "Lubrication performance of pipejacking in soft alluvial deposits," *Tunnelling and Underground Space Technology Incorporating Trenchless Technology Research*, vol. 91, 2019.
- [43] J.-H. Shen, R. Wang, and Y. Zheng, "Research on regional microstructure characteristics of structural clay of Zhanjiang formation," *Rock and Soil Mechanics*, vol. 34, no. 7, pp. 1931–1936, 2013.
- [44] X. W. Zhang, L. W. Kong, A. G. Guo, and Y. F. Tuo, "Experiment study of pore distribution of strong structural clay under different consolidation pressures," *Rock and Soil Mechanics*, vol. 35, no. 10, pp. 2794–2800, 2014.
- [45] X. W. Zhang, L. W. Kong, A. Guo, and Y. Tuo, "Evolution of microscopic pore of structured clay in compression process

- based on SEM and MIP test,” *Chinese Journal of Rock Mechanics and Engineering*, vol. 31, no. 2, pp. 406–412, 2012.
- [46] X.-W. Zhang, L. W. Kong, and C. Cheng, “Effects of hydrochemistry on structural strength of Zhanjiang formation clay,” *Chinese Journal of Geotechnical Engineering*, vol. 39, no. 11, pp. 1967–1975, 2017.
- [47] J.-H. Shen, R. Wang, and C. Q. Zhu, “Research on spatial distribution law of gray clays of Zhanjiang formation,” *Rock and Soil Mechanics*, vol. 34, no. S1, pp. 331–336, 2013.
- [48] L. W. Zhong, L.-J. He, and X.-W. Zhang, “Creep model of Zhanjiang clay and plastic components with variable parameters,” *Rock and Soil Mechanics*, vol. 33, no. 8, pp. 2241–2246, 2012.

Research Article

Bending Capacity of Concrete-Encased Underground Electrical Duct Banks under Monotonic Loading: An Experimental Study

Ting-jin Liu ^{1,2,3}, Liang-yi Cai,³ Qiang Liao,³ and Yu-bing Yang⁴

¹South China Institute of Geotechnical Engineering, South China University of Technology, Guangzhou 510640, Guangdong, China

²State Key Laboratory of Subtropical Building Science, South China University of Technology, Guangzhou 510640, Guangdong, China

³School of Civil Engineering and Transportation, South China University of Technology, Guangzhou 510640, Guangdong, China

⁴College of Water Conservancy and Civil Engineering, South China Agricultural University, Guangzhou 510642, Guangdong, China

Correspondence should be addressed to Ting-jin Liu; liu_tingjin@163.com

Received 22 September 2020; Revised 9 December 2020; Accepted 21 December 2020; Published 23 January 2021

Academic Editor: Zhushan Shao

Copyright © 2021 Ting-jin Liu et al. This is an open access article distributed under the Creative Commons Attribution License, which permits unrestricted use, distribution, and reproduction in any medium, provided the original work is properly cited.

The bending capacity of concrete-encased underground electrical duct banks has been the subject of considerable investigation using the load-structure method; however, the role of high-density polyethylene (HDPE) conduits and the thresholds of electrical duct banks has not been fully scrutinized. This study examines the bending behaviors of electrical duct banks subjected to monotonic vertical loading in a soil box using an advanced monitoring device to measure the conduit diameter change. An analysis of the experiment shows the effective role of HDPE conduits in improving the bending capacity of electrical duct banks. The results suggest 5% and 7.5% as the deformation rate thresholds with respect to the ultimate states of serviceability and bearing capacity, respectively. The threshold of the longitudinal curvature radius is determined to be 18000 m. Finally, the evolution trends of the stress and deformation rates of HDPE conduits are recommended for the monitoring indexes and control standards of electrical duct banks.

1. Introduction

Overhead lines, underground cables, and substations are critical infrastructure components in electricity transmission. In the central urban area of Shanghai, the proportion of underground cables has exceeded 80% [1]. In London, most of the electricity supply is also transmitted via underground cables, which are traditionally found just below the road surface [2]. Cables can be laid under a road, across open land, or in tunnels. They operate at a range of voltages reaching 400 kV [3]. In most cases, high-voltage underground cables are laid in a duct bank rather than being buried directly in the ground. Therefore, it is very important to guarantee the safety of these underground structures [4, 5]. In a duct bank, electrical cables are typically laid out within polyvinyl chloride (PVC)/modified polypropylene

(MPP)/high-density polyethylene (HDPE) conduits that are bundled together. These groupings of conduits are often protected by concrete casings. PVC spacers are also used to separate the internal conduits from concrete walls, as shown in Figure 1. In general, all concrete-encased electric conduit duct banks contain steel reinforcement throughout their entire length. The reinforcing steel is installed longitudinally at each corner of a duct bank (in cross section) and along the top and bottom. Stirrups are also needed to hold the longitudinal steel in place during the placement of the concrete.

An investigation of four high-voltage cable lines (110 kV/220 kV) of the Zhuhai Power Supply Bureau of Guangdong Province showed that 5.35 km of electrical duct bank was laid along a 15.25 km long line—a considerable proportion. Generally, an electrical duct bank is laid 1~3 m underground. Because of factors such as defects in early design,

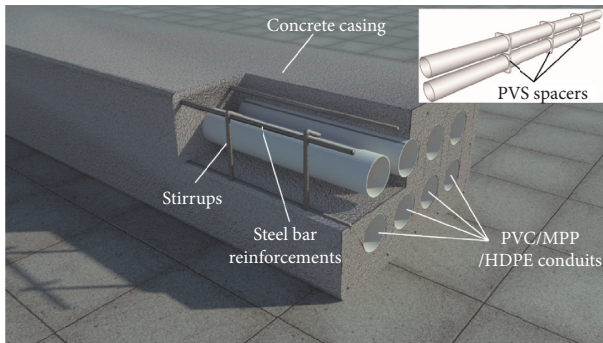


FIGURE 1: Sketch of concrete-encased underground electrical duct bank.

construction, and nearby infrastructure, deficiencies such as the differential settlement, tilting, and cracking of concrete and HDPE conduits can appear in electrical duct banks and working wells, as shown in Figure 2. Hence, protecting electrical cable duct banks and controlling their deformation and damage has become an important issue.

Most previous studies on electrical duct banks have focused on cable ampacity and thermal resistivity. Kelly et al. [6] provided a reference for various ampacity ratings that were dependent on installation. Nagley and Nease [7] conducted different installations to determine the relative thermal characteristics of two types of duct banks that differed in terms of duct spacing and the amount of concrete. Kellow [8–10] employed a numerical procedure to calculate the ampacity and rise in temperature rise and conducted experiments to study the ampacity of cables and the thermal performance of duct banks with and without forced cooling. El-Kady and Horrocks [11] described an efficient finite-element-based technique for calculating geometric factors for extended values of the external thermal resistance of cables in duct banks. Bascom [12] evaluated various cable and magnetic shielding configurations to minimize the resulting magnetic fields in an underground cable system along duct banks and near manholes. Hwang [13] described a combined magnetothermal analysis for calculating the thermal fields of a cable duct bank taking into account the effects of structural steels. Malmedal et al. [14] determined the effects of concrete mixtures on the resulting thermal resistivity. In addition, the optimization of cost and electrothermal performance has gradually become a research topic of interest. A multi-objective self-adaptive optimization method was proposed for the first time in 2018 to maximize ampacity and minimize the cost of underground cable duct banks [15]. Ocoñ et al. [16] used a modified Jaya algorithm to optimize the material costs and electrothermal performance of an underground power cable system (UPCS). Charerndee et al. [17] evaluated the effects of concrete duct bank dimensions and the thermal properties of concrete on the sensitivity of underground power cable ampacity.

When a duct bank deforms, the mechanical behaviors are key factors that affect the thermal performance and the magnetic fields. Experimental studies have been conducted to explore these mechanical behaviors. Liu et al. [18, 19] conducted small-scale experiments to study the flexural

performance and shear bearing capacity of concrete cable ducts reinforced with GFRP bars. In general, research on electrical cable duct banks has mainly focused on cable ampacity, thermal resistivity, and the optimization of cost and electrothermal performance. Wang and Guo [20] carried out a numerical simulation and data analysis to assess the settlement and damage of a working shaft of an underground high-voltage electricity cable duct and determined the threshold of differential settlement. However, research on the mechanical behaviors and thresholds of deformation and damage has been limited.

This paper presents the results of an experimental investigation on concrete cable ducts subjected to monotonic vertical loading with a soil-structure method. An innovative displacement measuring device is used to measure the change in conduit diameter of HDPE conduits during the experiment. Previous tests have concentrated on the cover concrete and reinforcements and disregarded the HDPE conduits [18, 19]. The experiment carried out within the framework of this study is unique in addressing the following objectives: (1) to study the role of HDPE conduits, (2) develop a set of thresholds for HDPE conduits, (3) study the bending behaviors of electrical duct banks, and (4) offer suggestions on monitoring indexes and control standards.

2. Experimental Procedure

2.1. Test Setup and Loading Protocol. The experimental program was based on a monotonic loading static test of four electrical duct banks. The test setup consisted of reaction frames made from hollow steel sections and a soil box providing lateral and vertical soil pressure. The electrical duct banks were tested vertically. Two hinge supports were set at the bottom of the soil box to prevent the excessive settlement of the specimens. The hinge supports were rectangular columns made of Q335 steel with dimensions of 800 mm × 300 mm × 300 mm. The specimens were placed 200 mm above the supports. The physical and mechanical properties of the soil used in the experiment are given in Table 1. The soil box was made of Q235 steel and tempered glass with a size of 4.2 m × 2.7 m × 2.7 m. An actuator was used to apply the load, and the load magnitude was measured by a force sensor. A load distributing beam was used to transfer the concentrated load into a distributed surface load. The test adopted monotonic static step loading, and the load of each stage was approximately 10 kN. When approaching the failure load, the loading mode was converted from force-control loading to displacement-control loading until a significant decrease in load appeared in the readings of the force sensor. The details of test setup are shown in Figure 3.

2.2. Test Specimens. Because the bending behaviors of the full-scale specimen and small specimen were similar [18], the specimens for the experiment were built with double conduits in different arrangements, section heights, and reinforcements. Figure 4 shows the configuration of the reinforcing bars, stirrups, concrete, and HDPE conduits in the specimen. The



FIGURE 2: Ground subsidence (a) and damage (b) caused by deficiencies in concrete-encased underground electrical duct banks.

TABLE 1: Physical and mechanical properties of soil.

Wet density ρ (g/cm ³)	Water content ω (%)	Cohesion c (kPa)	Friction angle φ (°)	Specific gravity G_s	Compression modulus E_s (MPa)	Liquid limit ω_L	Plastic limit ω_P
1.88	30.40	15	7.8	2.72	5.9	0.422	0.276

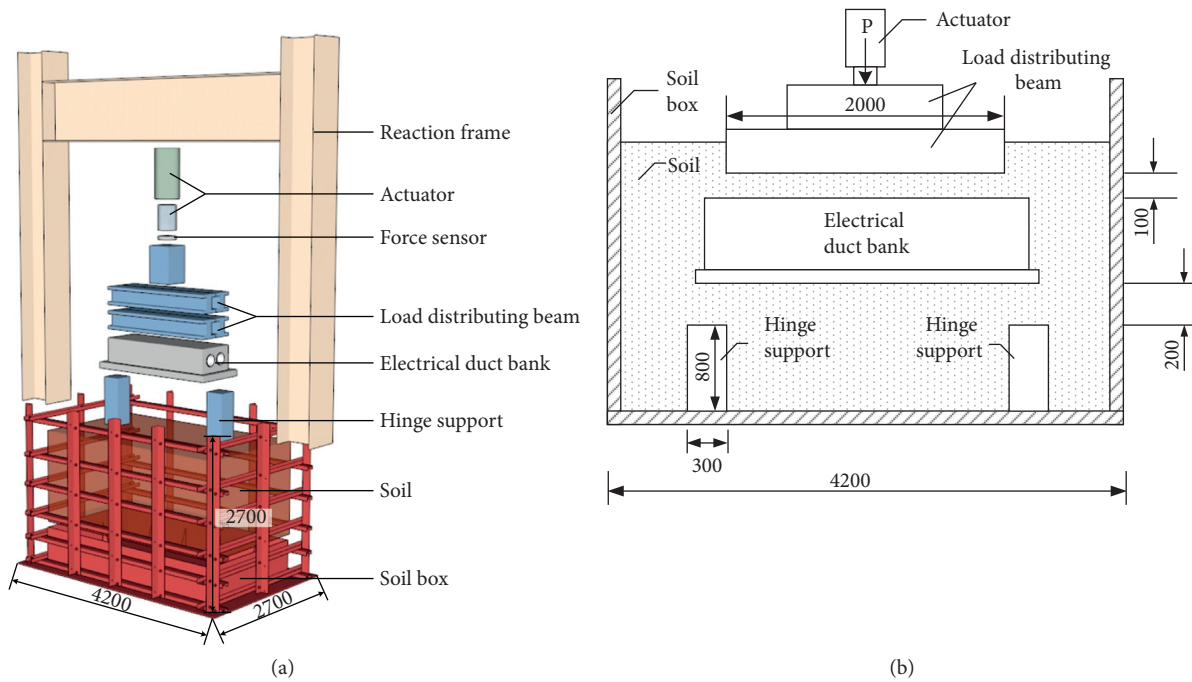
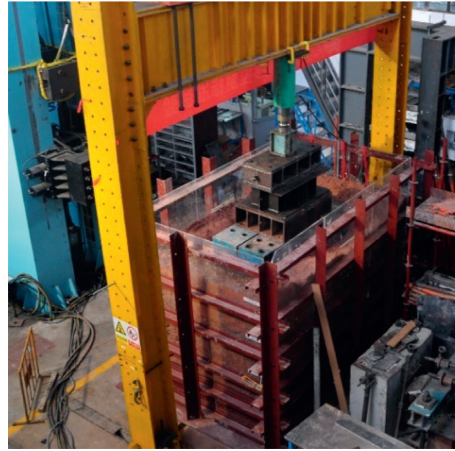


FIGURE 3: Continued.



(c)

FIGURE 3: Test setup details (millimeters).

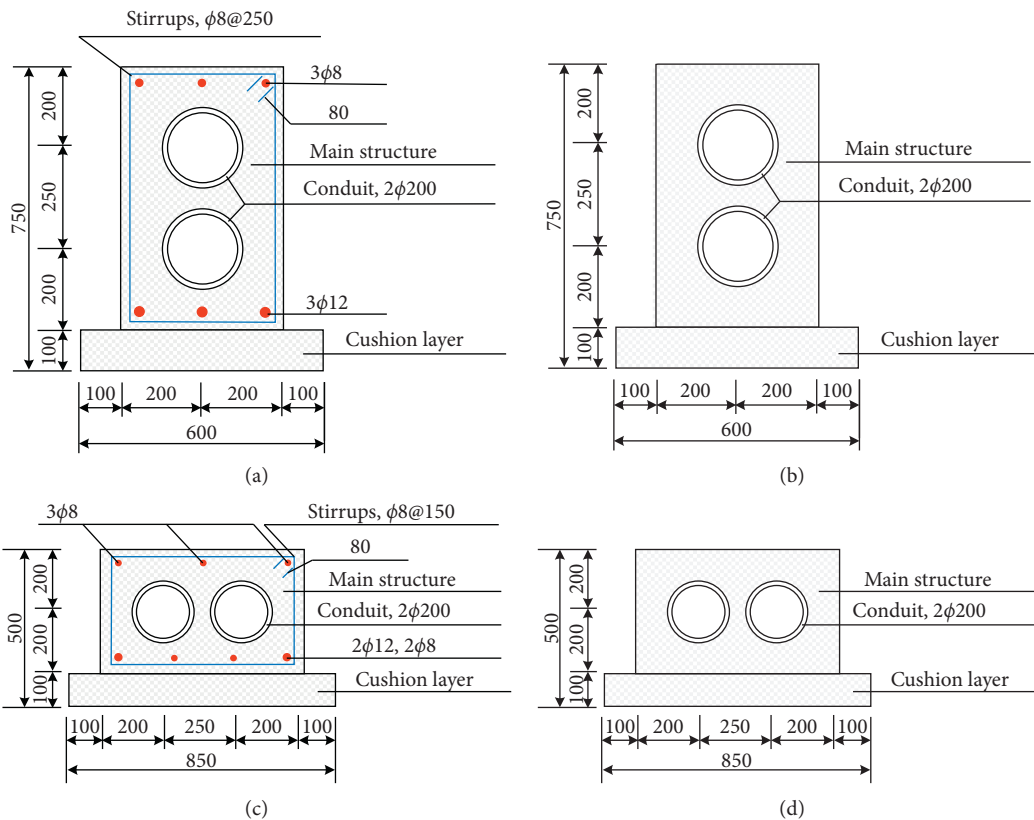


FIGURE 4: Test specimen arrangement (millimeters): (a) A1, (b) A2, (c) B1, and (d) B2.

geometric dimensions and reinforcement specifications for the specimens are shown in Table 2. For A-type specimens, the section height of the main structure was 650 mm, and the conduits were laid vertically, while B-type specimens were 400 mm, and the conduits were laid horizontally. Specimens A1 and B1 were reinforced, but there were no rebars in A2 and B2. The reinforcing rebars in specimens A1 and B1 were HRB335 with diameters of 8 mm and 12 mm. The stirrups for A1 and B1 were closed with 135° hooks on both ends. The compressive

strength values of concrete f_{ck} in the main structure and cushion layer were 21.2 MPa and 10.0 MPa, respectively; the tensile strength values f_{tk} were 2.43 MPa and 1.15 MPa; the elastic modulus values E_c were 25.5 GPa and 17.5 GPa. The yield strength values σ_y of HPB300 and HRB335 were 300 MPa and 335 MPa, respectively; the ultimate strength values σ_u of HPB300 and HRB335 were 420 MPa and 455 MPa, respectively; the elastic modulus values E_f were 200 GPa and 210 GPa. The HDPE conduits were made of high-density polyethylene

TABLE 2: Geometric dimensions and reinforcement specifications for specimens.

Specimen	B (mm)	H (mm)	D (mm)	Conduit layout	Longitudinal bars (HRB335)	Stirrups (HPB300)
A1	400	650	200	2×1	Top: $3\phi 8$ Bottom: $3\phi 12$	$\phi 8@250$
A2	400	650	200	2×1	0	0
B1	650	400	200	1×2	Top: $3\phi 8$ Bottom: $2\phi 12 \& 2\phi 8$	$\phi 8@150$
B2	650	400	200	1×2	0	0

Notes. B: section width of main structure; H: section height of main structure; D: diameter of conduit; $3\phi 8$: three 8 mm longitudinal bars; $\phi 8@150$: 150 mm distance between 8 mm stirrups.

(HDPE) with a 200 mm outside diameter and 10 mm thickness. The tension strength value f_{tp} was 18 MPa. The elastic modulus value E_p was 800 MPa. PVC spacers were set every 0.5 m along the longitudinal direction.

2.3. Monitoring System. Accurate monitoring technologies play an important role in physical experiments. In this study, the change in conduit diameter was a key factor. Thus, a conduit diameter-change measuring device was employed to measure the diameter change of the HDPE conduits, which could replicate the deformation behaviors inside the conduits. Figure 5 shows details of the conduit diameter-change measuring device.

The conduit diameter-change measuring device was provided with two round limit disks at both ends that matched the inner diameter of the measured conduits to ensure that there was no relative displacement between the measuring device and the measured conduits. Between the two limit disks, two fixed round disks with four displacement gauges installed orthogonally were used to measure the displacement change of the quarter-span and midspan of the measured conduits. To ensure the stability of the fixed round disks and the accuracy of the measuring points, the round disks and limit disks were connected in series on one steel rod. Thus, there was little relative slip or shedding between the device and the conduits.

In addition, there are other monitoring devices shown in Table 3. Soil pressure cells were used to record the soil pressure variation during the loading process. Strain gauges were used to measure the strain of the cover concrete, reinforcements, and HDPE conduits. Displacement gauges were used to measure the overall displacement of the specimens. The positions of the measuring points are shown in Figure 6. Note that the data of numbered measuring points were analyzed and those without numbers were either lost or unreasonable.

3. Results and Discussion

3.1. Damage Pattern. Figure 7 shows the load-displacement curve. Due to improper instrument operation, the load-displacement curve of specimen B1 was lost. As shown in Figure 7, the failure loads of specimens A1, A2, and B2 are 1275 kPa, 900 kPa, and 400 kPa, respectively. Specimen A1 contains the reinforcements, while A2 does not. Specimen A2 has a higher section height than specimen B2. Hence, it

can be concluded that the reinforcements and higher section height have an effect on improving the bending capacity and the section height may be a larger contributor than the reinforcements. After the failure load, a steep load drop appears in A1, but the load drops in A2 and B2 are gentle. In addition, the midspan deflections of A1, A2, and B2 are close within the range of 60 mm~80 mm. Although the bending capacity of the specimens differs greatly, their midspan deflections are close. Furthermore, a visible yield stage can be seen in A1, while no yield stage can be seen in A2. Thus, it can be speculated that the reinforcements cause the yield stage. The displacement of B2 shows an approximately linear increase without a yield stage, which means that B2 underwent brittle failure.

Figure 8 shows the damage patterns of the four specimens. The main cracks of specimens A2, B1, and B2 appear at the midspan, while the main crack of A1 is a diagonal crack that appears near the left hinge support. The main crack widths in the main structure of A1, A2, B1, and B2 are approximately 10 mm, 40 mm, 25 mm, and 20 mm, respectively. In addition, there are other secondary cracks. For specimen A1, there is one 4 mm diagonal crack near the left support and one 3 mm vertical crack at the midspan. For specimen A2, the main crack is split into one 10 mm crack and one 20 mm crack extending to the top of the main structure. For specimen B1, one 8 mm crack appears 180 mm to the left of the main crack. For specimen B2, the main crack is split into one 2 mm crack and one 10 mm crack extending to the top of the main structure. Furthermore, the concrete on the compression side is crushed in the A-type specimens, while no crushing is found in the B-type specimens. In summary, it can be seen that the damage pattern of specimens A2, B1, and B2 is similar to that of simply supported beams.

3.2. Soil Pressure. Figures 9(a) and 9(b) show the arrangement of measuring points. As shown in Figures 7 and 9(c), the curve of the 1/2-bottom soil pressure evolution is similar to the load-displacement curve. For example, when the load is 0~400 kPa, the displacement and soil pressure of A1 increase approximately linearly, after which a yield stage appears. This means that as the displacement increases, the soil is compacted, and then the soil pressure provided to the specimen is increased. Thus, the increase in displacement and soil pressure can be considered to occur almost simultaneously. As shown in Figure 9(c), the maximum 1/2-bottom soil pressures of the four specimens are close within

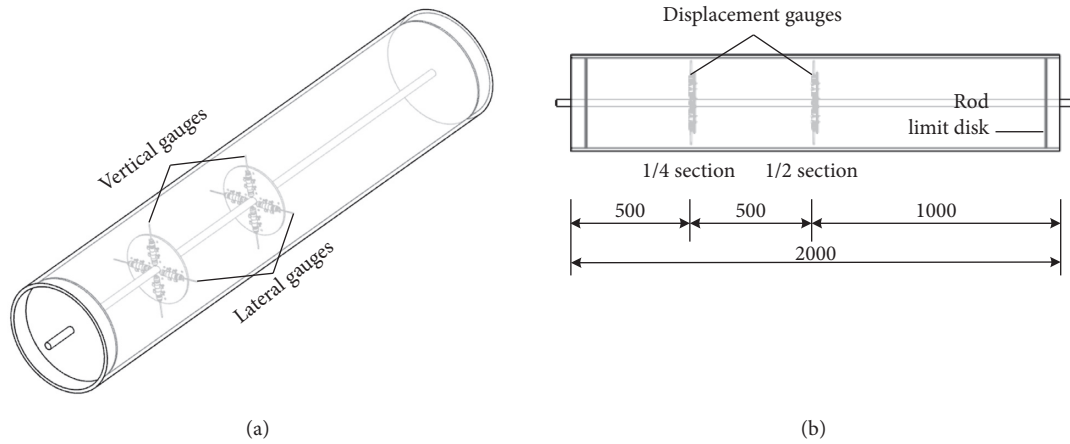


FIGURE 5: Conduit diameter-change measuring device. (a) Perspective drawing. (b) Elevation.

TABLE 3: Monitoring system.

Monitoring devices	Monitoring object	Precision
Strain gauges	Length change	≤1.0% FS
Soil pressure cells	Soil pressure in soil stratum	≤1.0% FS
Force sensor	Applied force	≤0.5% FS
Displacement gauges	Displacement of specimens	≤0.5% FS
Conduit diameter-change measuring device	Diameter change	≤0.5% FS

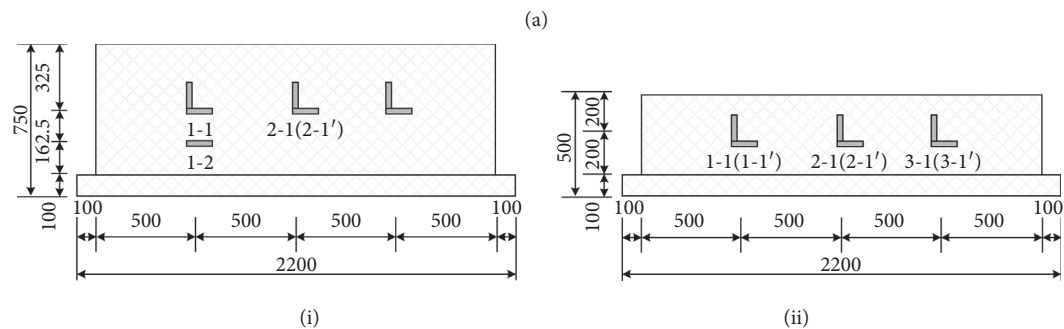
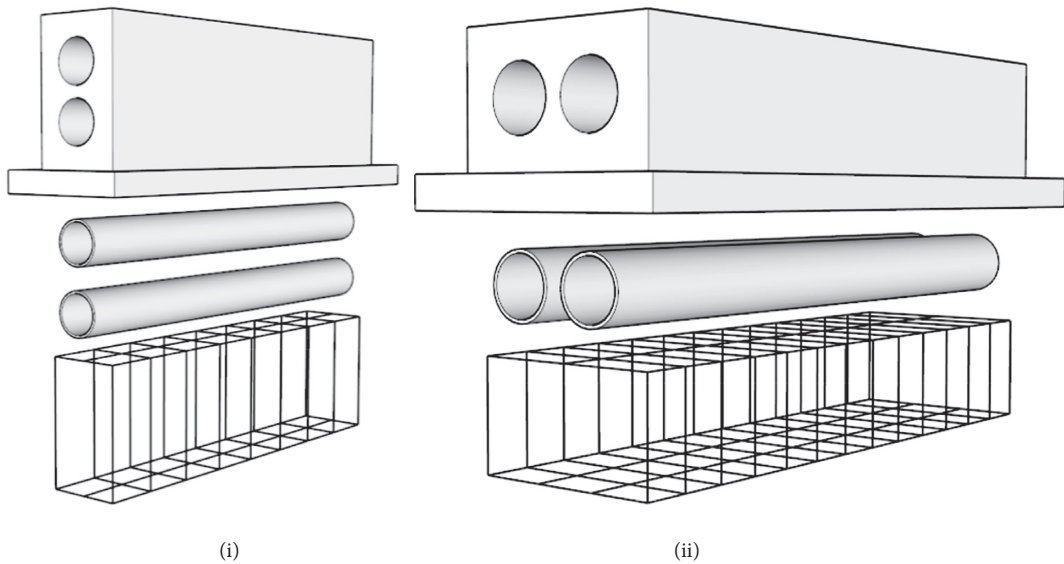


FIGURE 6: Continued.

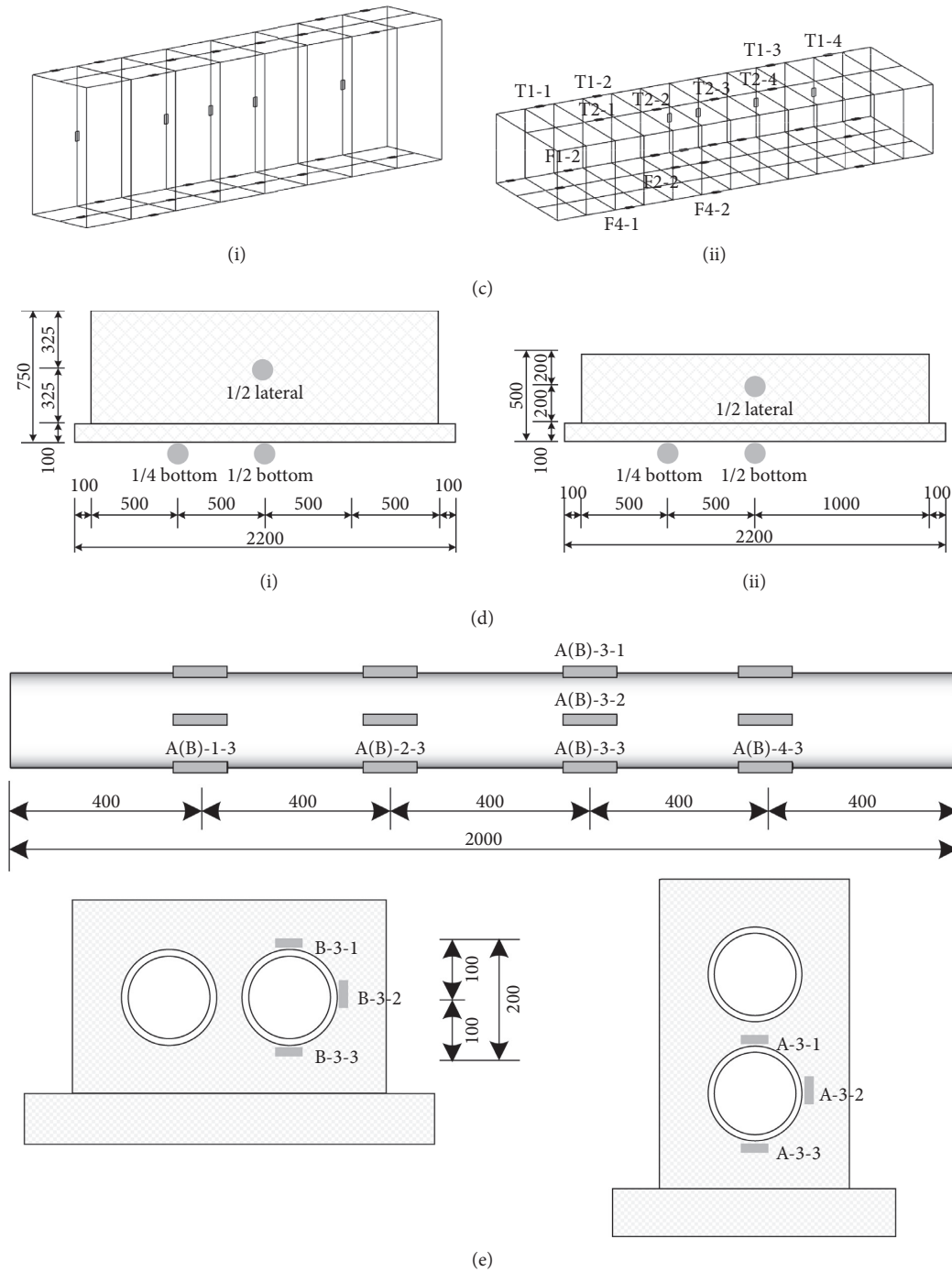


FIGURE 6: Specimen diagram and measurement points in the experiment (millimeters). (a) Specimen diagram: (i) A-type and (ii) B-type. (b) Cover concrete: (i) A-type and (ii) B-type. (c) Reinforcements: (i) A-type and (ii) B-type. (d) Soil pressure: (i) A-type and (ii) B-type. (e) HDPE conduits.

a range of 140 kPa ~ 160 kPa. Figure 9(d) shows that the maximum 1/4-bottom soil pressures of A1, A2, and B2 are within a range of 80 kPa ~ 130 kPa. The maximum of the 1/4-bottom soil pressure is less than that of the 1/2-bottom soil pressure. However, as shown in Figure 9(e), the maximum soil pressures at the 1/2 lateral side are approximately 10 kPa, which are much less than the maximum soil pressures at the bottom. The cause might be that the soil on the lateral side was not under proper compaction during the experiment.

3.3. Strain or Stress Analysis

3.3.1. Cover Concrete. As shown in Figure 10(a), measuring points A-1-1, A-2-1, and A-2-1' (' representing the back side) were arranged at a height of 1/2H, and A-1-2 was arranged at a height of 1/4H; A-1-1 and A-1-2 were arranged at a 1/4 span; A-2-1 and A-2-1' were arranged at a 1/2 span. Figure 10(b) shows the strain curve of the cover concrete. As shown in Figure 10(b), all the strains are tensile strains.

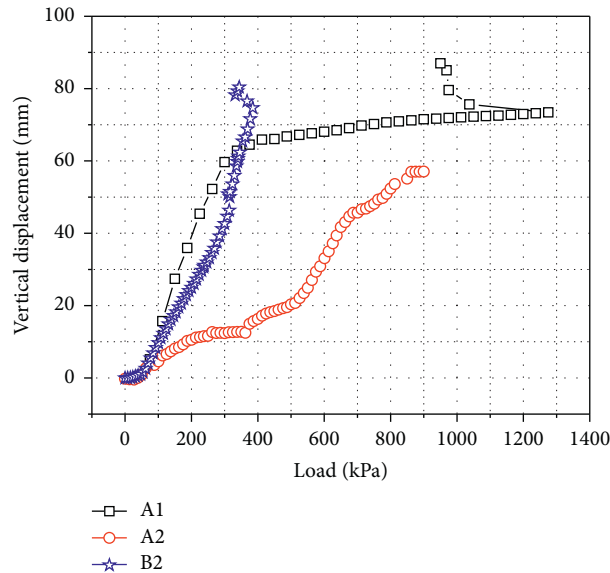


FIGURE 7: Load-displacement curve.

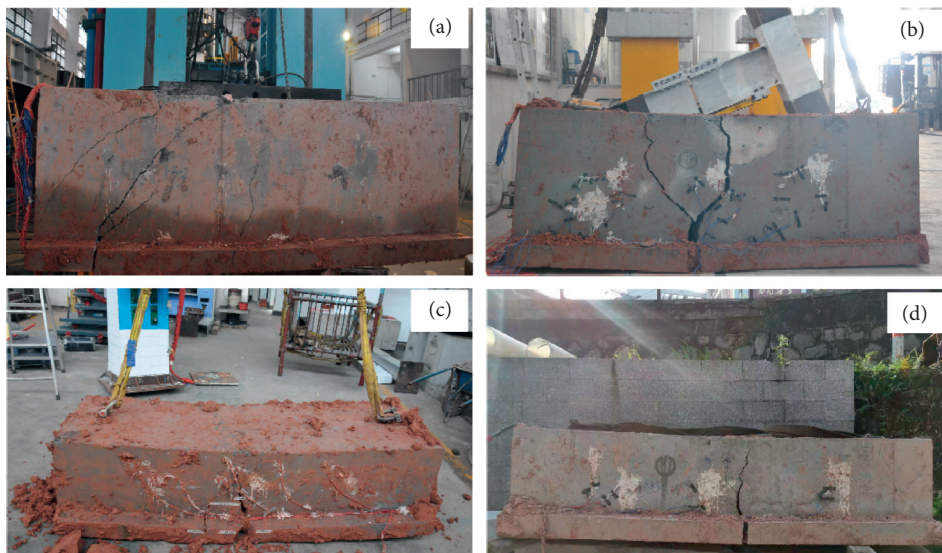


FIGURE 8: Damage patterns: (a) for A1, (b) for A2, (c) for B1, and (d) for B2.

When the load is less than 375 kPa, the strain barely increases. When the load exceeds 375 kPa, the strains of A-1-2, A-2-1, and A-2-1' are larger than the tensile cracking strain ($100 \mu\epsilon$), which means that cracks appear at $1/2 H$ of the $1/2$ span and $1/4 H$ of the $1/4$ span. When the load reaches 500 kPa, the strain of A-1-1 exceeds $100 \mu\epsilon$; hence, cracks appear at $1/2 H$ of the $1/4$ span. Thus, it can be inferred that cracks extend from $1/4 H$ to $1/2 H$ at the $1/4$ span when the load increases from 375 kPa to 500 kPa. In the meantime, the neutral axis moves upwards, and the crack width starts to grow after the strain exceeds $100 \mu\epsilon$. Furthermore, a visible inflection point appears in the four curves. The inflection points of A-2-1, A-2-1', A-1-2, and A-1-1 appear at loads of 375 kPa, 551 kPa, 701 kPa, and 763 kPa, which corresponds to the maximum crack width.

As shown in Figure 11(b), measuring points B-1-1, B-2-1', and B-3-1' (' representing the back side) are arranged at a height of $1/2 H$ at lengths of $1/4$ span, $1/2$ span, and $3/4$ span, respectively. As shown in Figure 11(a), when the load reaches 300 kPa, the tensile strain of B-1-1 reaches $100 \mu\epsilon$. When the load exceeds 400 kPa, the tensile strain of B-2-1' is larger than $100 \mu\epsilon$. Hence, it can be speculated that the cracks at the $1/4$ span and $1/2$ span appear at loads of 300 kPa and 400 kPa, respectively. The strain of B-3-1' is considered compressive strain during the experiment. Because the compressive strain of B-3-1' does not exceed the compressive cracking strain ($1470 \mu\epsilon$), there are no cracks at approximately $1/2 H$ of the $3/4$ span. The maximum crack widths of B-2-1' and B-1-1 appear at loads of 462 kPa and 504 kPa, respectively.

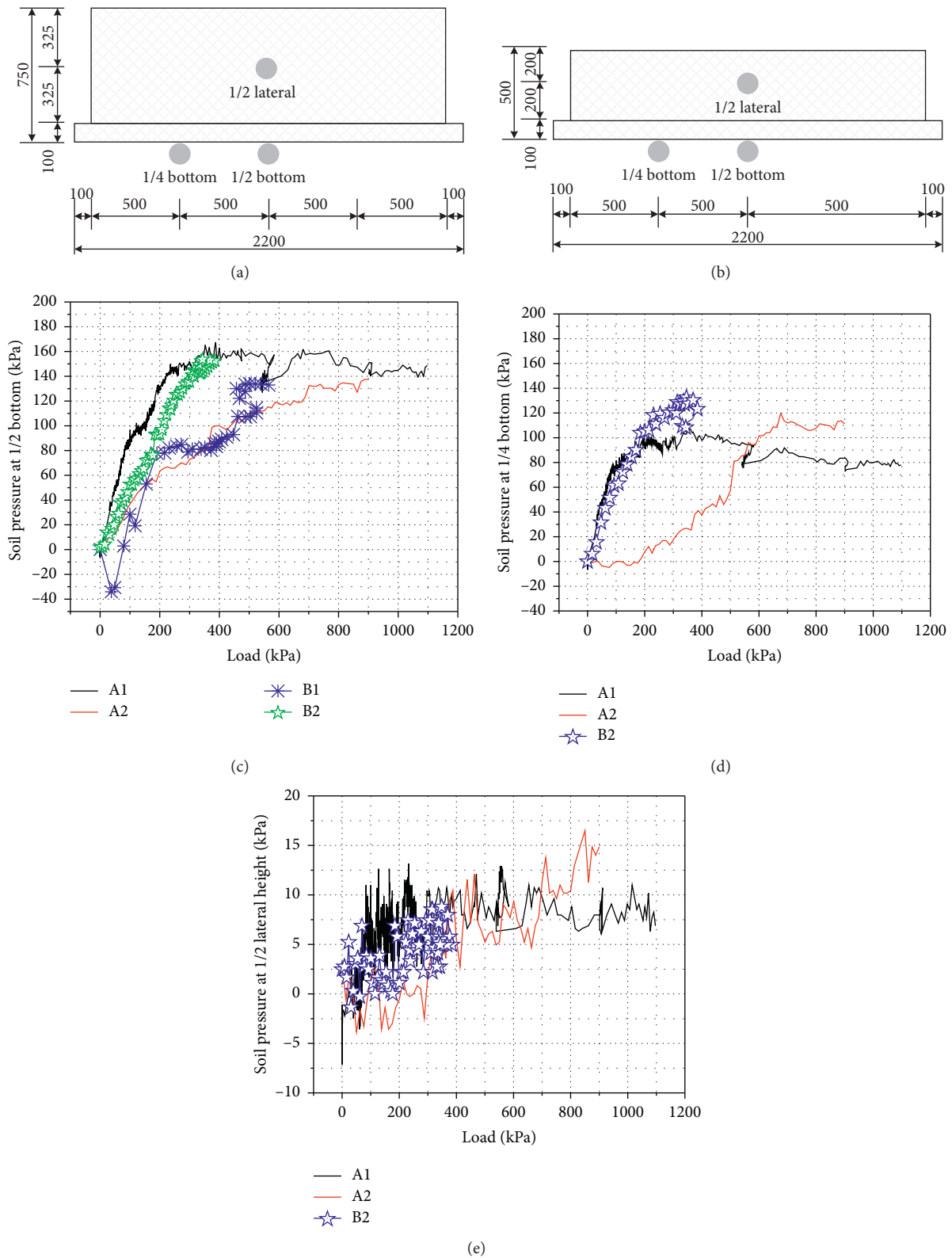


FIGURE 9: Soil pressure evolution. (a) A-type. (b) B-type. (c) 1/2 bottom. (d) 1/4 bottom. (e) 1/2 lateral.

3.3.2. Reinforcements. As shown in Figure 12(b), measuring points T1-1 ~ T1-4 and T2-1 ~ T2-4 are arranged on the top rebar of specimen B1. As shown in Figure 12(a), the stresses of the rebar increase linearly when the load is less than

400 kPa. When the load reaches 400 kPa, the compressive stress of T2-3 reaches its maximum, which is less than the yield stress of rebar (335 MPa). Thus, the top rebar T2 did not yield. When the load exceeds 400 kPa, the compressive

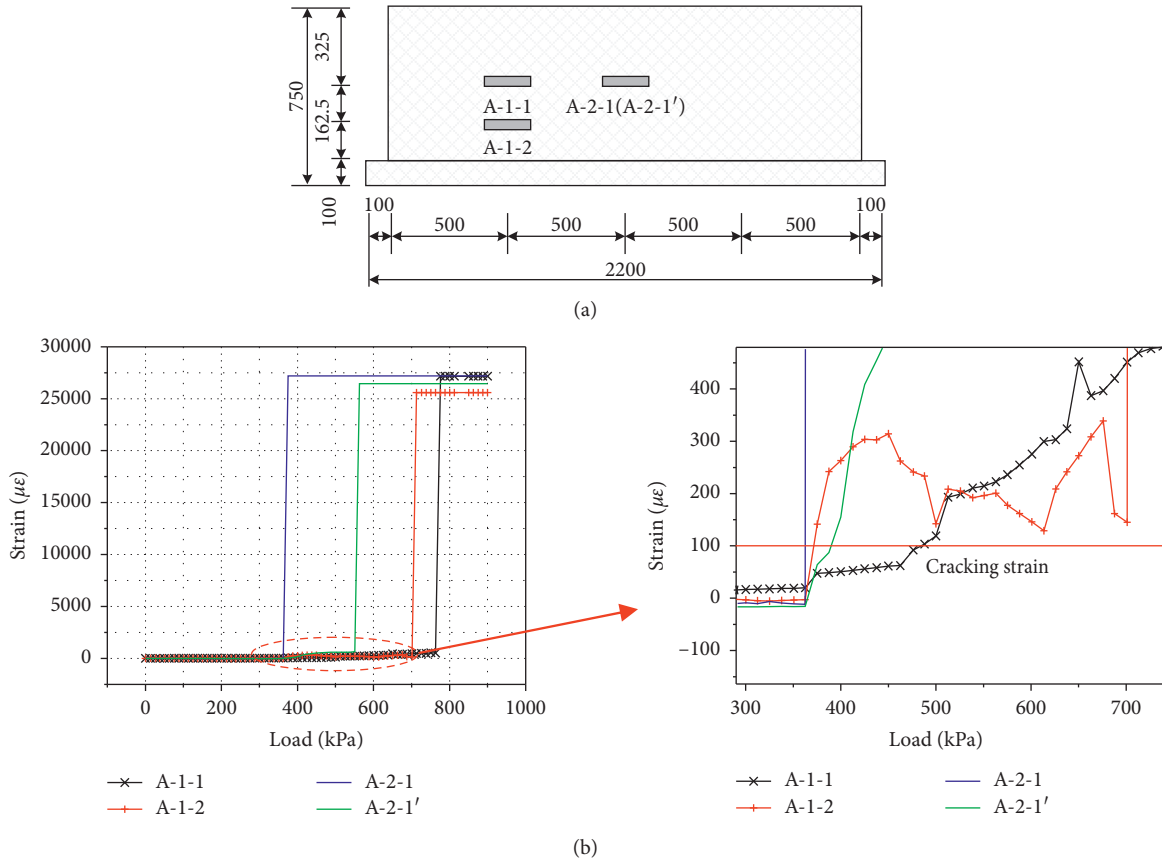


FIGURE 10: Strain evolution of A2. (a) Measuring points of cover concrete. (b) Load-strain curve.

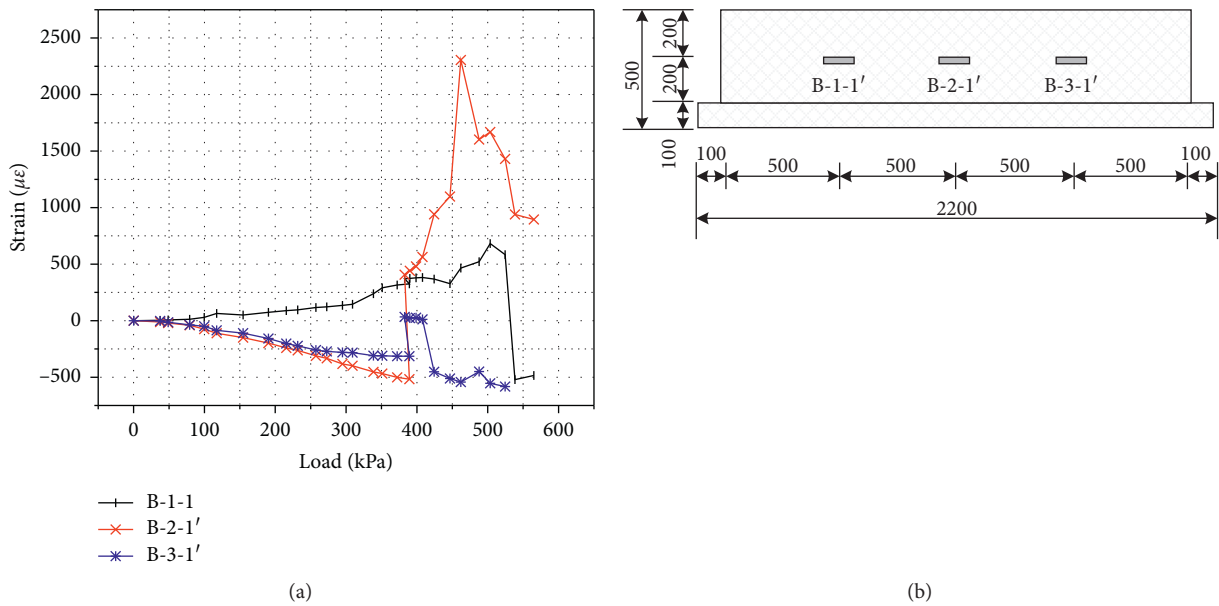


FIGURE 11: Strain evolution of B1. (a) Load-strain curve. (b) Measuring points of cover concrete.

stress starts to decrease. When the load approaches 525 kPa, the stress becomes tense. Then, the stress becomes larger than the yield stress at a load of 539 kPa, which means that the top rebar T2 yielded.

As shown in Figure 11(a) and 12(a), when the load is within a range of 0 ~ 400 kPa, the strain in the concrete and the stresses in the top rebar increase linearly. Cracks at the 1/2 span appear at a load of 400 kPa. Then, the neutral axis

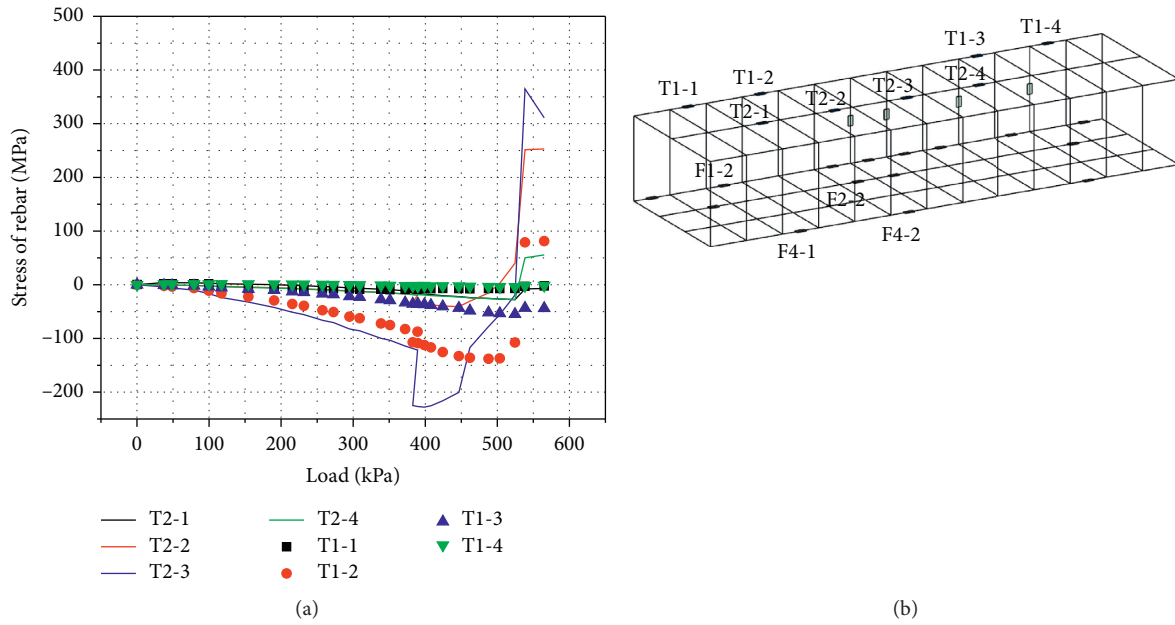


FIGURE 12: Stress evolution of B1. (a) Load-stress curve of top rebars. (b) Measuring points of rebars.

moves upwards. In the meantime, the crack width keeps growing. The maximum crack width of $1/2 H$ at the $1/4$ span and $1/2$ span appears at loads of 462 kPa and 504 kPa. It can be inferred that the concrete below $1/2 H$ of the midspan is out of work at 504 kPa. Then, a steep drop in strain appears. The cause of the steep drop may be the bonding failure between the strain gauges and cover concrete due to the development of cracks. When the load reaches 525 kPa, the neutral axis moves above the top rebars, and the stresses become tense. Then, the rebar T2 yields at a load of 539 kPa. Because the crack at midspan extends to the compression zone and the top rebars yield, 539 kPa can be considered the failure load.

As shown in Figure 12(b), measuring points F1-2, F2-2, F4-1, and F4-2 are arranged on the bottom rebar of specimen B1. When the load is less than 400 kPa, the stresses barely increase. When the load reaches 400 kPa, the tensile stress of F1-2 and F2-2 increases steeply, reaching the yield strength. This indicates that the bottom rebars yielded. In the meantime, a crack develops from the bottom to a height of $1/2$ at the midspan. Thus, it can be speculated that the failure mode is brittle because the bottom rebar yields in a short time and midspan cracks develop rapidly. At a failure load of 539 kPa, the stresses of F1-2 remain at 455 MPa, and the stresses of F2-2 exceed 455 MPa, which means that rebars F1 and F2 reached the ultimate strength.

As seen from the analysis in Sections 3.3.1 and 3.3.2, the bending behaviors of the concrete and reinforcements are similar to those of the simply supported beam.

3.3.3. HDPE Conduit. As shown in Figure 13(a), measuring points A (B)-3-1, A (B)-3-2, and A (B)-3-3 are arranged on the same transverse section; B-1-3, B-2-3, B-3-3, and B-4-3

are arranged on the same profile. As shown in Figure 13(b), when the load is less than 300 kPa, the stresses barely increase. When the load exceeds 300 kPa, the stresses start to increase linearly. Then, the stresses of A2 and B2 undergo a sharp increase at loads of 500 kPa and 350 kPa, respectively, exceeding the tensile strength of the conduit (18 MPa). As shown in Figure 13(c), when the load exceeds 400 kPa, the stresses start to increase linearly. Similarly, the stress of B1 exceeds the tensile strength at a load of 525 kPa. The three curves have the same evolution trend, which is similar to that of the bottom rebar F1 given in Figure 14.

As shown in Figures 13(c) and 14, rebar F1 yields at a load of 400 kPa, and, at the same time, the stress of the conduit starts to increase. As shown in Figures 13(c) and 12(a), the stress of the conduit exceeds the tensile strength at a load of 525 kPa, and rebar T2 exceeds the yield strength at a load of 539 kPa. During the upward movement of the neutral axis, the stresses of rebar F1, the HDPE conduit, and rebar T2 exceed their designed tensile strengths. Thus, it can be inferred that HDPE conduits serve as the rebars during the experiment. Moreover, the stresses of different measuring points on the same conduit are close.

3.4. Vertical Deformation of HDPE Conduits. When a vertical load is applied to the specimen, the HDPE conduits are compressed vertically and stretched horizontally. Because the vertical compressive deformation may affect the cable inside the conduits and the horizontal tensile deformation has little effect on the cable, the vertical deformation should be studied. To describe the deformation of HDPE conduits, the deformation rate of the conduit vertical diameter is introduced [21]:

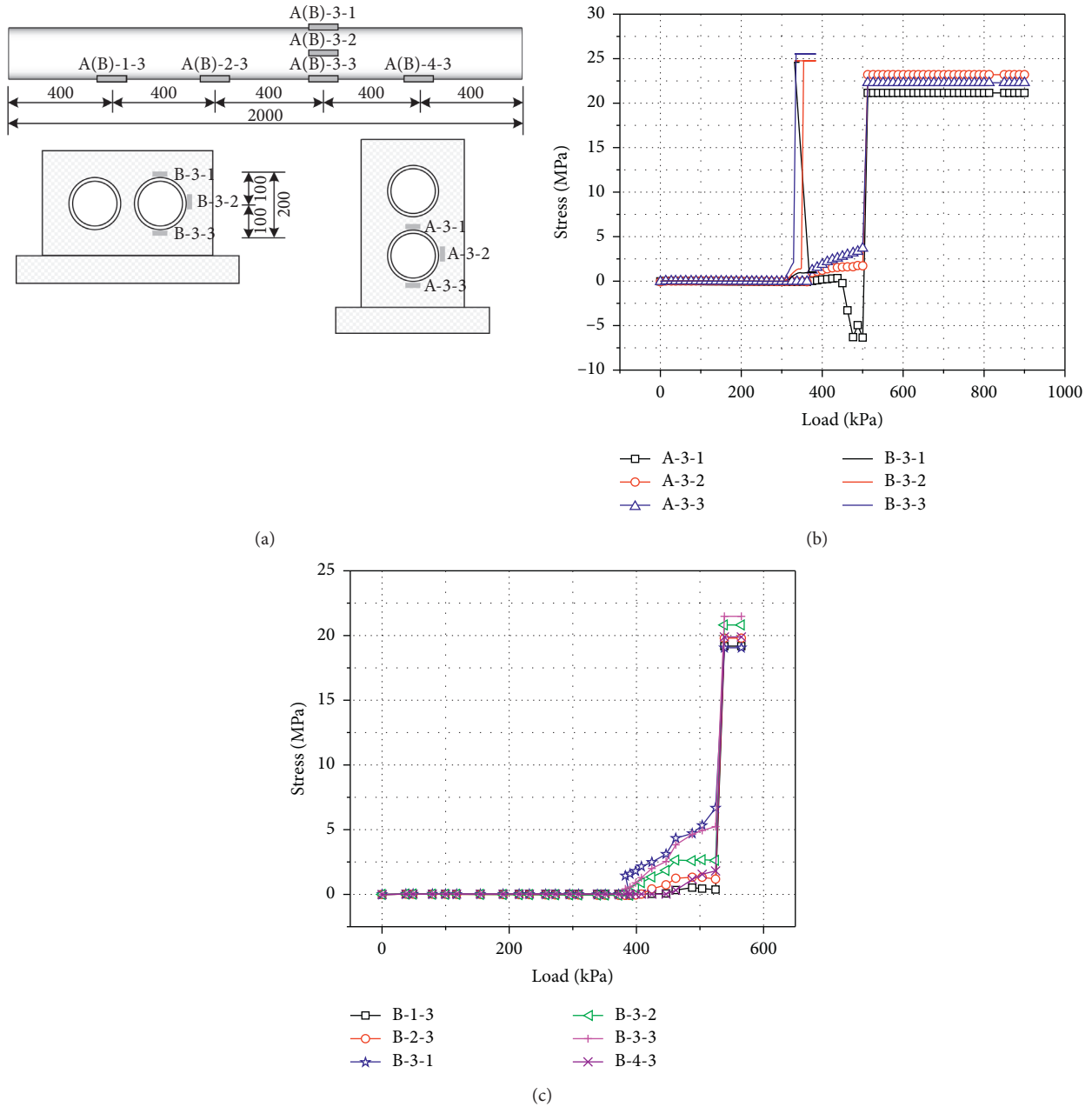


FIGURE 13: Stress evolution of HDPE conduits. (a) Measuring points of HDPE conduits. (b) Load-stress curve of A2 and B2. (c) Load-stress curve of B1.

$$\varepsilon = \frac{W_{d,max}}{D} \times 100\% \quad (1)$$

$W_{d,max}$: maximum deformation of the conduit vertical diameter

D : outer diameter of conduit

ε : deformation rate of conduit vertical diameter

As shown in Figure 15(a), the measuring points are arranged on a 1/2 section and 1/4 section of the conduit. As

shown in Figure 15(b), the compressive deformation of A1 and B1 at the midpoint exceeds 10 mm (5% conduit diameter), while B2 is below 5%; the compressive deformation of A1 exceeds 15 mm (7.5% conduit diameter), while B1 is below 7.5%. Moreover, a visible yield stage appears in the A-type specimens. As shown in Figure 15(c), the deformation rates of A1 (bottom conduit) and A2 (both conduits) are larger than 7.5%; the compressive deformation of A2 (bottom conduit) reaches 30 mm (15% of conduit diameter). Thus, it can be concluded that the deformation rate of A2 is larger than that of A1. For A-type specimens, the

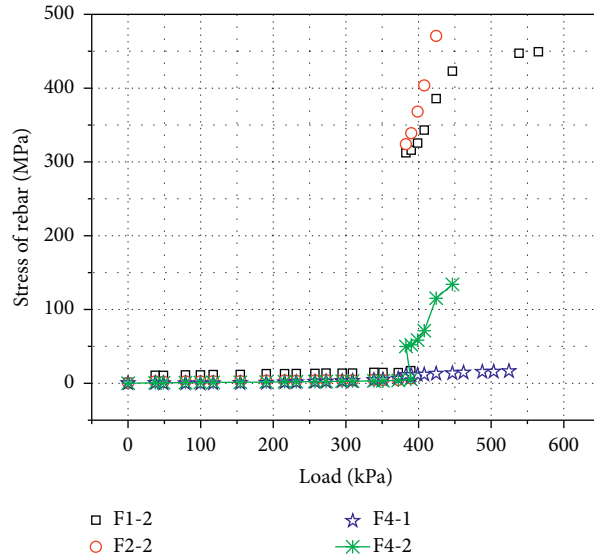


FIGURE 14: Load-stress curve of bottom rebars.

deformation rate of the bottom conduit is larger than that of the top conduit, which corresponds to the typical characteristics of bending specimens. The reason may be that the bottom conduit carries a larger bending moment and reaches the tensile strength earlier.

4. Discussion

4.1. Bending Capacity. The analysis in Section 3 shows that the bending characteristics of electrical duct banks are similar to those of simply supported beams. This section will discuss the bending capacity of the specimens during the experiment. First, HDPE conduits have a positive effect on improving the bending capacity of specimens, which can be found in Section 3.3.3. Hence, from the perspective of safety, the contribution of HDPE conduits can be neglected in the calculation of the bending capacity. The code [22] for the design of concrete structures in China gives the formulas for the design of the bending capacity of a normal section with holes. Thus, the bending capacity of the normal section of the concrete cable duct can be calculated according to the formulas in the code.

4.1.1. Conversion of Cross Section. The cross section of the concrete cable duct can be converted into an I-shaped cross section regardless of the cushion layer. As shown in Table 2, B, H, and D represent the width of the cross section, the height of the cross section, and the diameter of the HDPE conduits, respectively. As shown in Figure 16, by the rule of equal area and moment of inertia, the round hole can be converted into a rectangular hole. The dimensions of the I-shaped section can be calculated by the following formulas. Table 4 shows the result:

$$h_r = \frac{\sqrt{3}}{2} D, \tag{2}$$

$$b_r = \frac{\sqrt{3}\pi}{6} D,$$

$$b_f = B,$$

$$h = H,$$

$$h_f = e - 0.5h_r, \tag{3}$$

$$b = b_f - nb_r,$$

$$h_w = h - 2h_f.$$

4.1.2. Theoretical Calculation. For the calculation of the I-shaped section, the code gives the solution. First, determine whether the height of the compression zone is within the flange by the following formulas:

$$F_s = f_y A_s, \tag{4}$$

$$F_c = \alpha_1 f_c b_j' h_j',$$

$$F_s < F_c. \tag{5}$$

For A1 and B1.

Hence, the compression zones of A1 and B1 are within the flange. Second, the bending capacity of the I-shaped section is calculated by the following formula. Table 5 shows the result. The theoretical bending capacities of A1 and B1 are 195.8 kPa and 67.7 kPa, respectively:

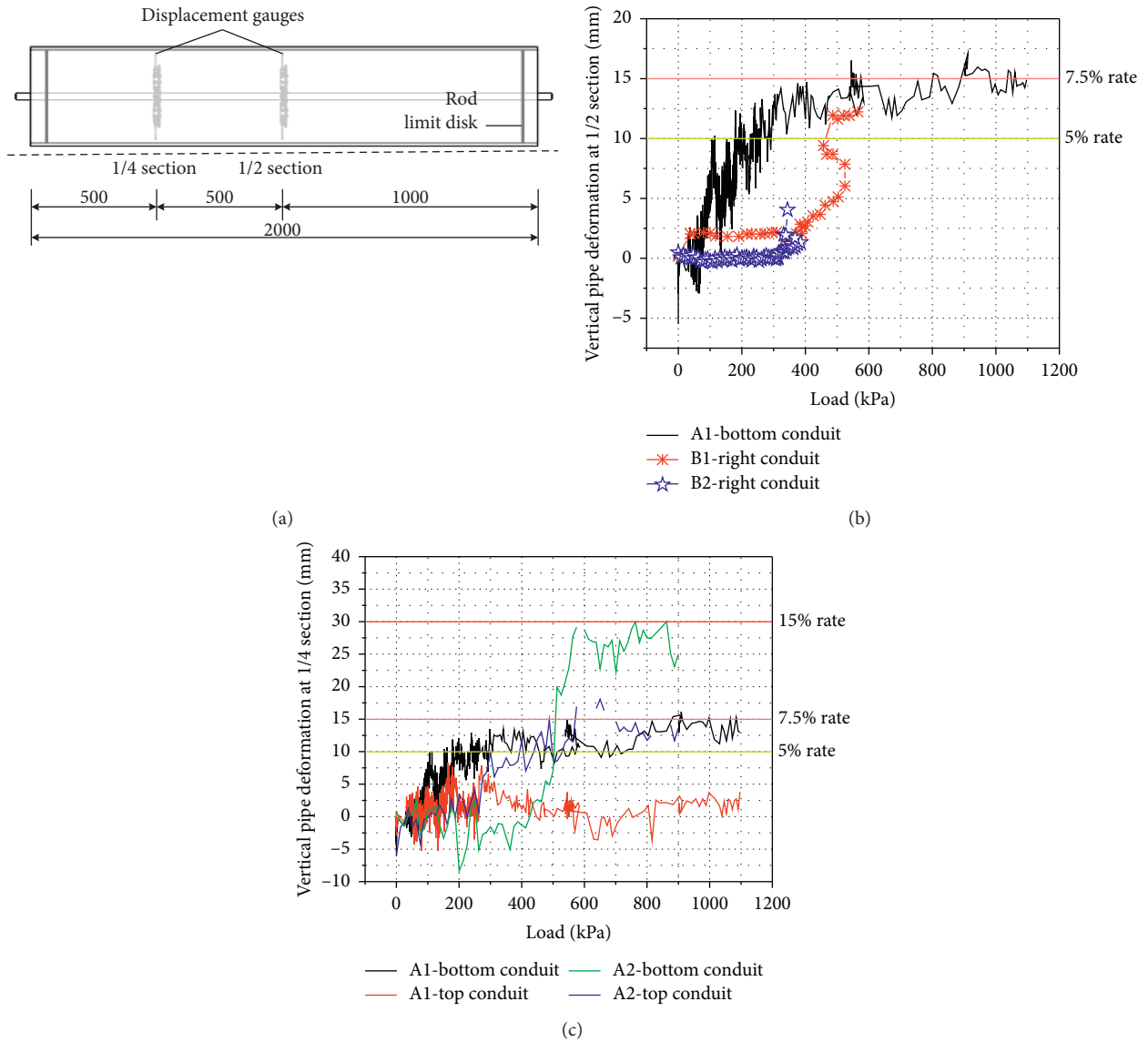


FIGURE 15: Vertical deformation of HDPE conduits. (a) Measuring points of HDPE conduits: (b) 1/2 section and (c) 1/4 section.

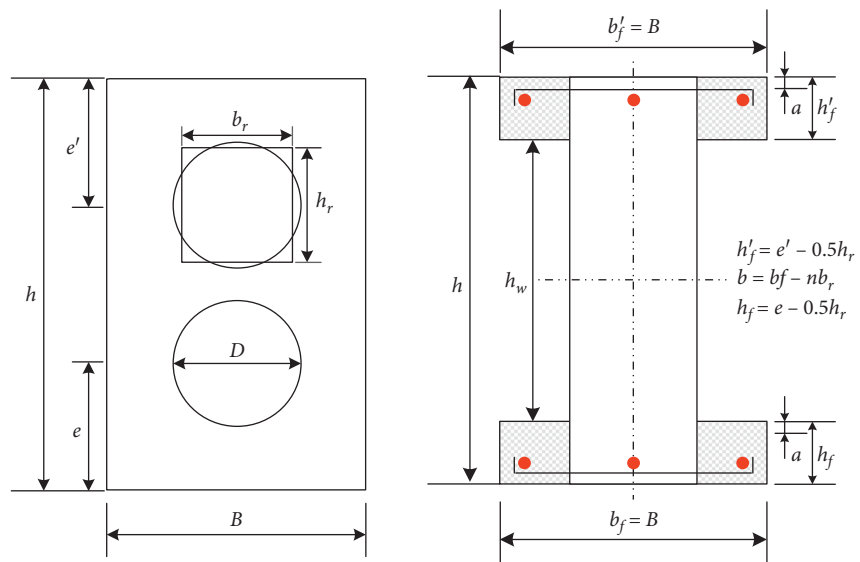


FIGURE 16: Equivalent I-shaped cross section of the concrete cable duct.

TABLE 4: Dimensions of I-shaped section (millimeters).

Specimen	n	h_r	b_r	b_f	h	e	h_f	b	h_w
A1	2	181.3	173.2	400	650	200	113.4	218.7	423.2
B1	1	181.3	173.2	650	400	200	113.4	287.4	173.2

Notes. n : number of conduits along the height; h_r : height of equivalent rectangle; b_r : width of equivalent rectangle; b_f : width of flange; h : height of cross section; e : distance between the center of hole and the lower edge; h_f : height of lower flange; b : width of web; h_w : height of web.

$$\begin{aligned}
 h_0 &= H - a_s, \\
 x &= \frac{f_y A_s}{\alpha_1 f_c b_f}, \\
 M_u &= f_y A_s \left(h_0 - \frac{x}{2} \right), \\
 P &= \frac{4M_u}{AL}.
 \end{aligned} \tag{6}$$

4.1.3. Comparison. The bending capacities of A1 and B1 in the experiment are 1275 kPa and 450 kPa, respectively. However, the theoretical bending capacities of A1 and B1 are 195.8 kPa and 67.7 kPa, respectively, which are much lower than the experimental values. There may be two reasons for this result. The first reason may be that the contribution of HDPE conduits to the bending capacity of the specimens is not taken into consideration. The second reason may be that the soil shared part of the upper load, and the subgrade reaction increased during the compaction of the soil, which indirectly improved the bending capacity of the specimens.

4.2. Allowable Deformation Rate of Conduit Vertical Diameter. Because there is no code for the concrete cable duct given the regulations for the deformation of HDPE conduits, the code [21] for the polyethylene drainage pipe is taken as the reference. The HDPE conduits are made of HPDE, which is the same as the drainage pipes. The drainage pipes are steel-reinforced, spiral-wound, and buried underground, while the HDPE conduits of the cable duct banks are covered by reinforced concrete. Furthermore, the minimum burial depths of the HDPE conduits and the drainage pipes are 0.9 m and 0.7 m, respectively. Therefore, it can be inferred that the HDPE conduits are under better protection.

Considering the factors mentioned above, it is reasonable to set a relatively larger allowable deformation rate for the HDPE conduits. The code [21] gives 5% as the allowable deformation rate. The analysis in Section 3.4 shows that 5%, 7.5%, and 15% are typical deformation rates for HDPE conduits. The analysis in Sections 3.3.1 and 3.4 shows that when the deformation rates of A-type bottom conduits reach 5%, cracks start to appear on the cover concrete; when the rate exceeds 7.5%, A-type specimens approach the failure

load. Moreover, the deformation rate of the bottom conduit is larger than that of the top conduit.

4.3. Suggestions for Monitoring Indexes and Control Standards. Several suggestions for the monitoring indexes and control standards can be obtained from the analysis above.

- (1) By the analysis in Sections 3.1 and 3.2, the midspan deflections of A1, A2, and B2 are within a range of 60 mm ~ 80 mm, and the soil pressure at the midspan bottom of the four specimens is within a range of 140 kPa ~ 160 kPa. The soil conditions are consistent throughout the experiment. It can be inferred that reinforcements and section height have little effect on the midspan deflection and the soil pressure. Furthermore, the soil condition may be the key factor. Therefore, the soil condition should be considered in the monitoring indexes.
- (2) The behaviors of the damage pattern are as follows: a small number of cracks appear on the cover concrete, and one main crack appears at the midspan, which is similar to that of the simply supported beams; a steep increase appears in the strain of the cover concrete and the stress of the steel bars and conduits. In conclusion, the damage pattern may be considered brittle damage. However, yield stages appear in the load-displacement curve and soil pressure evolution curve, which corresponds to ductile damage. The reason may be that the compaction of soil is a relatively long process. Thus, electrical duct banks should be monitored continuously, and it is recommended to take the relative magnitudes and the evolution trends as the control standards rather than the absolute magnitudes of evolution.
- (3) The analysis in Section 3.3.3 shows that HDPE conduits serve as rebars with respect to the cover concrete and that the stresses of different measuring points on the same conduit are close. Furthermore, the stresses of the conduits on the same row are close. Therefore, measuring points should be arranged on a certain conduit of each row. In practical applications, at least one conduit in each row should be reserved for monitoring according to the on-site situation.
- (4) Generally, the space required for high-voltage cables with an outer diameter of 110 mm is 1.5 times the outer diameter, which is 165 mm. However, the inner diameter of the conduit is 180 mm. Thus, for the normal operation of high-voltage cables, the allowable deformation of the conduit cannot exceed 15 mm, which is 7.5% of the outer diameter. Considering the above analysis and the analysis in Section 4.2, 5% and 7.5% can be taken as the deformation rates of the ultimate states of serviceability and bearing capacity, respectively.

TABLE 5: Parameters in formula (6).

Specimen	A_s (mm ²)	α_1	x (mm)	h_0 (mm)	M_u (kN·m)	A (m ²)	L (m)	P (kPa)
A1	339	1.0	28.1	600	66.5	0.8	1.7	195.8
B1	327	1.0	16.7	350	37.4	1.3	1.7	67.7

Notes. A_s : area of tension bars; α_1 : ratio of the magnitude of concrete rectangular stress diagram in compression zone to the design value of concrete axial compressive strength; x : height of compression zone; h_0 : effective height; M_u : bending capacity of normal section; A : area of top surface; L : distance between two hinge supports; P : theoretical bending capacity of specimens.

Furthermore, the deformation rate of the bottom conduit is larger than that of the top conduit. Hence, measuring points should be arranged on the conduits of the bottom row in practical applications.

- (5) For shield tunnels, the longitudinal deformation is generally described by the curvature radius. Because the structures of the underground electrical duct banks and the shield tunnels are similar in the longitudinal direction, the longitudinal deformation of the underground electrical duct bank can be described by the curvature radius. However, an underground electrical duct bank is generally a cast-in-place reinforced concrete structure without joints, and its damage pattern is brittle, which is different from that of a shield tunnel. Therefore, it is recommended to take 20 mm of the midspan deflection as the threshold. With respect to the 20 mm midspan deflection, the curvature radius R is 18063 m. In summary, $R_{min} = 18000$ m can be taken as the threshold of the longitudinal curvature radius for an underground electrical duct bank.

From the perspective of safety and convenience, it is recommended to use the stress and deformation rate of HDPE conduits to formulate the monitoring indexes and control standards for electrical duct banks.

5. Conclusion

This paper presented an experimental investigation of the bending behaviors of concrete-encased underground electrical duct banks. This study is aimed at determining a set of thresholds for electrical duct banks. The experimental study was realized in a soil box using an advanced monitoring device, which can measure the diameter change of HDPE conduits. In addition, the HDPE conduit played a critical role in the improvement of the bending capacity of the electrical duct bank. Experiments were conducted on four specimens: two A-type specimens ($H = 650$ mm) and two B-type specimens ($H = 400$ mm). Based on this study, the following conclusions can be drawn:

- Reinforcements and section height have little effect on the midspan deflection and the soil pressure. The soil condition should be considered in the monitoring indexes.
- HDPE conduits and underlying soil have a positive effect on improving the bending capacity of electrical duct banks.

- The damage pattern of an electrical duct bank is brittle damage. Electrical duct banks should be monitored continuously, and it is recommended to take the relative magnitudes and evolution trends as the control standard.
- Measuring points of stress and deformation rates of HDPE conduits should be arranged on each row and the bottom row, respectively.
- Deformation rates of 5% and 7.5% can be taken as the thresholds for HDPE conduits with respect to the serviceability ultimate state and the bearing capacity ultimate state, respectively.
- $R_{min} = 18000$ m can be taken as the threshold of the longitudinal curvature radius for the underground electrical duct bank.

In conclusion, it is recommended to use the stress and deformation rate of HDPE conduits to formulate monitoring indexes and control standards for electrical duct banks.

To quantify the contribution of the HDPE conduits and the subgrade reaction to the bending capacity of the specimens, three experiments are designed:

- Specimens A1 and B1 are simply supported, and a distributed surface load is monotonically applied.
- Specimens without HDPE conduits are monotonically subjected to a distributed surface load under the same soil conditions as the experiment mentioned above.
- Specimens A1 and B1 apply a distributed surface load monotonically under different soil conditions.

Furthermore, the authors will carry out studies on the influence of cyclic or vibration loadings (triggered by driving or earthquakes, etc.) on mechanical behavior in future research.

Data Availability

The data used to support the findings of this study are included within the article.

Conflicts of Interest

The authors declare that there are no conflicts of interest regarding the publication of this paper.

Acknowledgments






This work was funded by the National Natural Science Foundation of China (nos. 51678248, 51878296, and 51808230) and the Technical Projects of China Southern Power Grid (no. GD-KJXM-20172975).

References

- [1] U. K. National Grid, "New essential infrastructure: london power tunnels," 2018, <https://www.nationalgridet.com/infrastructure-projects/london-power-tunnels>.
- [2] National Grid UK. Technical Guidance Note 287, Third-party guidance for working near National Grid Electricity Transmission equipment.
- [3] J. Yu and Y. Zhou, "Genetic algorithm for reasonable laying length of power cable piping," *East China Electric Power*, vol. 40, no. 5, pp. 861–863, 2012, in Chinese.
- [4] W.-C. Cheng, G. Li, N. Liu, J. Xu, and S. Horpibulsuk, "Recent massive incidents for subway construction in soft alluvial deposits of Taiwan: a review," *Tunnelling and Underground Space Technology*, vol. 96, Article ID 103178, 2020.
- [5] K. Wu and Z. Shao, "Visco-elastic analysis on the effect of flexible layer on mechanical behavior of tunnels," *International Journal of Applied Mechanics*, vol. 11, no. 3, Article ID 1950027, 2019.
- [6] L. J. Kelly, "Cable ampacity practice for low voltage and medium voltage power cables," in *Proceedings of the IEEE Textile Industry Technical Conference IEEE*, Greenville, SC, USA, May 1988.
- [7] D. Nagley and R. Nease, "Thermal characteristics of two types of concrete conduit installations," *IEEE Transactions on Power Apparatus and Systems*, vol. PAS-86, no. 9, pp. 1117–1124, 1967.
- [8] M. Kellow, "A numerical procedure for the calculation of the temperature rise and ampacity of underground cables," *IEEE Transactions on Power Apparatus and Systems*, vol. PAS-100, no. 7, pp. 3322–3330, 1981.
- [9] M. Kellow, H. St-Onge, and R. Mier-Maza, "Thermal behaviour of an underground duct bank cable system under normal and forced cooling conditions," in *Underground Cable Thermal Backfill*, pp. 192–205, Pergamon Press, Oxford, UK, 1982.
- [10] M. Kellow, "Experimental investigation of the ampacity of distribution cables in a duct bank with and without forced cooling," *IEEE Transactions On Power Apparatus & Systems*, vol. PAS-100, no. 7, pp. 3274–3283, 2007.
- [11] M. El-Kady and D. Horrocks, "Extended values for geometric factor of external thermal resistance of cables in duct banks," *IEEE Transactions on Power Apparatus & Systems*, vol. PER-104, no. 8, pp. 1958–1962, 1988.
- [12] E. Bascom, "Magnetic field management considerations for underground cable duct bank," in *Proceedings of the Transmission & Distribution Conference & Exhibition IEEE*, Atlanta, Georgia, May 2006.
- [13] C. C. Hwang, "Calculation of thermal fields of underground cable systems with consideration of structural steels constructed in a duct bank," *IEE Proceedings-Generation, Transmission and Distribution*, vol. 144, no. 6, pp. 541–545, 2002.
- [14] B. Malmedal, C. Bates, D. Cain et al., "Engineering the thermal resistivity of concrete duct banks," in *Proceedings of the Cement Industry Conference IEEE*, Dallas, TX, USA, May 2015.
- [15] Z. D. Abootorabi and V. Behrooz, "Multi objective self adaptive optimization method to maximize ampacity and minimize cost of underground cables," *Journal of Computational Design & Engineering*, vol. 5, no. 4, pp. 401–408, 2018.
- [16] P. Ocoń, P. Cisek, and M. Rerak, "Thermal performance optimization of the underground power cable system by using a modified Jaya algorithm," *International Journal of Thermal Sciences*, vol. 123, pp. 162–180, 2018.
- [17] K. Charendeek, R. Chatthaworn, P. Khunkitti, A. Kruesubthaworn, A. Siritaratiwat, and C. Surawanitkun, "Effect of concrete duct bank dimension with thermal properties of concrete on sensitivity of underground power cable ampacity," in *Proceedings of the 18th International Symposium on Communications and Information Technologies (ISCIT)*, Bangkok, Thailand, September 2018.
- [18] C. Liu and J. Ying, "Experimental study on flexural performance of concrete cable duct reinforced with glass fiber reinforced polymer bars," *Fuhe Cailiao Xuebao/Acta Materiae Compositae Sinica*, vol. 35, no. 1, pp. 70–80, 2018.
- [19] C. Liu, J. Wang, Y. Chen et al., "Shear bearing capacity of concrete cable duct reinforced with GFRP bars," *Fuhe Cailiao Xuebao/Acta Materiae Compositae Sinica*, vol. 35, no. 12, pp. 3331–3341, 2018.
- [20] Y. Wang and J. Guo, "Settlement and damage analysis of working shaft for underground high-voltage electricity cables," *IOP Conference Series Earth and Environmental Ence*, vol. 304, Article ID 32063, 2019.
- [21] China Association for Engineering Construction Standardization, *Technical Specification for Steel-Reinforced Spirally Wound Polyethylene of Drainage Pipeline Engineering (CECS 248:2008)*, China Planning Press, Beijing, China, 2008, in Chinese.
- [22] Ministry of Construction of the People's Republic of China, *Code for Design of Concrete Structures (GB 50010-2010)*, China Architecture & Building Press, Beijing, China, 2010, in Chinese.

Research Article

Construction Sequence Optimization and Settlement Control Countermeasures of Metro Tunnels Underpassing Expressway

Chengzhong Zhang ^{1,2}, Qiang Zhang ^{1,2}, Ziming Pei ^{1,2}, Zhanping Song ^{1,2}
and Junbao Wang ^{1,2}

¹School of Civil Engineering, Xi'an University of Architecture and Technology, Xi'an, Shaanxi 710055, China

²Shaanxi Key Laboratory of Geotechnical and Underground Space Engineering, Xi'an, Shaanxi 710055, China

Correspondence should be addressed to Qiang Zhang; nndsyzq@163.com and Ziming Pei; 281083195@qq.com

Received 24 September 2020; Revised 9 December 2020; Accepted 30 December 2020; Published 11 January 2021

Academic Editor: Zhushan Shao

Copyright © 2021 Chengzhong Zhang et al. This is an open access article distributed under the Creative Commons Attribution License, which permits unrestricted use, distribution, and reproduction in any medium, provided the original work is properly cited.

The Chongqing metro line 6 underpass expressway around the city is taken as an engineering background, and the optimal excavation sequence and corresponding control countermeasures for the triangular-distributed three-line metro tunnel underpass expressway are studied. The influences of excavation sequence on the tunnel surrounding rock deformation, surrounding rock stress, supporting structure stress, plastic zone, and surface settlement are analyzed by using MIDAS/GTS NX finite element software. The numerical simulation results showed that Case 1 is the optimal excavation sequence of the metro tunnel. However, the surface settlement under the optimal excavation sequence exceeds the limit value of 30 mm, which cannot guarantee the safety of expressway traffic. On this basis, the control measure for strengthening the three-line tunnels with advanced small pipe grouting and reinforcing the middle tunnel with concrete-filled steel tube piles are proposed. Moreover, the excavation process of the metro tunnel with and without reinforcement schemes is numerically simulated. The results show that the reinforcement scheme can effectively control the surface settlement value within the limited value (16.47 mm), which is close to the maximum surface settlement of 18.31 mm after the metro tunnel excavation is completed, indicating that the proposed reinforcement scheme is beneficial to ensure the safety of metro tunnel construction and the driving safety of the expressway.

1. Introduction

Newly built metro tunnels underpassing through the upper existing buildings (structures) and traffic lines are common engineering problems in urban infrastructure construction [1–3]. During the construction of metro tunnels, it is very easy to cause large surface settlement, which will threaten the safety of existing buildings (structures) and traffic lines on the upper part [4–6]. Therefore, it is necessary to study the impact of metro tunnel construction on the existing buildings (structures) and traffic lines and the corresponding construction control countermeasures [7–9].

In order to ensure the safety of metro tunnel construction and reduce the impact on existing buildings (structures) and traffic lines, relevant scholars have conducted a lot of research studies on metro tunnel

underpassing projects and corresponding control measures [10–12]. Lu [13] used the CAESAR II software to establish the stress analysis model of Yanyingshan tunnel pipeline based on the Lantsang tunnel crossing pipeline project and studied the change law of pipeline stress state and displacement during tunnel construction. Liu et al. [14] used the MIDAS/GTS NX finite element software to analyze the impact of shield tunnel construction on the existing railway by taking Zhengzhou metro line 4 under the Longhai railway as an example. Chung et al. [15] studied the influence of continuous excavation of new metro tunnels on the stability of existing metro tunnels using numerical simulation methods and proposed the best excavation sequence and reinforcement methods to ensure the stability of metro tunnel entrances and exits. Xing et al. [16] studied the impact of precipitation and new metro excavation on existing metro

tunnels through theoretical analysis and finite element simulation and proposed groundwater treatment measures and protection schemes for existing metro tunnels. Zhang et al. [17] used real-time monitoring data to analyze the impact of the construction of a new metro tunnel on the existing tunnel, and the results showed that advanced grouting can achieve the overall uplift within the reinforced area, and jack hoisting is the key to suppressing the settlement. Lai et al. [18] proposed a method for predicting the surface settlement caused by the construction of a metro double tunnel underneath the existing tunnel based on the comprehensive analysis of the coupling effect of the new tunnel, soil, and existing tunnel, with the effectiveness of the method verified by engineering examples. Jin et al. [19] studied the influence of shield tunnels on the surface settlement of existing tunnels during the construction process based on the monitoring data of a large number of underpass metro tunnel construction cases and pointed out that the longitudinal additional stress of the existing tunnels is the main reason which caused the tunnel lining water seepage and structure damage. Wu et al. [20] used a combination of the numerical simulation and model test to study the influence of the construction method of a new metro tunnel on the deformation and stability of the existing structure. Zhou et al. [21] established a theoretical model of deformation prediction caused by a new tunnel underpassing an existing tunnel based on the Peck formula and used the Beijing metro line 10 underpassing metro line 1 as an engineering case to verify the rationality of the model. Castaldo et al. [22] used the results of the numerical model of the boundary value problem and proposed a simplified probabilistic method to evaluate the impact of the new tunnel excavation on the adjacent existing buildings. Lai et al. [6] studied the influence of shield tunnel construction on the settlement characteristics of existing tunnels based on on-site monitoring data and numerical simulation software, and the results showed that the deformation of existing tunnels caused by shield tunneling was mainly the vertical settlement, accompanied by the torsion deformation. At present, most of the two-line or three-line metro tunnels under construction and already built are in parallel in a straight line, while the triangular-distributed three-line tunnel section is still rare in metro construction [23–26]. The tunnel structure of this section is more complicated. Different construction methods and excavation sequence differences will have an important impact on the tunnel support structure, surrounding rock stress, deformation characteristics, surface settlement, upper existing buildings (structures), and traffic routes [27–32]. In the case in which the construction method is determined, determining the optimal excavation sequence is of great significance for reducing the disturbance of the surrounding rock and ensuring the stability of the tunnel structure, upper existing buildings (structures), and traffic safety [33–37].

Based on the Chongqing metro tunnel line 6 underpassing through the expressway around the city, the MIDAS/GTS NX numerical simulation software is used to simulate the surrounding rock deformation, supporting structure stress distribution, and surface settlement of the metro tunnel under different excavation sequences, and the

optimal excavation sequence is determined. On this basis, the control measure for strengthening the three-line tunnels with advanced small pipe grouting and reinforcing the middle tunnel with concrete-filled steel tube piles is proposed, and the numerical simulation of the metro tunnel excavation process with and without reinforcement schemes is carried out.

2. Project Overview and Construction Difficulties

2.1. Project Overview. Chongqing metro line 6 from Qingxi River to Liujiayuanzi section of the two-lane tunnel (left and right lines) and Caojiawan access section right line (middle line), a total of three tunnels at K17+520 ~ K17+960 (YCK0+380 ~ YCK0+870), with the mileage section underpassing through the expressway around the city and the service area. The excavation section of this part of the tunnel is about 7.11 m high and 7.06 m wide, and the section is underpassing through the fill area. In the mileage section of K17+680 ~ K17+720, these three tunnels are distributed in a triangle and underpassing through the expressway around the city. The intersection angle between the axis of the metro tunnel and axis of the expressway is about 69°, underpassing distance is about 40 m, overlying fill range is about 135 m, and minimum distance from the tunnel vault to the expressway around the city is about 7.2 m. The schematic plan and cross-sectional distribution diagram for the metro tunnel underpassing through the expressway around the city are shown in Figures 1 and 2, respectively.

2.2. Engineering Geological Conditions and Hydrogeological Conditions. The metro tunnel stratum mainly includes the Quaternary Holocene fill layer (Q_4^{ml}), Quaternary Holocene residual slope clay (Q_4^{el+dl}), Jurassic Middle Shaximiao Formation (J_2^s) sandstone, and sandy mudstone. The Quaternary Holocene system fill layer (Q_4^{ml}) is mainly plain fill, distributed in the artificial reconstruction area along the tunnel, with a maximum thickness of about 28.3 m. The Quaternary Holocene residual slope cohesive soil (Q_4^{el+dl}) is mainly silty clay, distributed in the nonartificially modified area along the tunnel; the thickness of the soil layer is about 0.2–5.2 m, and the local thickness can reach 8.5 m. The Middle Jurassic Shaximiao Formation (J_2^s) is mainly composed of moderately weathered sandstone and sandy mudstone; the rock mass is not developed with cracks, and the rock mass is relatively complete, which belongs to class III surrounding rock; however, the sandy mudstone in some sections has a relatively large sand content and large strength variability and belongs to the V-level surrounding rock.

The groundwater along the tunnel is mainly Quaternary loose layer pore water and bedrock fissure water. The loose layer pore water is mainly distributed in the artificial fill layer and residual slope layer. The amount of water is small, and it is greatly affected by climate and seasonal changes. Bedrock fissure water is mainly distributed in the strong weathering zone of the shallow bedrock and the middle and



FIGURE 1: The schematic diagram for the underpassing.

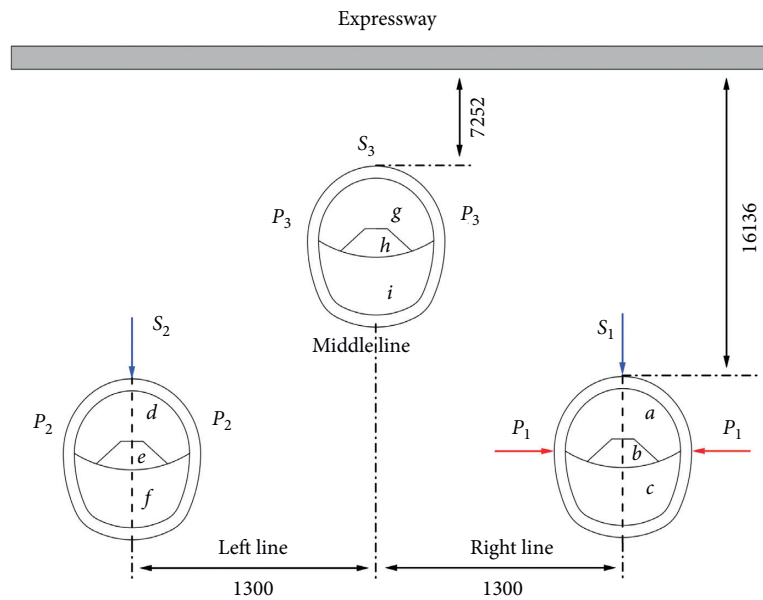


FIGURE 2: The cross-section distribution map for the metro tunnel underpassing through the expressway (unit: mm).

lower-middle-thick massive bedrock fissures. The amount of water is small, and it is greatly affected by seasonality.

2.3. Engineering Difficulties

(1) Most of the two-line or three-line metro tunnels currently under construction and already built are distributed in parallel in a straight line. However, in this project, the three tunnels are distributed in a triangular shape, that is, the middle tunnel is located directly above the middle point of the left and right tunnels, and the arch bottom of the middle tunnel is higher than the vaults of the left and right tunnels (as shown in Figure 2). This type of distribution of tunnel sections is still rare in metro tunnel construction. In particular, the maximum distance between the vault of the tunnel in the middle of the

section and the ground surface is only 15 m, which is a shallow tunnel. Therefore, the determination of a reasonable excavation plan, excavation sequence, and construction parameters have become the key issues for the safe and rapid construction of this project.

- (2) The underground excavation is carried out under the condition of backfilled soil. Due to the poor self-stability of the surrounding rock of the tunnel, the surrounding rock should be reinforced in advance to ensure the safety and stability of the excavation section before tunnel excavation in this layer.
- (3) The expressway around Chongqing city where the new metro tunnels underpassing in this project are in operation. To ensure driving safety, the surface settlement should be strictly controlled during the tunnel construction. Therefore, selecting appropriate

control countermeasures to strictly control the surface settlement is the most difficult point of this project.

3. The Construction Sequence Optimization of the Triangle-Distributed Three-Line Metro Tunnels Underpassing through the Expressway

The section structure of the triangular-distributed three-line metro tunnels is more complicated. Different construction methods and different excavation sequences will have an important impact on the tunnel support structure, surrounding rock stress, deformation characteristics, and surface settlement. Especially when the construction method is determined, determining the optimal excavation sequence is of great significance for reducing the disturbance of the surrounding rock and ensuring the stability of the surrounding rock of the tunnel. The MIDAS/GTS NX finite element software is used in this paper to carry out numerical simulations of different excavation sequences for Chongqing metro line 6 underpassing the expressway project. And, the most excellent tunnel excavation sequence scheme is determined by comparing and analyzing the numerical simulation results under different schemes.

3.1. Numerical Calculation Model and Relevant Parameters.

In the numerical simulation, according to the geological survey of the section of the underpass expressway, since the geological conditions of the K17+720 section are relatively complicated, this section is selected as the research object, with the two bench-cut method of core soil reserved on the upper step. In order to simplify the calculation, each rock and soil layer is regarded as a horizontal distribution, and it is regarded as an isotropic homogeneous elastic material. According to the actual project, the center line tunnel is completely in the backfilled stratum, and the left and right line tunnels are in the silty clay and sandy mudstone stratum. Since deep-well point precipitation has been used before tunnel excavation, there is no groundwater in the construction interval, so the influence of groundwater is ignored in the numerical simulation. At the same time, it is assumed that the initial stress is only the self-weight stress of each rock and soil layer. When meshing, the rock and soil layers are divided by 2D units, and the Mohr-Coulomb constitutive model is selected as the constitutive model of the rock and soil layers. 1D beam elements are used to divide the supporting structure and central diaphragm, and an elastic model is selected as the constitutive model of the supporting structure and central diaphragm; the model is divided into 1921 nodes and 2047 elements.

The excavation of the tunnel will cause deformation of the surrounding rock and soil, and its influence range is generally 3 to 5 times that of the tunnel diameter. Combined with the actual project, the dimensions of the numerical model in the X -axis and Y -axis directions are 80 m and 46.4 m, respectively. The X -axis direction is horizontal and perpendicular to the tunnel axis, and the Y -axis direction is the vertical direction. The upper surface is a free surface, and

the left side, right side, and lower part are displacement constraints. The finite element model is shown in Figure 3.

According to the on-site geological survey report, the section of the tunnel underneath the expressway is composed of artificial fill, silty clay, sandy mudstone, and sandstone from top to bottom, and the middle line tunnel is completely in the artificial fill. Most of the left and right tunnels are in sandy mudstone, and the partial vault structure is in silty clay rock. The thickness of roadbed, artificial fill layer, silty clay layer, sandy mudstone layer, and sandstone layer are 1.4 m, 15 m, 3 m, 7 m, and 20 m in order. The physical and mechanical parameters of each rock and soil layer are shown in Table 1.

All three tunnels adopt composite lining structure, and the initial supporting structure adopts C25 concrete with a thickness of 300 mm. In the tunnel support, two layers of $\Phi 8$ steel mesh with a grid spacing of $20\text{ cm} \times 20\text{ cm}$ are used; the steel frame adopts an I28b type full-ring arrangement with a spacing of 0.5 m the secondary lining adopts C40 concrete with a thickness of 500 mm. During model analysis, the initial support structure is simulated with an elastic model. According to the Code for Design of Concrete Structures of China (GB 50010-2011), the elastic modulus of C25 concrete and steel bars are 28 GPa and 200 GPa, respectively. The elastic modulus of the primary support adopts the equivalent elastic modulus and is calculated according to Equation (1). The physical and mechanical parameters of each support are shown in Table 2.

where E is the converted elastic modulus of the initial support, E_0 is the elastic modulus of sprayed concrete, E_g is the elastic modulus of the steel bar, S_g is the cross-sectional area of the steel bar, and S_0 is the cross-sectional area of concrete.

$$E = E_0 + \frac{S_g E_g}{S_0}, \quad (1)$$

3.2. *Excavation Schemes.* In order to avoid the influence of time and space effects during the excavation process, the load is released three times during the tunnel construction phase, and the load release coefficients are 0.4, 0.3, and 0.3, respectively. According to the actual engineering situation of Chongqing metro line 6, the three tunnels are distributed in a triangular shape, and the two bench-cut method of core soil reserved on the upper step is adopted for construction. The construction sequence of each tunnel is given as follows (taking the tunnel on the right in Figure 1 as an example): (1) excavate the pilot tunnel a and then construct the primary support; (2) excavate the core soil b and construct the middle partition; (3) excavate the pilot tunnel c , construct the primary support, and remove the middle partition; (4) construct the secondary lining. According to the above-mentioned construction sequence of a single tunnel, the following three excavation schemes of the numerical simulation in this paper are proposed.

Case 1. Right line tunnel \longrightarrow left line tunnel \longrightarrow middle line tunnel.

Case 2. Right line tunnel \longrightarrow middle line tunnel \longrightarrow left line tunnel.

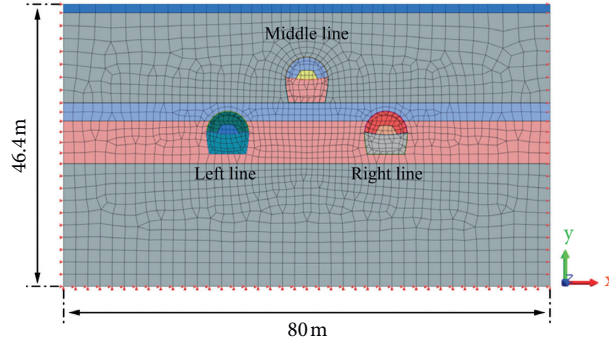


FIGURE 3: The finite element model diagram.

TABLE 1: Physical and mechanical parameters of rock and soil layers.

Type	Bulk density (kN/m ³)	Internal friction angle (°)	Cohesion (kPa)	Elastic modulus (MPa)	Poisson's ratio
Roadbed	20	36	30	15	0.3
Artificial fill	20	25	5	17	0.35
Silty clay	20	10.2	20.9	20	0.23
Sandy mudstone	25.6	31.2	440	2030	0.35
Sandstone	24.7	35	2100	4260	0.14

TABLE 2: Supporting physical and mechanical parameters.

Type	Bulk density (kN/m ³)	Modulus of elasticity (GPa)	Poisson's ratio	Thickness (mm)
Initial support	25	28	0.2	300
Middle partition	25	28	0.3	300
Secondary lining	25	32.5	0.2	300

Case 3. Center line tunnel → right line tunnel → left line tunnel.

3.3. Analysis of Numerical Simulation Results

3.3.1. Deformation of the Surrounding Rock and Supporting Structure. Figures 4 and 5, respectively, show the vertical and horizontal displacement cloud diagrams of the surrounding rock under different excavation schemes. It can be seen that, after the tunnel excavation is completed, the influence of different excavation schemes on the deformation of the surrounding rock is basically the same: (1) the maximum settlement values under the three excavation schemes all appear at the tunnel vault, and the maximum values are -42.13 mm, -48.04 mm, and -53.26 mm, respectively; (2) the inverted arch of the tunnel is uplifted, but due to the poor nature of the surrounding rock of the middle line tunnel, the uplift of the inverted arch is more obvious than that of the left and right line tunnels, and the maximum values under the three excavation schemes are 20.59 mm, 22.82 mm, and 12.36 mm, respectively; (3) the maximum horizontal displacements all appear on the left side of the middle line tunnel (X -axis negative direction), and the maximum values under the three excavation schemes are 12.36 mm, 12.36 mm, and 12.60 mm, respectively. It can be seen from the above results that compared with Cases 2 and 3, Case 1 has a more obvious effect on controlling the surrounding rock deformation of the tunnel.

In order to study the influence of the three excavation schemes on the primary support deformation of the tunnel, the vault settlement of the tunnel and haunch horizontal convergence were selected as reference values for analysis, and the layout of each monitoring point is shown in Figure 2. P_i ($i = 1, 2, \text{ and } 3$) is the monitoring point of the vault settlement, and S_i ($i = 1, 2, \text{ and } 3$) is the monitoring point of the haunch horizontal convergence. Table 3 shows the vault settlement value and haunch horizontal convergence value of the three tunnels under different excavation schemes. Due to the poor nature of the surrounding rock in the middle line tunnel, the vault settlement value and haunch horizontal convergence value are significantly greater than that of the left and right line tunnels. It can be seen from Table 3 that the vault settlement value of the tunnel and haunch horizontal convergence value under Case 3 are the largest, followed by Case 2, and Case 1 is the smallest. The vault settlement values of the tunnel under the three schemes are -42.13 mm, -46.89 mm, and -52.58 mm, respectively, and the haunch horizontal convergence value are -12.24 mm, -12.36 mm, and -12.60 mm, respectively. Although the three kinds of schemes cause large vault settlement values and on the basis of only considering the construction sequence, Case 1 is recommended for excavation.

3.3.2. Surrounding Rock Stress. Figures 6 and 7, respectively, show the maximum and minimum principal stress

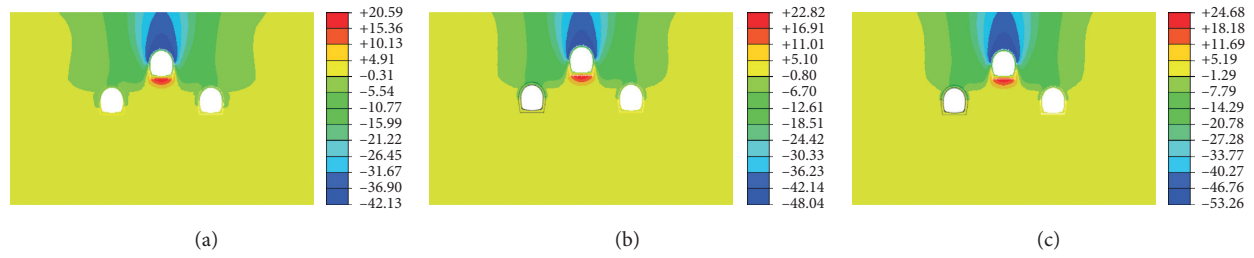


FIGURE 4: The vertical displacement distribution cloud map of the surrounding rock (unit: mm). (a) Case 1. (b) Case 2. (c) Case 3.

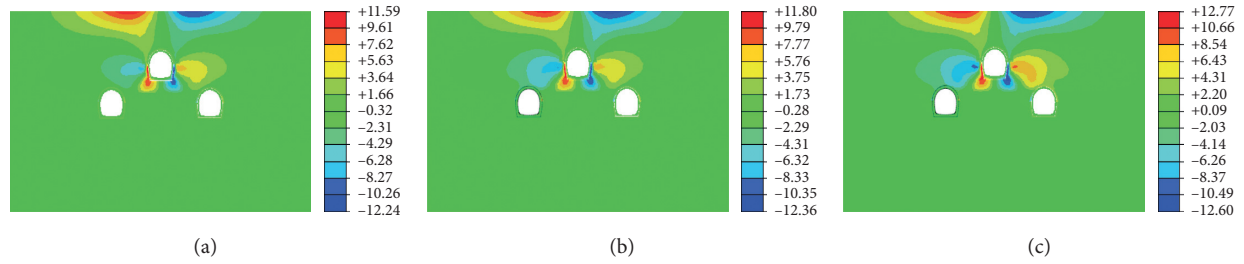


FIGURE 5: The horizontal displacement distribution cloud map of the surrounding rock (unit: mm). (a) Case 1. (b) Case 2. (c) Case 3.

TABLE 3: The vault settlement value of the tunnel and haunch horizontal convergence value under different construction schemes (unit: mm).

Monitoring points	P_1	P_2	P_3	S_1	S_2	S_3
Case 1	-6.81	-6.28	-42.13	-4.76	-4.24	-12.24
Case 2	-8.16	-9.18	-46.89	-4.72	-4.23	-12.36
Case 3	-10.32	-9.38	-52.58	-4.83	-4.26	-12.60

distribution cloud maps of the tunnel surrounding rock under different excavation schemes. It can be seen that the distribution law of the maximum and minimum principal stresses of the tunnel surrounding rock under the three excavation schemes are basically the same, and the excavation scheme has little influence on the stress of the tunnel surrounding rock. Through analysis, it can be seen that the maximum principal stresses of the tunnel surrounding rock under the three schemes are all distributed at the spandrel of the right tunnel, and the maximum values are 346.55 kPa, 346.75 kPa, and 352.03 kPa, respectively. The minimum principal stresses are all distributed at the haunch of the right tunnel, and the values are -1513.31 kPa, 1508.94 kPa, and 1556.29 kPa, respectively.

3.3.3. Surrounding Rock Stress. Figures 8 and 9 show the distribution cloud maps of the axial force and bending moment of the supporting structure under different excavation schemes, respectively. It can be seen from Figure 8 that the supporting structure under different excavation schemes is dominated by compressive stress, and the compressive stress distribution is relatively uniform. It can be seen from Figure 9 that the maximum positive bending moment and maximum negative bending moment of the supporting structure under different excavation schemes are located at the inverted arch and arch

foot of the middle line tunnel, respectively. It can be seen that there will be obvious uplift deformation at the inverted arch of the middle line tunnel. Through analysis, in Case 1, the maximum compressive stress on the tunnel haunch is 1280.98 kN, maximum compressive stress on the middle line tunnel is 454.21 kN, and maximum bending moment of the supporting structure is 336.72 kN m. In Case 2, the maximum compressive stress on the tunnel haunch is 1300.85 kN, maximum stress on the middle line tunnel is 454.21 kN, and maximum bending moment of the supporting structure is 337.12 kN m. In Case 3, the maximum stress on the tunnel haunch is 1313.40 kN, maximum stress of the middle tunnel is 468.74 kN, and maximum bending moment of the supporting structure is 337.43 kN m.

Through the above analysis, it can be seen that, under the same supporting conditions, the distribution of axial force and bending moment of the tunnel support structure under the three excavation schemes is basically the same, and the difference between the axial force value and bending moment value is small, that is, the three excavation schemes have little influence on the tunnel supporting structure.

3.3.4. Surface Settlement. Figure 10 shows the surface settlement curves under three excavation schemes. It can be seen that due to the close distance between the three tunnels, the surface settlement caused by the excavation of each

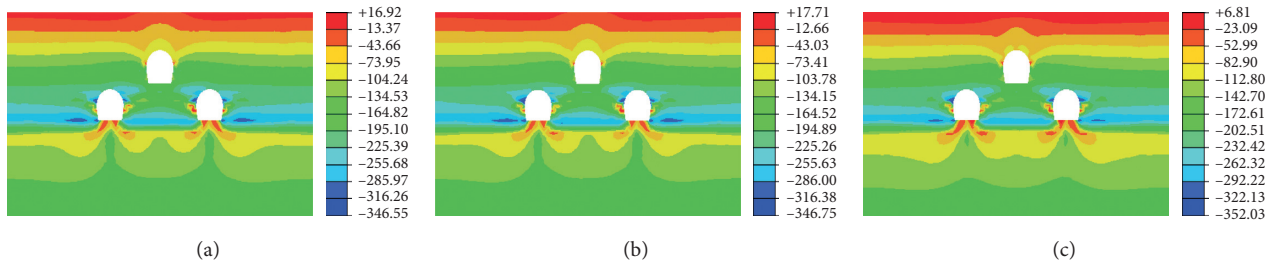


FIGURE 6: The maximum principal stress distribution cloud map of the surrounding rock (unit: kPa). (a) Case 1. (b) Case 2. (c) Case 3.

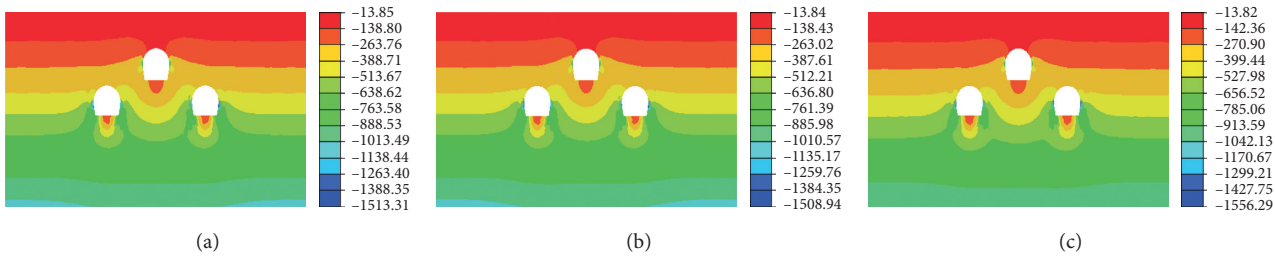


FIGURE 7: The minimum principal stress distribution cloud map of the surrounding rock (unit: kPa). (a) Case 1. (b) Case 2. (c) Case 3.

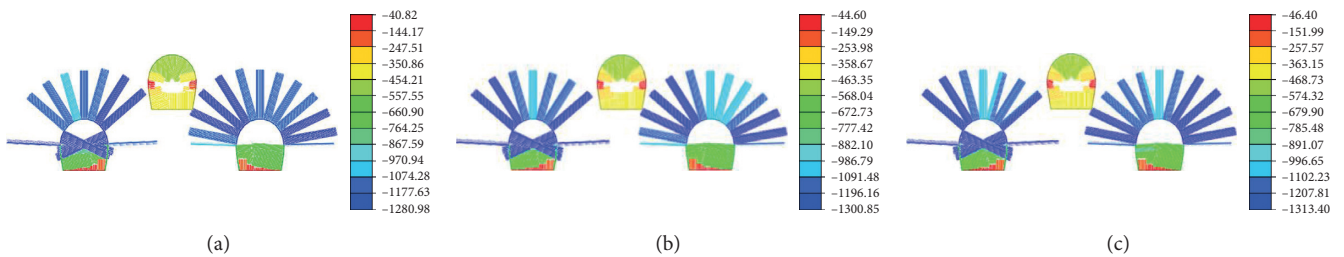


FIGURE 8: The axial force cloud map of the supporting structure (unit: kN). (a) Case 1. (b) Case 2. (c) Case 3.

tunnel gradually superimposes, resulting in the largest surface settlement in the middle part, and a “single peak” settlement curve with a small one on both sides and a large one on middle appears. In addition, it can be seen from Figure 10 that the width of the settlement tank under the three schemes is basically the same, and the first construction of the middle line tunnel in Cases 2 and 3 leads to the larger surface settlement. The maximum surface subsidence values under Cases 1–3 are 32.52 mm, 36.74 mm, and 41.55 mm in sequence. Although the surface settlement of the three cases exceeds the limit value of 30 mm, in comparison, Case 1 is more conducive to controlling the surface settlement during the construction process.

3.3.5. Plastic Zone Distribution. Figure 11 shows the plastic zone distribution cloud map of the tunnel surrounding rock under three excavation schemes. It can be seen that, under the three excavation schemes, the plastic zone of the surrounding rock of the tunnel is mainly distributed at the spandrel, haunch, arch foot, and inverted arch of the middle line tunnel. There is basically no plastic zone distribution

near the left and right tunnels. Through the comparative analysis of the distribution of the tunnel plastic zone under the three excavation schemes, it can be found that the plastic zone caused by Case 1 is slightly smaller than the size of the surrounding rock plastic zone caused by the other two schemes. Therefore, from the perspective of considering the plastic zone, the preferred choice for tunnel excavation is Case 1.

Through comparative analysis of the displacement, internal force, surface settlement, and plastic zone distribution of the tunnel surrounding rock and support system under the three excavation schemes, it can be seen that Case 1, namely, firstly excavate the right tunnel, then excavate the left tunnel, and finally excavating the middle line tunnel is the most effective way to control the deformation of the surrounding rock and the stress and shape change of the supporting structure. In addition, the plastic zone of the surrounding rock caused by Case 1 is smaller than the plastic zones caused by Cases 2 and 3. On comprehensive comparison, it is recommended to carry out on-site construction in accordance with Case 1, namely, the excavation sequence of right line tunnel → left line tunnel → middle line

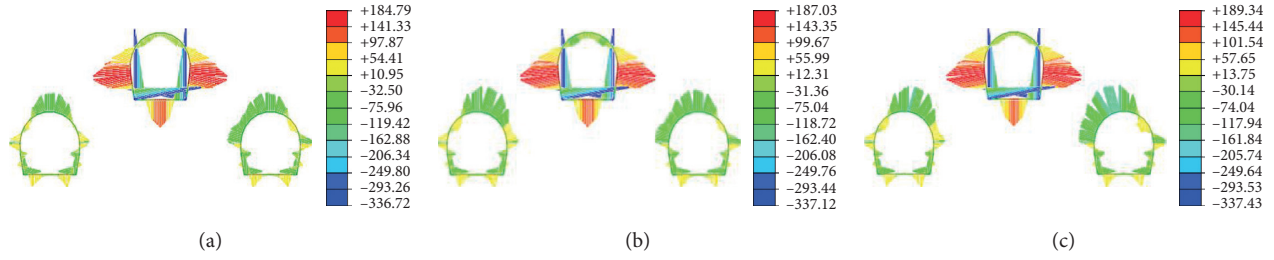


FIGURE 9: The bending moment cloud map of the supporting structure (unit: kN·m). (a) Case 1. (b) Case 2. (c) Case 3.

tunnel. However, the surface settlement under the three schemes all exceeded the limit value of 30 mm, which cannot guarantee the safety of expressway traffic. Therefore, it is necessary to adopt advanced small pipe grouting pre-reinforcement measures for the left, middle, and right tunnels and use steel tube concrete piles to reinforce the base of the middle tunnel in order to improve the stability of the tunnel surrounding rock.

4. Control Countermeasures for the Construction of Triangular Three-Line Metro Tunnels Undercrossing the Expressway

The advanced small pipe grouting is the most commonly used pre-reinforcement treatment method in the construction of shallow burying and undercutting. The principle is that the surrounding rock in a certain range in front of the tunnel is excavated and drilled at a certain inclination angle, and a small pipe with holes is installed or a small pipe with holes is directly drilled, and then, the surrounding rock is pressure injected through the small pipe cementing slurry. After the grout is hardened, on the one hand, the surrounding rock can be cemented into a hole, which improves the self-stability of the surrounding rock and plays a role in reinforcement. On the other hand, it plugs the fissures of the surrounding rock and plays a role in blocking water. Combining the actual situation of the project of Chongqing metro line 6 underpassing through the expressway around the city, according to the design, the soil in the 180° area of the arch of the three tunnels is driven into a $\Phi 42$ double-row advanced small pipe. The layout of the advanced small pipe is shown in Figure 12, and as indicated in Figure 12, the relevant parameters are given in Table 4.

In order to reduce the risk of inverted arch uplift and to ensure the operational safety of the tunnel, the steel tube concrete piles are adopted to strengthen the soft foundation of the tunnel inverted arch during the construction process of the Chongqing metro line 6. The on-site steel pipe piles are made of 406×5.6 mm steel pipes, $6\Phi 20$ steel cages are installed, and C40 waterproof concrete is poured. The length of the steel pipe piles is about 12 m, and the depth of the rock (sandstone) embedded in the actual construction is guaranteed to be 2 m. Figures 13 and 14, respectively, show the reinforced cross-section and plan layout of concrete-filled steel tube piles.

4.1. Numerical Model and Parameters. The numerical model after reinforcement is established on the basis of the model in Section 3. The physical and mechanical parameters of the

ground and supporting structure are shown in Tables 1 and 2. The selection of the constitutive model and other model conditions are the same as in Section 3, and the numerical model is divided into 1973 nodes and 2095 elements.

At present, the effect of advanced presupport can be equivalently analyzed by changing the physical and mechanical parameters of the surrounding rock in a certain area. The thickness of the grouting reinforcement zone can be calculated by Equation (2), taking 0.6 m. The physical and mechanical parameters of the surrounding rock after grouting can be determined by Equation (3). The final parameter determination results are shown in Table 5.

$$D = 2 \left[R^2 - \left(\frac{S}{2} \right)^2 \right]^{0.5}, \quad (2)$$

where D is the thickness of the reinforcement ring, R is the grout diffusion radius, taking S (0.6 ~ 0.8), and S is the distance between adjacent grouting holes.

$$E = \frac{E_1 I_1 + k_w E_2 I_2}{I_1 + I_2}, \quad (3)$$

where E is equivalent stiffness (GPa), E_1 is steel tube elastic modulus (GPa), I_1 is steel tube moment of inertia (m^4), E_2 is steel tube filled with elastic modulus of mortar (GPa), I_2 is moment of inertia of mortar filled in steel pipe (m^4), and k_w is considered the coefficient of mortar stiffness reduction caused by mortar cracking, and 0.6 is taken.

When simulating steel pipe piles in finite element software, the interaction between the pile circumference, pile tip, and rock and soil should be considered. In this paper, the 1D beam element is used to simulate a concrete-filled steel tube pile, and a pile element is built around the steel tube pile to simulate the contact between the pile circumference and rock and soil, with a pile end element established at the bottom of the beam element to simulate the interaction between the pile end and rock and soil. Table 6 shows the relevant parameters of concrete-filled steel tube piles.

4.2. Reinforcement Optimization Scheme Design. It can be seen from Section 3 that, compared with Cases 2 and 3, the excavation sequence of Case 1 is more reasonable to ensure the stability of the surrounding rock of the triangularly distributed three-line metro tunnels. Therefore, this section optimizes the reinforcement scheme on the basis of Case 1. Taking the right tunnel as an example, the

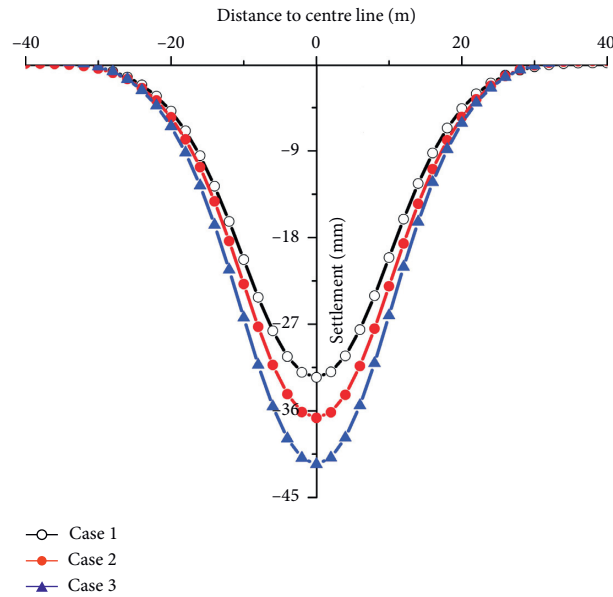


FIGURE 10: Comparison of the surface settlement.

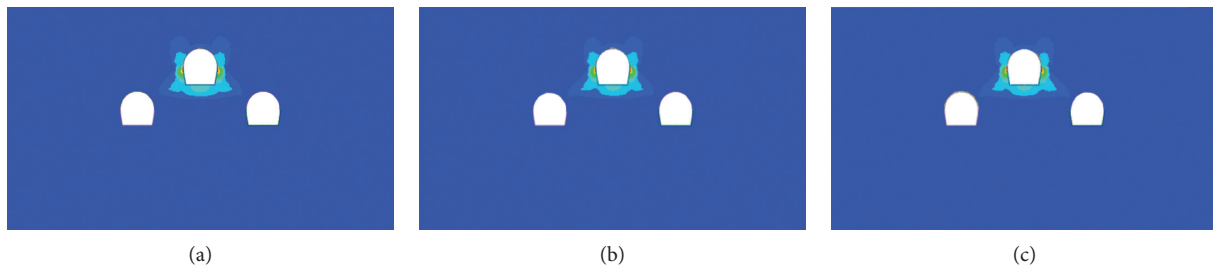


FIGURE 11: The cloud map of plastic zone distribution. (a) Case 1. (b) Case 2. (c) Case 3.

specific reinforcement sequence is given as follows (as shown in Figure 15): (1) reinforce area by using advanced small pipe grouting; (2) excavate pilot tunnel and implement primary support; (3) excavate the core soil of the right hole and construct the middle partition; (4) excavate pilot tunnel, construct primary support, and remove the middle partition; (5) construct the secondary lining and complete the construction of the right tunnel. In accordance with the above sequence, according to Case 1, the construction of the left tunnel and middle tunnel were completed in turn.

4.3. Analysis of Numerical Simulation Results

4.3.1. Deformation of the Surrounding Rock and Supporting Structure. Figures 16 and 17, respectively, show the vertical and horizontal displacement cloud maps of the tunnel surrounding rock before and after the reinforcement scheme is adopted. It can be seen that, after the tunnel excavation is completed, the surrounding rock deformation distribution law is basically the same before and after the reinforcement scheme is adopted. Due to the

poor nature of the surrounding rock in the middle line tunnel, the vault settlement and inverted arch uplift are more obvious than those of the left and right line tunnels. The maximum settlement occurred at the vault of the middle line tunnel, with the maximum values of -42.13 mm and -20.17 mm, respectively. The maximum uplift occurred at the inverted arch of the tunnel, with the maximum values of 20.59 mm and 18.50 mm, respectively. The maximum horizontal displacements all appear on the right side of the middle line tunnel, in the negative direction along the X -axis, and the maximum horizontal displacements are 12.36 mm and 13.08 mm, respectively. It can be seen from the calculation results that the reinforcement scheme has a significant control effect on the deformation of the tunnel surrounding rock.

In order to study the influence of the reinforcement scheme on the initial support deformation of the tunnel, the settlement of the tunnel vault and horizontal convergence of the arch waist were selected as reference values for analysis (the monitoring points are the same as in Section 3). Table 7 shows the settlement value of the tunnel vault and level of the arch waist before and after

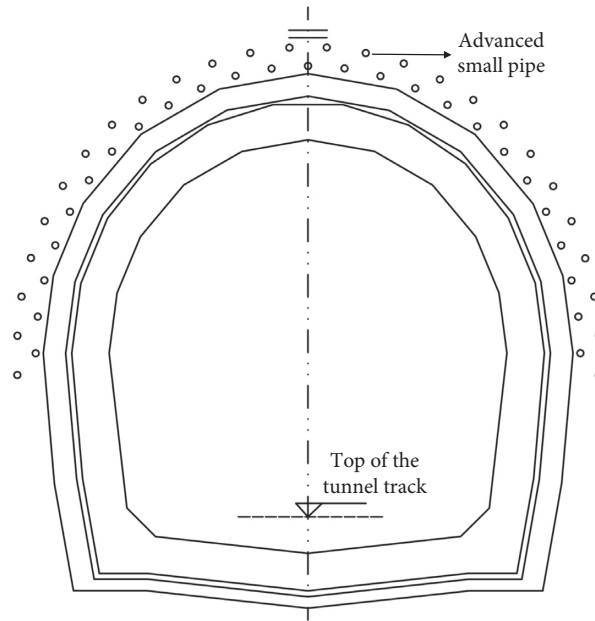


FIGURE 12: The layout of the advanced small pipes.

TABLE 4: Parameters of the advanced small pipes.

Small pipes	Length (mm)	Longitudinal spacing (mm)	Circumferential spacing (mm)	Extrapolation angle (°)	Grouting hole	Notes
Inner layer	5	2.5	0.4	40	Plum blossom arrangement with 0.5 m spacing	Chemical grouting
Outer layer	3.5	2.0	0.3	10~15		

the reinforcement scheme. It can be seen from Table 7 that the deformation of the supporting structure is very different before and after the reinforcement scheme is adopted. The deformation of the supporting structure after the reinforcement scheme is adopted and is significantly smaller than that without the reinforcement scheme. After adopting the reinforcement scheme at the same time, the maximum deformation can be controlled within 30 mm.

4.3.2. Surrounding Rock Stress. Figures 18 and 19 show the distribution cloud maps of the maximum and minimum principal stress of the tunnel surrounding rock before and after reinforcement measures are adopted. It can be seen that there is no obvious difference between the maximum principal stress of the surrounding rock after the tunnel excavation is completed before and after the use of reinforcement measures, but the minimum principal stress has changed significantly. Before adopting the reinforcement scheme, the maximum principal stress and minimum principal stress of the surrounding rock appeared at the arch shoulder and haunch of the right tunnel, respectively, and the values are 346.55 kPa and -1513.31 kPa, respectively; after the reinforcement

scheme is adopted, the maximum principal stress of the surrounding rock appears at the vaults of the left and right tunnels, and the minimum principal stress appears at the haunch of the right tunnel and the values are 333.14 kPa and -1886.04 kPa, respectively.

4.3.3. Supporting Structure Force. Figures 20 and 21 show the distribution cloud maps of the axial force and bending moment of the supporting structures before and after the reinforcement scheme is adopted. It can be seen that, before and after the reinforcement scheme is adopted, the axial force of the supporting structure is mainly pressure, and the pressure distribution is relatively uniform. The maximum positive bending moment of the supporting structure is located at the inverted arch of the middle line tunnel, and the maximum negative bending moment is located at the arch foot of the middle line tunnel, indicating that there will be obvious uplift deformation at the inverted arch. The analysis shows that, before the reinforcement scheme is adopted, the maximum pressure of the tunnel appears at the haunch of the left and right tunnels, and its value is 1280.98 kN. The maximum pressure on the middle line tunnel is 454.21 kN, and the maximum bending moment of the supporting structure is

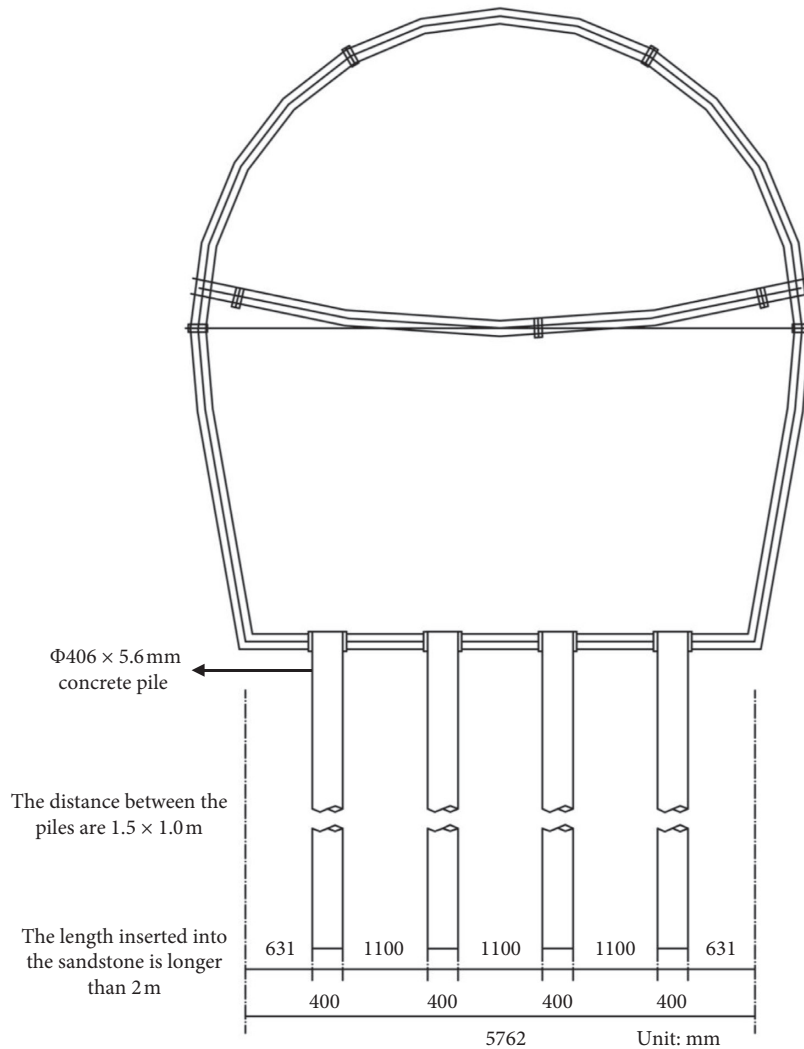


FIGURE 13: The reinforced section view of the steel tube concrete pile.

336.72 kN m. After the reinforcement scheme is adopted, the maximum pressure of the tunnel appears at the haunch of the left and right tunnels, with a value of 1071.39 kN. The maximum pressure on the middle line tunnel is 342.50 kN, and the maximum bending moment of the supporting structure is 328.34 kN-m. The above phenomenon shows that the reinforcement scheme can play a good control effect on the axial force and bending moment of the supporting structure.

4.3.4. Surface Settlement. Figure 22 shows the surface settlement curves before and after the reinforcement scheme is adopted. It can be seen that the surface settlement curves before and after adopting the reinforcement scheme still show a "single peak" settlement curve with small sides on both sides and large sides in the middle. Moreover, the width of the settlement tank before and after the reinforcement scheme is basically the same. The maximum settlement value after reinforcement is 16.47 mm, which is close to the surface settlement value of 18.31 mm after the tunnel excavation is

completed after 170 days, and is much smaller than that before the reinforcement measures (32.52 mm). Therefore, the reinforcement scheme in this section can effectively control the surface settlement value within the limit value of 30 mm, indicating that the reinforcement scheme has an obvious control effect on the surface settlement during tunnel construction.

4.3.5. Plastic Zone Distribution. Figure 23 shows the plastic zone distribution cloud map of the tunnel surrounding rock before and after the reinforcement scheme is adopted. It can be seen that, before and after the reinforcement scheme is adopted, the plastic zones are mainly concentrated at the arch shoulder, haunch, arch foot, and inverted arch of the middle line tunnel. However, compared with no reinforcement scheme, the plastic zone distribution area of the arch shoulder is greatly reduced after the reinforcement plan is adopted, indicating that the reinforcement scheme has a significant inhibitory effect on the development of the plastic zone of the surrounding rock.

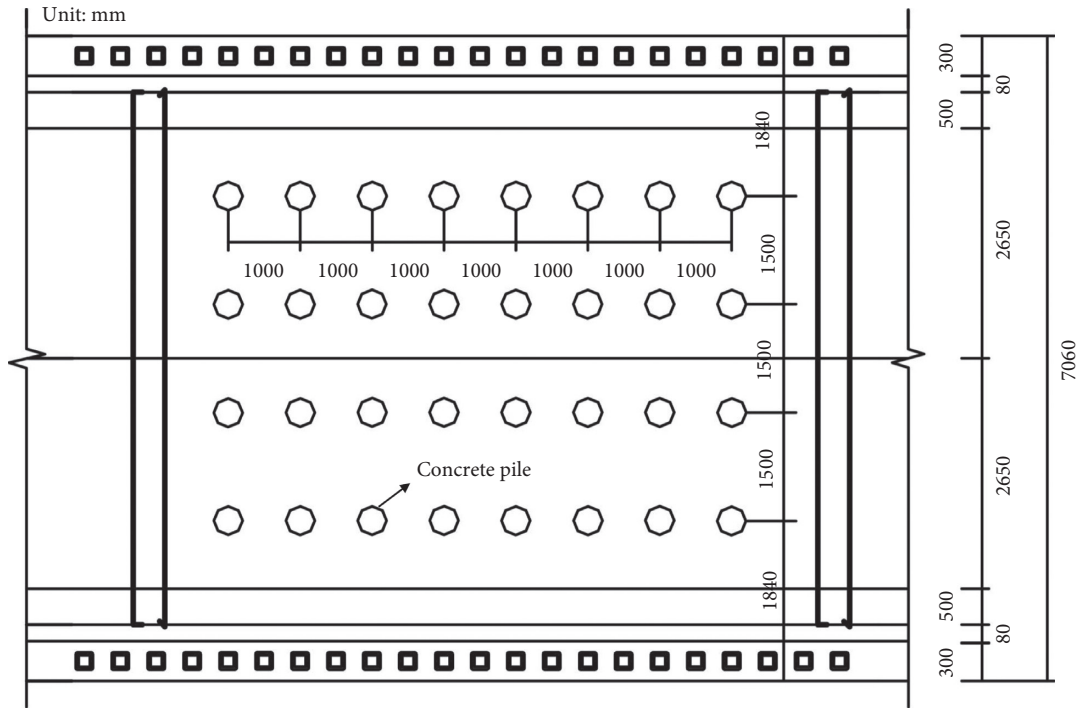


FIGURE 14: The layout plan of concrete-filled steel tube piles.

TABLE 5: Physical and mechanical parameters of the surrounding rock in the grouting reinforcement area.

Type	Elastic modulus (MPa)	Internal friction angle (°)	Cohesion (kPa)	Poisson's ratio
Advanced small-pipe grouting reinforcement area	103.55	23.5	108	0.2

TABLE 6: Numerical simulation parameters of concrete-filled steel tube piles.

Type	Shear stress (kPa)	Shear stiffness modulus (kN·m ⁻³)	Normal stiffness modulus (kN·m ⁻³)	Pile-end bearing capacity (kN)	Bulk density (kN·m ⁻³)	Elastic modulus (MPa)	Poisson's ratio
Pile unit	306	48465	126000	-	-	-	-
Pile end unit	-	-	-	300	-	-	-
Concrete-filled steel tube pile	-	-	-	-	23	3000	0.2

Through the above analysis, it can be seen that the use of advanced small pipe grouting and steel tube concrete piles to strengthen the control measures of the tunnel base in the middle tunnel not only is conducive to controlling the deformation and force of the surrounding rock and supporting structure but also the deformation value is controlled within the specified range. Moreover, the distribution range of the plastic zone after the

reinforcement is smaller. Therefore, for this project, it is recommended to excavate according to Case 1, namely, in the sequence of right line tunnel → left line tunnel → middle line tunnel. At the same time, the site construction was carried out in cooperation with the control plan of advanced small pipe grouting and steel tube concrete piles to strengthen the base of the middle line tunnel.

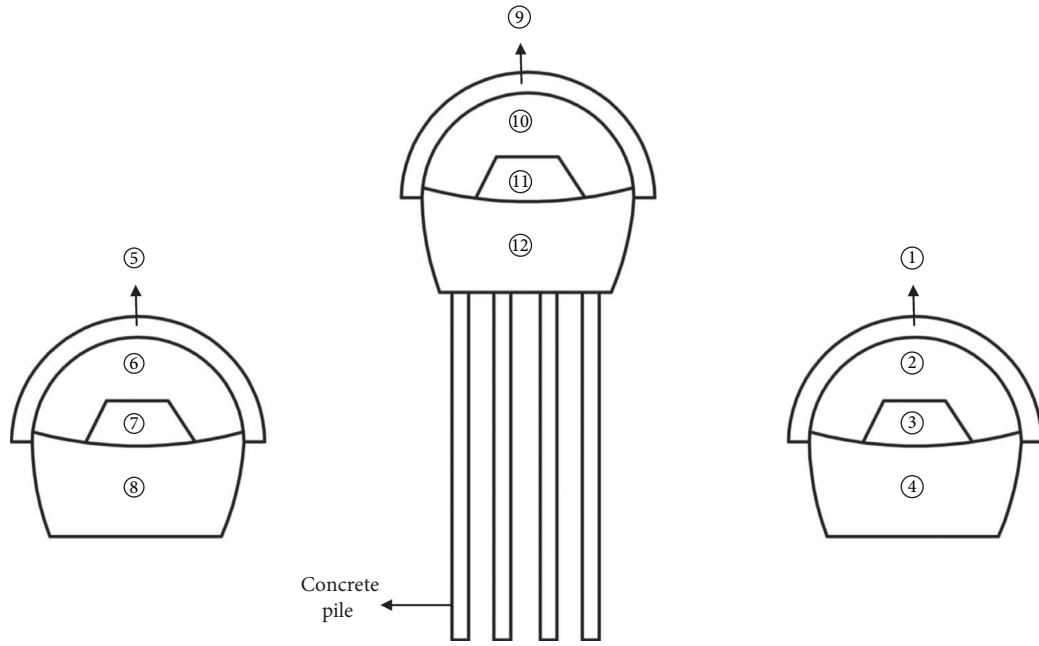


FIGURE 15: Tunnel reinforcement construction sequence.

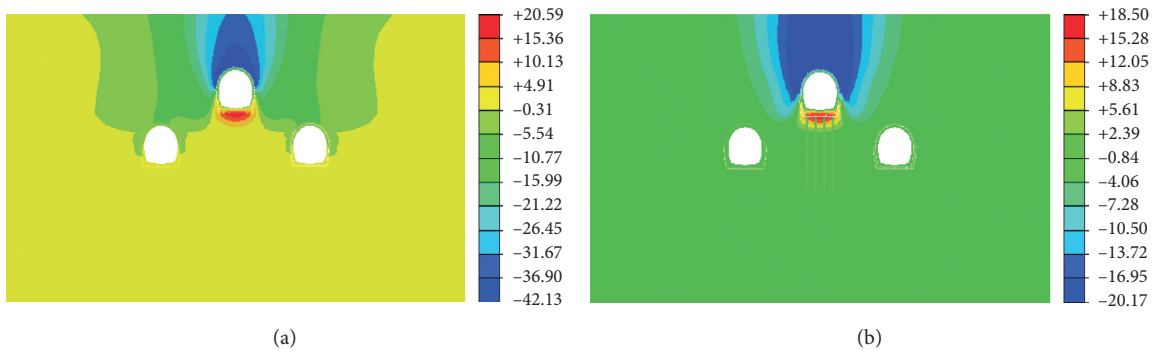


FIGURE 16: The vertical displacement distribution cloud map of the surrounding rock (unit: mm). (a) Not reinforced. (b) Reinforced.

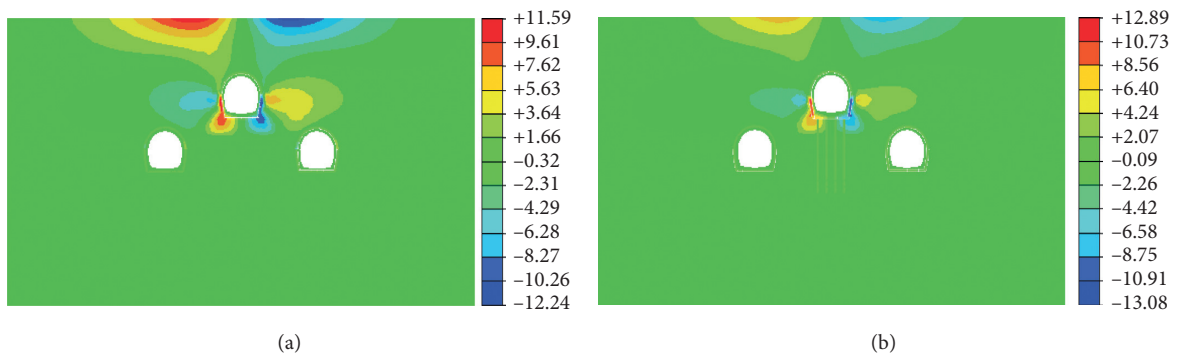


FIGURE 17: The horizontal displacement distribution cloud map of the surrounding rock (unit: mm). (a) Not reinforced. (b) Reinforced.

TABLE 7: The vault settlement value of the tunnel and haunch horizontal convergence value under different construction schemes (unit: mm).

Feature points	P_1	P_2	P_3	S_1	S_2	S_3
Before reinforcement	-6.81	-6.28	-42.13	-4.56	-4.14	-12.24
After reinforcement	-1.50	-1.51	-20.17	-1.21	-1.04	-13.08

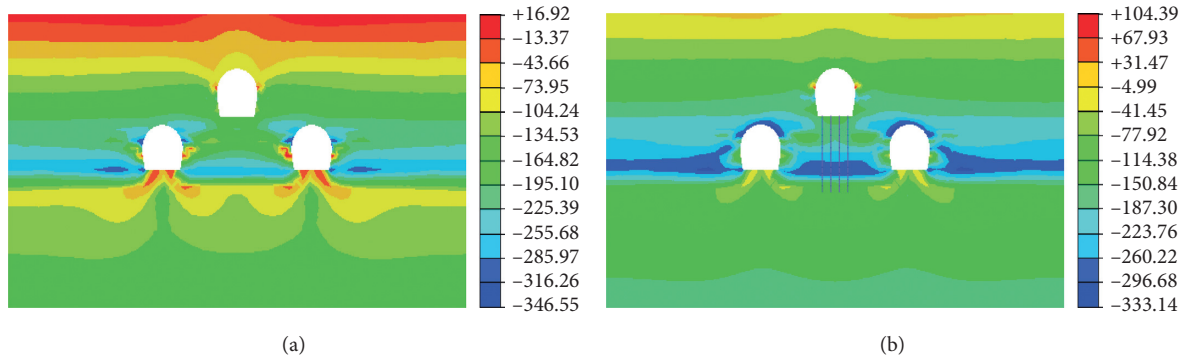


FIGURE 18: The maximum principal stress cloud map of the surrounding rock (unit: kPa). (a) Not reinforced. (b) Reinforced.

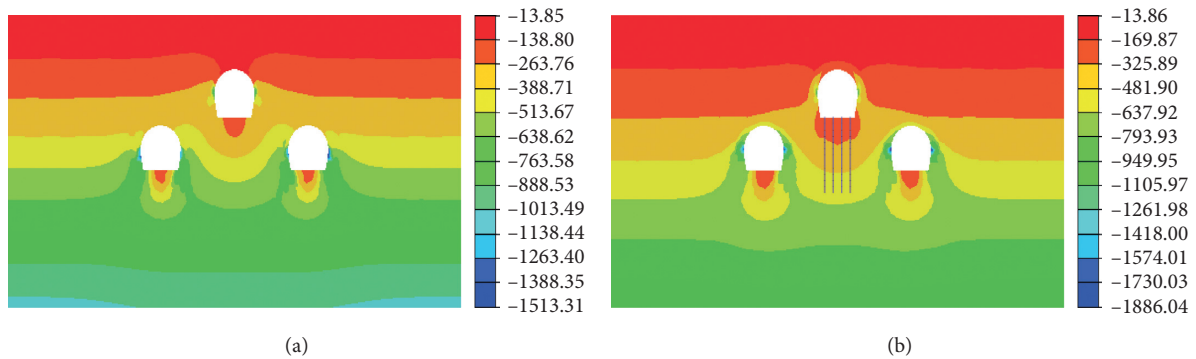


FIGURE 19: The minimum principal stress cloud map of the surrounding rock (unit: kPa). (a) Not reinforced. (b) Reinforced.

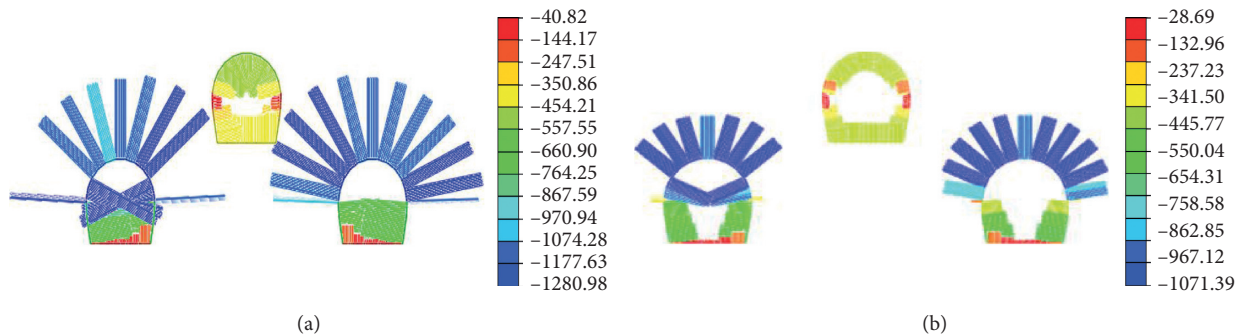


FIGURE 20: The axial force cloud map of the supporting structure (unit: kN). (a) Not reinforced. (b) Reinforced.

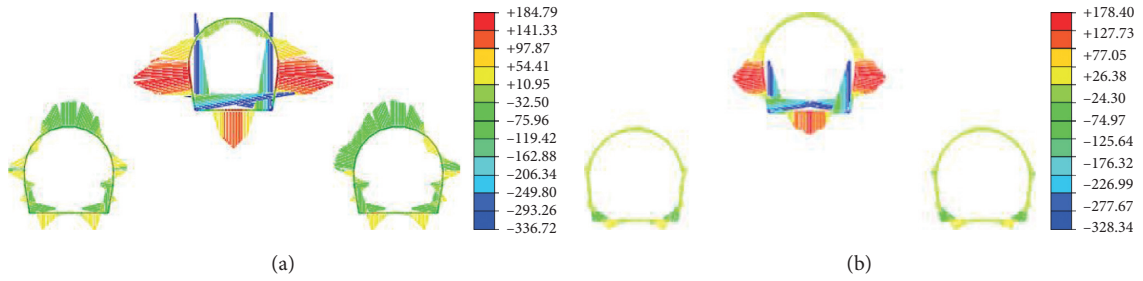


FIGURE 21: The bending moment cloud map of the supporting structure (unit: kN·m). (a) Not reinforced. (b) Reinforced.

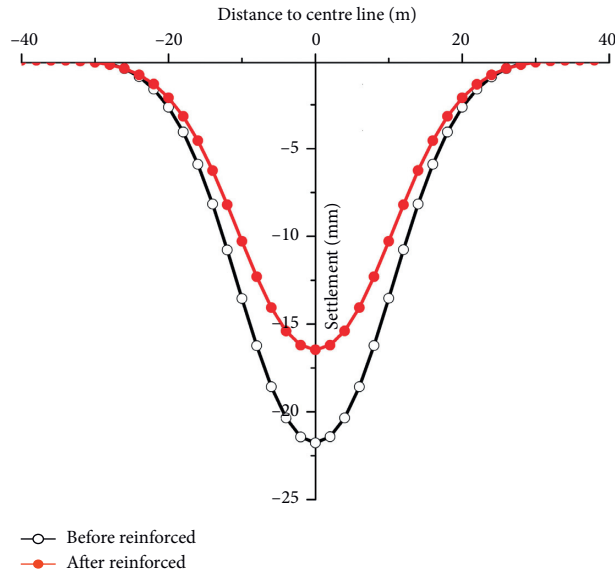


FIGURE 22: Comparison of the surface settlement before and after the reinforcement scheme is adopted.

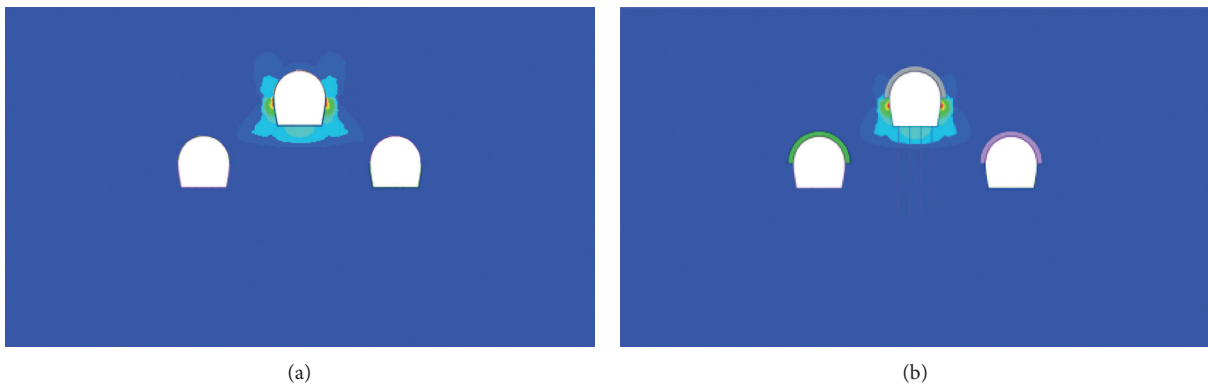


FIGURE 23: The plastic zone distribution cloud map before and after reinforced. (a) Not reinforced. (b) Reinforced.

5. Conclusions

In this paper, relying on the project of Chongqing metro tunnel line 6 underpassing through the expressway around the city, numerical simulation methods are used to study the

surrounding rock deformation, surface settlement, and stress distribution of the supporting structure of the three-line metro tunnels with a triangular distribution under different excavation sequences, and the optimal excavation sequence is determined. On this basis, the control measure

for strengthening the three-line tunnels with advanced small pipe grouting and reinforcing the middle tunnel with concrete-filled steel tube piles are proposed. The main conclusions obtained are as follows:

- (1) Numerical simulation results under three different excavation schemes show that the excavation sequence of Case 1 (right line tunnel → left line tunnel → middle line tunnel) is effective in controlling the deformation of surrounding rock, supporting structure stress, and surface settlement. The control effects of the surface settlement and development of plastic zone are the best, which helps ensure the rapid and safe construction of metro tunnels.
- (2) Although the excavation sequence of Case 1 is conducive to ensuring the safe construction of the triangularly distributed three-line metro tunnel, the surface settlement exceeds the limit value (30 mm), which is not conducive to the safety of the upper expressway. Therefore, in order to reduce the impact of metro tunnel construction on the upper expressway, a treatment method is proposed to pre-reinforce the three tunnels by grouting with small pipes in advance, and to use concrete-filled steel tube piles to strengthen the base of the middle line tunnel.
- (3) The numerical simulation of the excavation process of the triangular-distributed three-line metro tunnel with and without the reinforcement scheme is carried out. The results show that the use of reinforcement schemes can effectively control surface settlement, tunnel surrounding rock deformation, support structure stress, and plastic zone development, which is conducive to the safety of tunnel construction and safe operation of the upper expressway.

Data Availability

The data used to support the findings of this study are available from the corresponding author upon request.

Conflicts of Interest

The authors declare that they have no conflicts of interests.

Acknowledgments

This work was supported by the Housing and Urban-Rural Construction Science and Technology Planning Project of Shaanxi Province (Grant no. 2019-K39) and Innovation Capability Support Plan of Shaanxi-Innovation Team (Grant no. 2020TD-005).

References

- [1] H. Wu, Y. J. Zhong, W. Shi, X. H. Shi, and T. Liu, "Experimental investigation of ground and air temperature fields of cold-region road tunnels in NW China," *Advances in Civil Engineering*, vol. 2020, Article ID 4732490, 13 pages, 2020.
- [2] W. C. Cheng, G. Li, D. E. L. Ong, S. L. Chen, and J. C. Ni, "Modelling liner forces response to very close-proximity tunnelling in soft alluvial deposits," *Tunnelling and Underground Space and Technology*, vol. 103, Article ID 103455, 2020.
- [3] Z. F. Chu, Z. J. Wu, Q. S. Liu, and B. G. Liu, "Analytical solutions for deep-buried lined tunnels considering longitudinal discontinuous excavation in rheological rock mass," *Journal of Engineering Mechanics*, vol. 146, no. 6, Article ID 04020047, 2020.
- [4] Z. P. Song, J. C. Mao, X. X. Tian, Y. W. Zhang, and J. B. Wang, "Optimization analysis of controlled blasting for passing through houses at close range in super-large section tunnels," *Shock and Vibration*, vol. 2019, Article ID 1941436, 16 pages, 2019.
- [5] K. Wu and Z. S. Shao, "Visco-elastic analysis on the effect of flexible layer on mechanical behavior of tunnels," *International Journal of Applied Mechanics*, vol. 11, no. 3, Article ID 1950027, 2019.
- [6] H. P. Lai, H. W. Zheng, R. Chen, Z. Kang, and Y. Liu, "Settlement behaviors of existing tunnel caused by obliquely under-crossing shield tunneling in close proximity with small intersection angle," *Tunnelling and Underground Space and Technology*, vol. 97, Article ID 103258, 2020.
- [7] K. Wu and Z. S. Shao, "Study on the effect of flexible layer on support structures of tunnel excavated in viscoelastic rocks," *Journal of Engineering Mechanics*, vol. 145, no. 10, Article ID 04019077, 2019.
- [8] Z. P. Song, X. X. Tian, Q. Liu, Y. W. Zhang, H. Li, and G. N. Zhou, "Numerical analysis and application of the construction method for small interval tunnel in the turn line of metro," *Science Progress*, vol. 103, no. 3, Article ID 0036850420932067, 2020.
- [9] J. B. Wang, Q. Zhang, Z. P. Song, and Y. W. Zhang, "Experimental study on creep properties of salt rock under long-period cyclic loading," *International Journal of Fatigue*, vol. 143, Article ID 106009, 2021.
- [10] J. Su, Q. Fang, D. L. Zhang, X. K. Niu, X. Liu, and Y. M. Jie, "Bridge responses induced by adjacent subway station construction using shallow tunneling method," *Advances in Civil Engineering*, vol. 2018, Article ID 8918749, 16 pages, 2018.
- [11] K. Wu, Z. S. Shao, S. Qin, N. N. Zhao, and H. K. Hu, "Analytical-based assessment of effect of highly deformable elements on tunnel lining within viscoelastic rocks," *International Journal of Applied Mechanics*, vol. 12, no. 3, Article ID 2050030, 2020.
- [12] Z. Zhang and M. Huang, "Geotechnical influence on existing subway tunnels induced by multiline tunneling in Shanghai soft soil," *Computers and Geotechnics*, vol. 56, pp. 121–132, 2014.
- [13] H. F. Lu, "Stress and displacement analysis of aerial oil and gas pipelines: a case study of Lantsang tunnel crossing project," *Journal of Engineering Research*, vol. 3, no. 3, pp. 141–156, 2015.
- [14] B. Liu, D. Xi, and P. Xu, "Study on the interaction of metro shield tunnel construction under-crossing the existing Longhai railway," *Geotechnical and Geological Engineering*, vol. 38, no. 2, pp. 2159–2168, 2020.
- [15] J.-S. Chung, J.-Y. Choi, and J.-H. Lee, "A study on the stability of existing subway tunnel due to construction of new underpass," *Journal of the Korean Society of Safety*, vol. 31, no. 2, pp. 57–63, 2016.
- [16] H. F. Xing, F. Xiong, and J. M. Wu, "Effects of pit excavation on an existing subway station and preventive measures,"

- Journal of Performance of Constructed Facilities*, vol. 30, no. 6, Article ID 04016063, 2016.
- [17] X. Zhang, C. P. Zhang, and J. C. Wang, "Effect of closely spaced twin tunnel construction beneath an existing subway station: a case study," *Journal of Testing and Evaluation*, vol. 46, no. 4, pp. 1559–1573, 2018.
- [18] H. P. Lai, X. Zhao, Z. Kang, and R. Chen, "A new method for predicting ground settlement caused by twin-tunneling under-crossing an existing tunnel," *Environmental Earth Sciences*, vol. 76, no. 21, 726 pages, 2017.
- [19] D. Jin, D. Yuan, X. Li, and H. Zheng, "Analysis of the settlement of an existing tunnel induced by shield tunneling underneath," *Tunnelling and Underground Space Technology*, vol. 81, pp. 209–220, 2018.
- [20] K. Wu, W. Zhang, H. T. Wu, Y. J. Wang, and Z. L. Liu, "Study of impact of metro station side-crossing on adjacent existing underground structure," *Journal of Intelligent and Fuzzy Systems*, vol. 31, no. 4, pp. 2291–2298, 2016.
- [21] Z. Zhou, Y. Chen, Z. Z. Liu, and L. W. Miao, "Theoretical prediction model for deformations caused by construction of new tunnels undercrossing existing tunnels based on the equivalent layered method," *Computers and Geotechnics*, vol. 123, Article ID 103565, 2020.
- [22] P. Castaldo, M. Calvello, and B. Palazzo, "Probabilistic analysis of excavation-induced damages to existing structures," *Computers and Geotechnics*, vol. 53, pp. 17–30, 2013.
- [23] Z. P. Song, Y. Cheng, X. X. Tian, J. B. Wang, and T. T. Yang, "Mechanical properties of limestone from Maixi tunnel under hydro-mechanical coupling," *Arabian Journal of Geosciences*, vol. 13, no. 11, 402 pages, 2020.
- [24] J. B. Wang, Q. Zhang, Z. P. Song, Y. W. Zhang, and X. R. Liu, "Mechanical properties and damage constitutive model for uniaxial compression of salt rock at different loading rates," *International Journal of Damage Mechanics*, vol. 30, Article ID 20048, 2021.
- [25] W. C. Cheng, G. Li, N. N. Liu, J. Xu, and S. Horpibulsuk, "Recent massive incidents for subway construction in soft alluvial deposits of Taiwan: a review," *Tunnelling and Underground Space and Technology*, vol. 96, Article ID 103178, 2020.
- [26] K. Wu, Z. S. Shao, S. Qin, W. Wei, and Z. Chu, "A critical review on the performance of yielding supports in squeezing tunnels," *Tunnelling and Underground Space Technology*, vol. 114, no. 1, 2021.
- [27] Z. Chu, Z. Wu, B. Liu, and Q. Liu, "Coupled analytical solutions for deep-buried circular lined tunnels considering tunnel face advancement and soft rock rheology effects," *Tunnelling and Underground Space Technology*, vol. 94, Article ID 103111, 2019.
- [28] J. B. Wang, X. R. Liu, Z. P. Song, J. Q. Guo, and Q. Q. Zhang, "A creep constitutive model with variable parameters for thenardite," *Environmental Earth Sciences*, vol. 75, no. 6, 979 pages, 2016.
- [29] B. Hu, M. Sharifzadeh, X. T. Feng, W. Guo, and R. Talebi, "Roles of key factors on large anisotropic deformations at deep underground excavations," *International Journal of Mining Science and Technology*, vol. 31, no. 2, 2021.
- [30] J. Wang, Q. Zhang, Z. Song, and Y. Zhang, "Creep properties and damage constitutive model of salt rock under uniaxial compression," *International Journal of Damage Mechanics*, vol. 29, no. 6, pp. 902–922, 2020.
- [31] K. Wu, Z. S. Shao, and S. Qin, "An analytical design method for ductile support structures in squeezing tunnels," *Archives of Civil and Mechanical Engineering*, vol. 20, 91 pages, 2020.
- [32] R. Liang, T. Xia, Y. Hong, and F. Yu, "Effects of above-crossing tunnelling on the existing shield tunnels," *Tunnelling and Underground Space Technology*, vol. 58, pp. 159–176, 2016.
- [33] H. Li, E. L. Ma, J. X. Lai et al., "Tunnelling induced settlement and treatment techniques for a loess metro in Xi'an," *Advances in Civil Engineering*, vol. 2020, Article ID 1854813, 20 pages, 2020.
- [34] W. C. Cheng, G. Li, A. N. Zhou, and J. Xu, "Rethinking the water leak incident of tunnel Luo09 to prepare for a challenging future," *Advances in Civil Engineering*, vol. 2019, Article ID 4695987, 11 pages, 2019.
- [35] X. G. Li and D. J. Yuan, "Response of a double-decked metro tunnel to shield driving of twin closely under-crossing tunnels," *Tunnelling and Underground Space Technology*, vol. 28, pp. 18–30, 2012.
- [36] J.-B. Wang, X.-R. Liu, X.-J. Liu, and M. Huang, "Creep properties and damage model for salt rock under low-frequency cyclic loading," *Geomechanics and Engineering*, vol. 7, no. 5, pp. 569–587, 2014.
- [37] T. Liu, Y. Xie, Z. H. Feng, Y. B. Luo, K. Wang, and W. Xu, "Better understanding the failure modes of tunnels excavated in the boulder-cobble mixed strata by distinct element method," *Engineering Failure Analysis*, vol. 116, Article ID 104712, 2020.

Research Article

Stability and Countermeasures for a Deposit Slope with Artificial Scarp: Numerical Analysis and Field Monitoring

Yong Hong,¹ Zhushan Shao ,¹ Guangbin Shi,¹ and Jiabao Liu²

¹*Xi'an University of Architecture and Technology, Xi'an 710055, China*

²*The 1st Engineering Co., Ltd. of China Railway 12th Bureau Group, Xi'an 710038, China*

Correspondence should be addressed to Zhushan Shao; shaozhushan@xauat.edu.cn

Received 7 June 2020; Revised 14 October 2020; Accepted 14 December 2020; Published 28 December 2020

Academic Editor: Nuwen Xu

Copyright © 2020 Yong Hong et al. This is an open access article distributed under the Creative Commons Attribution License, which permits unrestricted use, distribution, and reproduction in any medium, provided the original work is properly cited.

This paper presents the results of the stability analysis of a deposit slope with an artificial scarp in a tunnel exit and an evaluation of the effectiveness of four proposed reinforcement schemes. A typical slope section was used to study the deposit slope stability and retaining mechanisms of the reinforcement systems. A series of two-dimensional (2D) finite element models (FEM), combined with a strength reduction technique, was established using the Phase² software. According to field monitoring results, the horizontal displacements of the front, middle, and rear of the slope decreased gradually, and the safety factor increased successively. The front of the deposit slope was in a state of limit equilibrium as a result of the artificial scarp formed by long-term manual excavation. Anchors and concrete frame beams provided stress compensation and improve the stability of the deposit slope, and front prestressed anchor cables and stability piles strengthened the mechanical properties of the rock and soil masses and provided resistance at the front of the deposit. Rear stability piles prevented the front of the deposit from being pushed and the middle and rear of the deposit from being pulled and provided resistance at the front of the deposit. The field monitoring also showed that the deformation of the deposit slope was effectively controlled. The study results provide insights into the effectiveness of measures for reinforcing and maintaining the stability of deposit slope with artificial scarps.

1. Introduction

Over the past few years, transportation facilities (e.g., railroads and highways) have increasingly been extended into mountainous and hilly areas in conjunction with rapid economic and social development [1–5]. During tunnelling in such areas, rock engineers normally encounter the problem of slope stability. Statistics data shows that there are up to 148 landslides and rockfalls along the Sichuan–Tibet railway [6], and along the Duijiangyan City to Siguniang Mountain railway the stability of 32 tunnel slopes needs to be measured and evaluated [7]. Slope instabilities have threatened the safety of tunnel portals. Slope failures cause not only economic losses but also the losses of human life [8, 9]. Therefore, stability assessment and reinforcement on slope in mountainous regions are the premise for tunnel construction and operation [10].

The analysis of slope stability is a difficult task that involves the evaluation of a large number of factors, including

geology, topography, slope materials, engineering activities, and rainfall [11]. In addition, a complete analysis, including geological and geomorphological fieldwork, field monitoring, and numerical modelling, is a necessary step for slope stability assessment [8]. Thus, this analysis and assessment of slope stability are crucial to the safe design and implementation of mitigation measures. Currently, slope stability can be analyzed by the limit equilibrium method, numerical methods [12, 13], and experimental methods [14]. Numerical methods, which have been widely applied to slope stability analyses, have significantly improved the speed and accuracy of slope stability analysis. In addition, the strength reduction method has gradually become a focus of theoretical research [15–17]. Various reinforcing measures (e.g., descending slopes, drainage, plugging cracks, piles, and rock bolts) have been applied to slope stabilization [18]. Stability piles and anchor frame beams are typical reinforcing measures used for large-scale slope engineering. Many

researchers have studied the reinforcement mechanisms and reinforcement parameters of individual reinforcement countermeasures [19–21]. However, given the complexity of geological conditions, environmental factors, geotechnical parameters, and other factors involved in slope engineering, especially large-scale slope engineering, comprehensive reinforcement countermeasures are becoming more commonly applied. Comprehensive reinforcement mechanisms and optimization of reinforcement parameters related to slope stability await further study. In recent decades, much deposit slope engineering had been constructed [22–24]. The deposit slope is a kind of mechanical medium with complex characteristics such as discontinuity, heterogeneity, and anisotropy, which is different from common rock slope and soil slope [23]. In view of the complexity of the deposit slope problem, there is still a long way to study and solve practical engineering problems.

This case study focused on evaluating how an artificial scarp can influence the stability of a deposit slope and on evaluating the effectiveness of the four proposed reinforcement schemes. A two-dimensional (2D) finite element model was developed and combined with a shear strength analysis technique to analyze a typical deposit slope section to obtain insight into the pile–anchor–soil interaction mechanism and its contribution to deposit slope stability. The analysis was conducted using the Phase² software. The movement of the deposit slope was monitored during construction, and the field measurements were compared to the numerical analysis results. Using a comparison analysis, we were able to perform a comprehensive evaluation of risks associated with the Taihedong tunnel deposit slope with an artificial scarp. Furthermore, we performed a reinforcement system design to ensure the safety of tunnel slope construction and operation.

2. Geological Conditions

2.1. General Description. The Taihedong tunnel, which is located in the northern Qingxin district of the city of Qingyuan in Guangdong Province, China, is a six-lane divided expressway tunnel (Figure 1). A scarp formed by manual excavation is above the tunnel exit. The scarp is 220 m long and 25 to 40 m high, and its slope ranges from 40 to 70°. The front edge of the scarp is a broad area formed by manual excavation. The right tunnel is inside the scarp, and the left tunnel is at the edge of the scarp. The supporting capacity has been seriously weakened by manual excavation at the toe of the deposit slope. The stability of the deposit slope has also diminished as deformation of the slope has occurred and tension cracks have formed as a result of excavation of the toe of the deposit.

The slope materials at the tunnel exit are mainly composed of Quaternary deposits. A slope stability analysis of the tunnel exit and reinforcement of the unstable sliding mass are needed to assess the effects of surface water, underground water, and human engineering activities [25, 26] and ensure slope safety.

The potentially unstable geological body at the tunnel exit is a colluvial deposit with multilayer and multistage

characteristics. This deposit can be divided into three subdomains: the existing deformation area (Zone I), a potential deformation area (Zone II), and a paleo deposit area (Zone III). The volume of the deposit is approximately 2.5 million m³ (including 0.55 million m³ in Zone I). The results of a geological survey indicate that there are eight tension cracks in the existing deformation area (Zone I). These cracks are typically 40–70 m long and 20–50 cm wide, with a maximum width of nearly 1 m. The tunnel exit is located at the front of Zone I. Reinforcement was necessary to limit the deformation of the deposit slope before the tunnel excavation.

2.2. Ground Conditions. Borehole exploration and ultra-high-density resistivity testing were performed to determine the deposit profiles, and soil samples were collected for laboratory tests. Figure 2 shows a representative cross section of the study site, based on the boring tests. The deposit slope is composed of four layers: from top to bottom, gravel soil, silty clay, fully weathered argillaceous siltstone, and strongly weathered argillaceous siltstone. The parent rock of the gravel soil is mainly strongly and moderately weathered argillaceous siltstone. Gravel, silty soil, and silty clay are interspersed with the gravel soil. The parent rock of the silty clay, which was formed by weathering of argillaceous siltstone after colluvium, is mainly strongly and moderately argillaceous siltstone. Fully weathered argillaceous siltstone had completely weathered into hard and plastic silty clay. The original structure of fully weathered argillaceous siltstone, which only retained the appearance of the original rock, was completely destroyed. The strongly weathered argillaceous siltstone, with an argillaceous silty structure, massive structural deterioration, and crack development, was broken, soft, and crushable by hand. The soil and rock properties determined from the site investigation and associated laboratory tests are summarized in Table 1.

2.3. Potential Sliding Plane. The various types of relevant strata at the study site exhibit significant differences in their engineering geological properties and permeability. To better guide the layout of the slope reinforcement system, the results of in situ tests (boring tests, geological surveying and mapping, and ultra-high-density resistivity surveying) were analyzed to estimate the potential slip surface of the deposit slope. Weak contact surface layers have developed in the following ways between the different soil and rock layers and could be potential sliding planes. (1) A weak contact surface layer has developed between layers of silty clay and fully weathered argillaceous siltstone. The gravel soil layer of the colluvial deposit is a permeable stratum. Consequently, relatively impermeable silty clay and fully weathered argillaceous siltstone have been infiltrated by rainwater. A weak layer has formed between them. (2) A weak contact surface layer has formed between fully weathered argillaceous siltstone and strongly weathered argillaceous siltstone. Shallow landslides and surface cracks have caused rainwater infiltration. A deep sliding surface has formed between the fully weathered argillaceous siltstone and the strongly weathered argillaceous siltstone, as confirmed by the results

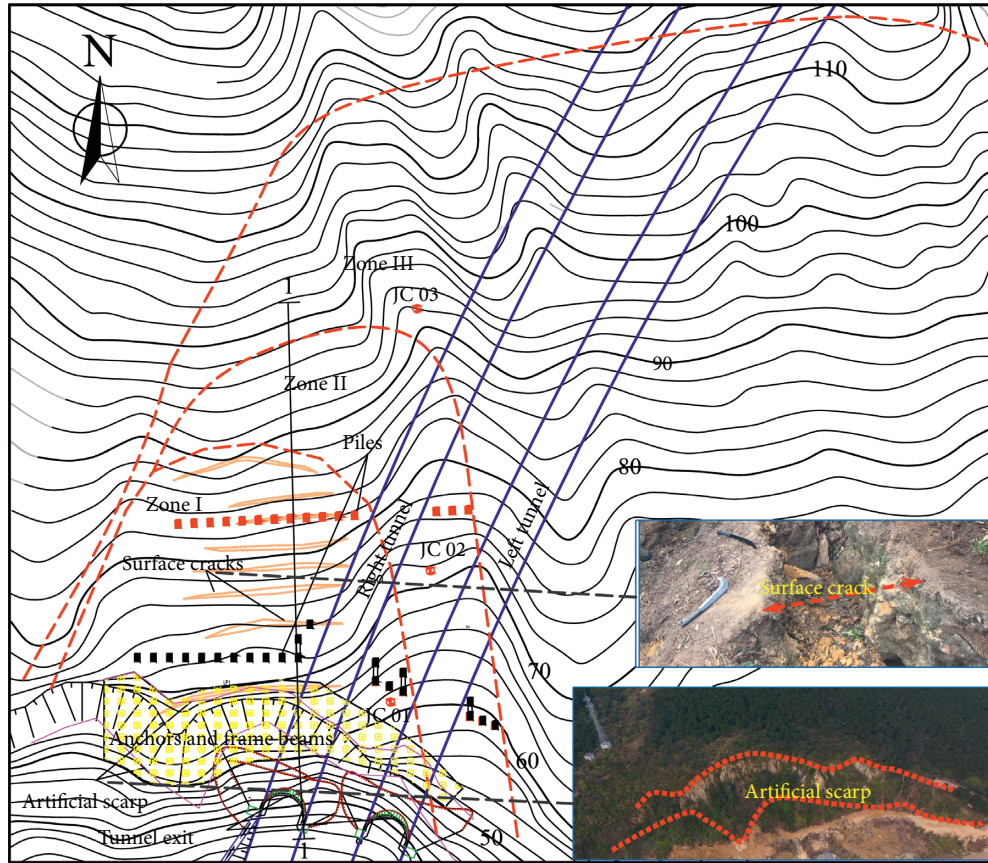


FIGURE 1: Layout of the tunnel and deposit slope.

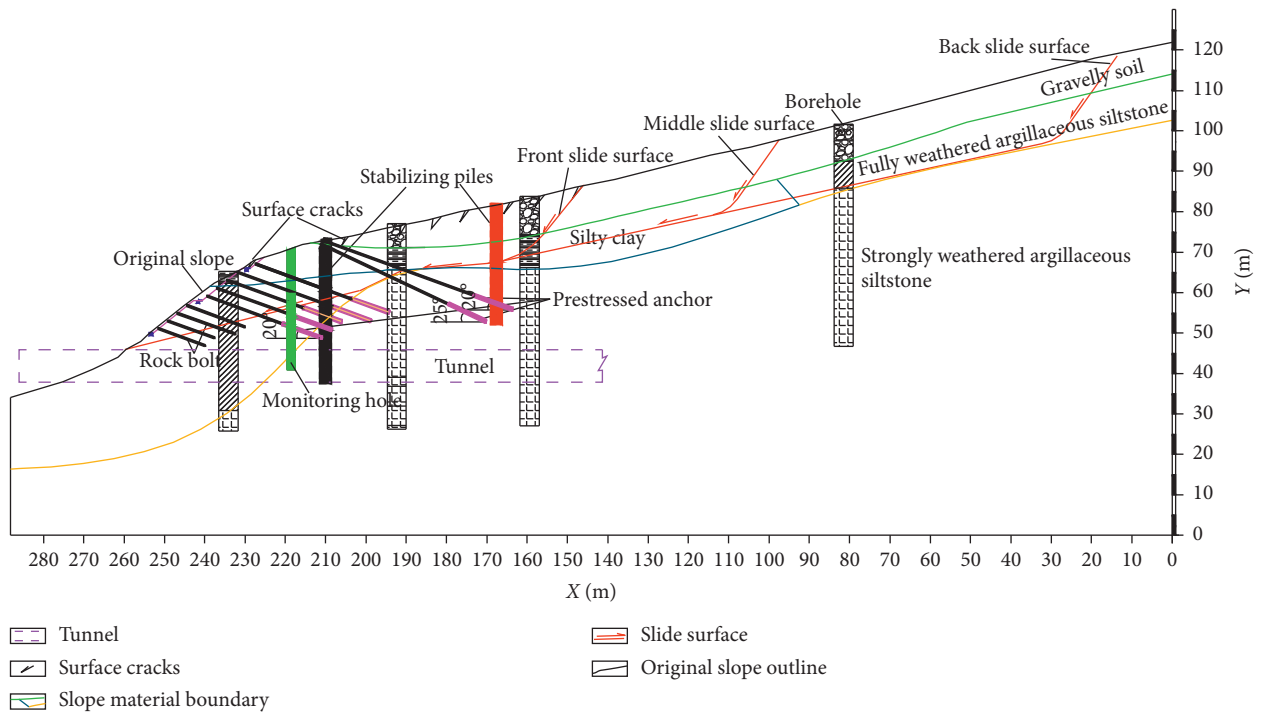


FIGURE 2: Representative geological profile along cross section 1-1 and the designed reinforcement system.

TABLE 1: Soil and rock properties.

Stratum	Total unit weight (kN/m ³)	Friction angle (°)	Cohesion (kPa)	Young's modulus (MPa)	Poisson's ratio
Gravel soil	20	18	8	35	0.13
Silty clay	19	12.5	15	25	0.25
Fully weathered argillaceous siltstone	20	15	17	32	0.30
Strongly weathered argillaceous siltstone	21	20	25	40	0.24

of the boring tests and the ultra-high-density resistivity survey.

On the basis of a comprehensive consideration of the structural conditions and activity characteristics of the deposit slope, sliding surfaces can be divided into existing sliding surfaces and potential sliding surface. The deposit slope can be divided into front, middle, and rear three-stage sliding surfaces. The leading edge of these is located at the toe of the deposit slope (Figures 1 and 2).

3. Numerical Simulation Method

3.1. Computer Program for Numerical Analysis. A 2D plane strain numerical model was developed to analyze the slope stability based on the actual geological conditions at cross section 1-1, using the Phase² software (version 8.0). One of the major features of Phase² is finite element slope stability analysis using the shear strength reduction (SSR) method. The model was developed on the basis of the mechanical properties of the soil and rock in each stratum summarized in Table 1.

Two-dimensional six-node triangular plane strain elements were used to discretize the 1-1 profile section of the deposit slope. The deposit model was uniformly meshed, with 2,183 elements connected with 4,496 nodes. All of the elements were found to be of good quality, on the basis of several trial-and-error tests. The number of bad elements was zero [27–29]. The boundary conditions of the slope model were set to constrain movement in both the x and y directions on the lateral sides and at the base of the slope, whereas the upper slope surface was unconstrained (Figure 3). Only gravity loading was applied to the model. The ratio of the horizontal to vertical stress was maintained at 1.0 [30]. The shear strength reduction (SSR) approach, with a tolerance of 0.001, was used to determine the critical strength reduction factor (SRF) [31, 32]. This approach involves the determination of the SRF or the factor of safety (SOF) by successive reduction of the cohesion (c) and internal friction angle (φ) of the soil until failure occurs.

An iterative nonconvergence failure criterion was used to determine the critical SRF [33]. The deposit slope material was considered to be an elastic and perfectly plastic substance obeying a Mohr–Coulomb failure criterion. This was controlled by keeping the peak values equal to the residual values [27, 34].

The discrete stability piles and concrete frame beams were modeled as standard linear beams with flexural rigidity [35]. The prestressed anchors were modeled as tiebacks. The anchors were modeled as fully bonded. Figure 3 illustrates

the finite element model established. The properties of the structural elements are summarized in Table 2.

3.2. Stability Analysis of Original Slope. The critical SRF and displacements for natural slope debris are shown in Figure 4. The numerical simulation results show that critical SRF values of 1.015, 1.017, and 1.029 and maximum displacements of 425 mm, 510 mm, and 855 mm were obtained for the front, middle, and rear of the deposit slope, respectively, along the 1-1 profile section. The stability analysis of the middle of the deposit slope included consideration of the front of the deposit slope. The stability analysis of the rear of the deposit slope included consideration of the front and middle of the deposit slope. The results indicate that the deposit slope is in a state of limit equilibrium. The results show very good agreement with the field measurements. The deformation area is located above the artificial scarp and the tunnel exit, at the front edge of the deformation of the deposit slope. The factors of safety for the middle and rear of the deposit slope are considerably larger than that for the front of the deposit slope. Thus, the front of the deposit slope must be reinforced before excavation.

4. Deposit Slope Reinforcement System and Analysis

4.1. Slope Reinforcement Schemes. To analyze the global stability of the deposit slope with and without a reinforcement system and to further study the effects of different reinforcement schemes, four reinforcement schemes were considered: (A) front prestressed anchor cables and stability piles; (B) front prestressed anchor cables and stability piles and rear stability piles; (C) front prestressed anchor cables and stability piles, anchors, and concrete frame beams; and (D) front prestressed anchor cables and stability piles, rear stability piles, and anchors and concrete frame beams (as adopted in engineering practice). These four schemes are summarized in Table 3. The symbol “x” indicates a type of reinforcement that was not included in the reinforcement system.

The critical SRF values (Table 4) and displacements for the deposit slope for the four different reinforcement schemes are shown in Figure 5. The results indicate that the SRF values are the lowest for the front of the deposit slope and the highest for the rear of the deposit slope for all four reinforcement cases, A, B, C, and D. These results were found to be in good agreement with the measured results. Figure 5 shows that the slope stability levels associated with schemes A and B were not significantly different. Similar

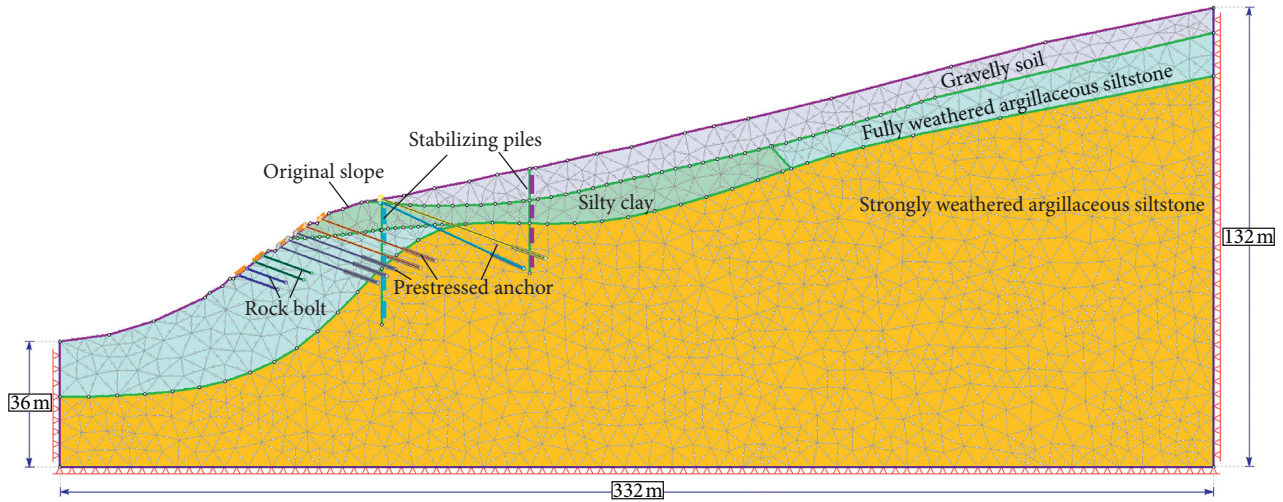


FIGURE 3: Finite element model for section 1-1.

TABLE 2: Properties of structural elements adopted in the finite element model.

Prestressed anchors	Parameter	Bolt modulus	Tensile capacity	Pretensioning force
	Value	19.5×10^4 MPa	1041 kN/1562 kN	183 kN/20 kN
Rock bolts	Parameter	Bolt modulus	Tensile capacity	Residual tensile capacity
	Value	20×10^4 MPa	220 kN	123 kN
Concrete frame beams/stabilizing piles	Parameter	Young's modulus	Poisson's ratio	Properties
	Value	3.0×10^4 MPa	0.2	Elastic

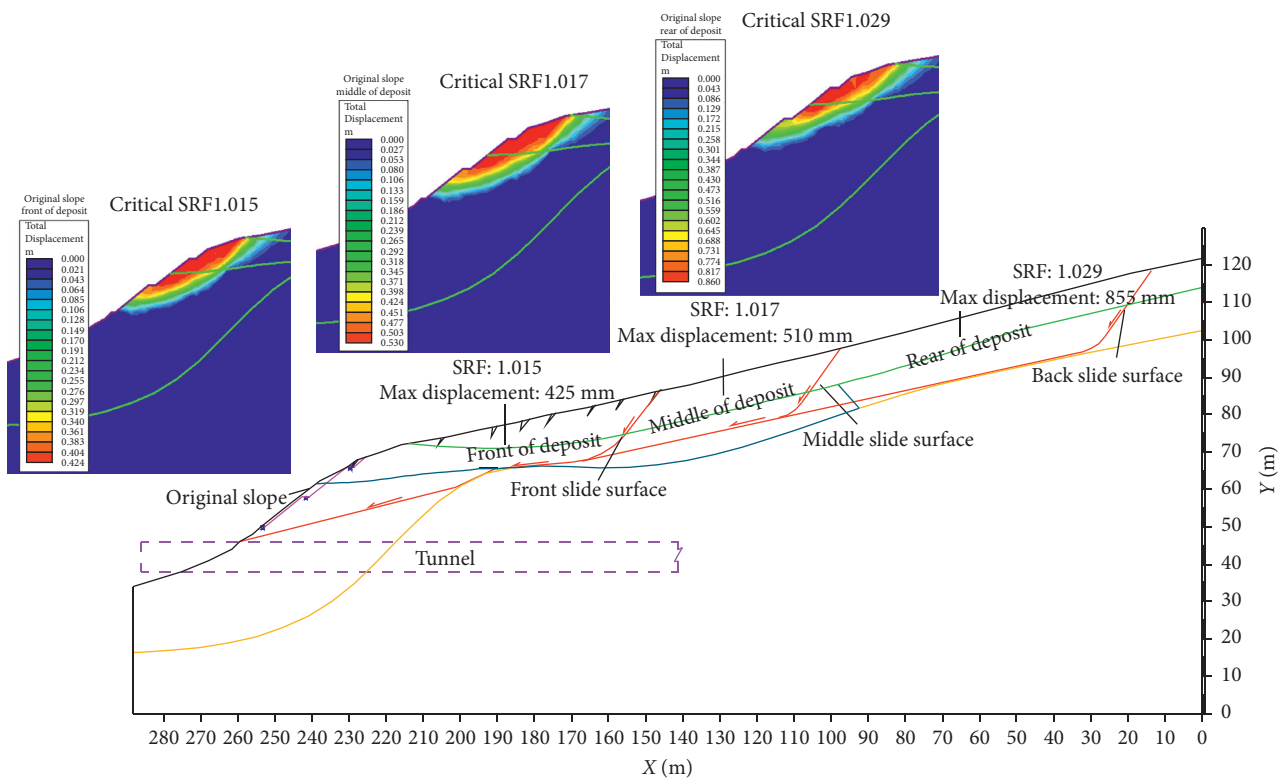


FIGURE 4: SSR analysis results for 1-1 profile section of natural deposit slope.

TABLE 3: Reinforcement schemes.

Scheme	Front prestressed anchor cables and stability piles	Rear stability piles	Anchors and concrete frame beams
O	×	×	×
A	√	×	×
B	√	√	×
C	√	×	√
D	√	√	√

TABLE 4: Critical strength reduction factor (SRF) of reinforcement schemes.

Deposit slope	SRF		
	Front	Middle	Rear
Scheme O (unreinforced)	1.015	1.017	1.029
Scheme A	1.045	1.047	1.049
Scheme B	1.047	1.050	1.055
Scheme C	1.422	1.432	1.459
Scheme D	1.428	1.440	1.515

results were obtained for schemes C and D. The reinforcement schemes differ primarily in whether the rear stability of the pile is considered. Schemes A and B were selected to analyze the function of stability piles and their influence on slope stability. Critical SRF values of 1.045 and 1.047 were obtained for schemes A and B, respectively. It appears that rear stability piles can effectively prevent the continued expansion of surface cracks, restrict deformation of the middle and rear of the deposit slope, and prevent the front soil from being pushed.

Critical SRF values of 1.045 and 1.015 were obtained for schemes A and O, respectively. The safety factor for scheme A was 3.0% higher than that for scheme O. This result shows that the front stability piles provided resistance to deformation of the soil at the front of the deposit. The prestressed anchor cables improved the mechanical properties of the rock and soil. The front of the deposit was reinforced by the prestressed anchor cables and stability piles, and its stability was improved.

Critical SRF values of 1.422 and 1.045 were obtained for schemes C and A. The safety factor for scheme C was 36.1% higher than that for scheme A and 40.1% higher than that for scheme O. As discussed previously, the deformation area was located at the front edge of the deformation body of the deposit slope. The anchors and concrete frame beams provided stress compensation for the artificial scarp and restricted the upper soil from continuing to be pulled. Thus, the analysis shows that the anchors and concrete frame beams significantly improved the stability of the deposit slope.

The front prestressed anchor cables and stability piles, the rear stability piles, and the anchors and concrete frame beams displayed different degrees of reinforcement effectiveness in the slope reinforcement system. Figure 6 and Table 4 show the numerical analysis results for the four different reinforcement schemes (Table 3). For scheme D, critical SRF values of 1.428, 1.440, and 1.515 were obtained for the front, middle, and rear of the deposit slope, respectively. These factors of safety are consistent with the GB

50330-2013 standard, which specifies a value of more than 1.30 for a grade III slope. Scheme D was therefore adopted for this engineering application.

4.2. Slope Reinforcement System. The deposit slope reinforcement systems were constructed before excavation to ensure the safe construction and operation of the Taihedong tunnel, including stabilization of piles, anchors, and concrete frame beams and establishment of groundwater drainage using collector wells. Figure 1 shows a plan view of the deposit slope reinforcement systems. Figure 2 shows a typical slope cross section used in this study.

Two rows of stabilizing piles were constructed as a primary slope reinforcement. These were buried piles with a cross section of $2.0 \times 3.0 \text{ m}^2$. The front stability piles, ranging in length from 15 to 25 m, were located approximately 4.9–12.3 m from the top of the scarp and were tied back by two prestressed anchor cables. The prestressed anchor cables were 45 m and 50 m in length and consisted of stranded wire cable. The prestressed anchor cables were installed at orientations of 20° to 25° downward, with a bond length of 10 m. A total of 13 stability piles were installed to the right of the right tunnel at a spacing of 6 m. A total of five stability piles were installed between the right tunnel and the left tunnel at a spacing of 5.5 m. A total of four stability piles were installed to the left of the left tunnel at a spacing of 5.5 m. The spacing between stability piles was 5 m near the tunnel.

The rear stability piles, which were 30 m long and spaced 6 m apart, were located at elevations of 82 to 84 m and were 50 m away from the front stability piles. Anchors and concrete frame beams were the other primary slope reinforcement measures. The rock bolts consisted of 40 mm diameter deformed steel bars, 12 and 15 m long, spaced 3 m apart. The prestressed anchor cables were stranded wire cables with lengths of 30 and 35 m. The prestressed anchor cables were installed at an orientation of 20° downward with a bond length of 10 m. Figure 7 shows the sequence of the completed reinforcement works.

4.3. Field Measurement. To observe the behavior of the deposit slope during the installation of the stability piles, anchors, and cable frame beams, three displacement monitoring holes were established, designed to monitor the deflections of the deformation body. Figures 1 and 2 show plane and cross-sectional plan views, respectively, of the displacement monitoring holes. The purposes of monitoring hole JC01, which was located ahead of the front stability pile, were to determine the deformation characteristics of the

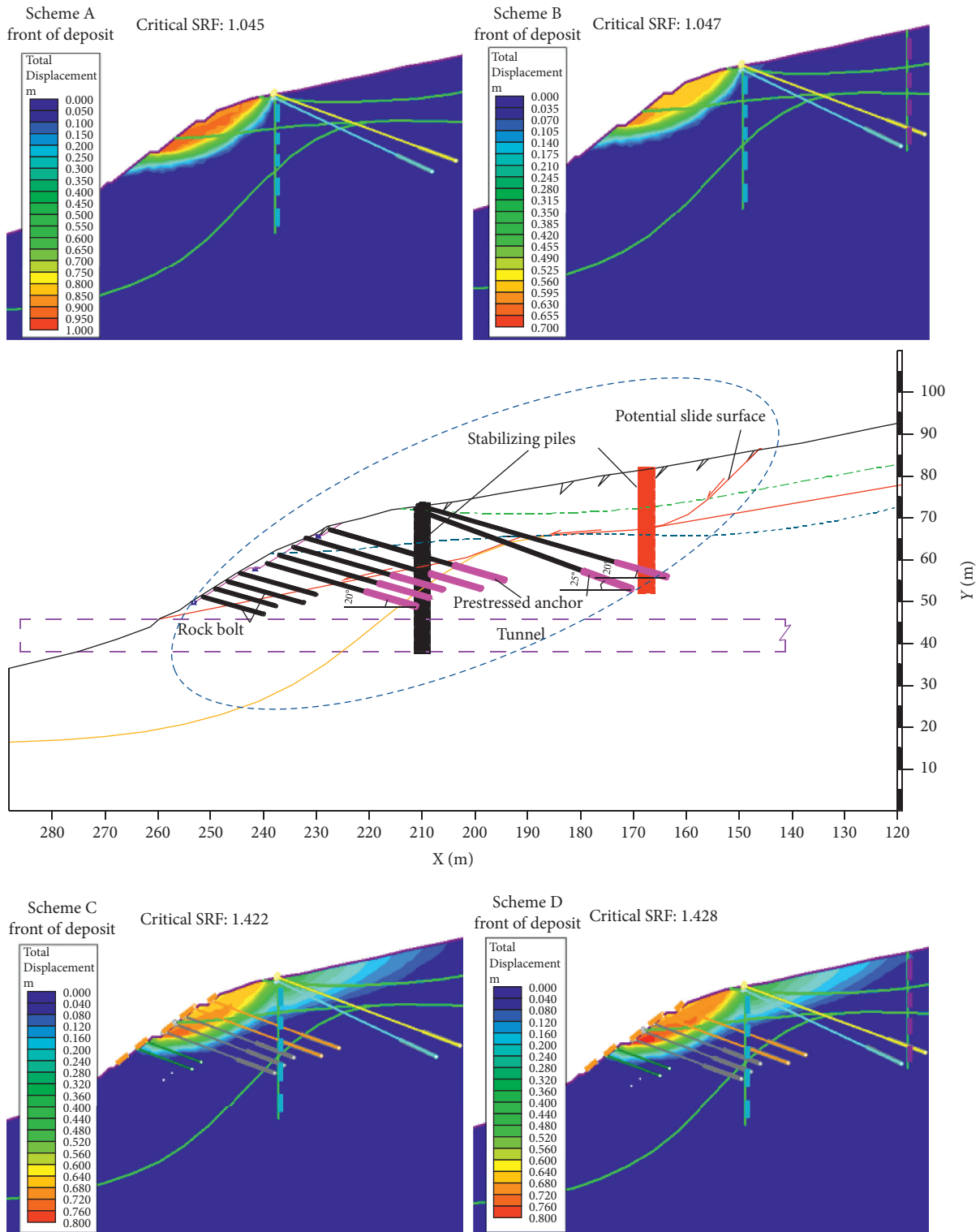


FIGURE 5: SSR analysis results for 1-1 profile section of deposit slope for different reinforcement schemes.

front slope and to forecast and warn geological disasters that may be caused by the construction of the slope reinforcement and tunnel excavation. The purpose of monitoring hole JC02, which was located between two rows of stability piles and between the left and right tunnel, was to monitor the potential sliding surface and the deformation of the deep

sliding surface. The purpose of monitoring hole JC03, which was located outside the boundary of the deformation body, was to monitor the deformation of the back edge of the deposit slope. Sliding borehole inclinometers were installed to measure the deflections of the deformation body. Figure 8 shows the instrumentation system and photograph of the in

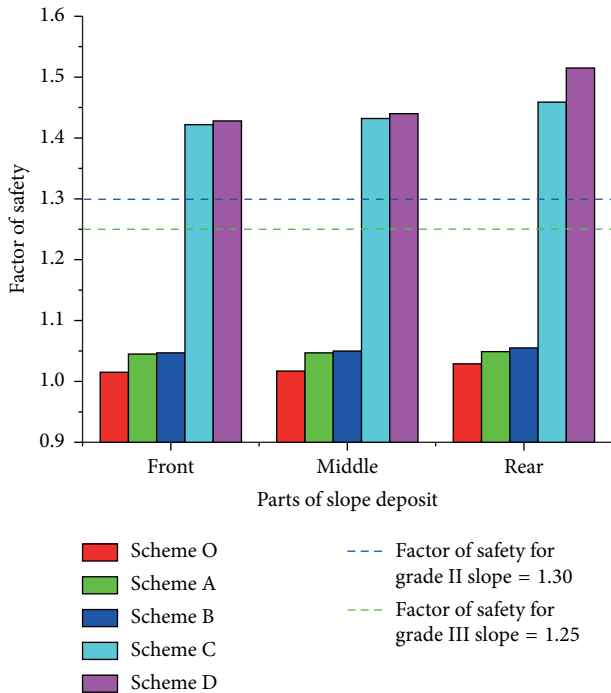


FIGURE 6: Changes in the FOS of the deposit slope for different reinforcement systems.

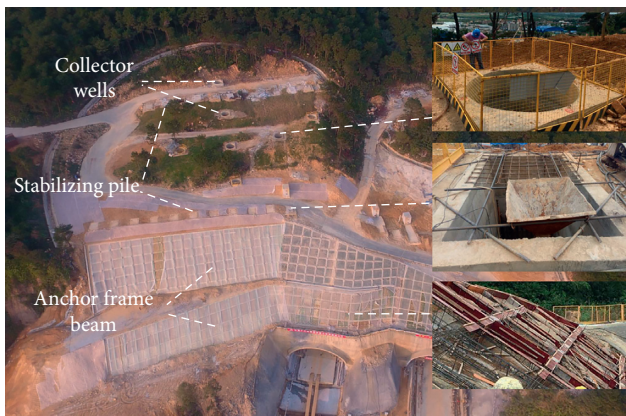


FIGURE 7: Deposit slope after stabilization work completed.

situ monitoring. An inspection of the deposit surface was also carried out.

The deformation of the deposit slope was analyzed based on the monitoring hole arrangement and the monitoring data collected. Monitoring hole JC01, which was located at the front slope and above the artificial scarp, fully reflected the deformation behavior of the front slope before, during, and after the reinforcement construction. Figure 9 shows the horizontal displacements at the three monitoring holes. The largest horizontal displacement, 56 mm, occurred at the front of the deposit slope. The maximum deformation occurred at the top of the inclinometer tube. Monitoring hole JC02, which was located in the potential deformation area, reflected the deformation of the middle slope. Figure 9(b) shows the larger deformation observed (within 28 m below the inclinometer tube). The largest horizontal displacement

of the middle deposit slope was 35 mm. The maximum deformation occurred near the top of the inclinometer tube. Monitoring hole JC03, which was located outside the potential deformation slope, reflected the deformation of the back edge of the slope and provided an early warning as to whether the deformation area of the slope would be enlarged. Figure 7 shows that the maximum horizontal displacement was 28 mm. The maximum deformation occurred near the top of the inclinometer tube.

The measurement results show that the horizontal displacement decreased gradually from the front to the rear of the deposit slope. The artificial scarp significantly reduced the stability of the slope and increased the deformation of the front slope. The horizontal displacement of the middle slope was caused by traction of the front slope. In addition, due to the thrust of the rear slope, the horizontal displacement was distributed to a certain depth. The horizontal displacement of the rear slope was small. The rear slope was pulled by the front and middle slopes. The rear edge of the slope had no obvious thrust effect on the rear slope. The results were confirmed by inspection of the deposit slope surface.

4.4. Deposit Slope Stability Analysis. Given the spatial relationship between the location of the monitoring holes and the section selected for numerical analysis, the monitoring results for hole JC01 and the numerical analysis results were judged to be comparable. Scheme D of Figure 5 shows the horizontal displacements for numerical analysis. Figure 10 shows a comparison of the measured and simulated horizontal displacements at JC01. The measured and simulated horizontal displacements exhibited the same deformation trend. The maximum horizontal displacement occurred at the borehole top, and the minimum displacement occurred at the borehole bottom. The maximum measured and simulated horizontal displacements were 56 mm and 66 mm, respectively. The measured value was approximately 84.8% of the simulated value.

As shown in Figure 10, the measured horizontal displacements of the deformation body differed from the numerical results. The reasons are as follows: (1) although monitoring hole JC01 is adjacent to the section considered in the numerical simulation, it is not in the same position, as shown in the plane layout in Figure 1. Both the measured and simulated horizontal displacements exhibit the same deformation trend, which indicates the accuracy of the simulated results to a certain extent. (2) A series of temporary measures were taken to reduce the groundwater level during the construction of the reinforcement system, which effectively improved the stability of the deposit slope. (3) Grouting reinforcement was used in a localized area above the tunnel roof during the construction of the reinforcement system. This further improved the deposit stability above the tunnel roof. The drainage holes and grouting reinforcement mentioned above were not simulated in the numerical model, but they did strengthen the reinforcement system during construction, which explains why the numerically simulated horizontal displacements were larger than the measured ones, as shown in Figure 10. The numerical

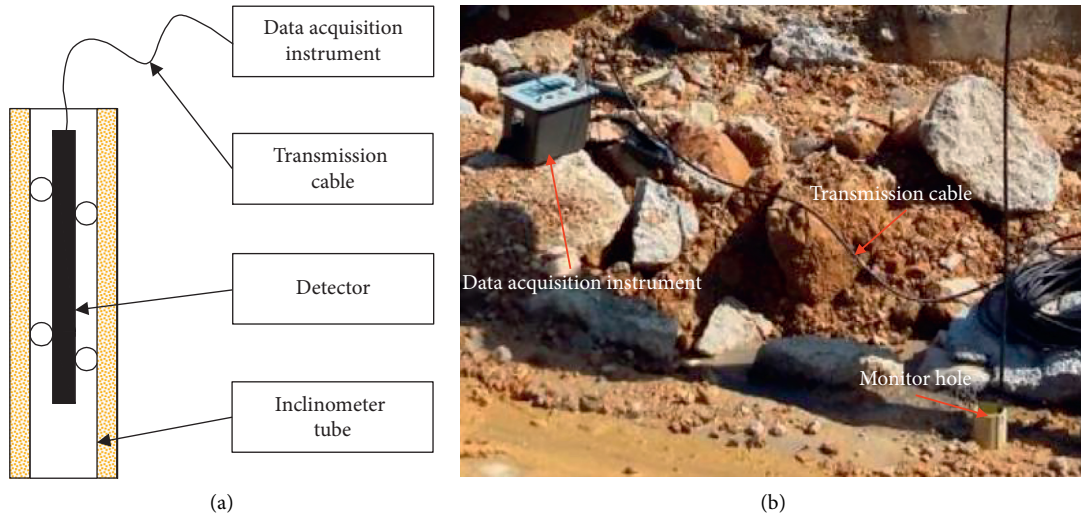


FIGURE 8: Instrumentation system and photographs of field monitoring.

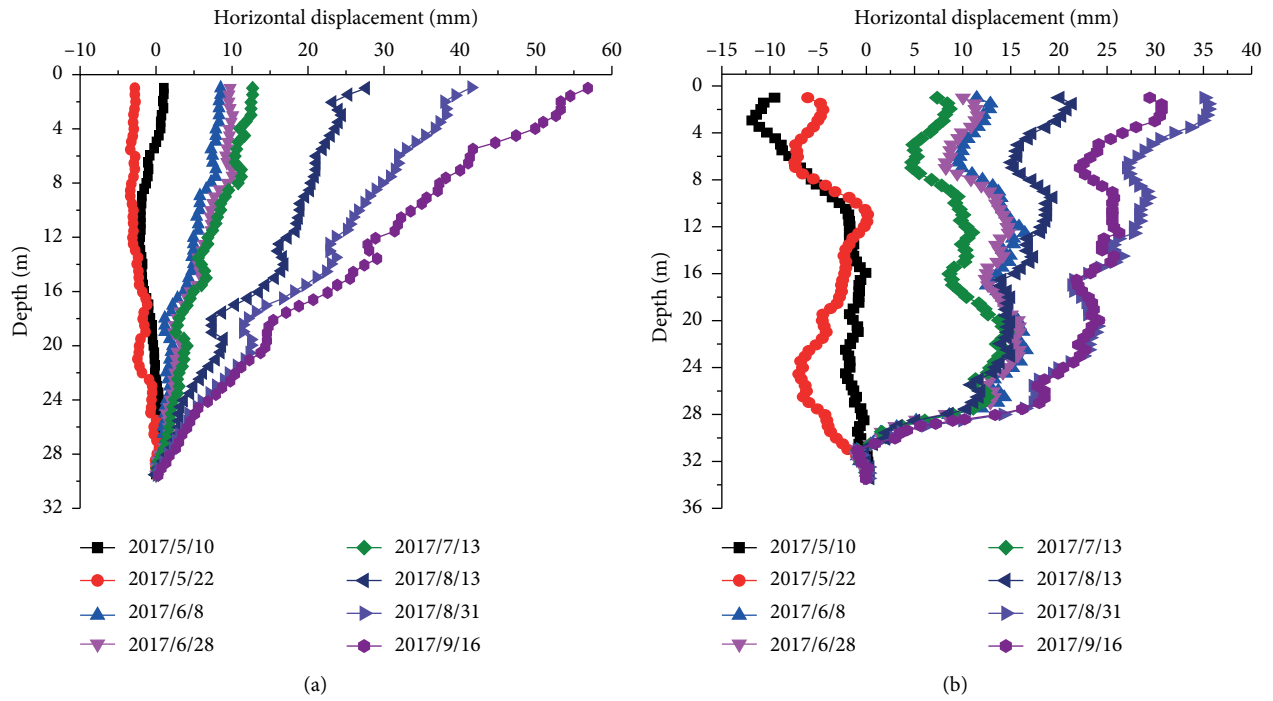


FIGURE 9: Continued.

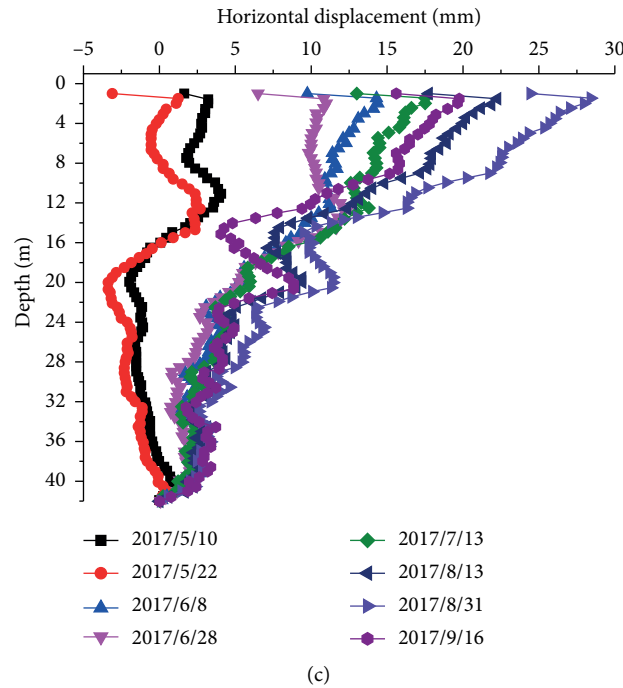


FIGURE 9: Horizontal displacements at monitoring holes: (a) JC01; (b) JC02; (c) JC03.

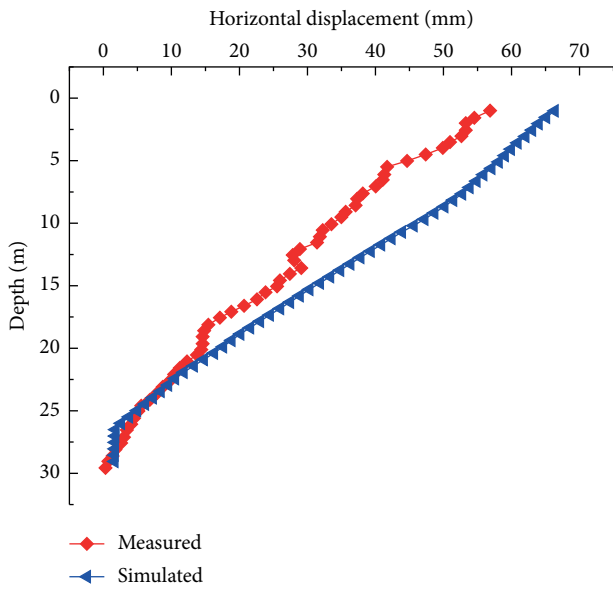


FIGURE 10: Comparison of measured and numerically predicted horizontal displacements.

simulation results were judged to be consistent with the measured results. The proposed comprehensive reinforcement scheme was therefore judged to be a suitable guide for tunnel slope reinforcement.

Figure 11 shows the displacement increment data for monitoring hole JC01 during the construction of the slope reinforcement and the initial excavation of the tunnel. The deposit slope reinforcement began in the middle of May and lasted for about two months. The tunnel excavation was carried

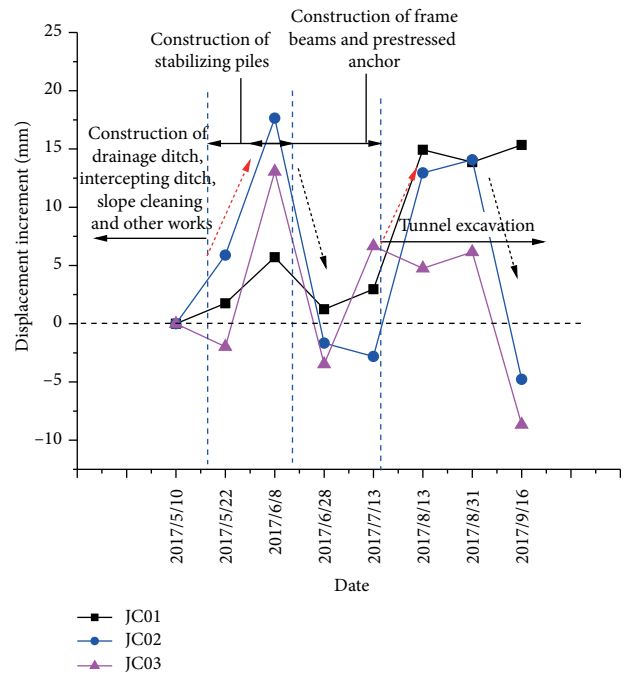


FIGURE 11: Field-monitored displacement increment data for the monitoring holes during slope reinforcement and tunnel excavation.

out after the completion of the reinforcement construction. The monitoring data indicated that the horizontal displacement of the deformation body was found to increase quickly at the beginning of the reinforcement construction and tunnel excavation data. The subsequent rate of horizontal displacement was notably reduced. Before the slope was disturbed, the

displacement increment was relatively small, less than 5 mm, and the slope was in the ultimate stability state. During the construction of the stabilizing piles, the excavation of the numerous pile holes disturbed the slope and caused a release of stress in the slope. The displacement of the slope tended to increase. However, no obvious deformation of the slope as a whole was observed. During the construction of the prestressed anchor cable frame beam, the displacement of the slope was significantly reduced because of the reinforcement effect of the stabilizing pile and the cessation of disturbance. After the completion of the comprehensive reinforcement construction, the whole reinforced slope was affected by the tunnel excavation. The displacement tended to increase, but the displacement values were all less than 18 mm. The displacement increase tended to be gentle as the tunnel excavation continued to advance. The whole slope was stable. In summary, the analysis results show that the comprehensive reinforcement treatment significantly improved the stability of the deposit slope and ensured the safety of the tunnel construction.

The measured and simulated results together indicate that the failure mode of the deposit was a typical retrogressive landslide type [36, 37]. The failure process is as follows: the scarp formed by a long-term excavation reduced the slip resistance of the toe of the deposit slope. Significant displacement occurred in front of the deposit. The strength of the rock and soil mass was further reduced by the surface cracks and rainwater infiltration. The front of the deposit slope was in a state of limit equilibrium. If no reinforcement measures are taken, the middle and rear of the deposit slope will be driven to slide. Finally, the whole deposit slope will slide. The slope failure will cause significant property damage and harm to those in the area. As for the retrogressive landslide, the optimal reinforcement site is the lower region of the deposit slope. In this engineering application, the anchors, concrete frame beams, prestressed anchor cables, and front stability piles that were installed at the front of the deposit slope effectively enhanced the safety factor and stability of the deposit slope. The rear stability piles are able to prevent the front deposit from being pushed and the middle and rear of the deposit from being pulled.

5. Conclusions

A deposit slope at an exit of the Taihedong tunnel, which is located in the city of Qingyuan in Guangdong Province, China, was analyzed in this study. The deposit slope, with surface cracks, had a scarp formed by a long-term excavation at the toe of the slope and was in a state of limit equilibrium. To determine how to best reinforce the deposit slope, four reinforcement schemes were analyzed based on field measurements and 2D numerical analysis results. The major findings of the study can be summarized as follows:

- (1) The maximum horizontal displacement and the minimum safety factor of the deposit slope with the artificial scarp formed by excavation were located at the front of the slope. The horizontal displacements of the middle and rear of the slope decreased gradually, and the safety factor increased steadily.

- (2) At the beginning of the reinforcement construction, a large number of excavation piles disturbed the slope and released stress within the slope, resulting in a significant increase in horizontal displacement. The construction of the prestressed anchor cable frame beam reinforcement resulted in less disturbance to the slope. The slope was strengthened by the stability pile, and the horizontal displacement of the slope was notably reduced as a result. The tunnel excavation disturbed the reinforced slope. The horizontal displacement increased notably at first and then became more stable. At all construction stages, the slope as a whole was in a stable state.
- (3) The slope stability of this retrogressive-type landslide was improved significantly by the use of prestressed anchor cable frame beam and front stability pile reinforcements, which provided stress compensation for the artificial scarp at the foot of the slope. The antisliding force of the slope was improved. The rear stability piles were found to be effective in preventing the front slope from being pushed and the middle and rear slopes from being pulled and in improving the overall stability of the deposit slope.

Data Availability

The data used in this study are available from the corresponding author upon request.

Conflicts of Interest

The authors declare that they have no conflicts of interest.

Acknowledgments

The authors would like to express their thanks for the financial support provided by the National Natural Science Foundation of China (Grant no. 11872287) and the Foundation of Shaanxi Key Research and Development Program (no. 2019ZDLGY01-10).

References

- [1] G. Barla, F. Antolini, and M. Barla, "Slope stabilization in difficult conditions: the case study of a debris slide in Nw Italian Alps," *Landslides*, vol. 10, no. 3, pp. 343–355, 2013.
- [2] K. Wu, Z. Shao, S. Qin, W. Wei, and Z. Chu, "A critical review on the performance of yielding supports in squeezing tunnels," *Tunnelling and Underground Space Technology*, vol. 114, no. 1, 2021.
- [3] K. Wu and Z. Shao, "Visco-elastic analysis on the effect of flexible layer on mechanical behavior of tunnels," *International Journal of Applied Mechanics*, vol. 11, no. 3, Article ID 1950027, 2019.
- [4] B. Hu, M. Sharifzadeh, X. T. Feng, W. B. Guo, and R. Talebi, "Roles of key factors on large anisotropic deformations at deep underground excavations," *International Journal of Mining Science and Technology*, vol. 31, no. 2, 2021.
- [5] K. Wu, Z. Shao, and S. Qin, "An analytical design method for ductile support structures in squeezing tunnels," *Archives of Civil and Mechanical Engineering*, vol. 20, Article ID 91, 2020.

- [6] Y. G. Xue, F. M. Kong, W. M. Yang et al., "Main unfavorable geological conditions and engineering geological problems along Sichuan—Tibet railway," *Chinese Journal of Rock Mechanics and Engineering*, vol. 39, no. 3, pp. 445–468, 2020.
- [7] J. P. Huang, C. W. Sun, X. Y. Wu, S. X. Ling, S. Wang, and R. Deng, "Stability assessment of tunnel slopes along the Dujiangyan city to Siguniang mountain railway, China," *Bulletin of Engineering Geology and the Environment*, vol. 79, 2020.
- [8] S. Sun, S. Li, L. Li et al., "Slope stability analysis and protection measures in bridge and tunnel engineering: a practical case study from Southwestern China," *Bulletin of Engineering Geology and the Environment*, vol. 78, no. 5, pp. 3305–3321, 2019.
- [9] K. Wu and Z. Shao, "Study on the effect of flexible layer on support structures of tunnel excavated in viscoelastic rocks," *Journal of Engineering Mechanics*, vol. 145, no. 10, Article ID 04019077, 2019.
- [10] N. Xu, J. Wu, F. Dai, Y. Fan, T. Li, and B. Li, "Comprehensive evaluation of the stability of the left-bank slope at the Baihetan hydropower station in southwest China," *Bulletin of Engineering Geology and the Environment*, vol. 77, no. 4, pp. 1567–1588, 2018.
- [11] D. Q. Song, J. D. Chen, and J. H. Cai, "Deformation monitoring of rock slope with weak bedding structural plane subject to tunnel excavation," *Arabian Journal of Geosciences*, vol. 11, no. 11, p. 251, 2018.
- [12] G. Zhao, Y. Yang, H. Zhang, and G. Zhang, "A case study integrating field measurements and numerical analysis of high-fill slope stabilized with cast-in-place piles in Yunnan, China," *Engineering Geology*, vol. 253, pp. 160–170, 2019.
- [13] Q. B. Zhan, X. J. Sun, C. Li et al., "Stability analysis and reinforcement of a high-steep rock slope with faults: numerical analysis and field monitoring," *Advances in Civil Engineering*, vol. 2019, p. 8, Article ID 3732982, 2019.
- [14] Z. L. Sun, L. W. Kong, and A. G. Guo, "Centrifuge modeling tests on seismic response of lower bedrock deposit slopes before and after reinforced with stabilizing piles," *Chinese Journal of Rock Mechanics and Engineering*, vol. 36, no. 6, pp. 118–128, 2017.
- [15] O. C. Zienkiewicz, C. Humpheson, and R. W. Lewis, "Associated and non-associated visco-plasticity and plasticity in soil mechanics," *Géotechnique*, vol. 25, no. 4, pp. 671–689, 1975.
- [16] M. Pirone and G. Urciuoli, "Analysis of slope-stabilising piles with the shear strength reduction technique," *Computers and Geotechnics*, vol. 102, pp. 238–251, 2018.
- [17] F. Tschuchnigg, H. F. Schweiger, and S. W. Sloan, "Slope stability analysis by means of finite element limit analysis and finite element strength reduction techniques. part I: back analyses of a case history," *Computers and Geotechnics*, vol. 70, pp. 178–189, 2015.
- [18] Z. Chen, Z. Wang, H. Xi et al., "Recent advances in high slope reinforcement in China: case studies," *Journal of Rock Mechanics and Geotechnical Engineering*, vol. 8, no. 6, pp. 775–788, 2016.
- [19] K. Wu, Z. Shao, S. Qin, and B. Li, "Determination of deformation mechanism and countermeasures in silty clay tunnel," *Journal of Performance of Constructed Facilities*, vol. 34, no. 1, Article ID 04019095, 2020.
- [20] Y. Huang, X. Xu, J. J. Liu, Huang, and W. W. Mao, "Centrifuge modeling of seismic response and failure mode of a slope reinforced by a pile-anchor structure," *Soil Dynamics and Earthquake Engineering*, vol. 131, pp. 1–11, 2020.
- [21] K. Wu, Z. Shao, S. Qin, N. Zhao, and H. Hu, "Analytical-based assessment of effect of highly deformable elements on tunnel lining within viscoelastic rocks," *International Journal of Applied Mechanics*, vol. 12, no. 3, Article ID 2050030, 2020.
- [22] W. C. Cheng, G. Li, N. N. Liu, J. Xu, and S. Horpibulsuk, "Recent massive incidents for subway construction in soft alluvial deposits of Taiwan: a review," *Tunnelling and Underground Space Technology*, vol. 96, Article ID 103178, 2020.
- [23] H. Q. Chen, R. Q. Huang, and F. Lin, "Study on the spatial engineering effect of large accumulation slope," *Chinese Journal of Geotechnical Engineering*, vol. 27, no. 3, pp. 323–328, 2005.
- [24] Z. Sun, L. Kong, A. Guo, and M. Alam, "Centrifuge model test and numerical interpretation of seismic responses of a partially submerged deposit slope," *Journal of Rock Mechanics and Geotechnical Engineering*, vol. 12, no. 2, pp. 381–394, 2020.
- [25] Y.-S. Song, W.-P. Hong, and K.-S. Woo, "Behavior and analysis of stabilizing piles installed in a cut slope during heavy rainfall," *Engineering Geology*, vol. 129–130, pp. 56–67, 2012.
- [26] G. Bicocchi, V. Tofani, M. D'Ambrosio et al., "Geotechnical and hydrological characterization of hillslope deposits for regional landslide prediction modeling," *Bulletin of Engineering Geology and the Environment*, vol. 78, no. 7, pp. 4875–4891, 2019.
- [27] V. Gupta, R. K. Bhasin, A. M. Kaynia et al., "Finite element analysis of failed slope by shear strength reduction technique: a case study for Surabhi Resort Landslide, Mussoorie township, Garhwal Himalaya," *Geomatics, Natural Hazards and Risk*, vol. 7, no. 5, pp. 1677–1690, 2016.
- [28] I. Jamir, V. Gupta, V. Kumar, G. T. Thong, and G. T. Thong, "Evaluation of potential surface instability using finite element method in Kharsali Village, Yamuna Valley, Northwest Himalaya," *Journal of Mountain Science*, vol. 14, no. 8, pp. 1666–1676, 2017.
- [29] D. P. Kanungo, A. Pain, and S. Sharma, "Finite element modeling approach to assess the stability of debris and rock slopes: a case study from the Indian Himalayas," *Natural Hazards*, vol. 69, no. 1, pp. 1–24, 2013.
- [30] P. Shilpa, M. K. Amir, K. B. Rajinder, and D. K. Paul, "Earthquake stability analysis of rock slopes: a case study," *Rock Mechanics and Rock Engineering*, vol. 45, pp. 205–215, 2012.
- [31] T. Matsui and K. C. San, "Finite element stability analysis method for reinforced slope cutting," in *Proceedings of the International Geotechnical Symposium on Theory and Practice of Earth Reinforcement*, pp. 317–322, Fukuoka, Japan, October 1988.
- [32] T. Matsui and K.-C. San, "Finite element slope stability analysis by shear strength reduction technique," *Soils and Foundations*, vol. 32, no. 1, pp. 59–70, 1992.
- [33] T. K. Nian, G. Q. Chen, S. S. Wan, and M. T. Luan, "Non-convergence criterion on slope stability FE analysis by strength reduction method," *Journal of Convergence Information Technology*, vol. 6, no. 5, pp. 78–88, 2011.
- [34] D. V. Griffiths and P. A. Lane, "Slope stability analysis by finite elements," *Géotechnique*, vol. 49, no. 3, pp. 387–403, 1999.
- [35] G. Tiwari and G. M. Latha, "Design of rock slope reinforcement: an himalayan case study," *Rock Mechanics and Rock Engineering*, vol. 49, no. 6, pp. 2075–2097, 2016.

- [36] J. W. Zhang, Y. Zou, and Y. L. Li, "Failure mechanism and stability analysis of big multi-layer deposit," *Chinese Journal of Rock Mechanics and Engineering*, vol. 35, no. 12, pp. 2479–2489, 2016.
- [37] G. H. Yang, Z. H. Zhong, Y. C. Zhang, and E. Q. Wang, "Dentification of landslide type and determination of optimal reinforcement site based on stress field and displacement field," *Chinese Journal of Rock Mechanics and Engineering*, vol. 31, no. 9, pp. 1879–1887, 2016.

Research Article

Analytical Solution of a Circular Opening considering Nonuniform Pressure and Its Engineering Application

Peng Wu,¹ Yanlong Chen ,¹ Liang Chen,^{2,3} Xianbiao Mao,¹ and Wei Zhang ²

¹State Key Laboratory for Geomechanics and Deep Underground Engineering, China University of Mining & Technology, Xuzhou 221116, China

²State Key Laboratory of Coal Resources and Safe Mining, China University of Mining & Technology, Xuzhou 221116, China

³School of Mines, China University of Mining & Technology, Xuzhou 221116, China

Correspondence should be addressed to Yanlong Chen; chenyanlong@cumt.edu.cn

Received 1 September 2020; Revised 7 November 2020; Accepted 29 November 2020; Published 24 December 2020

Academic Editor: Zhushan Shao

Copyright © 2020 Peng Wu et al. This is an open access article distributed under the Creative Commons Attribution License, which permits unrestricted use, distribution, and reproduction in any medium, provided the original work is properly cited.

Based on the Mohr–Coulomb criterion, a new analytical solution of a circular opening under nonuniform pressure was presented, which considered rock dilatancy effect and elastic-brittle-plastic failure characteristics. In the plastic zone, the attenuation of Young's modulus was considered using a radius-dependent model (RDM), and solution of the radius and radial displacement of plastic zone was obtained. The results show that many factors have important impact on the response of the surrounding rock, including lateral pressure coefficient, dilation coefficient, buried depth, and Young's modulus attenuation. Under nonuniform pressure condition, the distribution of plastic zone and deformation around the opening show obvious nonuniform characteristic: with the increasing of lateral pressure coefficient, the range of plastic zone and deformation decrease gradually at side, while they increase at roof and floor, and the location of the maximum value of support and surrounding rock response curve transfers from side to roof. Based on the analytical results and engineering practice, an optimization method of support design was proposed for the circular opening under nonuniform pressure.

1. Introduction

It is important to predict the distribution of stress and deformation accurately for a deep circular opening, which is the basis for evaluating the stability of surrounding rock and reliability of support design in deep mining and other underground engineering. Many efforts have been paid on this topic, based on the linear Mohr–Coulomb (M-C) criterion or nonlinear Hoek–Brown (H-B) criterion, considering ideal elastic-plastic model (EPM), elastic-brittle-plastic model (EBM), or strain-softening model [1–11]. In the previous researches, the stress was usually assumed to be uniform, and the influence of lateral pressure coefficient on the stress-state distribution of surrounding rock was ignored. However, many engineering practices indicate that the gravity stress of the overlying strata and the tectonic stress usually lead to the nonuniform stress distribution in the surrounding rock [12–16]. Some theoretical analysis and

numerical simulation results indicate that the lateral pressure coefficient has a remarkable influence on the stress state of surrounding rock [17–19]. Therefore, the research results without considering the effect of lateral pressure coefficient are inconsistent with the engineering conditions. In the present research, a mechanical model for circular opening with nonuniform confining pressure is first proposed. Then, the impacts of the lateral pressure coefficient on the distribution of plastic zone in the surrounding rock and the response curve of the support system were analyzed.

When the surrounding rock undergoes plastic deformation, the mechanical properties of the rock mass may change due to rock damage, such as the attenuations of internal friction angle, cohesion, Young's modulus, and Poisson's ratio. As for Young's modulus, at present, there are two methods to define the attenuation process for the postpeak rock. In the first method, Young's modulus of the postpeak rock is determined by confining pressure and minimum

principal stress, which is named the pressure-dependent Young's modulus model (PDM) [20–22]. In the other method, Young's modulus decreases with some function relationship along the radius direction of the surrounding rock, which is called the radius-dependent Young's modulus model (RDM) [23–26]. The RDM is regarded as the extension of PDM. It is thought that the close relationship between Young's modulus attenuation and rock fracture can explain efficiently the large deformation problems of surrounding rock in the deep underground engineering [27]. In the present work, the RDM is adopted to account for the effect of Young's modulus attenuation. In addition, some scholars regard the surrounding rock as viscoelastic model [28–33] and deduce a series of simplified formulas for lining pressure and tunnel convergence, which provides an effective method for predicting the time-varying displacement and stress field of surrounding rock of deep-buried circular tunnel. Wu and Shao [34–36] proposed using flexible layer to deal with large deformation of tunnel in viscoelastic rock mass. Theory and engineering practice shows that flexible layer has a good absorption effect on rock rheological deformation.

Based on the proposed mechanical model, the closed-form solutions of stress, deformation, and radius of plastic zone of the surrounding rock in circle opening with non-uniform confining pressure was obtained. The influence of the lateral pressure coefficient, dilation coefficient, and Young's modulus attenuation on the response of the surrounding rock was studied. Then, according to the engineering practices in different geological conditions, a support design method was proposed considering non-uniform stress state.

2. Analytical Solution of the Circular Opening

2.1. Fundamental Assumptions

2.1.1. Yield Criterion. As shown in Figure 1, a circular opening with a radius of r_0 is excavated in the uniform, isotropic, and continuous rock media. The internal support pressure (p_{in}) acts on the location of r_0 , and the vertical stress (σ_0) and the lateral pressure ($\lambda\sigma_0$) act at the outer boundaries, where λ is the lateral pressure coefficient. The stress of surrounding rock redistributes after excavation. When the stress reaches the yield strength of the rock mass, plastic deformation will occur, and the radius of plastic zone is represented by r_j in Figure 1.

In the paper, the linear M-C yield criterion was adopted as yield condition of surrounding rock, and it is expressed as [5, 8, 23]

$$\sigma_1 = \xi\sigma_3 + Y, \quad (1)$$

where σ_1 and σ_3 are the maximum stress and minimum principal stress, respectively, $Y = 2c \cos \varphi / (1 - \sin \varphi)$, $\xi = (1 + \sin \varphi) / (1 - \sin \varphi)$, and c and φ are the cohesion and internal friction angle of the rock, respectively.

For the plane strain problem of the circular tunnel, the hoop stress (σ_θ) and radial stress (σ_r) are the maximum and minimum principal stress, respectively [17], which means that $\sigma_1 = \sigma_\theta$ and $\sigma_3 = \sigma_r$. Then, equation (1) could be represented as

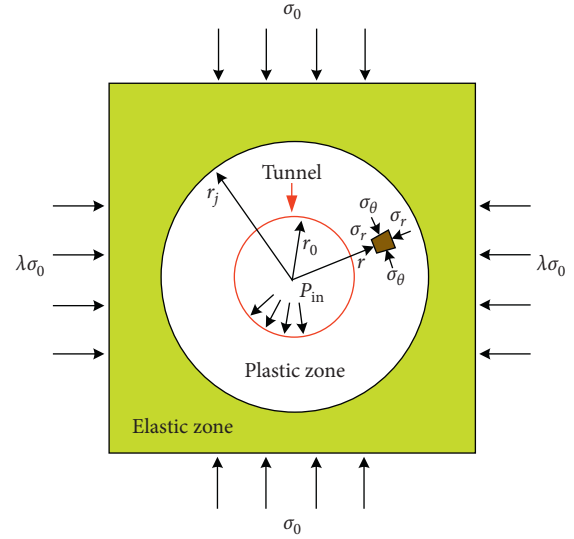


FIGURE 1: Mechanical model of a deep circular opening.

$$\sigma_\theta = \xi\sigma_r + Y. \quad (2)$$

Considering the elastic-brittle characteristic of rock mass, there is a stress drop after the peak strength [5, 9, 10], after which the rock mass undergoes postpeak-flow state. In the postpeak region, the residual rock parameters are used (residual cohesion c_r , residual internal frictional angle φ_r , and residual Poisson's ratio ν_r).

2.1.2. Attenuation of Young's Modulus. The mechanical behavior of surrounding rock is closely related with its damage in the plastic zone. The higher damage usually leads to larger deformation ability. Then, the attenuation of Young's modulus should be considered in the plastic zone. In general, the damage of the rock mass can be expressed by the attenuation of Young's Modulus. Based on previous researches [23, 24], a radius-dependent Young's modulus attenuation model (RDM) with a power function is adopted here as follows:

$$E(r) = E_r \left(\frac{r}{r_0} \right)^\alpha, \quad (3)$$

where E and E_r are the initial and residual Young's modulus, respectively, $\alpha = \log(E/E_r) / \log(r_j/r_0)$, if $\alpha = 0$ and $E = E_r$.

Equation (3) shows that the attenuation of Young's modulus is not only related to the initial and residual Young's modulus but also closely related to the radius of the plastic zone. Compared with the solution presented by Zhang and Ewy [23, 24], the solution of this paper is obtained under nonuniform pressure, and the influence of lateral pressure coefficient on the surrounding rock state is considered. Therefore, the radius of plastic zone in different positions around the surrounding rock varies, and the attenuation degree of Young's modulus is also nonuniform around the opening.

According to equation (3), at the boundaries of the plastic zone, Young's modulus should be

$$\begin{aligned} E(r)_{r=r_j} &= E, \\ E(r)_{r=r_0} &= E_r. \end{aligned} \quad (4)$$

2.2. *Fundamental Equations.* The equilibrium equation in the elastic zone and the plastic zone is

$$\frac{d\sigma_r}{dr} + \frac{(\sigma_r - \sigma_\theta)}{r} = 0. \quad (5)$$

The strain-displacement relationship is

$$\begin{aligned} \varepsilon_r &= \frac{du}{dr}, \\ \varepsilon_\theta &= \frac{u}{r}. \end{aligned} \quad (6)$$

For the plane strain problem, the constitute equation, i.e., Hooke's law, is

$$\begin{cases} \varepsilon_r = \frac{1+\nu}{E} [(1-\nu)(\sigma_r - \sigma_0) - \nu(\sigma_\theta - \sigma_0)], \\ \varepsilon_\theta = \frac{1+\nu}{E} [(1-\nu)(\sigma_\theta - \sigma_0) - \nu(\sigma_r - \sigma_0)]. \end{cases} \quad (7)$$

where ν is Poisson's ratio.

2.3. *Solution of Stress and Deformation in Elastic Zone.* To solve the problems of a circular opening under nonuniform stress field, the stress conditions at boundaries are divided into two parts [37], as shown in Figure 2. The first part (Figure 2(a)) is uniform compressive stress field with a value of $\sigma_0^u = (1+\lambda)\sigma_0/2$; and the second one (Figure 2(b)) is the stress field with horizontal tensile stress and vertical compressive stress, the value is $\sigma_0^v = (1-\lambda)\sigma_0/2$. In addition, R represents an infinite position that the stress state is equal to in situ stress.

2.3.1. *Solution of Uniform Compressive Stress Field.* Computational mechanics model of uniform compressive stress field is presented in Figure 2(a). Based on elastic theory, the stress of the elastic zone under uniform pressure is obtained on the consideration of stress boundary conditions $\sigma_{re} = p_y$ on elastic-plastic interface $r = r_j$ (where p_y is the radial stress in elastic-plastic interface):

$$\begin{cases} \sigma_{re}^U = \frac{(1+\lambda)\sigma_0}{2} \left(1 - \frac{r_j^2}{r^2}\right) + p_y \frac{r_j^2}{r^2}, \\ \sigma_{\theta e}^U = \frac{(1+\lambda)\sigma_0}{2} \left(1 + \frac{r_j^2}{r^2}\right) - p_y \frac{r_j^2}{r^2}. \end{cases} \quad (8)$$

where the subscript notation e represents the elastic zone.

2.3.2. *Solution of Stress Field with Horizontal Tensile Stress and Vertical Compressive Stress.* As shown in Figure 2(b), for a point in the surrounding rock with the position of $r = R$, the stress at the point is original rock stress, and the stress boundary conditions are $\sigma_x = -(1-\lambda)\sigma_0/2$, $\sigma_y = (1-\lambda)\sigma_0/2$, and $\tau_{xy} = 0$. So the stress expression in polar the coordinate is as follows:

$$\begin{cases} \sigma_r = -\frac{1}{2}(1-\lambda)\sigma_0 \cos 2\theta, \\ \tau_{r\theta} = \frac{1}{2}(1-\lambda)\sigma_0 \sin 2\theta. \end{cases} \quad (9)$$

Equation (9) gives the outer boundary conditions at the position of $r = R$. And the internal boundary condition under $r = r_j$ is shown as follows:

$$\begin{cases} (\sigma_r)_{r=r_j} = 0, \\ (\tau_{r\theta})_{r=r_j} = 0. \end{cases} \quad (10)$$

From equations (9) and (10), using the semi-retro-solution method [37], the stress function in the elastic zone is

$$F = f(r)\cos 2\theta. \quad (11)$$

Substituting equation (11) into the compatible equation in the polar coordinate system, i.e., $((\partial^2/\partial r^2) + (1/r)\partial/\partial r + (1/r^2) + (\partial^2/\partial\theta^2))F = 0$, the expression of stress function is determined as follows:

$$F = \left(A_1 r^4 + A_2 r^2 + A_3 + \frac{A_4}{r^2} \right) \cos 2\theta, \quad (12)$$

where A_1, A_2, A_3 , and A_4 are all constants.

The stress component is solved by equation (12), combined with the boundary condition expressions (9) and (10). The result is as follows:

$$\begin{cases} \sigma_{re}^N = \frac{1}{r} \frac{\partial F}{\partial r} + \frac{1}{r^2} \frac{\partial^2 F}{\partial \theta^2} = -\frac{(1-\lambda)\sigma_0}{2} \left(1 - 4\frac{r_j^2}{r^2} + 3\frac{r_j^4}{r^4} \right) \cos 2\theta, \\ \sigma_{\theta e}^N = \frac{\partial^2 F}{\partial r^2} = \frac{(1-\lambda)\sigma_0}{2} \left(1 + 3\frac{r_j^4}{r^4} \right) \cos 2\theta. \end{cases} \quad (13)$$

By superposing the two stress fields mentioned above, the stress equation of elastic zone of a circular opening under nonuniform stress field can be obtained:

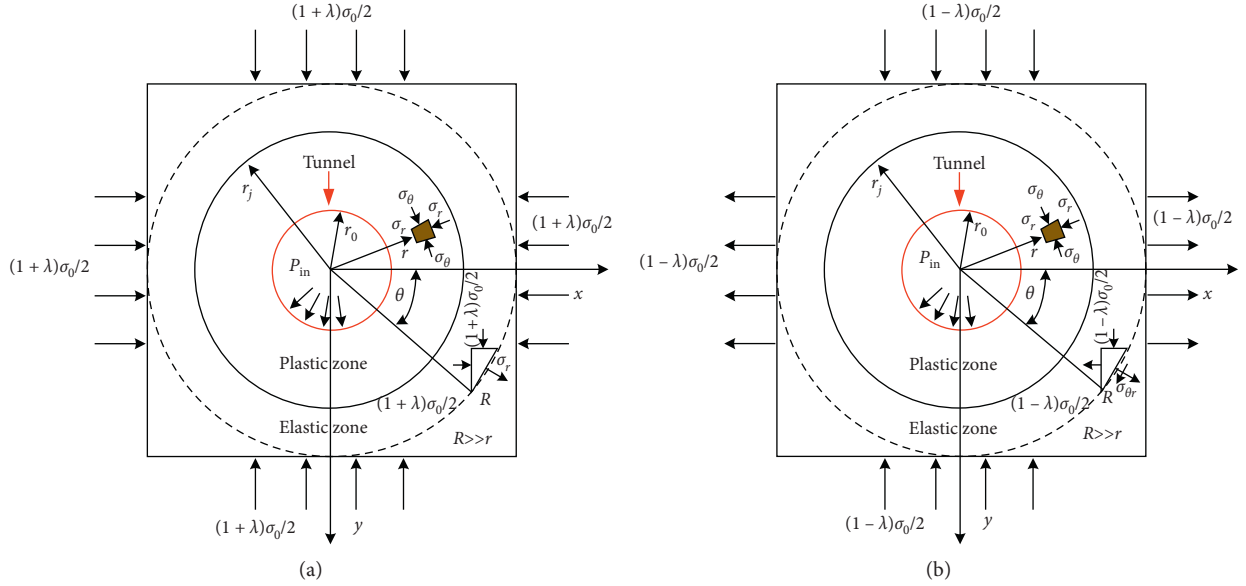


FIGURE 2: Equivalent mechanical model of a deep circular opening. (a) Uniform compressive stress field. (b) The stress field with horizontal tensile stress and vertical compressive stress.

$$\begin{cases} \sigma_{re} = \sigma_{re}^U + \sigma_{re}^N = \frac{(1 + \lambda)\sigma_0}{2} \left(1 - \frac{r_j^2}{r^2}\right) + p_y \frac{r_j^2}{r^2} - \frac{(1 - \lambda)\sigma_0}{2} \left(1 - 4\frac{r_j^2}{r^2} + 3\frac{r_j^4}{r^4}\right) \cos 2\theta, \\ \sigma_{\theta e} = \sigma_{\theta e}^U + \sigma_{\theta e}^N = \frac{(1 + \lambda)\sigma_0}{2} \left(1 + \frac{r_j^2}{r^2}\right) - p_y \frac{r_j^2}{r^2} + \frac{(1 - \lambda)\sigma_0}{2} \left(1 + 3\frac{r_j^4}{r^4}\right) \cos 2\theta. \end{cases} \quad (14a)$$

When $\lambda = 1$, equation (14a) will be transferred into the stress expression in the elastic zone under uniform pressure, as given in equation (14b), which is consistent with the results of other researchers [5]:

$$\begin{cases} \sigma_{re} = \sigma_0 - (\sigma_0 - p_y) \frac{r_j^2}{r^2}, \\ \sigma_{\theta e} = \sigma_0 + (\sigma_0 - p_y) \frac{r_j^2}{r^2}. \end{cases} \quad (14b)$$

Substituting equations (7) and (14a) into equation (6), the displacement of the elastic zone on consideration of stress instantaneous release is

$$u_{re} = \frac{(1 + \nu)r}{E} \left(\alpha_1 + \alpha_2 \frac{r_j^2}{r^2} + \alpha_3 \frac{r_j^4}{r^4} \right), \quad (15)$$

where $\alpha_1 = (1 - \lambda)\nu\sigma_0$, $\alpha_3 = (3(1 - \lambda)\sigma_0/2)$, and $\alpha_2 = ((1 + \lambda)\sigma_0/2) - 2(1 - \lambda)\nu\sigma_0 \cos 2\theta - p_y$.

When $r = r_j$, the radial displacement at elastoplastic interface is

$$u_{r_j} = \frac{(1 + \nu)r_j}{E} (\alpha_1 + \alpha_2 + \alpha_3). \quad (16)$$

As the surrounding rock is at the state of critical yield stress at elastoplastic interface, its circumferential and radial stresses both satisfy the yield criterion at peak point. Then, substituting equation (14a) into equation (2), the radial contact stress of elastoplastic zone with M-C criterion is

$$p_{y1} = \frac{1}{1 + \xi} [(1 + \lambda)\sigma_0 + 2(1 - \lambda)\sigma_0 \cos 2\theta - Y]. \quad (17)$$

When $\lambda = 1$, equation (17) can be transferred into radial contact stress in the elastoplastic zone with uniform pressure as given in equation (18), which is the same with the result given by Park [5]:

$$p_{y2} = \frac{2\sigma_0 - Y}{1 + \xi}. \quad (18)$$

2.4. Solution of Stress and Deformation of Plastic Zone

2.4.1. Stress and Radius of Plastic Zone. The stress of the plastic zone should satisfy the yield criterion and equilibrium equation under the postpeak state. By combining equations (2) and (5) with the stress boundary condition $\sigma_{rp} = p_{in}$ in the position of $r = r_0$, the expression of stress can be deduced as follows:

$$\begin{cases} \sigma_{rp} = H_1 \left(\frac{r}{r_0} \right)^{\xi_r - 1} + H_2, \\ \sigma_{\theta p} = \xi_r H_1 \left(\frac{r}{r_0} \right)^{\xi_r - 1}. \end{cases} \quad (19)$$

where the subscript notation p represents the plastic zone, $H_1 = p_{in} - (Y_r/1 - \xi_r)$, and $H_2 = (Y_r/1 - \xi_r)$.

From equations (14a) and (14b), it shows that the radius of the plastic zone should be determined first to obtain the closed analytical solution of the stress in the surrounding rock. According to the boundary conditions at the elastoplastic interface, $r = r_j$, and $(\sigma_{rp})_{r=r_j} = p_{y_1}$, the radius of the plastic zone is proposed by combining equations (17) and (19):

$$r_{j_1} = r_0 \left[\frac{(1 + \lambda)\sigma_0 + 2(1 - \lambda)\sigma_0 \cos 2\theta - Y - H_2}{(1 + \xi)H_1} - \frac{H_2}{H_1} \right]^{(1/\xi_r - 1)}. \quad (20)$$

2.4.2. Displacement of Plastic Zone. It is assumed that the circumferential strain and radial strain in the plastic zone are both composed of elastic and plastic strain, and the total strain is

$$\begin{cases} \varepsilon_{rp} = \varepsilon_r^e + \varepsilon_r^p, \\ \varepsilon_{\theta p} = \varepsilon_{\theta}^e + \varepsilon_{\theta}^p, \end{cases} \quad (21)$$

where ε_{rp} and $\varepsilon_{\theta p}$ are the total radial and circumferential strain, respectively; ε_r^p and ε_{θ}^p are the radial and circumferential plastic strain, respectively; and ε_r^e and ε_{θ}^e are the radial and circumferential elastic strain, respectively.

In any cases, the plastic deformation of rock should satisfy the flow rule, which is determined by the plastic potential function. Corresponding to the Mohr-Coulomb yield criterion, the following potential function is used:

$$\phi = \sigma_{\theta} - \beta_r \sigma_r, \quad (22)$$

where $\beta_r = (1 + \sin \psi)/(1 - \sin \psi)$ and ψ is the dilation angle of rock. If the dilation angle is not equal to the frictional angle, a nonassociated flow rule is used.

Based on plastic potential theory, the circumferential and radial plastic stresses in plastic zone are

$$\begin{cases} \varepsilon_{\theta}^p = \lambda_p \frac{\partial \phi}{\partial \sigma_{\theta p}}, \\ \varepsilon_r^p = \lambda_p \frac{\partial \phi}{\partial \sigma_r}, \end{cases} \quad (23)$$

where λ_p is the parameter related to plastic strain.

Substituting equation (22) into equation (23), the plastic strain in the plastic zone should satisfy the following relationship:

$$\varepsilon_r^p + \beta_r \varepsilon_{\theta}^p = 0. \quad (24)$$

And substituting equations (21) and (24) into equation (6), the differential equation of radial displacement of the plastic zone is

$$\frac{du_{rp}}{dr} + \beta_r \frac{u_{rp}}{r} = g(r), \quad (25)$$

where $g(r) = \varepsilon_r^e + \beta_r \varepsilon_{\theta}^e$.

According to radial displacement continuous condition $u_{rp} = u_{r_j}$ in the position of $r = r_j$, the radial displacement of the plastic zone is obtained by solving equation (25):

$$u_{rp} = \frac{1}{r^{\beta_r}} \int_{r_j}^r g(r) r^{\beta_r} dr + u_{r_j} \left(\frac{r_j}{r} \right)^{\beta_r}. \quad (26)$$

According to equation (26), it may be seen that the displacement of the plastic zone is closely related to the elastic strain $g(r)$. By taking into account Young's modulus attenuation along the radial direction, the elastic strain at a specific position in the plastic zone can be expressed as follows:

$$\begin{cases} \varepsilon_{\theta}^e = \frac{1 + \nu_r}{E(r)} [(1 - \nu_r)(\sigma_{\theta p} - \sigma_0) - \nu_r(\sigma_{rp} - \sigma_0)], \\ \varepsilon_r^e = \frac{1 + \nu_r}{E(r)} [(1 - \nu_r)(\sigma_{rp} - \sigma_0) - \nu_r(\sigma_{\theta p} - \sigma_0)]. \end{cases} \quad (27)$$

Substituting equation (27) into equation $g(r) = \varepsilon_r^e + \beta_r \varepsilon_{\theta}^e$, the expression of $g(r)$ is

$$g(r) = \frac{1 + \nu_r}{E(r)} [(1 - \nu_r - \nu_r \beta_r) \sigma_{rp} + (\beta_r - \nu_r \beta_r - \nu_r) \sigma_{\theta p} + (2\nu_r - 1)(1 + \beta_r) \sigma_0]. \quad (28)$$

Substituting equation (19) into (28), equation $g(r)$ with M-C criterion can be obtained:

$$g(r) = \frac{1 + \nu_r}{E(r)} \left[\delta_1 \left(\frac{r}{r_0} \right)^{\xi_r - 1} + \delta_2 \right], \quad (29)$$

where $\delta_1 = [(1 - \nu_r - \nu_r \beta_r) + \xi_r (\beta_r - \nu_r \beta_r - \nu_r)] H_1$ and $\delta_2 = (1 - 2\nu_r)(1 + \beta_r)(H_2 - \sigma_0)$.

From equations (26) and (29), it is known that the deformation of surrounding rock is closely related with Young's modulus in the plastic zone. In order to analyze the influence of different attenuation functions of Young's modulus on the rock deformation, based on the RDM in equation (3), three expressions for Young's modulus attenuation are proposed:

- (i) Case 1: when $\alpha = 0$ and $E = E(r) = E_r$, Young's modulus of rock in the plastic zone is the initial one, which means that the effect of Young's modulus attenuation on rock deformation is ignored
- (ii) Case 2: when $\alpha = 0$ and $E \neq E(r) = E_r$, Young's modulus of rock in the plastic zone is the residual one, which is a constant

- (iii) Case 3: when $\alpha > 0$ and $E(r) = E_r (r/r_0)^\alpha$, Young's modulus of rock in the plastic zone decreases, as defined in RDM

For Cases 1 and 2, substituting equations (29) into (26), the displacement of the plastic zone without considering the RDM is

$$u_{rp}^{\text{case1,2}} = \frac{1}{2G_r r^{\beta_r}} \left[\delta_1 f_1(r) + \delta_2 f_2(r) - \delta_1 f_1(r_j) - \delta_2 f_2(r_j) + 2G_r u_{rj} r_j^{\beta_r} \right], \quad (30)$$

where $G_r = E_r / [2(1 + \nu_r)]$, $f_1(r) = (1/r_0^{\xi_r-1}) (r^{\beta_r + \xi_r} / \xi_r + \beta_r)$, $f_1(r_j) = (1/r_0^{\xi_r-1}) (r_j^{\beta_r + \xi_r} / \xi_r + \beta_r)$, $f_2(r) = (r^{\beta_r+1} / 1 + \beta_r)$, and $f_2(r_j) = (r_j^{\beta_r+1} / 1 + \beta_r)$.

Similarly, with Case 3, substituting equations (3) and (29) into (26), the displacement of the plastic zone considering the RDM is

$$u_{rp}^{\text{case3}} = \frac{1}{2G_r r^{\beta_r}} \left[c_3 (r^{c_1} - r_j^{c_1}) + c_4 (r^{c_2} - r_j^{c_2}) + 2G_r u_{rj} r_j^{\beta_r} \right], \quad (31)$$

where $c_1 = \beta_r + \xi_r - \alpha$, $c_2 = \beta_r - \alpha + 1$, $c_3 = (\delta_1 / r_0^{\xi_r - \alpha - 1} (\beta_r + \xi_r - \alpha))$, and $c_4 = (\delta_2 / r_0^{-\alpha} (\beta_r - \alpha + 1))$.

3. Analytical Results

3.1. Model Validation and Comparison. Comparing with the closed-form solutions in the literature, the presented work takes lateral pressure coefficient and Young's modulus attenuation into consideration. When $\lambda = 1$, $\alpha = 0$, and $\nu = \nu_r$, the model provides solution for the condition of uniform stress and constant Young's modulus, which has been studied by Park [5]. To verify the accuracy of the proposed model, results of the proposed model and Park's solution were compared, as shown in Figure 3. The geometric and physical parameters are listed in Table 1.

As shown in Figure 3, when $\lambda = 1$, $\alpha = 0$, and $\nu = \nu_r = 0.2$, the proposed model in the present study provides the same result as that of Park's research. Therefore, the result of Park's research is a special case of present work.

3.2. Effect of Lateral Pressure Coefficient on the Distribution of Plastic Zone. The elastoplastic radial contact stress and the radius of the plastic zone under nonuniform pressure can be obtained by equations (17) and (19). The distribution of the plastic zone is shown in Figure 4, which shows that the lateral pressure coefficient has important influence on the distribution of the plastic zone. When $0 < \lambda < 1$, the ranges of the plastic zone in side walls are larger than those in the roof and floor; when $\lambda > 1$, the results are on the contrary. Besides, when the lateral pressure coefficient increases, the ranges of the plastic zone in side walls shrink, while those in roof and floor increase.

3.3. Effect of Lateral Pressure Coefficient on the Surface Displacement of Surrounding Rock. The radial displacement on the surface of opening under nonuniform pressure was

obtained by equations (30) and (31), as shown in Figure 5. It shows that the lateral pressure coefficient has remarkable effects on the surface displacement. With the increase of lateral pressure coefficient, the surface displacement decreases at the sides of opening and increases around the roof. For example, when $\beta_r = 2$ and λ increases gradually from 0.8 to 1.2~1.5, the displacement at roof increases by 1.07 mm to 1.37 mm, which is 202 to 258 percent; while the displacement at side wall decreases by approximately 0.39 mm to 0.67 mm, which is 30 to 52 percent. Meanwhile, when $0 < \lambda < 1$, the surface displacement at side wall is larger than at roof and floor; however, when $\lambda > 1$, the results are on the contrary.

From Figure 5, it is also known that the surface displacement increases greatly with the increase of the dilation coefficient. For example, when $\lambda = 0.8$ and β_r changes from 1 to 1.5~2, the surface displacement at roof, spandrel (60°) and side wall increase about 0.06 to 0.13 mm, 0.11 to 0.24 mm, and 0.25 to 0.63 mm, respectively, which vary by 15 to 32.5, 22.91 to 50, and 37.31 to 94.03 percent, respectively. We may conclude that the dilation coefficient also has great influence on surface displacement of surrounding rock.

3.4. Effect of the Buried Depth on Maximum Surface Displacement of Surrounding Rock. The maximum surface displacement of surrounding rock is given in Figure 6. It may be seen that the surface displacement increases with the burial depth by exponential law. For example, when $\lambda = 1.2$ and σ_0 varies from 1 to 1.2~1.8 MPa, the displacement increases from 3.3 to 20.7 mm, which means a great influence of the buried depth on the deformation of surrounding rock. It is important to note that the location of the maximum displacement is also different with different lateral pressure coefficients. When $0 < \lambda < 1$, the location of the maximum surface displacement occurs in two sides (0°); otherwise, when $\lambda > 1$, the maximum displacement distributes in the roof and floor (90° or 270°).

3.5. Effect of Lateral Pressure Coefficient on Response Curve between Surrounding Rock and Support. According to the analytical solution, the response curve between the surrounding rock and support can be deduced (Figure 7). It can be seen that the lateral pressure coefficient influences the response curve in two aspects. First, that response curve varies at different sites under specific lateral pressure coefficient. Second, the location of the maximum value of response curve transfers from side (0°) to roof (90°) with the increasing of lateral pressure coefficient, which is in accordance with the deformation of surrounding rock.

As shown by the above analysis, the influence of lateral pressure coefficient should be taken into full consideration for the design of the primary support under nonuniform pressure, and the reinforced support should be carried out in the key parts to prevent rock instability.

Table 2 illustrates the critical support resistance of each position when the surrounding rock begins to show the plastic state. If $p_{in} > p_{yc}$, it means that the part of surrounding rock is in the elastic state, whose response curve could be

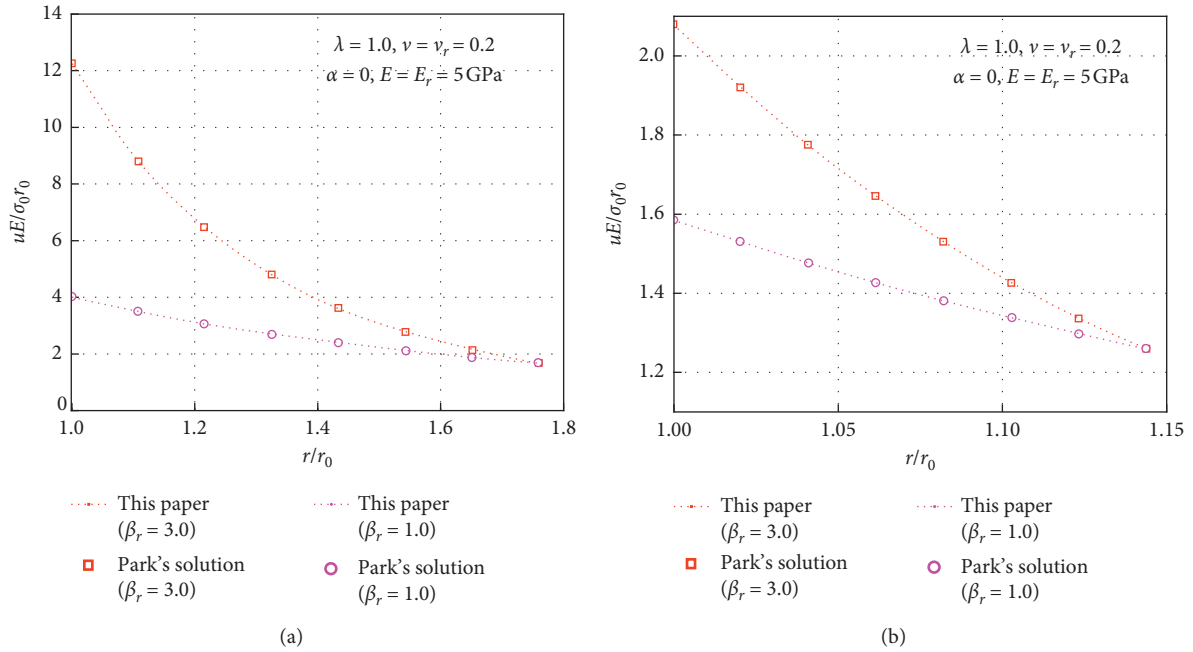


FIGURE 3: Comparisons between displacement of plastic zone in this paper and Park's solution. (a) The solution with soft rock parameters. (b) The solution with hard rock parameters.

TABLE 1: Geometrical and physical parameters of a circular opening [5].

Parameters	Hard rock	Soft rock
Radius of opening, r_0 (m)	1	1
Initial stress, σ_0 (MPa)	1	1
Internal pressure, p_{in} (MPa)	0	0
Young's modulus, E (MPa)	50,000	5000
Poisson's ratio, ν	0.2	0.2
Shear modulus, G (MPa)	20,833	2083
β_r (°)	3	3
c (MPa)	0.173	0.276
φ (°)	55	35
c_r (MPa)	0.061	0.055
φ_r (°)	52	30

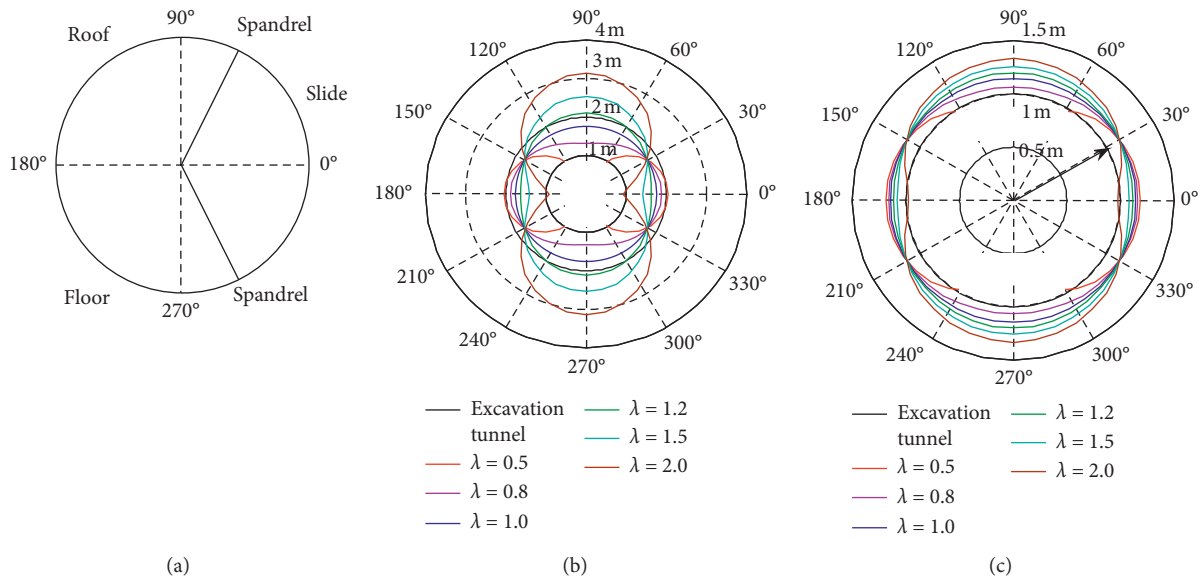


FIGURE 4: Effect of lateral pressure coefficient on the distribution of the plastic zone. (a) The polar coordinate system for the postprocessing of the results. (b) The result with soft rock parameters. (c) The result with hard rock parameters.

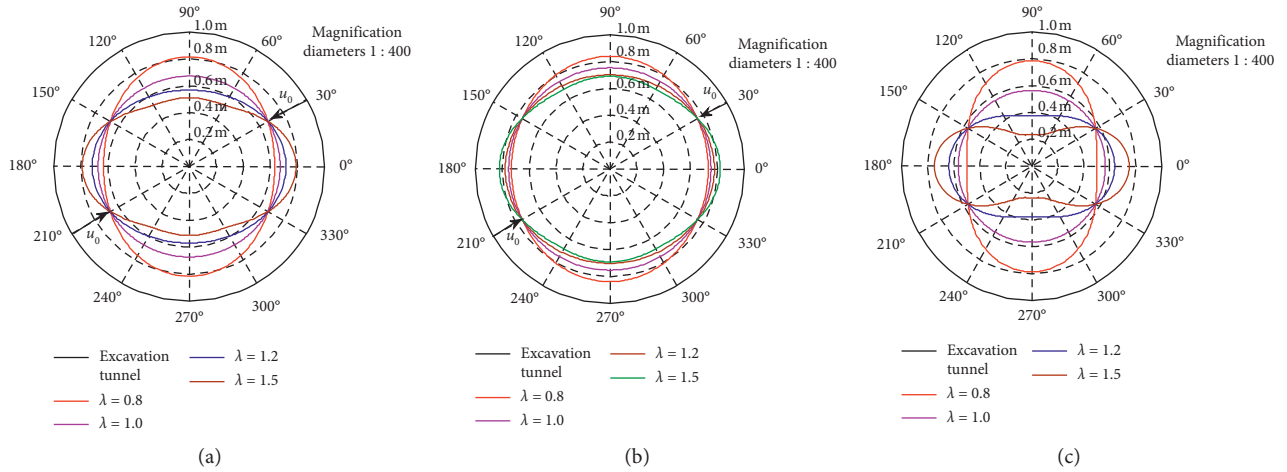


FIGURE 5: Effect of lateral pressure coefficient on the surface displacement of surrounding rock. Parameter values: $\nu = \nu_r = 0.2, \alpha = 0, E = E_r = 5 \text{ GPa}$. (a) $\sigma_0 = 1 \text{ MPa}, \beta_r = 1.5$. (b) $\sigma_0 = 1 \text{ MPa}, \beta_r = 1.0$. (c) $\sigma_0 = 1 \text{ MPa}, \beta_r = 2$. u_0 is the radial displacement at the surface of tunnel. Note. As the displacement at the surface of surrounding rock is small, the result is scaled up by 1 : 400 to give a more intuitive illustration.

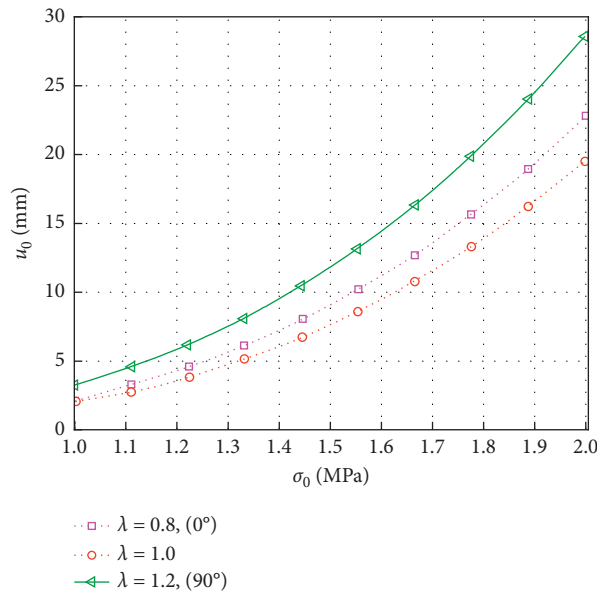


FIGURE 6: Effect of the maximum surface displacement of surrounding rock with burial depth. Parameter values: $\nu = \nu_r = 0.2, \alpha = 0, E = E_r = 5 \text{ GPa}$, and $\beta_r = 3.0$.

obtained by equation (15); on the contrary, if $p_{in} < p_{yc}$, it means the part of surrounding rock is in the plastic state, whose response curve could be obtained by equation (30) or (31).

3.6. *Effect of Young’s Modulus Attenuation on Radial Displacement of Plastic Zone.* The change law of radial displacement of the plastic zone with the increasing radius is shown in Figure 8 in different cases of Young’s modulus attenuation. It is known that Young’s modulus attenuation has great influence on radial displacement of the plastic zone when using RDM. For example, at side position (0°), comparing Case 2 and Case 3 with Case 1, the surface

displacement of plastic zone ($uE/\sigma_0 r_0$) increases 9.91 and 2.77, respectively, which is increased by 103 and 29 percent. Therefore, it indicates that the damage of surrounding rock in Case 2 is largest, while the one in Case 1 is smallest.

3.7. *Effect of Young’s Modulus Attenuation on the Response Curve between Surrounding Rock and Support.* The response curves between surrounding rock and support are shown in Figure 9 in different cases of Young’s modulus attenuation. It shows that when Young’s modulus attenuation is ignored (Case 1), the deformation of the surrounding rock and support force will be underestimated; however, when a residual value of Young’s modulus is assumed in the plastic

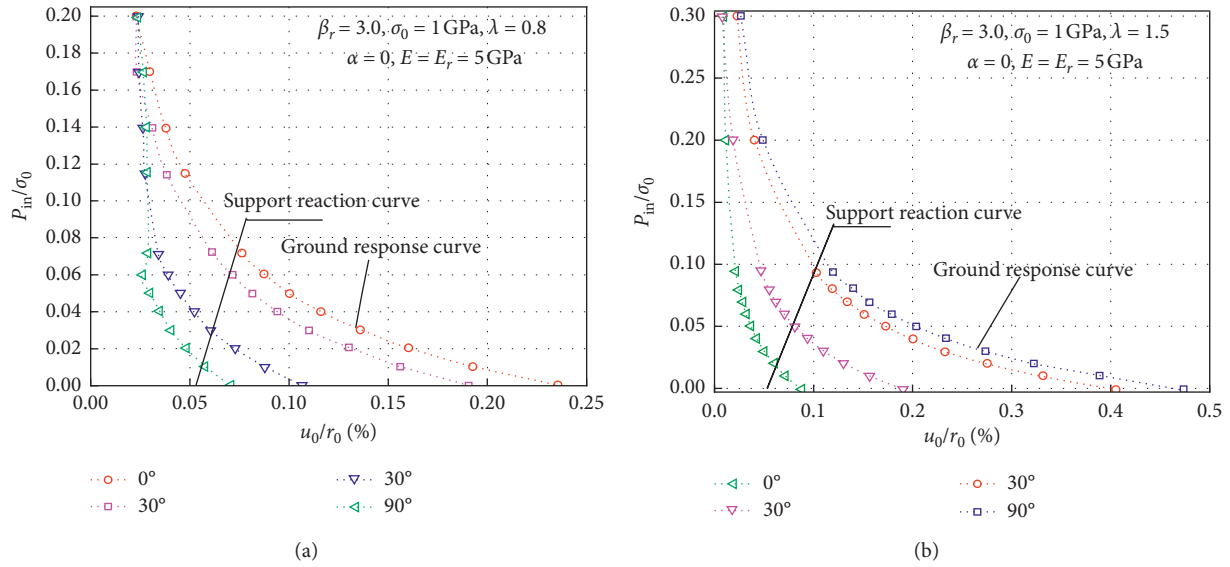


FIGURE 7: Changes of the response curve between rock wall and support frame with different lateral pressure coefficients. Parameter values: soft rock $\nu = \nu_r = 0.2$, $\beta_r = 3.0$, $\alpha = 0$, and $E = E_r = 5$ GPa. The lateral pressure coefficient of (a) $\lambda = 0.8$ and (b) $\lambda = 1.5$.

TABLE 2: The changes of critical support resistance (p_{yc}) when the surrounding rock changes from elastic to plastic state.

Lateral pressure coefficient	0° side (MPa)	30° spandrel (MPa)	60° spandrel (MPa)	90° roof (MPa)
$\lambda = 0.8$	0.243	0.200	0.115	0.072
$\lambda = 1.5$	0.094	0.200	0.414	0.520

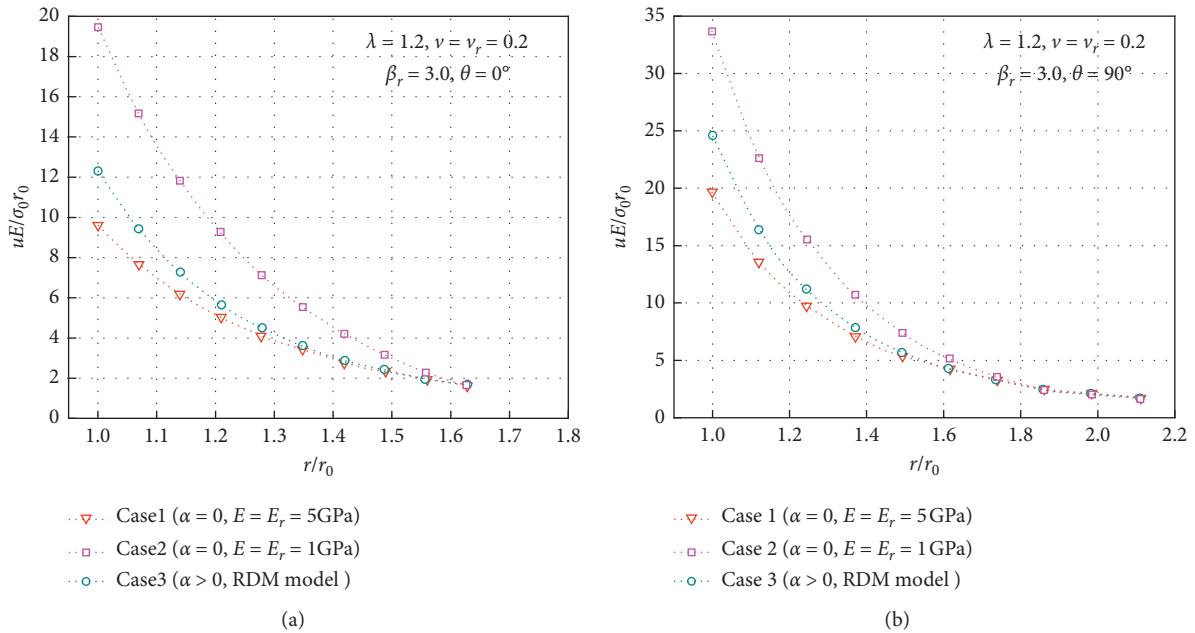


FIGURE 8: Effect of Young's modulus attenuation model on the surface displacement of surrounding rock. Soft rock, $\sigma_0 = 1$ MPa, $\lambda = 1.2$, $\nu = \nu_r = 0.2$, and $\beta_r = 3$. (a) The curve at side position (0°). (b) The curve at the roof (90°).

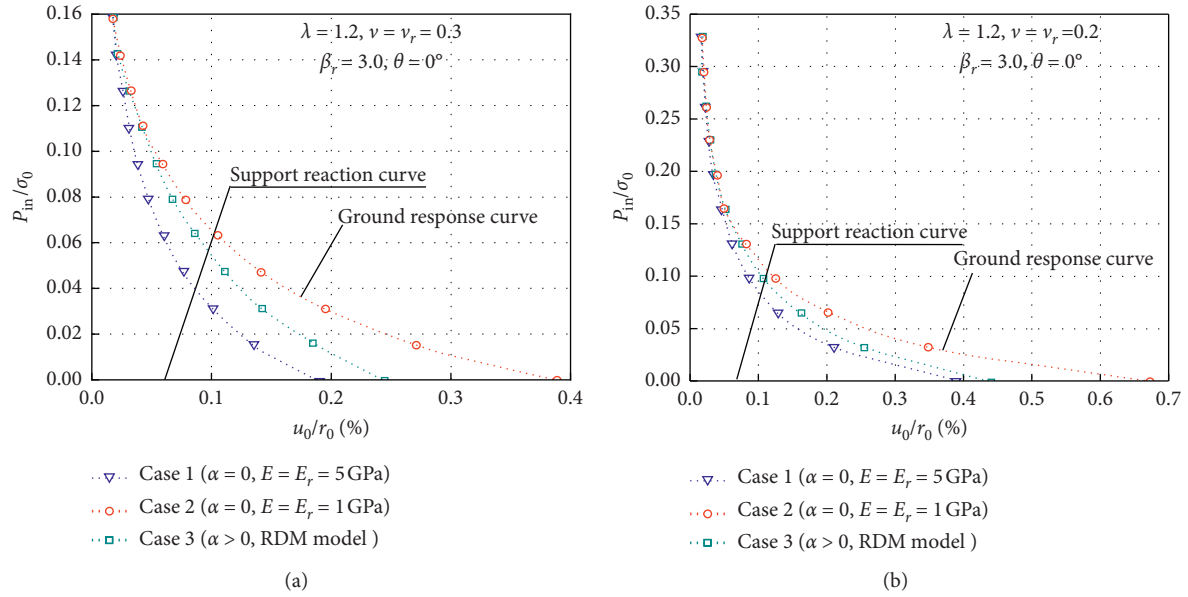


FIGURE 9: Effect of Young's modulus attenuation on the response curve between surrounding rock and support. Soft rock, $\lambda = 1.2$, $\nu = \nu_r = 0.2$, and $\beta_r = 3$. (a) The curve at side position (0°). (b) The curve at roof position (90°).

TABLE 3: Summary of cases on fracture and support scheme of opening under nonuniform pressure.

Site	Buried depth (m)	In situ stress state	Deformation features	Support schemes	Support effects
No. 1 coal mine [13]	930	$\lambda = 1.2$	Roof (floor) > side	Deep hole grouting + shallow hole grouting + whole section high-strength bolt (rope) support	Stable
No. 2 coal mine [12]	535	$\lambda = 0.3$	Roof (floor) < side	Shallow hole grouting + high-strength bolt (rope) support	Stable
No. 3 coal mine [16]	640	$\lambda = 1.5$	Roof (floor) > side	Grouting + cable anchor + flexible truss yield support	Stable
No. 4 coal mine [38]	860	$\lambda = 1.36$	Roof (floor) > side	Cable anchor + concrete lining + steel pipe arch support	Stable

zone (Case 2), the deformation of the surrounding rock and support force will be overestimated. The RDM (Case 3) seems to give more reasonable results and is recommended for design of support parameters and stability analysis of surrounding rock in the circular tunnel.

4. Support Design for Opening under Nonuniform Pressure

According to the above analysis, it is known that the lateral pressure coefficient is the main reason for nonuniform distribution of the plastic zone and deformation of surrounding rock. When $0 < \lambda < 1$, the range of the plastic zone and deformation presents larger at side than roof positions, while when $\lambda > 1$, the result is on the contrary. The rule was also verified well in many engineering practices in deep openings [12–16], as shown in Table 3.

Many support techniques of deep opening under non-uniform pressure were put forward, such as bolt-grouting support, bolt-grouting and flexible arch combined support, and bolt-mesh-cable and bolt-grouting combined support.

The principles of support design can be concluded in three aspects as follows:

- (1) Allocate the key parts (where the surrounding rock fails easily) and provide reinforced support in these areas. Due to the nonuniform deformation around the opening induced by the nonuniform initial pressure, the deformation of the support structure is inhomogeneous, which may cause buckling failure of the support. Therefore, reinforced support around the key parts is needed to control the nonuniform deformation of surrounding rock and make the support structure bear uniform pressure [38]. Specifically speaking, when $0 < \lambda < 1$, the key locations are around the side wall, and when $\lambda < 1$, the key locations are around the roof and floor.
- (2) Improve the self-bearing capacity of surrounding rock by grouting reinforcement. The grouting reinforcement can increase the strength of rock mass and make it response elastically. Based on the results of present research, the distribution of grouting boreholes can be optimized to account for the nonuniform plastic zone extent.

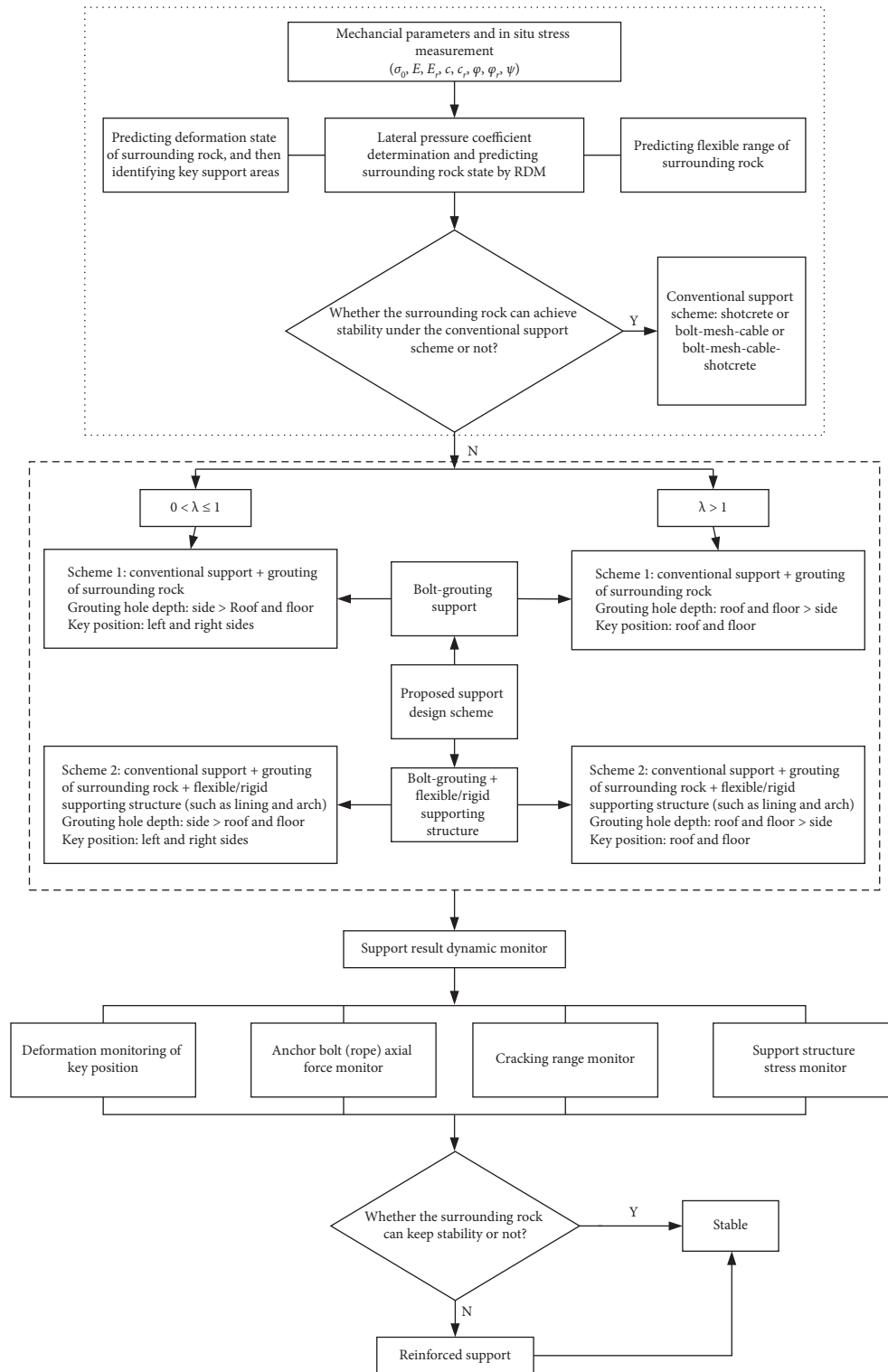


FIGURE 10: Optimization flow of support scheme of deep circular opening under nonuniform pressure.

- (3) Use flexible support structure if rigid support bears too heavy load, especially for the key parts.

Combining engineering practices and theoretical analysis results, an optimization method for support design was proposed for deep circular opening under nonuniform pressure. The specific optimization flow is shown in Figure 10.

5. Conclusions

The mechanical model of a circular opening with nonuniform pressure was proposed, which takes into account the nonassociated flaw rule and Young’s modules attenuation. The closed-form solutions of stress, deformation, and radius of the plastic zone of surrounding rock were obtained. The

influences of some factors including lateral pressure coefficient, dilation coefficient, buried depth, and Young's modulus attenuation on the state of surrounding rock were analyzed. The following conclusions can be drawn:

- (1) An analytical solution of a circular opening with nonuniform pressure was obtained. Compared with the results under uniform pressure in the literature, the proposed analytical solution is verified.
- (2) The lateral pressure coefficient has remarkable influence on the distribution of the plastic zone. When $0 < \lambda < 1$, the ranges of the plastic zone around side walls are larger than those of the roof and floor; when $\lambda > 1$, the results are on the contrary. Besides, with the increasing of lateral pressure coefficient, the range of the plastic zone in side walls shrinks gradually, while that in the roof and floor increases.
- (3) The lateral pressure coefficient has an impact on surrounding rock deformation and response curve of the support. With the consideration on the effect of lateral pressure coefficient, both the deformation and response curve show nonuniform characteristic around the tunnel.
- (4) The surface displacement of surrounding rock increases with dilation coefficient and buried depth. Therefore, their effect on deformation of surrounding rock should be taken a full account on support design.
- (5) Young's modulus attenuation has important influence on radial displacement of plastic zone. When the attenuation effect is ignored, it will cause underestimation for the deformation of surrounding rock. The RDM can be more effective on the design of support parameters and stability analysis of surrounding rock in deep circular opening.

Data Availability

The data used to support the findings of this study are available from the corresponding author upon request.

Conflicts of Interest

The authors declare that there are no conflicts of interest regarding the publication of this paper.

Acknowledgments

The authors acknowledge financial support by the National Natural Science Foundation of China (nos. 51974295 and 51874278), the Natural Science Foundation of Jiangsu Province of China (no. BK20181357), the Foundation Research Project of Jiangsu Province (no. BK20181357), the "Six Talent Peaks" Project of Jiangsu Province (no. JNHB-087), the Talent Support Project of Jiangsu Association for Science and Technology (no. 2019-134), and the Independent Research Project of State Key Laboratory of Coal Resources and Safe Mining (no. SKLCSRSM2020X04).

References

- [1] A. L. Florence and L. E. Schwer, "Axisymmetric compression of a Mohr-Coulomb medium around a circular hole," *International Journal for Numerical & Analytical Methods in Geomechanics*, vol. 2, no. 4, pp. 367–379, 2010.
- [2] C. Carranza-Torres and C. Fairhurst, "Application of the Convergence-Confinement method of tunnel design to rock masses that satisfy the Hoek-Brown failure criterion," *Tunnelling and Underground Space Technology*, vol. 15, no. 2, pp. 187–213, 2000.
- [3] S. K. Sharan, "Exact and approximate solutions for displacements around circular openings in elastic-brittle-plastic Hoek-Brown rock," *International Journal of Rock Mechanics and Mining Sciences*, vol. 42, no. 4, pp. 542–549, 2005.
- [4] S. K. Sharan, "Analytical solutions for stresses and displacements around a circular opening in a generalized Hoek-Brown rock," *International Journal of Rock Mechanics and Mining Sciences*, vol. 45, no. 1, pp. 78–85, 2008.
- [5] K.-H. Park and Y.-J. Kim, "Analytical solution for a circular opening in an elastic-brittle-plastic rock," *International Journal of Rock Mechanics and Mining Sciences*, vol. 43, no. 4, pp. 616–622, 2006.
- [6] K.-H. Park, B. Tontavanich, and J.-G. Lee, "A simple procedure for ground response curve of circular tunnel in elastic-strain softening rock masses," *Tunnelling and Underground Space Technology*, vol. 23, no. 2, pp. 151–159, 2008.
- [7] Y.-K. Lee and S. Pietruszczak, "A new numerical procedure for elasto-plastic analysis of a circular opening excavated in a strain-softening rock mass," *Tunnelling and Underground Space Technology*, vol. 23, no. 5, pp. 588–599, 2008.
- [8] S. Wang, X. Yin, H. Tang, and X. Ge, "A new approach for analyzing circular tunnel in strain-softening rock masses," *International Journal of Rock Mechanics and Mining Sciences*, vol. 47, no. 1, pp. 170–178, 2010.
- [9] R. C. F. Tonon, "Closed-form solutions for a circular tunnel in elastic-brittle-plastic ground with the original and generalized Hoek-Brown failure criteria," *Rock Mechanics & Rock Engineering*, vol. 44, no. 2, pp. 169–178, 2011.
- [10] Q. Zhang, B. S. Jiang, X. S. Wu, H. Q. Zhang, and L. J. Han, "Elasto-plastic coupling analysis of circular openings in elasto-brittle-plastic rock mass," *Theoretical and Applied Fracture Mechanics*, vol. 60, no. 1, pp. 60–67, 2012.
- [11] J.-x. Han, S.-c. Li, S.-c. Li, and W.-m. Yang, "A procedure of strain-softening model for elasto-plastic analysis of a circular opening considering elasto-plastic coupling," *Tunnelling and Underground Space Technology*, vol. 37, pp. 128–134, 2013.
- [12] W. Li, S. Li, C. Xuan et al., "Mechanism and control of failure of rock roadway support in highly stressed soft rock," *Chinese Journal of Rock Mechanics and Engineering*, vol. 34, no. 9, pp. 1836–1848, 2015.
- [13] R. Yang, Y. Li, D. Guo, L. Yao, T. Yang, and T. Li, "Failure mechanism and control technology of water-immersed roadway in high-stress and soft rock in a deep mine," *International Journal of Mining Science and Technology*, vol. 27, no. 2, pp. 245–252, 2017.
- [14] F. T. Wang, C. Zang, S. F. Wei et al., "Whole section anchor-grouting reinforcement technology and its application in underground roadways with loose and fractured surrounding rock," *Tunnelling and Underground Space Technology*, vol. 51, pp. 133–143, 2016.
- [15] X. Yang, J. Pang, D. Liu et al., "Deformation mechanism of roadways in deep soft rock at Hegang Xing'an Coal Mine,"

- International Journal of Mining Science and Technology*, vol. 23, no. 2, pp. 307–312, 2013.
- [16] P. Cao and H. Y. Li, “Instability mechanism and control measures of surrounding rock in deep tunnel under high lateral pressures,” *Chinese Journal of Geotechnical Engineering*, vol. 38, pp. 2262–2270, 2016.
- [17] Z.-H. Zhao, W.-M. Wang, and L. Wang, “Response models of weakly consolidated soft rock roadway under different interior pressures considering dilatancy effect,” *Journal of Central South University*, vol. 20, no. 12, pp. 3736–3744, 2013.
- [18] J.-f. Zou, S.-s. Li, X. Yuan, Y. Xu, H.-c. Dan, and L.-h. Zhao, “Theoretical solutions for a circular opening in an elastic-brittle-plastic rock mass incorporating the out-of-plane stress and seepage force,” *KSCSE Journal of Civil Engineering*, vol. 20, no. 2, pp. 687–701, 2016.
- [19] Z. Zhang, C. a. Tang, Q. L. Yu, and D. Duan, “Numerical simulation on influence coefficient of lateral pressure on broken zone of circular aperture,” *Rock and Soil Mechanics*, vol. 30, no. 2, pp. 413–418, 2009.
- [20] E. T. Brown, J. W. Bray, and F. J. Santarelli, “Influence of stress-dependent elastic moduli on stresses and strains around axisymmetric boreholes,” *Rock Mechanics and Rock Engineering*, vol. 22, no. 3, pp. 189–203, 1989.
- [21] M. R. Asef and D. J. Reddish, “The impact of confining stress on the rock mass deformation modulus,” *Géotechnique*, vol. 52, no. 4, pp. 235–241, 2002.
- [22] M. Verman, B. Singh, M. N. Viladkar, and J. L. Jethwa, “Effect of tunnel depth on modulus of deformation of rock mass,” *Rock Mechanics and Rock Engineering*, vol. 30, no. 3, pp. 121–127, 1997.
- [23] C. Zhang, J. Zhao, Q. Zhang, and X. Hu, “A new closed-form solution for circular openings modeled by the Unified Strength Theory and radius-dependent Young’s modulus,” *Computers and Geotechnics*, vol. 42, pp. 118–128, 2012.
- [24] R. T. Ewy and N. G. W. Cook, “Deformation and fracture around cylindrical openings in rock-I. Observations and analysis of deformations,” *International Journal of Rock Mechanics and Mining Sciences & Geomechanics Abstracts*, vol. 27, no. 5, pp. 387–407, 1990.
- [25] P. A. Nawrocki and M. B. Dusseault, “Modelling of damaged zones around openings using radius-dependent Young’s modulus,” *Rock Mechanics and Rock Engineering*, vol. 28, no. 4, pp. 227–239, 1995.
- [26] X. Chen, C. P. Tan, and C. M. Haberfield, “Solutions for the deformations and stability of elastoplastic hollow cylinders subjected to boundary pressures,” *International Journal for Numerical & Analytical Methods in Geomechanics*, vol. 23, no. 8, pp. 779–800, 2015.
- [27] P. K. Kaiser, “A New Concept to Evaluate Tunnel Performance-Influence of Excavation Procedure,” in *Proceeding of the 22nd US Symposium on Rock Mechanics*, pp. 264–271, Cambridge, MA, USA, 1981.
- [28] Z. F. Chu, Z. J. Wu, Q. S. Liu et al., “Analytical solutions for deep-buried lined tunnels considering longitudinal discontinuous excavation in rheological rock mass,” *Journal of Engineering Mechanics*, vol. 146, no. 6, Article ID 04020047, 2020.
- [29] Z. Chu, Z. Wu, B. Liu, and Q. Liu, “Coupled analytical solutions for deep-buried circular lined tunnels considering tunnel face advancement and soft rock rheology effects,” *Tunnelling and Underground Space Technology*, vol. 94, Article ID 103111, 2019.
- [30] F. Song, H. Wang, and M. Jiang, “Analytically-based simplified formulas for circular tunnels with two liners in viscoelastic rock under anisotropic initial stresses,” *Construction and Building Materials*, vol. 175, pp. 746–767, 2018.
- [31] F. Song, H. Wang, and M. Jiang, “Analytical solutions for lined circular tunnels in viscoelastic rock considering various interface conditions,” *Applied Mathematical Modelling*, vol. 55, pp. 109–130, 2018.
- [32] K. Wu and Z. S. S. Qin, “An analytical design method for ductile support structures in squeezing tunnels,” *Archives of Civil and Mechanical Engineering*, vol. 20, no. 3, pp. 1–13, 2020.
- [33] K. Wu, Z. Shao, S. Qin, N. Zhao, and H. Hu, “Analytical-based assessment of effect of highly deformable elements on tunnel lining within viscoelastic rocks,” *International Journal of Applied Mechanics*, vol. 12, no. 3, Article ID 2050030, 2020.
- [34] W. Kui, S. Z. Shan, S. Qin et al., “Determination of deformation mechanism and countermeasures in silty clay tunnel,” *Journal of Performance of Constructed*, vol. 34, no. 1, 2020.
- [35] K. Wu and Z. S. Shao, “Visco-elastic analysis on the effect of flexible layer on mechanical behavior of tunnels,” *International Journal of Applied Mechanics*, vol. 11, no. 3, 2019.
- [36] K. Wu and Z. S. Shao, “Study on the effect of flexible layer on support structures of tunnel excavated in viscoelastic rocks,” *Journal of Engineering Mechanics*, vol. 145, no. 10, 2019.
- [37] Z. L. Xu, *Elasticity*, Higher Education Press, Beijing, China, 2010.
- [38] M. He, X. Lu, and H. Jing, “Characters of surrounding rockmass in deep engineering and its non-linear dynamic-mechanical design concept,” *Chinese Journal of Rock Mechanics and Engineering*, vol. 21, no. 8, pp. 1215–1224, 2002.

Research Article

Experimental Study on the Soil Conditioning Materials for EPB Shield Tunneling in Silty Sand

Chi-Hao Cheng ^{1,2}, Shao-Ming Liao ¹, Xiao-Bo Huo ³, and Li-Sheng Chen ⁴

¹Department of Geotechnical Engineering, Tongji University, 1239 Siping Road, Shanghai 200092, China

²Shenzhen Tagen Group Co., Ltd., Shenzhen 518034, China

³Shanxi Electric Power Survey and Design Institute, Taiyuan 030001, China

⁴Shanghai Urban Construction Municipal Engineering (Group) Co., Ltd., Shanghai 200065, China

Correspondence should be addressed to Shao-Ming Liao; metroshield@foxmail.com

Received 22 September 2020; Revised 18 November 2020; Accepted 27 November 2020; Published 17 December 2020

Academic Editor: Zhushan Shao

Copyright © 2020 Chi-Hao Cheng et al. This is an open access article distributed under the Creative Commons Attribution License, which permits unrestricted use, distribution, and reproduction in any medium, provided the original work is properly cited.

Earth pressure balance (EPB) shield tunneling in a silty sand stratum is frequently faced with the wear of rotary cutter disc, clogging, or even collapse of workface due to its noncohesive and discrete properties of silty sand material. Soil conditioning is an effective way to reduce the discrete and friction properties of silty sand and to increase its rheology and fluidity, thus improving the cutting performance of EPB machines. However, soil conditioning materials were generally prepared and injected based on past limited field experiences or lab tests which were far from reality. In this article, a ground suitability test system for simulating shield tunneling in a conditioned ground was specially developed and used in a series of tests to investigate the influences of key factors of soil conditioning on the shield cutting performance. In addition, a field experiment of shield tunneling in silty sand of Wuhan Metro was conducted for verification. The major findings were obtained as follows. (1) The proposed test system performed well in simulating and assessing the cutting performance of EPB shield in conditioned soils, and the test results agreed well with the field test. (2) The soil conditioning materials can significantly reduce the cutting torque of shield tunneling in silty sand by up to 60%–70%. (3) The optimal foam and slurry parameters are suggested in the paper for shield tunneling in silty sand, respectively. (4) The test results reveal that the slurry conditioning is better than the foam in decreasing the cutter torque in silty sand. To achieve the same effect of soil conditioning, the injection ratios of foam and slurry should be 45% and 10%, respectively, to achieve the torque reduction ratio of 60%. These findings can provide a practical reference for engineers to determine the best-fit conditioning materials and construction parameters in the silty sand stratum.

1. Introduction

Tunnel engineering has played a very important role in the rapid development of infrastructure construction [1–4]. Massive earth pressure balance (EPB) shields have been put into building comprehensive networks of underground transportation in megacities of China and around the world [5–8]. However, the widespread unfavorable geologic conditions often severely hamper the normal operation of this mechanized tunneling equipment [3, 9–11]. For instance, the shield tunneling in sand is prone to serious abrasion of cutter disk, downtime of advancement, and even collapse of the workface [12–14]. The use of soil conditioning

material is an effective way to improve the applicability of EPB shields in different geological conditions [15–17].

Many researchers and engineers have paid much attention to the soil conditioning materials and their injection parameters, as well as their effects on the shield driving performance [18–29]. Wei [30] proposed that excavated soils should ideally have a “paste flow” (e.g., low inner friction, preferable consistency, low permeability, and compressibility). Massive projects [31–35] considered the injection of conditioning agents such as foams, bentonite slurry, and polymers ahead of the cutter head, into the working chamber, and along the screw conveyor, to mix with the original soil during the excavation process. Peila et al. [36]

performed a slump test to evaluate the flowability of conditioned soils, reaching a consensus that the ideal slump value is 100–250 mm [37–40]. Although the slump test is easy to perform and can reflect an overall plastic index on the behavior of the conditioned soil, the state of the prepared conditioned sample in the test is quite different from its actual states at the shield workface or in its working chamber. Several experimental devices have been developed to simulate the operation of shield machines [39, 41–48]. Sotiris et al. [46] utilized a mixing apparatus to simulate the mixing process in a shielded chamber so that the friction properties of conditioned soils can be assessed based on the difficulty in mixing. Merritt [42], Peila et al. [39], Rivas et al. [45], and Thewes and Budach [47] developed microscrew conveyor models for laboratory tests to investigate the performance of conditioned soils based on different screw speeds and tank pressures. Nevertheless, most of these experiments were carried out at atmospheric pressure without considering soil confining pressure and thus still far from application to field construction. In fact, the soils at the excavation face and in the working chamber or screws are under highly variable confining pressures. Therefore, it is necessary to perform a close-to-field dynamic simulation test on the relationship between the shield cutting performance and soil conditioning.

In this paper, a special ground suitability test system for simulating shield driving was developed, and a series of tests were conducted to investigate the effect of different conditioners on the shield cutting performance. The simulation test considered four key factors (moisture content, soil pressure, soil conditioner type, and injection ratio) that affect soil conditioning performance the most. Finally, the laboratory test results were verified by the field observations of a real tunneling project in Wuhan, China.

2. Test Setup

The test system consists of a main test device and two soil conditioning devices (a foaming device and a slurry device), as shown in Figure 1. The main test device was designed and manufactured to simulate the cutting and driving process of shield machine and automatically to measure and record the interactions between the cutter head and soils. The foaming device was used for foam generation and injection for different foaming materials. The slurry device was used for preparation and injection of bentonite slurry into the cutter head.

2.1. Foaming Device. Figure 2 shows the working principle of the foam generator, which consists mainly of a feeding system, air control system, foam mixer, and foam generator connected in series with a reducing valve, pressure gauge, flowmeter, and stop valve to gather and regulate the pressure and flow in the air and liquid mixer. Firstly, the foaming material is stored in the storage silo and connected to the air and liquid mixer. Then, it is delivered to the air-liquid mixer by the air compressor. Finally, the foam is produced by the

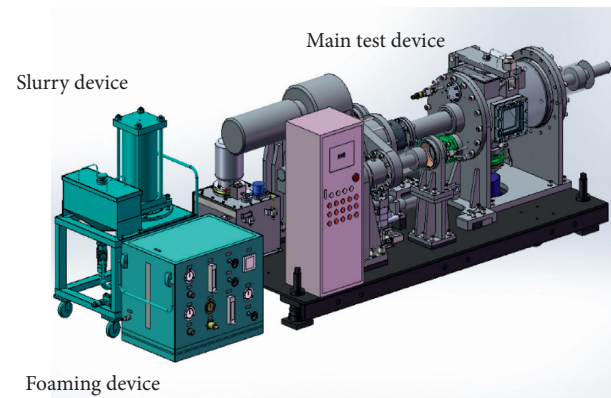


FIGURE 1: Ground suitability test system for EPB tunneling.

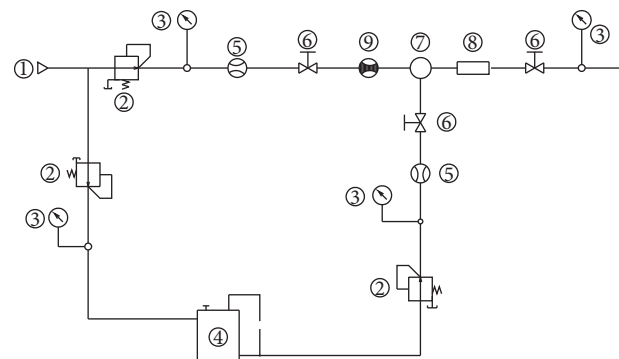


FIGURE 2: System schematic of foam device. 1, air compressor; 2, reducing valve; 3, pressure gage; 4, storage silo; 5, flowmeter; 6, stop valve; 7, air and liquid mixer; 8, foam generator; 9, air flow sensor.



FIGURE 3: Image of foam generator.

foam generator after thorough mixing. Figure 3 shows an image of the assembled foaming device, and the dimension is 0.6 meters long, 0.4 meters wide, and 0.6 meters high.

2.2. Slurry Device. The slurry device mainly includes a storage silo, syringe, and cylinder (Figure 4). The dimension of length, width, and height is 0.7 meters, 0.53 meters, and 1.3 meters. The prepared slurry is transferred from the storage silo to the syringe by controlling the ball valve. Then, the slurry is injected into the drain pipe by the extension of the cylinder. The injection pressure and rate are automatically recorded.

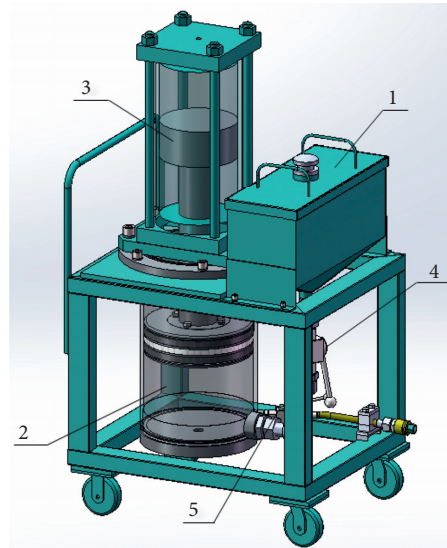


FIGURE 4: Slurry device. 1, storage silo; 2, syringe; 3, cylinder; 4, ball valve; 5, drain pipe.

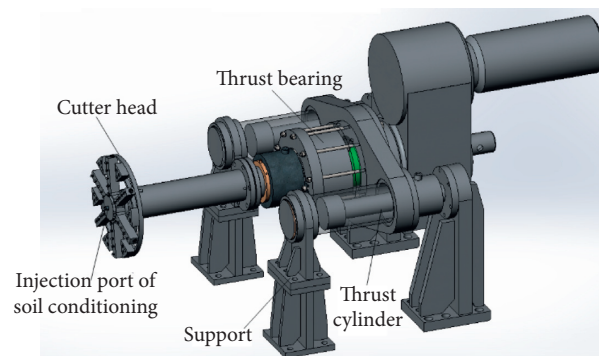


FIGURE 5: Propulsion and cutting system.

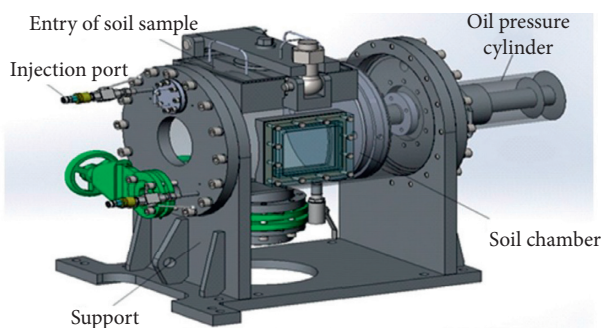


FIGURE 6: Soil chamber system.

2.3. Main Device. The main device is composed of a propulsion system, cutter head, and soil chamber system used to simulate the driving process of EPB shield machine (Figures 5 and 6). The external dimension is 3.1 meters long, 1.2 meters wide, and 1.2 meters high. The response data from the main device are automatically recorded to assess the performance of cutter head under different soil conditioning situations. Firstly, the soil sample in the soil

chamber is pressurized to a required value equivalent to the target ground pressure. By regulating oil pressure cylinder and monitoring pressure gauge, the ground overload can also be taken into consideration. Then, the soil is cut using the cutter head driven by a propulsion system under a set advance rate and rotation speed. At the same time, soil conditioning materials are injected into the front of cutter head at a rate set by the foaming device and slurry device. The torque and thrust of cutter head, earth pressure, are automatically recorded in the driving process.

According to the similarity principles of scaled test, the cutter torque for actual shield machine can be determined by the simulation test as follows:

$$T = \alpha k^3 T_0, \quad (1)$$

where T is the cutter torque of actual shield machine, T_0 is the cutter torque from the simulation test, k is the similarity ratio of the cutter diameter between the test device and shield machine, and α is the calibration coefficient of the test system ($\alpha = 1.1 \sim 1.3$).

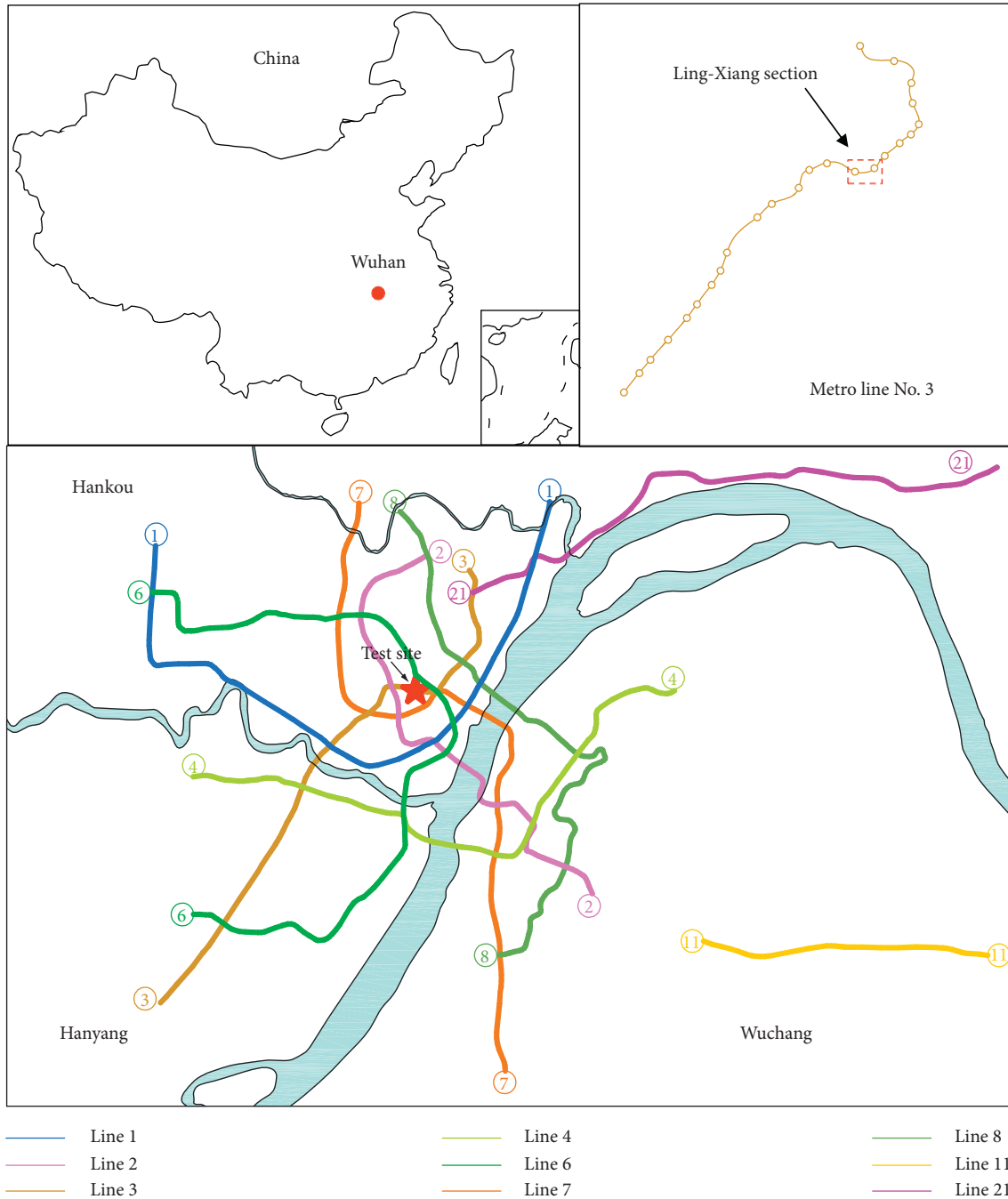


FIGURE 7: Metro lines of Wuhan city and the location of field test site.

3. Material Preparation

Material preparation involves a series of material tests on soil samples, foam, and slurry, which should be all prepared and optimized before the main test begin.

3.1. Soil. The soil samples for the test were silty sand taken from the tunnel site of Ling-Xiang tunnel section, of Wuhan Metro Line 3, which is 1200 m, mainly located in silty sand,

as shown in Figures 7–9. The natural moisture content of the silty sand ranges from 10% to 30% with internal friction angle of 30° , as shown in Table 1. The silty sand from the tunnel site was remixed with water and reconsolidated to be the same moisture content and friction angle as its natural state in the pressurized soil chamber. The processing steps begin with the air drying of the soil sample, then followed by grinding, sieving, mixing, sealing, and storing. Finally, the soil samples are layered compacted to achieve the required moisture content and density. Otherwise, considering the

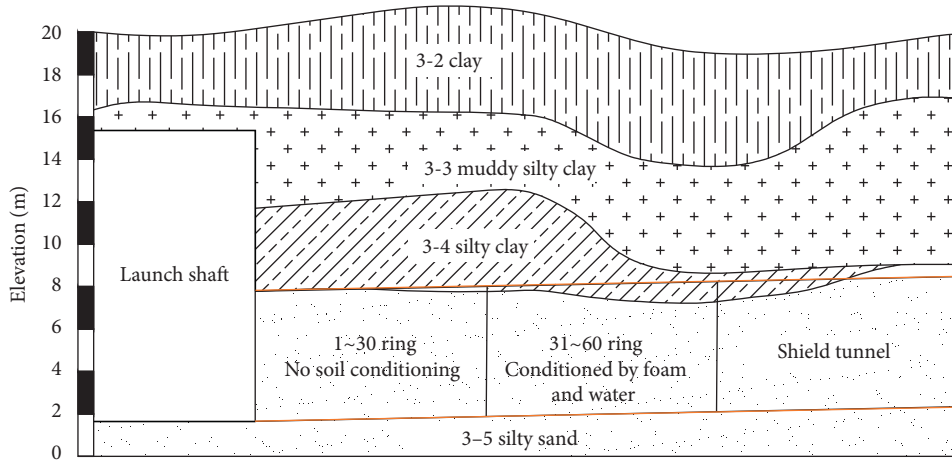


FIGURE 8: Geological profile of the experimental tunnel.



FIGURE 9: Test sample of silty sand from the tunnel site.

TABLE 1: Physical and mechanical parameters of soils.

No.	Soil layers	γ (kN/m ³)	ω (%)	c (kPa)	φ (°)	E_s (MPa)
3-2	Clay	18.0	18.6	18	10	5.0
3-3	Muddy clay	17.5	22.5	10	4	3.0
3-4	Silty clay	18.0	29.2	13	14	5.5
3-5	Silty sand	18.5	30.5	0	30	14

Note. γ is the unit weight; ω is the water content; c is the cohesion; φ is the friction angle; E_s is the constrained modulus.

difference in mechanical property between original soil and remolded soil, the calibration coefficient α is adopted in equation (1). According to the natural particle grading curve of the silty sand (marked by red line in Figure 10), the recommended soil conditioning material for the soil is either foam or slurry [49, 50].

3.2. Foam. The foam conditioning material for shield tunneling is usually prepared by a foaming device to mix water with foaming agent, which is a surfactant that reduces surface tension of water to create the foam or increases its colloidal stability by inhibiting coalescence of bubbles. In order to find the best fit foaming and injection parameters for the silty sand, the foams were prepared by adjusting the foaming device to have a different foam expansion ratio (F_{er} , see equation (2)) and foam stability (F_s , see equation (3)), which were described in detail by Wu et al. [51].

The recommended value of F_{er} for shield tunneling is 20–40:

$$F_{er} = \frac{V_f}{V_l}, \quad (2)$$

where V_f is the volume of foam and V_l is the volume of the foaming solution.

F_s can be measured by the foam dissipation test using the following equation:

$$F_s = \frac{m_d}{m_o}, \quad (3)$$

where m_d is the weight of the dissipated foam and m_o is the initial weight of the foam. In shield tunneling practice, the weight of dissipated foam is changing over time, and thus, the half-dissipation time ($T_{1/2}$) (i.e., the time during when $F_s = 0.5$) of foam is generally used to assess the stability of foam. The value ranges from 15–20 min for shield tunneling.

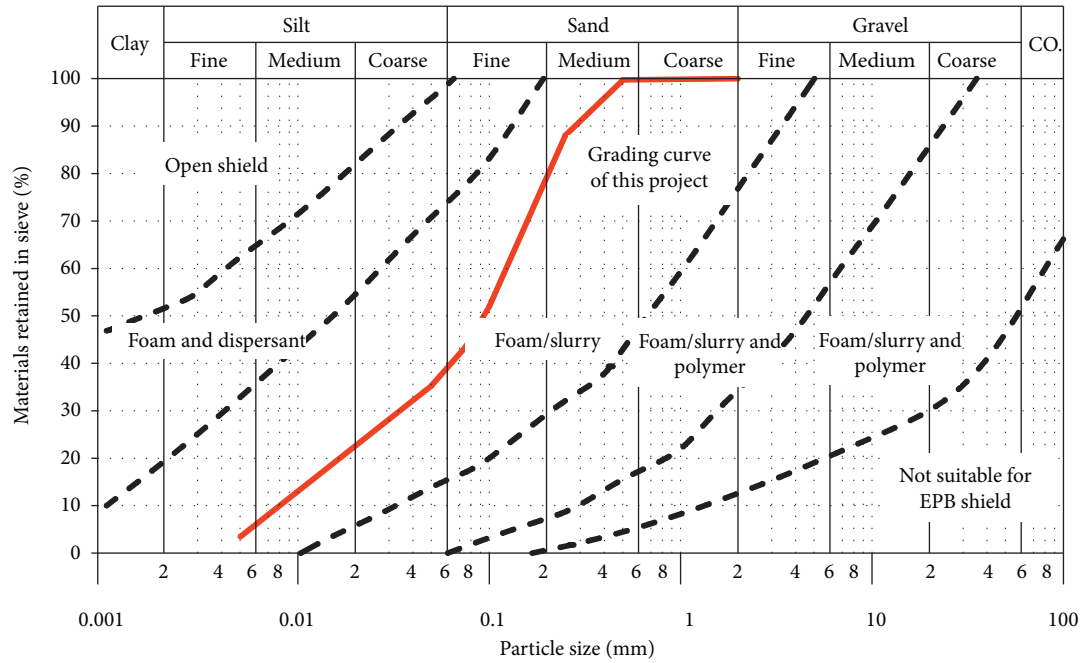


FIGURE 10: Particle grading curves of soils and suitable conditioning materials.

TABLE 2: Test levels and foaming parameters.

Level	Concentration of foam solution (A) (%)	Air pressure (B) (MPa)	Air flow (C) (L/min)	Liquid pressure (D) (MPa)	Liquid flow (E) (mL/min)
1	2.0	0.2	1.0	0.2	50
2	3.0	0.3	2.0	0.3	100
3	4.0	0.4	3.0	0.4	150
4	5.0	0.5	4.0	0.5	200

TABLE 3: Scheme of orthogonal test.

No.	Concentration of foam solution (A) (%)		Air pressure (B) (MPa)		Air flow (C) (L/min)		Liquid pressure (D) (MPa)		Liquid flow (E) (ml/min)	
	Level	Value	Level	Value	Level	Value	Level	Value	Level	Value
1	1	2.0	2	0.3	3	3.0	2	0.3	3	150
2	3	4.0	4	0.5	1	1.0	2	0.3	2	100
3	2	3.0	4	0.5	3	3.0	3	0.4	4	200
4	4	5.0	2	0.3	1	1.0	3	0.4	1	50
5	1	2.0	3	0.4	1	1.0	4	0.5	4	200
6	3	4.0	1	0.2	3	3.0	4	0.5	1	50
7	2	3.0	1	0.2	1	1.0	1	0.2	3	150
8	4	5.0	3	0.4	3	3.0	1	0.2	2	100
9	1	2.0	1	0.2	4	4.0	3	0.4	2	100
10	3	4.0	3	0.4	2	2.0	3	0.4	3	150
11	2	3.0	3	0.4	4	4.0	2	0.3	1	50
12	4	5.0	1	0.2	2	2.0	2	0.3	4	200
13	1	2.0	4	0.5	2	2.0	1	0.2	1	50
14	3	4.0	2	0.3	4	4.0	1	0.2	4	200
15	2	3.0	2	0.3	2	2.0	4	0.5	2	100
16	4	5.0	4	0.5	4	4.0	4	0.5	3	150

In practice, the F_{er} and $T_{1/2}$ are greatly influenced by concentration of the foam solution, air flow, liquid flow, air pressure, and liquid pressure. Considering the complex influences of these five factors, the multivariable tests

(orthogonal tests of 4 levels and 5 variables) were performed firstly to determine the possible set of optimal foaming parameters, with test conditions shown in Tables 2 and 3. And then, single-variable tests were

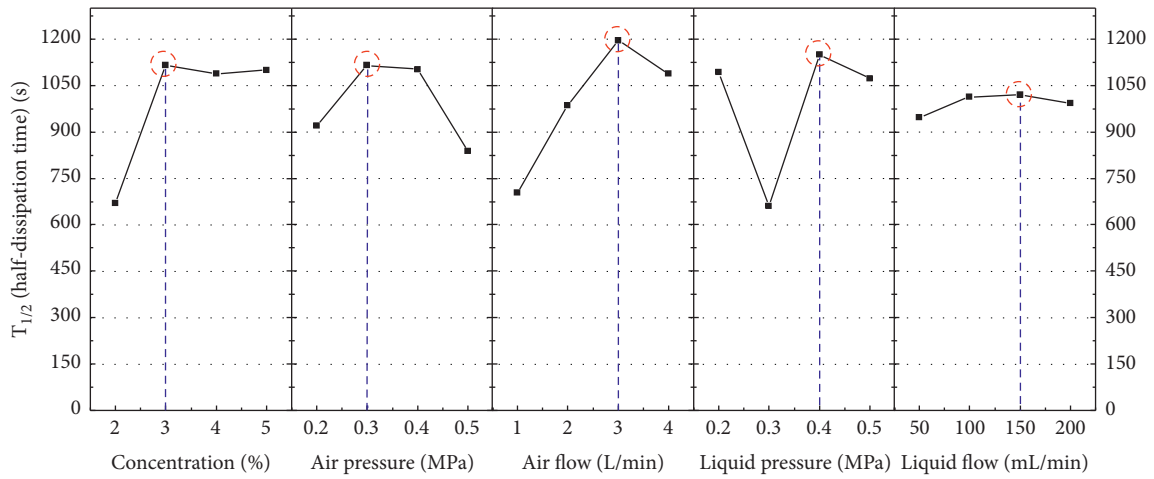


FIGURE 11: Effect of foaming parameters on half-dissipation time.

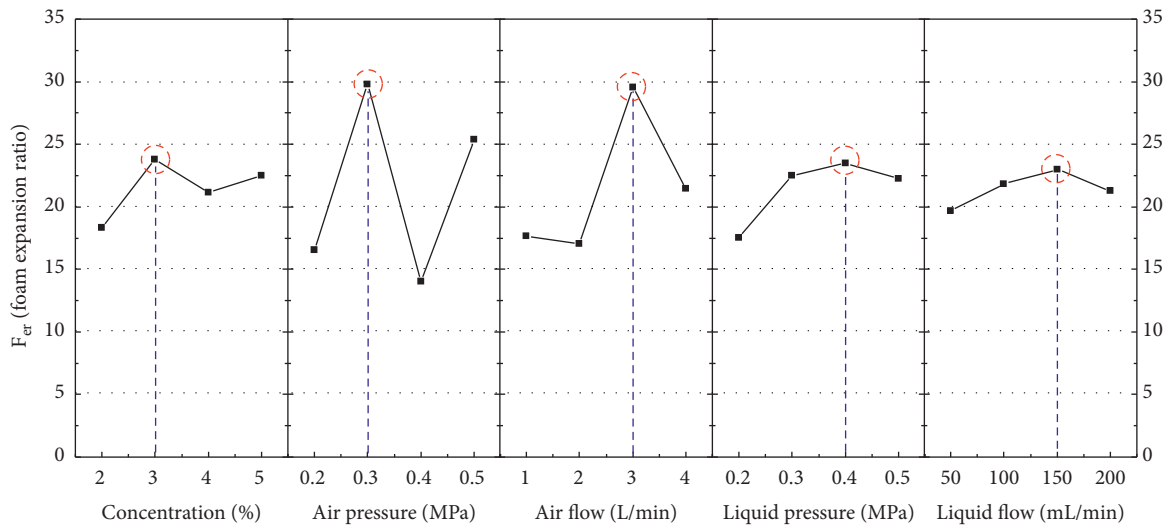


FIGURE 12: Effect of foaming parameters on foam expansion ratio.

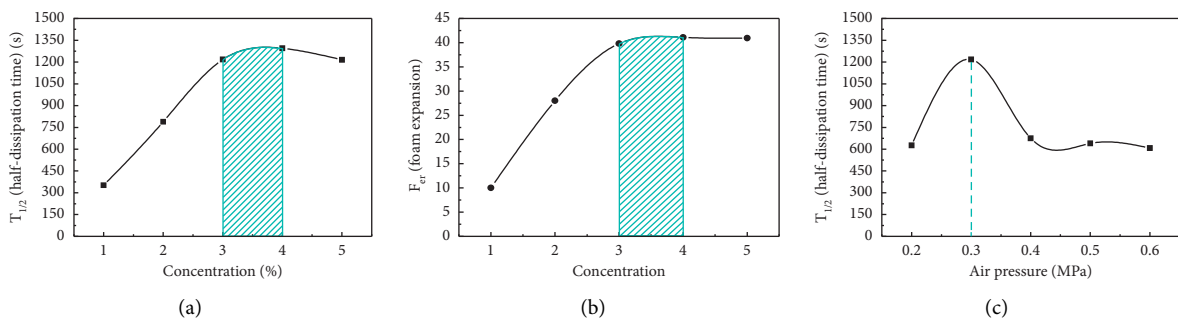


FIGURE 13: Continued.

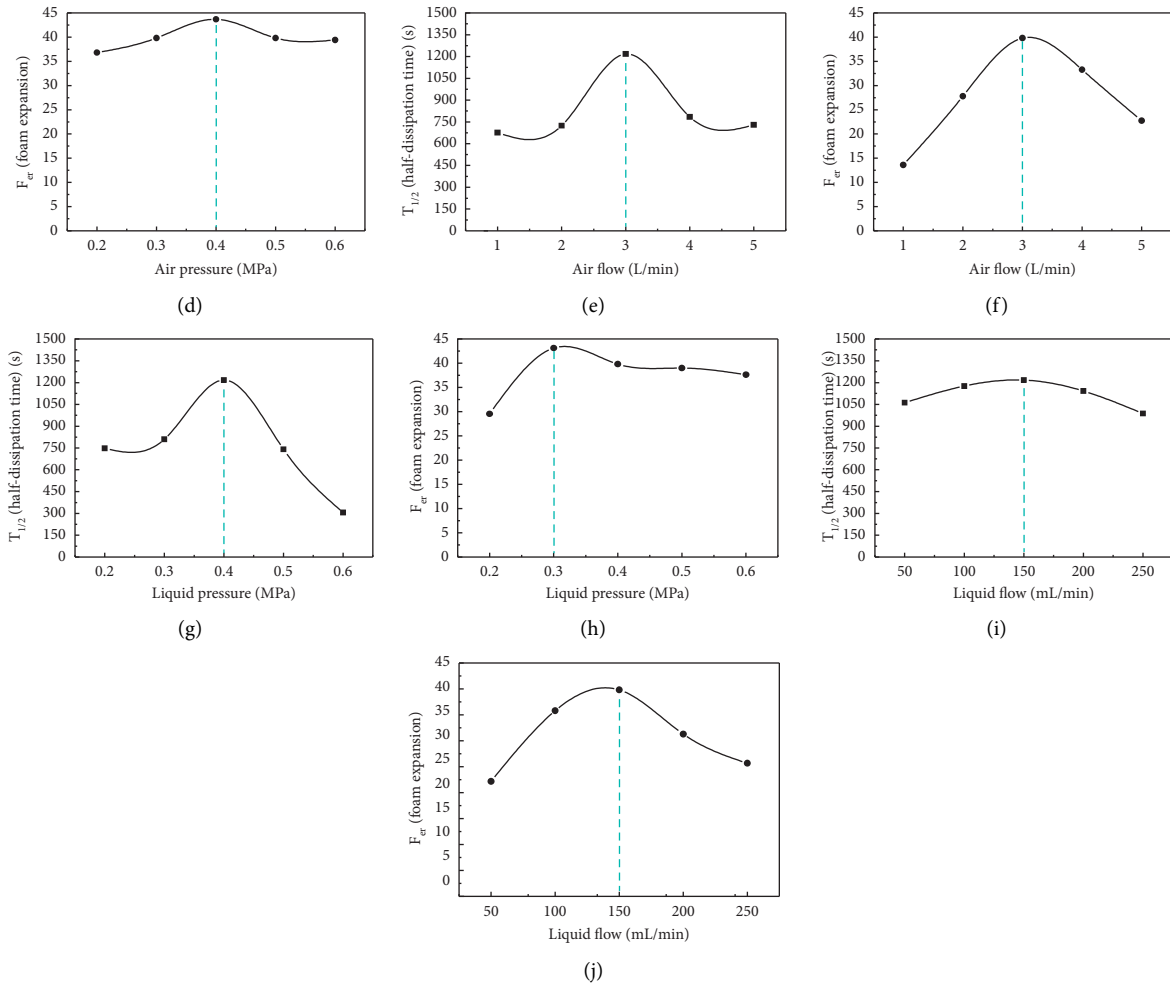


FIGURE 13: Effect of foaming parameters on foam properties.



FIGURE 14: Bentonite.

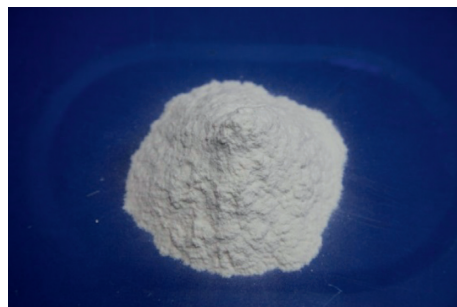


FIGURE 15: Carboxyl methyl cellulose (CMC).

TABLE 4: Results of slurry optimization experiment.

Type	No.	Water (g)	Bentonite (%)	Bentonite (g)	CMC (%)	CMC (g)	Density (g/cm ³)	Viscosity (s)
Initial tests	1	4000	1	40	0	0	1.017	15.26
	2	4000	2	80	0	0	1.022	15.63
	3	4000	3	120	0	0	1.027	16.50
	4	4000	4	160	0	0	1.032	17.61
	5	4000	5	200	0	0	1.037	19.01
	6	4000	6	240	0	0	1.044	22.81
	7	4000	7	280	0	0	1.048	27.96
	8	4000	8	320	0	0	1.053	32.81
	9	4000	9	360	0	0	1.059	49.96
	10	4000	10	400	0	0	1.063	77.23
	11	4000	11	440	0	0	1.071	138.56
	12	4000	12	480	0	0	1.074	238.00
Combination tests	13	4000	5	200	0.15	0.3	1.036	22.73
	14	4000	5	200	0.3	0.6	1.037	23.88
	15	4000	5	200	0.5	1	1.036	25.54
	16	4000	5	200	0.7	1.4	1.037	30.58
	17	4000	8	320	0.15	0.48	1.056	47.46
	18	4000	8	320	0.3	0.96	1.062	59.46
	19	4000	8	320	0.5	1.6	1.054	79.36
	20	4000	8	320	0.7	2.24	1.062	117.43
	21	4000	10	400	0.15	0.6	1.062	88.18
	22	4000	10	400	0.3	1.2	1.071	133.30
	23	4000	10	400	0.5	2	1.072	185.30
	24	4000	10	400	0.7	2.8	1.071	245.60

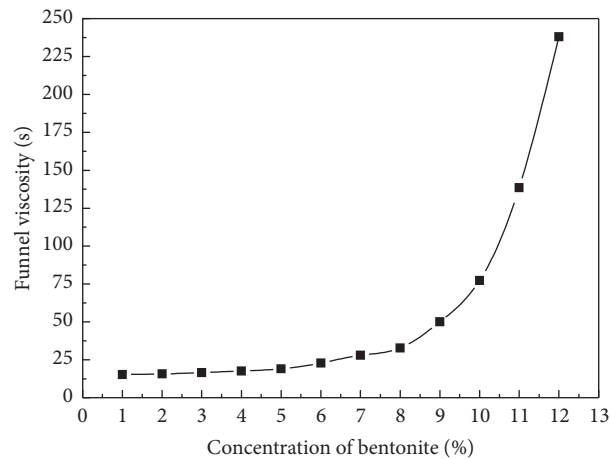


FIGURE 16: Effect of bentonite concentration on funnel viscosity.

performed further to verify and confirm the foaming parameters.

According to the multivariable test results shown in Figures 11 and 12, the possible set of optimal foaming parameters is 3.0% foam solution concentration, 3.0 L/min air flow, 150 mL/min liquid flow, 0.3 MPa air pressure, and 0.4 MPa liquid pressure. To further verify and amend the results of multivariable test, the single-variable tests are conducted, and the results are summarized in Figure 13. As shown in Figures 13(a) and 13(b), when the concentration of foam solution increases to 3%, the half-dissipation time and expansion ratio nearly reach the maximum values of

1200 s and 40, respectively. Figure 13(c) illustrates that the foam has the best stability when the air pressure is 0.3 MPa, and the expansion ratio is controlled in 20–40 (see Figure 13(d)). Figures 13(e) and 13(f) show the relationship between the foam properties and air flow; the preferred air flow is 3 L/min. Additionally, the liquid pressure and liquid flow should be 0.4 MPa and 150 mL/min, respectively, as shown in Figures 13(g)–13(j). Hence, the optimized foaming parameters were confirmed as follows: 3.0% foam solution concentration, 3.0 L/min air flow, 150 mL/min liquid flow, 0.3 MPa air pressure, and 0.4 MPa liquid pressure. The corresponding half-dissipation time and the

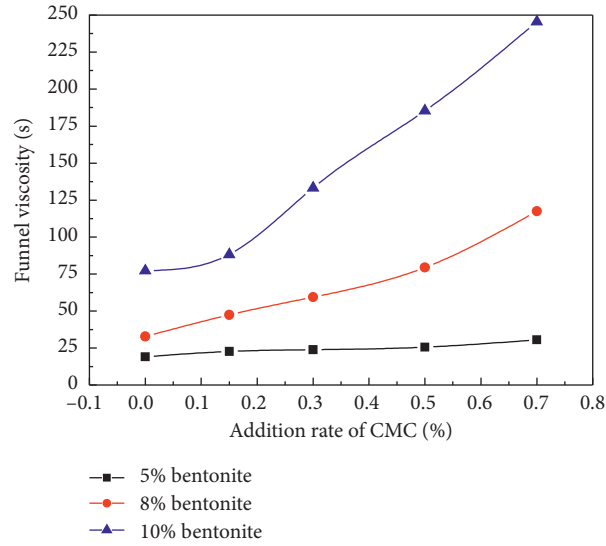


FIGURE 17: Effect of addition rate of CMC on funnel viscosity.

TABLE 5: Testing conditions for soil conditioning.

No.	Soil pressure (MPa)	Water content (%)	Soil conditioner	Injection ratio of volume
1	0.1	10	Foam	0–100%
2	0.1	10	Slurry	0–30%
3	0.1	30	Foam	0–100%
4	0.1	30	Slurry	0–30%
5	0.25	10	Foam	0–100%
6	0.25	10	Slurry	0–30%
7	0.25	30	Foam	0–100%
8	0.25	30	Slurry	0–30%

TABLE 6: Relationship between foam injection ratio and advance distance.

Advance distance (mm)	0–30	31–60	61–90	91–120	121–150	151–180
Injection ratio (%)	0	10–15	30–35	50–55	70–75	90–100

TABLE 7: Relationship between slurry injection ratio and advance distance.

Advance distance (mm)	0–30	31–60	61–90	91–120	121–150	151–180	181–210	211–240
Injection ratio (%)	0	3–5	7–8	10–12	14–16	18–20	24–26	28–30

TABLE 8: Driving parameters of shield cutter head.

Opening ratio (%)	Rotating speed	Advance speed
50	1 r/min	30 mm/min

foam expansion ratio are recommended as 1217 s and 39.81, respectively.

3.3. Bentonite Slurry and CMC. The other conditioning material for the test is the bentonite with addition of carboxyl methyl cellulose (CMC, $[C_6H_7O_2(OH)_2CH_2COO Na]_n$) which can significantly increase the viscosity of bentonite slurry as thickener when it is dissolved in water. The influences of the bentonite (Figure 14) and CMC

(Figure 15) concentration were investigated via an optimization experiment of the slurry properties (density and funnel viscosity) (Table 4). In the 12 initial try tests shown in the table, only the concentration of bentonite was adjusted, and the results show that the funnel viscosity is more sensitive to the bentonite concentration than the density. As shown in Figure 16, the funnel viscosity increases with the bentonite concentration. When the concentration reaches 11%, the viscosity increases sharply and part of bentonite tends to be insoluble in water. To maintain the viscosity

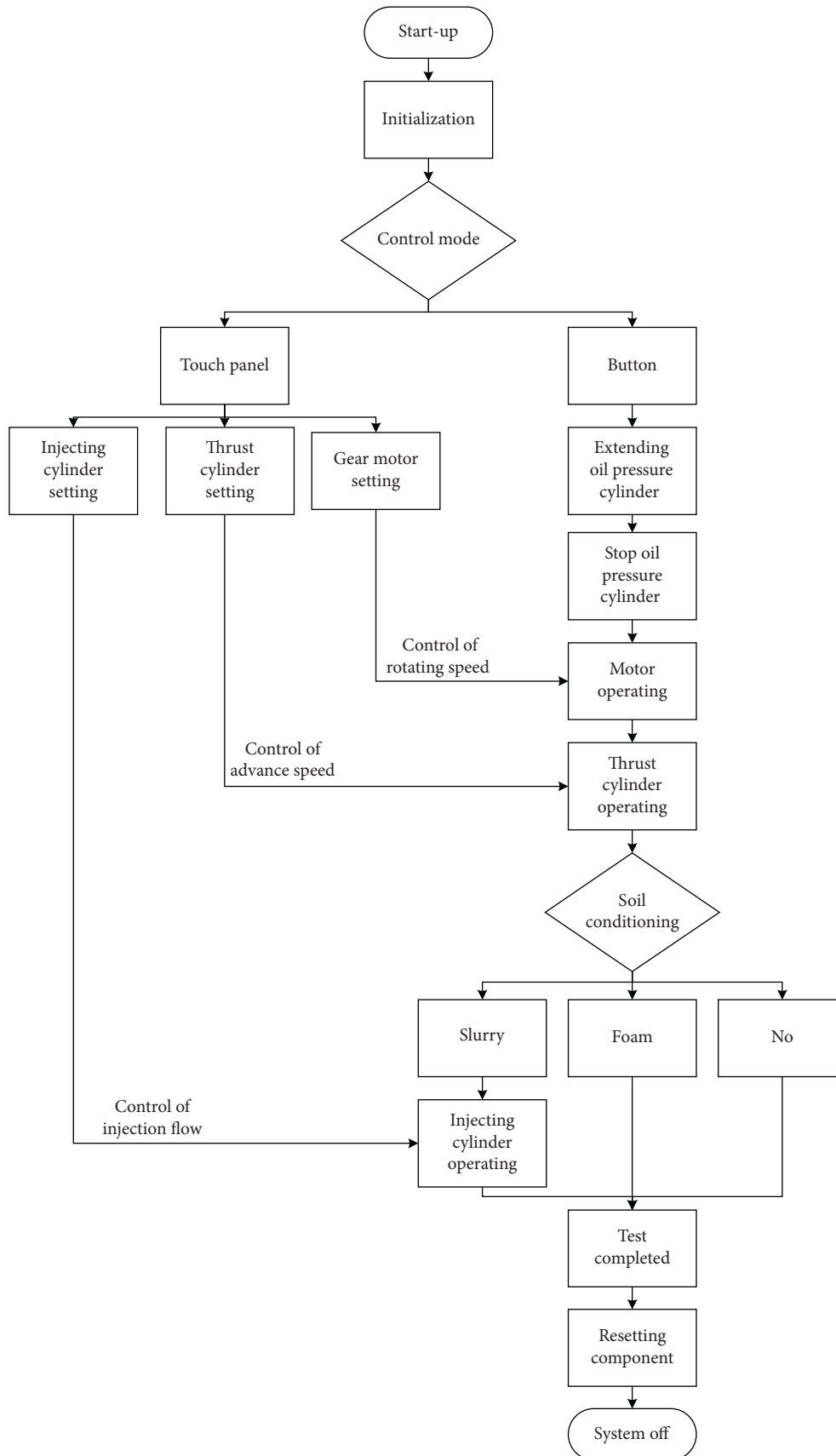


FIGURE 18: The testing process.

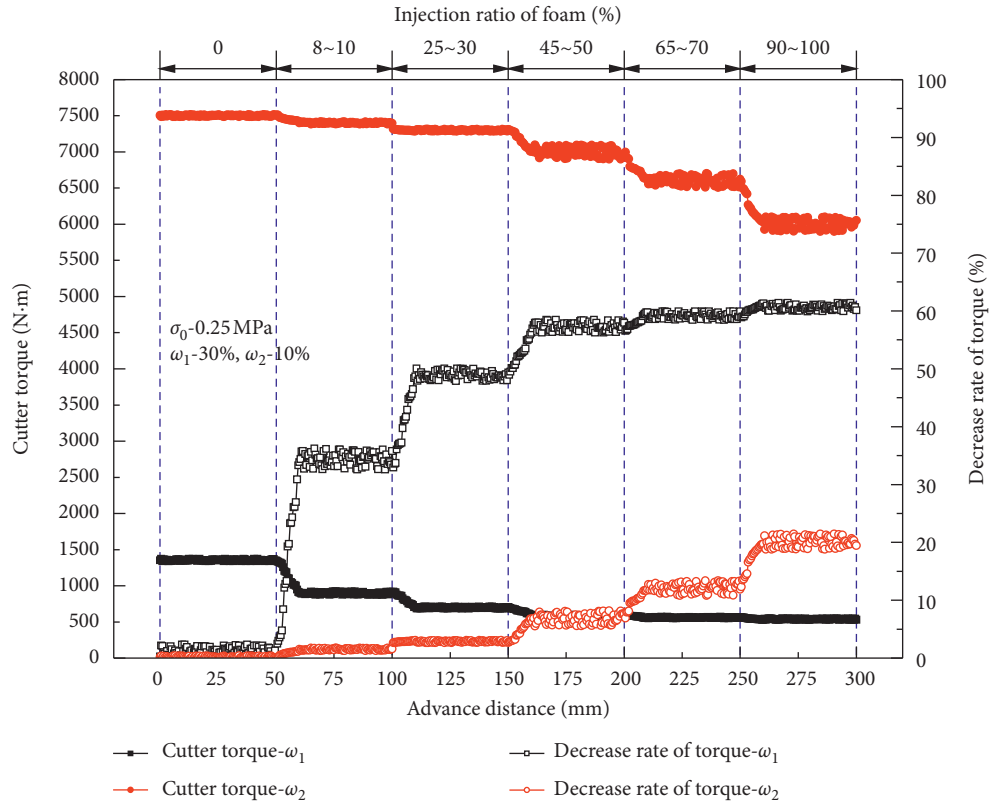


FIGURE 19: Effect of foam conditioning and soil water contents on cutter torque at soil pressure 0.25 MPa.

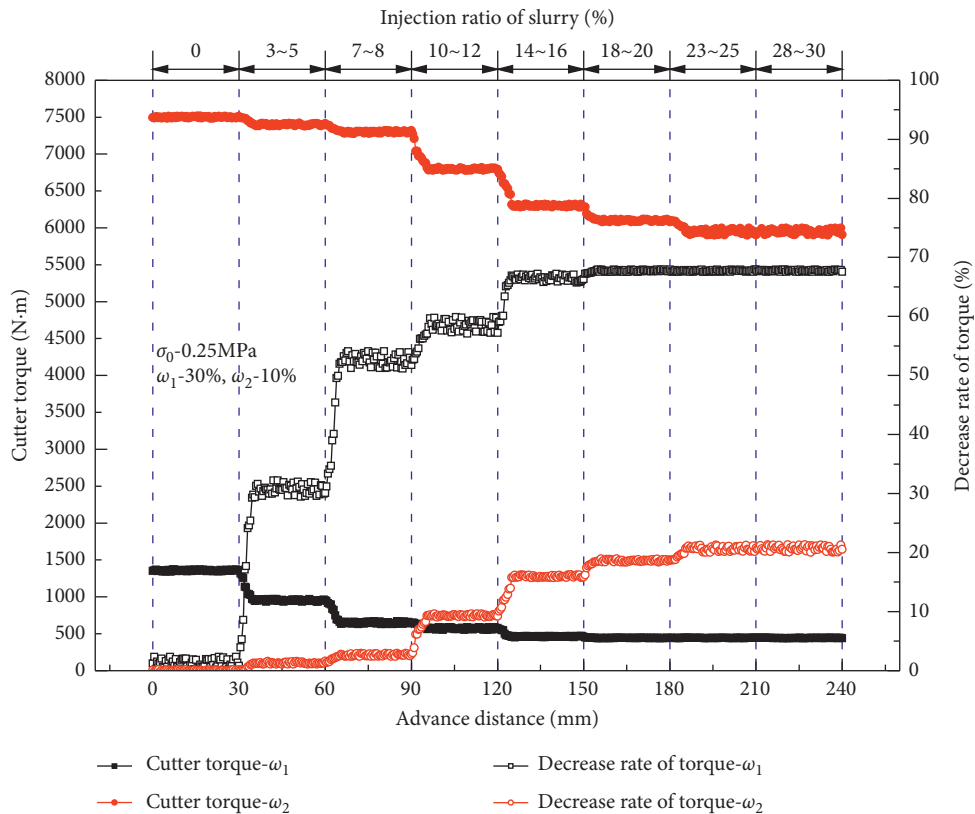


FIGURE 20: Effect of slurry conditioning and soil water contents on cutter torque at soil pressure 0.25 MPa.

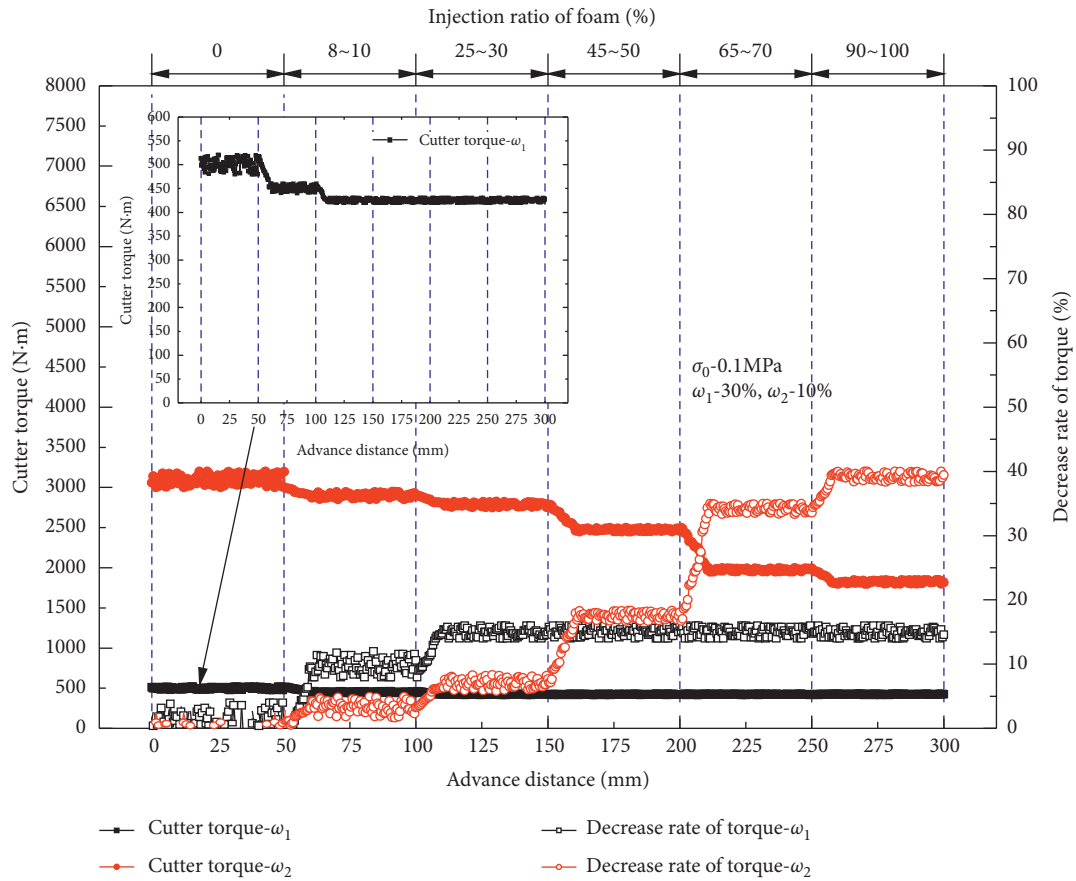


FIGURE 21: Effect of foam conditioning and soil water contents on cutter torque at soil pressure 0.1 MPa.

between 60 and 80 s, which is suitable for this type of ground, bentonite concentrations of 5%, 8%, and 10% are mixed with CMC (test no. 13 to test no. 24 in Table 4). According to Figure 17, the addition rate of CMC has an obvious effect on the funnel viscosity for bentonite concentrations of 8% and 10%. Hence, part of bentonite can be replaced with CMC to improve the solubility of the slurry. The recommended slurry proportioning is 8% bentonite and 0.5% CMC, resulting in a density and funnel viscosity of 1.054 g/cm³ and 79.36 s, respectively.

4. Main Test

4.1. Test Procedure. The testing conditions and parameters are shown in Tables 5–7. The soil samples were configured with two moisture contents of 10% and 30% and then pressurized at 0.1 MPa and 0.25 MPa, respectively. Based on the abovementioned optimized parameters of foam and slurry, the injection process was performed in several stages with different injection ratios, as shown in Tables 6 and 7. The driving parameters of the shield cutter head were set, as shown in Table 8, in compliance with the onsite construction parameters of shield. During the test process, the cutter torque was automatically recorded by the torque sensor installed on the

ground suitability test system. The cutter torque is regarded as a comprehensive index in the test for accessing the cutting performance because the changes in cutter torque closely reflect the abrasion of cutters and cutting efficiency. The process of testing is shown in Figure 18.

4.2. Test Results. According to the above test procedure, the influences of the moisture content and confining pressure of soil, the conditioner type, and the injection ratio on the cutting performance were experimentally investigated, respectively, and summarized below.

4.2.1. The Effect of Moisture Content of Silt Sand. As shown in Figures 19–22, the moisture content of the silty sand affects significantly the cutting torque, which increased by 5 to 7 times when the moisture content increased from 10% to 30% in case of no soil conditioning. However, it was only when the foam injection ratio reached 30% or when the slurry injection ratio exceeded 5% that the cutter torque began to reduce remarkably.

The maximum reduction in the cutter torque was a result of combined effect of the moisture content and soil pressure. When the moisture content was 10% at a soil pressure of

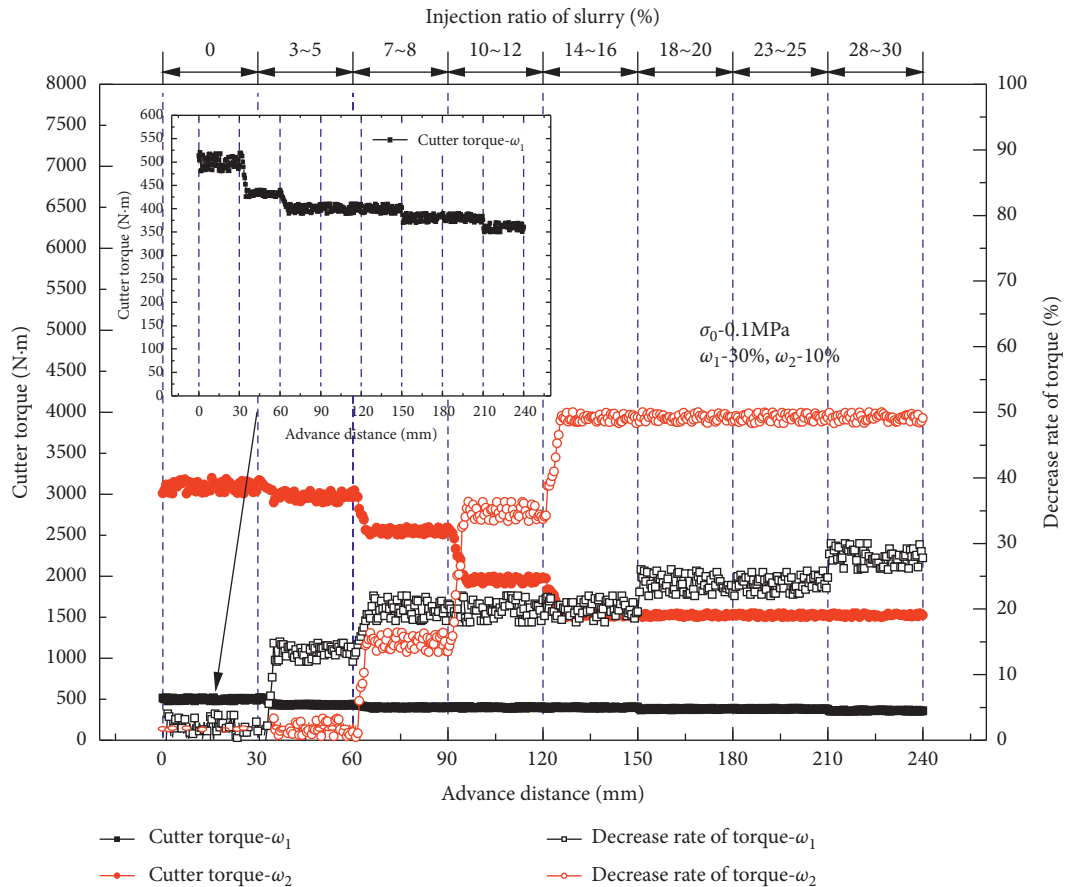


FIGURE 22: Effect of slurry conditioning and soil water contents on cutter torque at soil pressure 0.1 MPa.

0.1 MPa, the maximum reduction ratio of cutter torque occurred as 40%–60%, while at the same moisture content and higher pressure of 0.25 MPa, the maximum reduction in cutter torque was only 20%–30%. However, the maximum reduction ratio could reach 60%–70% when the moisture content was 30% and soil pressure was 0.25 MPa.

4.2.2. The Effect of Confining Pressure. As shown in Figures 23–26, the cutter torque in silty sand is positively correlated with the soil confining pressure. When the soil confining pressure increased from 0.1 MPa to 0.25 MPa, the cutter torque increased by 2 to 3 times in case of no soil conditioning.

When the soil moisture content was 30%, even a high soil confining pressure could result in a larger decrease in the cutter torque with soil conditioning. For instance, a maximum decrease in the cutter torque of 60% could be obtained when the soil confining pressure was 0.25 MPa, while only a 15% decrease occurred when the soil confining pressure was 0.1 MPa, as shown in Figure 23.

However, the opposite was observed when the moisture content was 10%. A higher soil pressure resulted in smaller decreases in the cutter torque with soil conditioning. However, the differences in the reduction of cutter torque under the two pressure conditions were close. As shown in Figure 24, the maximum reduction was only 1200–1500 N m under different soil pressures.

4.2.3. The Effect of Conditioning Material. The effect of different kinds of soil conditioners on the cutting performance was compared under the same moisture content and soil pressure conditions, as shown in Figures 27–30.

The results revealed that the effect of soil conditioning is limited when the injection ratio reaches a certain value. For example, Figure 27 shows that when the injection ratio of slurry exceeds 15% or that of foam exceeds 45%, the decrease rate of the cutter torque tends to be stable.

Judging from the maximum decrease of the torque, slurry was a better option than foam for decreasing the cutter torque. In order to achieve the same effect of soil conditioning, the

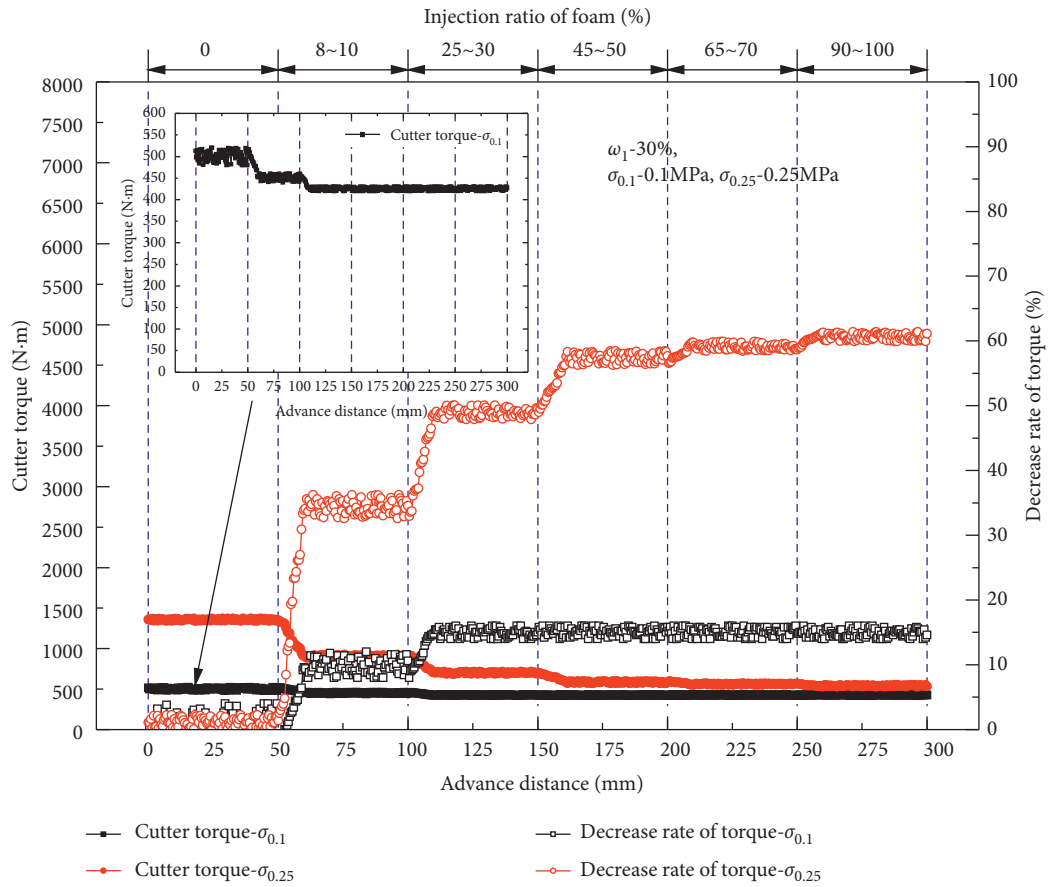


FIGURE 23: Effect of foam conditioning and soil pressure on cutter torque at water content 30%.

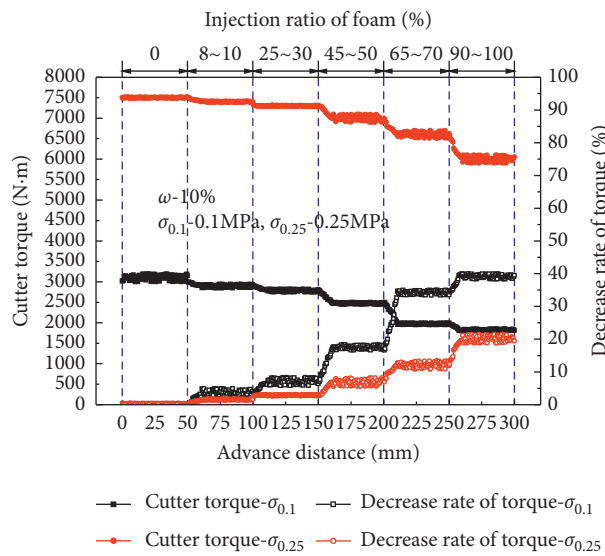


FIGURE 24: Effect of foam conditioning and soil pressure on cutter torque at water content 10%.

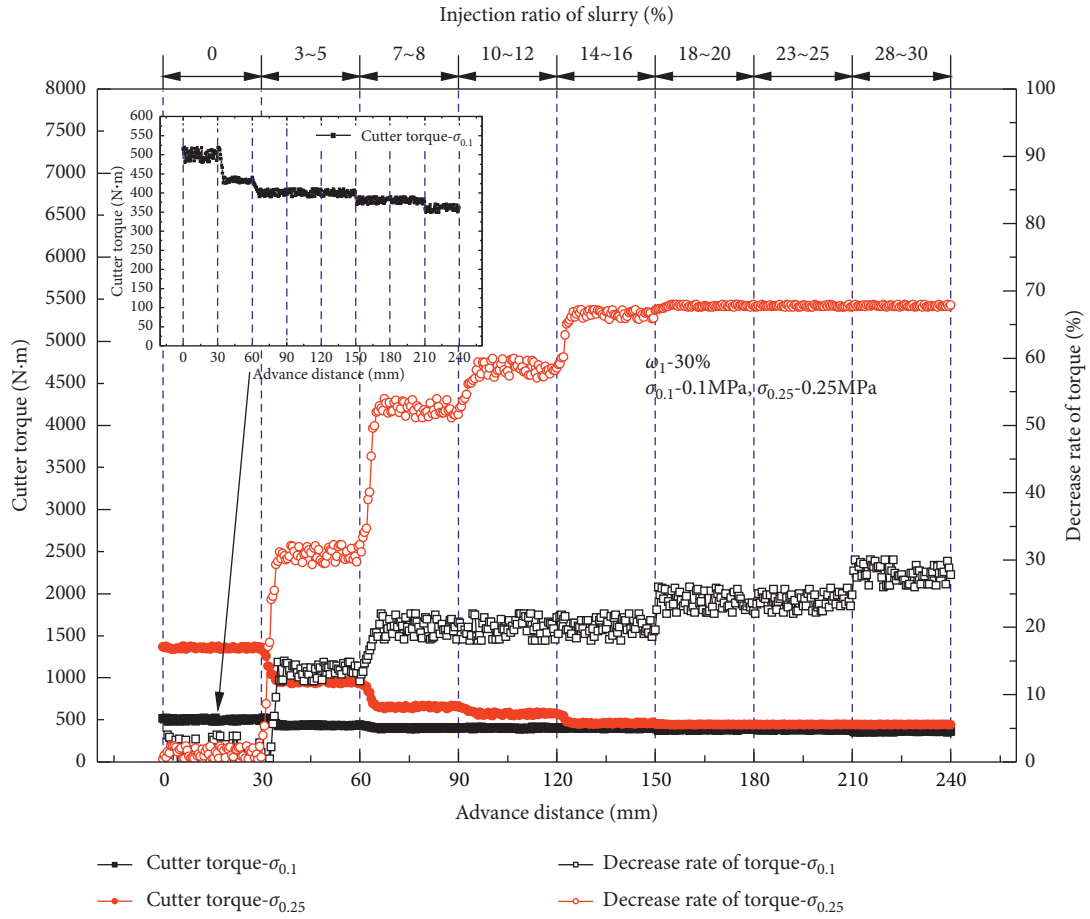


FIGURE 25: Effect of slurry conditioning and soil pressure on cutter torque at water content 30%.

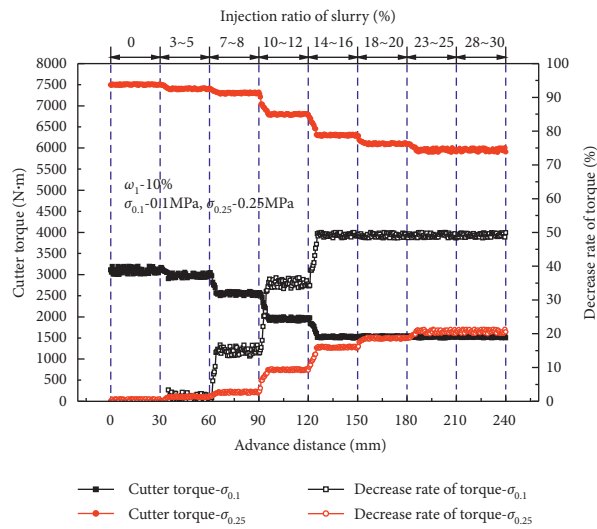


FIGURE 26: Effect of slurry conditioning and soil pressure on cutter torque at water content 10%.

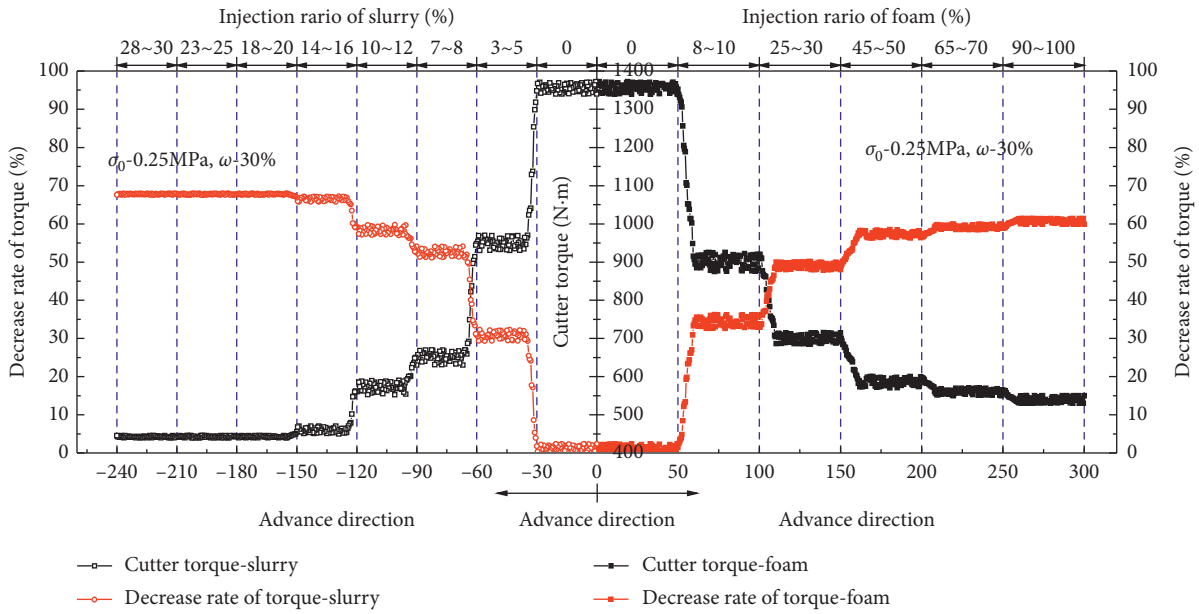


FIGURE 27: Effect of two types of soil conditioners on cutter torque at water content 30% and soil pressure 0.25 MPa.

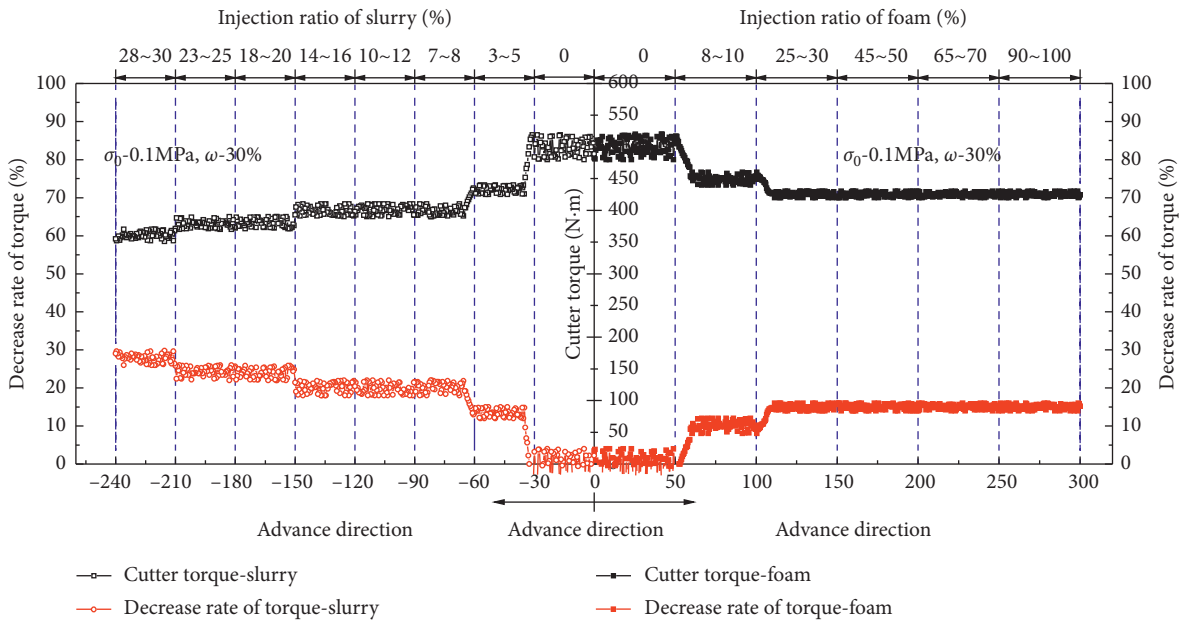


FIGURE 28: Effect of two types of soil conditioners on cutter torque at water content 30% and soil pressure 0.1 MPa.

injection ratios of the two types of soil conditioners were different. As shown in Figure 27, the injection ratios of foam and slurry should be 45% and 10%, respectively, to achieve the same maximum reduction of torque at 60%.

5. Field Test and Verification

To realize the onsite effect of soil conditioning on the cutting performance of the shield machine, a field experiment was

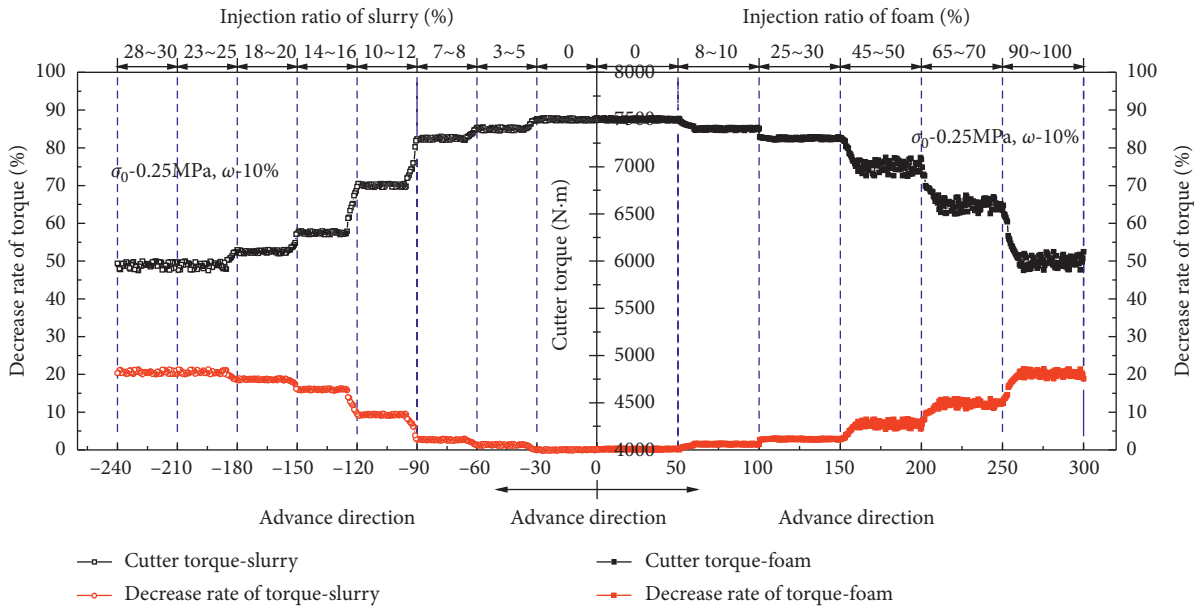


FIGURE 29: Effect of two types of soil conditioners on cutter torque at water content 10% and soil pressure 0.25 MPa.

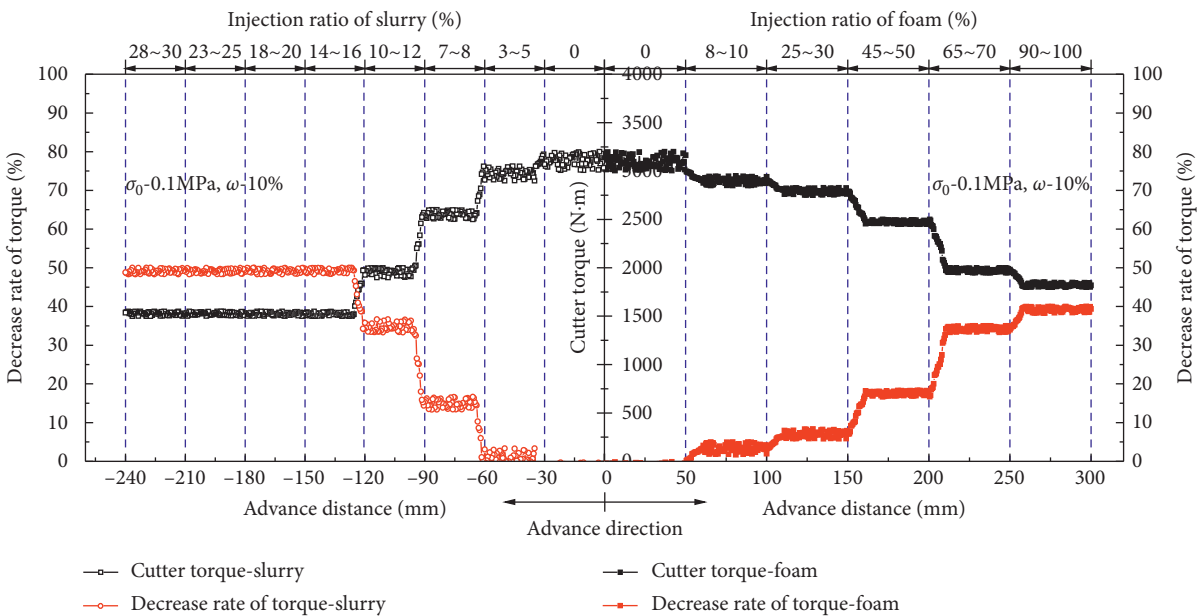


FIGURE 30: Effect of two types of soil conditioners on cutter torque at water content 10% and soil pressure 0.1 MPa.

conducted on a real tunneling project in Wuhan with $\Phi 6.26\text{m}$ EPB shield (shown in Figure 31). The tunneling parameters of the cutter head are listed in Table 9. There were totally 60 rings taken for the field experiment, in which the 1st to 30th rings were driven without soil conditioning while the 31st to 60th rings with foam conditioning at

different injection ratios, as shown in Figure 8. The foaming parameters adopted in the field test were the same as the laboratory test.

As shown in Figure 32, soil conditioning had an evident effect on shield cutting. During tunneling in the first 30 rings, the cutter torque fluctuated over a wide range from



FIGURE 31: Picture of EPB shield.

TABLE 9: Tunneling parameters of cutter head.

Mode	EPB
Diameter	6260 mm
Open ratio	50%
Rated torque	7206 kN m
Total thrust	40000 kN
Soil pressure	0.16–0.22 MPa
Advance speed	30 mm/min
Rotating speed	1 r/min

6. Conclusion

In order to realize the effect of soil conditioning on the shield cutting performance and to optimize the conditioning materials, a series of laboratory tests were conducted using a self-developed ground suitability test system. The effect of four key factors was comprehensively investigated on the shield cutting performance and verified by field experiment of a real tunnel project. The major findings were obtained as follows:

- (1) The ground suitability test system performed well, and the prediction of the cutter torque based on the test agreed well with the field test. It can prospectively be served as an onsite real time testing equipment for shield tunneling.
- (2) The optimal foam parameters are suggested for shield tunneling in silty sand as 3.0% foam solution concentration, 3.0 L/min air flow, 150 mL/min liquid flow, 0.3 MPa air pressure, and 0.4 MPa liquid pressure with half-dissipation time and expansion ratio as 1217 s and 39.81, respectively. The optimal slurry is recommended as 8% bentonite and 0.5% CMC with resulted density and funnel viscosity as 1.054 g/cm³ and 79.36 s, respectively.
- (3) The shield cutter torque is also sensitive to the moisture content and confining pressure of silty sand and the injection ratio of conditioners. The torque at moisture content of 10% is 5 to 7 times more than that at moisture content of 30% in case of no soil conditioning. When the foam injection ratio exceeds 30% or the slurry injection ratio exceeds 5%, the shield cutter torque starts to significantly decrease. The maximum decrease in cutter torque by 40%–60% was achieved by optimized soil conditioning, moisture content, and soil pressure. However, the effect of soil conditioning is limited when the injection ratio reaches a certain value.
- (4) In comparison, slurry is better than foam in decreasing the cutter torque in silty sand. To achieve

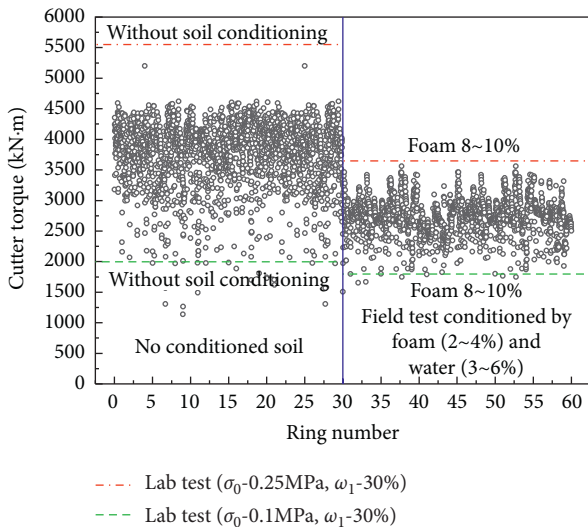


FIGURE 32: Comparison of laboratory test with field test result.

3000 kN·m to 4500 kN m. When the soil was conditioned with foam and water from the 31th ring onward, the torque sharply decreased to 2200–3200 kN m, about 25%–50% drop.

The predictions of the shield cutter torque based on the laboratory test results were compared with those from the field test in Figure 32, which shows they were in good agreement and most of the measured values were within the range of predicted values.

the same effect of soil conditioning, the injection ratios of foam and slurry should be 45% and 10%, respectively, to achieve the maximum decrease in the torque at 60%.

Data Availability

The data used to support the findings of this study are included within the article.

Conflicts of Interest

The authors declare that they have no conflicts of interest.

Acknowledgments

This research was funded by the National Basic Research Program of China (973 Program) (Grant no. 2015CB057806). This financial support is gratefully acknowledged.

References

- [1] Z. Chu, Z. Wu, Q. Liu, and B. Liu, "Analytical solutions for deep-buried lined tunnels considering longitudinal discontinuous excavation in rheological rock mass," *Journal of Engineering Mechanics*, vol. 146, no. 6, Article ID 4020047, 2020.
- [2] F. Song, H. Wang, and M. Jiang, "Analytically-based simplified formulas for circular tunnels with two liners in viscoelastic rock under anisotropic initial stresses," *Construction and Building Materials*, vol. 175, pp. 746–767, 2018.
- [3] K. Wu, Z. Shao, S. Qin, and B. Li, "Determination of deformation mechanism and countermeasures in silty clay tunnel," *Journal of Performance of Constructed Facilities*, vol. 34, no. 1, Article ID 4019095, 2020.
- [4] K. Wu and Z. Shao, "Visco-elastic analysis on the effect of flexible layer on mechanical behavior of tunnels," *International Journal of Applied Mechanics*, vol. 11, no. 3, p. 1950027, 2019.
- [5] S.-M. Liao, J.-H. Liu, R.-L. Wang, and Z.-M. Li, "Shield tunneling and environment protection in Shanghai soft ground," *Tunnelling and Underground Space Technology*, vol. 24, no. 4, pp. 454–465, 2009.
- [6] S.-M. Liao, C.-H. Cheng, and L.-S. Chen, "The planning and construction of a large underpass crossing urban expressway in Shanghai: an exemplary solution to the traffic congestions at dead end roads," *Tunnelling and Underground Space Technology*, vol. 81, pp. 367–381, 2018.
- [7] M.-B. Liu and S.-M. Liao, "A case study on the underground rapid transport system (URTS) for the international airport hubs: planning, application and lessons learnt," *Tunnelling and Underground Space Technology*, vol. 80, pp. 114–122, 2018.
- [8] C. Yang, S.-L. Shen, D.-W. Hou, S.-M. Liao, and D.-J. Yuan, "Material properties of the seal gasket for shield tunnels: a review," *Construction and Building Materials*, vol. 191, pp. 877–890, 2018.
- [9] Z. Chu, Z. Wu, B. Liu, and Q. Liu, "Coupled analytical solutions for deep-buried circular lined tunnels considering tunnel face advancement and soft rock rheology effects," *Tunnelling and Underground Space Technology*, vol. 94, p. 103111, 2019.
- [10] C. H. Cheng, S. M. Liao, S. J. Peng, J. W. Zhu, and Y. Liu, "Study on ground suitability of slurry shield in water-rich sandy cobble ground in Shenyang," *Chinese Journal of Underground Space and Engineering*, vol. 13, pp. 190–196, 2017, in Chinese.
- [11] D.-J. Ren, S.-L. Shen, A. Arulrajah, and W.-C. Cheng, "Prediction model of TBM disc cutter wear during tunnelling in heterogeneous ground," *Rock Mechanics and Rock Engineering*, vol. 51, no. 11, pp. 3599–3611, 2018.
- [12] H. T. Jiang, Q. M. Gong, and X. L. Du, "Experimental study on soil conditioning in cobble layer by use of earth pressure balanced machine," *Chinese Journal of Geotechnical Engineering*, vol. 35, pp. 284–292, 2013, in Chinese.
- [13] D. Peila, "Soil conditioning for EPB shield tunnelling," *KSCSE Journal of Civil Engineering*, vol. 18, no. 3, pp. 831–836, 2014.
- [14] R. Vinai, C. Oggeri, and D. Peila, "Soil conditioning of sand for EPB applications: a laboratory research," *Tunnelling and Underground Space Technology*, vol. 23, no. 3, pp. 308–317, 2008.
- [15] L. Mori, E. Alavi, and M. Mooney, "Apparent density evaluation methods to assess the effectiveness of soil conditioning," *Tunnelling and Underground Space Technology*, vol. 67, pp. 175–186, 2017.
- [16] D. Peila, A. Picchio, D. Martinelli, and E. D. Negro, "Laboratory tests on soil conditioning of clayey soil," *Acta Geotechnica*, vol. 11, no. 5, pp. 1061–1074, 2015.
- [17] R. Zumsteg and L. Langmaack, "Mechanized tunneling in soft soils: choice of excavation mode and application of soil-conditioning additives in glacial Deposits," *Engineering*, vol. 3, no. 6, pp. 863–870, 2017.
- [18] K. Chaidachatorn, J. Suebsuk, S. Horpibulsuk, and A. Arulrajah, "Extended water/cement ratio law for cement mortar containing recycled asphalt pavement," *Construction and Building Materials*, vol. 196, pp. 457–467, 2019.
- [19] C. H. Cheng, G. Q. Zhao, S. M. Liao, and X. B. Huo, "Adaptability study of EPB shield machine in hard clay in Wuhan," *Construction Technology*, vol. 45, pp. 105–109, 2016, in Chinese.
- [20] O. D. G. G. De, M. Thewes, M. S. Diederichs, and L. Lars, "EPB tunnelling through clay-sand mixed soils: proposed methodology for clogging evaluation," *Geomechanics and Tunneling*, vol. 11, pp. 375–387, 2018.
- [21] Q. Gong, L. Yin, H. Ma, and J. Zhao, "TBM tunnelling under adverse geological conditions: an overview," *Tunnelling and Underground Space Technology*, vol. 57, pp. 4–17, 2016.
- [22] E. A. Zhao, J. Rostami, and K. Talebi, "Experimental study of the effect of conditioning on abrasive wear and torque requirement of full face tunneling machines," *Tunnelling and Underground Space Technology*, vol. 41, pp. 127–136, 2014.
- [23] P. Li, D. Huang, J. Huang, and W. Ding, "Experimental study on soil conditioning of shield construction in hardplastic high-viscosity layer," *Journal of Tongji University (Natural Science)*, vol. 44, pp. 59–66, 2016.
- [24] F. Liu, S.-L. Shen, D.-W. Hou, A. Arulrajah, and S. Horpibulsuk, "Enhancing behavior of large volume underground concrete structure using expansive agents," *Construction and Building Materials*, vol. 114, pp. 49–55, 2016.
- [25] L. Mori, M. Mooney, and M. Cha, "Characterizing the influence of stress on foam conditioned sand for EPB tunneling," *Tunnelling and Underground Space Technology*, vol. 71, pp. 454–465, 2018.
- [26] S. Pourmand, H. Chakeri, M. Sharghi, and Y. Ozelcik, "Investigation of soil conditioning tests with three-dimensional

- numerical modeling,” *Geotechnical and Geological Engineering*, vol. 36, no. 5, pp. 2869–2879, 2018.
- [27] C. G. O. Salazar, C. Todaro, F. Bosio, E. Bassini, D. Ugues, and D. Peila, “A new test device for the study of metal wear in conditioned granular soil used in EPB shield tunneling,” *Tunnelling and Underground Space Technology*, vol. 73, pp. 212–221, 2018.
- [28] S.-L. Shen, D.-W. Hou, J.-L. Zhao, S. Horpibulsuk, and Z.-Y. Yin, “Assessment of internal forces for intermediate anchorage zone of post-tensioned concrete structure,” *Construction and Building Materials*, vol. 64, pp. 370–378, 2014.
- [29] P. Sukmak, S. Horpibulsuk, S.-L. Shen, P. Chindapasirt, and C. Suksiripattanapong, “Factors influencing strength development in clay-fly ash geopolymer,” *Construction and Building Materials*, vol. 47, pp. 1125–1136, 2013.
- [30] K. L. Wei, “On the “ideal soil” in the earth pressure balanced shield tunneling,” *Urban Mass Transit*, vol. 10, pp. 67–70, 2007, in Chinese.
- [31] K. Elbaz, S.-L. Shen, W.-C. Cheng, A. Arulrajah, and J. N. Shirlaw, “Discussion: cutter-disc consumption during earth pressure balance tunnelling in mixed strata,” *Proceedings of the Institution of Civil Engineers-Geotechnical Engineering*, vol. 171, no. 6, pp. 559–561, 2018.
- [32] J. Li, “Key technologies and applications of the design and manufacturing of non-circular TBMs,” *Engineering*, vol. 3, no. 6, pp. 905–914, 2017.
- [33] Z. H. Tang, Q. W. Xu, X. A. Yang, Y. Qiu, Z. Y. Gong, and S. Zhang, “Soil conditioning technology for shield tunnelling in a water-rich sandy stratum,” *Modern Tunnelling Technology*, vol. 53, pp. 153–158, 2016.
- [34] X. Ye, S. Wang, J. Yang, D. Sheng, and C. Xiao, “Soil conditioning for EPB shield tunneling in argillaceous siltstone with high content of clay minerals: case study,” *International Journal of Geomechanics*, vol. 17, Article ID 5016002, 2016.
- [35] S. C. Zhang, S. H. He, Z. P. Zhu, and C. H. Li, “Research on soil conditioning for earth pressure balance shield tunneling in Lanzhou sandy pebble strata with rich water,” *Rock and Soil Mechanics*, vol. 38, pp. 279–286, 2017.
- [36] D. Peila, C. Oggeri, and L. Borio, “Using the slump test to assess the behavior of conditioned soil for EPB tunneling,” *Environmental and Engineering Geoscience*, vol. 15, no. 3, pp. 167–174, 2009.
- [37] T. Liu, L. S. Chen, and Q. Yao, “Experimental Study of ground conditioning of Earth Pressure Balance (EPB) shield in sandy strata,” *Tunnel Construction*, vol. 37, pp. 1018–1025, 2017, in Chinese.
- [38] D. Martinelli, D. Peila, and E. Campa, “Feasibility study of tar sands conditioning for earth pressure balance tunnelling,” *Journal of Rock Mechanics and Geotechnical Engineering*, vol. 7, no. 6, pp. 684–690, 2015.
- [39] D. Peila, C. Oggeri, and R. Vinai, “Screw conveyor device for laboratory tests on conditioned soil for EPB tunneling operations,” *Journal of Geotechnical and Geoenvironmental Engineering*, vol. 133, no. 12, pp. 1622–1625, 2007.
- [40] D. Peila, A. Picchio, and A. Chierigato, “Earth pressure balance tunnelling in rock masses: laboratory feasibility study of the conditioning process,” *Tunnelling and Underground Space Technology*, vol. 35, pp. 55–66, 2013.
- [41] A. Bezuijzen and P. E. L. Schaminee, “Tunnelling. a decade of progress. geodelft 1995–2005, in Simulation of the EPB-Shield TBM in Model Tests with Foam as Additive,” in *Informa UK Limited*, pp. 157–163, London, UK, 2006.
- [42] T. Merritt, *Conditioning for Clay Soils for Tunnelling Machine Screw Conveyors*, University of Cambridge, Cambridge, England, 2004.
- [43] A. S. Merritt and R. J. Mair, “Mechanics of tunnelling machine screw conveyors: model tests,” *Géotechnique*, vol. 56, no. 9, pp. 605–615, 2006.
- [44] T. Nomoto, S. Imamura, T. Hagiwara, O. Kusakabe, and N. Fujii, “Shield tunnel construction in centrifuge,” *Journal of Geotechnical and Geoenvironmental Engineering*, vol. 125, no. 4, pp. 289–300, 1999.
- [45] J. Rivas, A. Jiménez, O. Videra, P. Gégout, F. Vallon, and J. Pegon, *Reducing the environmental impact of tunnel boring (OSCAR)*. in *Technology Innovation in Underground Construction*, G. Beer, Ed., pp. 239–259, CRC Press, Rotterdam, Netherlands, 2009.
- [46] P. Sotiris, *Properties of Foam/sand Mixtures for Tunnelling Applications*, University of Oxford, Oxford, England, 2001.
- [47] M. Thewes and C. Budach, “Soil conditioning with foam during EPB tunnelling/. Konditionierung von Lockergesteinen bei Erddruckschilden,” *Geomechanics and Tunnelling*, vol. 3, no. 3, pp. 256–267, 2010.
- [48] Q. W. Xu, H. H. Zhu, S. M. Liao, Q. Z. Zheng, and K. Zhou, “Experimental study on EPB shield tunnel construction in soft ground,” *Chinese Journal of Geotechnical Engineering*, vol. 29, pp. 1849–1857, 2007, in Chinese.
- [49] C. Budach and M. Thewes, “Application ranges of EPB shields in coarse ground based on laboratory research,” *Tunnelling and Underground Space Technology*, vol. 50, pp. 296–304, 2015.
- [50] H. Jiang, *Feasibility Study on EPB TBM Applied in Typical Gravel Strata in Beijing Metro*, China University of Mining and Technology, Beijing, China, 2012, in Chinese.
- [51] Y.-L. Wu, M. Mooney, and M.-S. Cha, “An experimental examination of foam stability under pressure for EPB TBM tunneling,” *Tunnelling and Underground Space Technology*, vol. 77, pp. 80–93, 2018.

Research Article

Effect of the Double-Line Spiral Tunnel Curvature on the Tunnel Construction Stability

Chao Zhang,¹ Chao Wang,¹ Xibin Niu,¹ Shaoqiang Zhang,¹ and Huiling Zhao ²

¹PowerChina Roadbridge Group Co., Ltd., Beijing 100048, China

²Department of Civil Engineering, Shanghai University, Shanghai 200444, China

Correspondence should be addressed to Huiling Zhao; hlzhao@shu.edu.cn

Received 29 July 2020; Revised 19 November 2020; Accepted 30 November 2020; Published 17 December 2020

Academic Editor: Wen-Chieh Cheng

Copyright © 2020 Chao Zhang et al. This is an open access article distributed under the Creative Commons Attribution License, which permits unrestricted use, distribution, and reproduction in any medium, provided the original work is properly cited.

In the construction of mountain highway, in order to avoid complicated geology and adapt to the requirements of the terrain of the large height difference and the large slope, the double-line spiral tunnels are gradually applied. The purpose of this paper is to analyze the mechanical behavior of the double-line spiral tunnel and its surrounding rock under different line curvatures, and to obtain the influence of the curvature of the spiral tunnel on the stability of the double-line tunnel construction. The analysis of this paper is based on the engineering background of double-line spiral tunnels in China's Yunnan province. The elastoplastic three-dimensional rock strata-tunnel by means of finite difference FLAC3D software was established to simulate the construction process. The model was verified by comparing the calculation results and the actual monitoring data of tunnel vault settlement. The small curvature radius spiral makes the mechanical behavior of the double-line tunnel uneven and the surrounding rock deformed unevenly. A quantitative analysis and qualitative evaluation of the influence of curvature radius were established by the systematic evaluation index of (1) ratio of compressive stress on both sides of the tunnel, (2) stress ratio of double-line tunnel, (3) convergent deformation of the cross section of the tunnel, and (4) deformation of the surrounding rock on the top of the tunnel. The results show that the small curvature radius (less than 200 m) will make the inner pressure of the inner tunnel significantly greater than the external pressure stress, showing obvious asymmetry, and the inner tunnel vault tensile stress is greater than the outer tunnel. With the increase of the curvature radius (about more than 400 m), the ratio of the compressive stress on the inside and outside of the tunnel tends to be constant, and the bias condition is weakened and stabilized. Meanwhile, the smaller curvature radius makes the convergent deformation of the cross section of the tunnel appear asymmetrical, and the compression quantity inside the tunnel center line is larger. It provides a reference basis for the stability control of the construction of the double-line spiral tunnels in the mountainous area.

1. Introduction

The mountainous area of the plateau tends to be characterized by the deep valley and high mountain. In order to avoid poor geology and adapt to the requirements of large height difference and large longitudinal slope terrain, the tunnel alignment is usually designed to be spiral [1–3]. The alignment of the spiral tunnel is composed of continuous codirectional curves. Due to the limitation of the terrain, obstacles, and the engineering investment, the curvature of the tunnel axis line is required to be tight [4]. Besides, the tunnel is designed as a two-way double-line to improve the traffic capacity effectively [5]. The construction technology

of double-line spiral curve tunnels with the small curvature radius in rock has gradually attracted attention. The deformation and stability of the surrounding rock during the excavation are critical to the safety of tunnel construction. It is significant to clarify the influence of the curvature of the double-line tunnel on the surrounding rock deformation under the specified geological conditions, and to predict the deformation range and deformation amount of the excavation face and near area.

Hao [6] found that the asymmetry of ground-surface settlement profile caused by the tunnel excavation is related to the curved alignment of the tunnel by observations. Under the dual action of asymmetric overcutting and

construction loadings, the surface settlement of the curved tunnel is larger than that of the straight-line tunnel [7]. Huynh studied an innovated mechanized tunneling technology to construct a twin spiral tunnel at once by multi-circular face shield, and also the cross section can be changed from a horizontal double circular shape to a vertical one [8]. Numerical simulations have been explored to study the stratum disturbance caused by the construction of a tunnel at curved alignment [9–12]. Mitsutaka et al. employed the proposed three-dimensional FEM kinematic model to compute immediate ground movements by a curved shield tunnel excavation in multilayered ground [13]. Li et al. [14] focused on the stress distribution of segments for a curved shield tunnel during construction, and segment stress variation from curvature of tunnel alignment, and deviation of the Jack. However, most of the above studies aimed at the curved shield tunnel in soft soil. Little literature was found to study the curved or spiral tunnels in rock. In the mountainous area of west China, tunnels are mostly constructed in rock. Ganhaizi Tunnel on Yalu Highway is a typical spiral twin tunnel in rock, and the curvature radius of the left and right lines is 600 m and 618 m, respectively [15]. Such type of tunnels in rock is widely constructed recently [16]. Systematic numerical simulations of a series of tunnels with different curvatures at curved alignments need to explore asymmetric mechanical behaviors of the single spiral. Also, the differences between the twin spiral tunnels at double lines need to be paid attention. There is a slight difference in curvature.

In this paper, based on the tunnel project in Honghe, Yunnan, a 3D elastoplastic numerical model for double-line spiral tunnels in rock was established. The model was verified by the on-site monitoring data. The deformation of the surrounding rock caused by the excavation of the double-line tunnels with the curvature radius from 122 m to 722 m was calculated. The stress and deformation distribution of the tunnels were studied and compared to obtain the asymmetric behaviors of the double-line spiral tunnels. The influence of the curvature radius on tunnel arch settlement, lateral convergence deformation, and tunnel stress distribution was analyzed. This result provides reference and guidance for safety control of tunnel design and construction in similar engineering cases.

2. Analysis of Double-Line Spiral Tunnel Excavation Process

2.1. Characteristics of Spiral Tunnel. The double-line spiral tunnel studied in this paper is in China's Yunnan province. The left-line tunnel has a total length of 3900 m and a curvature radius of 703 m. The right-line tunnel has a total length of 4015 m and a curvature radius of 741 m. The longitudinal gradient of the unidirectional slope of the tunnel is 3.9%. The tunnel alignment at the entrance is the direction of 13°, and the tunnel alignment at the exit is the direction of 167°. The tunnel is deeply buried, and the maximum buried depth is 366 m. The height difference between the tunnel entrance and exit is about 80 m. The left tunnel was excavated firstly, then the right line was

excavated. The excavation faces of the two tunnels are about 80 m apart during the construction process. The rock through which the tunnel passes is mainly granite.

2.2. Establishment of 3D Numerical Model. The interval of K36 + 395~K36 + 545 in the double-line spiral tunnel is selected as the object of three-dimensional numerical simulation analysis. The length of the tunnel alignment is 150 m. The outer diameter of the single tunnel is 12.08 m, and the clear distance between the left and right tunnels is 25 m. The depth of the tunnel center is 215 m. The surrounding rock of the tunnel is of grade III. The rock range considered in the numerical model is 3–5 times the outer diameter of the single tunnel. The width and height dimensions of the three-dimensional rock-tunnel model are 130 m and 110 m, respectively. The X-axis is the transverse direction of the initial section of the tunnel, the Y-direction is the tunnel axis direction, and the Z-axis is the vertical direction. The bottom boundary of the numerical model is fixed, and the lateral boundary constraint is normally horizontal translation. The numerical calculation model is shown in Figure 1. The thickness of the primary lining of the tunnel is 10 cm, and the thickness of the secondary lining is 35 cm. During the construction of the tunnel, $\phi 44$ mm bolts were used for support, with a bolt depth of 2.5 m and a spacing of 1.45 m.

The Mohr-Coulomb constitutive model was adopted for the rock mass, while the elastic material model was adopted for the concrete tunnel lining and the anchor rod. The material parameters are shown in Table 1.

In order to eliminate the influence of complicate initial stress distribution, the initial stress of the rock in the numerical model was simplified. The initial stress of the original rock was a geostatic field type, on which the set of vertical initial stress was based. Both horizontal stresses were proportional to the vertical stress, and the proportionality factor is 0.5. The ground water was not considered in the simulation. The rock mass was a uniform rock stratum without consideration of tectonic activities in the rock. The parallel integrated contact was set between the different rock layers. In the simulation, the tunnel excavation was a step-by-step excavation. The single excavation step completed 3 m excavation forward. The excavated rock and soil were set as empty model. The lining and anchor support structure were established during the excavation.

2.3. Comparison with the Actual Monitoring Data. The tunnel crown settlements were monitored when the right line tunnel was excavated to the points YK21 + 640 m, YK21 + 680 m, YK21 + 700 m, and YK21 + 720 m during construction. The monitoring results were compared with the results obtained by numerical simulation in order to verify the numerical simulation in this paper. As shown in Figure 2, the vertical ordinate indicates the amount of settlement of the vault, and the abscissa ordinate indicates the number of construction days from the excavation face. It can be seen from Figure 2 that the settlement of the tunnel vault from the 1st to 8th day developed faster, then it got slowly in 8–15 days, and the final cumulative settlement was

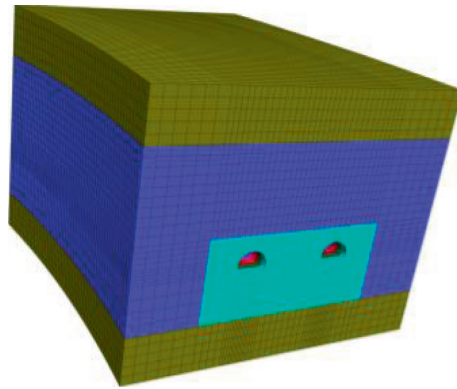


FIGURE 1: A numerical model for tunnel excavation simulation in FLAC3D.

TABLE 1: The material parameters of the tunnel numerical model.

Rock				
Cohesion (kPa)	Friction angle (°)	Volumetric weight (kNm ⁻³)	Elastic modulus (GPa)	Poisson's ratio
900	45	26.5	6.5	0.20
Anchor				
Stiffness of cement slurry per unit length (MPa)	Elastic modulus (GPa)		Cross-sectional area (mm ²)	
17.6	210		380	
Initial lining			Secondary lining	
Elastic modulus (GPa)	Poisson ratio	Elastic modulus (GPa)	Poisson ratio	
10	0.2	10	0.2	

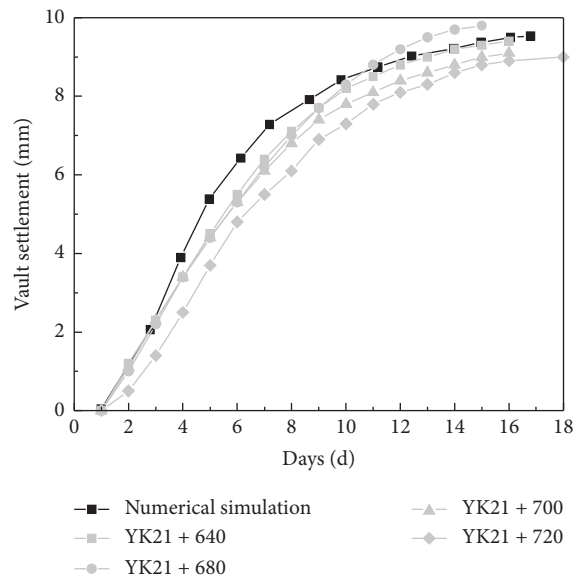


FIGURE 2: Comparison of numerical simulation and monitoring of tunnel vault settlement.

in the range of 8–14 mm. The development of settlement by numerical simulation is similar to the monitoring settlement, and the overall trend is relatively consistent. The average deviation between the maximum settlement simulation result and the monitoring data is about 11%. Except for accidental construction factors, the numerical simulation result is reasonable and credible.

2.4. Comparison with the Analytical Solution. The analytical methods offer a rapid analysis of the stress and strain fields and are practical for predicting the mechanical behaviors of the tunnel and the surrounding rock. The calculation model of the shallow tunnels is more complicated than the deep tunnels, which are so distant from the ground surface that the stress boundary condition is equal to the initial stress

[17, 18]. As for the shallow double-tunnel, the elastic analytical solution can be obtained by the complex variable method together with the Schwartz alternating method [19, 20]. In the references [21, 22], the elastic region in the z -plane was mapped conformally onto a circular ring in the ζ -plane, bounded by the circles $|\zeta| = 1$ and $|\zeta| = \alpha$, as shown in Figure 3. The conformal mapping transformation is

$$z = \omega(\zeta) = -ih \frac{1 - \partial^2}{1 + \partial^2} \frac{1 + \zeta}{1 - \zeta} \quad (1)$$

By the ζ -plane, the complex variable solution for a circular tunnel in an elastic half plane was obtained under boundary conditions of the stress-free surface and the assumed displacement around the tunnel. And then the effect of the interaction between the two parallel tunnels was calculated by the Schwarz alternating method on one tunnel to another iteratively to satisfy the boundary conditions. The solution is limited to the tunnels with the circular cross section. Few analytical methods were conducted for the shallow double-tunnel with three-centered arch cross section. What is more, this paper focuses on the effect of the alignment of the spiral tunnel on the tunnel and surrounding rock. Three-dimensional elastic body with the double uncircular holes brings about challenge to the analytic solution. Therefore, this paper turns to the numerical analysis. Conventionally, the stability of tunnel structures can be analyzed with, e.g., finite element method and discrete element method [23–26]. In the paper, Fu's [21] analytic solution of shallow double tunnels in two-dimensional plane is used for a preliminary estimation and validation for the numerical analysis in some degree. Figure 4 shows the surface settlement curves by the analysis results by the 3D numerical model in Section 2.2 and Fu's 2D analytic solution for shallow circular double-tunnel, respectively. The two curves are close to each other. By the numerical analysis, due to the spiral tunnel alignment, the settlement of the left tunnel side is larger than the right tunnel side, while the 2D analytic solution is incapable of considering the effect of the spiral alignment.

3. Influence of Curvature on Mechanical Behaviors of Tunnels

3.1. Parametric Analysis of Numerical Experiments. In order to systematically analyze the influence of the curvature radius of the double-line spiral tunnel on the deformation and stress of the tunnel and surrounding rock, seven models with different curvature radii of tunnel alignment were set for numerical simulations, as shown in Table 2. The variation range of curvature radius in the table was selected based on the actual project, and 7 equal interval levels were determined to conduct parametric analysis.

The quantitative analysis and qualitative evaluation of the influence of the curvature radius on the tunnel construction stability were comprehensively analyzed to obtain the influence of the curvature radius on the unevenness of the mechanical behavior of the double-line tunnel and the overall surrounding rock. Four indicators were selected for

stability evaluation as 1) compressive stress ratio of both sides at cross section of a single spiral tunnel, (2) stress ratio of the two tunnels at double-line, (3) tunnel cross section convergence deformation, and (4) rock deformation on the top of tunnels. Index 1 reflects the influence of curvature radius on the stress asymmetry between the inner and outer sides of the tunnel lining. Index 2 reflects the influence of curvature radius on the stress asymmetry between the left and right tunnel linings. Index 3 reflects the influence of curvature radius on the deformation unevenness of tunnel. Index 4 reflects the influence of curvature radius on the deformation tendency of surrounding rock.

3.2. Influence on Stress Asymmetry of Tunnel Lining.

Figure 5 shows the minimum principal stress cloud diagram of the tunnel lining when the curvature radius R of the center line of the double-line spiral tunnel is 122 m, 422 m, and 722 m. The asymmetry of the internal and external stresses is significant when R is 122 m. The asymmetry of the tunnel stress is not obvious when R is 422 m and 722 m.

Figure 6 shows the maximum principal stress cloud diagram of the tunnel lining when the curvature radius R is 122 m, 422 m, and 722 m. When R is 122 m, the tensile stresses of the left and right tunnel arches at the beginning of the excavation are significantly different. When R is 422 m and 722 m, the difference in tensile stress between the left and right tunnels is not obvious.

The curve of stress ratio varying with curvature radius in Figure 7 is to quantify the influence of the curvature radius on the stress unevenness of the tunnel. As shown in Figure 7(a), when R is 122 m, the compressive stress ratio between the inside and outside of the left tunnel lining is the largest, reaching 1.38. As the curvature radius increases, the ratio of the inner and outer compressive stresses of the left line gradually decreases. When the curvature radius is greater than 422 m, the ratio approaches 1.1. The compressive stress inside the left tunnel is always greater than the compressive stress outside. When R is 122 m, the ratio of the compressive stress between the inside and the outside of the lining of the right line tunnel is the largest, reaching 1.09. At this time, the compressive stress on the inside is greater than the outside. As the curvature radius increases, the ratio of the inner and outer compressive stresses on the right line gradually decreases. When the curvature radius increases to 322 m, the ratio is less than 1.0. At this time, the inner compressive stress is less than the outer compressive stress, and the final ratio approaches 0.95.

As for the double-line spiral tunnel, the tensile stress at the vault of the inner (left) line tunnel is always greater than that of the outer line tunnel. When R is 122 m, the tensile stress ratio of the inner and outer line lining is the largest, reaching 1.14. As the curvature radius increases, the ratio gradually decreases, as shown in Figure 7(b). It can be seen that there is a significant difference in the unevenness and distribution of the compressive stress on the inside and outside of the left and right tunnels, which should be paid attention to in the design and construction of the tunnel.

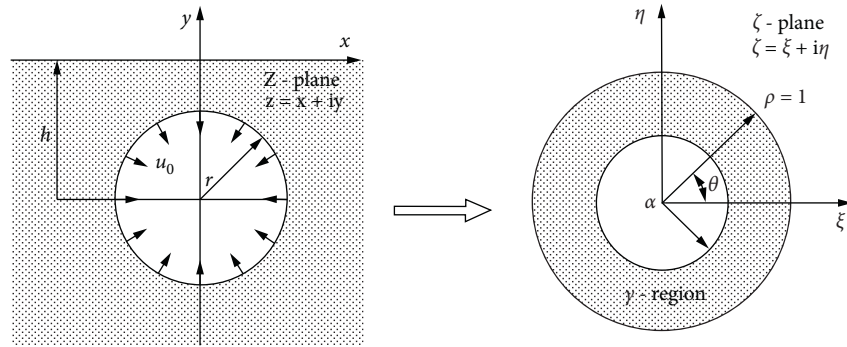


FIGURE 3: Conformal mapping from z -plane to ζ -plane [17].

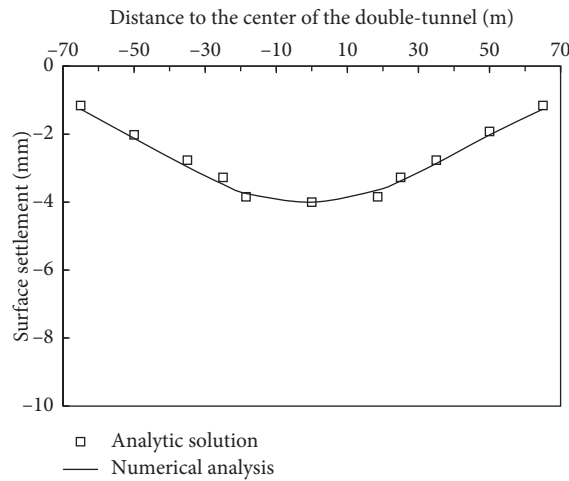


FIGURE 4: Comparison between the numerical results and Fu's analytic solution.

TABLE 2: Different curvature radius of the tunnel alignment for numerical simulations.

Model no.	Curvature radius of left line- R_L/m	Curvature radius of right line R_R/m	Center line radius of two line- R/m
1	103	141	122
2	203	241	222
3	303	341	322
4	403	441	422
5	503	541	522
6	603	641	622
7	703	741	722

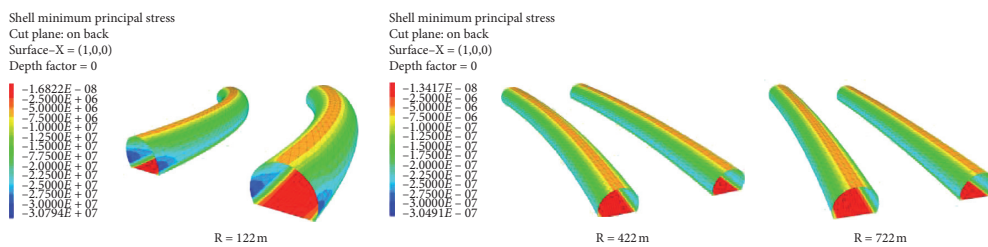


FIGURE 5: Minimum principal stress of tunnels with different curvature radii (Pa).

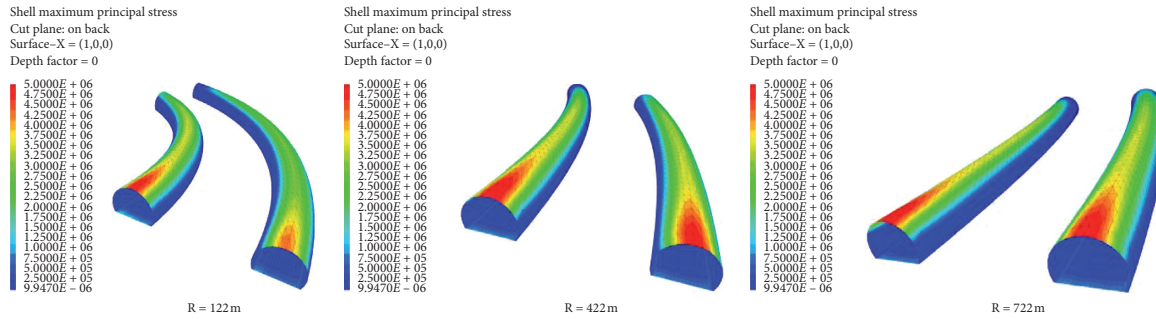


FIGURE 6: Maximum principal stress of tunnels with different curvature radii (Pa).

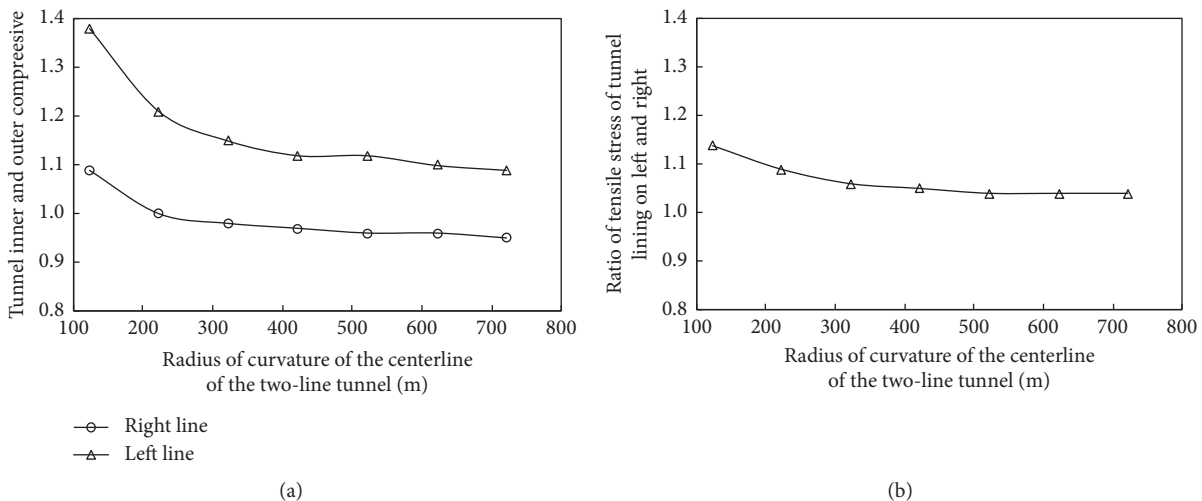


FIGURE 7: Variation curve of asymmetric stress ratio with the curvature radius.

3.3. Influence on the Unevenness of Tunnel Deformation.

The small curvature radius of the tunnel causes the uneven deformation of the cross section of the double-line spiral tunnel. As shown in Figure 8, as the tunnel excavation depth increases, the amount of convergence deformation of the initial cross section gradually increases and tends to be stable. Among them, the distance between the two points B and C increases, and the distance between the two points A and B and the distance between the two points A and C decrease, indicating that the entire section is deformed by transverse compression, and the vault A settles downward. The vault settlement of the double-line spiral tunnel with a curvature radius of 122 m is greater than that with a radius of 722 m.

As shown in Figures 8(a) and 8(b), when R is 122 m, the AB convergence deformation is less than AC, indicating that the convergence deformation on both sides of the tunnel center line is uneven. The entire cross section deformation is compressed inward, and asymmetry is shown. It can be seen from the figure that the asymmetry of the inner line (left line) tunnel is greater than that of the outer line tunnel, which is consistent with the distribution law of compressive stress inside and outside the tunnel. As shown in Figure 8(c), when R is 722 m, the AB convergence deformation is slightly smaller than AC but very close, indicating that the

convergence deformation unevenness on both sides of the tunnel center line is not obvious.

3.4. Influence on Deformation of Surrounding Rock.

Figure 9 shows the vertical deformation cloud diagram of the tunnel surrounding rock when the curvature radius R of the center line of the double spiral tunnel is 122 m and 722 m, respectively. It can be seen from the figure that the clear distance between the left and right tunnels is greater than 2 times the diameter of the tunnel, so the mutual disturbance caused by the construction of the double-line tunnel is weak. At this time, two settlement grooves appear in the vertical deformation curve of the surrounding rock.

It should be noted that when R is 122 m, the deformation of the surrounding rock of the left and right tunnels shows an obvious asymmetry. Within the tunnel height range, the amount and range of vertical deformation of the surrounding rock of the inner tunnel are larger than those of the outer tunnel. As for the area above the tunnel vault, the vertical deformation range of the surrounding rock inside the inner tunnel is smaller than that outside the outer tunnel. Differently, when R is 722 m, the vertical deformation of the surrounding rock of the tunnel is a typical W-shaped symmetrical trend, which is in line with the trend of the

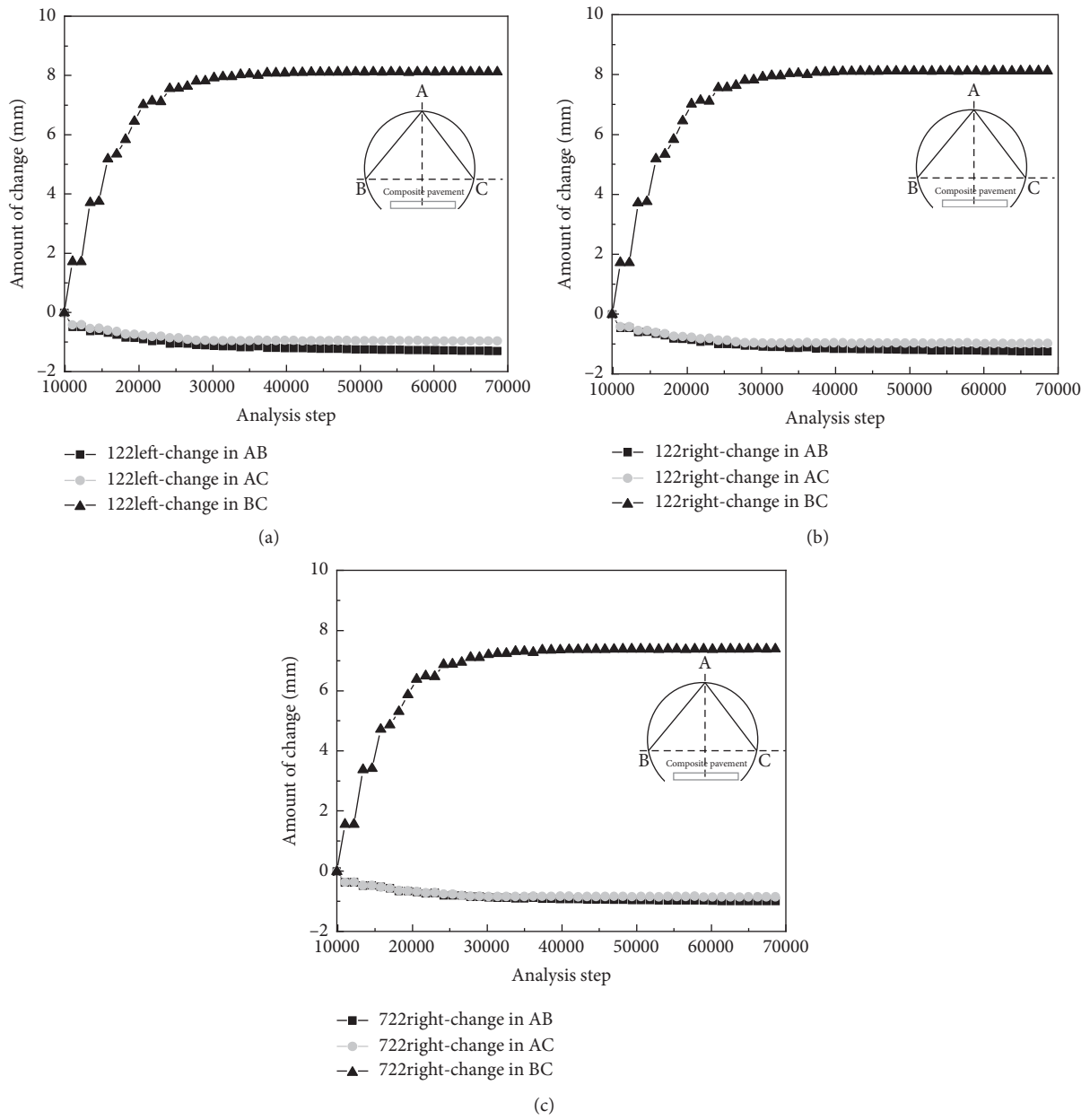


FIGURE 8: Convergent deformation curve of the tunnel cross section during construction.

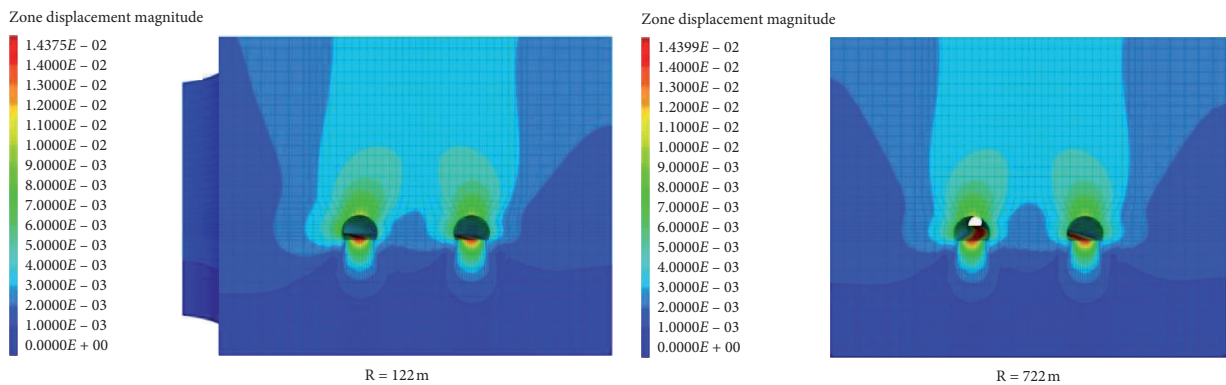


FIGURE 9: Deformation of the tunnel surrounding rock (m).

deformation of the surrounding rock for the separated double-line tunnel at straight-line alignment.

4. Conclusions

Based on the project of a double-line spiral tunnel in China's Yunnan province, a three-dimensional elastoplastic finite difference model of rock-tunnel was established in FLAC3D. Furthermore, by numerical simulation, the influence of the curvature radius on the mechanical behaviors of the double-line spiral tunnel during the construction process is studied. The following conclusions can be obtained:

- (1) When the curvature radius of the double-line spiral tunnel is small (about less than 200 m), the stress distribution of tunnels shows asymmetry. The compressive stress at the internal side is greater than the external one. Compared with outside tunnel, the asymmetry of inside tunnel is more significant. As the curvature radius increases (approximately greater than 400 m), the compressive stress ratio of the inside side to the outside side tends to be fixed. The smaller curvature radius results in the fact that the tensile stress at the vault of the inner tunnel is significantly larger than that of the outer tunnel.
- (2) The convergence deformation of the tunnel cross section gradually increases and then tends to be stable as the construction process. Transverse compression deformation occurred on both cross sections of the double-line tunnel, and point A at the vault settled downward. It should be noted that when the curvature radius of the spiral tunnel is small, asymmetry occurs in the convergence deformation on both sides of the tunnel center line. The entire cross section deformation is compressed inwards, and the asymmetry of the inner tunnel is greater than that of the outer tunnel. What is more, the small curvature radius results in a large settlement at vault of the tunnel.
- (3) The distance between the left and right tunnels is greater than 2 times the diameter of the tunnel, so the mutual disturbance of the construction of the double-line tunnel is weak. Two settlement slots appear in the vertical deformation curve of the surrounding rock. When the curvature radius of the double-line spiral tunnel is small (about less than 200 m), the deformation of the surrounding rock of the left and right tunnels is obviously asymmetric. The vertical deformation of the surrounding rock on top of the inner line tunnel is greater than that of the outer line tunnel. When the curvature radius is large, the vertical deformation curve of the surrounding rock is typical W-shaped symmetrical, which is consistent with the trend of the deformation of the surrounding rock of the separated double-line tunnel at straight-line alignment.

The influence of the curvature radius of the tunnel alignment on the deformation and stress of the double-line

spiral tunnel and its surrounding rock provides a reference for the construction stability control measures of the similar double-line spiral tunnel.

Data Availability

This is an open-access article distributed under the Creative Commons Attribution License, which permits unrestricted use, distribution, and reproduction in any medium, provided the original work is properly cited.

Conflicts of Interest

The authors declare that they have no conflicts of interest.

References

- [1] Wogli G. Railway Network Switzerland. Swiss Federal Railways, General Secretariat, 1980.
- [2] M. David, "Spiral tunnel runs rings around arctic circle dam site," *Tunnels and Tunnelling International*, vol. 16, no. 11, pp. 15–17, 1987.
- [3] B. Chen, H. Ren, and L. X. Fu, "On the portal construction technology of spiral tunnel in special stratum," *Applied Mechanics and Materials*, vol. 94–96, pp. 1879–1884, 2011.
- [4] N. Losacco and G. M. B. Viggiani, "Class A prediction of mechanised tunnelling in Rome," *Tunnelling and Underground Space Technology*, vol. 87, pp. 160–173, 2019.
- [5] A. Paithankar, "Critical appraisal of double spiral cut in tunnel blasting," in *Proceedings of International Society for Rock Mechanics and Rock Engineering International Symposium*, pp. 370–388, Madrid, Spain, September 1988.
- [6] F. Hao, "Analysis and prediction of uneven settlement due to a curved shield metro tunnel," *Civil Engineering Research Journal*, vol. 7, no. 4, Article ID 555720, 2019.
- [7] M. Zhang, S. Li, and P. Li, "Numerical analysis of ground displacement and segmental stress and influence of yaw excavation loadings for a curved shield tunnel," *Computers and Geotechnics*, vol. 118, Article ID 103325, 2020.
- [8] T. Huynh, M. Sugimoto, and J. Chen, "Study on steering method of H&V shield to construct a spiral tunnel," in *Proceedings of ITA WTC 2015 Congress*, Dubrovnik, Croatia, May 2015.
- [9] A. Alsahly, J. Stascheit, and G. Meschke, "Advanced finite element modeling of excavation and advancement processes in mechanized tunneling finite element modeling of excavation and advancement processes in mechanized tunneling," *Advances in Engineering Software*, vol. 100, pp. 198–214, 2016.
- [10] S. Miliziano and A. de Lillis, "Predicted and observed settlements induced by the mechanized tunnel excavation of metro line C near S. Giovanni station in Rome," *Tunnelling and Underground Space Technology*, vol. 86, pp. 236–246, 2019.
- [11] T. N. Huynh, J. Chen, and M. Sugimoto, "Analysis on shield operational parameters to steer articulated shield," *Japanese Geotechnical Society Special Publication*, vol. 2, no. 42, pp. 1497–1500, 2016.
- [12] T. Huynh, H. Pham, and M. Sugimoto, "Simulation of H&V shield behavior at sharp curve by kinematic shield model," *Geotechnical Engineering Journal of the SEAGS & AGSSEA*, vol. 2, no. 48, pp. 96–103, 2017.
- [13] S. Mitsutaka, S. Aphichat, K. Shinji, and S. Yutaka, "Simulation of shield tunneling behavior along a curved alignment

- in a multilayered ground,” *Journal of Geotechnical and Geoenvironmental Engineering*, vol. 133, no. 6, pp. 684–695, 2007.
- [14] S. Li, G. Gu, P. Li, and M. Zhang, “Numerical simulation of mechanical properties of the segments for a curved shield tunnel during construction stage: a case study,” in *Proceedings of International Conference on Geotechnical and Earthquake Engineering*, pp. 61–69, Chongqing, China, October 2018.
- [15] X. Wu, “Safe construction technology of ganhaizi spiral tunnel,” *Southwest Highway*, vol. 4, pp. 85–89, 2009, in Chinese.
- [16] S. He, Y. Wu, and J. Zang, “Study on ventilation characteristics of high-drop spiral tunnel during operation period,” in *Proceedings of the 11th International Symposium on Heating, Ventilation and Air Conditioning (ISHVAC 2019)*, Singapore, March 2019.
- [17] M.-B. Wang and S.-C. Li, “A complex variable solution for stress and displacement field around a lined circular tunnel at great depthfield around a lined circular tunnel at great depth,” *International Journal for Numerical and Analytical Methods in Geomechanics*, vol. 33, no. 7, pp. 939–951, 2009.
- [18] A.-z. Lu, L.-q. Zhang, and N. Zhang, “Analytic stress solutions for a circular pressure tunnel at pressure and great depth including support delay,” *International Journal of Rock Mechanics and Mining Sciences*, vol. 48, no. 3, pp. 514–519, 2011.
- [19] A. R. Kargar, R. Rahmancejad, and M. A. Hajabasi, “A semi-analytical elastic solution for stress field of lined non-circular tunnels at great depth using complex variable methodfield of lined non-circular tunnels at great depth using complex variable method,” *International Journal of Solids and Structures*, vol. 51, no. 6, pp. 1475–1482, 2014.
- [20] A.-Z. Lu, N. Zhang, and L. Kuang, “Analytic solutions of stress and displacement for a non-circular tunnel at great depth including support delay,” *International Journal of Rock Mechanics and Mining Sciences*, vol. 70, pp. 69–81, 2014.
- [21] J. Fu, J. Yang, L. Yan, and S. M. Abbas, “An analytical solution for deforming twin-parallel tunnels in an elastic half plane,” *International Journal for Numerical and Analytical Methods in Geomechanics*, vol. 39, no. 5, pp. 524–538, 2015.
- [22] F. Kong, D. Lu, X. Du, and C. Shen, “Elastic analytical solution of shallow tunnel owing to twin tunnelling based on a unified displacement function,” *Applied Mathematical Modelling*, vol. 68, pp. 422–442, 2019.
- [23] J. P. Sahoo and J. Kumar, “Stability of long unsupported twin circular tunnels in soils,” *Tunnelling and Underground Space Technology*, vol. 38, pp. 326–335, 2013.
- [24] F. Yang and J. S. Yang, “Stability of shallow tunnel using rigid blocks and finite-element upper bound solutions,” *International Journal of Geomechanics*, vol. 10, no. 6, pp. 242–247, 2010.
- [25] Y. Zhang, X. Zhuang, and R. Lackner, “Stability analysis of shotcrete supported crown of NATM tunnels with discontinuity layout optimization,” *International Journal for Numerical and Analytical Methods in Geomechanics*, vol. 42, pp. 1–18, 2018.
- [26] Z. Sun, Y. Zhang, Y. Yuan, and H. Mang, “Stability analysis of a fire-loaded shallow tunnel by means of a thermo-hydro-chemo-mechanical model and discontinuity layout optimization,” *International Journal for Numerical and Analytical Methods in Geomechanics*, vol. 43, pp. 1–14, 2019.

Research Article

Experimental Study on the Transverse Effective Bending Rigidity of Segmental Lining Structures

Yong-feng Tang,¹ Han-cheng Chen,¹ Zhen-wei Ye,¹ Ting-jin Liu ,^{2,3,4} and Yu-bing Yang ⁵

¹School of Civil Engineering and Transportation, South China University of Technology, Guangzhou 510640, Guangdong, China

²South China Institute of Geotechnical Engineering, South China University of Technology, Guangzhou 510640, Guangdong, China

³State Key Laboratory of Subtropical Building Science, South China University of Technology, Guangzhou 510640, Guangdong, China

⁴School of Engineering, University of Tasmania, Hobart 7005, Tasmania, Australia

⁵College of Water Conservancy and Civil Engineering, South China Agricultural University, Guangzhou 510642, Guangdong, China

Correspondence should be addressed to Ting-jin Liu; liu_tingjin@163.com

Received 6 September 2020; Revised 13 November 2020; Accepted 24 November 2020; Published 10 December 2020

Academic Editor: Wen-Chieh Cheng

Copyright © 2020 Yong-feng Tang et al. This is an open access article distributed under the Creative Commons Attribution License, which permits unrestricted use, distribution, and reproduction in any medium, provided the original work is properly cited.

The transverse effective rigidity ratio is a key parameter when the uniform rigidity ring model is adopted to design or numerically analyse segmental lining structures commonly used on a shield-driven tunnel. Traditionally, the transverse effective rigidity ratio η is treated as a constant, which can be evaluated through theoretical analysis and model tests. In this study, scale models were designed and tested to investigate the variation of the transverse effective rigidity ratio in the segmental linings' flattening deformation process. The test results suggested that in the elastic stage, the transverse effective rigidity ratio fluctuated between 0.667 and 0.734 for the stagger-jointed rings and fluctuated between 0.503 and 0.642 for the straight-jointed rings. When segmental linings were squashed and started to crack at the circumferential joints, the transverse effective rigidity ratio decreases sharply. Then, a regression equation was obtained to fit the variation trend of η with the increase of horizontal convergence to the outer-diameter ratio ($\Delta D/D_{out}$). Finally, in a case study, the regression equation was adapted to determine the value of η of an operated shield tunnel which was once surcharged accidentally and deformed severely so as to numerically predict the prospective deformation induced by the upcoming adjacent excavation. Numerical results indicated that as the value of η decreases, the horizontal convergences of shield tunnel induced by adjacent excavation increase significantly and even more than doubled in the case study. Comparatively, through taking account of the operating tunnels' exiting transverse deformation, the predicted deformation tends to be unfavourable.

1. Introduction

The shield-driven tunnelling method has been widely used for the construction of underground tunnels in urban areas because it has advantages including flexibility, highly safe construction efficiency, and minimum impact on the surrounding environment. Most shield-driven tunnels have utilised segmental linings connected by steel bolts. Besides, tunnel segments are often articulated or coupled at longitudinal and circumferential joints. Therefore, the characteristics

of joints have a notable influence on the behaviour of the segmental linings. As a result, the effect of the joints on internal forces and deformation characteristic should be taken into consideration in the design or safety evaluation of the tunnel lining. In the engineering and numerical analyses related to the underground shield-driven tunnel problems, figuring out accurately the mechanism performance of segmental linings has always been one of the major foci [1–3].

Consequently, appropriate design models, which can accurately reflect the internal force and the loading

condition imposed by the various surrounding ground, are essentially required. In 1978, the International Tunnelling Association [4] set up a professional team to collect design model for shield tunnel linings applied in different countries. Lee et al. [5] classified the typical methods of shield tunnel lining design into four major categories: (a) empirical design methods based on past tunnelling practices; (b) design methods based on the in situ measurement and laboratory testing; (c) circular ring in elastic foundation method; and (d) continuum mechanics models including analytical methods and numerical methods.

Generally, shield tunnel lining behaviour is often approached as two plane problems along the transverse and longitudinal direction in the design process although it is a three-dimensional problem [6, 7]. Accordingly, the shield tunnel lining is usually regarded as a planar problem in the transverse direction. Among the design models mentioned above, more often than not, the circular ring in the elastic foundation method is utilised for both design and analysis purposes. This method can also be categorized according to how the joints of concrete segments are regarded, namely: (1) uniform rigidity ring method [8]; (2) average uniform rigidity ring [9–12]; (3) multihinge ring [13]; and (4) beam-spring model [14–16]. The structural models that correspond to these approaches are illustrated in Figure 1.

The uniform rigidity ring method is carried out by absolutely ignoring the existence of the segment joints and that resulting in an inaccurate bending moment at the joint area. The multihinge ring method takes the segment joints as perfect pins and is suitable and appropriate for the tunnelling boring machine- (TBM-) driven tunnel in hard rock [17], where the surrounding rock can maintain self-stability and transfer enough reaction to the lining. The beam-spring model, which simulates segmental joints with rotational springs and reflects relatively accurate stiffness of the segmental joints, is comparatively complex in calculation and limited in application. In fact, after a great number of practices and experience, especially in soft ground, the average uniform rigidity ring method has been widely employed in segmental lining design of shield tunnel for its clear mechanical concept and the simple calculation. In the average uniform rigidity ring method, the presence of the joints is considered by introducing two factors [12], namely, the effective ratio of bending rigidity η reflecting the relative stiffness between the segmental lining and the continuous lining structure and the transfer ratio of bending moment ξ reflecting the relative stiffness between segment and joint. Accordingly, the equivalent stiffness of the segmental lining ring is ηEI ($\eta \leq 1$), as shown in Figure 2, and the bending moments of the segment and the joint are modified to be $(1 + \xi) M_0$ and $(1 - \xi) M_0$, respectively, as shown in Figure 3.

Thus, it can be seen that the value of the effective ratio of the transverse bending rigidity has great theoretical significance because the maximum bending moment of segments and the diameter convergence of linings are closely associated with the effective rigidity. Until now, the research studies mainly focus on the value and influence of the effective ratio of the transverse bending rigidity, typically by the means of analytical solution and laboratory structural testing.

Wood [10] presented an analytical approach to compute the effective ratio of the transverse bending rigidity taking the influence of joint stiffness and segment number into consideration. Through assuming the deformation mode of the circular tunnel is an ellipse, Liu and Hou [19] proposed the elastic analytical formula for the value of η of the segmental lining. Lee et al. [5] proposed the iterative analytical method of η through employing the multihinge ring model, and the fitting formula of the relationship between the effective ratio of the transverse bending rigidity and the parameters (tunnel radius, lining thickness, strata resistance coefficient, joint stiffness ratio, etc.) was obtained for the segment assembling types with the straight joint. Accordingly, their research concluded that the value of η ranges from 0.1~0.6 in most of the soft ground. Zhong et al. [20] qualitatively analysed the effective ratio of the transverse bending rigidity after comparing the results calculated by the average uniform rigidity ring and beam-spring models. Also, they suggested that the effective ratio of the transverse bending rigidity η of Chinese subway tunnels generally ranges from 0.4 to 0.8.

Xu [21] and Huang et al. [22] fabricated the segments and joints with polyethylene (PE) and PE sheets separately and assembled into two-ring tunnel models. The laboratory model test result indicated that the effective rigidity ratios of the tunnel with straight joints and stagger joints were 0.67 and 0.75, respectively, for Shanghai Metro and the effect of soil resistance on the effective rigidity of shield tunnel was very small in soft ground. Ye et al. [23] designed and manufactured three types of circular ring model, namely, straight-jointed ring, stagger-jointed ring, and uniform ring, which were made of PMMA simulating segments and aluminium welding wire simulating bolts. It is reported that the range of the effective ratio of the transverse bending rigidity value is between 0.09 and 0.23 under straight-jointed condition and 0.30 and 0.80 under stagger-jointed condition. Zheng et al. [24] also adopted polyethylene and aluminium wire to fabricate the shield tunnel models, and the effective rigidity ratios of the tunnel were investigated through testing the model under the concentrated load and realistic loading pattern in sandy soil. Taking the Shanghai Yan-Jiang Tunnel as an example, Li et al. [25] analysed the influence of buried depth on the effective ratio of the transverse bending rigidity and found that the buried depth has a great influence on η . Feng et al. [26] carried out prototype tests on segmental lining structure for shield tunnel with a large cross section and attained the variation pattern of η and ξ with load conditions; the experiment also showed that as the section increases, η increases while ξ decreases. Many Japanese scholars suggested that the method of the whole ring loading test should be used to determine η . In the design of Tokyo Bay expressway shield tunnel, Uchida [27] adopted the uniform circular ring model with $\eta = 0.8$ and then carried out the prototype loading test of the whole ring to prove the reasonability and validity of the value. Kashima et al. [28] conducted prototype loading tests on the stagger-jointed mode of the DPLEX shield tunnel and determined that an η value of 0.8 was meaningful. In conclusion, Japan Society of Civil Engineers recommends

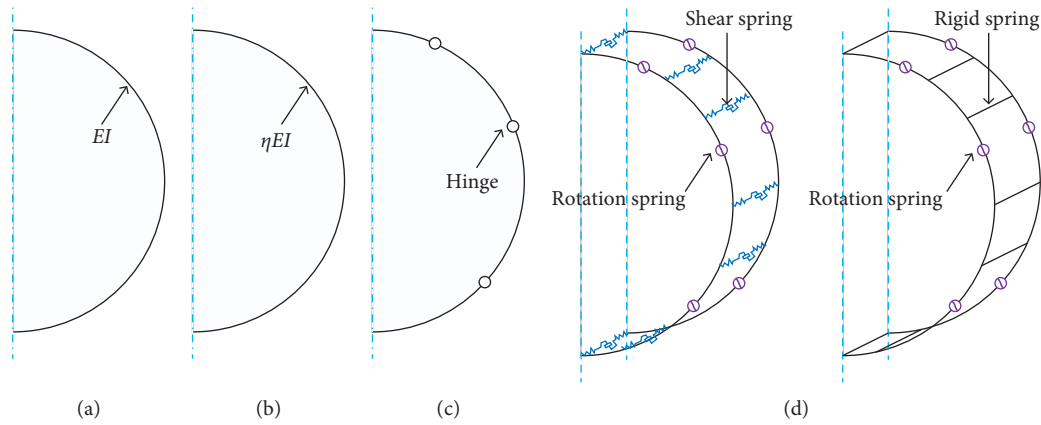


FIGURE 1: Structural models of the shield segment. (a) Uniform rigidity ring method. (b) Average uniform rigidity ring. (c) Multihinge ring. (d) Beam-spring model.

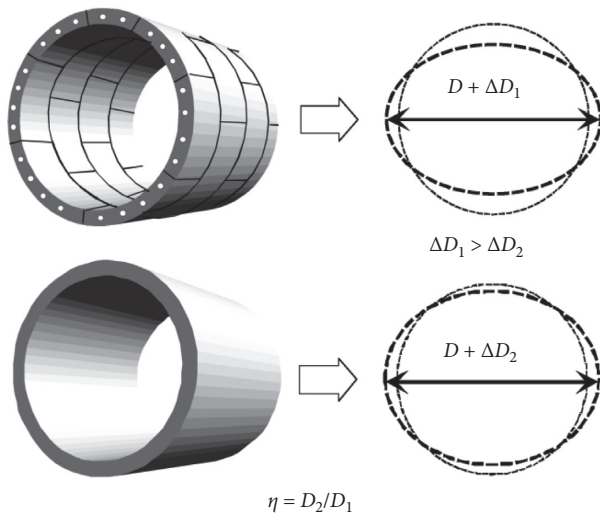


FIGURE 2: Concept of the effective ratio of bending rigidity [11].

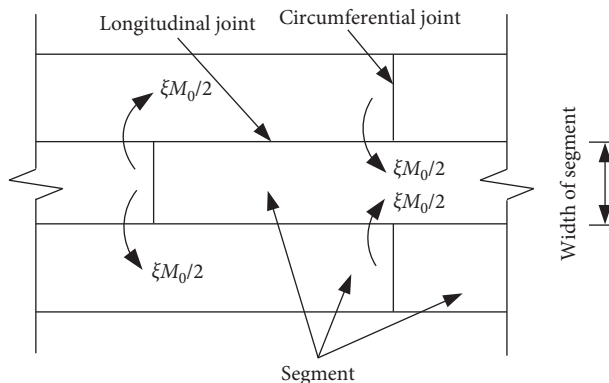


FIGURE 3: Transferring of bending moment between adjacent rings [18].

values of η and ζ of 0.8 and 0.3, respectively. At present, model tests are still the mainstream method to investigate the effective ratio of the transverse bending rigidity.

It is common to treat the segmental linings as a continuous ring with a discounted rigidity in the numerical analyses related to the shield tunnel. For instance, Chen et al. [1] set the effective rigidity ratios of the lining for circumferential directions to be 0.7 in order to numerically investigate the influence of large excavation on tunnel. Zheng et al. [29] performed finite element analyses to investigate the effect of cutoff wall on protecting the tunnel from deformation. And the transverse effective rigidity ratio of tunnel lining was also set to 0.7.

Previous studies mainly focus on the transverse effective bending rigidity ratio in the elastic stage. For example, elastic materials are always used in model tests [22–24]. However, the damage process of the material of segment rings as the load increases can also conversely influence the value of the transverse effective bending rigidity ratio. In this paper, lining structure model tests, which are fabricated by brittle gypsum material rather than the conventional elastic polymer materials, are first carried out to investigate the transverse effective bending rigidity ratio in the whole process of loading. Second, a regression equation is developed to reflect the variation trend of η with the increase of diameter convergence based on the experimental results. Third, for numerical modelling purposes, a practical method is suggested to determine the value of η based on the existing horizontal deformation of an operated shield-driven tunnel that can be obtained from on-site measurement.

2. Physical Model Tests

2.1. The Similarity of Model Tests. Physical models need to satisfy a variety of similarity relationships in terms of geometry and physical-mechanical properties so that the conclusions of the model can represent the prototype. The similar model test is based on the model similarity theory, which has three common points that can guide the design of the model test and the processing of test data. In the model test, the segmental tunnel linings used in Guangzhou city are taken as the prototype.

The geometric similarity ratio $C_l=20$ and elastic modulus $C_E=20$ are chosen as basic similarity ratios. The weights of segmental rings are not considered because of their negligible impact compared to those caused by the overburden pressure and the ground overload. Accordingly, a series of similarity ratio between the prototype parameters and the model parameters can be deduced, including the similarity ratio of displacement $C_\delta=C_l=20$, stress $C_\sigma=C_E=20$, rotation $C_\theta=C_l=1$, and strain $C_\epsilon=C_\delta/C_l=1$.

2.2. Modelling of the Segment. Figure 4 shows a typical shield tunnel cross section with an outer diameter of 6 m and an inner diameter of 5.4 m. The segmental lining is composed of a universal segment combination of three standard segments, i.e., B1, B2, and B3, two counter key segments, i.e., L1 and L2, and one key segment, F. The width of the segmental lining is 1.5 m. Adjacent segments are connected with two circumferential M24 curve bolts, and adjacent segmental rings are connected with ten longitudinal M24 curve bolts.

The strength grade of the concrete used for the segmental linings is C50 in Chinese concrete code. For the purpose of simulating the concrete effectively, the segmental lining model is made of a mixture of gypsum with diatomite and water, which has similar brittleness and failure mechanics to that of concrete [30]. In this experiment, a number of proportioning tests and compressive strength tests were performed until the mechanical parameters can meet the requirements. The final proportion in the mixture is gypsum : diatomite : water = 1 : 0.3 : 1. Figure 5 shows one of the compressive strength tests of the gypsum specimen. In addition, the circumferential reinforcement and longitudinal reinforcement of prototype concrete segments are of HRB400E grade, the elastic modulus of which is 210 GPa. But the detailing reinforcement of concrete segments is ignored for its little effect on the lining models' overall performance. After comparing the mechanical property of a variety of metal wires, the tinned iron wire whose elastic modulus is 165 GPa is chosen to simulate the reinforcement of concrete segments. According to the equivalent principle of tensile rigidity, the diameter of the tinned wire distributed in the inner and outer cambered surface of segments is 0.5 mm and 0.6 mm, respectively, and the spacing of the double layer tinned wire is equally 35 mm both in the inner and outer cambered surfaces of segments. Meanwhile, the diameter of the longitudinal wire is 0.4 mm and the spacing is 30 mm. The longitudinal wires and circumferential wires were welded into wire mesh, as shown in Figure 6. Table 1 provides the geometrical parameters and material property of the segmental lining.

2.3. Modelling of the Circumferential Joints. The circumferential joints influence the segmental linings' overall behaviour seriously, but the complicated structural characteristics of joints bring great difficulties to their simulation. In fact, the compression stiffness and shear stiffness of circumferential joints have little influence on the internal force and deformation of the segmental lining, and

it is feasible to only consider the bending stiffness. Usually, as the segmental lining is under the external load and deformed, joints at different positions will open inward or outward. Therefore, the inner and outer dividing groove method is used to simulate the circumferential joints [31–33]. In the segmental lining models, the dividing grooves with a certain width and depth were cut at the locations corresponding to the circumferential joints. The detailed structure of the circumferential joint of shield tunnel is shown in Figure 7, and the circumferential joint of the segmental lining is regarded as an articulation with a certain bending rigidity. In the experiment, the simplified method of the equal absolute value of bending stiffness under positive and negative bending moment is used to simulate the segment joint, although the bending rigidity of positive and negative bending moment is not the same. The bending stiffness of the groove must meet the requirements of similarity ratio. According to the research findings [5], the value of the bending rigidity of circumferential joint can be approximately 5×10^4 kN·m/rad, so the width and depth of the groove are calculated by using formulas (1) and (2) developed in [32]. Generally, it is recommended that the central angle of the groove is $3^\circ \sim 5^\circ$ for the accuracy of the simulation and the convenience of fabricating. Finally, both of the groove width and depth are coincidentally determined to be 5 mm.

$$H_1 = \sqrt[3]{\frac{12L_1kI}{b(EI+kL)}} = \sqrt[3]{\frac{12Ik\alpha(D_1+D_2)}{2bEI+bka\alpha(D_1+D_2)}}, \quad (1)$$

$$H = \frac{((t-H_1)/C_L)}{2}, \quad (2)$$

where H_1 and L_1 represent the width and depth of the groove based on prototype segmental lining, respectively, H represents the depth of the groove based on the scaled model, k represents the rotational stiffness of the prototype circumferential joint, E and I represent the elastic modulus and area moment of inertia of the prototype segment respectively, b represents the width of the prototype segment, D_1 and D_2 represent the external diameter and the internal diameter of the prototype segment, and α represents the central angle of the groove.

2.4. Modelling of the Longitudinal Joints. To simulate the boundary condition, the three-ring segmental lining structure was assembled by longitudinal joints for testing. Guo et al. [34] and Wang et al. [33] considered the stiffness of the longitudinal joint which was large enough to be assumed as infinite, and simplistically, the straight steel bars were used to simulate the joints between segmental rings in their experiment. To be more exact, the stiffness between segmental rings is finite and relative deformation, for example, joint opening and dislocation will occur commonly in actual projects. Also, the shear force possibly varied in different assembly modes, and that is why straight-jointed and stagger-jointed rings have obviously different deformation characteristic. Therefore, the

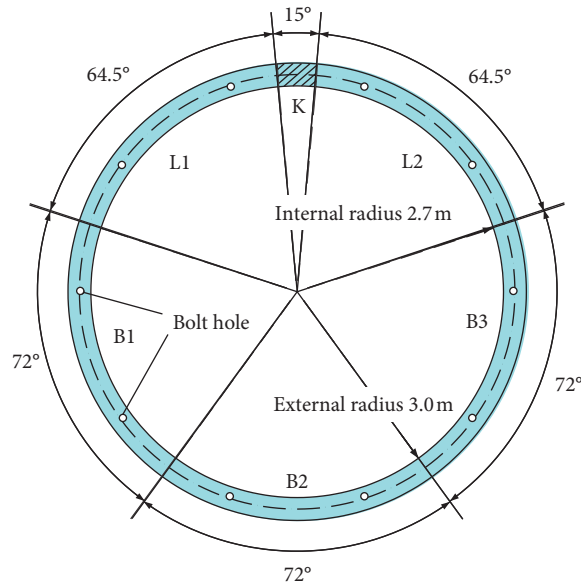


FIGURE 4: Cross section of the segmental lining.



FIGURE 5: Compressive strength tests of the gypsum specimen.

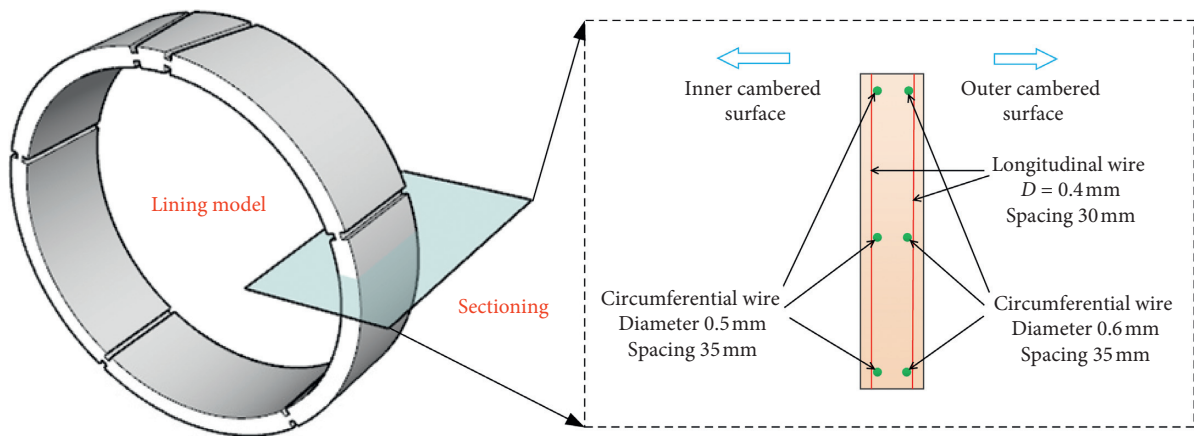


FIGURE 6: Distribution of the segment reinforcements.

longitudinal bolts are considered as elastic spring and the stiffness relationship between the prototype and the model is expressed by

$$\left(\frac{nE_b A_b}{l_b}\right)_p = \left(\frac{nE_b A_b}{l_b}\right)_m C_E C_L^2, \quad (3)$$

TABLE 1: Mechanical and geometrical parameters of the model tunnel.

Parameters	Relation	Prototype	Model
Inner diameter (mm)	$C_d = C_l = 20$	2700	135
Thickness of the segmental lining (mm)	$C_t = C_l = 20$	300	15
Width of the segmental lining (mm)	$C_w = C_l = 20$	1500	75
Elastic modulus of the segmental lining (GPa)	$C_E = 20$	35.5	1.83
Compressive strength of the segmental lining (MPa)	$C_R = C_E = 20$	59.8	3.3
Total tensile stiffness of the reinforcement in the inner cambered surface of segments (kN)	$C_{EA} = C_E C_l^2 = 8000$	938700	140
Total tensile stiffness of the reinforcement in the outer cambered surface of segments (kN)	$C_{EA} = C_E C_l^2 = 8000$	551460	97

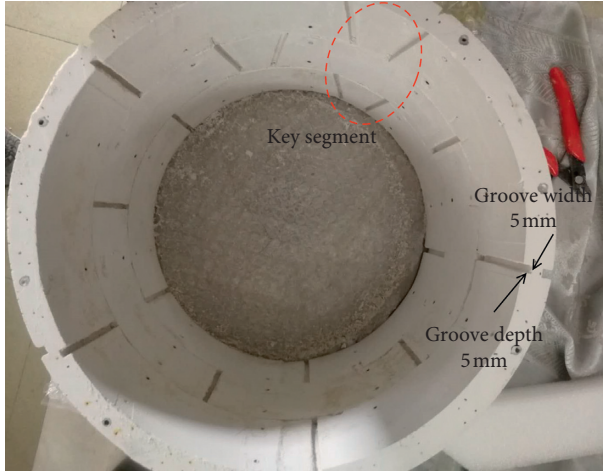


FIGURE 7: Circumferential joint processing diagram.

where n is the number of longitudinal bolts, E_b is the elastic modulus of bolts, A_b is the area of a single bolt, and l_b is the length of bolts.

The material selection of longitudinal bolts can be determined based on the similarity ratio requirement and the manufacturing requirements; several materials including aluminium welding wires, iron wires, and brass wires were taken as samples for testing. The tensile result shows that the elastic modulus of the aluminium welding wire (type 1060) is 2.45×10^4 MPa, and it is suitable to be bent into the needed shape for its flexibility. Thus, we decided to select aluminium welding wire to simulate bolts and calculate the diameter and length of aluminium welding wire using equation (3). The geometric and mechanical properties of longitudinal bolts of model and prototype segmental lining are shown in Table 2.

2.5. Model Fabrication. The fabrication process involves many steps. First of all, a handmade and detachable mould was designed and manufactured for the casting of segmental linings. The handmade mould was mainly made up of two thin aluminium sheets and several circular wooden boards. When assembling the mould, the two thin aluminium sheets were rolled into cylinders, the diameter of which was the inner and outer diameters of the segmental lining model, respectively, and the wooden boards are used to support and keep the shape of the aluminium sheets. Also, the double layer wire mesh (simulating reinforcement), rubber strips (forming circumferential dividing grooves), and hollow

aluminium tubes (forming longitudinal bolt holes) were positioned precisely and embedded inside the mould in advance. Next, the gypsum mixture was poured into the mould, forming multiple ring model, as shown in Figure 8. Then, the multiple ring model was cut into single rings according to the width of the segmental linings, and the embedded hollow aluminium tubes were simultaneously cut in half. Finally, the single rings were assembled into three-ring segmental linings through longitudinal joints.

Figure 9 shows the details of the longitudinal joints. After cutting out the single rings, the aforementioned aluminium welding wires (simulating longitudinal bolts) pass through the bolt hole formed by the hollow aluminium tubes. Both ends of longitudinal bolts were fixed by fixators, and the pretension force of longitudinal bolts was applied so that the adjacent rings were assembled firmly.

2.6. Apparatus of Model Tests and Experimental Procedure.

Figure 10 shows the overall view of the apparatus of the model loading test. The model tests were conducted through the load structure method on a specially designed experimental bench. According to the research proposed by Huang et al. [22], the transverse effective rigidity ratio of segmental linings in the soft ground (the typical ground resistance coefficient is 10000 kN/m^3) is almost the same as that of segmental linings without lateral confinement. Therefore, the lateral confinement was not imposed in the test. The segmental rings were supported on the experimental bench, and the line load was applied by a loading box at vault position of linings. There were two rubber strips sticking on both sides of contact line between the segmental lining and the experimental bench. Through the rubber strips, the displacement of the segmental lining's bottom was constrained, and the physical model's rigid-body displacement and rotation were in turn constrained. Also, four vertical rods were installed to ensure that the loading box only has the freedom of vertical movement, and then the line load can be applied exactly at vault position of segmental lining.

Since the weight of the loading box was 1.6 kg approximately, placing the loading box on the top of the segmental lining was regarded as the first loading stage. Then, each subsequent loading was applied through placing standard weights (1.5 kg) into the loading box. The loading was applied step by step until the segmental linings were destroyed.

The middle ring among the assembled three-ring segmental linings was the target ring to be measured. To reveal the

TABLE 2: The geometric and mechanical properties of model and prototype segmental lining.

Type	Elastic modulus (MPa)	Length of bolt (mm)	Diameter of bolt (mm)	Longitudinal bolt number
Prototype	2.06×10^5	470	24	10
Model	2.45×10^4	31.8	0.9	10

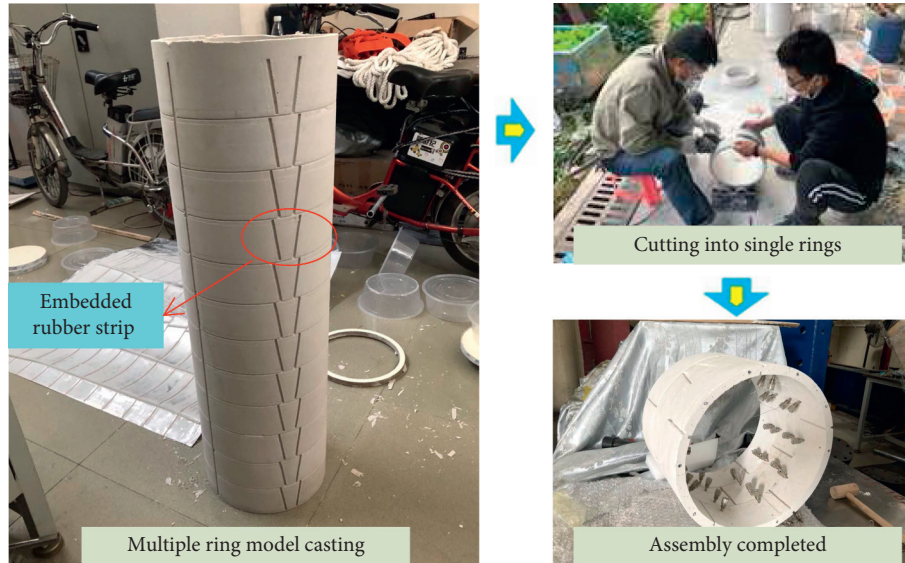


FIGURE 8: Brief fabrication process of segmental linings.

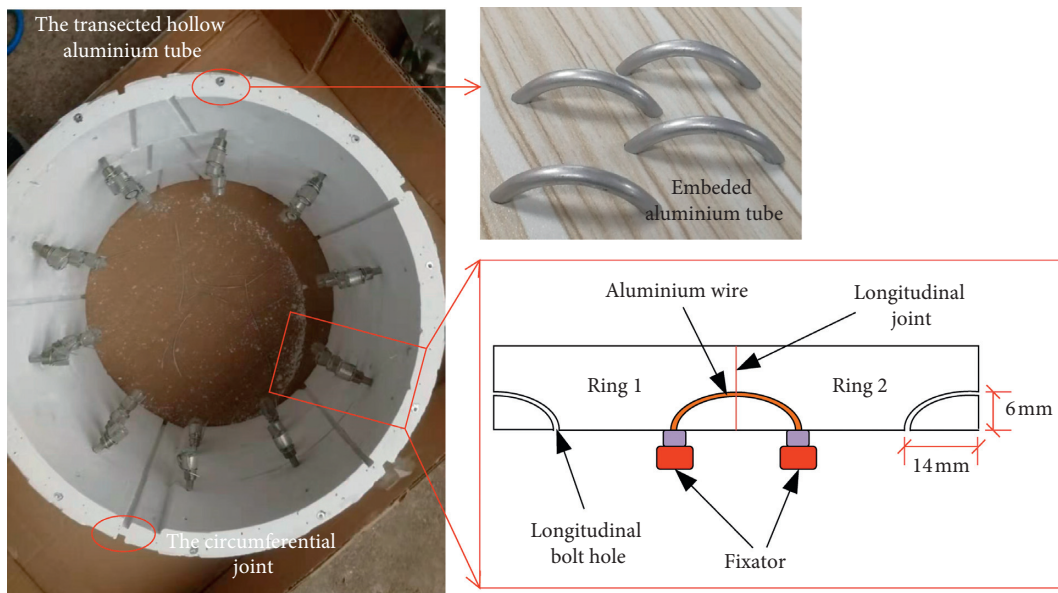


FIGURE 9: The details of the longitudinal joints.

radial deformation of the target ring effectively, digital micrometres and static data collecting gauge were used to measure and collect the displacement during the test. Eight digital micrometres were distributed symmetrically around the circular direction at an equal angle interval of 45 degrees, and an extra digital micrometre was used to monitor the possible movement of the experimental bench. A diagrammatic sketch of the arrangement of the devices is shown in Figure 11.

2.7. *Grouping and Test Content.* To investigate the deformation characteristic of segmental linings under different assembled conditions, three types of segmental linings in different assembled modes were tested, including uniform ring (only longitudinal joint), straight-jointed rings, and stagger-jointed rings, which are shown in Figure 12. Besides, the key blocks of the straight-jointed rings and the stagger-jointed rings are located at the vault and the vault offset of 18°.

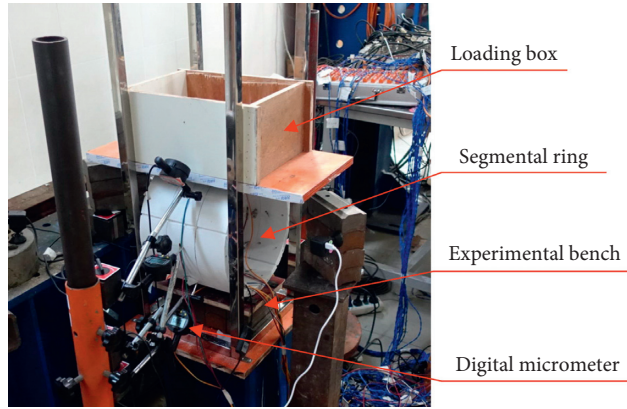


FIGURE 10: Apparatus of model loading test.

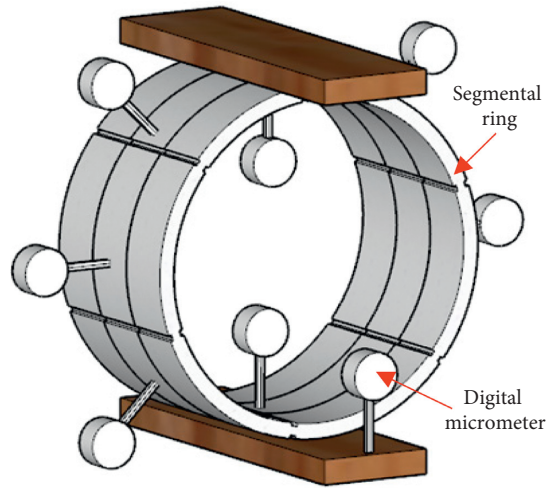


FIGURE 11: Arrangement of the measurement devices.

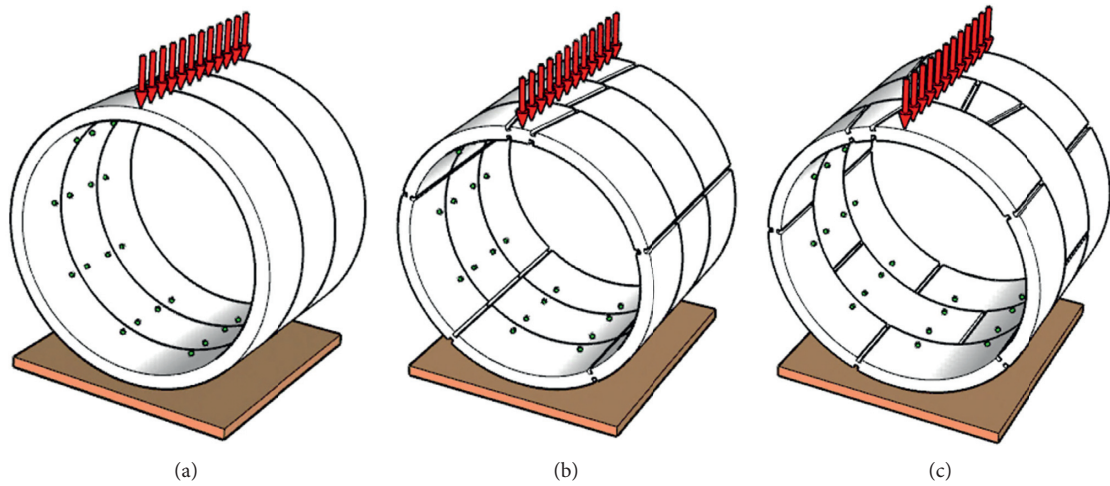


FIGURE 12: Three types of segmental lining. (a) Uniform rings. (b) Straight-jointed rings. (c) Stagger-jointed rings.

3. Experiment Results and Analysis

The experimental results of the segmental linings are converted into the corresponding prototype segmental lining according to the general law of similarity of the model test. Also, the weights applied on the vault are converted to line load along the width of the lining.

3.1. Transverse Deformation Characteristic. Figure 13 shows the deformation results in several loading stages, and the deformed shapes are reproduced through the measured radial displacement of the representative points of the middle ring, from which it can be seen that both the uniform rings and the straight-jointed rings deformed symmetrically while the stagger-jointed rings were not. Besides, the largest deformation occurs in the vault of the three types of segmental linings and the horizontal diameter is the second. However, the position at 135° of stagger-jointed rings also shows relatively large deformation, which may be attributed to the key segment of the middle ring tilted to the right side.

In the model tests, the displacement towards the outside of the tunnel is defined as positive, and in contrast, the displacement towards the inside of the tunnel is defined as negative. It can be seen from Figure 14 that for these three types of segmental lining structure, the vertical and horizontal diameter variation increases almost linearly as the concentrated load increases at the initial loading process. The value of the horizontal and vertical displacement is small, and there is no obvious elliptic deformation for the lining structures, which indicates that the segmental lining structures are in the elastic stage.

However, after the linear stage, the behaviour of different segmental linings has diverged. For the uniform rings, after the concentrated load increases linear to 550 kN/m, the displacement increased with a slight acceleration. Finally, when the concentrated load reached 594 kN/m, the vertical and horizontal diameter variation increased sharply and collapsed quickly, which showed brittle failure characteristics. As for the straight-jointed rings and stagger-jointed rings, the displacement still increased with an approximately linear slope after the linear stage, but there is an obvious acceleration trend in the increase rate. Meanwhile, the lining structure exhibited obvious elliptic deformation. In the end, the straight-jointed rings and stagger-jointed rings collapsed as the concentrated load reached 280 kN/m and 419 kN/m, respectively. In fact, it should be added that the horizontal and vertical displacement of the model test may be larger than practical engineering for the lateral confinement was not considered and imposed in the model.

3.2. Failure of the Lining Structure. It can be seen from Figure 15 that the failure modes of segmental linings have different characteristics for different assembly conditions. For the uniform rings, the deformation was small until four main cracks started to emerge at the lining hance, vault, and the bottom of the arc. The cracks at the lining vault and the bottom of the arc of each ring were consecutive in the longitudinal direction while the cracks at the hance were not,

which was possibly caused by the assembly error or the existing defects of lining material. Then, the cracks expanded rapidly and caused the exposure of the circumferential wires embedded in the segments. As the loading continued to increase, the exposed reinforcement wires also broke and the whole lining structure collapsed all of a sudden.

For the straight-jointed rings, the first observed longitudinal crack emerged at the outer surface of the circumferential joint at the lining hance. As the load increased, the crack expanded quickly and more cracks appeared at the inner surface at the vault and arc bottom. After that, the cracks penetrated the circumferential joints, and the lining structure finally collapsed.

For the stagger-jointed rings, cracks also firstly emerged at the circumferential joint. However, because the distribution of the circumferential joints between the adjacent ring is different, cracks were not consecutive in the longitudinal direction. Besides, the rotation angle of circumferential joints was apparently larger than that of adjacent segments. Therefore, the deformed shapes of the adjacent rings were different, which caused obvious dislocations between the adjacent rings and the longitudinal bolts to undergo shear fracture.

3.3. Transverse Bending Rigidity Ratio. According to the experiment results of various segmental rings conducted by Huang et al. [22] and Ye et al. [23], the transverse bending rigidity ratio can be determined by comparing the variation value of the horizontal or vertical diameter of different segmental rings under the same loading condition. The calculation definition of η can be expressed as follows:

$$\left\{ \begin{array}{l} \eta_1 = \frac{\Delta D_{hy}}{\Delta D_{hp}}, \\ \eta_2 = \frac{\Delta D_{vy}}{\Delta D_{vp}}, \end{array} \right. \quad (4)$$

$$\eta = \frac{EI^*}{EI} = \frac{\Delta D_2}{\Delta D_1}, \quad (5)$$

where EI and EI^* are the transverse bending rigidities of the uniform rings and the assembled segmental rings, respectively, and ΔD_1 and ΔD_2 are the maximum diameter variation values (including horizontal diameter and vertical diameter) of the assembled segmental rings and the uniform rings, respectively.

According to the definition, the value of η of the segmental linings can be calculated under each loading stage. The curves of the transverse bending rigidity ratio during loading are shown in Figure 16. As shown in Figure 16, for the straight-jointed rings, when the concentrated load is less than 176 kN/m, the calculated value of the transverse bending rigidity ratio η is fluctuating between 0.503 and 0.642, and a slight upward trend can be observed at the same time. When the concentrated load increases to 202 kN/m, which is corresponding to the cracking loading in the aforementioned failure process of the straight-jointed rings,

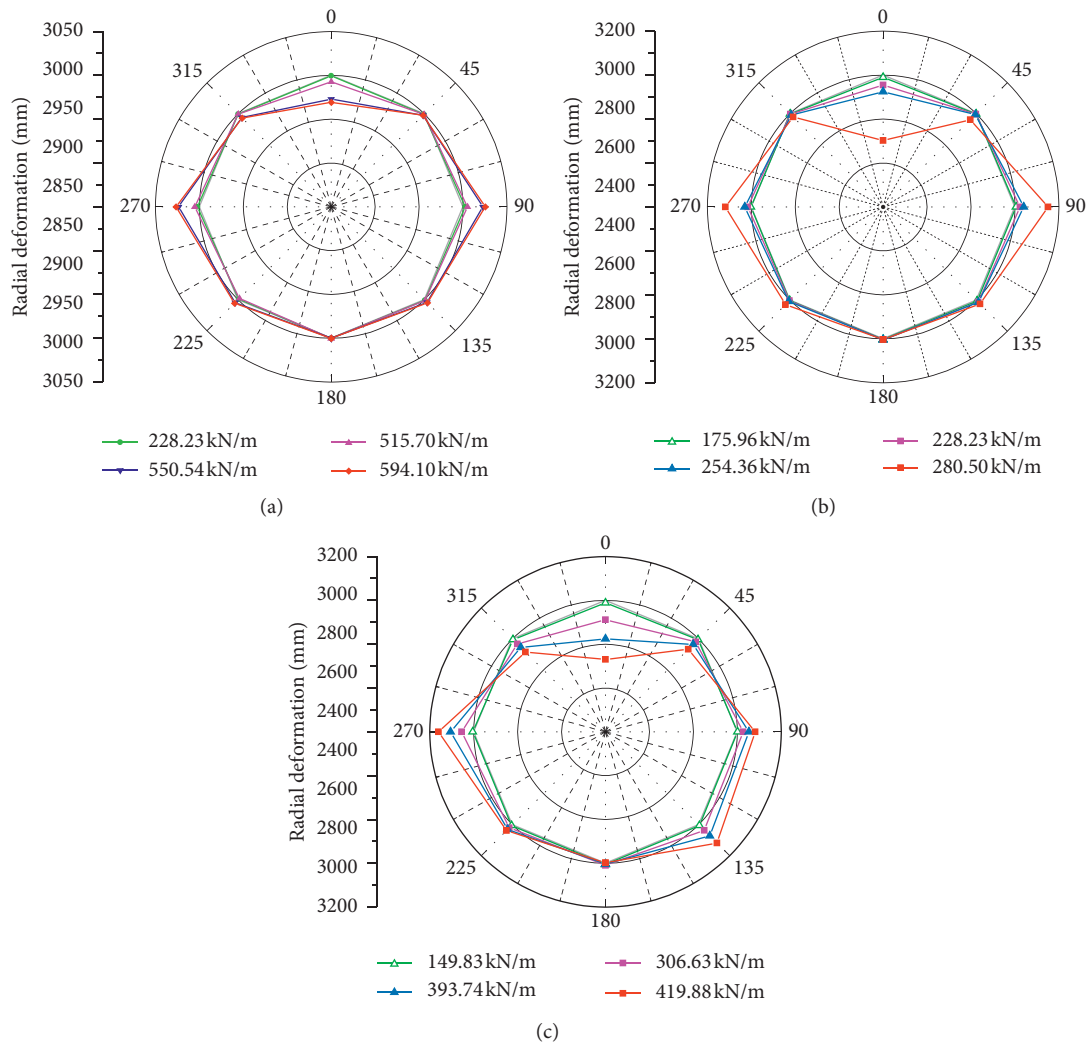


FIGURE 13: The deformed shape of lining models. (a) Uniform rings. (b) Straight-jointed rings. (c) Stagger-jointed rings.

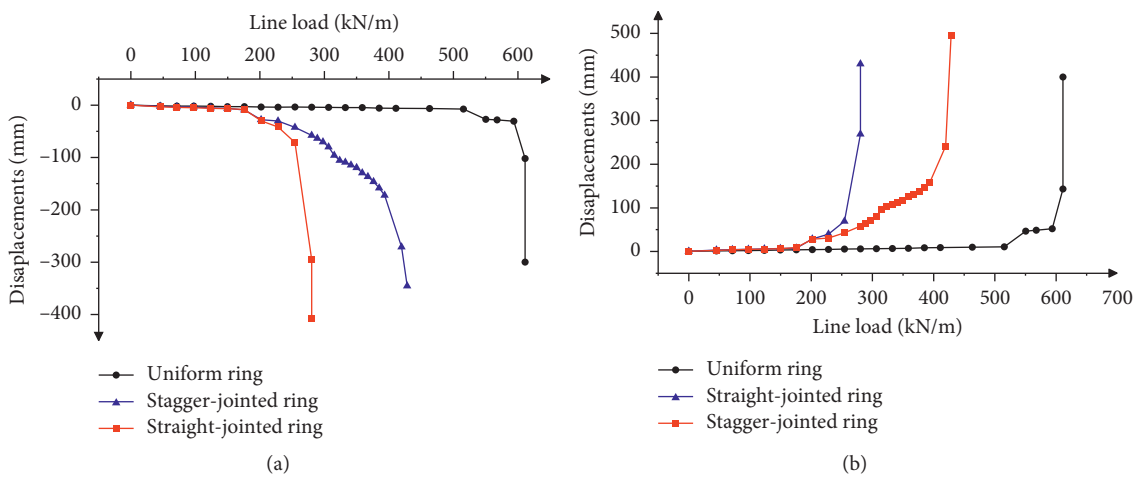


FIGURE 14: Variation of diameters of the target ring with the increase of the concentrated load. (a) Vertical diameters. (b) Horizontal diameters.

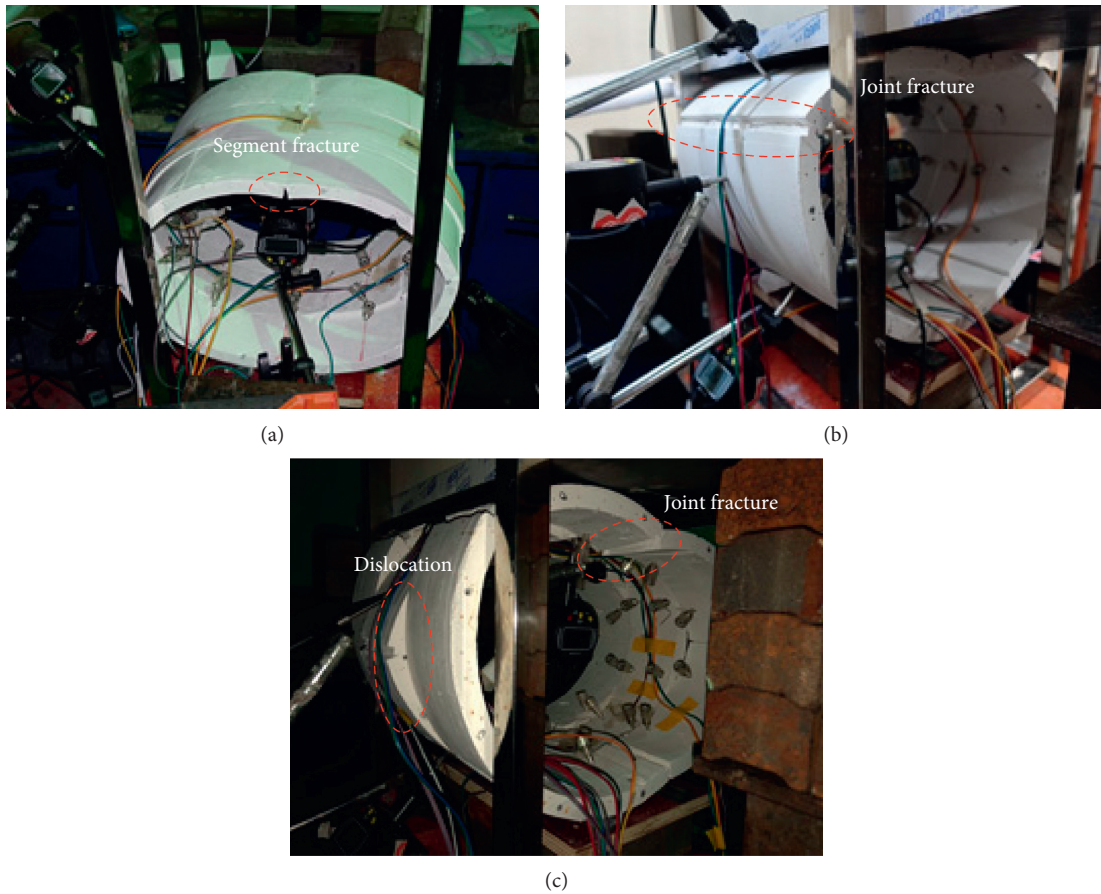


FIGURE 15: Failure of the lining structure. (a) Uniform rings. (b) Straight-jointed rings. (c) Stagger-jointed rings.

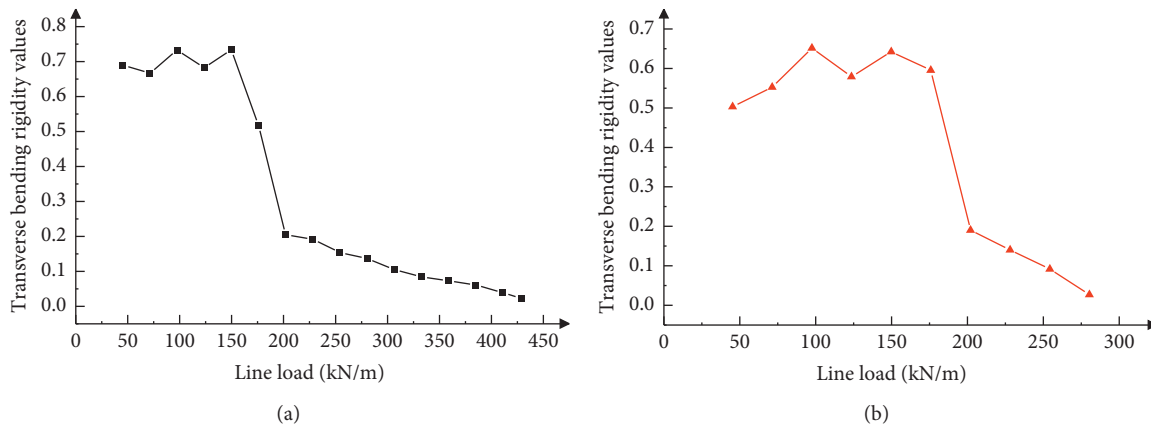


FIGURE 16: Relationship of the value of η and the line load. (a) Stagger-jointed rings. (b) Straight-jointed rings.

η decreases sharply to 0.190. When the concentrated load continued to increase to 280 kN/m, the decline rate of η slows down and the value of η decreases from 0.190 to 0.027. For the stagger-jointed rings, the relationship between the transverse bending rigidity ratio and loading condition is similar to that of the straight-jointed rings. When the concentrated load is less than 150 kN/m, the calculated value of the transverse bending rigidity ratio η is fluctuating between 0.667 and 0.734, and a slight upward trend can be

observed. When the concentrated load increases to 202 kN/m, which is also corresponding to the cracking process of stagger-jointed rings mentioned above, η decreases sharply to 0.204. When the concentrated load is greater than 202 kN/m, the value of η descends relatively slowly from 0.191 at 228 kN/m to 0.022 at 428 kN/m.

To summarize, the stagger-jointed rings have a larger overall transverse rigidity than that of the straight-jointed rings. Before the transverse bending rigidity sharply

decreases, the average value of η of the stagger-jointed rings is 0.701 and the average value of η of the straight-jointed rings is 0.587. The variation trends in the η value of both assembled conditions are basically the same.

3.4. Regression Analysis. It is worth considering that the loading condition applied to the lining structure on the tests is different from the actual loading condition because of the surrounding soil pressure. However, the loading condition is varied under complicated stratum condition in the actual shield tunnel engineering. Therefore, it will be more meaningful to establish the relationship between the transverse bending rigidity ratio and the deformation characteristic quantity of segmental linings. Moreover, in the engineering practice, the deformation parameters are often adapted as the key performance indicators (KPIs) for evaluation of the serviceability and structural safety [35]. For instance, the ratio of convergence of horizontal diameter over the initial outer diameter, i.e., $(\Delta D/D_{out})$, is commonly regarded as the KPI. Therefore, considering that the experiment results reveal the transverse bending rigidity ratio is dependent on the deformation of tunnel lining, the relationship between the transverse bending rigidity ratio and the horizontal convergence to diameter ratio $(\Delta D/D_{out})$ is obtained by regression analysis, as shown in Figure 17.

For the stagger-jointed rings, the regression equation is

$$\eta = \begin{cases} 0.70, & \text{when } \frac{\Delta D}{D_{out}} < 1.00\%, \\ 0.719 \left(\frac{\Delta D}{D_{out}} \right)^{-0.785}, & \text{when } \frac{\Delta D}{D_{out}} > 1.00\%. \end{cases} \quad (6)$$

For the straight-jointed rings, the regression equation is

$$\eta = \begin{cases} 0.59, & \text{when } \frac{\Delta D}{D_{out}} < 1.35\%, \\ 0.773 \left(\frac{\Delta D}{D_{out}} \right)^{-0.872}, & \text{when } \frac{\Delta D}{D_{out}} > 1.35\%. \end{cases} \quad (7)$$

Accordingly, the variation of the transverse bending rigidity ratio could be divided into two stages, and the convergence to diameter ratio $(\Delta D/D_{out})$ of turning points is defined as the critical diameter convergence $(\Delta D/D_{out})_{cr}$, the values of which are 1.00‰ and 1.35‰ for the stagger-jointed rings and straight-jointed rings, respectively. Because of the effect of surrounding soil pressure and the lateral restriction, the value of the $(\Delta D/D_{out})_{cr}$ will possibly increase.

The formulas proposed can be valuable guidance for the evaluation of shield tunnel serviceability and safety, especially for the operated shield tunnel whose diameter convergence is larger than the critical diameter convergence. For example, according to a case study of operated shield tunnel subjected to an extreme surcharge, the field measurement results showed that the convergence to diameter ratio $(\Delta D/D_{out})$ of lower line tunnel and the upper line is on

average at 6.88‰ and 25.8‰, respectively [35]. Meanwhile, another case study [36], which researches the response of the Taipei Rapid Transit System shield tunnel induced by adjacent excavation, presents that the diameter convergence of the lining structure is 4.26‰ in the horizontal direction and 7.38‰ in the vertical direction. Therefore, it can be deduced that the diameter convergences of tunnel lining in both cases have far exceeded the critical diameter convergence $(\Delta D/D_{out})_{cr}$ and consequently the transverse bending rigidity of the operated shield tunnel lining has possibly declined sharply. In the next section, another engineering case involving an operated tunnel that was also subjected to surcharges will be discussed. Besides, the relationship between the transverse bending rigidity ratio and the horizontal convergence to diameter ratio based on the experimental results will be applied to numerical analysis.

4. Case Study of an Operated Shield Tunnel and the Numerical Analysis Based on the Experimental Results

The operated shield tunnel, one of the sections of Guangzhou Metro Line 3, was once subjected to accidental surface surcharges, and relatively large diameter convergences of the segmental linings were measured. However, a foundation pit that is close to the tunnel will be excavated and the effect of the adjacent excavation is urgent to be predicted. In Sections 4.1 and 4.2, an overview of the operated tunnel and the upcoming adjacent excavation will be firstly illustrated.

Meanwhile, based on the experimental result, the transverse bending rigidity ratio η of the shield tunnel is dependent on the diameter convergence $\Delta D/D_{out}$. When diameter convergences $\Delta D/D_{out}$ are relatively large and especially exceed the critical diameter convergence $(\Delta D/D_{out})_{cr}$, the value of η decreases rapidly. To consider the exiting horizontal diameter convergence which can be obtained by on-site measurement, regression equations (6) and (7) based on the model test are employed to determine the value of the key parameter η . Moreover, a practical method was put forward to consider the variation of the parameter η and numerically predict the further deformation of the operated shield tunnel.

The specific deformation prediction method which considers the existing deformation of tunnel linings is illustrated as follows. On the one hand, the existing diameter convergence of tunnel linings can be obtained by the way of on-site measurement, so that the transverse bending rigidity ratio η_0 of operated shield tunnel can be determined through substituting the measured horizontal convergence into regression equations (6) and (7). Then, η_0 is introduced into the first excavation step of numerical model as the original value of the transverse bending rigidity ratio. On the other hand, the numerically calculated results of horizontal diameter convergence in each excavation step can be used to back-calculate the transverse bending rigidity ratio and then adopted as the original transverse bending rigidity ratio for the next excavation step. After several iterations, a final transverse

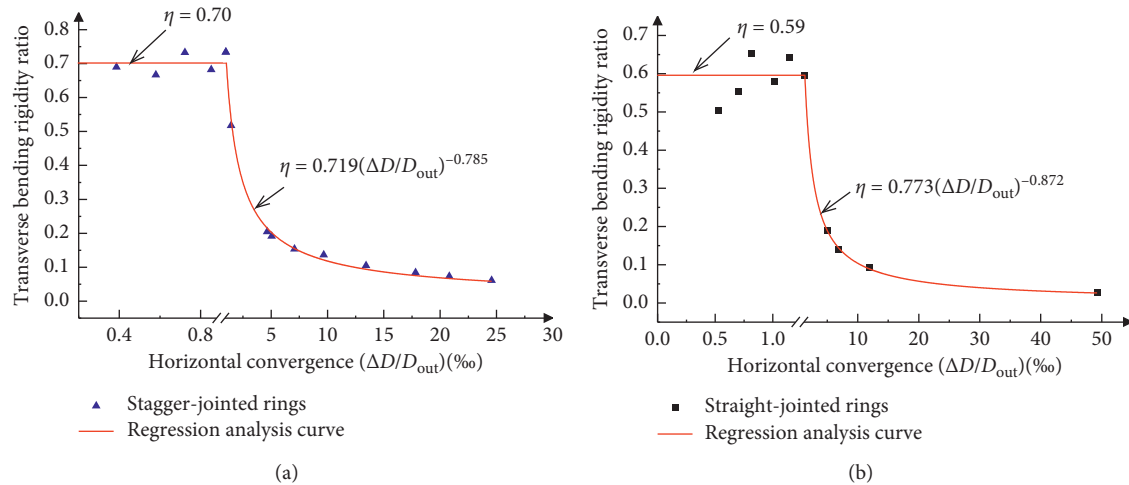


FIGURE 17: Regression analysis result. (a) Stagger-jointed rings. (b) Straight-jointed rings.

deformation $\Delta D/D_{out}$ is obtained as a prediction. The flow-chart for the proposed prediction process of the operated shield tunnel's transverse deformation is shown in Figure 18.

4.1. Surcharge History of Shield Tunnel. A brief overview of the operated shield tunnel is described as follows. The lining structures' cross section is the same as that exhibited in Section 2.2, and the lining structure is assembled with a stagger-jointed condition. The buried depth of the tunnel crown varies from 6 m to 9 m. The soil layer at the construction site mainly includes surface fill (layer ①), medium-coarse sand (layer ②), silty clay (layer ③), hard plastic sandy clay (layer ④), plastic sandy clay (layer ④m), fully weathered granite (layer ⑤), and strongly weathered granite (layer ⑥) (see Figure 19).

The shield-driven tunnel was completed in June 2006, and after that, two accidental surface surcharges occurred. On 18 January 2013, a large amount of waste soil from a nearby construction site was piled up on the ground surface above the tunnel, and the height of the waste soils was on average 4 m. The abnormal settlement of the tunnel caused by surcharge was quickly monitored, and the waste soil was removed in two days. Figure 20(a) shows the settlement curve of the tunnel beneath the surcharged area. It can be seen that the maximum settlement of tunnel was 20.40 mm, and the settlement of the tunnel rebounded 4~9 mm after the overloading was removed. Another accidental surcharge happened on 8 December 2018, and more of the waste soil was abandoned on almost the same area and the height of the waste soils was up to 6 m. Similarly, the overloading was carried away after the sudden increase in displacement was monitored. Figure 20(b) shows the curve of the tunnel settlement after the second surcharge. It can be seen that at the overlapping area of two surcharging, the maximum settlement increased to 27.98 mm.

On 1 January 2019, the FARO three-dimensional laser scanning technique was used to measure the configuration of the segment rings that were seriously affected by the surcharging accidents. Figure 21 shows the variation of the

segment rings' horizontal diameter from mileage ZDK18+604~ZDK18+754. As shown in Figure 21, the diameter convergence of segment rings was significantly increased after two surcharging accidents, and the maximum horizontal diameter convergence reaches 8.85‰ at No. 50 segment ring.

4.2. Adjacent Excavation Project. In 2019, high-rise buildings adjacent to the shield tunnel were planned and designed, and a five-level basement on the site was needed to construct. The plan view is shown in Figure 22, and the profile of section A-A is shown in Figure 23. It can be seen that the boundary of the excavation was an irregular polygon and was retained by a diaphragm wall in vertical and three levels of reinforced concrete struts in horizontal. One of the boundaries of the excavation is along the tunnel from the metro station, and the horizontal distance between the diaphragm wall and the tunnel approximately equals 5.2 m. The depth of the excavation is 21.55 m. The thickness of the diaphragm wall is 1.2 m. The length and the width of the cross sections of struts were varied in different positions and range from 1.0 m to 1.5 m. The foundation pit is excavated at four layers, which is followed in each level by strut installation.

4.3. Numerical Analysis. In the aforementioned on-site measurement data after the surcharging accidents, the maximum horizontal diameter convergence ratio of the tunnel lining was up to 8.85‰. It is of significance to consider the influence of the existing transverse deformation on the prospective deformation induced by adjacent excavation. Therefore, the effective transverse rigidity ratio η that was introduced to the numerical analysis was calculated by regression equation (6), and the convergence to diameter ratio ($\Delta D/D_{out}$) in equation (6) was based on the on-site measured horizontal diameter convergence ratio of the operated tunnel.

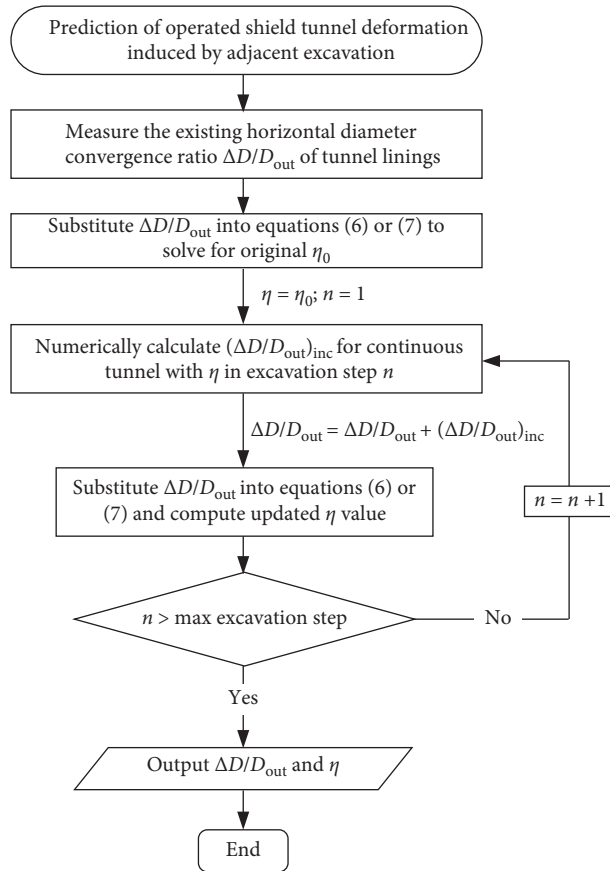
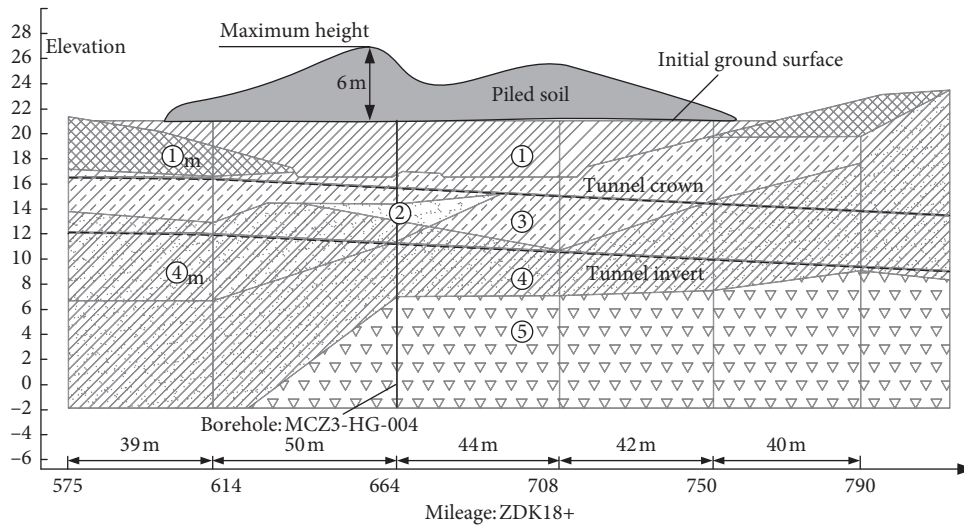


FIGURE 18: The flowchart of the specific deformation prediction method.



- ①: fill
- ②: medium-coarse sand
- ③: silty clay
- ④: hard plastic sandy clay
- ④m: plastic sandy clay
- ⑤: fully weathered granite

FIGURE 19: The detailed soil profile along the longitudinal direction.

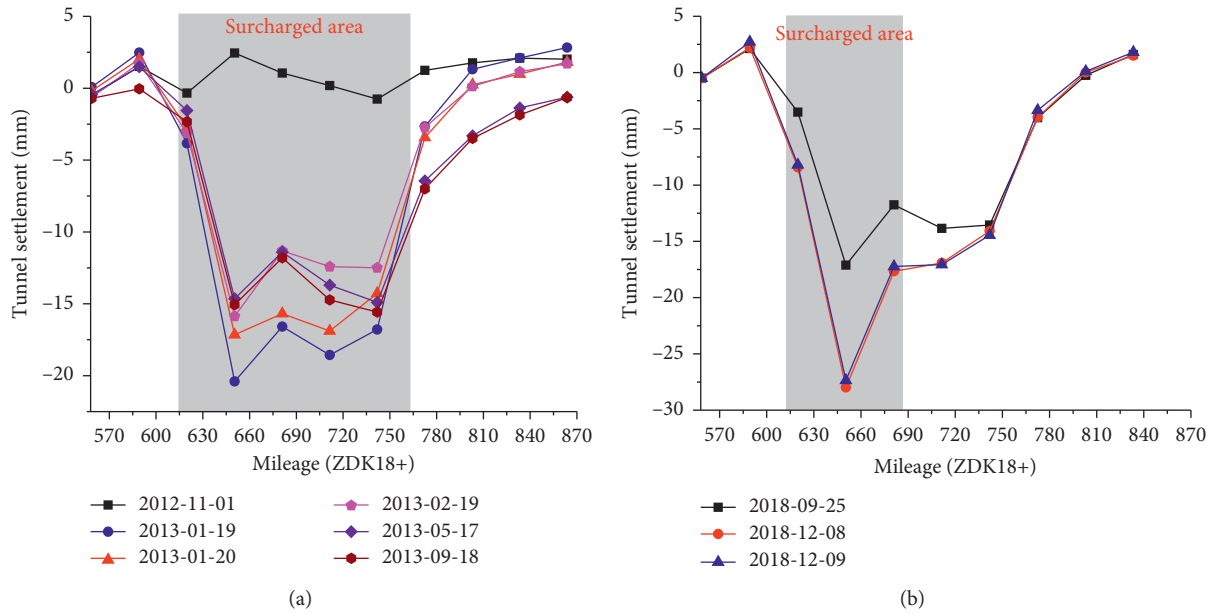


FIGURE 20: Tunnel settlement around the surcharged area. (a) First surcharge. (b) Second surcharge.

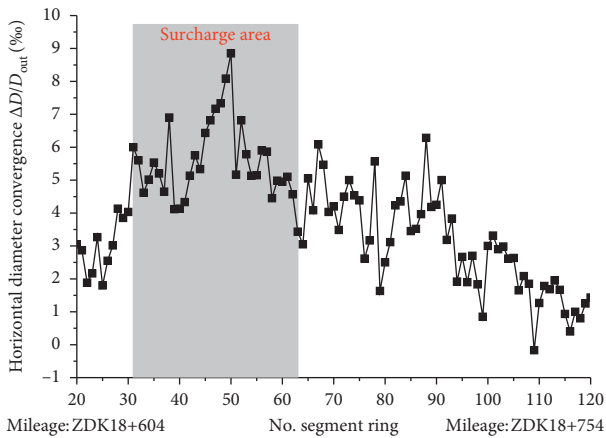


FIGURE 21: Diameter convergence of segment rings through on-site measurement.

Before the adjacent foundation pit was excavated, it was urgent to predict the influence of the excavation on the operated tunnel deformation. Therefore, the FEM program PLAXIS was adapted to simulate the excavation process. Considering that the surrounding environment was complicated and the concerns were mainly focused on the tunnel section that was once surcharged, the FE model based on section A-A is analysed in a plane strain condition. The domain of the model is 150 m × 60 m. Lateral boundaries are fixed in the horizontal direction and on the bottom boundary in both vertical and horizontal directions. The mesh of the FE model is shown in Figure 24.

In the model, the hardening soil model with small strain model (HSS), which can reflect the small strain behaviour of the soil [37], is used to simulate the soil. The soil parameters used in the numerical model are listed in Table 3. The diaphragm wall, struts, and tunnel lining are defined as linear

material, and the elastic modulus and Poisson’s ratio are 30 GPa and 0.2. The interaction between the structure and the soil is modelled with an interface element that is 0.1 m in virtual thickness. The excavation of soil layers and the installation of struts was conducted step by step. The influence of pit dewatering on the deformation of structure and soil was also simulated in the model.

In particular, for the tunnel lining under the surcharged area, the horizontal diameter convergence was up to 8.85%, whose effective transverse rigidity ratio η can be calculated as 0.130 based on equation (6). For the purpose of studying the prospective transverse deformation of tunnel linings with different transverse rigidities, seven sets of tunnel linings with different original effective transverse rigidity ratios are involved in the numerical model, i.e., 0.7, 0.6, 0.5, 0.4, 0.3, 0.2, and 0.1, which correspond to different degrees of transverse deformation. As described in detail in Figure 18, the variation of the parameter η in each excavation step is also included in the numerical model. The transverse deformation of the tunnel linings caused by the lateral unloading in the process of adjacent excavation will result in the decline of the effective transverse rigidity ratio, which will in turn exacerbate the transverse deformation of the tunnel linings in the subsequent excavation step. The final transverse deformation states of tunnel lining are shown in Figure 25, and the variations of horizontal convergence during excavation are shown in Figure 26.

As shown in Figure 26, the horizontal convergences ΔD of the tunnel lining increase when the adjacent foundation pit is excavated from step 1 to 4, and the increment is significant from step 3 to step 4. As the original effective transverse rigidity ratio η decreases from 0.7 to 0.1, the horizontal convergences ΔD increase obviously. When the foundation pit was excavated to layer 4, the horizontal convergences ΔD increase from 12.29 mm to 27.95 mm as

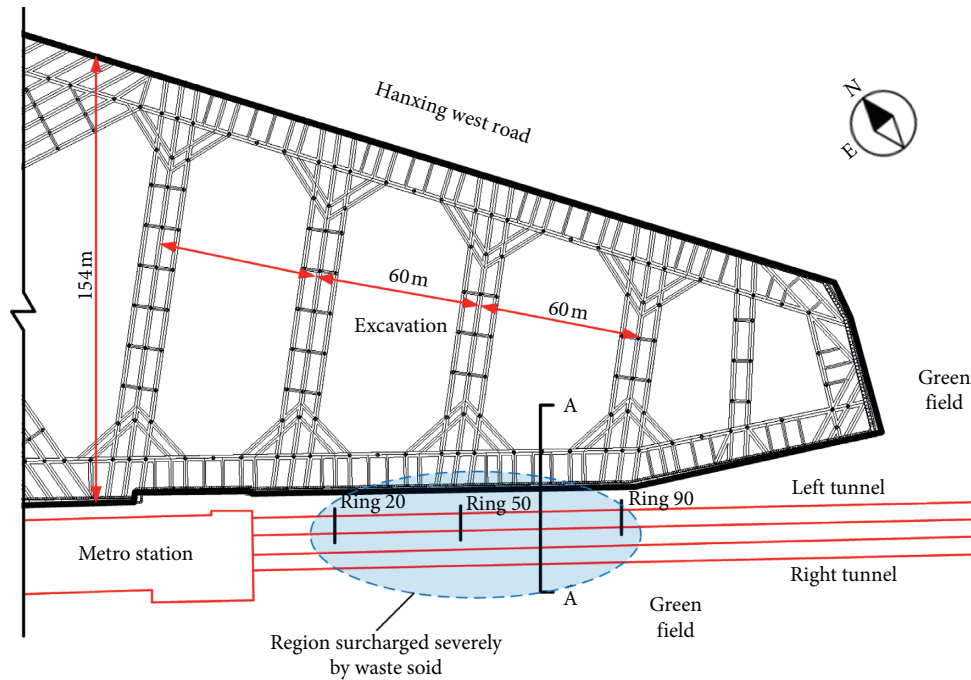


FIGURE 22: Plan view of the construction site.

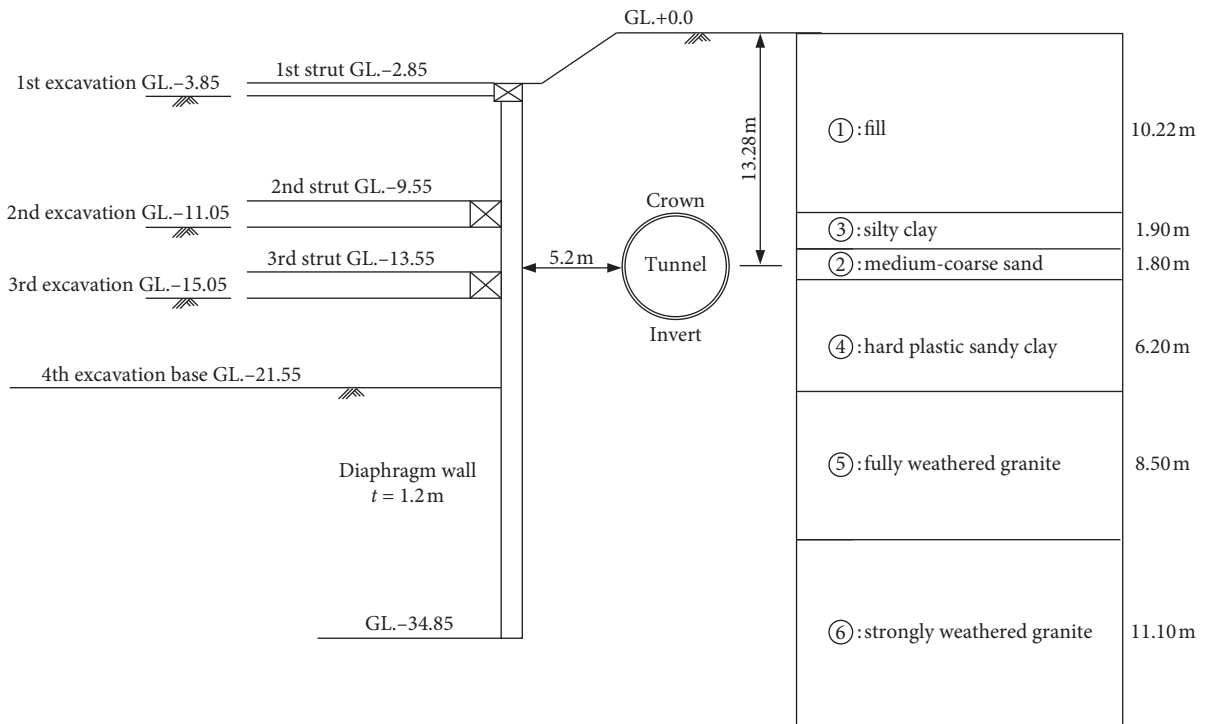


FIGURE 23: Profile of soil layer, excavation, and tunnel (section A-A).

the original η decreases from 0.70 to 0.1, which increases by 1.27 times. Besides, as shown in Figure 25, differing from the previous concept that regarded the effective transverse rigidity as a constant value, the final deformed shape is apparently becoming larger as the tunnel linings' original effective transverse rigidity decreases.

This indicates that the original horizontal diameter convergences of operated shield tunnel have a significant effect on the subsequent deformation induced by adjacent excavation. When the lining structure is under the same excavation stage, the lateral unloading will cause different effects on the deformation of the lining structure with

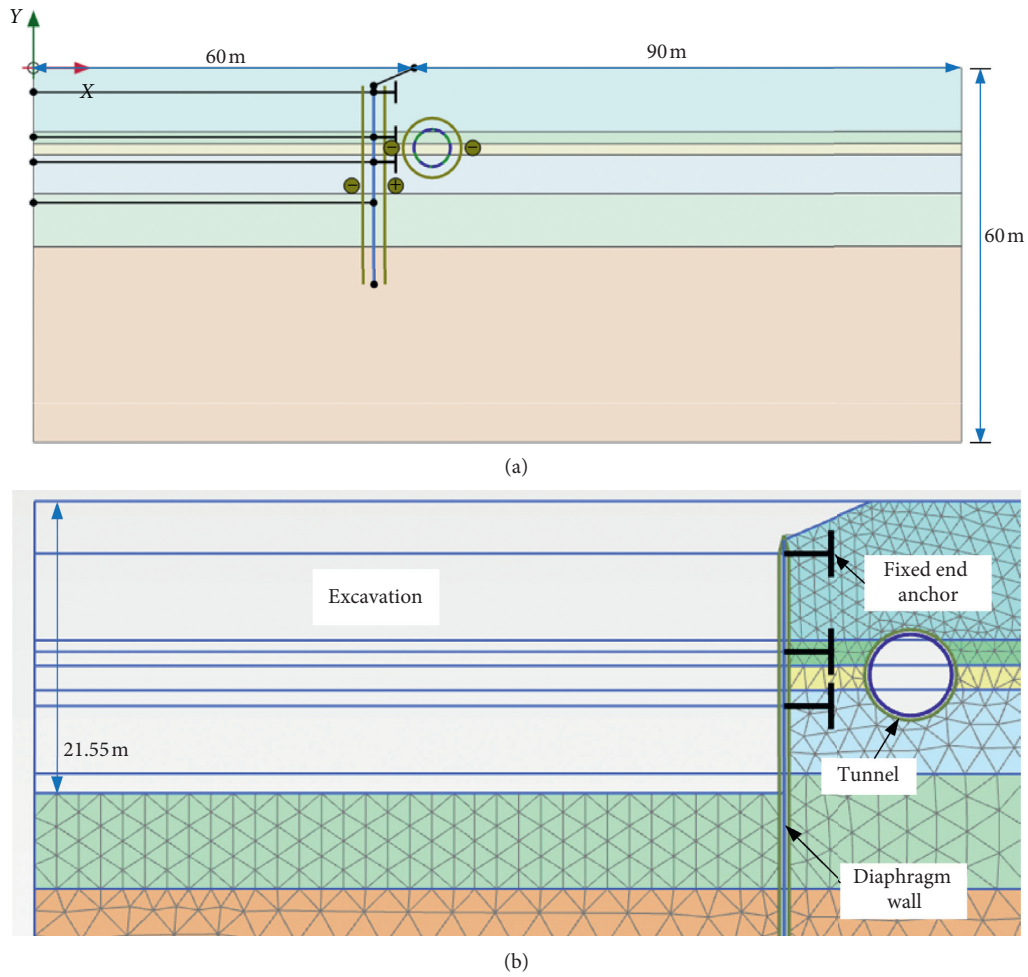


FIGURE 24: Finite element mesh of the simulation model.

TABLE 3: Input values of HSS parameters.

Soil layer type	Fill	Medium coarse sand	Silty clay	Hard plastic sandy clay	Fully weathered granite	Strongly weathered granite
γ ($\text{kN}\cdot\text{m}^{-3}$)	19.5	18.9	18.7	19.6	20	21
$E_{\text{oed}}^{\text{ref}}$ (kPa)	3000	6200	6000	7500	12000	30000
E_{50}^{ref} (kPa)	4000	7500	6200	7500	12000	30000
$E_{\text{ur}}^{\text{ref}}$ (kPa)	15000	45200	37200	47000	60000	180000
c' (kPa)	15	1	19.7	25	32	200
ϕ'	19	31	15.5	21	26	30
ψ	0	1	0	0	0	0
ν_{ur}	0.3	0.26	0.26	0.23	0.23	0.21
m	0.5	0.7	0.7	0.5	0.5	0.5
$\gamma_{0.7}$ (10^{-4})	2.0	3.0	2.0	2.0	2.0	3.2
G_0 (kPa)	30000	130600	110000	133000	180000	620000
R_f	0.9	0.9	0.9	0.9	0.9	0.9

different effective transverse rigidity ratios. With the decline of the effective transverse rigidity ratio, the horizontal convergence increases gradually and the deformation of lining structure tends to be unfavourable. Therefore, it is

highly probable that the deformation results of tunnel lining will be more dangerous if a modified value of η is introduced into numerical analyses of shield tunnel-related problems.

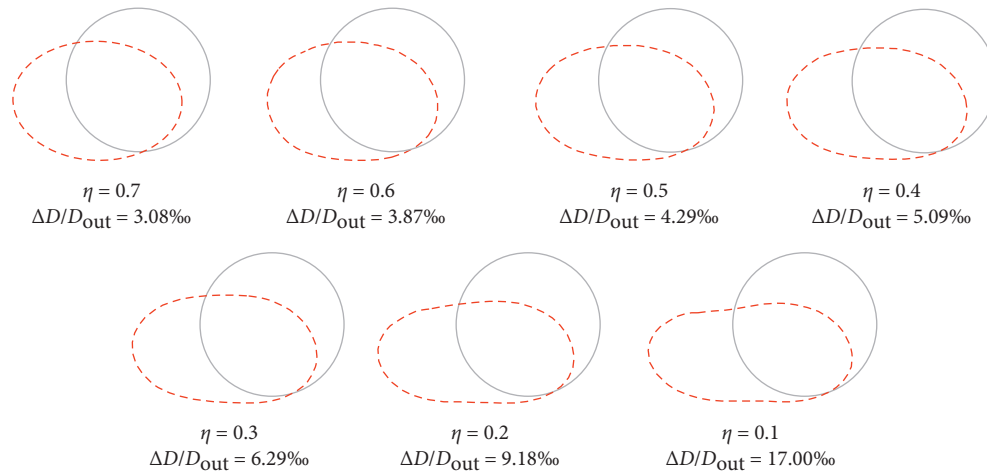


FIGURE 25: Final deformation state (100x magnification).

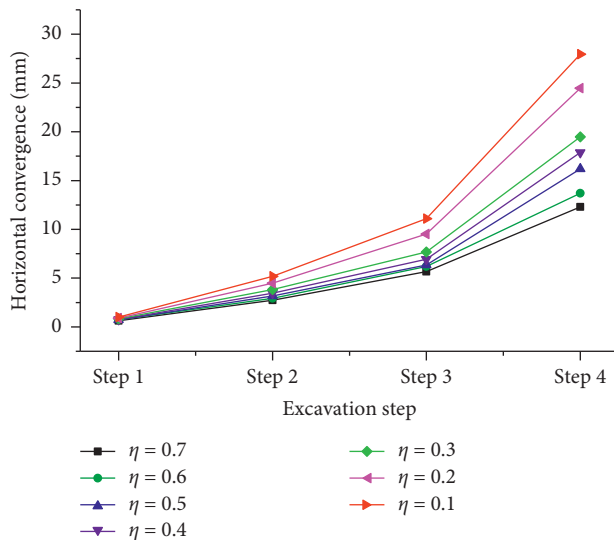


FIGURE 26: Horizontal convergence deformation curves of different values of η .

5. Conclusions

In this paper, experimental investigations for different assembled lining structures were first conducted to study the transverse bending rigidity, and the regression relationship between the effective transverse bending rigidity ratio and the horizontal diameter convergence was established. Besides, a case study of an operated tunnel that was once surcharged and deformed severely was presented in detail. Then, based on the regression relationship proposed from the experimental results, the influence of the transverse effective rigidity ratio on the shield tunnel's subsequent deformation induced by adjacent excavation was explored. The main conclusions can be drawn as follows:

- (1) Based on the similarity theory, brittle gypsum material was used to simulate the segment concrete and featured the deformation characteristic of lining structures after the elastic stage. A detachable mould

was designed for the casting of segmental rings. Hollow aluminium tubes were embedded between segmental rings to form the shape of bolts hole, through which the longitudinal joint bolts can pass. The meticulous fabrication of segmental rings revealed well the detailed structure of segmental rings.

- (2) The deformation characteristic and failure process of the segmental linings are as follows: in the elastic stage, the horizontal and vertical diameter variation of three kinds of lining structure increased approximately linearly as the load increases. Cracks first appeared at the circumferential joints for both of the straight-jointed rings and the stagger-jointed rings. Finally, the fractures at the circumferential joints resulted in the collapse of lining structures. Besides, obvious dislocations between the adjacent rings occurred in the flattening deformation process of stagger-jointed rings.
- (3) The model test results show that before the model cracked, the values of the transverse bending rigidity ratio η fluctuate between 0.503 and 0.642 for the straight-jointed rings and 0.667 and 0.734 for the stagger-jointed rings. But the values of η decrease sharply when the ratio of horizontal diameter convergence exceeds the critical value.
- (4) Existing transverse deformation will cause the decline of transverse stiffness of operated tunnel lining and subsequently result in much unfavourable transverse deformation when subjected to lateral unloading caused by adjacent excavation. It is highly suggested to introduce the modified value of η , which is obtained through substituting on-site measurement data of the tunnel diameter convergence into the regression equation summarized from experimental results, into the numerical analyses of underground shield-driven tunnel problems so that the tunnel deformation and the lining structure safety can be predicted more precisely.

Data Availability

The data used to support the findings of this study are included within the article.

Conflicts of Interest

The authors declare that there are no conflicts of interest regarding the publication of this paper.

Acknowledgments

The authors would like to acknowledge the support from the National Natural Science Foundation of China (grant nos. 51678248 and 51878296), Independent Research Program of State Key Laboratory of Subtropical Building Science (grant no. 2017KB15), South China University of Technology, and Open Research Fund of State Key Laboratory of Simulation and Regulation of Water Cycle in River Basin (grant no. IWHR-SKL-KF201818).

References

- [1] R. Chen, F. Meng, Z. Li, Y. Ye, and J. Ye, "Investigation of response of metro tunnels due to adjacent large excavation and protective measures in soft soils," *Tunnelling and Underground Space Technology*, vol. 58, pp. 224–235, 2016.
- [2] W. C. Chen, Z. P. Song, W. Tian, and Z. F. Wang, "Shield tunnel uplift and deformation characterisation: a case study from Zhengzhou metro," *Tunnelling and Underground Space Technology*, vol. 79, pp. 83–95, 2018.
- [3] T.-j. Liu, S.-w. Chen, and H.-y. Liu, "Deformation characterisation and distress diagnosis of a metro shield tunnel by adjacent constructions," *Advances in Civil Engineering*, vol. 2020, Article ID 4216349, 17 pages, 2020.
- [4] ITA, "Guidelines for the design of shield tunnel lining," *Tunnelling and Underground Space Technology*, vol. 15, pp. 303–331, 2000.
- [5] K. M. Lee, X. Y. Hou, X. W. Ge, and Y. Tang, "An analytical solution for a jointed shield-driven tunnel lining," *International Journal for Numerical and Analytical Methods in Geomechanics*, vol. 25, no. 4, pp. 365–390, 2001.
- [6] H. Yu, C. Cai, A. Bobet, X. Zhao, and Y. Yuan, "Analytical solution for longitudinal bending stiffness of shield tunnels," *Tunnelling and Underground Space Technology*, vol. 83, pp. 27–34, 2019.
- [7] S.-M. Liao, F.-L. Peng, and S.-L. Shen, "Analysis of shearing effect on tunnel induced by load transfer along longitudinal direction," *Tunnelling and Underground Space Technology*, vol. 23, no. 4, pp. 421–430, 2008.
- [8] H. D. Morgan, "A contribution to the analysis of stress in a circular tunnel," *Géotechnique*, vol. 11, no. 1, pp. 37–46, 1961.
- [9] R. B. Peck, A. J. Hendron, and B. Mohraz, "State of the art of soft-ground tunneling," *North American Rapid Excavation & Tunneling Conference Proceedings*, vol. 1, 1972.
- [10] A. M. M. Wood, "The circular tunnel in elastic ground," *Géotechnique*, vol. 25, no. 1, pp. 115–127, 1975.
- [11] Y. Koyama, "Present status and technology of shield tunneling method in Japan," *Tunnelling and Underground Space Technology*, vol. 18, no. 2-3, pp. 145–159, 2003.
- [12] JSCE, *The Design and Construction of Underground Structures*, JSCE, Tokyo, Japan, in Japanese, 1977.
- [13] Y. Tang, "The mechanism study of the staggering assembly of shield-driven tunnel," M.Phil. thesis, Tongji University, Shanghai, China, 1988.
- [14] H. H. Zhu and L. B. Tao, "Study on two beam-spring models for the numerical analysis of segments in shield tunnel," *Rock and Soil Mechanics*, vol. 19, no. 2, pp. 26–32, 1998, in Chinese.
- [15] Y. Koyama and T. Nishimura, "The design of lining segment of shield tunnel using a beam-spring model," *Quarterly Reports RTRI*, vol. 39, no. 1, pp. 23–27, 1998.
- [16] X. Hu, Z. Zhang, and L. Teng, "An analytical method for internal forces in DOT shield-driven tunnel," *Tunnelling and Underground Space Technology*, vol. 24, no. 6, pp. 675–688, 2009.
- [17] Z. Guan, T. Deng, G. Wang, and Y. Jiang, "Studies on the key parameters in segmental lining design," *Journal of Rock Mechanics and Geotechnical Engineering*, vol. 7, no. 6, pp. 674–683, 2015.
- [18] W. Ding, Z. Yue, L. Tham, H. Zhu, C. Lee, and T. Hashimoto, "Analysis of shield tunnel," *International Journal for Numerical and Analytical Methods in Geomechanics*, vol. 28, no. 1, p. 57e91, 2004.
- [19] J. H. Liu and X. Y. Hou, *Shield-Driven Tunnels*, China Railway Press, Beijing, China, 1991, in Chinese.
- [20] X. C. Zhong, W. Zhu, Y. P. Ji, and Y. Xu, "The method to confirm the effective bending stiffness of shield-driven tunnel lining," *Geology and Prospecting*, vol. 39, no. 2, pp. 185–189, 2003, in Chinese.
- [21] L. Xu, "Study on the longitudinal settlement of shield tunnel in soft soil," D.Phil. thesis, Tongji University, Shanghai, China, 2005.
- [22] H. W. Huang, L. Xu, J. L. Yan, and Z. K. Yu, "Study on transverse effective rigidity ratio of shield tunnels," *Chinese Journal of Geotechnical Engineering*, vol. 28, no. 1, pp. 11–18, 2006, in Chinese.
- [23] F. Ye, C.-f. Gou, H.-d. Sun, Y.-p. Liu, Y.-x. Xia, and Z. Zhou, "Model test study on effective ratio of segment transverse bending rigidity of shield tunnel," *Tunnelling and Underground Space Technology*, vol. 41, pp. 193–205, 2014.
- [24] G. Zheng, Y. Lei, T. Cui et al., "Experimental research on the transverse effective bending rigidity of shield tunnels," *Advances in Civil Engineering*, vol. 2019, Article ID 2174562, 17 pages, 2019.
- [25] X. Li, B. Huang, and Z. Yang, "Lateral equivalent stiffness of large diameter shield tunnel lining structure at various buried depths," *Journal of Tongji University*, vol. 43, no. 8, pp. 1159–1166, 2015.
- [26] K. Feng, C. He, and S. L. Xia, "Prototype tests on effective bending rigidity ratios of segmental lining structure for shield tunnel with large cross-section," *Chinese Journal of Geotechnical Engineering*, vol. 33, no. 11, pp. 1750–1758, 2011, in Chinese.
- [27] K. Uchida, "Design and engineering of large bore slurry shield tunnel lining system for trans-Tokyo bay highway," *Civil Engineering in Japan*, vol. 30, pp. 54–67, 1992.
- [28] Y. Kashima, N. Kondo, and M. Inoue, "Development and application of the DPLEX shield method: results of experiments using shield and segment models and application of the method in tunnel construction," *Tunnelling and Underground Space Technology*, vol. 11, no. 1, pp. 45–50, 1996.
- [29] G. Zheng, J. Pan, Y. Li, X. Cheng, and X. Li, "Deformation and protection of existing tunnels at an oblique intersection angle to an excavation," *International Journal of Geomechanics*, vol. 20, no. 8, Article ID 05020004, 2020.

- [30] S. M. Wang, Q. Y. Yu, S. W. Duann, and B. Peng, "A model test for the progressive failure mechanism of lining segment structure of underwater shield tunnels," *China Civil Engineering*, vol. 4, pp. 111–120, 2016, in Chinese.
- [31] C. He, J. G. Zhang, and Z. Yang, "Model test study on the mechanical characteristics of segment lining for the Wuhan Yangtze river tunnel," *China Civil Engineering Journal*, vol. 41, no. 12, pp. 85–90, 2008.
- [32] D. W. Huang, S. H. Zhou, X. Z. Wang, H. B. Liu, and R. L. Zhang, "Design method for longitudinal segment joints of shield tunnel model," *Chinese Journal of Geotechnical Engineering*, vol. 37, no. 6, pp. 1068–1076, 2015.
- [33] S. Wang, X. Wang, B. Chen, Y. Fu, Y. Jian, and X. Lu, "Critical state analysis of instability of shield tunnel segment lining," *Tunnelling and Underground Space Technology*, vol. 96, Article ID 103180, 2020.
- [34] R. Guo, M. Zhang, H. Xie, C. He, Y. Fang, and S. Wang, "Model test study of the mechanical characteristics of the lining structure for an urban deep drainage shield tunnel," *Tunnelling and Underground Space Technology*, vol. 91, Article ID 103014, 2019.
- [35] H. Huang, H. Shao, D. Zhang, and F. Wang, "Deformational responses of operated shield tunnel to extreme surcharge: a case study," *Structure and Infrastructure Engineering*, vol. 13, no. 3, pp. 345–360, 2016.
- [36] C.-T. Chang, C.-W. Sun, S. W. Duann, and R. N. Hwang, "Response of a Taipei rapid transit system (TRTS) tunnel to adjacent excavation," *Tunnelling and Underground Space Technology*, vol. 16, no. 3, pp. 151–158, 2001.
- [37] T. Benz, R. Schwab, and P. Vermeer, "Small-strain stiffness in geotechnical analyses," *Bautechnik*, vol. 86, no. S1, pp. 16–27, 2009.

Research Article

The Effects of Multipropped Deep Excavation-Induced Ground Movements on Adjacent High-Rise Building Founded on Piled Raft in Sand

Mukhtiar Ali Soomro ¹, Naeem Mangi,¹ Wen-Chieh Cheng,² and Dildar Ali Mangnejo³

¹Department of Civil Engineering, Quaid-e-Awam University of Engineering, Science & Technology, Nawabshah, Sindh, Pakistan

²School of Civil Engineering, Xi'an University of Architecture and Technology, Xi'an 710055, China

³Department of Civil Engineering, Mehran University of Engineering & Technology, Shaheed Zulfiqar Ali Bhutto Campus, Khairpur Mirs, Pakistan

Correspondence should be addressed to Mukhtiar Ali Soomro; eng.soomro@gmail.com

Received 6 July 2020; Revised 9 September 2020; Accepted 15 September 2020; Published 24 October 2020

Academic Editor: Jinyang Xu

Copyright © 2020 Mukhtiar Ali Soomro et al. This is an open access article distributed under the Creative Commons Attribution License, which permits unrestricted use, distribution, and reproduction in any medium, provided the original work is properly cited.

In this paper, a three-dimensional numerical parametric study was conducted to predict the deformation mechanism of a 20-storey building sitting on a (4×4) piled raft to an adjacent 25 m deep basement excavation. The influences of different excavation depths were investigated. An advanced hypoplastic sand model (which is capable of taking small-strain stiffness into account) was adopted to capture soil behaviour. The computed results revealed that excavation adjacent to a building resting on the piled raft caused significant settlement, differential settlement, lateral deflection, and interstorey drift in the building. With settlement due to working load (i.e., $4.8d_p\%$), the total settlements of the building ($7.8d_p\%$) exceed the maximum allowable foundation settlement (i.e., 50 mm). In addition, substantial bending moment, shear forces, and changes in axial load distribution along pile length were induced. The findings from this study revealed that the building and pile responses are significantly influenced by the excavation depth.

1. Introduction

Underground space has become increasingly important in relieving the shortage of lands in megacities with rapid economic development and dramatic increase of population [1]. Deep basements for underground facilities such as subway stations are usually excavated near existing buildings and bridges. Basement excavation-induced stress relief and ground movements inevitably cause additional deformation and stress on adjacent pile foundations [2, 3]. It is highly likely that excavation-induced ground movement and stress relief may lead to severe damage and might result in collapse of structure. Thus, it is a major concern for designers and engineers to evaluate adverse effects of basement excavation on buildings. To ensure the safety and serviceability of existing pile foundations, several researchers have studied

this complex problem by means of different approaches. Rocha [4] systematically described scale modeling for problems in soil mechanics in a 1g gravitation field. Moncarz and Krawinkler [5] considered that if an adequate model correctly scales the primary features of the problem, the scaling relations between the prototype and model are not significantly affected. In the previous research study, Sawwaf and Nazir [6] analyzed the results of laboratory model tests on the influence of deep excavation-induced lateral soil movements on the behaviour of a model strip footing adjacent to the excavation and discussed the variation of the footing measured vertical settlements with different parameters. Fang et al. [7] conducted physical model tests of highway tunnel construction and examined the stability of the surrounding rocks regarding different caved zone-tunnel distances and dip angles of the coal seam.

Yang et al. [8] investigated the mechanical behaviour of a typical jointed rock block located adjacent to an underground excavation by comparing the failure modes of the numerical simulations with the corresponding experimental physical jointed block test results. Shahin et al. [9–11] studied about the influence of existing building load on the deformation and earth pressure of the ground in shallow tunnelling by two-dimensional model tests and numerical analysis. Kusui et al. [12] conducted a large number of scaled-down tunnel experiments to investigate the response of unsupported walls to an increased stress field. Xu et al. [13] carried out a series of three-dimensional shaking table tests to investigate the mechanism and effect of seismic measures of the mountain tunnel using a scaled model based on a real tunnel. Furthermore, the centrifuge test was often used to study the effect of excavation construction, and Liyanapathirana and Nishanthan [14] and Zhang et al. [15] analyzed the excavation-induced pile behaviour using the finite element method and the centrifuge test. In terms of influence parameters of excavation construction, Yashiro et al. [16] conducted parameter analysis focusing on the overburden and the stiffness coefficient of the ground by anecdotal surveying and numerical analysis. Boone et al. [17] provided a modified approach for estimating potential damage and compared to case histories using construction data from a large braced excavation. Hsiao et al. [18, 19] considered the calculated settlement as the load in the context of reliability analysis and proposed a simplified model for evaluating the damage potential of a building adjacent to a braced excavation. Long [20] summarized the general trends and patterns based on some 300 case histories of wall and ground movements due to deep excavations worldwide. Among those numerical studies, however, responses of the framed building to excavation were reported in a limited number of studies. Most of these aforementioned research studies only examined the tunnelling effects on buildings founded on shallow footings [21–24]. Therefore, there is a gap of systematic research on the responses of a high-rise building subjected to live load and resting on the piled raft to advancement of adjacent excavation. The paper aims to understand the responses of a 20-storey building to ground movement due to excavation-induced stress relief. To achieve this, three-dimensional finite element analysis was conducted. The building deformation (i.e., differential settlement, deflection, and interstorey drift) and piled raft (i.e., induced bending moment and shear forces in the piles) were presented and discussed.

2. Development of Three-Dimensional Finite Element Model

2.1. General. With the prime objective of investigating the excavation building interaction, three-dimensional finite element analysis was adopted in this study. An excavation was carried out in the close proximity of a 20-storey high rising building which is resting on a (4×4) piled raft foundation in sand. Figure 1(a) illustrates the general setup of the 20-storey building founded on a piled raft and a basement. In practice, the final excavation depth of the

basement commonly varied from 12 to 26 m, and the thickness of the retaining wall varied from 0.3 to 1.0 m [1, 6, 25]. To simulate an actual construction in practice, the basement with a final excavation depth of 25 m (staged excavation) and a wall thickness of 0.3 m was simulated in this study. The depth of first and eighth (i.e., final) stages was 2 m and the depth of each of remaining stages (i.e., second to seven) was taken as 3 m. The ratio of wall penetration depth to excavation depth is typically 0.5–2 in engineering practice [1, 6, 26], and thus a value of 0.6 is adopted in this study. The retaining wall was supported by eight levels of props with vertical and horizontal spacing of 3.0 m and 5 m, respectively. The first level of props was installed at 2.0 m below the ground surface. The props are modeled as soft with axial rigidity of 81×10^3 kNm [21–26]. A 60 m high, 15 m wide 20-storey, concrete building with three spans in each direction was selected in the study. The building was founded on a square raft, which was 15 m wide and 1.5 m thick supported by a group of piles in a 4×4 configuration with a centre-to-centre distance of 3.75 m (see Figure 1(b)). The diameter (d_p) and length (L_p) of each pile were 1 m and 20 m, respectively. The clear distance between the closest pile and the diaphragm wall was 2.0 m ($2d_p$). Since the prime objective of this parametric study is to assess the impact of excavation on the 20-storey building under dead and live loads, the live load of 5 kPa [27] was adopted in this study. With this adopted piled raft system, the numerical prediction showed that settlement of the building due to dead and live load was 45.2 mm ($4.52\%d_p$) which is within the limit of the allowable foundation settlement of 50 mm given by Skempton and Macdonald [28] and O'Brien [29].

2.2. Features of the Building. Figure 2 illustrates the building and its sections of structural components. The structural sections were adopted from Rasouli and Fatahi [30]. They designed the sections by conducting a routine design procedure by conducting analysis and design using SAP2000 [31] based on AS3600 [32], AS1170.1 [27], and AS1170.4 [33]. The details of all sections are summarized in Table 1. The specific compressive strength (f'_c) and mass density of the concrete members in the building were considered to be 32 MPa and 2400 kg/m³, respectively, and the modulus of elasticity of concrete was estimated to be equal to 30.1 GPa.

2.3. Characteristics of the Numerical Model. Figure 3 shows the finite element mesh developed in Abaqus software. The size of the mesh numerical run was taken as 50 m×50 m×60 m. The different structural components of the building (i.e., columns and slabs) were modeled by using two-node linear beam elements (B31) and four-node shell elements (S4). The mechanical behaviour of structural elements of the building was modeled using an elastic-perfectly plastic constitutive model to capture any possible inelastic behaviour of the structural elements; these structural elements could behave elastically until they reached yielding stress that was equal to the compressive strength of concrete (i.e.,

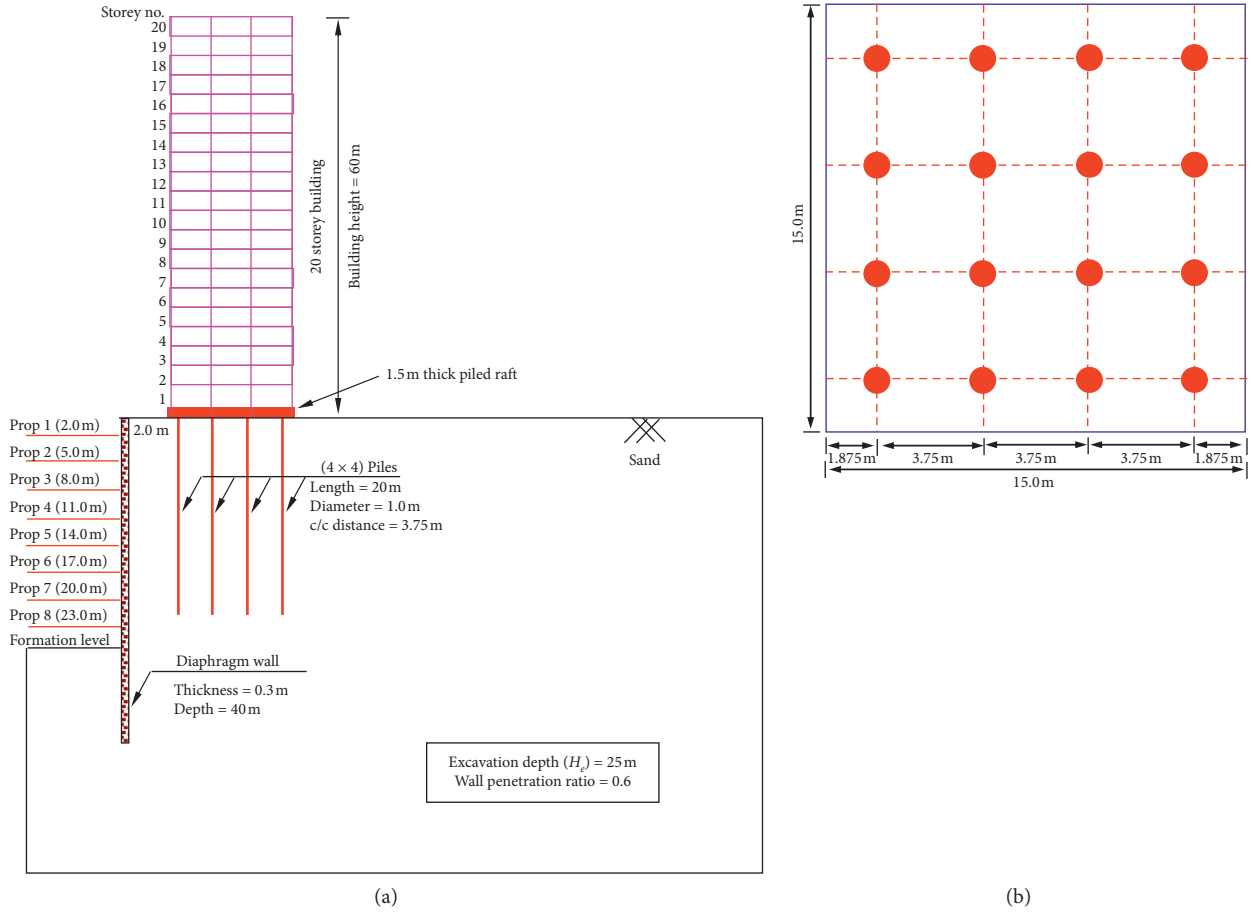


FIGURE 1: (a) General setup of building, piled raft, and excavation. (b) Piles arrangement in the raft.

$f'_c = 32$ MPa) taken from the study of Shing and Tanabe [25]. Eight-noded hexahedral brick elements are used to model the soil, the pile, and the diaphragm wall, while two-noded truss elements are adopted to model the props.

Since the stress-strain relationship of soils is highly nonlinear even at very small strain and the stiffness of soil depends on the recent stress or strain history of the soil [34–38], an advanced hypoplastic model was used to simulate the behaviour of sand in this study. The basic hypoplastic soil model requires eight material parameters to describe the nonlinear behaviour of sand (ϕ'_c , h_s , n , e_{d0} , e_{c0} , e_{i0} , α , and β). Parameter ϕ'_c is the soil frictional angle at a critical state. Parameters h_s and n are used to describe the shape of limiting void ratio lines. Parameters e_{d0} , e_{c0} , and e_{i0} are reference void ratios of isotropic normal compression line, critical state line, and minimum void ratio line, respectively. Effects of soil relative density on peak frictional angle and shear stiffness are characterized by parameters of α and β . To consider the small-strain stiffness and stress path-dependent soil behaviour, the concept of intergranular strain is incorporated into the basic model [39], which includes additional five parameters (m_R , m_T , R , β_r , and χ). By using the concept of intergranular strain, the modified hypoplastic sand model has the ability to capture effects of shear strain and stress path on soil stiffness [40]. These five parameters were obtained by fitting the stiffness degradation curves of Toyoura sand (see Figure 4) obtained from the stress-

path triaxial tests carried out by Ng et al. [41]. Figure 4 shows the measured secant modulus degradation curves corresponding to four varying recent stress histories (i.e., $\theta = 0, 90, -90,$ and 180°), based on the GDS and CKC triaxial automated testing systems. It can be seen that the measured results in the tests for $u = 180^\circ$ by the GDS and CKC triaxial testing systems had fairly similar trends. Quantitatively, the percentage differences between the secant modulus measured by the two triaxial testing systems were less than 18%. The model parameters were taken from a study by Shi et al. [21]. They calibrated and validated all the parameters of the hypoplastic sand model against their centrifuge test results (which was performed to simulate excavation in sand). These parameters are summarized in Table 2. The lateral coefficient of earth pressure (K_0) is estimated by the empirical equation $(1 - \sin \phi')$ proposed by Jáky [42], where ϕ' is internal frictional of soil at the critical state. Since the internal friction angle of Toyoura sand at the critical state is 31° , the K_0 value is estimated as 0.5.

2.4. Soil Structure Interactions and Boundary Conditions. While modeling excavation-pile-soil problem, one of the important aspects of modeling soil structure interaction (SSI) is to establish interaction between pile and surrounding soil. To incorporate the interactions between pile-

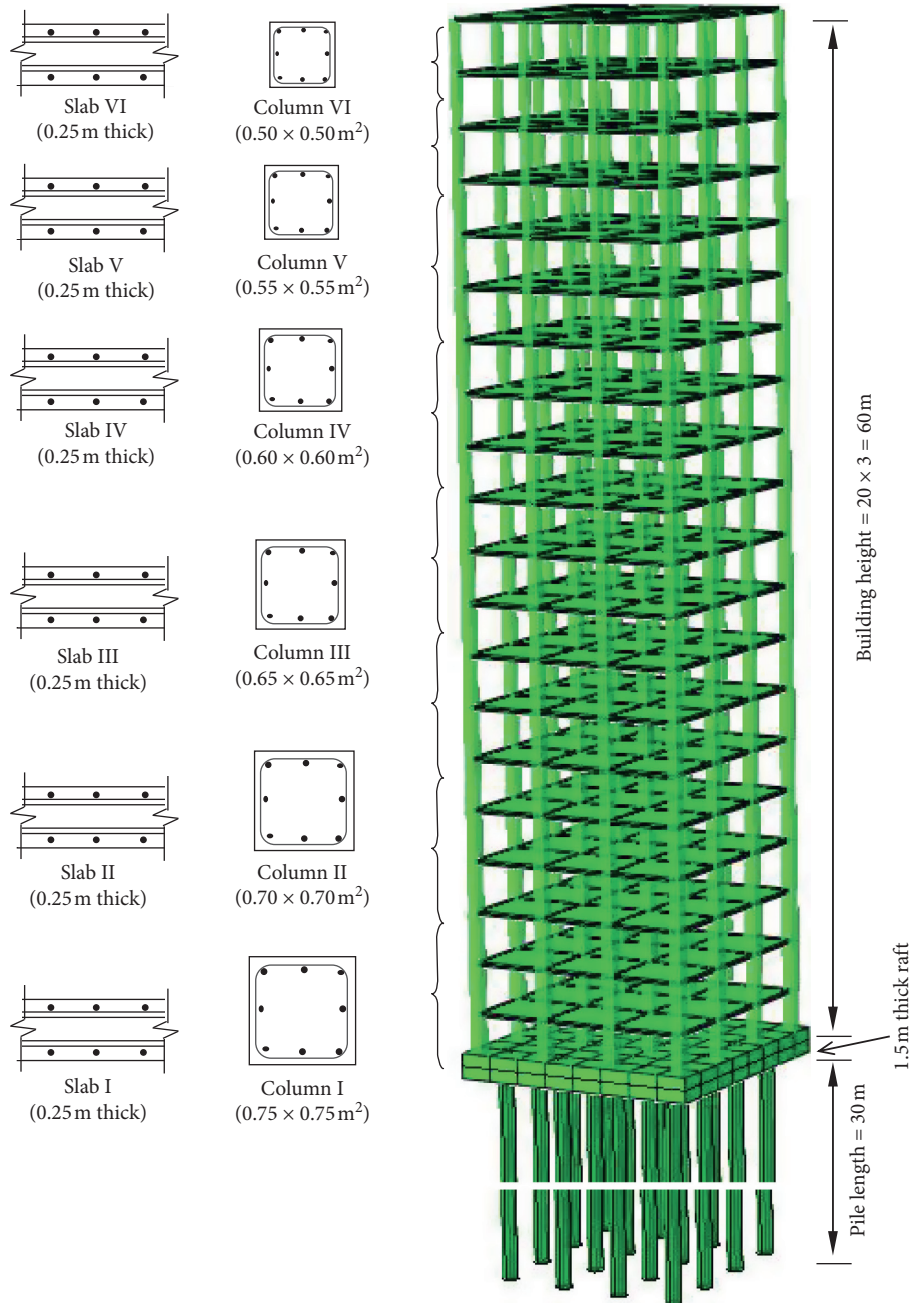


FIGURE 2: Designed sections of columns and slabs.

TABLE 1: Summary of numerical simulations [30].

Section type	Column I	Column II	Column III	Column IV	Column V	Column VI	Slab
Dimension (m)	0.75 × 0.75	0.70 × 0.70	0.65 × 0.65	0.6 × 0.6	0.55 × 0.55	0.50 × 0.50	13.5 × 13.5 × 0.25
Distribution level	1–3	4–7	8–11	12–15	16–18	19–20	All levels
Cross-sectional area, A (m ²)	0.5625	0.49	0.4225	0.36	0.3025	0.25	0.25 (1 m width)
Flexural rigidity, EI (GPa.m ⁴)	0.794	0.602	0.448	0.325	0.230	0.157	0.039

soil and raft-soil, the surface-to-surface contact technique provided in the Abaqus software package was used [43]. In this approach, two surfaces in contact were assigned as the master and slave surfaces. The penalty approach was used for

tangential contact, and the normal behaviour is modeled as hard contact with no normal relative displacement between the pile and surrounding soil. The interface was modeled by the Coulomb friction law, in which the interface friction

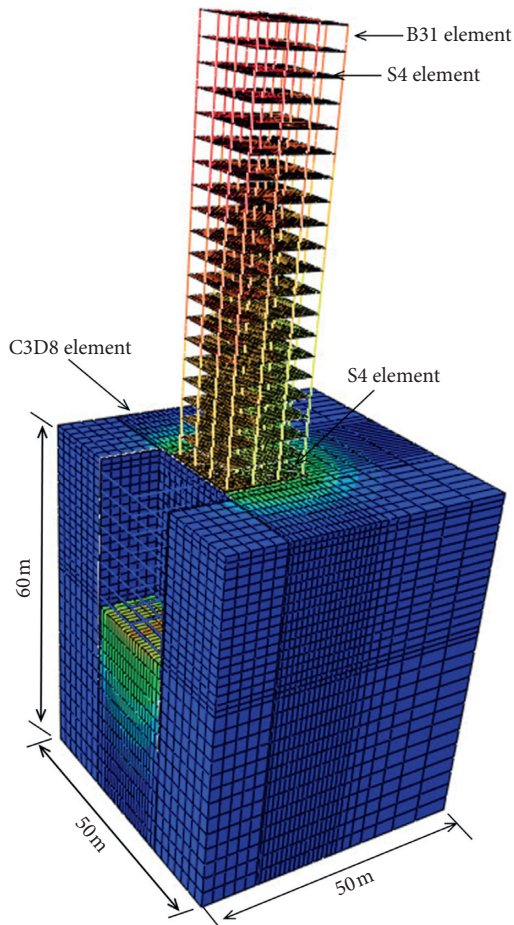


FIGURE 3: 3D finite element mesh (showing the model of building, raft, and ground).

coefficient (μ) and limiting displacement (γ_{lim}) are required as input parameters. A limiting shear displacement of 5 mm was assumed to achieve full mobilization of the interface friction equal to $\mu \times p'$, where p' is the normal effective stress between two contact surfaces, and a typical value 0.35 of μ for a bored pile was used in all analyses [35]. Roller and pin supports were applied to the vertical sides and the base of the mesh, respectively. Therefore, movements normal to the vertical boundaries and in all directions of the base were restrained. The excavation process will be simulated by deactivating soil elements inside the excavation zone. In the meantime, the truss elements representing the props will be activated.

The concrete pile, the diaphragm wall, and the props were assumed to be linear elastic with Young's modulus of 35 GPa and Poisson's ratio of 0.25. The unit weight of the concrete was assumed to be 24 kN/m³. The parameters for the piles and the diaphragm wall are summarized in Table 3.

2.5. Numerical Simulation. The numerical simulations of all the three cases were carried out in the following steps.

- (a) Step 1: initial geostatic stresses are generated in the mesh by applying gravity load and the coefficient of lateral earth pressure of 0.5.

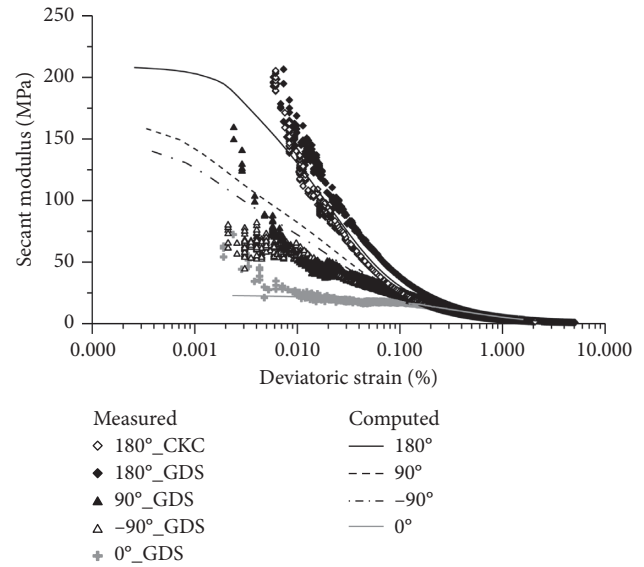


FIGURE 4: Measured and computed degradation curves of Toyoura sand subjected to varying recent stress histories [41].

- (b) Step 2: the piles are constructed, and then a raft is placed on the top of the pile group and soil deposit.
- (c) Step 3: the 20-storey building is constructed on the top of the piled raft. A live load of 5 kPa is applied on the floor slab of each storey.
- (d) Step 4: the brick elements representing the diaphragm wall are activated.
- (e) Step 5: staged multipropped excavation is simulated as described in Section 2.1. After excavating to 2 m depth, the first level of props is installed at 2 m below the ground surface.
- (f) Step 6: repeat step 6 to excavate the next stages and install props until the last stage of excavation (i.e., $H_e = 25$ m) is completed.

2.6. Validation of Numerical Modeling against Centrifuge Test Result.

Before conducting any numerical parametric study, the measured ground surface settlement in centrifuge test results reported by Shi et al. [21] was used to validate the soil constitutive model and model parameters adopted in the finite element analyses. Figure 5 shows the comparison between measured and computed ground surface settlement trough developed on completion of the excavation. Both the ground surface settlement (S) and the distance behind the wall in the transverse direction are normalised by final excavation depth (H_e). It can be observed from the figure that the measured and computed settlement troughs show reasonable agreement. In this study, multipropped basement excavation is simulated. Thus, concave-shaped profile of ground settlement behind the wall is observed, as expected. The measured maximum soil settlement is observed at a distance of $0.375H_e$, while the induced settlement is negligible when the distance from the wall exceeds $2.5H_e$. When the normalised distance from the basement is $0.375H_e$, the

TABLE 2: Hypoplastic model parameters of sand adopted in this study.

Description	Parameter
Effective angle of shearing resistance at critical state, ϕ'	31°
Coefficient of at-rest earth pressure, K_o	0.5
Hardness of Granulates, h_s	2.6 GPa
Exponent n	0.27
Minimum void ratio at zero pressure, e_{do}	0.61
Maximum void ratio at zero pressure, e_{io}	1.10
Critical void ratio at zero pressure, e_{co}	0.98
Exponent α	0.14
Exponent β	6
Parameter controlling initial shear modulus upon 180° strain path reversal, m_R	11
Parameter controlling initial shear modulus upon 90° strain path reversal, m_T	6
Size of elastic range, R	2×10^{-5}
Parameter controlling degradation rate of stiffness with strain, β_r	0.1
Parameter controlling degradation rate of stiffness with strain, χ	1.0

TABLE 3: Concrete parameters adopted in finite element analysis.

Description	Parameter
Young's modulus, E	35 GPa
Poisson's ratio, ν	0.3
Density, ρ	2400 kg/m ³

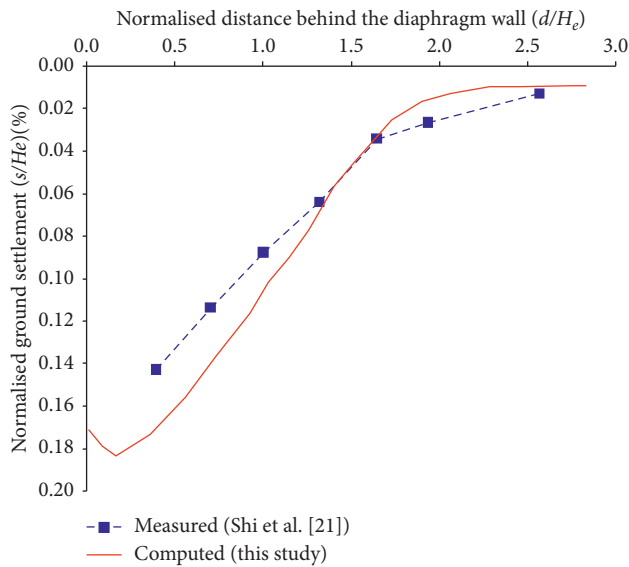


FIGURE 5: Comparison of the measured and computed ground surface settlement.

computed ground surface settlement at the end of basement excavation is $0.17\%H_e$, which is 18% larger than the measured one ($0.143\%H_e$).

3. Interpretation of Computed Results

3.1. Settlement of Piled Raft. Settlement of the piled raft at its centre (S_p) induced due to different excavation stages is plotted in Figure 6. The piled settlement is normalised by the pile diameter. Excavation depths are indicated by h which is normalised by final excavation depth (H_e). It can be seen

from the figure that bilinear increment in S_p was observed with increasing excavation depth. S_p increased linearly when excavation depth reached $h/H_e = 0.68$; however, the rate of induced settlement further increased until final excavation depth ($h/H_e = 1.00$). This was because of degradation of sand stiffness due to excavation-induced stress and the plastic strain generated surrounding the piles due to excavation-induced stress release. Since the initial excavation stages ($0 < h/H_e < 0.68$) are adjacent to the pile shaft, the shafts of the piles were affected by excavation-induced plastic strain. However, the toes of the piles were resting on the intact (from plastic strain) stiffer layer, whereas toes of the piles were severely influenced by the plastic strain as excavation stages passed beyond the pile toes ($h/H_e > 1.00$). Consequently, the piled raft experienced larger settlement due to excavation stages beyond $h/H_e > 0.68$ as compared to the initial excavation stages. On completion of the excavation, the piled raft settlement was 30 mm ($3.0d_p\%$). With settlement due to working load (i.e., $4.8d_p\%$), the total settlements of the building ($7.8d_p\%$) exceed the maximum allowable foundation settlement (i.e., 50 mm) according to Skempton and Macdonald [28] and O'Brien [29]. Hence, the numerical prediction implies that the serviceability limit state of a building founded on the pile can be affected when excavation is carried out adjacent to the building.

3.2. Differential Settlement of Piled Raft. In addition to the discussion of piled raft settlement in the previous section, differential settlement induced in the building is an important parameter to investigate. During the excavation of nearby piled raft foundation, as expected, piles closest to the excavation are subjected to larger ground movement and stress release than those which are farthest from the excavation. As a result, differential settlement is induced in the piles. Figure 7 shows settlements of the piled raft induced at various positions along the centreline of the raft (see inset in the figure) at different excavation stages (i.e., $h/H_e = 0.08, 0.32, 0.56, 0.80$, and 1.00). The settlement before excavation is added in the figure for reference. It can be seen that after completion of the building construction (before excavation), the settlement occurred in the building was uniform through

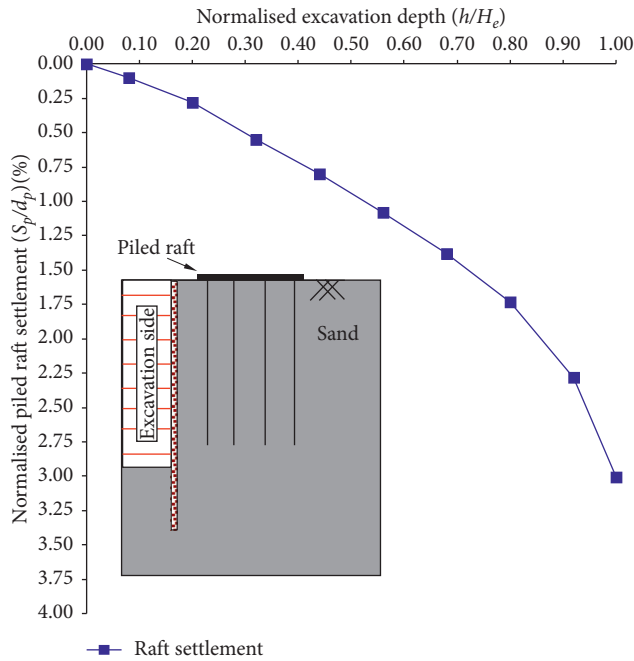


FIGURE 6: Piled raft settlement during excavation.

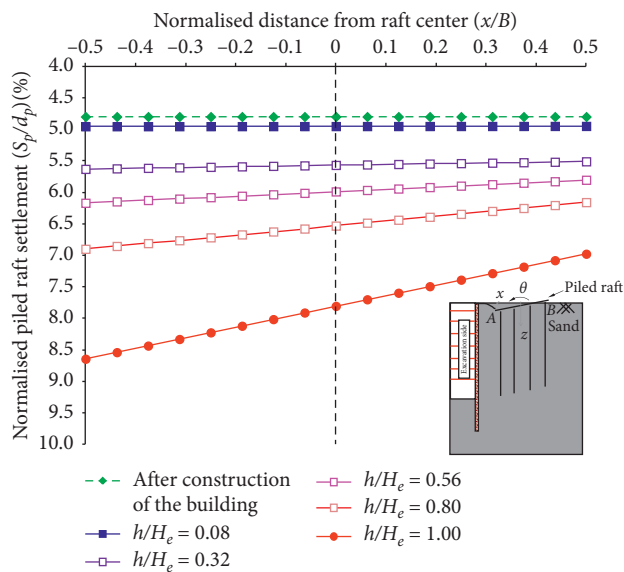


FIGURE 7: Evolution of differential settlement in the raft.

the centreline of the raft. However, as excavation was carried out, the raft corner closest to the diaphragm wall settled larger than that furthest from the wall. After the completion of the first excavation stage (i.e., $h/H_e = 0.08$), negligible differential settlement was predicted. However, as excavation depth increases, the differential settlement increases. This observation is attributed to excavation-induced stress release which is larger and smaller around the pile closest to and farthest from the excavation. The induced differential settlement caused the building permanent interstorey drifts (discussed in Section 3.3). The differential settlement in the

raft of 3.6, 7.4, and 16.7 mm was induced on completion of excavation stages $h/H_e = 0.56, 0.80, \text{ and } 1.00$, respectively.

3.3. Flooring Lateral Displacement and Interstorey Drifts. The numerical predictions in the previous section showed that the excavation resulted in differential settlement of the raft. This led to displace the 20-storey building laterally towards the excavation. Figure 8(a) illustrates the induced lateral deflection of the building along each storey at different excavation stages (i.e., $h/H_e = 0.08, 0.32, 0.56, 0.80, \text{ and } 1.00$). It can be seen from the figure that lateral deflection increased with the height of the building. Negligible lateral deflection was computed after the first excavation stage (i.e., $h/H_e = 0.08$). However, as the excavation continues, the substantial lateral deflection was induced in the building. This observation is consistent with induced settlement in the piled raft. The maximum lateral deflection occurred at the top of the building (the roof level of 20th storey). The general trend of the lateral deflection profile is consistent with differential settlement. Since interstorey drift may induce distress in structural component of the building, it is necessary to predict the drift induced in the building due to excavation at different stages. Figure 8(b) illustrates interstorey drift of the building during excavation. The interstorey drift of the building can be defined as ratio of difference of deflections at two storeys to storey height. It is noted that interstorey drift shows similar trend as that of lateral deflection. The drift of 0.024%, 0.05%, and 0.11% was predicted on completion of excavation stages $h/H_e = 0.56, 0.80, \text{ and } 1.00$, respectively.

3.4. Computed Ground Deformation Mechanism and Deviatoric Strain. Figure 9 shows computed incremental displacement vectors due to excavation. In addition, computed incremental shear strain of the excavation-induced stress release is also superimposed in the figure. It can be observed that soil on the retained side moved towards the excavation, whereas the soil underneath the excavation heaved upwards due to vertical stress relief inside the excavation zone. Furthermore, it can be seen that excavation-induced ground movement is mainly bounded by a wedge at an angle of 45° drawn from the wall toe. In addition to ground movement, significant shear strain (up to 1.0%) is also developed extending nearly at 45° from the wall toe. A similar pattern and magnitude of excavation-induced shear strain were calculated from the measured centrifuge test in sand [21]. This indicates that the finite element analysis results are appropriate to analyze the excavation pile interaction problem.

It can be seen that all the piles are located at the zone of ground movement. Moreover, the piles closest to the diaphragm wall are subjected to larger ground movement as compared to farthest piles. This caused the differential settlement (see Figure 7) in the piled raft. Because the entire pile length is affected by the ground movement due to excavation-induced stress release, shaft resistance decreased. To maintain equilibrium, the pile had to settle which resulted in increment in end bearing (explained in Section 3.6). On

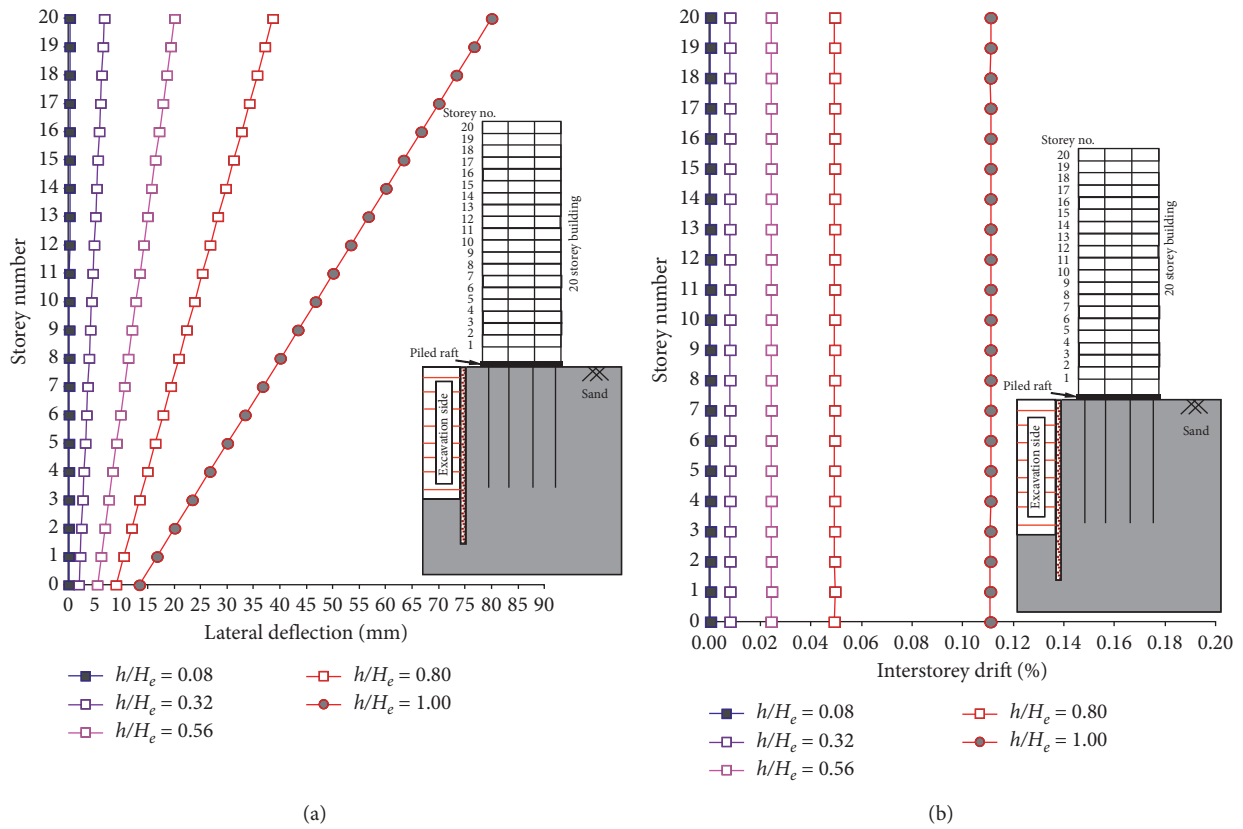


FIGURE 8: Lateral deflection and interstorey drift of the building on completion of excavation.

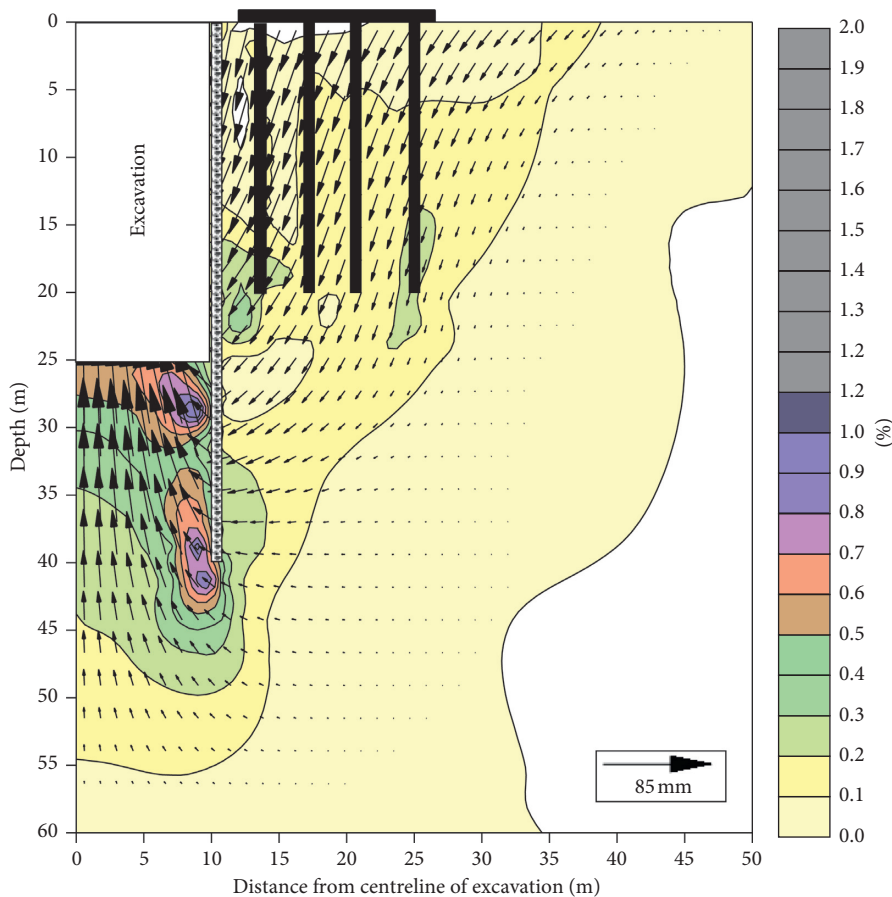


FIGURE 9: Computed soil displacement vectors and incremental deviatoric strain contours due to excavation.

the other hand, the toe of the closest pile is located within the region where shear strain is developed. As illustrated, the presence of the pile further increases the shear strain of soil near the pile toe, as more end bearing has to be mobilized to support vertical load transferred from the pile shaft to the pile toe after excavation.

3.5. Changes in Load Taken by the Raft during Excavation.

After construction of the building resting on a piled raft system, some of the building load is sustained by the raft and remaining load is transferred to the piles. However, the load taken by the raft can be altered when excavation is performed close to piles. Figure 10 represents the change in load sharing by the raft at different depths of excavations. It can be seen that before excavation (after application of working load), about 5.9% of the building load (i.e., 57.6 MN) was carried by the raft and the rest of the load was transferred to sixteen piles. It can be observed that the load taken by the raft kept decreasing during excavation. As the excavation depth increases, rate of reduction of the load is the highest. This indicates that the building load was transferred to piles on completion of excavation. This can be attributed to the raft settlement and induced ground settlement. On completion of the excavation, the load resisted by the raft reduced to 4.85% of the total load.

3.6. Changes in Axial Load Distribution along Piles.

As discussed in the previous section, the load taken by the raft altered substantially due to the excavation. It suggests that changes in axial load distribution along 16 piles can be induced. Since arrangement of the 16 piles in the piled raft system is in a square pattern (i.e., 4×4 piles), the piles at critical positions are selected for discussion in this section. The piles are designated as P1, P2, P3, and P4 (see the inset in Figure 11). Figure 11(a) compares axial load distribution along the lengths of piles P1 and P4. For comparison, load distribution along the length of each pile before the excavation is included in each figure. It can be observed from the figure that the load taken by the piles positioned at the corner of the raft (i.e., P1 and P4) is same, whereas piles in the middle of the raft shared equal load before excavation. Before excavation, the load taken by the piles P1 and P4 is 3517 kN. Both piles resisted the load by shaft resistance (36% of the load), and the remainder resisted by end bearing. On completion of the excavation, the axial load along the entire pile length of piles P1 and P4 increased. This indicates that shaft resistance decreased along the length of both the piles. This observation can be attributed to excavation-induced shear strain due to stress release at the midportion of the pile (discussed in Section 3.4). To support the load, shaft resistance was mobilized at the lower portion of the pile. Figure 11(b) compares axial load distribution along the length of piles P2 and P3. For comparison, load distribution along the length of each pile before the excavation is included in each figure. It can be seen from the figure that before excavation, the load transferred to each of the piles P2 and P3 was 3160 kN. The piles resisted the load by mobilizing shaft resistance (40% of load) along the lower portion the

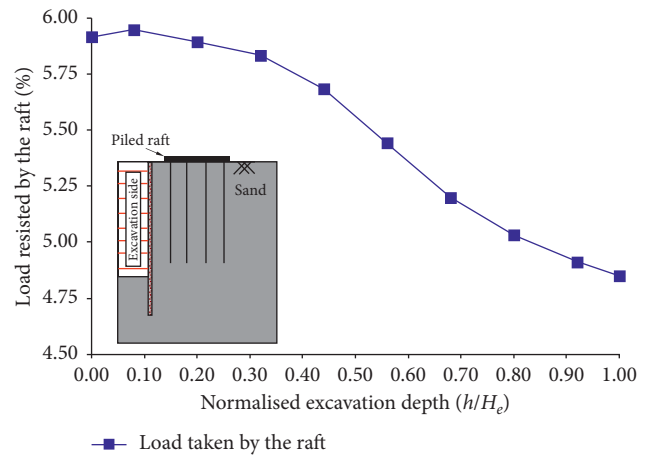


FIGURE 10: Changes in load resisted by the raft during excavation.

pile length, and remainder 60% of the load was resisted by end bearing. It can be seen from the figure that similar to the changes in axial load distribution along the pile length of P1 and P4, the axial load along the entire pile length of P2 and P4 increased on completion of the excavation. This load redistribution is ascribed to excavation-induced stress release and load transfer from the raft to piles. The end bearing of both the piles P2 and P3 increased by 10% to carry the transferred load from the raft.

3.7. Structural Response of Pile (Induced Bending Moment and Shear Forces along Piles).

Before excavation, the piles are horizontally confined by the surrounding soil and are subjected to negligible shear forces and bending moments. However, when excavation is carried out near piles and induces stress release in the ground, the substantial shear forces and bending moment can be produced in the piles. Thus, the shear forces and bending moment induced along piles due to excavation are important parameters to be predicted. Figure 12 illustrates the induced shear forces along normalised depth of four selected piles (i.e., P1, P2, P3, and P4) on completion of excavation. A highly nonlinear shear force distribution was predicted along each pile in each case. Due to rigid connection between the piles and raft, the maximum shear force generated is at the head of the piles. However, the magnitude of the maximum shear force was dependent on the location of the piles in the raft. The piles at the corners of the raft (P1 and P4) and the middle of the raft (P2 and P3) are subjected to positive and negative shear forces, respectively. The maximum shear forces developed at pile heads P1, P2, P3, and P4 were 730 kN, 600 kN, 550 kN, and 250 kN, respectively. This is because of excavation-induced stress release and ground movement towards excavation.

Since the piles are mostly designed to carry vertical load, the bending moment induced in the piles is another important parameter to investigate due to adjacent excavation. Figure 13 shows the induced bending moments along the normalised depth of four selected piles (i.e., P1, P2, P3, and P4) on completion of excavation. It is clear evidence from the figures that the maximum bending moment is induced at

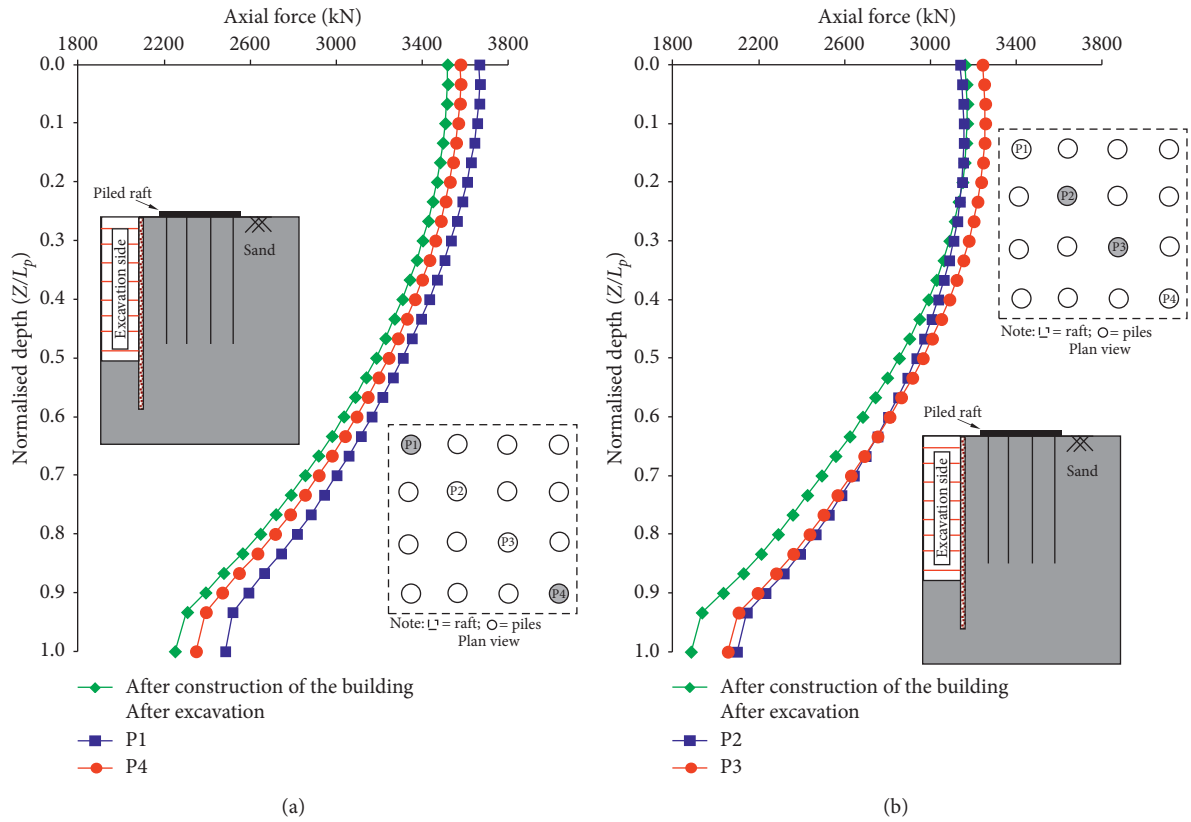


FIGURE 11: Axial load distribution before and after tunnelling in each case along the lengths of piles. (a) P1 and P4. (b) P2 and P3.

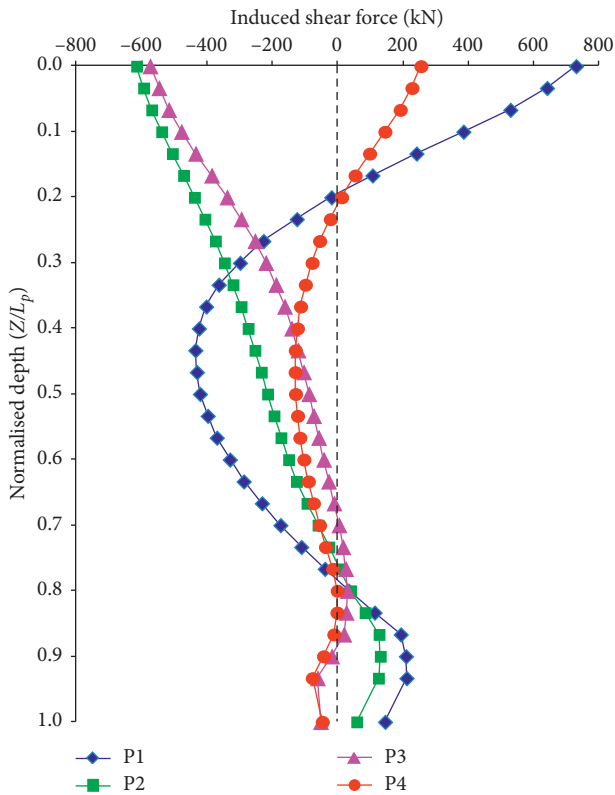


FIGURE 12: Induced shear force along four piles (i.e., P1, P2, P3, and P4).

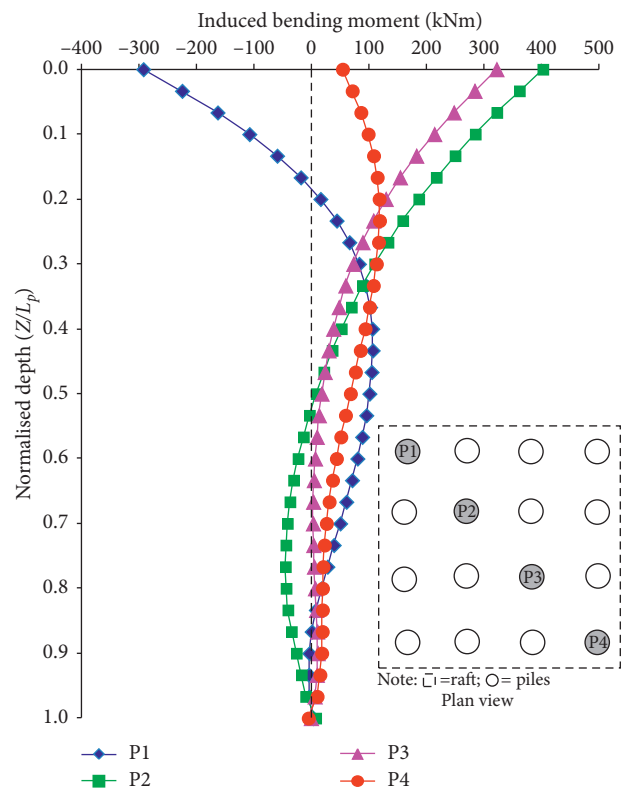


FIGURE 13: Induced bending moment along four piles (i.e., P1, P2, P3, and P4).

the head of each pile. This is because the piles are rigidly connected to the raft. The maximum negative bending moment (300 kNm) was predicted at the head of pile P1. To counterbalance the negative bending moment, positive bending moment was induced at the lower portion of the pile ($Z/L_p > 0.2$). The remaining piles (P2, P3, and P4) were subjected to positive bending moment at their heads. Since the pile toes were free to move, negligible bending moment was induced at the toes of each pile.

4. Conclusions

Based upon the analysis and results, the following specific conclusions are drawn:

- (1) Owing to degradation of soil stiffness, bilinear increment in S_p was observed with increasing of excavation depth. S_p increased linearly when excavation depth reached $h/H_e = 0.68$; however, the rate of induced settlement further increased until final excavation depth ($h/H_e = 1.00$). With settlement due to working load (i.e., $4.8d_p\%$), the total settlements of the building ($7.8d_p\%$) exceed the maximum allowable foundation settlement (i.e., 50 mm) according to Skempton and Macdonald and O'Brien.
- (2) After the completion of the first excavation stage (i.e., $h/H_e = 0.08$), negligible differential settlement was induced. However, as excavation depth increases, the differential settlement increases. This observation is attributed to excavation-induced stress release which is larger and smaller around the pile closest to and farthest from the excavation. The differential settlement in the raft of 3.6, 7.4, and 16.7 mm was induced on completion of excavation stages $h/H_e = 0.56$, 0.80, and 1.00, respectively.
- (3) The excavation resulted in differential settlement of the raft. This led to displace the 20-storey building laterally towards the excavation which caused the building permanent interstorey drifts. The interstorey drift may induce distress in structural component of the building.
- (4) The load taken by the raft (about 5.9% of the building loads, i.e., 57.6 MN before excavation) can be altered when excavation is performed close to piles. On completion of the excavation, the load resisted by the raft reduced to 4.85% of the total load.
- (5) Apart from induced settlement, differential settlement, lateral movement, and interstorey drift in the building due to excavation, the piles are also subjected to substantial shear forces and bending moment along pile lengths.

Data Availability

The data used to support the findings of this study are available from the corresponding author upon request.

Conflicts of Interest

The authors declare that they have no conflicts of interest.

Acknowledgments

The authors would like to acknowledge the financial support provided by the Quaid-e-Awam University of Engineering, Science & Technology, Sindh, Pakistan.

References

- [1] J. Shi, C. Ding, C. W. W. Ng, H. Lu, and L. Chen, "Effects of overconsolidation ratio on tunnel responses due to overlying basement excavation in clay," *Tunnelling and Underground Space Technology*, vol. 97, Article ID 103247, 2020.
- [2] J. Shi, G. Liu, P. Huang, and C. W. W. Ng, "Interaction between a large-scale triangular excavation and adjacent structures in Shanghai soft clay," *Tunnelling and Underground Space Technology*, vol. 50, pp. 282–295, 2015.
- [3] M. Son and E. J. Cording, "Evaluation of building stiffness for building response analysis to excavation-induced ground movements," *Journal of Geotechnical and Geoenvironmental Engineering*, vol. 133, no. 8, pp. 995–1002, 2007.
- [4] M. Rocha, "The possibility of solving soil mechanics problems by use of models," in *Proceedings of 4th International Conference on Soil Mechanics and Foundation Engineering*, vol. 1, pp. 183–188, London, UK, August 1957.
- [5] P. Moncarz and H. Krawinkler, "Theory and application of experimental model analysis in earthquake engineering," John A. Blume Earthquake Engineering Center Stanford University, Stanford, CA, USA, Rpt. No. 50, 1981.
- [6] M. E. Sawwaf and A. K. Nazir, "The effect of deep excavation induced lateral soil movements on the behavior of strip footing supported on reinforced sand," *Journal of Advanced Research*, vol. 3, no. 4, pp. 337–344, 2012.
- [7] Y. Fang, C. Xu, G. Cui, and B. Kenneally, "Scale model test of highway tunnel construction underlying mined-out thin coal seam," *Tunnelling and Underground Space Technology*, vol. 56, pp. 105–116, 2016.
- [8] X. Yang, P. H. S. W. Kulatilake, H. Jing, and S. Yang, "Numerical simulation of a jointed rock block mechanical behavior adjacent to an underground excavation and comparison with physical model test results," *Tunnelling and Underground Space Technology*, vol. 50, pp. 129–142, 2015.
- [9] H. M. Shahin, E. Sung, T. Nakai et al., "2D model tests and numerical simulation in shallow tunneling considering existing building load," *Underground Construction and Ground Movement*, vol. 155, pp. 304–311, 2006.
- [10] H. M. Shahin, T. Nakai, M. Hinokio, T. Kurimoto, and T. Sada, "Influence of surface loads and construction sequence on ground response due to tunnelling," *Soils and Foundations*, vol. 44, no. 2, pp. 71–84, 2004.
- [11] W.-C. Cheng, J. C. Ni, A. Arulrajah, and H.-W. Huang, "A simple approach for characterising tunnel bore conditions based upon pipe-jacking data," *Tunnelling and Underground Space Technology*, vol. 71, pp. 494–504, 2018.
- [12] A. Kusui, E. Villaescusa, and T. Funatsu, "Mechanical behaviour of scaled-down unsupported tunnel walls in hard rock under high stress," *Tunnelling and Underground Space Technology*, vol. 60, pp. 30–40, 2016.
- [13] H. Xu, T. Li, L. Xia, J. X. Zhao, and D. Wang, "Shaking table tests on seismic measures of a model mountain tunnel,"

- Tunnelling and Underground Space Technology*, vol. 60, pp. 197–209, 2016.
- [14] D. S. Liyanapathirana and R. Nishanthan, “Influence of deep excavation induced ground movements on adjacent piles,” *Tunnelling and Underground Space Technology*, vol. 52, pp. 168–181, 2016.
- [15] R. Zhang, J. Zheng, H. Pu, and L. Zhang, “Analysis of excavation-induced responses of loaded pile foundations considering unloading effect,” *Tunnelling and Underground Space Technology*, vol. 26, no. 2, pp. 320–335, 2011.
- [16] K. Yashiro, K. Shimamoto, and Y. Kojima, “Proposal of guideline for judgment of adjacent level on adjacent construction of existing tunnels,” *Quarterly Report of RTRI*, vol. 49, no. 2, pp. 79–84, 2008.
- [17] S. J. Boone, J. Westland, and R. Nusink, “Comparative evaluation of building responses to an adjacent braced excavation,” *Canadian Geotechnical Journal*, vol. 36, no. 2, pp. 210–223, 1999.
- [18] E. C. L. Hsiao, C. H. Juang, G. T. C. Kung, and M. Schuster, “Reliability analysis and updating of excavation-induced ground settlement for building serviceability excavation,” in *Proceedings of Probabilistic Applications in Geotechnical Engineering*, vol. 170, pp. 1–10, Denver, CO, USA, February 2007.
- [19] E. C. Hsiao, M. Schuster, C. H. Juang, and G. T. Kung, “Reliability analysis and updating of excavation-induced ground settlement for building serviceability assessment,” *Journal of Geotechnical and Geoenvironmental Engineering*, vol. 134, no. 10, pp. 1448–1458, 2008.
- [20] M. Long, “Database for retaining wall and ground movements due to deep excavations,” *Journal of Geotechnical and Geoenvironmental Engineering*, vol. 127, no. 3, pp. 203–224, 2001.
- [21] J. Shi, J. Wei, C. W. W. Ng, and H. Lu, “Stress transfer mechanisms and settlement of a floating pile due to adjacent multi-propped deep excavation in dry sand,” *Computers and Geotechnics*, vol. 116, Article ID 103216, 2019.
- [22] J. Shi, Z. Fu, and W. Guo, “Investigation of geometric effects on three-dimensional tunnel deformation mechanisms due to basement excavation,” *Computers and Geotechnics*, vol. 106, pp. 108–116, 2019.
- [23] S. Yu and Y. Geng, “Influence analysis of underground excavation on the adjacent buildings and surrounding soil based on scale model test,” *Advances in Civil Engineering*, vol. 2019, p. 15, Article ID 6527175, 2019.
- [24] W.-C. Cheng, L. Wang, Z.-F. Xue, J. C. Ni, M. Rahman, and A. Arulrajah, “Lubrication performance of pipejacking in alluvial deposits,” *Tunnelling and Underground Space Technology*, vol. 91, p. 102991, 2019.
- [25] P. B. Shing and T. Tanabe, *Modeling of Inelastic Behavior of RC Structures under Seismic Loads*, ASCE Publications, Reston, VI, USA, 2001.
- [26] M. A. Soomro, D. A. Mangnejo, R. Bhanbhro, N. A. Memon, and M. A. Memon, “3D finite element analysis of pile responses to adjacent excavation in soft clay: effects of different excavation depths systems relative to a floating pile,” *Tunnelling and Underground Space Technology*, vol. 86, pp. 138–155, 2019.
- [27] Standards Australia, *Structural Design Actions; Part 1 Permanent, Imposed and other Actions*, Standards Australia, Sydney Australia, AS1170.1, 2002.
- [28] A. W. Skempton and D. H. Macdonald, “The allowable settlements of buildings,” *Proceedings of the Institution of Civil Engineers*, vol. 5, no. 6, pp. 727–768, 1956.
- [29] A. S. O’Brien, “Chapter 52 foundation types and conceptual design principles,” *ICE Manual of Geotechnical Engineering*, vol. II, pp. 733–764, 2012.
- [30] H. Rasouli and B. Fatahi, “A novel cushioned piled raft foundation to protect buildings subjected to normal fault rupture,” *Computers and Geotechnics*, vol. 106, pp. 228–248, 2019.
- [31] Computers and Structures Inc, *SAP2000 14 [Computer Software]*, Computers and Structures Inc., Berkeley, CA, USA.
- [32] Standards Australia, *Concrete Structures*, Standards Australia, Sydney, Australia, AS3600, 2009.
- [33] Standards Australia, *Structural Design Actions; Part 4: Earthquake Actions in Australia*, Standards Australia, Sydney, Australia, AS1170.4, 2007.
- [34] J. H. Atkinson, D. Richardson, and S. E. Stallebrass, “Effect of recent stress history on the stiffness of overconsolidated soil,” *Géotechnique*, vol. 40, no. 4, pp. 531–540, 1990.
- [35] M. A. Soomro, M. Kumar, H. Xiong, D. A. Mangnejo, and N. Mangi, “Investigation of effects of different construction sequences on settlement and load transfer mechanism of single pile due to twin stacked tunnelling,” *Tunnelling and Underground Space Technology*, vol. 96, Article ID 103171, 2020.
- [36] M. A. Soomro, A. Saand, N. Mangi, D. A. Mangnejo, H. Karira, and K. Liu, “Numerical modelling of effects of different multipropped excavation depths on adjacent single piles: comparison between floating and end-bearing pile responses,” *European Journal of Environmental and Civil Engineering*, 2020.
- [37] W.-C. Cheng, J. C. Ni, H.-W. Huang, and J. S. Shen, “The use of tunnelling parameters and spoil characteristics to assess soil types: a case study from alluvial deposits at a pipejacking project site,” *Bulletin of Engineering Geology and the Environment*, vol. 78, no. 4, pp. 2933–2942, 2019.
- [38] W.-C. Cheng, G. Li, N. Liu, J. Xu, and S. Horpibulsuk, “Recent massive incidents for subway construction in soft alluvial deposits of Taiwan: a review,” *Tunnelling and Underground Space Technology*, vol. 96, p. 103178, 2020.
- [39] A. Niemunis and I. Herle, “Hypoplastic model for cohesionless soils with elastic strain range,” *Mechanics of Cohesive-Frictional Materials*, vol. 2, no. 4, pp. 279–299, 1997.
- [40] I. Herle and G. Gudehus, “Determination of parameters of a hypoplastic constitutive model from properties of grain assemblies,” *Mechanics of Cohesive-Frictional Materials*, vol. 4, no. 5, pp. 461–486, 1999.
- [41] C. W. W. Ng, Y. Hong, and M. A. Soomro, “Effects of piggyback twin tunnelling on a pile group: 3D centrifuge tests and numerical modelling,” *Géotechnique*, vol. 65, no. 1, pp. 38–51, 2015.
- [42] J. Jáky, “The coefficient of earth pressure at rest,” *Journal of the Society Hungarian Society of Engineers and Architects*, vol. 78, no. 22, pp. 355–358, 1944, in Hungarian.
- [43] K. Hibbitt, *Sorensen, Abaqus User’s Manual, Version 6.14-2*, Hibbitt, Karlsson & Sorensen Inc, Providence, RI, USA, 2014.

Research Article

Research and Application of Support Resistant Limiting Dampers in the Deep-Buried Large-Section Loess Tunnel

Yong Deng, Jiangsheng Xie, and Shuguang Li 

China Railway 20th Bureau Group Co. Ltd., Xian 710016, China

Correspondence should be addressed to Shuguang Li; lssgg2015@163.com

Received 9 September 2020; Revised 17 September 2020; Accepted 18 September 2020; Published 30 September 2020

Academic Editor: Zhushan Shao

Copyright © 2020 Yong Deng et al. This is an open access article distributed under the Creative Commons Attribution License, which permits unrestricted use, distribution, and reproduction in any medium, provided the original work is properly cited.

The paper aims to solve the problem that the primary support of the deep-buried large-section loess tunnel of the Haolebaoji-Ji'an Railway was damaged due to excessive force. Based on indoor tests, on-site construction feedback, and monitoring measurement data, the surrounding rock deformation and structural forces with different support schemes were compared and analyzed. The engineering application methods and mechanism of the support resistant limiting damper (SRLD) technology were studied. The results show that for the deep-buried large-section loess tunnels, under the premise of ensuring the self-supporting capacity of the surrounding rock is not significantly reduced, and the loose pressure is not significantly increased, the resistance-limiting and high-ductility support concept that can control the deformation and the energy release of the surrounding rock is reasonable and feasible. The support resistant limiting damper (SRLD) is a reasonable and practical resistance-limiting and high-ductility support method, which successfully solved the failure of the primary support of the deep-buried large-section loess tunnel. The SRLD's integrity and safety are guaranteed, the materials are easy to obtain, the processing is convenient, and the construction is simple and easy to operate. The SRLD is a safe and economic support structure.

1. Introduction

With the development of transportation construction, more and more new tunnels need to traverse complex geology. Excavation and support problems caused by high ground stress, weak surrounding rocks, and other unfavourable geology have become the bottleneck of tunnel construction [1–3]. The special engineering characteristics of loess cause the loess tunnel large deformation during the excavation process [4], which brings challenges to theoretical research and design of the loess tunnel.

The colour of loess is from yellow to red-yellow; its bedding is not apparent; it is rich in carbonate, and it has a loose honeycomb-type metastable structure [5, 6]. Li et al. [7] pointed out that the loess tunnel has large settlements at the arch and ground surface. It is recommended to adopt the seven-step method. Xue et al. [8] established the Delphi extended model to evaluate the deformation of the surrounding rock of the loess with a super-large section. The support structure with large rigidity can allow a small

amount of deformation, and it is difficult to release the energy stored in the surrounding rock entirely, so the support problem is challenging to solve. In recent years, based on the concepts of energy absorption and energy dissipation in surrounding rocks, the “yield pressure support” or “flexible support” scheme has begun to be explored and implemented in scientific research and engineering. In the late 1990s, Kovári [9] pointed out that if the deformation of the surrounding rock is forcibly suppressed, it will cause excessive surrounding rock pressure, causing the internal force of the structure to exceed the bearing capacity. The only feasible support scheme in the construction of squeezing confining pressure tunnels is to allow the support structure to deform with the surrounding rock before failure and develop a “yield control” support concept. Anagnostou and Cantièni [10] pointed out that there are two ways to achieve yield control support: one is to fill the compressible layer behind the rigid support, which is more effective in the shield or TBM excavation support. The other way is to use the combination of a sliding steel frame and shotcrete, which

can be sprayed when the sliding steel frame is deformed to a preset value or sprayed immediately after the steel frame is erected. At the same time, a “lining stress controller” [11] or “high compression concrete” [12] is inserted into the concrete at the sliding joint of the steel frame, so that the steel frame and the concrete can be compressed and deformed simultaneously. This kind of yield-controlled support has been widely used in tunnels such as Alpine Tunnel, Galgenberg Tunnel, Semmering Pilot Tunnel, and Saint Martin-La Porte Connection Channel [13–16]. Wu et al. [17–20] conducted a systematic theoretical study on the application of the yielding support concept in the tunnel support structure. Sun et al. [21] proposed an anchoring technology to control the continuous development of large deformations of the surrounding rock—a new type of large-scale let-down anchor rod. Wang et al. [22] started from the idea of the appropriate release of the deformation energy of surrounding rock and proposed a new design concept of timely strong-yield compression support. Based on this design concept, a pressure-relief support system is proposed.

At present, the pressure-relief and yield-controlled support technology are in the stage of theoretical research and summary of construction experience. There is no unified theoretical system and support plan. It is based on the “support resistant limiting dampers” (SRLDs) developed by Qiu et al. [23]. This paper focuses on its engineering application in the deformation control of deep-buried large-section loess tunnels, which provides a reference for the construction of similar tunnels in the future.

2. Working Principle of Support Resistant Limiting Dampers (SRLDs)

2.1. Energy Release Mechanism of Surrounding Rock. In the construction of high-energy geological environment tunnels, the surrounding rock often releases much energy after being disturbed. The primary support of the tunnel is the combination of bolts, steel frames, and shotcrete, and the deformation of these supports during the normal working phase is minimal. The small deformation of the primary support is difficult to fully release the large amount of energy stored in the surrounding rock, which brings a high surrounding rock pressure and causes the internal force of the primary support to exceed its ultimate bearing capacity.

When the primary support of the tunnel is cracked, the existing countermeasures mostly adopt the principle of “never weaker than strong” to strengthen support parameters. However, practice shows that merely increasing the support parameters cannot effectively solve the problem of primary support cracking [24, 25]. The behaviour of the primary support with severe deformation and damage caused by repeated dismantling and replacement during construction is essentially the process of gradual deformation under certain constraints to release the deformation pressure of the surrounding rock. The cavern cannot stabilize until the pressure of the surrounding rock is released (see Figure 1). Therefore, in the high-energy geological environment, the tunnel construction should not adopt the measures of “strong support and hard resistance” but should

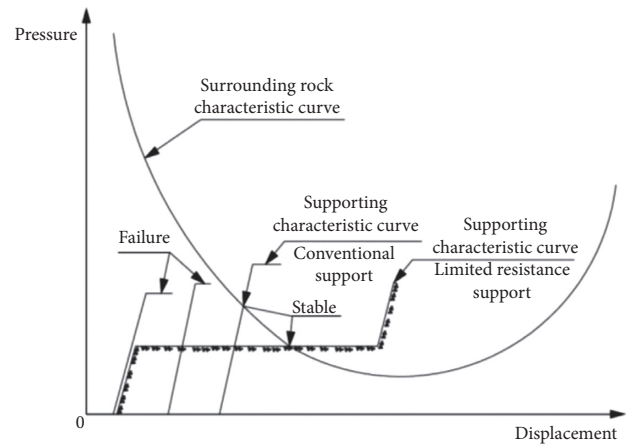


FIGURE 1: Characteristic curve of convergence-confinement.

adopt a structure that can produce a large amount of deformation and fully release the energy stored in the surrounding rock and carry out the support method of “combination of resistance and release.” The use of a resistance-limiting energy-consuming support structure can limit the support resistance in the early stage and allow large deformations of the surrounding rock and support structure. In the later stage, the support resistance increases, and its support characteristic curve can finally intersect with the surrounding rock characteristic curve to achieve stability (see Figure 1).

2.2. SRLD Structure. The SRLD is composed of upper and lower connection steel plates and vertical resistance-limiting steel plates. The upper and lower connection steel plates are placed in parallel, and the vertical resistance-limiting steel plates are vertically welded on the upper and lower connection steel plates [23], as shown in Figure 2.

2.3. Working Process of SRLD. The working process of the SRLD is shown in Figure 3. A vertical pressure P is applied to the connecting plate. When the pressure P reaches the peak load of the vertical steel plate, the vertical steel plate begins to yield and deform until the resistance limiter is compacted.

2.4. Loading-Deformation Characteristics of SRLD. The SRLD samples were made, and the performance verification test was carried out on the universal press (see Figure 4). The typical pressure-deformation curves of the resistance limiter are shown in Figure 5.

According to the verified test results, the working period of the SRLD is mainly divided into four stages. The first stage is the elastic deformation stage, and the pressure increases linearly with the deformation. The second stage is the yield decrease stage, and the pressure decreases with the deformation. The third stage is the yield constant resistance deformation stage, and the pressure is constant with the deformation. The fourth stage is the compaction deformation stage, and the pressure increases sharply with the deformation. The third stage is the main working stage of the

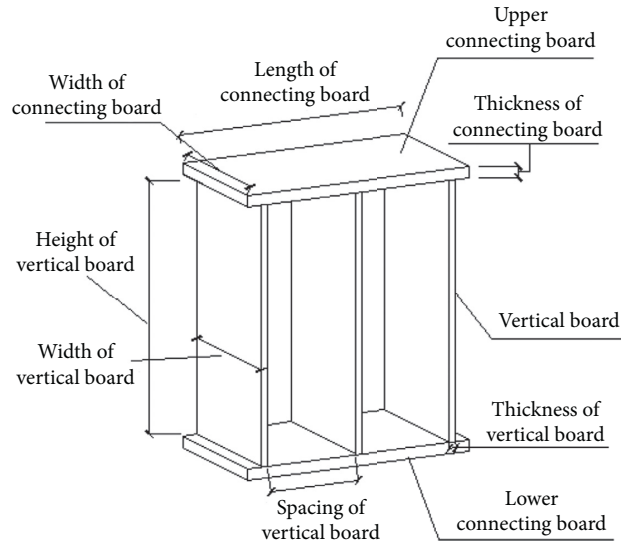


FIGURE 2: SRLD structure.

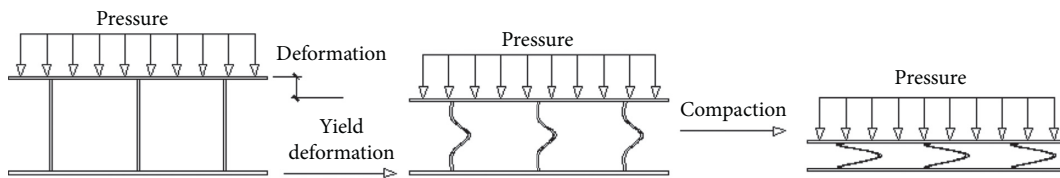


FIGURE 3: SRLD working process.



FIGURE 4: Mechanical performance test of SRLD [23].

deformation of the SRLD. The limiter undergoes large-stroke deformation under the constant pressure. The pressure-deformation curve of the limiter is simplified as shown in Figure 6.

It can be seen from Figure 6 that the SRLD has high initial rigidity and a massive working stroke. At the same time, it can provide stable support resistance and can meet the requirement of guiding the surrounding rock to release energy through deformation while controlling the deformation rate of the surrounding rock. Through the on-site monitoring and measurement of the vault subsidence and clearance convergence data, the deformation rate and acceleration can be analyzed and calculated to

determine whether the current support parameters are reasonable.

3. Engineering Application of SRLD

3.1. Engineering Overview. This paper takes the Yangshan Tunnel of the Haolebaoji-Ji'an Railway as the engineering background. The lithology of the cave in the deep-buried old loess section of this railway is the Quaternary Middle Pleistocene alluvial (Q_2^{pl}) clay old loess. The colour of the soil is brown-yellow, brown-red, brown-red, and yellow-brown. The soil is hard plastic to stern, with a small number of calcareous nodules and a large compacted structure. No groundwater was found during excavation. The plastic limit of the soil was 20%, and the liquid limit was 33.4%, showing soft swelling. The surrounding rock is classified as IV soil, with a burial depth of 120–140 m (see Figure 7), and the soil moisture content of the excavated face is about 15%. Water seeps out after the primary branch is destroyed, and the tested soil has a water content of 20% to 23%. The typical geological section of the tunnel is shown in Figure 8.

The Yangshan Tunnel is a single-hole double-line tunnel with an excavation area of 101.43 m². It is constructed by the three-step method. The deep-buried old loess section (DK390 + 528 ~ DK390 + 708) at the exit of the tunnel suffered damage to the primary support and caused the primary support infringement. The damage is manifested as concrete cracking and spalling at the left and right arch waist to the arch foot of the upper step, the steel

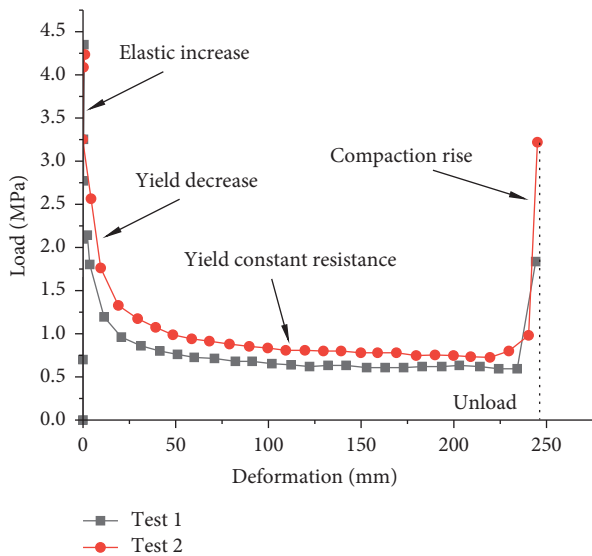


FIGURE 5: Typical loading-deformation curves of SRLD [23].

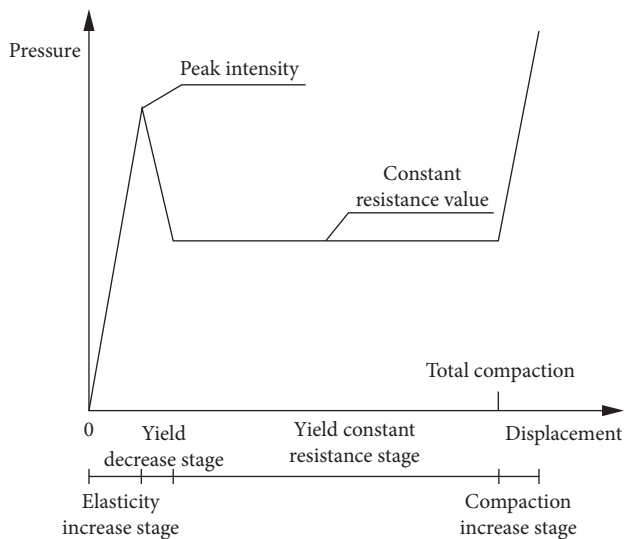


FIGURE 6: Simplified loading-deformation curve of SRLD.

frame is buckled and staggered, and the falling block runs through in the longitudinal direction. The primary support invasion limit after failure is 30–40 cm, as shown in Figure 8.

3.2. Support Scheme of Yangshan Tunnel. In the initial construction, the designed primary support scheme (scheme I) was adopted. After the primary support of the tunnel was destroyed, the support scheme was changed to reinforced support (scheme II). The initial support failure phenomenon was significantly reduced after using reinforced support. However, concrete spalling occurred in the DK390 + 462~DK390 + 467 section, indicating that the reinforced support failed to control the cracking phenomenon of the initial support fully. Therefore, an optimization scheme (scheme III) based on SRLD was designed. The

specific schemes are shown in Table 1. Construction of the SRLD test is carried out in the DK390 + 152 ~ DK390 + 168 of the Yangshan Tunnel (see Figures 9 and 10).

3.3. Deformation Analysis of Test Sections

3.3.1. Monitoring Scheme. According to [26], six measurement sections were laid out: DK390 + 175, DK390 + 170, DK390 + 165, DK390 + 160, DK390 + 155, and DK390 + 150. The measuring points were arranged as the vault settlement point, a horizontal line was set up and down 50 cm above and below the SRLD, and a horizontal line was set up 1.5 m above the bottom of the excavation, that is, one vault sinking measurement point and three horizontal convergence measurement lines (see Figure 11). Two measurement sections were set up on DK390 + 163 and DK390 + 159 to test the surrounding rock pressure. The layout of the measurement points is shown in Figure 12.

3.3.2. Analysis of Monitoring Results

(1) *Analysis of Displacement Monitoring Results.* The monitoring results are shown in Table 2 and Figure 13. For scheme II, the vault subsidence of the monitoring sections is between 20.7 and 40.9 mm, the horizontal convergence of line 1 is between 34.2 and 106.8 mm, the horizontal convergence of line 2 is between 27.0 and 65.0 mm, and the horizontal convergence of line 3 is between 30.5 and 66.9 mm. For scheme III, the vault subsidence of the sections is between 47.7 and 57.6 mm, the horizontal convergence of line 1 is between 62.5 and 136.1 mm, the horizontal convergence of line 2 is between 34.2 and 95.1 mm, and the horizontal convergence of line 3 is between 30.5 and 71.4 mm (see Table 2). The deformation rate in the first 2~3 days after the excavation is relatively large, reaching 30~40 mm/d. The deformation tends to converge about one week after excavation. After converging for a period of time, the deformation has a weak tendency to increase (see Figure 13).

(2) *Analysis of Surrounding Rock Pressure Monitoring Results.* The surrounding rock pressure of the monitored section is shown in Figure 14, and the pressure distribution of the surrounding rock of each section is shown in Figure 15. The surrounding rock pressure tested on each section tends to converge in about one week (see Figure 14). The surrounding rock pressure at the arch waist is significantly higher than other locations, and the two test sections DK390 + 163 and DK390 + 159 have the highest surrounding rock pressure at the right arch waist (0.44 MPa and 0.51 MPa), which is consistent with the actual structure cracks.

(3) *Analysis of Concrete Stress Monitoring Results.* It can be seen from the figure that the measured concrete stress of each section exceeds the convergence in about one week. The concrete of the monitored section is basically in a compressed state, and the maximum compressive stress is at the inner left arch waist of the DK390 + 163 section

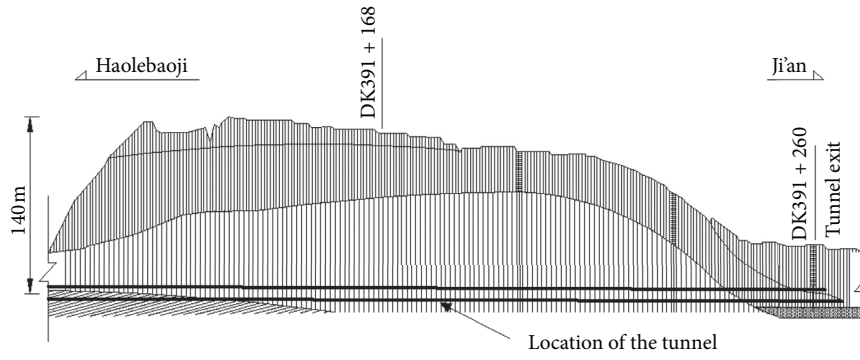


FIGURE 7: Typical geological section of the tunnel.

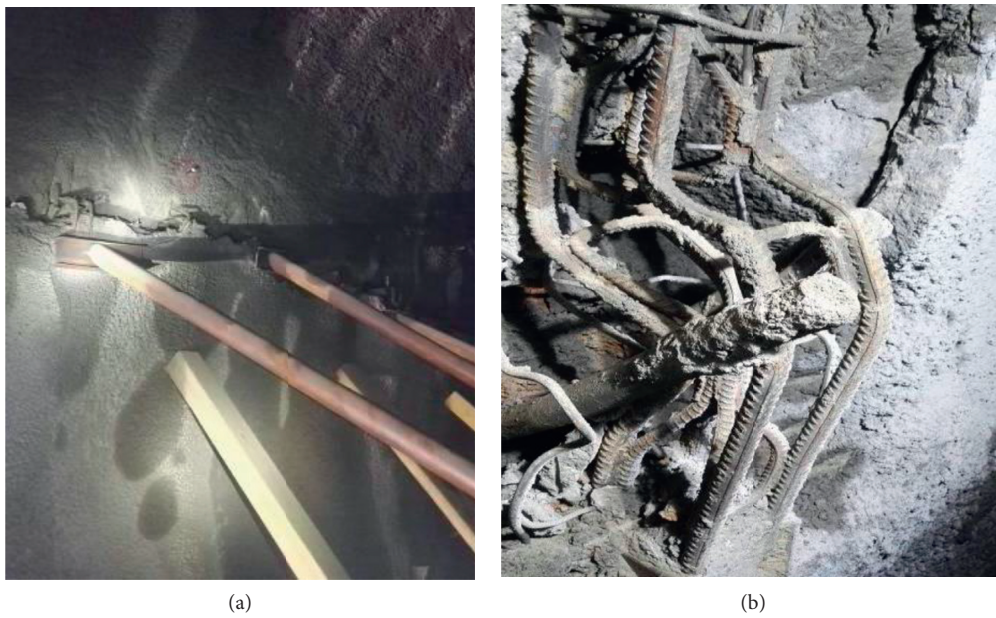


FIGURE 8: Damage of primary lining in the deep-buried loess tunnel. (a) Concrete cracking. (b) Steel frame twisted.

TABLE 1: Statistical table of displacement monitoring results.

Scheme	Steel frame	Steel frame spacing (m)	Main rib diameter (mm)	C25 shotcrete thickness (cm)	SRLD
I	H150	1.0	22	22	—
II	H230	0.6	28	30	—
III	H150	1.0	22	22	Set the SRLD on the left and right arch feet of the upper step (vertical steel plate thickness: 7.5 mm; height: 28 cm; spacing: 10–15 cm)



FIGURE 9: The assembled SRLD.



FIGURE 10: SRLD after construction. (a) Upper step. (b) Middle step.

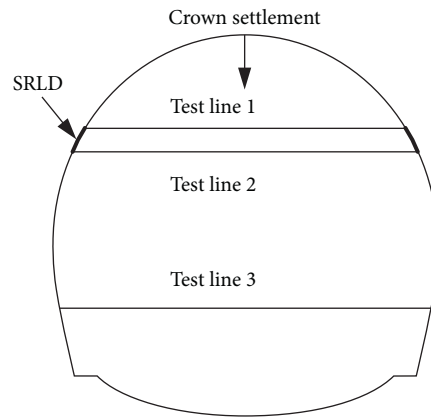


FIGURE 11: Diagram of crown settlement point and the horizontal convergence line.

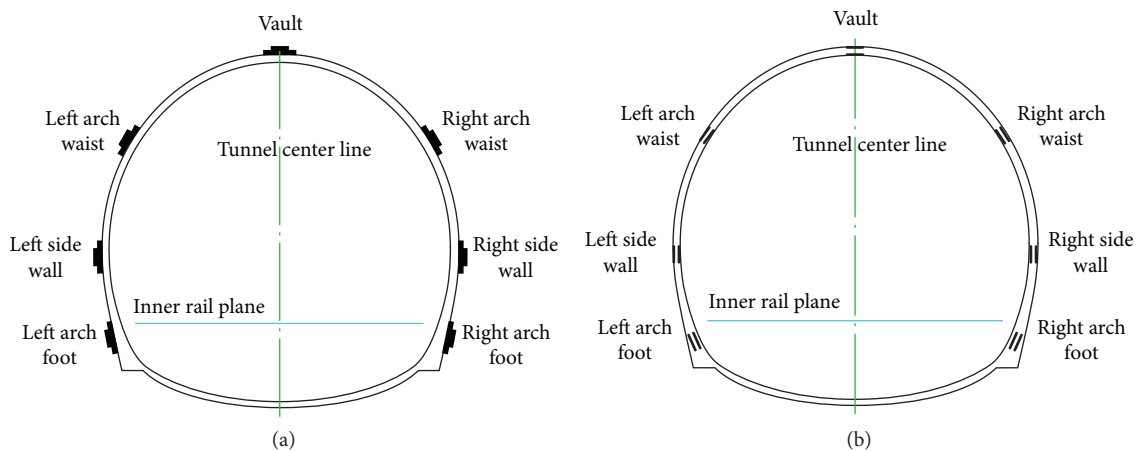


FIGURE 12: Layout of the monitoring points for internal force. (a) Surrounding rock pressure. (b) Internal stress of shotcrete.

with the value of 42.05 MPa (see Figure 16(a)), which is consistent with the actual deformation.

About 7 to 10 days after the component is embedded, the time-history curves of the various parameters of the internal force of the structure begin to converge. Around 15 days, the surrounding rock pressure and stress deformation decreased and tended to converge gradually,

indicating that the structural parameters of the test section can meet the actual needs of the project.

4. Applicability Analysis of SRLD

The construction progress, economy, and safety of different scheme conditions are compared, and the results are shown

TABLE 2: Statistical table of displacement monitoring results.

Mileage	Scheme	Vault subsidence	Cumulative deformation (mm)		
			Test line 1	Test line 2	Test line 3
DK390 + 175	II	20.7	66.5	54.8	50.7
DK390 + 170	II	40.9	106.8	65.0	66.9
DK390 + 165	III	47.7	77.4	87.0	67.0
DK390 + 160	III	55	136.1	95.1	71.4
DK390 + 155	III	57.6	62.5	34.2	30.5
DK390 + 150	II	21.6	34.2	42.0	50.1

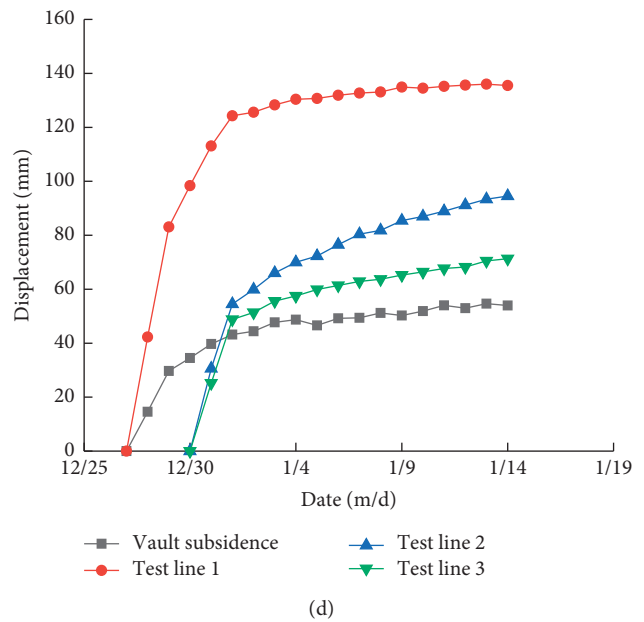
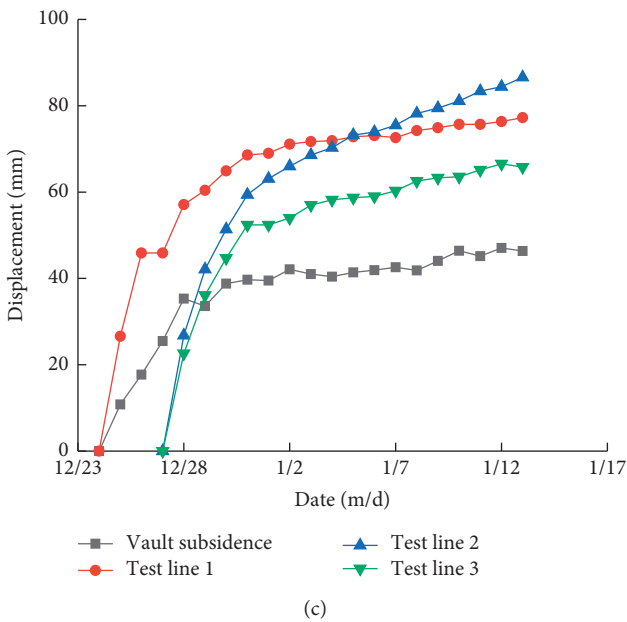
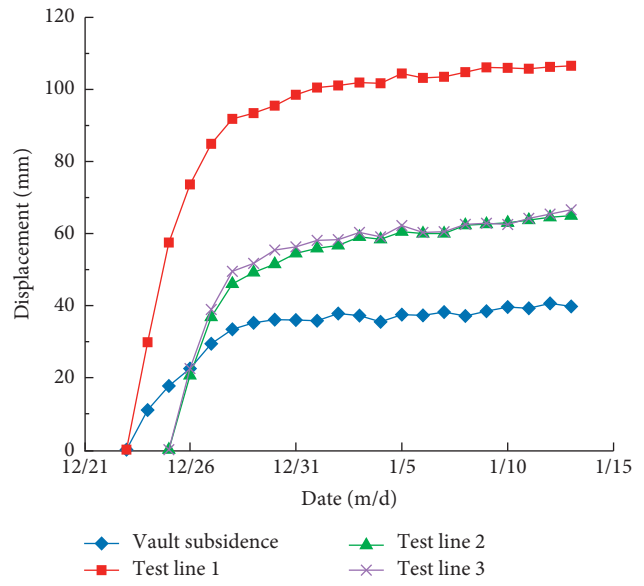
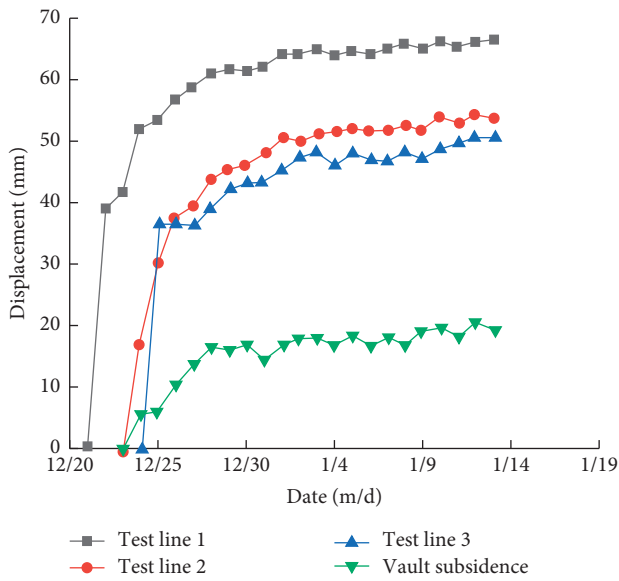


FIGURE 13: Continued.

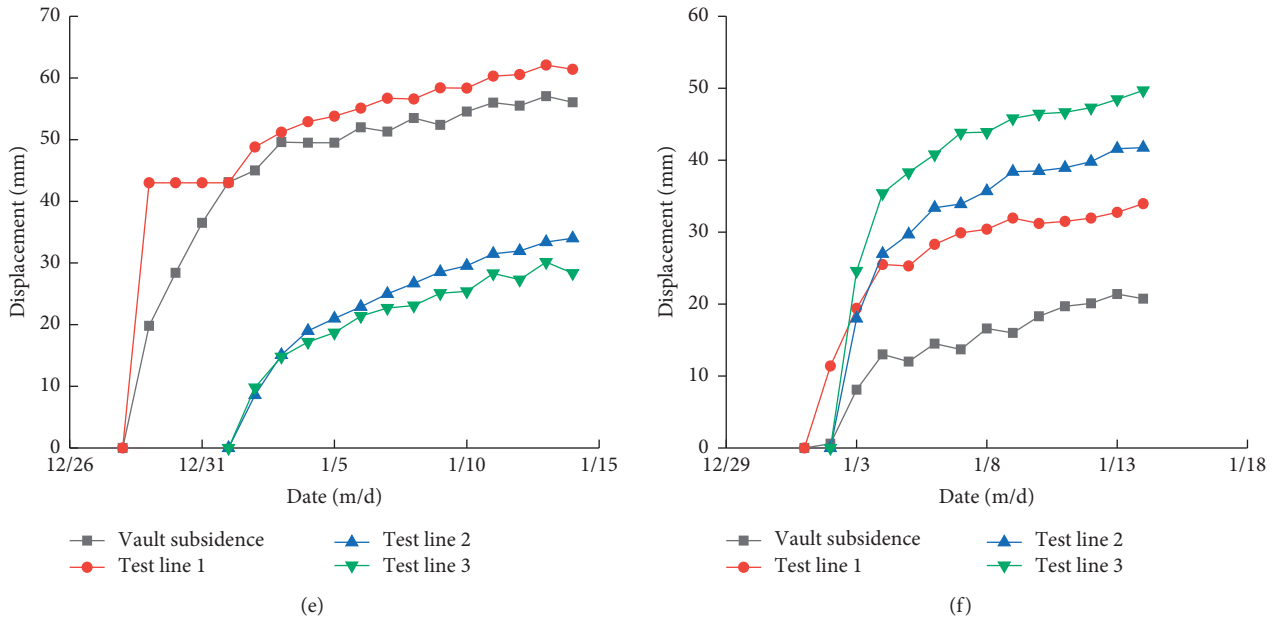


FIGURE 13: Time-history curves of vault subsidence and horizontal convergence. (a) DK390 + 175. (b) DK390 + 170. (c) DK390 + 165. (d) DK390 + 160. (e) DK390 + 155. (f) DK390 + 150.

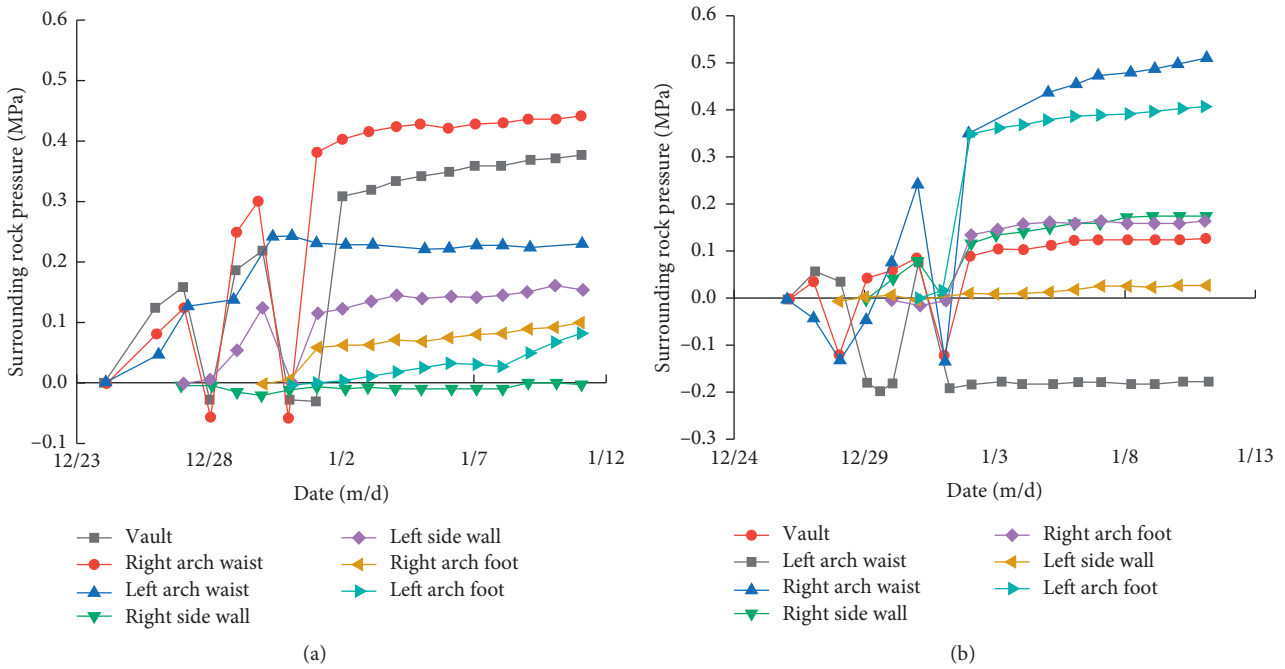


FIGURE 14: Time-history curves of surrounding rock pressure. (a) DK390 + 163. (b) DK390 + 159.

in Tables 3–5. Under the condition that the technical proficiency is unskilled, the progress of scheme III is better than scheme II but slightly slower than scheme I (Table 3). Compared with scheme I, the amount of excavation, shotcrete, and steel mesh in scheme III increased by 0.8%~1.6%, and the amount of steel frame increased by 16.8%. Compared with scheme II, the amount of excavation in scheme III is reduced by 2.5%,

the amount of shotcrete and steel mesh is reduced by 27%, and the amount of steel frame is reduced by 47% (Table 4). Compared with scheme I and II (Figures 8 and 17), there will be no damages such as initial support cracking and spalling, long cracks, steel frame deformation, and misalignment using scheme III (Figure 18).

From the aspects of the economy, construction progress, and safety, the SRLD scheme is better than the other two

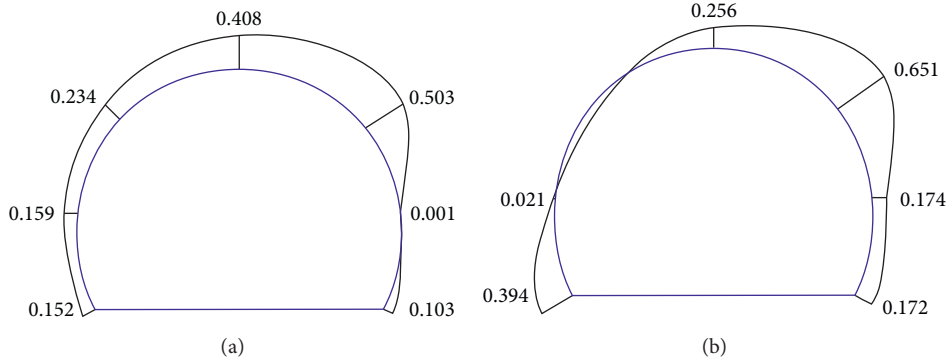


FIGURE 15: Circumferential distribution of surrounding rock pressure. (a) DK390 + 163. (b) DK390 + 159.

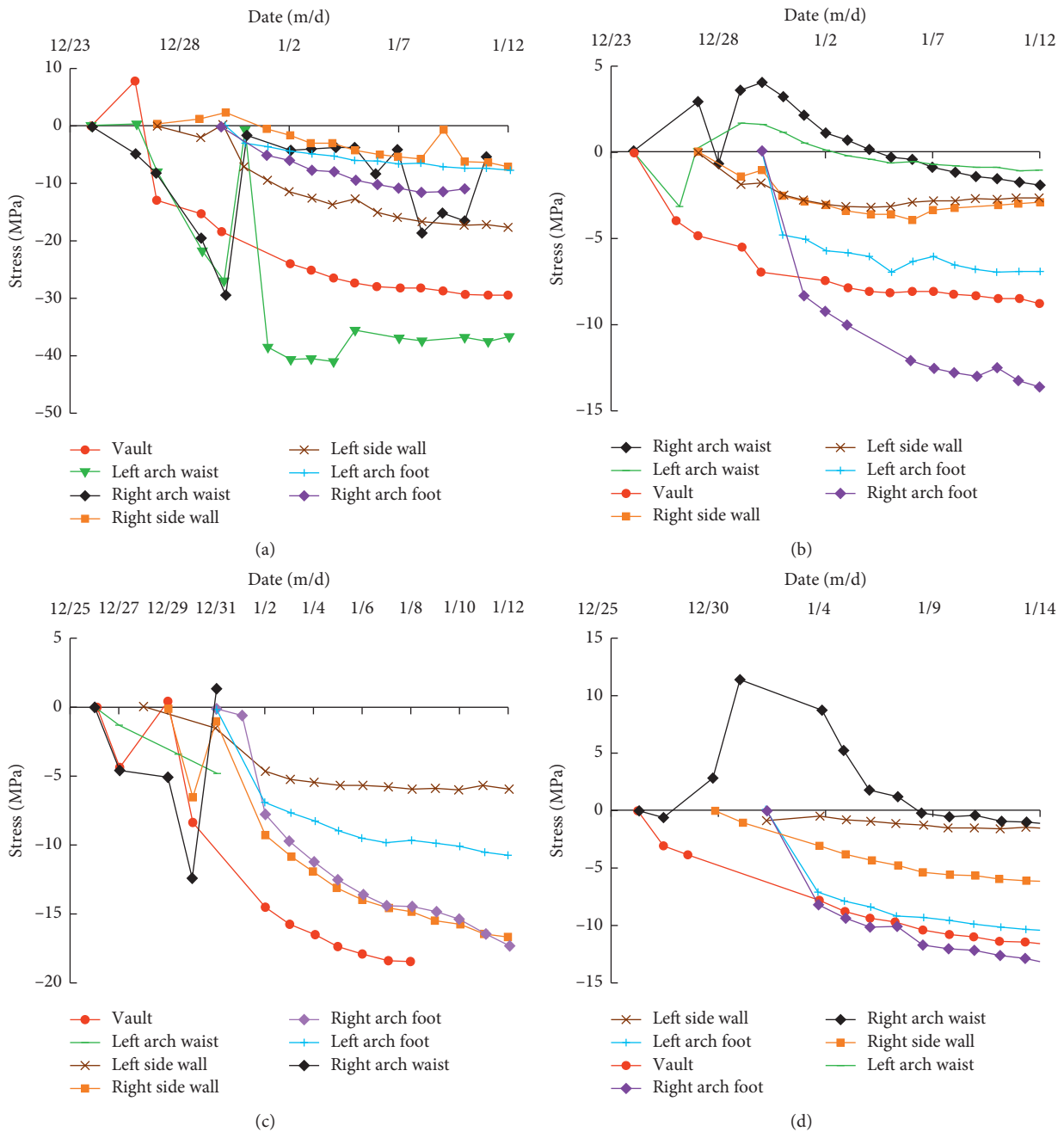


FIGURE 16: Time-history curves of concrete stress. (a) DK390 + 163 inside. (b) DK390 + 163 outside. (c) DK390 + 159 inside. (d) DK390 + 159 outside.

TABLE 3: Construction progress comparison table.

Scheme	Construction time (days)	Mileage	Tunneling length (m)	Progress rate (m/d)	Process proficiency
I	149	DK390 + 960~ +520	440	4.0	Very skilled
II	140	DK390 + 520~ +168	352	2.4	Skilled
III	5	DK390 + 168~ +152	16	3.2	Unskilled

TABLE 4: Engineering quantity comparison table.

Project unit		Quantity comparison			Scheme III/scheme I (%)	Scheme III/scheme II (%)
		Scheme I	Scheme II	Scheme III		
Soil and rock excavation	m ³	101.44	105.69	103.04	101.6	97.5
C25 shotcrete	m ³	8.43	11.62	8.50	100.8	73.1
Steel mesh	kg	105.95	146.87	106.78	100.8	72.7
Steel used for steel frame	kg	1036.80	2297.54	1211.42	116.8	52.7
Steel frame spacing	m	1.00	0.60	1.00	—	—

TABLE 5: Safety comparison table.

Scheme	Mileage	Cracked or not	Cause of cracking	Structural safety
I	DK390 + 786~DK390 + 520	Along the longitudinal direction of the tunnel, a continuous crack and dislocation of about 180 m occurred on the left and right arch waist	On the action of surrounding rock pressure, the primary support at the arch waist bears great hoop stress, and the structure is compressed, and shear failure occurs	Both the left and right arches were damaged, and the structure is unsafe
II	DK390 + 520~DK390 + 168	The left and right arches are easy to produce diagonal cracks and longitudinal cracks of about 1 m in length	Changing the scheme increases the rigidity of the structure, but the internal force of the structure increases. Once the internal force of the structure is greater than the ultimate strength of the material, the structure will crack	Cracking, peeling, and falling pieces occur at the arch waist, and the structural safety is insufficient
III	DK390 + 168~DK390 + 152	Longitudinal cracks above the SRLD	The weak surface formed by the shotcrete above the SRLD is easy to crack and peel off	The vertical steel plate of the SRLD deforms and only accounts for about 10%, and the amount of deformation is less than 10% of the design estimate, and the structure is safe



(a)



(b)

FIGURE 17: Primary support cracking and spalling (scheme II).



FIGURE 18: Primary support cracking (scheme III).

schemes, and the SRLD scheme is worthy of promotion and application.

5. Conclusions

- (1) The traditional rigid support allows small deformation and releases less energy from the surrounding rock. It is challenging to solve the problem of support failure during the construction of deep-buried large-section loess tunnels. When dealing with geological problems such as large deformation of loess tunnels, the design concept should be changed from a large rigidity and strong support method to a limited resistance and release energy support method that allows the deformation of the surrounding rock and controls its energy release.
- (2) Embedding the SRLD into the primary support can transform the traditional rigid support into a limited resistance and energy release support. By setting the SRLD in the essential force-bearing parts, the final deformation of the surrounding rock is significantly increased and the problem of primary support cracking can be effectively solved. It shows that the SRLD can limit the internal force of the structure and release the surrounding rock pressure in a controllable manner. It is a feasible and effective way of supporting deep-buried large-section loess tunnels.
- (3) The surrounding rock deformation of the experimental section tends to converge about one week after excavation, indicating that the support-surrounding rock system of the SRLD scheme can quickly reach a stable state. The maximum value of surrounding rock pressure and internal structural force occurred at the arch waist. From the comprehensive comparison and analysis of the economy, construction process, and safety, it can be seen that the construction plan of the SRLD support is worthy of popularizing and using.

Data Availability

The data included in this study are available from the corresponding author upon request.

Conflicts of Interest

The authors declare that they have no conflicts of interest.

Acknowledgments

The author would like to thank the National Key R&D Program of China (2018YFC0808701), China Postdoctoral Science Foundation (2020M673525), and China Railway 20th Bureau Group Co. Ltd. (YF2000SD01A).

References

- [1] M. Bayati and J. Khademi Hamidi, "A case study on TBM tunnelling in fault zones and lessons learned from ground improvement," *Tunnelling and Underground Space Technology*, vol. 63, pp. 162–170, 2017.
- [2] S. Wang, C. Li, Z. Liu, and J. Fang, "Optimization of construction scheme and supporting technology for HJS soft rock tunnel," *International Journal of Mining Science and Technology*, vol. 24, no. 6, pp. 847–852, 2014.
- [3] W. Yu, W. Wang, X. Chen, and S. Du, "Field investigations of high stress soft surrounding rocks and deformation control," *Journal of Rock Mechanics and Geotechnical Engineering*, vol. 7, no. 4, pp. 421–433, 2015.
- [4] M. Sharifzadeh, F. Kolivand, M. Ghorbani, and S. Yasrobi, "Design of sequential excavation method for large span urban tunnels in soft ground—Niayesh tunnel," *Tunnelling and Underground Space Technology*, vol. 35, pp. 178–188, 2013.
- [5] I. Jefferson, N. Mavlyanova, K. O'Hara-Dhand, and I. Smalley, "The engineering geology of loess ground: 15 tasks for investigators—the Mavlyanov programme of loess research," *Engineering Geology*, vol. 74, no. 1–2, pp. 33–37, 2004.
- [6] J. Qiu, X. Wang, J. Lai, Q. Zhang, and J. Wang, "Response characteristics and preventions for seismic subsidence of loess in Northwest China," *Natural Hazards*, vol. 92, no. 3, pp. 1909–1935, 2018.
- [7] P. Li, Y. Zhao, and X. Zhou, "Displacement characteristics of high-speed railway tunnel construction in loess ground by using multi-step excavation method," *Tunnelling and Underground Space Technology*, vol. 51, pp. 41–55, 2016.
- [8] Y. Xue, X. Zhang, S. Li et al., "Analysis of factors influencing tunnel deformation in loess deposits by data mining: a deformation prediction model," *Engineering Geology*, vol. 232, pp. 94–103, 2018.
- [9] K. Kovári, "Tunnelling in squeezing rock," *Rock Mechanics and Rock Engineering*, vol. 29, no. 3, p. 111, 1996.
- [10] G. Anagnostou and L. Cantieni, "Design and analysis of yielding support in squeezing ground," in *Proceedings of the 11th International Society for Rock Mechanics and Rock Engineering (ISRM) Congress*, Lisbon, Portugal, July 2007.
- [11] W. Schubert, "Dealing with squeezing conditions in Alpine tunnels," *Rock Mechanics and Rock Engineering*, vol. 29, no. 3, pp. 145–153, 1996.
- [12] K. Kovári, "Design methods with yielding support in squeezing and swelling rocks," in *Proceedings of the World Tunnel Congress Ed.*, pp. 1–10, Budapest, Hungary, May 2009.
- [13] A. Thut, D. Naterop, P. Steiner, and M. Stolz, "Tunnelling in squeezing rock—yielding elements and face control," in *Proceedings of the 8th International Symposium on Tunnel Construction and Underground Structures Ed.*, Ljubljana, Slovenia, November 2006.
- [14] L. Cantieni and G. Anagnostou, "The interaction between yielding supports and squeezing ground," *Tunnelling and*

- Underground Space Technology*, vol. 24, no. 3, pp. 309–322, 2009.
- [15] G. Barla, M. Bonini, and M. Semeraro, “Performance monitoring and analysis of a yieldcontrol support system in squeezing rock,” in *Rock Mechanics in Civil and Environmental Engineering*, J. Zhao, V. Labiouse, J. P. Dudd, and J. F. Mathier, Eds., pp. 459–462, Taylor & Francis Group, London, UK, 2010.
- [16] G. Barla, M. Bonini, and M. Semeraro, “Analysis of the behaviour of a yield-control support system in squeezing rock,” *Tunnelling and Underground Space Technology*, vol. 26, no. 1, pp. 146–154, 2011.
- [17] K. Wu and Z. Shao, “Study on the effect of flexible layer on support structures of tunnel excavated in viscoelastic rocks,” *Journal of Engineering Mechanics*, vol. 145, no. 10, Article ID 04019077, 2019.
- [18] K. Wu and Z. Shao, “Visco-elastic analysis on the effect of flexible layer on mechanical behavior of tunnels,” *International Journal of Applied Mechanics*, vol. 11, no. 3, Article ID 1950027, 2019.
- [19] K. Wu, Z. Shao, and S. Qin, “An analytical design method for ductile support structures in squeezing tunnels,” *Archives of Civil and Mechanical Engineering*, vol. 20, no. 3, pp. 1–13, 2020.
- [20] K. Wu, Z. Shao, S. Qin, N. Zhao, and H. Hu, “Analytical-based assessment of effect of highly deformable elements on tunnel lining within viscoelastic rocks,” *International Journal of Applied Mechanics*, vol. 12, no. 3, Article ID 2050030, 2020.
- [21] J. Sun, X. Pan, and Y. Wang, “Study on non linear rheologic mechanical property of squeezing deformation of soft surrounding rock in tunneling and its anchorage mechanism,” *Tunnel Construction*, vol. 35, no. 10, p. 969, 2015.
- [22] B. Wang, J. Wang, and D. Wu, “Study of application of yielding supporting system for large deformation in soft rock highway tunnel,” *Journal of Railway Science and Engineering*, vol. 13, no. 10, p. 1985, 2016.
- [23] W. Qiu, G. Wang, and L. Gong, “Research and application of resistance-limiting and energy-dissipating support in large deformation tunnel,” *Chinese Journal of Rock Mechanics and Engineering*, vol. 37, no. 8, pp. 1786–1795, 2018.
- [24] M. Huang, J. Zhao, and Z. Tao, “Analysis of the deformation and mechanical characteristics of the surrounding rock-lining structure of the Muzhailing tunnel,” *Modern Tunnelling Technology*, vol. 53, no. 6, p. 89, 2016.
- [25] C. B. He and L. H. Shu, “Deformation mechanization and construction control of high ground stresses soft rock tunnel in Lanzhou-Chongqing railway,” *Journal of Railway Engineering Society*, vol. 31, no. 5, pp. 68–73, 2014.
- [26] Q/CR 9218-2015, *Technical Specification for Monitoring Measurement of Railway Tunnel*, China Railway Publishing House, Beijing, China, 2015.

Research Article

The Influence of Physical and Chemical Reactions on Water Leakage in a Multiarch Tunnel

Jian-Xun Shi ^{1,2} Zhao-Hui Li,^{1,2} Yong-Qiang He,^{1,2} Guo-Ming Zhang,^{1,2}
and Ming-Qiang Wei^{1,2}

¹School of Civil Engineering, Northwest Minzu University, Lanzhou 730030, China

²State Key Laboratory Base of New Building Materials and Energy-Efficient Building in Gansu Province, Lanzhou 730030, China

Correspondence should be addressed to Jian-Xun Shi; sjxnxu@163.com

Received 23 July 2020; Revised 30 August 2020; Accepted 11 September 2020; Published 23 September 2020

Academic Editor: Zhushan Shao

Copyright © 2020 Jian-Xun Shi et al. This is an open access article distributed under the Creative Commons Attribution License, which permits unrestricted use, distribution, and reproduction in any medium, provided the original work is properly cited.

In many tunnels in China, the groundwater is acidic and carbonated, causing in challenges in the prevention and control of leakages of the existing tunnels and tunnels under construction. Research on tunnel leakage and the physical and chemical effects of water due to water-rock interactions is a trending topic. In addition, there is a big difference between the waterproof and drainage of multiarch tunnels and separate tunnels. In this study, the mechanism of the interaction between the groundwater and the surrounding rock of a multiarch tunnel were analyzed. The relationship between the leakage of a multiarch tunnel and the interaction between the surrounding rocks and groundwater was determined by analyzing the interaction between the chemical components in the groundwater, rocks, and the concrete lining. A mathematical model was established based on the physical and chemical reactions in the rock surrounding the tunnel, and the RNCDX.FOR program was compiled using the simplex Monte Carlo method. The total free energy in the entire system varied significantly, and the value of objective function (J) reflected the trend of the system's spontaneous reaction. As J decreased, the reaction power of the system increased. The more significant the erosion of the rocks was by the groundwater, the more channels were created by the groundwater in the rock, and the more likely the water leakage was.

1. Introduction

Water-rock interaction research is one of the leading topics in mechanics and earth sciences. The interaction is referred to as “solid-fluid coupling” in mechanics and “water-rock interaction” in earth sciences. The focus of the former research is on the fundamental laws of mechanical coupling between solids and fluids; the latter is concentrated on the laws of the physicochemical reactions and the physical and chemical characteristics of the rocks and water under high-temperature high-pressure conditions. As an interdisciplinary discipline that integrates civil engineering and geology, geotechnical engineering has focused on rock body hydraulics, i.e., a study of the laws from the perspective of the interaction of the seepage field and stress field. Hellevang et al. [1] provided a guide to model kinetically constrained

CO₂-water-rock interactions. Kaszuba et al. [2] demonstrated that the interaction between CO₂, water, and rock could lead to the massive dissolution and precipitation of minerals, and numerous techniques existed for obtaining experimental data. Zhao et al. [3] used the discrete element method to analyze the effect of water-rock mechanical interaction and the combination of physical and chemical effects on the deformation of a reservoir bank slope. Recently, the chemical interaction between water and rocks has been increasingly investigated [4–8], especially in the construction of tunnels in China, where the groundwater is acidic and carbonated. These conditions have caused significant challenges in the prevention and control of leakages of existing tunnels and tunnels under construction, as shown in Figure 1. Wang et al. [9] analyzed the mineral origin of carbonate cement, the mechanism of precipitation, the



FIGURE 1: Chemical deposition of seepage water.

evolution and distribution of pore fluids, and the interaction between water and rock and its impact on reservoir quality. At present, there are few random physical and chemical simulation studies on water leakage caused by water-rock interaction in tunnels.

In terms of physical chemistry, the main elements that exhibit chemical reactions in geotechnical engineering include the groundwater and its chemical components, rock formations, organic matter, and materials used in engineering, such as concrete. These elements will interact under certain temperature, pressure, and concentration conditions, produce energy exchange, and generate energy output using input from the environment [10–14]. In addition, the external environment promotes or prevents interactions. Zheng and Liu [5] first used physical and chemical simulations to analyze an aquifer in the surrounding rock of a tunnel, and the model was an optimized linear model. Wang et al. [15] analyzed the mechanism of water-rock interaction inside the aquifer. Many Chinese scholars have investigated the water-rock interaction [16–19]. However, these studies had two limitations. First, most studies used linear programming models, and nonlinearity has not been analyzed in detail. Second, insufficient sample data were used. Most studies did not use sample data from multiple trials, but only from a single trial. The sample data were averaged, and the average value was used for analysis and calculation. Therefore, the mutual influence of the system inside and outside the surrounding rock of the multiarch tunnel and the random changes were ignored, which produced simulation results that did not represent actual conditions.

In this study, the internal energy of the surrounding rock of the tunnel is simulated to determine the degree of erosion and the connectivity of the surrounding rock.

There is a big difference between the waterproof and drainage of multiarch tunnels and separate tunnels. Mao et al. [20, 21] used 3D numerical simulation to analyze the water leakage susceptible area of the loess multiarch tunnel. The results show that the water disaster susceptible areas for loess multiarch tunnels during the construction period mainly concentrated in the midpartition, arch springs of the

left and right tunnels, and the tunnel face. In this study, the prevention and control of water leakage in a multiarch tunnel is mainly discussed from the perspective of the interaction mechanism between groundwater and surrounding rock.

A mathematical programming model of the physical-chemical conditions of the rock is established. In other words, the chemical reaction inside the surrounding rock of the multiarch tunnel is used as the objective function, and the equilibrium principle, mass conservation law, charge conservation law, and other conditions are used as constraints of the model. After obtaining a model solution, the water-rock interaction inside the surrounding rock of the multiarch tunnel is analyzed to determine the degree of erosion of the surrounding rock caused by the groundwater.

The use of random numbers in the Monte Carlo analysis ensures that the data provide a realistic simulation of actual conditions to reflect the mechanism of water-rock interaction in the surrounding rock of multiarch tunnels. The analysis of the internal chemical reaction of the surrounding rock can provide a theoretical basis for the waterproofing, drainage design, and construction of multiarch tunnels and the prevention and treatment of water leakage.

2. Mathematical Model of Water-Rock Interaction

2.1. Mathematical Model. The water-rock interaction can be regarded as an organic connection or a large system of mutual influence [22–25]. In a system with certain pressure, temperature, and concentration conditions, the chemical reaction always proceeds in the direction where the free energy becomes smaller and tends to balance. According to the principle of thermodynamics, the smaller the value of ΔG_{fi} , the stronger the positive reaction trend. Accordingly, take the minimum sum of the free energy changes of each physical and chemical reaction in the groundwater system as the objective function. The constraint conditions are established based on the laws of the conservation of mass, conservation of charge, and neutrality among the chemical components in the groundwater system. The objective

has been rapidly developed since it was developed and has become an indispensable and important part of computational mathematics.

Each b_j in the Monte Carlo system is a random variable. According to the linear programming model, the internal b_j implementation is always true. In this way, we randomly extract a $[b'_1, b'_2, \dots, b'_m]$ corresponding to b_j from the random numbers and use the simplex method to find a set of solutions to $X'_i = [x'_1, x'_2, \dots, x'_n]_I$ using equation (1). By analogy, this step is repeated to produce N sets of solutions until N tends to infinity. When all the physical quantities in the system have been described, the characteristics of the physical quantities in the system and the distribution are obtained.

Equation (6) is the definition of the mean value and equation (7) is the definition of the standard deviation:

$$\mu = \frac{1}{N} \sum_{i=1}^N X_i, \quad (6)$$

$$\sigma = \left[\frac{1}{N-1} \sum_{i=1}^N (X_i - \mu)^2 \right]^{(1/2)}. \quad (7)$$

The Monte Carlo method is implemented and a program is written (RNDDX.FOR) for use in the subsequent case study.

3. Case Study

3.1. Hydrogeological and Topographic Features in the Tunnel Site Area. The exit of the multiarch tunnel is located on the east side of the downslope of low- and midelevation mountains. The slope is covered with gravel and soil layers and consists of strongly~weakly weathered marl and limestone. The gravel soil layer has a maximum thickness of 2.80 m, the thickness of the strongly weathered marl is 1.10~9.20 m, and the exposed thickness of the weakly weathered marl and limestone is 22.94~37.38 m. The natural slope of the hillside is 30~40°, the azimuth angle of the free slope of the hillside is 162°, and the slope oblique to the course is about 75°. The occurrence of bedrock is 5°~30°, and the gravel soil cover at the entrance is thin (0.60~2.80 m). The weathered fissures of the underlying bedrock are well developed, and the rock mass is highly fragmented, showing a fragmented-fissured block structure with poor integrity. The vertical slope velocity of the surrounding rock is $V_p = 380\text{--}1800$ m/s, and the surrounding rock is classified as grade V. The conditions for the formation of caves are poor, and the surrounding rock is prone to collapse.

The gravel soil is above the groundwater level and has strong water permeability. Karst water occurs about 500 m from the cave entrance, and the water volume is large. Due to a large amount of water during the construction, grouting was used as an antiseepage curtain to facilitate construction. However, after one year of operation of the tunnel, significant water leakage occurred,

especially at a distance of 500 m from the entrance of the tunnel. The field data indicated that the pH value at a distance of 1000 m from the cave entrance was low, and the water had high concentrations of dissolved CO₂. The bedrock is quartz sandstone containing 10% shale, and the dominant minerals are mica, quartz, a small amount of pyrophyllite, kaolinite, and montmorillonite. Part of the bedrock is carbon shale, with an organic matter content of 4% to 8% [26, 27]. The rocks are highly broken. Due to the long-term immersion in the groundwater and resulting corrosion, some rocks have softened. The field investigation also found that the groundwater had eroded the antiseepage curtain due to cement hydrates in the groundwater, indicating that the chemical components in the groundwater and rock had interacted with the concrete.

Under certain conditions, the water-rock interaction in the area surrounding the tunnel can cause different materials in the surrounding rock to undergo chemical reactions, as shown in Table 1. The physicochemical reactions in the system are mutually reinforcing, and one reaction will promote another reaction, thus forming a reaction chain of the entire system. Over time, the physicochemical reactions continue, and a groundwater channel is formed and is being continuously connected and unblocked, increasing the water leakage in the tunnel. Depending on the interaction between the components in the surrounding rock, the groundwater components, the organic substances, the components of the concrete grouting curtain, the free energy produced by the reactants and products during the processes determine the reactant's standard free energy change (ΔG_f).

The monitoring data of the groundwater and surrounding rock in the tunnel and the drainage holes created during construction indicate that the groundwater behind the grouting curtain is the dominant source of recharge. Thus, the groundwater is the initial liquid in the tunnel area, and the discharge liquid of the drainage holes is the dissolution liquid. The chemical composition and the differences between the initial liquid and the dissolution liquid are shown in Table 2. Both variables follow a normal distribution. The difference between the two can be expressed by statistical parameters. The mean of the difference equals the mean of the dissolution solution minus the mean value of the initial solution. The variance of the difference is the square root of the sum of squares of the variance of the dissolution solution and the initial solution; it follows a normal distribution. Four drainage holes are selected as examples for the analysis, namely hole 1, hole 2, hole 3, and hole 4 (Table 2).

3.2. The Establishment of the Mathematical Model.

According to the physicochemical reactions and the free energy changes (Table 1) and the random samples of the difference between the initial solution and the dissolution solution of the components in Table 2, the following model is established:

TABLE 1: Physicochemical reactions and free energy change (ΔG_f) of the water-rock system.

Number	Reaction volume	Reactant	Physicochemical reaction	ΔG_f (J·mmol ⁻¹)
1	X_1	Soda feldspar	$\text{NaAlSi}_3\text{O}_8 + \text{CO}_2 + 5.5\text{H}_2\text{O} \rightarrow 0.5\text{NaAlSi}_3(\text{OH})_4 + \text{Na}^+ + 2\text{H}_4\text{SiO}_4 + \text{HCO}_3^-$	79.97
2	X_2	Calcareous spar	$\text{CaCO}_3 + \text{CO}_2 + \text{H}_2\text{O} \rightarrow \text{Ca}^{2+} + \text{HCO}_3^-$	27.66
3	X_3	Ca (OH) ₂	$\text{Ca}(\text{OH})_2(\text{s}) + \text{CO}_2 \rightarrow \text{Ca}^{2+} + 2\text{HCO}_3^-$	-56.77
4	X_4	Organic matter	$\text{CH}_2\text{O} + \text{O}_2 \rightarrow \text{CO}_2 + \text{H}_2\text{O}$	-405.78
5	X_5	CO ₂	$\text{CO}_2 + \text{H}_2\text{O} \rightarrow \text{H}^+ + \text{HCO}_3^-$	38.9
6	X_6	HCO ₃ ⁻	$\text{H}^+ + \text{HCO}_3^- \rightarrow \text{CO}_2 + \text{H}_2\text{O}$	-38.9
7	X_7	Maria glass	$\text{KMg}_3\text{AlSi}_3\text{O}_{10}(\text{OH})_2 + 7\text{H}^+ + 0.5\text{H}_2\text{O} \rightarrow 0.5\text{Al}_2\text{Si}_2\text{O}_5(\text{OH})_4 + \text{K}^+ + 3\text{Mg}^{2+} + 2\text{H}_4\text{SiO}_4$	348.94
8	X_8	Mg (OH) ₂	$\text{Mg}(\text{OH})_2(\text{s}) + \text{CO}_2 \rightarrow \text{Mg}^{2+} + 2\text{HCO}_3^-$	-53.24
9	X_9	Ca ²⁺	$\text{Ca}^{2+} + \text{Na}(\text{s}) \rightarrow \text{Na}^+ + \text{Ca}(\text{s})$	30.74
10	X_{10}	Mg ²⁺	$\text{Mg}^{2+} + 2\text{Na}(\text{s}) \rightarrow \text{Na}^+ + \text{Mg}(\text{s})$	-70.01

TABLE 2: Differences in the ion contents between the initial solution and dissolution solution.

Hole number	Statistics	Cation content/(mmol·L ⁻¹)			Anion content/(mmol·L ⁻¹)			Erosion CO ₂ /(mmol·L ⁻¹)
		Na ⁺ + K ⁺	Ca ²⁺	Mg ²⁺	SO ₄ ²⁻	HCO ₃ ⁻	Cl ⁻	
Hole 1	Mean value	0.061	0.029	0.0818	-0.0005	0.281	0.0135	0.306
	Mean square error	0.1259	0.0935	0.0495	0.0491	0.2317	0.0255	0.145
Hole 2	Mean value	0.071	-0.131	0.0045	-0.0117	-0.127	0.0075	0.68
	Mean square error	0.1425	0.0685	0.0366	0.0521	0.1564	0.0237	0.199
Hole 3	Mean value	0.066	-0.006	-0.0017	-0.0192	0.09	0.0085	0.304
	Mean square error	0.1371	0.0567	0.0354	0.045	0.1472	0.0232	0.115
Hole 4	Mean value	0.14	-0.046	0.0758	0.001	0.222	0.0075	0.623
	Mean square error	0.2163	0.061	0.0426	0.0541	0.1298	0.0238	0.161

$$\begin{aligned}
J = \min(X) = & 79.97X_1 + 23.66X_2 - 56.77X_3 \\
& - 405.78X_4 + 38.9X_5 - 38.9X_6 \\
& + 348.94X_7 - 53.24X_8 + 30.74X_9 - 70.01X_{10}.
\end{aligned} \quad (8)$$

Constraint equations:

$$\begin{cases}
X_2 + X_3 - X_9 = \Delta m\text{Ca}^{2+}, \\
3X_7 - X_8 - X_{10} = \Delta m\text{Mg}^{2+}, \\
X_1 + X_7 - 2X_9 + 2X_{10} = \Delta m\text{Na}^+, \\
X_1 + 2X_2 + 2X_3 + X_5 + X_6 = \Delta m\text{Na}^+, \\
-X_1 - 2X_2 - 2X_3 + X_4 - X_5 + X_6 - X_8 = \Delta m\text{CO}_2,
\end{cases} \quad (9)$$

where $X_1 \sim X_{10}$ is the number of millimoles of reactants participating in the reaction per liter of groundwater and Δm is the difference between the dissolution liquid and the initial liquid content, mmol/L.

The reaction amounts of the different components are obtained by solving equations (8) and (9).

In the processing of random numbers, some random numbers may not conform to the principles of equilibrium, the conservation of mass, the conservation of charge, and the principle of minimum energy, resulting in a mathematical

model with no solution. In the calculation analysis, these random numbers are removed, and the Monte Carlo principle is used to obtain the characteristic value of the reaction amount of each water-rock interaction.

3.3. Mathematical Model Solution. Studies have shown that the number of simulations is crucial in the simulation of Monte Carlo random numbers and affects not only the rationality of the simulation results but also the accuracy of the simulation. Therefore, we tested different numbers of simulations and considered the calculation time and other factors. Ultimately, 1000 simulations were deemed reasonable and met the accuracy requirements. The results of the random simulation of the state of the water-rock interaction system are shown in Table 3.

4. Results and Discussion

The results show that the reaction amounts $X_1 \sim X_2$ in Table 3 are zero, indicating that the reaction of albite and calcite did not occur, i.e., $\text{NaAlSi}_3\text{O}_8 + \text{CO}_2 + 5.5\text{H}_2\text{O} \rightarrow 0.5\text{NaAlSi}_3(\text{OH})_4 + \text{Na}^+ + 2\text{H}_4\text{SiO}_4 + \text{HCO}_3^-$, $\text{CaCO}_3 + \text{CO}_2 + \text{H}_2\text{O} \rightarrow \text{Ca}^{2+} + \text{HCO}_3^-$. However, this is not the case. The model of the water-rock interaction does not reflect this type of chemical reaction process but only reflects the direction of the chemical reaction of the entire water-rock

TABLE 3: Random simulation results of the state of the water-rock interaction system.

Hole number	Statistics	Reaction volume (mmol·L ⁻¹)									Objective function/ <i>J</i>
		$X_1 \sim X_2$	X_3	X_4	X_5	X_6	X_7	X_8	X_9	X_{10}	
Hole 1	Mean value (XM)/(mmol·L ⁻¹)	0	0.142	0.59	0.149	0.083	0.031	0.036	0.062	0.002	-234.238
	Mean square error (STD)	0	0.082	0.281	0.201	0.152	0.021	0.027	0.043	0.004	103.27
	Coefficient of variation (Cv)	0	0.577	0.476	1.349	1.831	0.677	0.75	0.694	2	0.442
Hole 2	Mean value (XM)/(mmol·L ⁻¹)	0	0.059	0.608	0.01	0.301	0.006	0.055	0.11	0.006	-259.258
	Mean square error (STD)	0	0.054	0.259	0.041	0.209	0.008	0.025	0.051	0.02	99.233
	Coefficient of variation (Cv)	0	0.915	0.426	4.1	0.694	1.33	0.455	0.464	3.33	0.383
Hole 3	Mean value (XM)/(mmol·L ⁻¹)	0	0.089	0.393	0.039	0.122	0.004	0.036	0.071	0.017	-167.281
	Mean square error (STD)	0	0.062	0.182	0.068	0.15	0.01	0.023	0.046	0.021	73.83
	Coefficient of variation (Cv)	0	0.7	0.463	1.74	1.23	2.5	0.64	0.648	1.235	0.441
Hole 4	Mean value (XM)/(mmol·L ⁻¹)	0	0.099	0.853	0.091	0.086	0.031	0.067	0.134	0.001	-340.257
	Mean square error (STD)	0	0.08	0.199	0.091	0.143	0.021	0.037	0.074	0.005	93.643
	Coefficient of variation (Cv)	0	0.808	0.23	1	1.662	0.677	0.552	0.552	5	0.275

system from the initial state to the final state. In other words, the spontaneous reaction is still in equilibrium. Therefore, the zero reaction amounts of albite and calcite does not mean that they did not participate in the reaction, but the dissolved amount and precipitation amount of these two minerals are equal, i.e., they offset each other. No. 2 in Table 1 indicates that the surrounding rock of the tunnel is in a process of relatively balanced dissolution and sedimentation. This result is consistent with the fact that white precipitate was observed on the secondary lining in the on-site investigation of the drainage hole orifice and the water leakage. In addition, No. 1 in Table 1 was not selected in the calculation. The reason is that in the physical and chemical reactions of No. 9, Ca^{2+} , and Na^+ were exchanged, which hindered the dissolution of albite in groundwater.

The numbers 3, 4, 5, 6, 7, 8, 9, and 10 in Table 1 indicate that the main components involved in the reaction are $\text{Ca}(\text{OH})_2$, organic matter, CO_2 , and HCO_3^- . The organic matter (No. 4) is the dominant component in the reaction, indicating that the composition of the rock 1000 m from the tunnel entrance has an important influence. Organic matter is found in the interlayer, and the reaction is strongly oxidized and is strong at all simulated pore numbers. The result shows that the groundwater at the drainage hole is acidic (pH < 7.0), and the groundwater at the grouting curtain and the water in the drainage hole are even more acidic (such as hole 3 and hole 4). Therefore, carbonic acid erosion by the groundwater occurs. Moreover, the water in the drainage holes contains large amounts of dissolved CO_2 , which is consistent with field observations.

The reaction number 3 in Table 1 describes the interaction with $\text{Ca}(\text{OH})_2$ due to the acid-base balance and organic oxidation. The component $\text{Ca}(\text{OH})_2$ in the grouting body of the concrete and curtain is alkaline, and the groundwater is acidic; thus, the system is not in an equilibrium state. In addition, dissolution and precipitation should also be considered, because the attenuation or loss of the waterproofing effect of the curtain body is caused by the loss of cement particles in the body. The durability of the secondary concrete lining will be affected by the precipitation of the cement hydration products in the body. These

processes will lead to the failure of the waterproofing and drainage measures of the multiarch tunnel. In the treatment of seepage water, these reactions should be suppressed by chemical grouting.

Equations (4) and (5) in the mathematical model indicate that the total free energy of the system varies significantly. The value of the objective function (*J*) reflects the trend of the reaction power of the system. As *J* decreases, the reaction power increases. Therefore, dynamic water-rock interaction occurs about 1000 m from the entrance of the cave. The variance value is also relatively large, which can cause a spontaneous reaction in the system.

5. Conclusion

- (1) The leakage of the multiarch tunnel was significantly affected by the groundwater. The chemicals in the groundwater interacted with the surrounding rocks, concrete, and other components. The groundwater was acidic, resulting in carbonate erosion and the subsequent leakage of the multiarch tunnel.
- (2) A physical-chemical model of the water-rock interaction was established by considering the mechanism of the interactions between the rock surrounding the tunnel, the concrete, and the groundwater. The Monte Carlo method was used to take into account the multidimensional and complex factors and perform random number simulation. We used trial and error to determine the number of simulations (1000 times). The obtained water-rock interaction system of the multiarch tunnel met the accuracy requirements, and the state of the system and chemical interactions were simulated. The proposed method provides a new approach for the determination of the connectivity of the rock surrounding the multiarch tunnel.
- (3) The results indicated that the total free energy in the system varied significantly. The value of *J* reflected the trend of the spontaneous reaction of the system. As *J* decreased, the reaction power increased.

Therefore, dynamic water-rock interaction occurred about 1000 m from the opening of the cave. The variance value was also relatively large, indicating the occurrence of a spontaneous reaction in the system. As a result, the connectivity of the surrounding rock of the multiarch tunnel was increased, resulting in continuous leakage.

Notations

P :	Free energy change of reaction in the system
X_i :	Amount of the i -th physicochemical reaction
a_{ij} :	Stoichiometric coefficient of the j -th element in the i -th physical and chemical reaction mineral
d_j :	Concentration difference between the dissolution solution and the initial solution in the j -th component
m :	Number of equations with constraint conditions
x :	Random variable
l, w :	Upper and lower limits of the distribution of the random variable
u :	Mean
σ^2 :	Variance
b_j :	Constant
σ :	Standard deviation
J :	Objective function value
$X_1 \sim X_{10}$:	Number of millimoles of reactants participating in the reaction per liter of groundwater.

Data Availability

The data used in the study are available upon request to the corresponding author.

Conflicts of Interest

The authors declare that they have no conflicts of interest.

Acknowledgments

The authors would like to express their gratitude to Tong Haitao and Song Hanzhou for their assistance with the experiments and the use of the data used in this study.

References

- [1] H. Hellevang, V. T. H. Pham, and P. Aagaard, "Kinetic modelling of CO₂-water-rock interactions," *International Journal of Greenhouse Gas Control*, vol. 15, pp. 3–15, 2013.
- [2] J. Kaszuba, B. Yardley, and M. Andreani, "5. Experimental perspectives of mineral dissolution and precipitation due to carbon dioxide-water-rock interactions," *Geochemistry of Geologic CO₂ Sequestration*, vol. 77, no. 1, pp. 153–188, 2013.
- [3] Z. Zhao, T. Guo, Z. Ning, Z. Dou, F. Dai, and Q. Yang, "Numerical modeling of stability of fractured reservoir bank slopes subjected to water-rock interactions," *Rock Mechanics and Rock Engineering*, vol. 51, no. 8, pp. 2517–2531, 2017.
- [4] H. T. Tong and H. Z. Song, "Water-rock of the system function random hydrogeochemical simulation," *Water Scientific Progress*, vol. 21, no. 2, pp. 211–215, 2004, in Chinese.
- [5] X. L. Zheng and H. J. Liu, "Shandong alumina water system of the environmental geochemical reaction model," *The Earth Chemistry*, vol. 3, pp. 270–276, 1990, in Chinese.
- [6] Y. Chen and M. Gao, "Water-rock interaction model and its application in water-basalt reaction," *Journal of Nanjing University*, vol. 1, pp. 118–123, 1994, in Chinese.
- [7] J. X. Lai, J. L. Qiu, H. B. Fan et al., "Structural safety assessment of existing multiarch tunnel: a case study," *Advances in Materials Sciences and Engineering*, vol. 2017, Article ID 1697041, 12 pages, 2017.
- [8] T. Liu, Y. Xie, Z. H. Feng, Y. Luo, K. Wang, and W. Xu, "Better understanding the failure modes of tunnels excavated in the boulder-cobble mixed strata by distinct element method," *Engineering Failure Analysis*, vol. 116, Article ID 104712, 2020.
- [9] J. Wang, Y. Cao, K. Liu, J. Liu, X. Xue, and Q. Xu, "Pore fluid evolution, distribution and water-rock interactions of carbonate cements in red-bed sandstone reservoirs in the Dongying depression, China," *Marine and Petroleum Geology*, vol. 72, pp. 279–294, 2016.
- [10] J. X. Shi, X. R. Liu, W. Z. Cao, C. Q. Chen, and Y. H. Yang, "Study on the water of leakage diseases caused by frost heave of multiple-arch tunnel," *Disaster Advances*, vol. 6, no. 2, pp. 20–26, 2013.
- [11] T. H. Yang, "Rock failure process permeability properties and stress coupling," Dissertation, Northeastern University, Boston, MA, USA, 2001, in Chinese.
- [12] E. M. Kweilin and R. W. Healy, "Numerical investigation of steady liquid water flow in a variably saturated fracture networks," *Water Resources*, vol. 29, no. 12, pp. 4091–4102, 1993.
- [13] Y. Meng and M. L. Lei, "Karst area tunnel gushing water research status and the suggestion," *China Karst*, vol. 37, no. 4, pp. 287–290, 2003, in Chinese.
- [14] K. Wu and Z. Shao, "Visco-elastic analysis on the effect of flexible layer on mechanical behavior of tunnels," *International Journal of Applied Mechanics*, vol. 11, no. 3, p. 20, 2019.
- [15] J. G. Wang, Z. F. Zhou, and R. L. Tang, "The water-rock effect linear programming model and application to cross the los hydropower project as an example," *Water Scientific Progress*, vol. 10, no. 2, pp. 118–122, 1999, in Chinese.
- [16] D. L. Zhu and Q. F. Li, "Forecast method of tunnel yield," *Engineering Survey*, vol. 38, no. 4, pp. 18–32, 2000, in Chinese.
- [17] P. A. Hsieh and S. P. Neuman, "Field determination of the three-dimensional hydraulic conductivity tensor of anisotropic media: 1. theory," *Water Resources Research*, vol. 21, no. 11, pp. 1655–1665, 1985.
- [18] S. S. Xu, H. Lei, C. Li, H. Q. Liu, J. X. Lai, and T. Liu, "Model test on mechanical characteristics of shallow tunnel excavation failure in gully topography," *Engineering Failure Analysis*, vol. 118, Article ID 104839, 2020.
- [19] T. Y. Xu, Z. J. Zhou, R. P. Yan et al., "Real-time monitoring method for layered compaction quality of loess subgrade based on hydraulic compactor reinforcement," *Sensors*, vol. 20, no. 15, Article ID 4288, 2020.
- [20] Z. Mao, X. Wang, N. An, X. Li, and R. Wei, "Water disaster susceptible areas in loess multi-arch tunnel construction under the lateral recharge condition," *Ksce Journal of Civil Engineering*, vol. 23, no. 10, pp. 4564–4577, 2019.
- [21] Z. J. Mao, X. K. Wang, N. An et al., "Water leakage susceptible areas in loess multi-arch tunnel operation under the lateral recharge conditions," *Environmental Earth Sciences*, vol. 79, no. 15, p. 32, 2020.

- [22] J. Bear, *Dynamics of Fluids in Porous Media*, Li Jing-Sheng, Chen Chong-Xi Translation, China Architecture & Building Press, Beijing, China, 1983.
- [23] D. S. Vincent, R. E. Williams, and G. L. Bloomsburg, "Groundwater flow patterns in the vicinity of underground openings in unsaturated rock," *Journal of Hydrology*, vol. 127, no. 1-4, pp. 1-21, 1991.
- [24] H. J. Yang and F. G. Li, "Buried deep groundwater treatment technology of long tunnel," *Geotechnical Engineering*, vol. 3, pp. 343-356, 2005, in Chinese.
- [25] Z. F. Zhou and Y. Li, "Complicated rock mass movement of groundwater problems limited analysis," *Water Scientific Progress*, vol. 3, pp. 102-108, 1997, in Chinese.
- [26] J. Wang, W. Li, and Z. Song, "Development and implementation of new triangular finite element based on MGE theory for bi-material analysis," *Results in Physics*, vol. 13, Article ID 102231, 2019.
- [27] J. Wang, Q. Zhang, Z. Song, and Y. Zhang, "Creep properties and damage constitutive model of salt rock under uniaxial compression," *International Journal of Damage Mechanics*, vol. 29, no. 6, pp. 902-922, 2020.

Research Article

Evaluation of Ground Displacements Caused by Installing Jet Grouted Columns Using Machine Learning Methods

Zhi-Feng Wang ¹, Xing-Bin Peng,¹ Yong Liu,¹ Wen-Chieh Cheng,^{2,3} Ya-Qiong Wang,¹ and Chao-Jun Wu⁴

¹School of Highway, Chang'an University, Xi'an 710064, China

²School of Civil Engineering, Xi'an University of Architecture and Technology, Xi'an 710055, China

³Shaanxi Key Laboratory of Geotechnical and Underground Space Engineering (XAUAT), Xi'an 710055, China

⁴Jinan Rail Transit Group Co. Ltd., Jinan 250101, China

Correspondence should be addressed to Zhi-Feng Wang; zhifeng.wang@chd.edu.cn

Received 27 May 2020; Revised 28 August 2020; Accepted 9 September 2020; Published 21 September 2020

Academic Editor: Zaobao Liu

Copyright © 2020 Zhi-Feng Wang et al. This is an open access article distributed under the Creative Commons Attribution License, which permits unrestricted use, distribution, and reproduction in any medium, provided the original work is properly cited.

During the jet grouting process, large volumes of high pressurized fluids injected into the soils will cause significant ground displacements, which may bring harmful impacts on surrounding environment. Therefore, it is essential to provide an accurate estimation of the ground displacement in the design stage. Based on multiple nonlinear regression (MNL) and support vector regression (SVR), the prediction approaches are established, respectively. The column radius (R_c), Young's modulus (E), and distance from column center to target point (L_{OA}) are selected as the input parameters, while the displacement of target point A at the radial direction (δ_A) is taken as the output parameter. Comparisons results on the prediction performance of ground displacements indicate that the MNL-based approach has a better prediction effect. The design charts of the MNL-based approach for predicting the ground displacement are created, which will be helpful for the practicing engineers to get a quick estimation.

1. Introduction

Jet grouting is invented based on the combination of hydraulic mining technology and grouting technique and has become one of the most popular ground improvement techniques in different construction fields for preventing geohazards in worldwide area [1–13]. Jet grouting is generally adopted to strengthen soft soil, such as ground improvement during deep excavations and tunnel construction [14–27] and reinforcement of embankment foundation [28–32]. Considering the types of fluids jetted from the nozzles, jet grouting systems can be divided into three categories [33–35]: (i) single fluid system (injection of high pressurized grout), (ii) double fluid systems (injection of high pressurized grout and compressed air), and (iii) triple fluid systems (injection of high pressurized water, compressed air, and low pressurized grout).

Because large volumes of high pressurized fluids are injected into the fine grained soils during the jet grouting process, it will cause significant ground displacements, which may bring harmful impacts on surrounding environment [36–38]. Therefore, it is essential to provide an accurate estimation of the ground displacement in the design stage. However, most researchers mainly focused on the prediction of diameter and strength of jet grouted columns [39–44], and there are few published literatures related to ground displacement caused by installation of jet grouted columns. Shen et al. [31] proposed a method to calculate the lateral displacements caused by installing vertical jet grouted columns in clayey soils based on the analytical solution developed by Verruijt [45]. Wang et al. [8] proposed an approach to estimate the ground displacements caused by installation of horizontal jet grouted columns. However, the practical engineers may lack relative mathematical

knowledge, which may bring difficulty in the use of these existed methods and will limit their widespread application. Intelligent approaches based on machine learning methods are becoming more and more popular in the field of engineering geology and geotechnical engineering [46–50], which can effectively overcome the difficulties of arbitrary assumptions adopted in the current methods and increase the confidence in predictions. Multiple nonlinear regression (MNLR) is a form of regression analysis in which the dependent variables are modeled by a nonlinear function of the independent variables [51–53]. MNLR can establish the models to describe the arbitrary relationships between the independent variables and the dependent variables, and this is different from traditional multiple linear regression (MLR), which is only used to obtain linear models. It has been proven that MNLR is an efficient prediction tool by many researchers in different fields (e.g., the field of economics, marketing, and engineering). As a new and efficient intelligent approach, the support vector machine (SVM) was produced on the basis of machine learning theory to solve the classification problems at the initial stage, and then, it was developed to deal with the regression problems after introducing the ϵ -insensitive loss function. The support vector regression (SVR) technique is based on the structural risk minimization (SRM) principle, which is not only to minimize the error on the training data but also to minimize a bound on the generalization error of a model [54].

In this paper, in order to control and mitigate environmental impacts due to installation disturbance of jet grouting, the machine learning methods including MNLR and SVR are taken as an attempt to propose an approach to predict the ground displacements caused by installing jet grouted columns. A series of field data on ground displacements caused by installing jet grouted columns were collected to conduct the analysis by MNLR and SVR. Finally, the design charts to estimate ground displacement are created to make it easy to use the proposed approach in this study for practical engineers.

2. Problem Description

Jet grouting is invented based on the combination of hydraulic mining technology and grouting technique. In the construction of jet grouting, high pressurized fluids (grout or water) are jetted from the nozzles that are fixed on the rod and have small diameters into the ground. Then, the in situ soils below ground surface can be eroded by the high pressurized fluid jets, and an approximate cylindrical soil-cement column will be formed by mixing the eroded soils with the injected grout. Figure 1 depicts the schematic view of ground displacements caused by installing a jet grouted column. As can be seen, the injection of large volumes of high pressurized fluids may cause an expansion effect in the internal stratum, which can induce movements in surroundings soil. Considering the jet grouting process, the factors influencing the ground displacements can be divided as follows: jetting parameters, soil properties, and distance to target point. Hence, the ground displacement caused by installing a jet grouted column can be expressed as a

function of construction issues, soil properties, and distance to target point:

$$\delta_A = f(\text{jetting parameters, soil properties, distance to target point}), \quad (1)$$

where δ_A is the displacement of point A at the radial direction, as shown in Figure 1.

For the effect of jetting parameters on ground displacements, the withdrawal rate of the rod, nozzle diameter, number of nozzles, flow rate of injected fluid, rotation speed of the rod, and jetting pressure of fluid are mainly concerned. The values of ground displacements will be larger if the higher values of jetting parameters are given when other conditions are the same. For the effect of soil properties on ground displacements, the soil strength and soil stiffness are mainly included. The values of ground displacements will be smaller if the higher values of jetting parameters are introduced when other conditions are the same. In this study, column radius R_c , Young's modulus E , and distance from column center to target point L_{OA} are selected to represent the effects of jetting parameters, soil properties, and distance to target point on ground displacements, and their relationship can be expressed as follows:

$$\delta_A = f(R_c, E, L_{OA}), \quad (2)$$

where R_c is the radius of jet grouted column, E is Young's modulus of surrounding soils, and L_{OA} is the distance from column center (point O) to target point A, as shown in Figure 1. In summary, to yield an accuracy prediction of ground displacements caused by installing a jet grouted column, a reasonable approach using MNLR and SVR should be capable of considering these three parameters: column radius R_c , Young's modulus E , and distance from column center to target point L_{OA} .

3. Data Preparation

Based on the above thought on influencing factors, considering the column radius R_c , Young's modulus E , and distance from column center to target point L_{OA} , 36 experimental data on ground displacements caused by installing a jet grouted column were collected from the published literature as regression data. Table 1 tabulates the collected experimental data on ground displacements caused by installing jet grouted columns. These field data were obtained from two case histories in two different soils. Figure 2 shows the geotechnical profile and soil properties for two case histories conducted in the soft clay and silty clay, respectively. As can be seen, the physical properties and mechanical parameters can be easily determined.

4. Methodology

4.1. Multiple Nonlinear Regression. Multiple nonlinear regression (MNLR) is a type of regression analysis in which the dependent variables are modeled by a nonlinear function of the independent variables. MNLR can establish the models to describe the arbitrary relationships between the

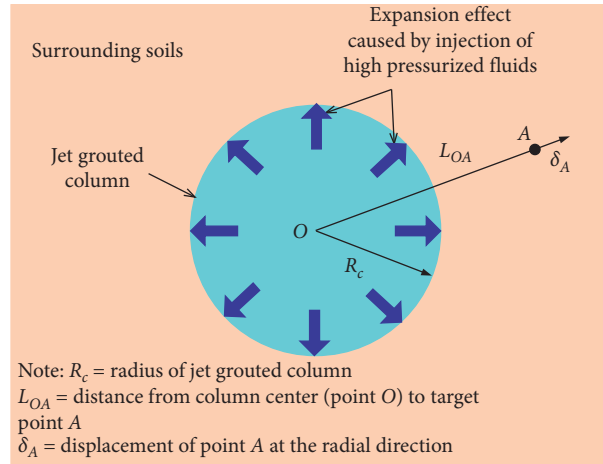


FIGURE 1: Schematic view of ground displacements caused by installing a jet grouted column.

TABLE 1: Data collected in this study.

Data number	Soil types	R_c (m)	E (kPa)	L_{OA} (m)	δ_A (mm)	References
1	Soft clay	0.88	5370	7.4	31.2	Shen et al. [31]
2	Soft clay	0.88	5882	7.4	26.9	Shen et al. [31]
3	Soft clay	0.88	6393	7.4	22.7	Shen et al. [31]
4	Soft clay	0.88	6905	7.4	17.7	Shen et al. [31]
5	Soft clay	0.88	7416	7.4	14.2	Shen et al. [31]
6	Soft clay	0.88	7927	7.4	9.6	Shen et al. [31]
7	Soft clay	0.88	8439	7.4	6.5	Shen et al. [31]
8	Soft clay	0.88	14321	7.4	3.7	Shen et al. [31]
9	Soft clay	0.88	15139	7.4	2.3	Shen et al. [31]
10	Soft clay	0.88	15957	7.4	1.5	Shen et al. [31]
11	Silty clay	0.5	2500	6.5	44.2	Wang et al. [8]
12	Silty clay	0.5	2500	6.5	47.4	Wang et al. [8]
13	Silty clay	0.5	5000	6.1	15.1	Wang et al. [8]
14	Silty clay	0.5	5000	5.8	13.9	Wang et al. [8]
15	Silty clay	0.5	5000	5.6	14.6	Wang et al. [8]
16	Silty clay	0.5	5000	5.4	15.1	Wang et al. [8]
17	Silty clay	0.5	5000	5.2	14.9	Wang et al. [8]
18	Silty clay	0.5	5000	5.1	14.9	Wang et al. [8]
19	Silty clay	0.5	5000	5.0	15.2	Wang et al. [8]
20	Silty clay	0.5	5000	5.0	18.0	Wang et al. [8]
21	Silty clay	0.5	5000	5.0	18.8	Wang et al. [8]
22	Silty clay	0.5	5000	5.1	15.0	Wang et al. [8]
23	Silty clay	0.5	5000	5.2	11.2	Wang et al. [8]
24	Silty clay	0.5	5000	5.4	10.9	Wang et al. [8]
25	Silty clay	0.5	5000	5.6	10.7	Wang et al. [8]
26	Silty clay	0.5	5000	5.8	10.6	Wang et al. [8]
27	Silty clay	0.5	5000	6.1	9.9	Wang et al. [8]
28	Silty clay	0.5	5000	6.4	9.2	Wang et al. [8]
29	Silty clay	0.5	5000	6.7	9.1	Wang et al. [8]
30	Silty clay	0.5	5000	7.1	8.6	Wang et al. [8]
31	Silty clay	0.5	5000	7.4	8.4	Wang et al. [8]
32	Silty clay	0.5	5000	7.8	7.6	Wang et al. [8]
33	Silty clay	0.5	5000	8.2	6.7	Wang et al. [8]
34	Silty clay	0.5	5000	8.6	6.3	Wang et al. [8]
35	Silty clay	0.5	5000	9.0	3.2	Wang et al. [8]
36	Silty clay	0.5	5000	9.4	2.3	Wang et al. [8]

Note. R_c : radius of jet grouted column; E : Young's modulus of soil; L_{OA} : distance from column center to target point; δ_A : measured displacement at the radial direction.

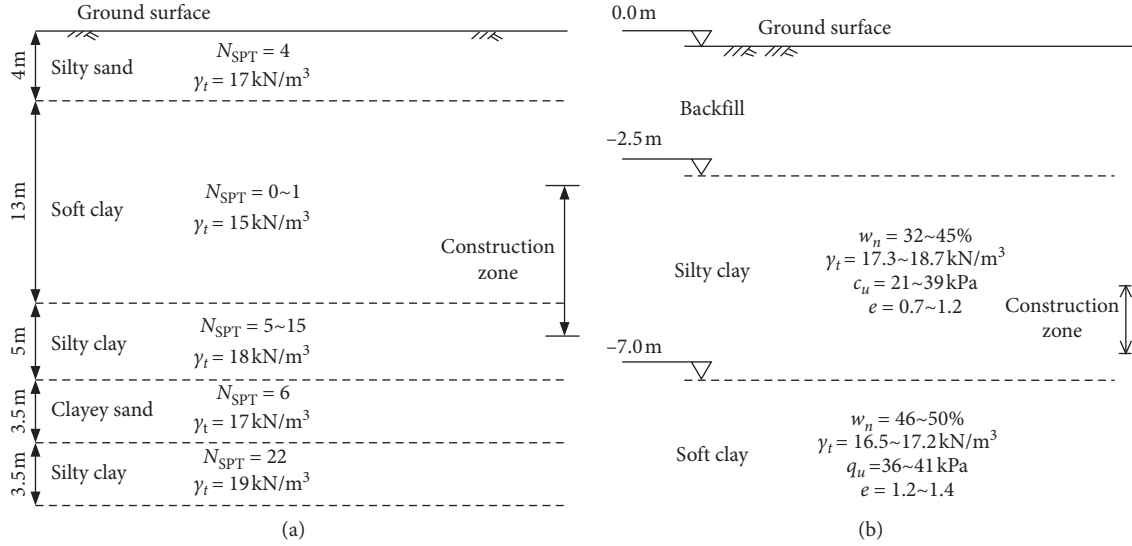


FIGURE 2: Geotechnical profile and soil conditions for two different cases: (a) case history conducted in soft clay (after [31]); note: γ_t = unit weight; N_{SPT} = blow counts of the standard penetration test (SPT); (b) case history conducted in silty clay (after [8]); note: w_n = water content; γ_t = unit weight; e = void ratio; q_u = unconfined compressive strength.

independent variables and the dependent variables, and this is different from traditional multiple linear regression (MLR), which is only adopted to obtain linear models. Based on the consideration of the influencing factors on ground displacements and equation (2), the following nonlinear function is proposed to conduct MNLR analysis:

$$\delta_A = \delta_{ref} \cdot \left(\frac{R_c}{0.5}\right)^a \cdot \left(\frac{E}{3000}\right)^b \cdot \left(\frac{L_{OA}}{5.0}\right)^c \text{ mm}, \quad (3)$$

where R_c is expressed in m; E is expressed in kPa; L_{OA} is expressed in m; and a , b and c are empirical coefficients. With such a formulation, δ_{ref} has the physical meaning of being the ground displacement produced under the condition having $R_c = 0.5$ m, $E = 3000$ kPa, and $L_{OA} = 5.0$ m.

MNLR model has been implemented using Statistics and Machine Learning Toolbox in MATLAB 2019a environment with a nonlinear regression code. Based on the running results of the nonlinear regression code, $\delta_{ref} = 40$ mm, $a = 1.8$, $b = -1.4$, and $c = -1.7$ are obtained with the best prediction performance.

4.2. Support Vector Regression. The support vector machine (SVM) is a new and efficient artificial intelligence method, which was produced on the basis of statistical learning theory to solve the classification problems at the initial stage, and then, it was developed to deal with the regression problems after introducing the ϵ -insensitive loss function. SVR can be divided as the linear SVR and the nonlinear SVR. In many cases, it is not suitable using the linear SVR due to the real-world problem is very complex. The principle of SVR technique is introduced briefly in this section.

Taking a series of training data into account $\{(x_1, y_1), \dots, (x_n, y_n)\}$, $x \in R^m$, $y \in R$, where x is the input parameter, y is the output parameter, n is the number of collected data, R^m is the m -dimensional vector space, and

R is the one-dimensional vector space. Figure 3 shows the principle of a linear SVR technique, ϵ -insensitive loss function, and slack variables. As can be seen, the shaded area is called as the ϵ -insensitive tube. For these training data outside of the ϵ -insensitive tube, they will be given a nonzero slack variable. When the predicted data are inside the ϵ -insensitive tube, there will be no other differences, which mean that the value of ϵ -insensitive loss is zero. While the predicted data are outside the ϵ -insensitive tube, the value of the loss will be equal to be the magnitude of the difference between the estimated data and the tube radius ϵ [54]. The ϵ -insensitive loss function may be determined by the following equation:

$$L_\epsilon(y) = |y - f(x)|_\epsilon = \begin{cases} 0, & \text{if } |y - f(x)| \leq \epsilon, \\ |y - f(x)| - \epsilon, & \text{otherwise,} \end{cases} \quad (4)$$

where $L_\epsilon(y)$ is the loss function.

The linear function for SVR can be given by the following equation in general:

$$f(x) = \langle \mathbf{w} \cdot \mathbf{x} \rangle + b, \quad (5)$$

where b is the bias, \mathbf{w} is the weight vector, and $\langle \mathbf{w} \cdot \mathbf{x} \rangle$ is the inner product of \mathbf{w} and \mathbf{x} .

In SVR, there exists a main goal that is to find out a function $f(x)$ that has the ability to minimize the complexity of model [54, 55]. The aforementioned goal can be achieved by the minimization of the weight vector (w):

$$\begin{aligned} & \text{minimize } \frac{1}{2} \|\mathbf{w}\|^2 \\ & \text{subjected to } \begin{cases} y_i - \langle \mathbf{w} \cdot \mathbf{x}_i \rangle - b \leq \epsilon, \\ \langle \mathbf{w} \cdot \mathbf{x}_i \rangle + b - y_i \leq \epsilon. \end{cases} \end{aligned} \quad (6)$$

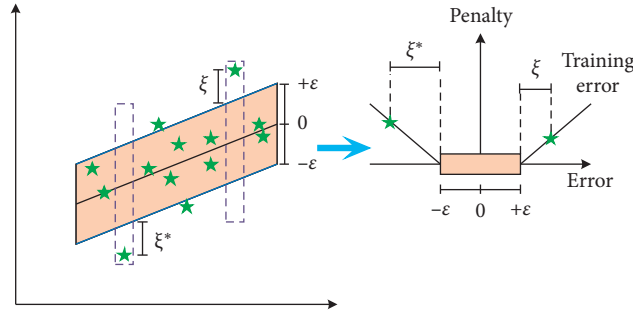


FIGURE 3: Schematic view of a linear SVR technique, ε -insensitive loss function, and slack variables.

However, by the introduction of slack parameters ξ_i, ξ_i^* ($i = 1, \dots, n$), the estimation error of training data outside the ε -insensitive tube could be incorporative. The function of

convex optimization could be determined by the following equation:

$$\begin{aligned} \text{minimize } \varphi(w, \xi, \xi^*) &= \frac{1}{2} \|w\|^2 + C \sum_{i=1}^n (\xi_i + \xi_i^*) \\ \text{subject to } \begin{cases} y_i - \langle \mathbf{w} \cdot \mathbf{x}_i \rangle - b \leq \varepsilon + \xi_i, \\ \langle \mathbf{w} \cdot \mathbf{x}_i \rangle + b - y_i \leq \varepsilon + \xi_i^*, \\ \xi_i, \xi_i^* \geq 0, \end{cases} \end{aligned} \quad (7)$$

where C is the penalty parameter that is >0 . In equation (8), the left term $(1/2)\|w\|^2$ stands for the structure risk, while the right term $C \sum_{i=1}^n (\xi_i + \xi_i^*)$ stands for the empirical risk. The penalty parameter C determines the trade-off between

the term $(1/2)\|w\|^2$ and the empirical risk. By introducing a Lagrange function, the function in equation (8) could be transformed as follows:

$$\begin{aligned} \text{maximize } L(\alpha^*, \alpha) &= -\varepsilon \sum_{i=1}^n (\alpha_i^* + \alpha_i) + \sum_{i=1}^n y_i (\alpha_i^* - \alpha_i) - \frac{1}{2} \sum_{i=1}^n \sum_{j=1}^n (\alpha_i^* - \alpha_i)(\alpha_i^* + \alpha_i)(\mathbf{x}_i \cdot \mathbf{x}_j) \\ \text{maximize } \begin{cases} \sum_{i=1}^n (\alpha_i^* + \alpha_i), \\ 0 \leq \alpha_i^* \leq C, \\ 0 \leq \alpha_i \leq C, \end{cases} \end{aligned} \quad (8)$$

where α^* and α are Lagrange multipliers and $L(\alpha^*, \alpha)$ is the Lagrange function. When the Lagrange multipliers after optimization are obtained, the regression problem in equation (9) can be expressed as follows:

$$\mathbf{w}_0 = \sum_{\text{Support vectors}} (\alpha_i^* + \alpha_i) \mathbf{x}_i, \quad (9)$$

$$b_0 = \frac{1}{2} \omega_0 [\mathbf{x}_r + \mathbf{x}_s], \quad (10)$$

$$f(x) = \sum_{\text{Support vectors}} (\alpha_i^* - \alpha_i)(\mathbf{x}_i \cdot \mathbf{x}) + b_0, \quad (11)$$

where \mathbf{x}_r and \mathbf{x}_s are the support vectors, b_0 is the optimum value for the bias, and w_0 is the optimum value for the weight vector. During the training process of SVR technique, the values of some Lagrange multipliers could become zero, indicating that these training data could be irrelevant for the final regression analysis. Training modes with nonzero Lagrange multipliers are generally called as the support vectors [56]. The abovementioned SVR model is capable of solving the linear regression problems in general.

By introducing a nonlinear kernel function, the following equations can be adopted to solve the nonlinear regression problems:

$$\begin{aligned}
f(\mathbf{x}) &= \sum_{\text{Support vectors}} (\alpha_i^* - \alpha_i) K(\mathbf{x}_i \cdot \mathbf{x}) + b_0, \\
\mathbf{w}_0 \cdot \mathbf{x} &= \sum_{\text{Support vectors}} (\alpha_i^* - \alpha_i) K(\mathbf{x}_i, \mathbf{x}), \\
b_0 &= \frac{1}{2} \sum_{\text{Support vectors}} (\alpha_i^* - \alpha_i) [K(\mathbf{x}_r, \mathbf{x}_i) + K(\mathbf{x}_s, \mathbf{x}_i)],
\end{aligned} \tag{12}$$

where $K(\mathbf{x}_i \cdot \mathbf{x})$ is the kernel function.

$$K(\mathbf{x}_i \cdot \mathbf{x}) = \langle \phi(x_i) \cdot \phi(x) \rangle. \tag{13}$$

By the use of a map ϕ , the input variables could be mapped onto the feature space. The dot product of $\phi(x_i) \cdot \phi(x)$ is calculated by using a linear combination of the training data [57].

In this study, a structure of the SVR technique for prediction of ground displacements is established, as shown in Figure 4. SVR model has been implemented using Statistics and Machine Learning Toolbox in MATLAB 2019a environment with a SVR code. Radial basis kernel function is one of the most widely used kernel functions in SVR and is adopted to analyze the collected data for prediction of ground displacements in this study.

5. Accuracy of Predicted Values by MNLR and SVR

In order to evaluate the accuracy of predicted values of ground displacement by MNLR and SVR, five regression indices, namely, correlation coefficient (R^2), mean squared error (MSE), mean absolute error (MAE), mean absolute percentage error (MAPE), and median absolute error (MEDAE), were adopted in this study. These five regression indices can be determined as follows:

$$\begin{aligned}
\text{correlation coefficient, } R &= \frac{\sum_{i=1}^n (l_i - \bar{l}_i)(m_i - \bar{m}_i)}{\sqrt{\sum_{i=1}^n (l_i - \bar{l}_i)^2 \sum_{i=1}^n (m_i - \bar{m}_i)^2}}, \\
\text{MSE} &= \frac{\sum_{i=1}^n (l_i - m_i)^2}{n}, \\
\text{MAPE} &= \frac{100\%}{n} \times \left[\sum_{i=1}^n \left| \frac{l_i - m_i}{l_i} \right| \right], \\
\text{MEDAE} &= \text{median}(l_i - m_i), \\
\text{MAE} &= \frac{1}{n} \sum_{i=1}^n |l_i - m_i|,
\end{aligned} \tag{14}$$

where l_i is the observed data, m_i is the predicted data, n is the number of adopted data, \bar{l}_i is the average value of the observed data, and \bar{m}_i is the average value of the predicted data.

Figure 5 shows the prediction performance of ground displacement with MNLR and SVR, in which training data and testing data are included. As can be seen, the prediction performance obtained by using MNLR ($\delta_{\text{ref}} = 40$ mm, $a = 1.8$, $b = -1.4$, and $c = -1.7$) is better, for training data: $R^2 = 0.96$, $\text{MSE} = 13.32$, $\text{MAPE} = 50.5\%$, $\text{MEDAE} = 3.2$, and $\text{MAE} = 3.3$; for testing data: $R^2 = 0.98$, $\text{MSE} = 14.05$, $\text{MAPE} = 12.5\%$, $\text{MEDAE} = 3.1$, and $\text{MAE} = 3.0$. While for the prediction performance obtained by SVR with radial basis function, these five regression indices are listed as follows: for training data: $R^2 = 0.80$, $\text{MSE} = 38.61$, $\text{MAPE} = 35.01\%$, $\text{MEDAE} = 3.0$, and $\text{MAE} = 0.84$; for testing data: $R^2 = 0.55$, $\text{MSE} = 59.8$, $\text{MAPE} = 21.5\%$, $\text{MEDAE} = 5.82$, and $\text{MAE} = 5.13$. From these comparison results, it is suggested that the MNLR has a better prediction performance and can be adopted to yield an accurate prediction of the ground displacement caused by installing a jet grouted column.

6. Design Charts to Estimate Ground Displacement Created by MNLR

Based on the analysis of prediction performance, it has been proven that the MNLR can be used to yield a good estimation of the ground displacement caused by installing a jet grouted column. In order to increase the application range of this MNLR method, the design charts for predicting the ground displacement caused by installing a jet grouted column for different cases are plotted, as shown in Figure 6, which will make it more convenient for the use of this MNLR method in engineering practice. As can be seen in this figure, the column radius R_c varies from 0.25 m to 1.25 m, and Young's modulus E is within the range of 2500 kPa to 30000 kPa, while the distance from column center to target point L_{OA} changes from 3 m to 18 m. These design charts basically cover the most situations that can be encountered in engineering practice. Considering the construction issues and soil conditions in engineering site, the column radius can be estimated using the existed method [39, 41–43] firstly, and then, the practicing engineers can get a quick prediction of the ground displacement caused by installing a jet grouted column based on the design charts proposed in this paper. In engineering practice, it is always encountered that multiple rows of jet grouted columns are installed. For such cases, based on the assumption of the principle of superposition, the ground displacements induced by installing a row of columns can be determined by the sum of the displacement caused by each individual column, as shown in the following equation and Figure 7:

$$\delta_{\text{Asum}} = \sum_{i=1}^n \delta_{Ai}, \tag{15}$$

where δ_{Asum} is the ground displacements induced by installing a row of columns; i stands for the number of the jet grouted column being installed; and δ_{Ai} is the displacement caused by installation of column i , which can be estimated by the design charts in this study.

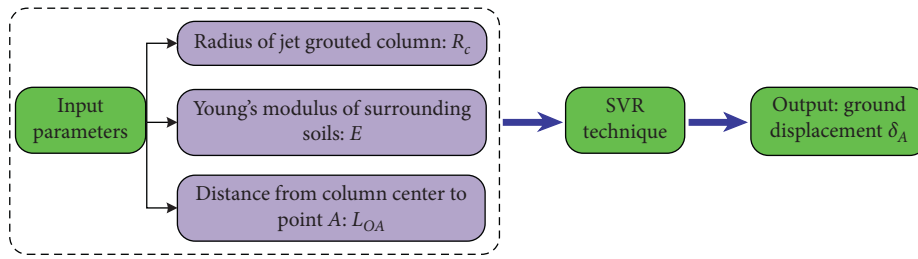


FIGURE 4: Prediction structure of the SVR technique in this study.

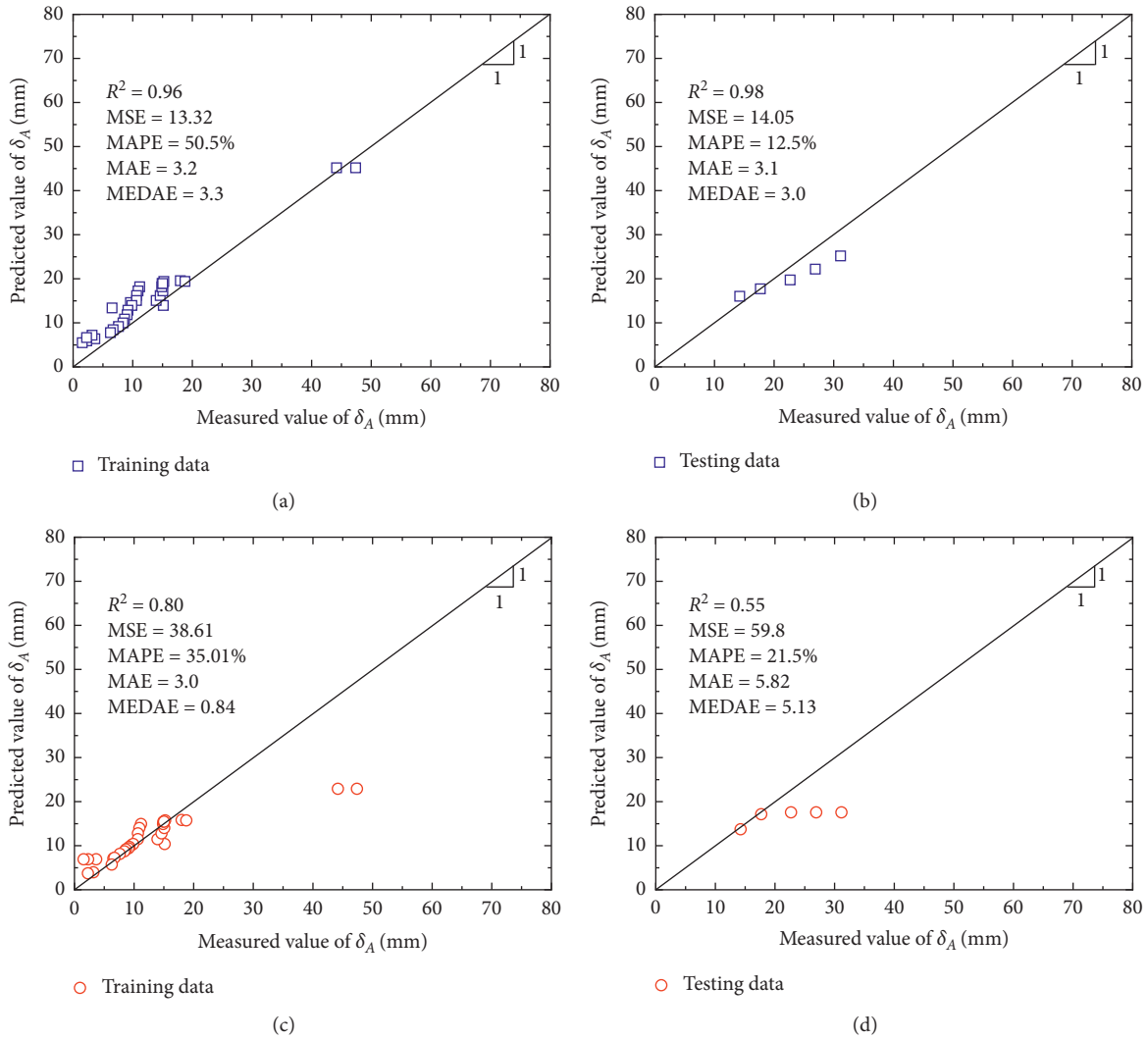


FIGURE 5: Prediction performance of ground displacement with different methods: (a) MNL model (training); (b) MNL model (testing); (c) SVR model (training); (d) SVR model (testing).

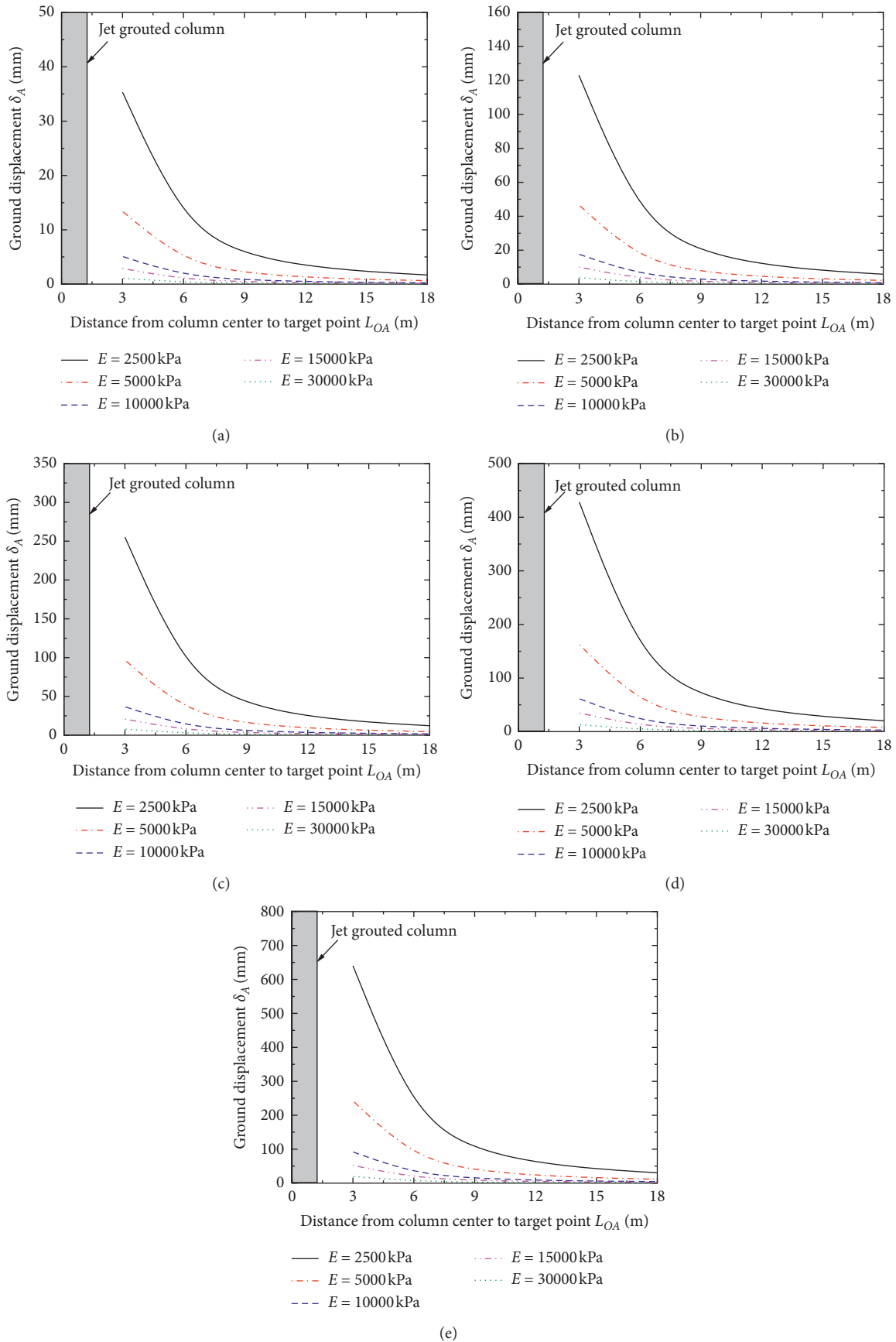


FIGURE 6: Design charts for estimating ground displacement caused by installing a jet grouted column: (a) $R_c = 0.25$ m; (b) $R_c = 0.50$ m; (c) $R_c = 0.75$ m; (d) $R_c = 1.00$ m; (e) $R_c = 1.25$ m.

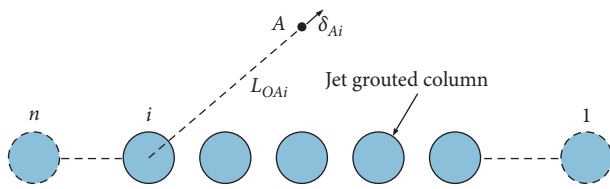


FIGURE 7: Illustration of ground displacements induced by installing a row of columns (after [31]).

7. Conclusions

Predicting the ground displacements caused by installing jet grouted columns is an important issue in the design stage of jet grouting, and large error in prediction may induce harmful results in engineering practice. Based upon the machine learning methods, prediction of the ground displacement caused during jet grouting is analyzed and discussed in this study, and the conclusions can be drawn as follows:

- (1) The factors influencing the ground displacements can be divided as jetting parameters, soil properties, and distance to target point. The column radius (R_c), Young's modulus (E), and distance from column center to target point (L_{OA}) are selected as the input parameters, while the displacement of target point A at the radial direction (δ_A) is taken as the output parameter.
- (2) The prediction approaches are established, respectively, based on MNLR and SVR. A nonlinear equation to express the relationship between the input parameters (R_c , E , and L_{OA}) and the output parameter (δ_A) is proposed in this study. Comparisons results on prediction performance of ground displacements indicate that the MNLR-based approach has a better prediction effect.
- (3) Using the MNLR-based approach, the design charts for predicting the ground displacement induced by installation of jet grouted columns are created to increase the convenience for the use of the MNLR model in engineering practice. Based on the proposed design charts, the practicing engineers can get a quick estimation of the ground displacements caused by installing jet grouted columns.

Data Availability

The data used to support the findings of this research work are included within the article.

Conflicts of Interest

The authors declare that there are no conflicts of interest.

Acknowledgments

The research described in this study was funded by the project supported by the Natural Science Basic Research Plan in Shaanxi Province of China (Program no. 2019JQ-

114), the National Nature Science Foundation of China (NSFC) (Grant nos. 41702287 and 41807245), and the Fundamental Research Funds for the Central Universities (Grant no. 300102218517). These financial supports are gratefully acknowledged.

References

- [1] X. Bian, Y.-J. Cui, and X.-Z. Li, "Voids effect on the swelling behaviour of compacted bentonite," *Géotechnique*, vol. 69, no. 7, pp. 593–605, 2019.
- [2] X. Bian, Y.-J. Cui, L.-L. Zeng, and X.-Z. Li, "Swelling behavior of compacted bentonite with the presence of rock fracture," *Engineering Geology*, vol. 254, pp. 25–33, 2019.
- [3] S. Coulter and C. D. Martin, "Effect of jet-grouting on surface settlements above the Aeschertunnel, Switzerland," *Tunnelling and Underground Space Technology*, vol. 21, no. 5, pp. 542–553, 2006.
- [4] S.-L. Shen, Z.-F. Wang, W.-J. Sun, L.-B. Wang, and S. Horpibulsuk, "A field trial of horizontal jet grouting using the composite-pipe method in the soft deposits of Shanghai," *Tunnelling and Underground Space Technology*, vol. 35, pp. 142–151, 2013.
- [5] S.-L. Shen, Z.-F. Wang, S. Horpibulsuk, and Y.-H. Kim, "Jet grouting with a newly developed technology: the twin-jet method," *Engineering Geology*, vol. 152, no. 1, pp. 87–95, 2013.
- [6] G. N. Karahan and O. Sivrikaya, "Designing singular jet grouting column for sandy soils," *Environmental Earth Sciences*, vol. 77, no. 12, p. 448, 2018.
- [7] Z.-F. Wang, W.-C. Cheng, and Y.-Q. Wang, "Investigation into geohazards during urbanization process of Xi'an, China," *Natural Hazards*, vol. 92, no. 3, pp. 1937–1953, 2018.
- [8] Z. F. Wang, J. S. Shen, and W. C. Cheng, "Simple method to predict ground displacements caused by installing horizontal jet-grouting columns," *Mathematical Problems in Engineering*, vol. 2018, Article ID 1897394, 11 pages, 2018.
- [9] C. Toraldo, G. Modoni, M. Ochmański, and P. Croce, "The characteristic strength of jet-grouted material," *Géotechnique*, vol. 68, no. 3, pp. 262–279, 2018.
- [10] Y.-Q. Wang, Z.-F. Wang, and W.-C. Cheng, "A review on land subsidence caused by groundwater withdrawal in Xi'an, China," *Bulletin of Engineering Geology and the Environment*, vol. 78, no. 4, pp. 2851–2863, 2019.
- [11] Z.-F. Wang, S.-L. Shen, and G. Modoni, "Enhancing discharge of spoil to mitigate disturbance induced by horizontal jet grouting in clayey soil: theoretical model and application," *Computers and Geotechnics*, vol. 111, pp. 222–228, 2019.
- [12] Y. Wei, X. Gao, F. Wang, and Y. Zhong, "Nonlinear strain distribution in a field-instrumented concrete pavement slab in response to environmental effects," *Road Materials and Pavement Design*, vol. 20, no. 2, pp. 367–380, 2019.
- [13] Y. Wei, Z. Wu, X. Yao, and X. Gao, "Quantifying effect of later curing on pores of paste subject to early age freeze thaw cycles by different techniques," *Journal of Materials in Civil Engineering*, vol. 31, no. 8, Article ID 04019153, 2019.
- [14] G. Modoni and J. Bzówka, "Analysis of foundations reinforced with jet grouting," *Journal of Geotechnical and Geoenvironmental Engineering*, vol. 138, no. 12, pp. 1442–1454, 2012.
- [15] M. Ochmański, G. Modoni, and J. Bzówka, "Numerical analysis of tunnelling with jet-grouted canopy," *Soils and Foundations*, vol. 55, no. 5, pp. 929–942, 2015.
- [16] Q. L. Cui, H. N. Wu, S. L. Shen, Z. Y. Yin, and S. Horpibulsuk, "Protection of neighbour buildings due to construction of

- shield tunnel in mixed ground with sand over weathered granite," *Environmental Earth Sciences*, vol. 75, no. 6, p. 458, 2016.
- [17] G. Modoni, A. Flora, S. Lirer, M. Ochmański, and P. Croce, "Design of jet grouted excavation bottom plugs," *Journal of Geotechnical and Geoenvironmental Engineering*, vol. 142, no. 7, Article ID 04016018, 2016.
- [18] C. E. Ho, "Groundwater management for sustainable underground subway development in Manhattan, New York City," in *Proceedings of the 1st Geo-Chicago Conference: Sustainability and Resiliency in Geotechnical Engineering, Geo-Chicago*, Geotechnical Special Publication No. 269, American Society of Civil Engineers (ASCE) Press, pp. 663–672, Chicago, IL, USA, August 2016.
- [19] J. Lai, H. Fan, J. Chen, J. Qiu, and K. Wang, "Blasting vibration monitoring of undercrossing railway tunnel using wireless sensor network," *International Journal of Distributed Sensor Networks*, vol. 11, no. 6, Article ID 703980, 2015.
- [20] J. Qiu, Y. Xie, H. Fan, Z. Wang, and Y. Zhang, "Centrifuge modelling of twin-tunnelling induced ground movements in loess strata," *Arabian Journal of Geosciences*, vol. 10, no. 22, p. 493, 2017.
- [21] J. X. Lai, S. Y. He, J. L. Qiu et al., "Characteristics of seismic disasters and aseismic measures of tunnels in Wenchuan earthquake," *Environmental Earth Science*, vol. 76, no. 2, p. 94, 2017.
- [22] J. L. Qiu, H. Q. Liu, J. X. Lai, H. P. Lai, J. X. Chen, and K. Wang, "Investigating the long-term settlement of a tunnel built over improved loessial foundation soil using jet grouting technique," *Journal of Performance Constructed Facilities*, vol. 32, no. 5, Article ID 04018066, 2018.
- [23] W.-C. Cheng, J. C. Ni, A. Arulrajah, and H.-W. Huang, "A simple approach for characterising tunnel bore conditions based upon pipe-jacking data," *Tunnelling and Underground Space Technology*, vol. 71, pp. 494–504, 2018.
- [24] W.-C. Cheng, J. C. Ni, H.-W. Huang, J. S. Shen, and J. S. Shen, "The use of tunnelling parameters and spoil characteristics to assess soil types: a case study from alluvial deposits at a pipejacking project site," *Bulletin of Engineering Geology and the Environment*, vol. 78, no. 4, pp. 2933–2942, 2019.
- [25] W.-C. Cheng, L. Wang, Z.-F. Xue, J. C. Ni, M. M. Rahman, and A. Arulrajah, "Lubrication performance of pipejacking in soft alluvial deposits," *Tunnelling and Underground Space Technology*, vol. 91, Article ID 102991, 2019.
- [26] W.-C. Cheng, G. Li, N. Liu, J. Xu, and S. Horpibulsuk, "Recent massive incidents for subway construction in soft alluvial deposits of Taiwan: a review," *Tunnelling and Underground Space Technology*, vol. 96, Article ID 103178, 2020.
- [27] X. Bian, Y.-J. Cui, L.-L. Zeng, and X.-Z. Li, "State of compacted bentonite inside a fractured granite cylinder after infiltration," *Applied Clay Science*, vol. 186, Article ID 105438, 2020.
- [28] P. Jamsawang, P. Voottipruex, P. Boathong, W. Mairaing, and S. Horpibulsuk, "Three-dimensional numerical investigation on lateral movement and factor of safety of slopes stabilized with deep cement mixing column rows," *Engineering Geology*, vol. 188, pp. 159–167, 2015.
- [29] P. Jamsawang, S. Jamnam, P. Jongpradist, P. Tanseng, and S. Horpibulsuk, "Numerical analysis of lateral movements and strut forces in deep cement mixing walls with top-down construction in soft clay," *Computers and Geotechnics*, vol. 88, pp. 174–181, 2017.
- [30] J. Han, F. Wang, M. Al-Naddaf, and C. Xu, "Progressive development of two-dimensional soil arching with displacement," *International Journal of Geomechanics*, vol. 17, no. 12, Article ID 04017112, 2017.
- [31] S. L. Shen, Z. F. Wang, and W. C. Cheng, "Estimation of lateral displacement induced by jet grouting in clayey soils," *Géotechnique*, vol. 67, no. 7, pp. 621–630, 2017.
- [32] Z. F. Wang, W. C. Cheng, and Y. Q. Wang, "Simple method to predict settlement of composite foundation under embankment," *International Journal of Geomechanics*, vol. 18, no. 12, Article ID 04018158, 2018.
- [33] J. C. Ni and W.-C. Cheng, "Quality control of double fluid jet grouting below groundwater table: case history," *Soils and Foundations*, vol. 54, no. 6, pp. 1039–1053, 2014.
- [34] P. G. A. Njock, J. Chen, G. Modoni, A. Arulrajah, and Y. H. Kim, "A review of jet grouting practice and development," *Arabian Journal of Geosciences*, vol. 11, no. 16, p. 459, 2018.
- [35] P. G. A. Njock, J. S. Shen, G. Modoni, and A. Arulrajah, "Recent advances in horizontal jet grouting (HJG): an overview," *Arabian Journal for Science and Engineering*, vol. 43, no. 4, pp. 1543–1560, 2018.
- [36] Z.-F. Wang, S.-L. Shen, C.-E. Ho, and Y.-H. Kim, "Investigation of field-installation effects of horizontal twin-jet grouting in Shanghai soft soil deposits," *Canadian Geotechnical Journal*, vol. 50, no. 3, pp. 288–297, 2013.
- [37] Z.-F. Wang, S.-L. Shen, C.-E. Ho, and Y.-S. Xu, "Jet grouting for mitigation of installation disturbance," *Proceedings of the Institution of Civil Engineers—Geotechnical Engineering*, vol. 167, no. 6, pp. 526–536, 2014.
- [38] Z.-F. Wang, S.-L. Shen, G. Modoni, and A. Zhou, "Excess pore water pressure caused by the installation of jet grouting columns in clay," *Computers and Geotechnics*, vol. 125, Article ID 103667, 2020.
- [39] G. Modoni, P. Croce, and L. Mongiovi, "Theoretical modelling of jet grouting," *Géotechnique*, vol. 56, no. 5, pp. 335–347, 2006.
- [40] C. E. Ho, "Fluid-soil interaction model for jet grouting," in *Proceedings of the Grouting for Ground Improvement: Innovative Concepts and Applications*, Geotechnical Special Publication No. 168, American Society of Civil Engineers (ASCE) Press, pp. 1–10, Denver, CO, USA, February 2007.
- [41] A. Flora, G. Modoni, S. Lirer, and P. Croce, "The diameter of single, double and triple fluid jet grouting columns: prediction method and field trial results," *Géotechnique*, vol. 63, no. 11, pp. 934–945, 2013.
- [42] S.-L. Shen, Z.-F. Wang, J. Yang, and C.-E. Ho, "Generalized approach for prediction of jet grout column diameter," *Journal of Geotechnical and Geoenvironmental Engineering*, vol. 139, no. 12, pp. 2060–2069, 2013.
- [43] M. Ochmański, G. Modoni, and J. Bzówka, "Prediction of the diameter of jet grouting columns with artificial neural networks," *Soils and Foundations*, vol. 55, no. 2, pp. 425–436, 2015.
- [44] S.-L. Shen, P. G. Atangana Njock, A. Zhou, and H.-M. Lyu, "Dynamic prediction of jet grouted column diameter in soft soil using Bi-LSTM deep learning," *Acta Geotechnica*, 2020.
- [45] A. Verruijt, "Deformations of an elastic half plane with a circular cavity," *International Journal of Solids and Structures*, vol. 35, no. 21, pp. 2795–2804, 1998.
- [46] A. T. C. Goh and S. H. Goh, "Support vector machines: their use in geotechnical engineering as illustrated using seismic liquefaction data," *Computers and Geotechnics*, vol. 34, no. 5, pp. 410–421, 2007.
- [47] P. Samui, T. G. Sitharam, and P. U. Kurup, "OCR prediction using support vector machine based on piezocone data,"

- Journal of Geotechnical and Geoenvironmental Engineering*, vol. 134, no. 6, pp. 894–898, 2008.
- [48] S. K. Das, P. Samui, and A. K. Sabat, “Prediction of field hydraulic conductivity of clay liners using an artificial neural network and support vector machine,” *International Journal of Geomechanics*, vol. 12, no. 5, pp. 606–611, 2012.
- [49] H. Güllü, “A new prediction method for the rheological behavior of grout with bottom ash for jet grouting columns,” *Soils and Foundations*, vol. 57, no. 3, pp. 384–396, 2017.
- [50] J. Tinoco, A. Gomes Correia, and P. Cortez, “Jet grouting column diameter prediction based on a data-driven approach,” *European Journal of Environmental and Civil Engineering*, vol. 22, no. 3, pp. 338–358, 2018.
- [51] İ. F. Öge and M. Çırak, “Relating rock mass properties with Lugeon value using multiple regression and nonlinear tools in an underground mine site,” *Bulletin of Engineering Geology and the Environment*, vol. 78, no. 2, pp. 1113–1126, 2019.
- [52] S. Shiripour, I. Mahdavi, and N. Mahdavi-Amiri, “A nonlinear model for a capacitated stochastic transportation network using multiple linear regression,” *International Journal of Management Science and Engineering Management*, vol. 11, no. 4, pp. 252–261, 2016.
- [53] J. Xu, X. Zhao, Y. Yu, T. Xie, G. Yang, and J. Xue, “Parametric sensitivity analysis and modelling of mechanical properties of normal- and high-strength recycled aggregate concrete using grey theory, multiple nonlinear regression and artificial neural networks,” *Construction and Building Materials*, vol. 211, pp. 479–491, 2019.
- [54] P. Debnath and A. K. Dey, “Prediction of bearing capacity of geogrid-reinforced stone columns using support vector regression,” *International Journal of Geomechanics*, vol. 18, no. 2, Article ID 04017147, 2018.
- [55] C. Cortes and V. Vapnik, “Support-vector networks,” *Machine Learning*, vol. 20, no. 3, pp. 273–297, 1995.
- [56] Y. B. Dibikey, S. Velickov, D. Solomatine, and M. B. Abbott, “Model induction with support vector machines: introduction and applications,” *Journal of Computing in Civil Engineering*, vol. 15, no. 3, pp. 208–216, 2001.
- [57] P. Samui, “Support vector machine applied to settlement of shallow foundations on cohesionless soils,” *Computers and Geotechnics*, vol. 35, no. 3, pp. 419–427, 2008.

Research Article

Analysis and Monitoring of Small-Scale Rock Fracture Zone Deformation and Shaft Failure in a Metal Mine

Rong Lu ^{1,2}, Fengshan Ma ¹, Jie Zhao ², Jianbo Wang ², Guilin Li ² and Bing Dai ³

¹Key Laboratory of Shale Gas and Geoenvironment, Institute of Geology and Geophysics, Chinese Academy of Science, Beijing 100029, China

²Deep Mining Laboratory Subsidiary of Shandong Gold Mining Technology Co. Ltd., Jinan 250101, China

³Nuclear Resource Engineering College, University of South China, Hengyang, China

Correspondence should be addressed to Fengshan Ma; fisma@mail.iggcas.ac.cn

Received 26 May 2020; Revised 23 July 2020; Accepted 5 August 2020; Published 3 September 2020

Academic Editor: Wen-Chieh Cheng

Copyright © 2020 Rong Lu et al. This is an open access article distributed under the Creative Commons Attribution License, which permits unrestricted use, distribution, and reproduction in any medium, provided the original work is properly cited.

Rock fracture zones were distributed in a metal mine, and their deformation was always neglected because they are available on a small scale. However, the deformation of the small-scale fracture zone may lead to serious consequences, such as underground building and structure failure. Combined with the ground movement and surface fissure monitoring, the deformation of several fracture zones was analyzed by field monitoring, experimental test, and numerical simulation. The results showed that fracture deformation promoted the surface fissure movement. The horizontal movement of the foot wall rock of the fracture was found to be larger than the hanging wall rock. Deep mining engineering resulted in the squeezing of the shallow fracture, and the shallow fracture deformed more severely than the deep fracture. In the study area, fracture zone displacements were estimated according to a numerical model. The deformation and stress comparison of the shallow fracture zone and the deep fracture zone provided the characteristic of the broken structure in the field investigation.

1. Introduction

The cut and backfill mining technology has been used in many metal mines with rapid progress. Initially, it was generally believed that the cut-and-fill mining method could effectively control the ground pressure and prevent the development of ground deformation and ground fissure [1–3]. However, some metal mines that used this mining method observed ground fissure and ground subsidence phenomenon during mining over the decades. Although backfill provides support to the surrounding rock mass and restrains its deformation, the mining also induces the rock mass movement and ground subsidence.

For the study of the rock mass movement and ground subsidence, Fengshan et al. set the monitoring network to record the ground movement in the Jinchuan mine and analyzed the monitoring data and confirmed a subsidence center [4]. For studying the subsidence evolution in the metal mine, Xin et al. analyzed the frequency-size

distribution of ground movement evolution [5]. Rong et al. combined monitoring points and underground backfill to analyze the rock movement influenced by the backfill deformation [6].

Besides ground subsidence, mining engineering also induced the major fault reactivation in the mining area. Haijun et al. studied F16 in the reactivation and deformation of the Jinchuan mine [7]. Kuo et al. investigated the fault movement induced by mining stope roof deformation in the mining process [8]. Researchers have paid attention to the deformation of the open-pit rock after the transition to underground mining [9–14]. It has become an important research area to explore the fault reactivation caused by excavation. Some researchers have also studied the patterns of the differential settlement result from the fault in the mining situation [15–19].

The rock mass movement in the mine could lead to some damages to shafts, buildings, roads, and other facilities. Islam and Sherman evaluated the building damage

influenced by the fault reactive caused by excavation [19]. The mechanism of the rock mass movement influenced by the fault was studied, and the reasons of ground fissures that occurred were analyzed.

Based on the above studies, the ground subsidence centers are found to be located on the hanging side of the ore body in the mine. The rock mass of the hanging wall can more easily move as compared to the foot wall. It was concluded that the foot wall rock mass is stable. Based on this concept, some mining facilities, structures, and buildings were set on the foot wall area in the mine. However, the rock mass in the foot wall contains some rock fracture zones with a small-scale and slow inclination. Some fracture zones were found to be severely broken. The mining influence of rock fracture zones was more obvious with an increase in the mining depth. The deformation of fracture zones resulted in some broken buildings and structures in the mining area. So, the rock fracture zones in the deformation and movement of the foot wall area are also considered vital in mining engineering.

2. Background of the Study Area

2.1. Overview of the Study Area. In China, the Jinchuan mine is the largest nickel mine. The mine deposit is about 6,500 m long, 200 m wide, and over 1,000 m deep, as shown in Figure 1(a). The native ore-bearing rocks are divided into four independent fields due to the major faults, as shown in Figure 1(b). The major study area in this article is the No.1 ore body attributed to the No.2 mining zone.

The backfill mining method helped in maintaining the overall stability of the Jinchuan mine during mining over the decades. However, ground subsidence and overlying rock mass movement occurred. The first fissure was observed in 2001, and in the same year, the monitoring points were set for the monitored displacement period. After nearly two decades of monitoring work, the subsidence center was found that was located in the hanging wall rock mass. The displacements of the hanging wall rock mass were found to be larger than the foot wall rock. The foot wall rock was observed to be basically stable. So, some structures were built in the foot wall area. However, the ventilating shaft located in the foot wall area was damaged. Investigation showed that the shaft went through several rock fracture zones. The deformation of the fracture zones resulted in the shaft damage.

2.2. Rock Fracture Zones and Ventilating Shaft Situation. The rock fracture zones were distributed in the profile of exploration line-14, and the surface elevation of exploration line-14 is approximately 1730 m. The profile map is shown in Figure 2. In this profile, more than five fracture zones were investigated, and the ventilating shaft went through these zones. From shallow to deep, the burial depths of these fracture zones are as follows: the burial depths of fracture zone 1 are -150 to -200 m (the corresponding elevation is 1580 m to 1530 m); the burial depths of fracture zone 2 are -220 to -280 m (the corresponding elevation is 1510 m to

1450 m); the burial depths of fracture zone 3 are -370 to -400 m (the corresponding elevation is 1360 m to 1330 m); the burial depths of fracture zone 4 are -480 to -530 m (the corresponding elevation is 1250 m to 1200 m); and the burial depths of fracture zone 5 are -580 to -630 m (the corresponding elevation is 1150 m to 1100 m). All these fracture zones are available in a small scale. Some fracture zones are gently inclined. The ventilating shaft was repaired after damage, and two cracks were observed on the wall of the shaft.

The major failure part was located on -170 m of the ventilating shaft. The shaft is seated in the scope of the depression induced by the underground mining, and displacement of the rock mass keeps increasing. The rock mass movement, rupture, and fall are the primary forms of the shaft deformation, and the fracture effects will be aroused again in the future under the present circumstances of mining. For the ventilating shaft, the rock rupture in the shallow part is more serious than the deep part.

3. Analysis of Ground Subsidence and Fissures in Exploration Line-14

For the problem of ground subsidence and fissures, 124 monitoring points were set, which gradually covered the entire mining area in 2001. The monitoring period was half a year. Based on the monitoring data, the characteristics of the ground subsidence and fissures of exploration line-14 were analyzed.

3.1. Ground Subsidence Analysis of Exploration Line-14. The monitoring work was performed for almost 20 years, and the subsidence basin evolved gradually. The distribution of the monitoring points is shown in Figure 3(a). The subsidence center is 340 m away from the ventilation shaft on exploration line-14 and 130 m away from the projection of the ore body on the surface. Monitoring point 1407, as the subsidence center, recorded the maximum vertical displacement (Figure 3(a)). The subsidence center was found on the hanging wall rock mass, which was located in exploration line-14 (point 1408 and point 1409). The cumulative settlement is over 3478.4 mm. The subsidence displacements of the hanging wall rock mass were about two or three times larger than the foot wall rock. Almost all displacement vectors of monitoring points were pointing to the direction of the mined-out area. Currently, only a subsidence center was determined on the ground. The rock mass of exploration line-14 moved strongly. The major reason of ground subsidence and overlying rock mass movement is large-scale stress adjustment, and redistribution resulted in the elastic-plastic deformation of the surrounding rocks and squeezing of the filling body.

Figure 3(b) shows the vertical displacement of points set in exploration line-14 from 2001 to 2017. Three points were located in the foot wall side and the upper part of rock fracture zones: point 1401, point 1402, and point 1403. The vertical displacement increased slowly in the initial monitoring of the foot wall rock (1401–1403). In the past five

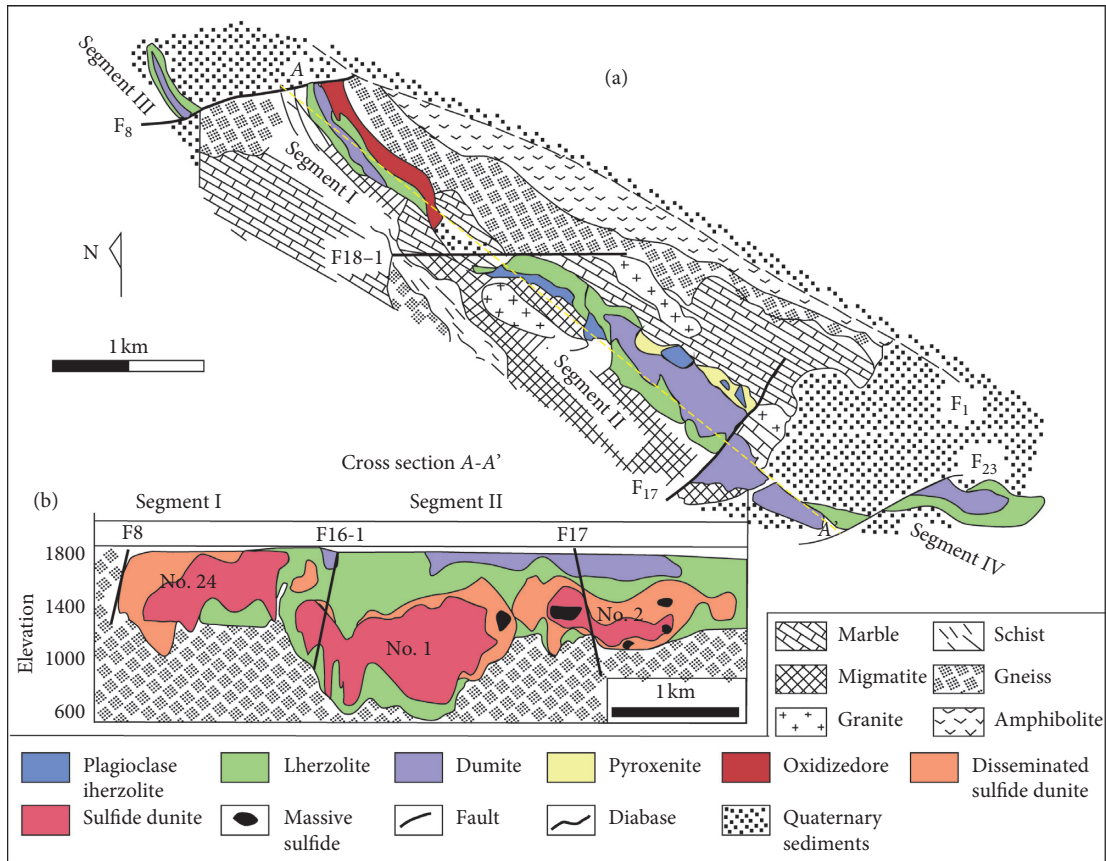


FIGURE 1: Geological map of the study area: (a) the main tectonic units of the Jinchuan mine; (b) simplified geological map and a cross section of the Jinchuan mine.

years, the cumulative curve of vertical displacements with relatively steep slopes showed that the increase rate of the vertical displacement was larger. For every curve of vertical displacement, the displacement changed slowly in the 1401–1404 area. Figure 3(c) shows horizontal displacements of monitoring points. The rock of 1402–1405 has moved strongly. The deformation of the rock fracture zones resulted in the large horizontal displacement in the foot wall rock.

3.2. *Fissure Characters in Exploration Line-14.* Besides ground subsidence monitoring, fissures in the mining area were also monitored, periodically. The distribution of fissures is shown in Figure 4(a). Fissure F011-F012 was located in the upper part of rock fracture zones. The deformation of fissures is shown in Figures 4(b)–4(d). From investigation, the integrity of the rock mass in fissure F001-F002 and fissure F091-F092 is found better. So, the deformation of fissure F001-F002 and fissure F091-F092 is considered as the control group for fissure F011-F012 analysis. Fissure F091-F092 located was on the hanging wall rock, and fissure F001-F002 and fissure F011-F012 were located on the foot wall rock. For every fissure, two points (#1 and #2) were set in relative positions in two sides of the fissure, as shown in Figure 4(a).

The curve of the relative tensile deformation of fissures is shown in Figure 4(b). Fissure F011-F012 deformed in the

stretching phase. On the contrary, fissure F001-F002 deformed in the closed phase. The tensile deformation indicates fissure stress to some degree. So, the major stress of fissure F011-F012 on the ground surface was tension stress.

The horizontal relative displacement showed rupture deformation along the fissure strike direction under shear stress. The horizontal displacements of fissure F011-F012 and fissure F001-F002 were found to be less than fissure F091-F092. So, the horizontal displacement of the hanging wall rock fissure is found to be larger than the foot wall rock fissure. The ground shear stress of fissure F011-F012 was small. The relative vertical displacement of fissures is shown in Figure 4(d). The relative vertical displacement equals displacement -#2 subtracted displacement -#1 in each fissure. The vertical displacement of points located near the ore-body side is found to be larger than the another side. The vertical displacement of fissure F011-F012 was the largest due to the influence of underground rock fracture zones.

4. Experimental Test of Soft Material

The simulation test of soft material was used to analyze the mechanism of rock fracture zone deformation influenced by mining engineering. The soft material test was applied in studying different issues, such as landslide deformation, open-pit slope tumbled, and rock mass movement in the mining area [20–24]. The advantage of the soft material

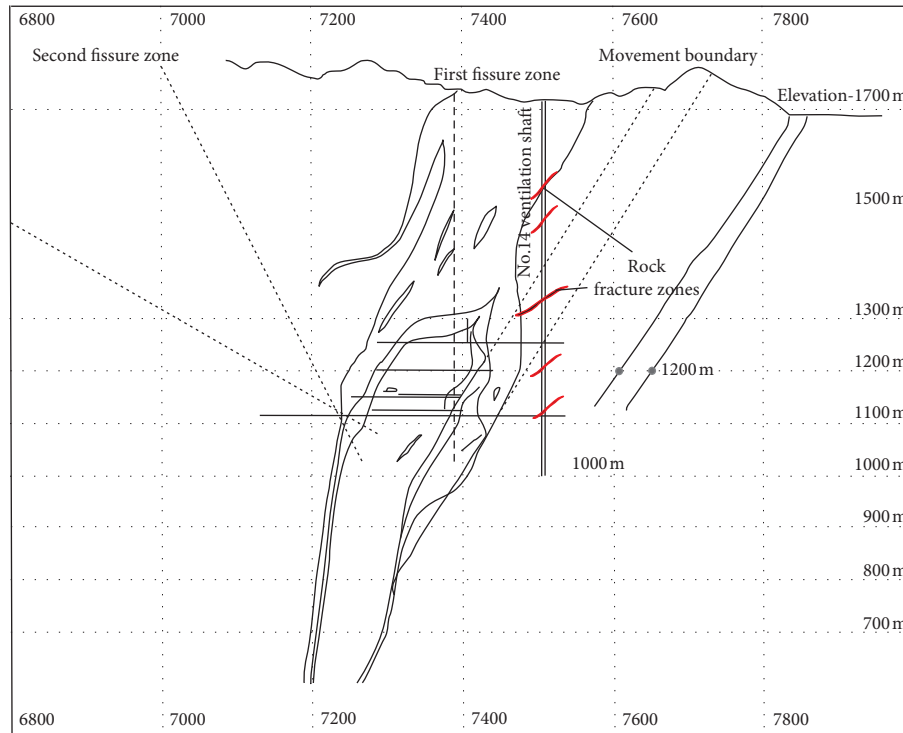


FIGURE 2: Sketch map of the exploration line-14 profile.

experiment is that it is conducted under self-weight stress conditions for rock deformation analysis in the mining area. The model demonstrated the relative positions of fracture zones, mining area, and overlying rock mass. The essential characteristics of the deformation of the fracture zones and the movement of overlying rock mass were analyzed by this soft material test. The empty area of the test model represents the upper-part ore-body mining (corresponding elevation is 1334–1280 m), and the mining area has been simplified.

4.1. Experiment Material and Procedure. The experimental model used synthetic, soft, and elastic-plastic material for the test, as shown in Figure 5. The experimental model used the vertical mold by two glass sheets with a fused mixture. The mixture was made of gelatine, glycerine, and water in proportions of 1 : 6 : 8 by weight. The elastic modulus of the solidified fused mixture was 0.01 MPa, and the Poisson ratio was about 0.4. The fused mixture was solidified in two days at room temperature, then the framework was laid flat, and finally, glass sheets were removed. The rock fracture zone and monitoring points were set, and the origin positions were labeled on the glass sheet. After this process, the designed excavation was cut. Then, deformation was observed under only self-weight stress conditions by reinstalling the glass sheets and restanding the model.

4.2. Deformation of the Rock Fracture Zone. The deformation of nodes of the physical experiment was handled by software, and the vectors of node displacement are shown in Figure 6(a). The relative displacements of the hanging wall

rock and the foot wall rock of the fracture zone (labeled by white box) are shown in Figures 6(b) and 6(c).

The deformation of the rock fracture zone in the model was mainly vertical compression. The value of the vertical displacement was found to be larger than the horizontal displacement. By comparing two sides of fracture zone deformation, horizontal displacements of the hanging wall rock were found to be smaller than the foot wall rock. However, vertical displacements of the hanging wall rock were found to be larger than the foot wall rock.

Four layers of the rock stratum displacement are analyzed in Figure 7. Layer-8 rock stratum located below the mining section occurred during floor heaving in the central part of the rock stratum. The vertical displacement decreased from layer-1 to layer-8. The vertical displacement of nodes located between the mining area and the fracture zone (labeled by the red line in Figure 7) resulted in a slight mutation caused by mining and the compression of the fracture zone. The compression of the fracture zone and mining work resulted in the ground tensile fissure, as shown in Figure 5. These physical models analyzed the mechanism and characteristics of deformation and movement of the fracture zone. Combined with the ground monitoring data, the characteristics and mechanism could provide some explanations for the situation in the field to some degree.

5. Numerical Simulation Analysis

5.1. Numerical Simulation Model Parameters. The simulation model was developed by the finite element method for analyzing the deformation of small-scale rock fracture zones located in the foot wall rock mass. According to the situation

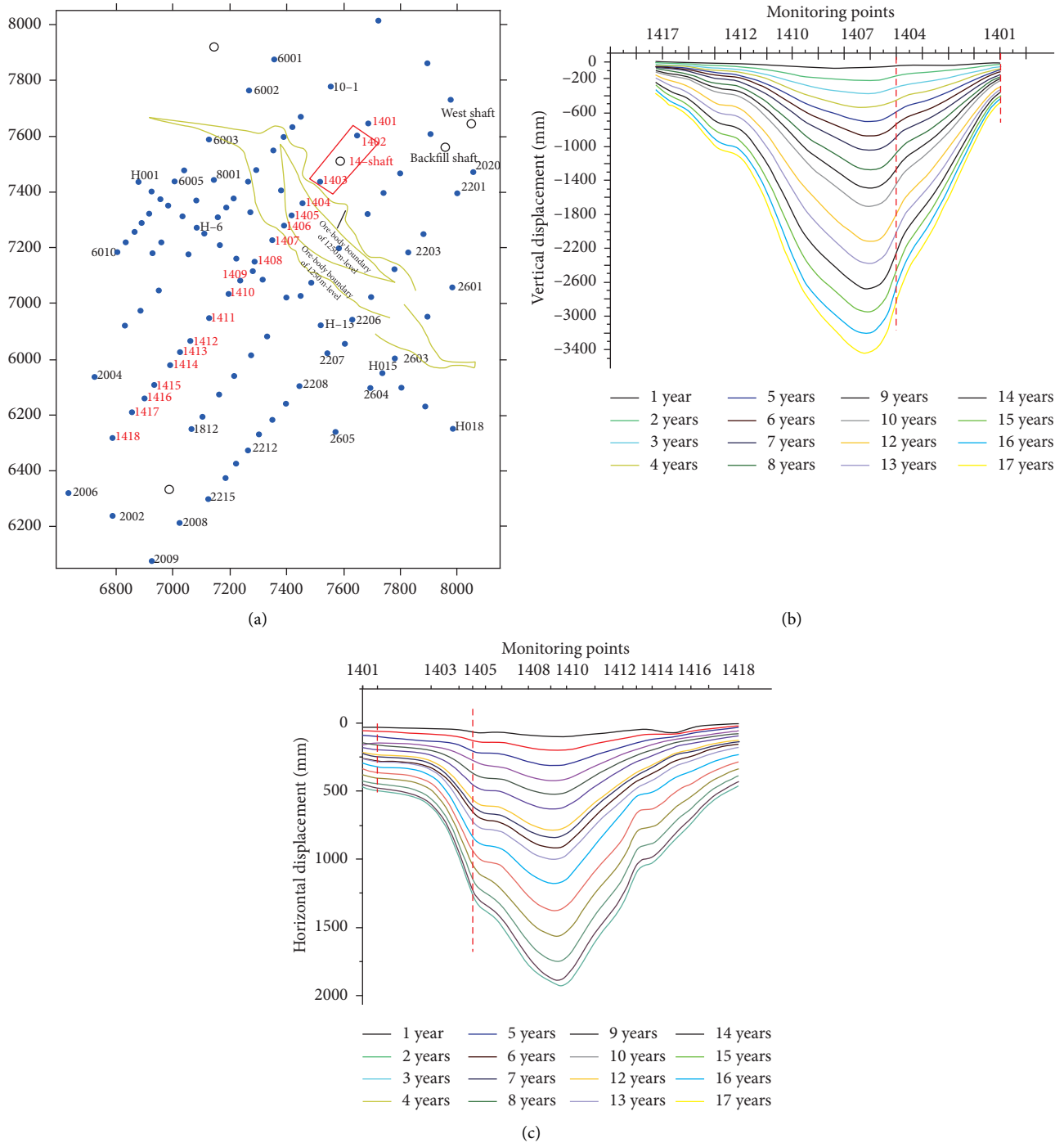
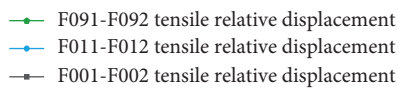
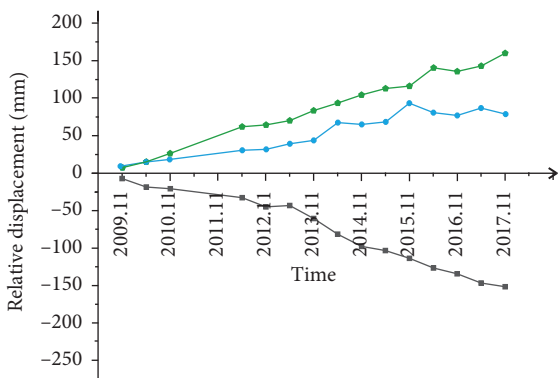
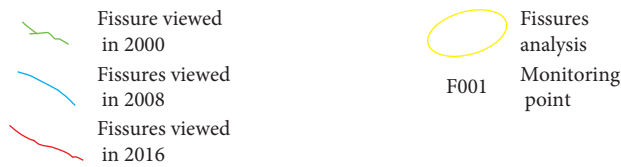
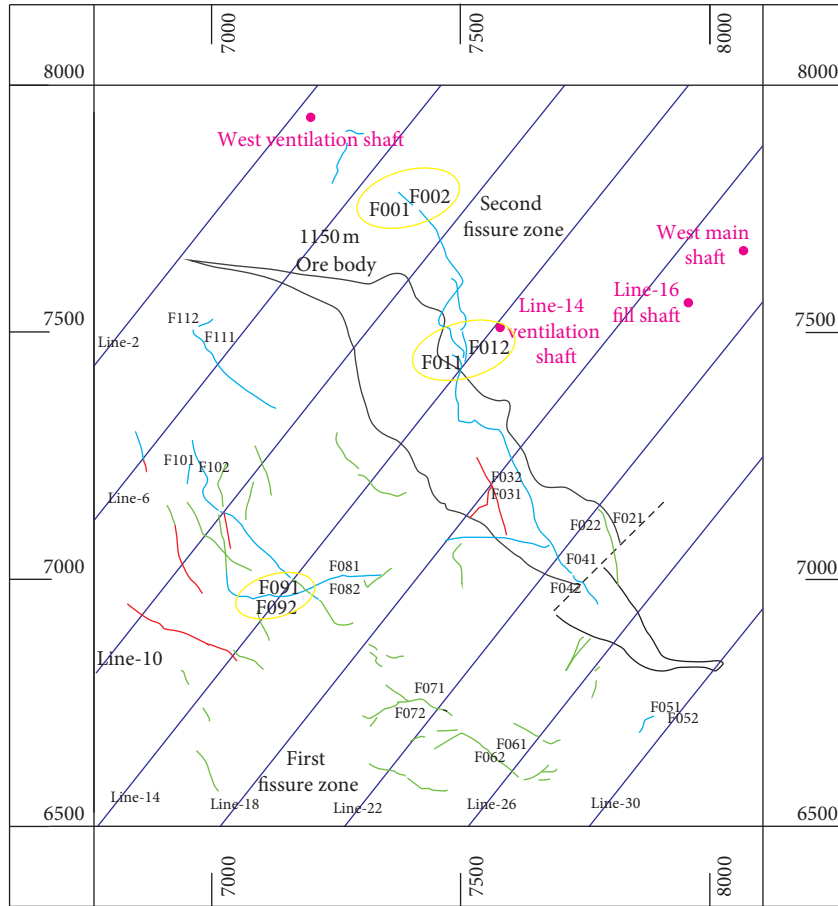


FIGURE 3: Distribution of monitoring points and the displacement of points set in exploration line-14: (a) monitoring point distribution; (b) vertical displacement of points set in exploration line-14; (c) horizontal displacement of points set in exploration line-14.

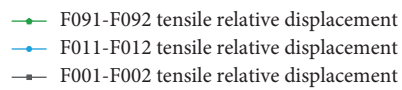
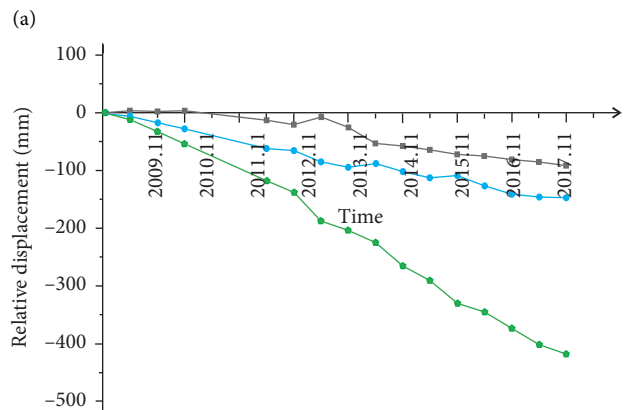
of the mining area, the development of the simulation model is shown in Figure 8.

The levels of the top layer and the first layer of the ore body were -100 m and -366 m . The surface elevation is approximately 1730 m , and the elevation of the first mining layer is 1334 m . The thickness of the mining level was set 50 m by practical mining engineering. In the simulation model, the total thickness of the ore body was 350 m ; finally, the thickness of backfill was 250 m . The distance of the ore-

body boundary to rock fracture zones was 100 m . In our investigation, five representative rock fracture zones were selected. These rock fracture zones were distributed from -180 m depth to -700 m depth. The numerical simulation model represents the area of the Jinchuan mine from -100 m to -750 m of the underground, and the corresponding elevation is 1600 m to 950 m , as shown in Figure 2. Numerical model parameters were set according to the test result of laboratory rock mechanics, as shown in Table 1.

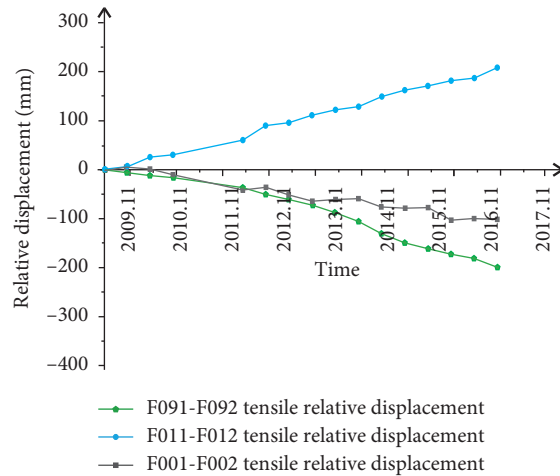


(b)



(c)

FIGURE 4: Continued.



(d)

FIGURE 4: Monitoring and displacement of fissures: (a) fissure monitoring distribution; (b) tensile relative displacement; (c) horizontal relative displacement; (d) vertical relative displacement.

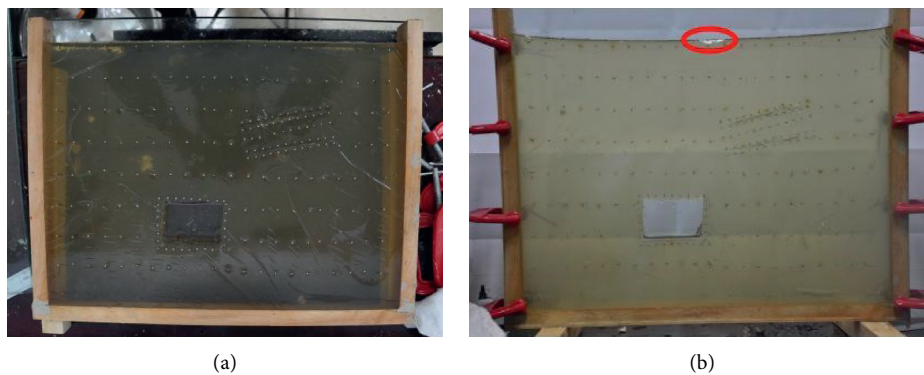


FIGURE 5: Soft material experimental model.

The ore body was downward mined by panels with a width of 50 m. Once excavation was completed within an access drift, the void was filled using backfill before the next access drift was excavated. After the last void was filled in one layer, mining work proceeded to the next layer. The horizontal stress coefficient was set as 1.5–2.

5.2. Validation of the Numerical Model. Three relative nodes, node 2952, node 5258, and node 5218, were distributed on the upper part of rock fracture zones in the numerical model. The corresponding ground monitoring points in the mining area are point 1402, point 1403, and point 14-well (point 1403 is located near the ore body, and point 14-well is located between point 1403 and point 1402; these three points have been labeled in Figure 3(a) by a red frame). Figure 9 shows vertical displacement rates and cumulative displacements in ground monitoring points. The vertical displacement of point 1403 was the largest, and the vertical displacement of point 1402 was the smallest.

Therefore, the vertical displacements of monitoring points decreased with an increase in the distance between

the point position and the ore body. In the numerical model, node 2952 was located near the ore body, and node 5318 was located between node 2952 and node 5258. The vertical displacement of numerical model points is shown in Figure 10. The maximum vertical displacement rate was -98 mm in field monitoring. The maximum value was -55 mm in the numerical model. The maximum value of the cumulative vertical displacement was -1650 mm in field monitoring. The maximum cumulative displacement was -1180 mm in the numerical model. The variation trend of displacements was consistent with field monitoring displacements. The numerical model was verified to some degree.

5.3. Stress and Deformation of the Rock Fracture Zones in the Numerical Model. In the numerical model, vertical displacements of four fracture zones (fracture zone-1 to fracture zone-4) are shown in Figure 11.

The maximum values of the vertical displacement of the hanging wall rock in four fracture zones were 1202.43 mm, 1099.18 mm, 1014.73 mm, and 630.959 mm, respectively.

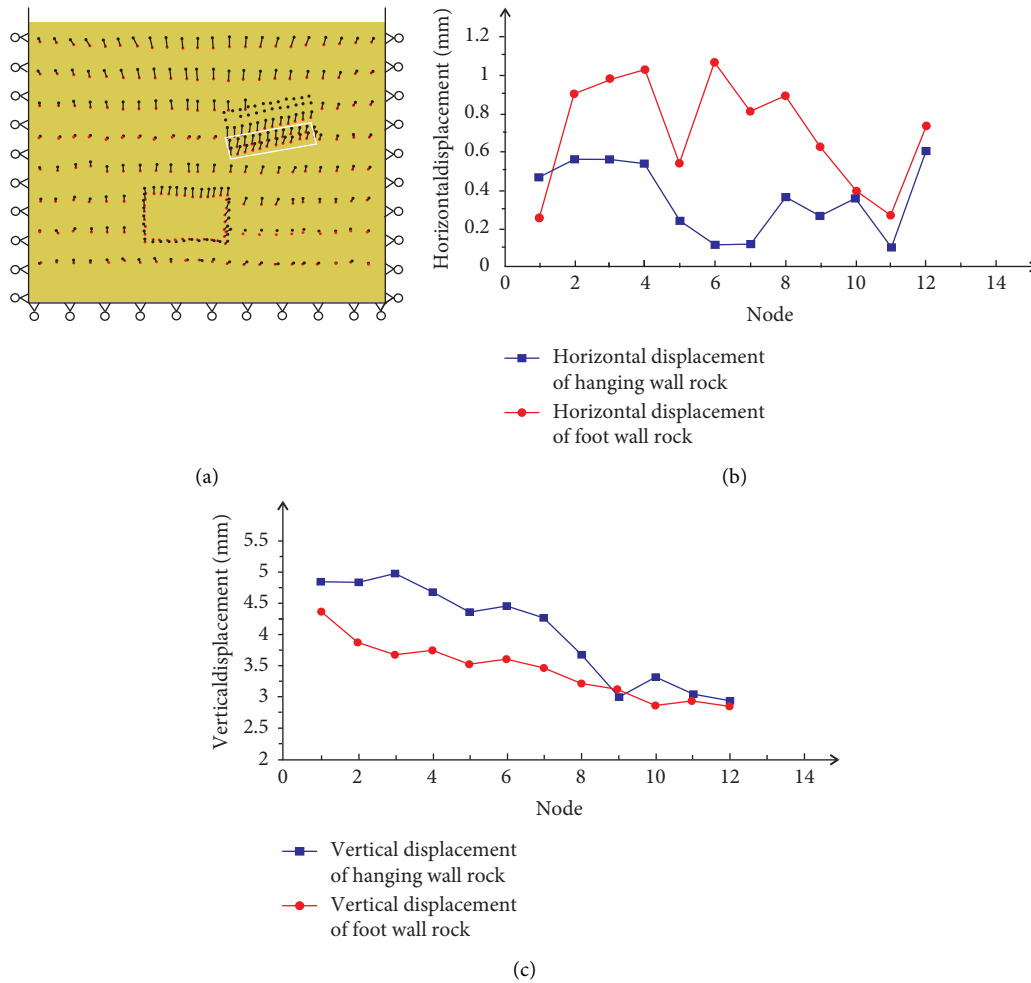


FIGURE 6: Physical experiment results using soft material: (a) deformation vectors of physical model nodes; (b) horizontal relative displacement; (c) vertical relative displacement.

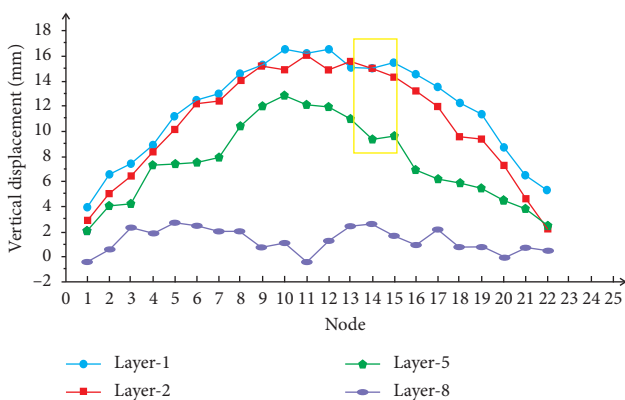


FIGURE 7: Vertical displacements of the rock stratum.

The maximum values of the vertical displacement of the foot wall rock were 1114.49 mm, 1021.84 mm, 815.098 mm, and 372.355 mm, respectively. Model validation showed that the numerical model results were slightly smaller than field monitoring. However, the results of rock fracture zones in the numerical model could represent the fracture

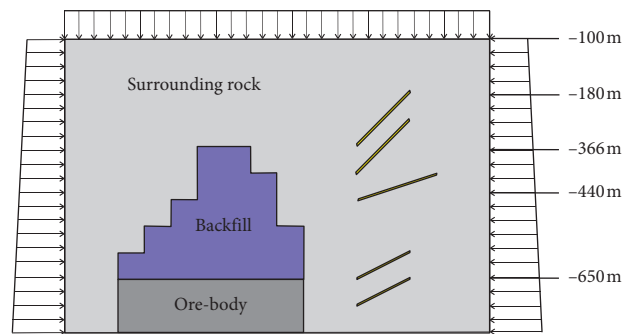


FIGURE 8: The sketch map of the simulation model.

deformation in the field mining area. The shallow fracture zone deformation of the hanging wall rock was about two times that of the deep fracture zone. However, the shallow fracture zone deformation of the foot wall rock was about three times that of the deep fracture zone.

For these rock fracture zones, the horizontal displacements were far smaller than vertical displacements, as

TABLE 1: Material parameters of the numerical model.

Material	Elastic modulus (GPa)	Poisson's ratio	Density (kg/m ³)	Friction angle (°)	Cohesion (MPa)
Surrounding rock	61	0.26	3200	56	14.5
Ore body	77	0.26	3000	56.5	18.2
Backfill	3.02	0.15	2700	49.3	0.87
Fracture zones	0.06-0.08	0.13	2000	35	—

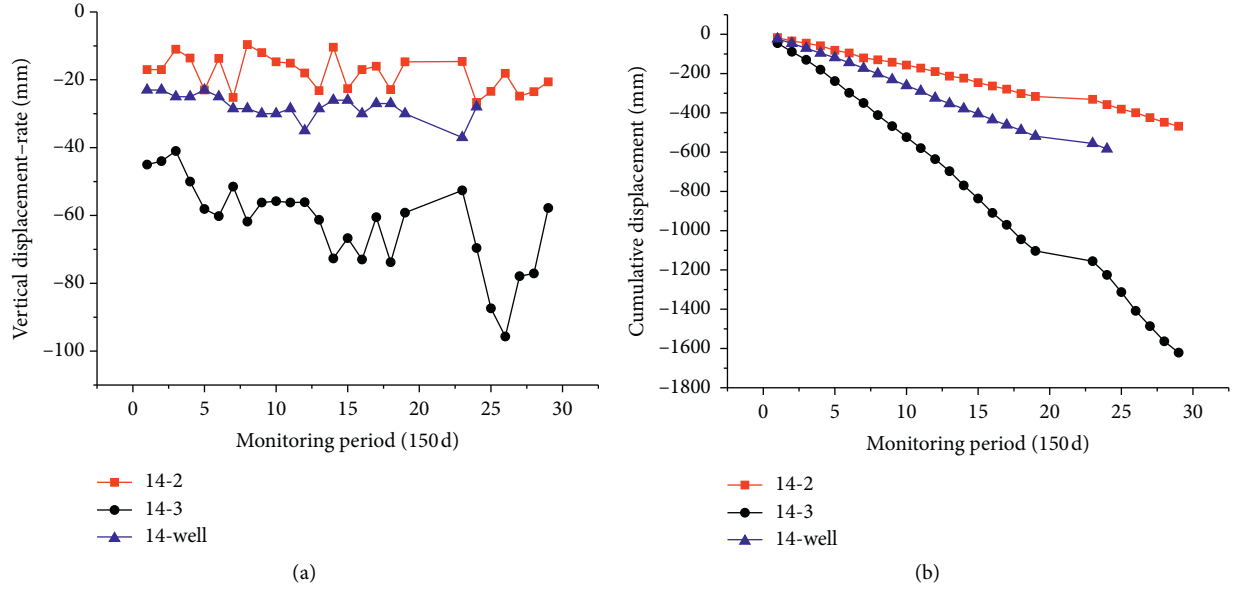


FIGURE 9: Displacements of field monitoring: (a) displacement rate; (b) cumulative displacement.

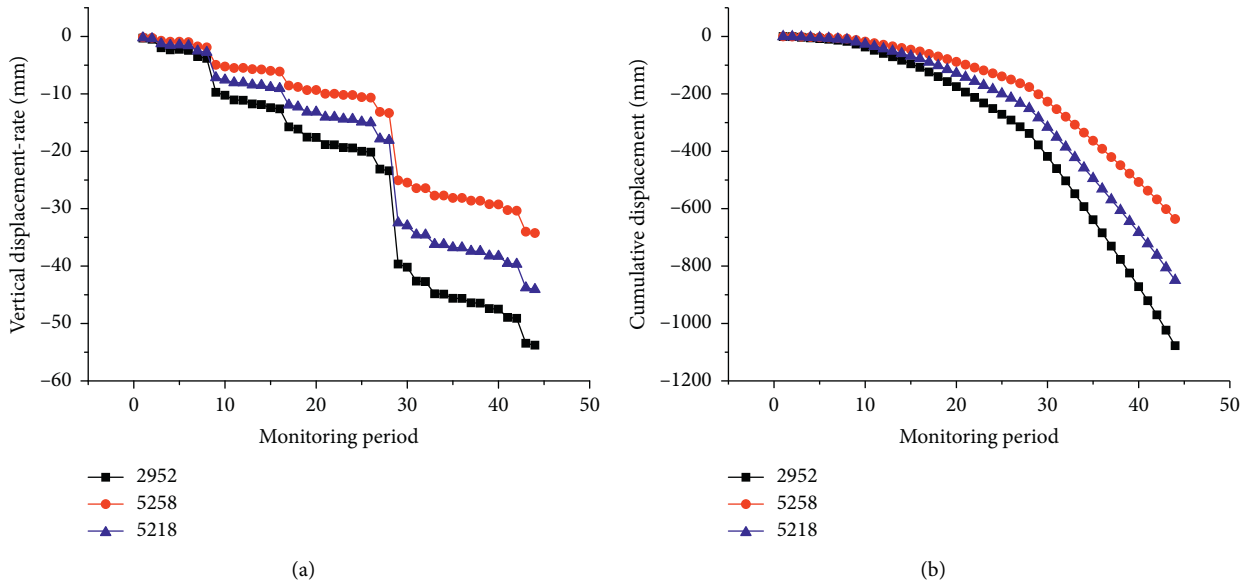


FIGURE 10: Displacements of the numerical model: (a) displacement rate; (b) cumulative displacement.

shown in Figure 12. Features of these fracture zones in horizontal deformation are different. The horizontal displacement of the hanging and the foot wall rock in fracture

zone-1 was the same as the physical model fracture zone deformation. However, for deeper fracture zones, horizontal displacements were moved in different directions.

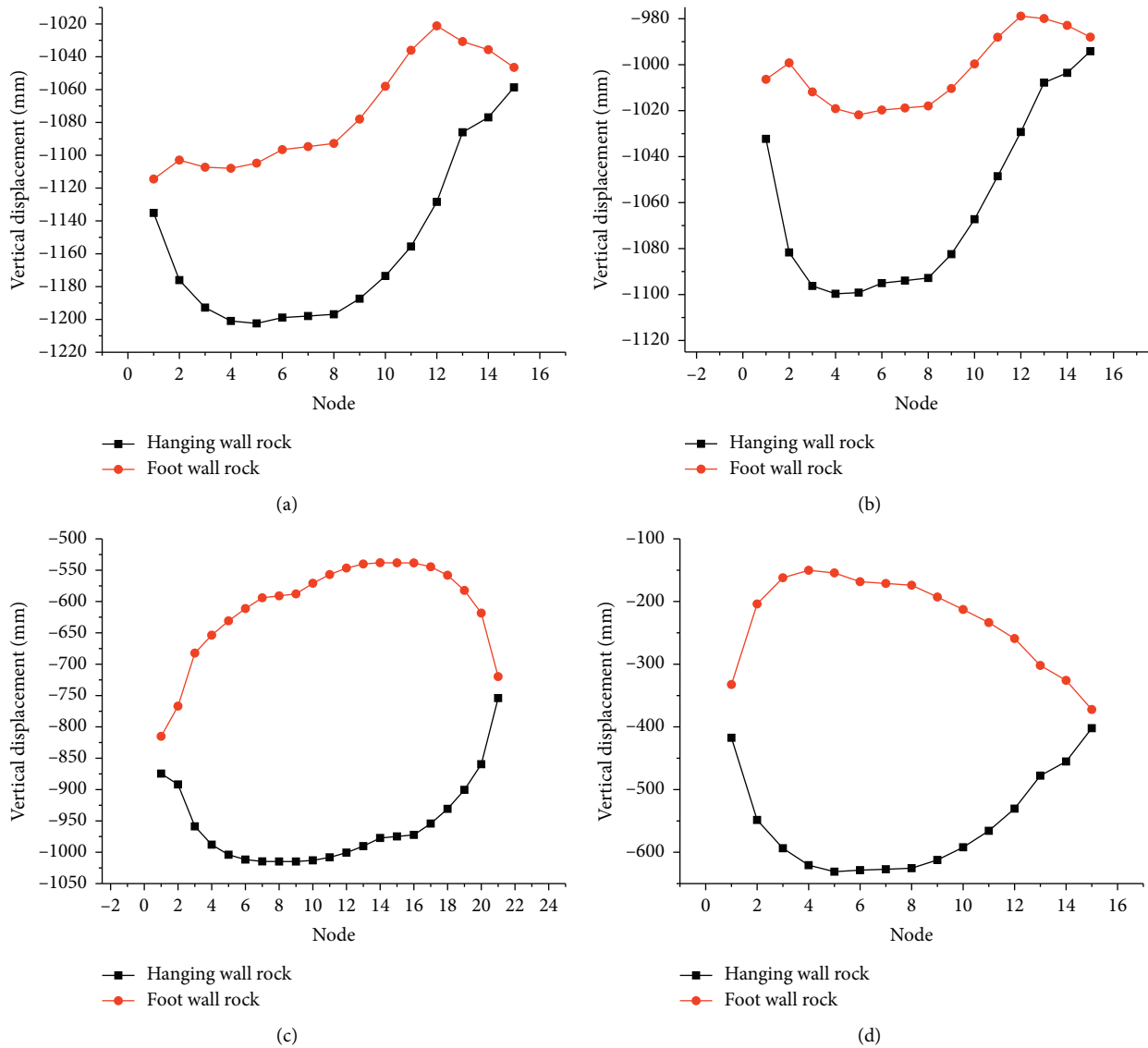


FIGURE 11: Vertical displacement of two sides of rock fracture zones in deep mining: (a) vertical displacement of fracture zone-1; (b) vertical displacement of fracture zone-2; (c) vertical displacement of fracture zone-3; (d) vertical displacement of fracture zone-4.

Basically, the foot wall rock was moved to the mining section, and the hanging wall rock was moved away from the mining section.

The difference of the effective stress for each node represents unbalance stress that influences the node movement. The shallow fracture zone deformation was larger than others, so the stress of rock fracture zone-1 located underground the shallow rock layer was analyzed in this part. Mining work, operated from the shallow layer to the deep layer in the underground, was divided into three phases according to the mining depth: mining in the shallow part, mining in the middle part, and mining in the deep part. Different mining phases resulted in different stress conditions for fracture zone-1. In Figure 13, blue labels represent the effective stress difference of the hanging wall rock, and red labels represent the effective stress difference of the foot wall rock. The effective stress differences of the foot wall rock

were found to be larger than the hanging wall rock in phases of mining in shallow and middle parts. However, unbalance stress distribution represented by the effective stress difference was totally changed in the deep mining phase, both the hanging and the foot wall rock. In the right part of fracture zone-1 stress curves, the unbalance stress changed sharply. This unbalance stress was the major reason for the movement of the fracture zone-1 rock.

5.4. Fracture Zone Deformation Analysis of the Hanging Wall Rock and the Foot Wall Rock. In the study area, underground rock fracture zone deformation has resulted in some structural damage. The mining depth increase induced to the movement and deformation of the surrounding rock. Figures 14 and 15 show the plastic deformation area distribution and the plastic strain vector distribution of rock

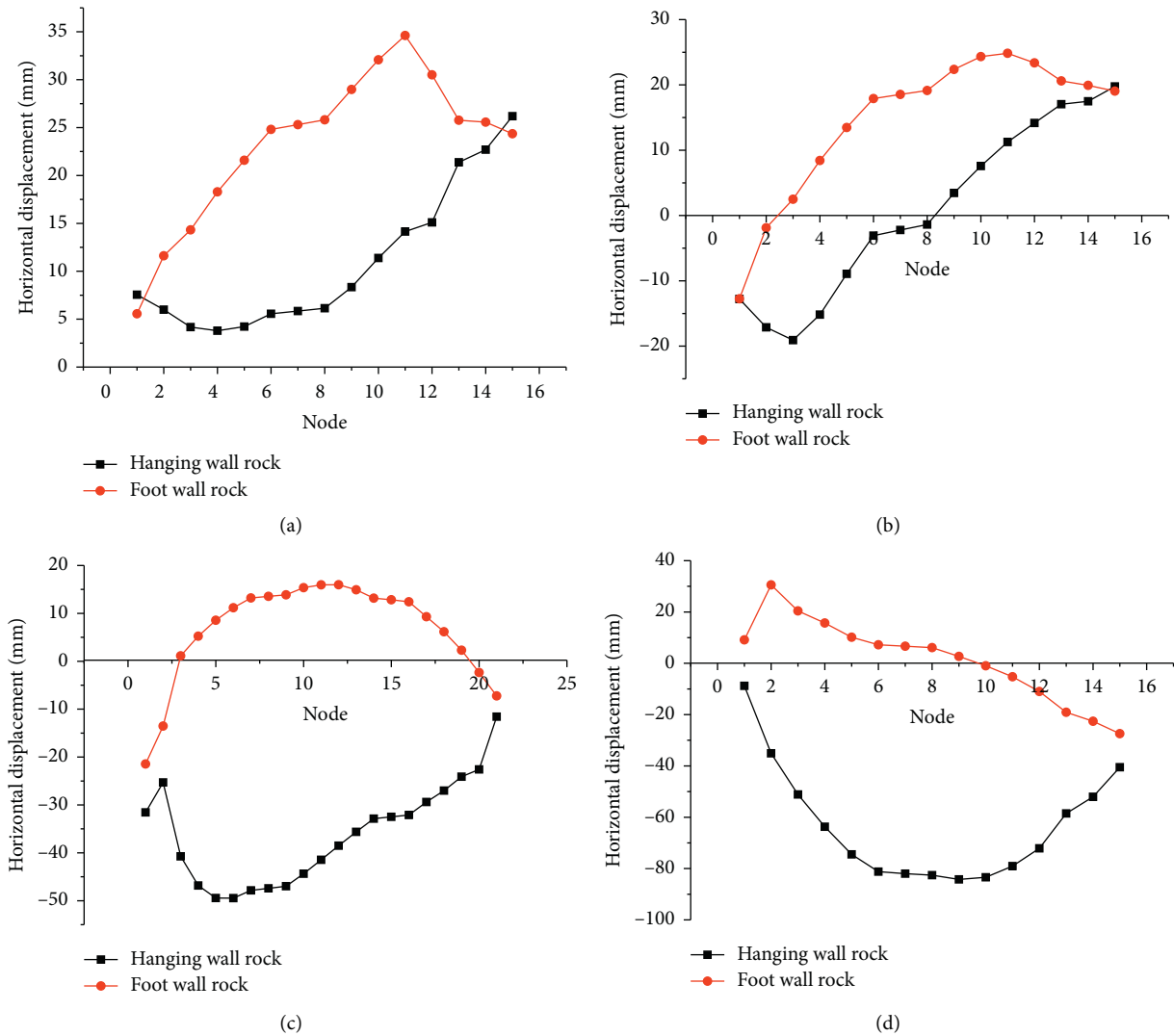


FIGURE 12: Horizontal displacement of two sides of rock fracture zones in deep mining: (a) horizontal displacement of fracture zone-1; (b) horizontal displacement of fracture zone-2; (c) horizontal displacement of fracture zone-3; (d) horizontal displacement of fracture zone-4.

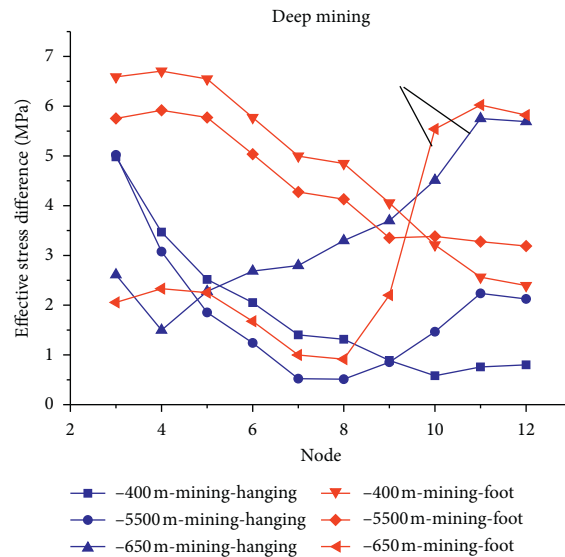


FIGURE 13: Curve of the effective stress difference in fracture zone-1 at different mining depths.

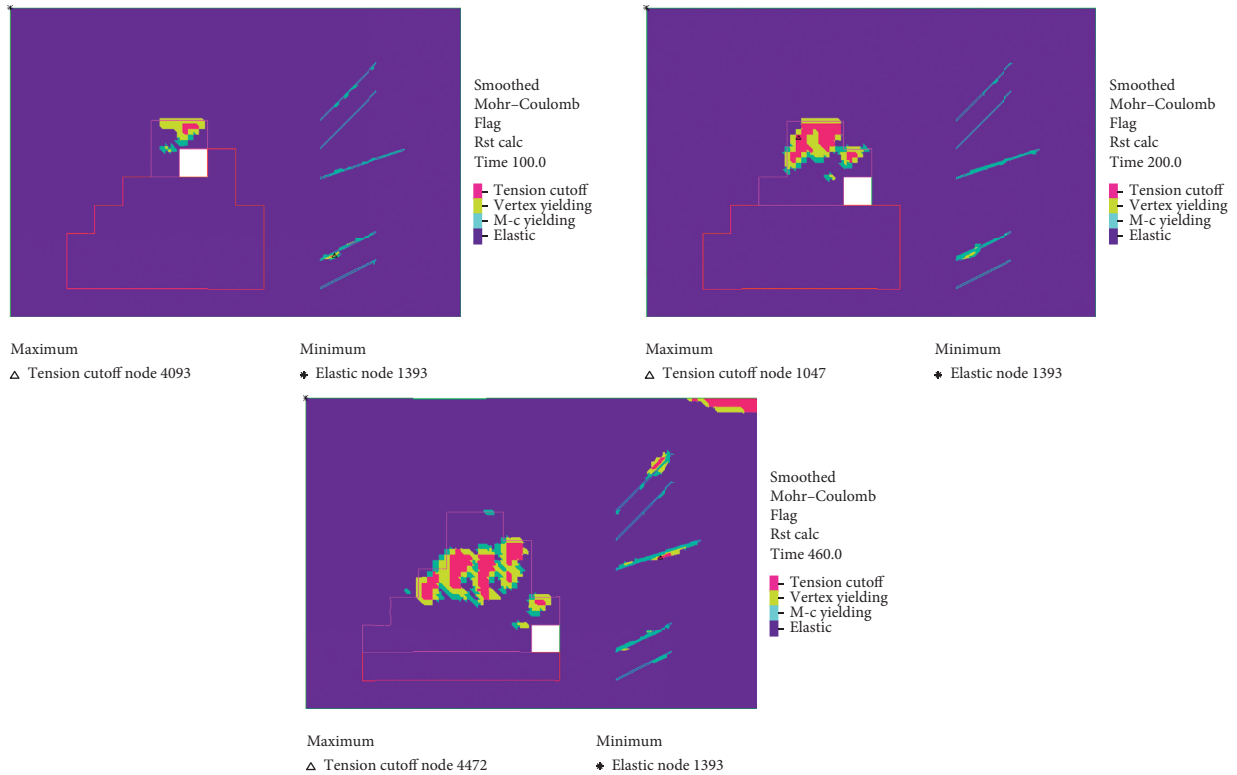


FIGURE 14: Plastic deformation distribution in the numerical model.

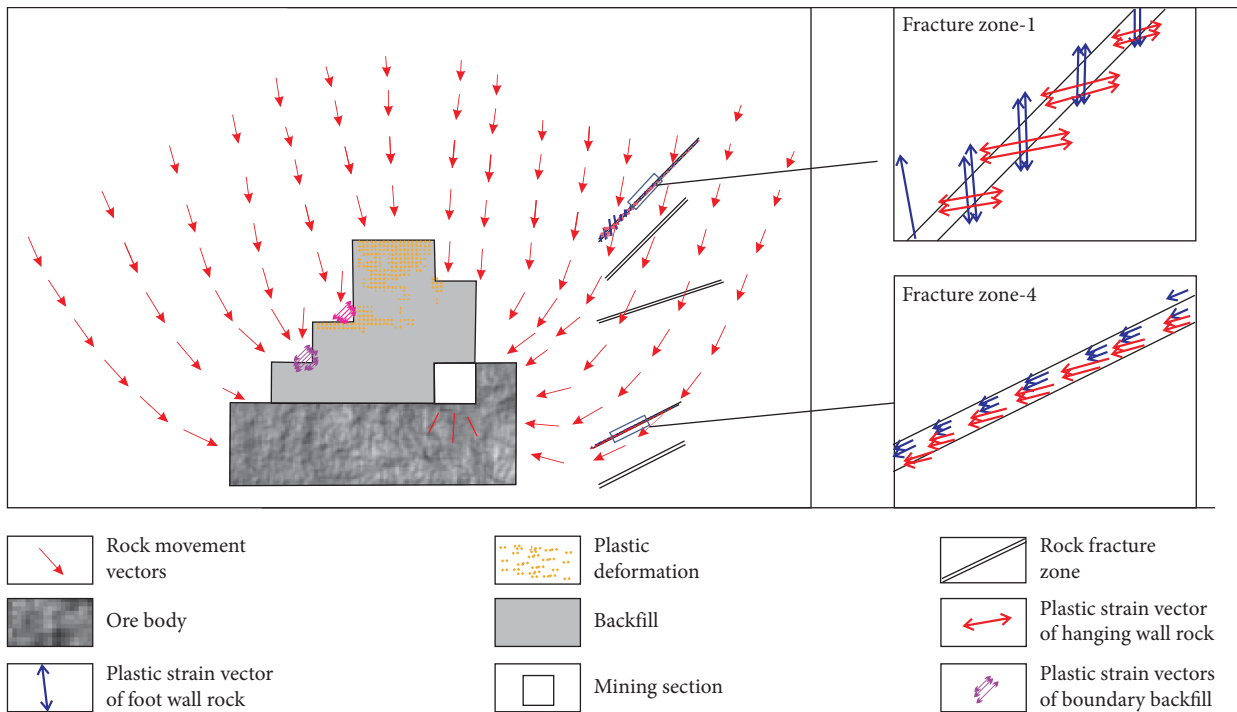


FIGURE 15: Plastic strain vectors of fracture zones and rock movement in the numerical model.

fracture zones in the deep mining phase. Typical fracture zones, fracture zone-1 and fracture zone-4, representing the shallow fracture and the deep fracture, respectively, were analyzed in this part. The plastic strain vectors of fracture

zone-1 were larger than fracture zone-4. So, the plastic deformation of the shallow fracture was larger than the deep one because the heavy vertical pressure of the deep fracture helps in stability. The vector direction indicates the trend of

rock movement. The plastic strain of fracture zone-4 vectors was found to be horizontal to both sides of the fracture. The rock of both sides of fracture zone-4 moved slightly and synchronously. However, characteristics of plastic strain vectors of fracture zone-1 were completely different.

The plastic strain of the hanging wall rock of fracture zone-1 vectors was found to be different from the foot wall rock. The vertical plastic strain vectors of the hanging wall rock of fracture zone-1 were dominated, whereas the plastic strain vectors of the foot wall rock were horizontal, caused by the horizontal tectonic stress. Fracture zone-1 deformed by the squeezing of the hanging wall rock.

As mentioned above, the ventilated shaft passed through these rock fracture zones. This shaft was damaged during the process of mining. The damaged area of the shaft concentrated on the scope of -165 to -220 m depth, and the deeper part of the shaft was found to be stable. Fracture zone-1 was matching to the location of the damaged zone. The damaged zone of the shaft was filled with a lot of waste rocks, which demonstrates that the rock mass of this zone was compressed.

Field monitoring and numerical simulation showed that mining engineering induced shallow fracture deformation, whereas the deep fracture was found to be relatively stable. The shaft was also damaged on the shallow part and would not cause multipart horizontal dislocation. The lower vertical stress and the heavy horizontal stress resulted in the large unbalance effective stress in the shallow part of the fracture zone. In addition, the overlying rock mass movement and the ground movement promoted the shallow fracture deformation. The vertical displacement of the shallow fracture zone increased the ground fissure tensile deformation.

6. Conclusion

The deformation of underground rock fracture zones was analyzed by field monitoring, physical experiment, and numerical simulation. The fracture deformation was broken structures in the mining area.

Field monitoring indicated features of the ground movement and the surface fissure deformation of the upper part of fracture zones. The vertical displacement increased slowly during the initial monitoring of the foot wall rock. The rock fracture zone deformation resulted in the large horizontal displacement in the foot wall rock. The major stress of the fissure located in the upper part of underground fracture zones was the tension stress. The vertical displacement of the fissure located in the upper part of underground fracture zones was large because of underground rock fracture zone deformation.

In the physical experiment, we studied the mechanism of underground fracture zone deformation induced by mining under self-weight conditions. The vertical displacement was found to be larger than the horizontal displacement in the whole model. The horizontal displacement of the foot wall rock of the shallow rock fracture zone was found to be larger than the hanging wall rock. The

vertical displacement of the fracture promoted ground fissure deformation.

Numerical simulation showed that the large unbalance effective stress in the shallow part of the fracture zone was compressed. Mining work showed that the shallow fracture deformed more severely than the deep fracture. The vertical displacement of the shallow fracture zone increased ground fissure tensile deformation.

Data Availability

The data used to support the findings of this study are included within the article.

Conflicts of Interest

The authors declare that there are no conflicts of interest regarding the publication of this paper.

Acknowledgments

The authors would like to express their sincere gratitude to the Jinchuan mine for their data support. This research was funded by the National Natural Science Foundation of China (Grant nos. 41831293, 41772341, and 41877274).

References

- [1] F. G. Bell, T. R. Stacey, and D. D. Genske, "Mining subsidence and its effect on the environment: some differing examples," *Environmental Geology*, vol. 40, no. 1-2, pp. 135–152, 2000.
- [2] G. Swift and D. Reddish, "Stability problems associated with an abandoned ironstone mine," *Bulletin of Engineering Geology and the Environment*, vol. 61, no. 3, pp. 227–239, 2002.
- [3] M. Alber, R. Fritschen, M. Bischoff, and T. Meier, "Rock mechanical investigations of seismic events in a deep longwall coal mine," *International Journal of Rock Mechanics and Mining Sciences*, vol. 46, no. 2, pp. 408–420, 2009.
- [4] M. Fengshan, Z. Haijun, Z. Yamin et al., "GPS monitoring and analysis of ground movement and deformation induced by transition from open-pit to underground mining," *Journal of Rock Mechanics and Geotechnical Engineering*, vol. 4, no. 1, pp. 82–87, 2012.
- [5] H. Xin, M. Fengshan, Z. Haijun, and X. Jiamo, "Monitoring and statistical analysis of mine subsidence at three metal mines in China," *Bulletin of Engineering Geology and the Environment*, vol. 78, pp. 3983–4001, 2019.
- [6] L. Rong, M. Fengshan, G. Jie, and Z. Haijun, "Monitoring and analysis of ground subsidence and backfill stress distribution in Jinchuan Mine, China," *Current Science*, vol. 115, no. 10, pp. 1970–1977, 2018.
- [7] Z. Haijun, M. Fengshan, Z. Yamin, and G. Jie, "Monitoring and analysis of the mining-induced ground movement in the longshou mine, China," *Rock Mechanics and Rock Engineering*, vol. 46, pp. 207–211, 2013.
- [8] D. Kuo, M. Fengshan, G. Jie, Z. Haijun, L. Rong, and L. Feng, "Investigation of the mechanism of roof caving in the jinchuan nickel mine, China," *Rock Mechanics and Rock Engineering*, vol. 51, pp. 1215–1226, 2018.
- [9] A. Vyazmensky, D. Stead, D. Elmo, and A. Moss, "Numerical analysis of block caving-induced instability in large open pit slopes: a finite element/discrete element approach," *Rock*

- Mechanics and Rock Engineering*, vol. 43, no. 1, pp. 21–39, 2010.
- [10] E. Bakhtavar, K. Shahriar, and K. Oraee, “Transition from open-pit to underground as a new optimization challenge in mining engineering,” *Journal of Mining Science*, vol. 45, no. 5, pp. 485–494, 2009.
- [11] N. D. Rose and O. Hungr, “Forecasting potential rock slope failure in open pit mines using the inverse-velocity method,” *International Journal of Rock Mechanics and Mining Sciences*, vol. 44, no. 2, pp. 308–320, 2007.
- [12] D. P. Adhikary and A. V. Dyskin, “Modelling of progressive and instantaneous failures of foliated rock slopes,” *Rock Mechanics and Rock Engineering*, vol. 40, no. 4, pp. 349–362, 2007.
- [13] M. Amini, A. Majdi, and Ö. Aydan, “Stability analysis and the stabilisation of flexural toppling failure,” *Rock Mechanics and Rock Engineering*, vol. 42, no. 5, pp. 751–782, 2009.
- [14] A. Carpinteri and M. Paggi, “Size-scale effects on strength, friction and fracture energy of faults: a unified interpretation according to fractal geometry,” *Rock Mechanics and Rock Engineering*, vol. 41, no. 5, pp. 735–746, 2008.
- [15] L.-g. Wang and X.-x. Miao, “Numerical simulation of coal floor fault activation influenced by mining,” *Journal of China University of Mining and Technology*, vol. 16, no. 4, pp. 385–388, 2006.
- [16] X. Li, S. J. Wang, T. Y. Liu, and F. S. Ma, “Engineering geology, ground surface movement and fissures induced by underground mining in the Jinchuan Nickel Mine,” *Engineering Geology*, vol. 76, no. 1-2, pp. 93–107, 2004.
- [17] L. J. Donnelly, “A review of coal mining induced fault reactivation in Great Britain,” *Quarterly Journal of Engineering Geology and Hydrogeology*, vol. 39, no. 1, pp. 5–50, 2006.
- [18] L. J. Donnelly, “A review of international cases of fault reactivation during mining subsidence and fluid abstraction,” *Quarterly Journal of Engineering Geology and Hydrogeology*, vol. 42, no. 1, pp. 73–94, 2009.
- [19] S. I. Sherman, “Natural triggers in violating the fault-and-block crust metastability in real time,” *Journal of Mining Science*, vol. 45, no. 5, pp. 438–451, 2009.
- [20] Z. Haijun, M. Fengshan, X. Jiamo, G. Jie, and Y. Guangxiang, “Experimental investigations of fault reactivation induced by slope excavations in China,” *Bulletin of Engineering Geology and the Environment*, vol. 73, pp. 891–901, 2014.
- [21] J. M. Xu, X. Li, and B. C. Han, “Original state of strain energy in a rock mass and its effect on excavation-induced displacement fields,” *International Journal of Rock Mechanics and Mining Sciences*, vol. 25, no. 12, pp. 2467–2474, 2006.
- [22] J. H. Zhang, Z. Y. Chen, and X. G. Wang, “Centrifuge modeling of rock slopes susceptible to block toppling,” *Rock Mechanics and Rock Engineering*, vol. 40, no. 4, pp. 363–382, 2007.
- [23] Z. X. Zhang, Y. Xu, P. H. S. W. Kulatilake, and X. Huang, “Physical model test and numerical analysis on the behavior of stratified rock masses during underground excavation,” *International Journal of Rock Mechanics and Mining Sciences*, vol. 49, pp. 134–147, 2012.
- [24] Q. Wu, M. Wang, and X. Wu, “Investigations of groundwater bursting into coal mine seam floors from fault zones,” *International Journal of Rock Mechanics and Mining Sciences*, vol. 41, no. 4, pp. 557–571, 2004.

Research Article

Study on the Large Deformation Characteristics and Disaster Mechanism of a Thin-Layer Soft-Rock Tunnel

Xiulian Zhang,^{1,2} Manchao He,^{1,2} Fengnian Wang,^{1,2} Gan Li,³ Shengxin Xu,⁴ and Zhigang Tao^{1,2}

¹State Key Laboratory for Geomechanics and Deep Underground Engineering, China University of Mining and Technology (Beijing), Beijing 100083, China

²School of Mechanics and Civil Engineering, China University of Mining and Technology (Beijing), Beijing 100083, China

³State Key Laboratory of Hydrosience and Engineering, Tsinghua University, Beijing 100084, China

⁴Deformation Survey Center, Yunnan Earthquake Agency, Kunming 650041, China

Correspondence should be addressed to Zhigang Tao; taozhigang@263.net

Received 20 May 2020; Revised 18 July 2020; Accepted 23 July 2020; Published 13 August 2020

Academic Editor: Wen-Chieh Cheng

Copyright © 2020 Xiulian Zhang et al. This is an open access article distributed under the Creative Commons Attribution License, which permits unrestricted use, distribution, and reproduction in any medium, provided the original work is properly cited.

In view of the large deformation of thin-layer soft rock in the No. 2 inclined shaft of the Muzhailing Tunnel, we performed an experimental investigation on the mineral composition, physical characteristics, and uniaxial compressive strength of the surrounding rock of the tunnel. The characteristics of the large deformation of the surrounding rock of the tunnel were analyzed, and the main factors influencing the deformation of the tunnel were revealed. The influence of various factors on the large deformation of the surrounding rock was analyzed using the 3DEC-Trigon discrete element numerical simulation method. The results show that (1) the deformation of the surrounding rock of the tunnel has remarkable asymmetry, the deformation of the initial support of the tunnel is significant, and the buried depth of the area where the maximum deformation of the tunnel exceeded 1 m is greater than 500 m; (2) the main factors influencing the deformation of a thin-layer slate tunnel include joint inclination, buried depth, water absorption, and softening of the surrounding rock; and (3) the maximum deformation of the surrounding rock is observed for a joint angle of 45°, at which the buried depth is directly proportional to the deformation and failure of the tunnel. Furthermore, after the surrounding rock was softened by water absorption, the floor of the tunnel, the left shoulder socket, and the right side of the tunnel are deformed greatly. The results of this study will provide a theoretical basis for the study of similar deformation control methods and supporting measures for tunnels excavated in thin-layer soft rock.

1. Introduction

The Muzhailing Tunnel in China is a critical control project along the Weiwu Expressway from Lanzhou to Haikou (G75), a national expressway. Because of its special geological conditions including deep burial, high ground stress, and a thin-layered slate structure, the tunnel deformation is extremely serious and has restricted the opening of the Weiwu Expressway. During the construction process, tunnel deformation and collapse occur frequently because of disturbance from excavation and the complex geological structure, seriously affecting the safety of the tunnel project [1–4]. Therefore, it is urgent to investigate the deformation mechanism of the surrounding rock of the thin-layered slate

tunnel to provide an important theoretical basis for support and control measures after future deformation of the surrounding rock.

Many researchers have investigated the deformation of deep-buried tunnels and have obtained useful findings [5–8]. In 1999, Brox and Hagedorn [9] studied the deformation characteristics of a tunnel crossing a fault along the Anatolian Highway in Turkey. The study revealed that structural stresses, weak surrounding rock, and stress concentrations after excavation were the main causes of the deformation of the tunnel. In 2000, Hoek and Marinos [10] identified through a study of rock and rock mass strength that rock mass strength and ground stress were the key factors affecting the stability of the surrounding rock of the

tunnel. In 2005, Liu et al. [11] studied the damage characteristics and causes of the large deformation of the Muzhailing Tunnel and suggested that the deformation and failure of the tunnel had serious, long-term and asymmetric characteristics. The deformation was found to be mainly caused by the plastic flow and expansion of the excavated unloaded surrounding rock under the combined action of lithology, groundwater, and ground stress field.

Apart from experimental investigations, many studies have numerically analyzed the deformation of deeply buried tunnels. In 2006, Meguid and Rowe [12] studied the deformation and stress distribution of the surrounding rock of a tunnel under different stress conditions by means of a three-dimensional numerical simulation method. Guo et al. [13] analyzed the anisotropy of the strength and deformation of layered surrounding rock through an experiment of basic mechanics and studied the deformation and failure mechanism of the highly stressed and steeply dipping layer of the Yangjiaping Tunnel by numerical analysis. Yu [14] in 2017 studied the deformation mechanism and control measures of the Shiziyuan Tunnel by means of theoretical analysis and on-site measurement and found that the main factors of the deformation were ground stresses, mechanical characteristics of surrounding rocks, type of tunnel-lining structure, and construction disturbance (blasting). In 2018, Cao et al. [15] analyzed the deformation and failure characteristics of the initial support of a typical weak tunnel, Dongshan Tunnel, and obtained the factors influencing the stability of surrounding rocks in the construction process. Sun et al. [16] in 2019 studied the application of a constant resistance large deformation anchor cable support system by performing a field test and numerical simulation. The results showed that the anchor cable effectively controlled the large deformation of the surrounding rock of the tunnel.

The above studies have revealed many beneficial findings on deep-buried soft-rock tunnels. However, there are few studies on the deformation and failure mechanisms of the surrounding rock in the complex engineering geological environment of the Muzhailing deep-buried thin-layered slate tunnel. The factors affecting large deformations of the surrounding rock and the degree of influence of each factor on the deformation of the surrounding rock of the tunnel are not adequately understood. Therefore, it is necessary to postulate relevant theories and perform numerical analysis.

This study considers the No. 2 inclined shaft of the Muzhailing Tunnel, investigating the deformation characteristics of the thin-layered slate tunnel by statistically analyzing the deformation of the tunnel under the original supporting conditions. Combined with laboratory experiments, the main factors affecting tunnel deformation are then analyzed. At the same time, the effects of different joint inclinations of the surrounding rock, buried depths, water absorption, and softening on the large deformation of the surrounding rock are analyzed by the 3DEC-Tragon numerical simulation method.

2. Project Overview

The Muzhailing Tunnel is located in the low and middle mountainous area of the West Qinling Mountains (Figure 1). It is located at the junction of several plates, crosses

the Muzhailing Watershed between the Zhanghe River and Taohe River and spans Zhangxian County and Minxian County of Gansu Province. The total length of the tunnel is 15.15 km, the maximum buried depth of the tunnel body is 629.1 m, and the minimum buried depth is 8 m. The tunnel is composed of three inclined shafts, of which the No. 2 inclined shaft is located in the Muzhailing Tunnel (middle section, red framed position in Figure 1). The starting and ending pile numbers are (z) K216 + 380 – (z) K220 + 300, and the length of the Muzhailing Tunnel is 3920 m. The opening of the No. 2 inclined shaft is located on the north side slope of Luzagou. The pile number in the main tunnel at its intersection with the inclined shaft is K218 + 400. The intersection angle with the main tunnel plane is 90°. For the inclined shaft, the starting pile number is K0 + 000 and the end pile number is K1 + 813 m, with the length of the shaft being 1813 m.

2.1. Formation Lithology Characteristics. According to the field investigation and exploration, the bank slope is covered with quaternary slope gravel and the underlying bedrock is the lower Permian slate. The main components of the surrounding rock are carbonaceous slate with local intercalations of sandstone, limestone, and shale. Quartzite is sporadically distributed in the rock formations, and the slate in this area is mainly grey-black. Joints are relatively developed, the rock mass is relatively broken, and the strength markedly decreases under the action of water-rock coupling. The surrounding geological structure largely affects the surrounding rock, and the whole area is essentially grade V rock.

2.2. Hydrogeological Characteristics. The distribution of groundwater was relatively uneven and was strongly related to the geological structure, lithology, and topography of the region. As the area was strongly affected by geological actions in the past, the joints and fissures in the area were well developed and the groundwater mainly was present in the form of fissure water. According to the geological survey, the valley area was relatively rich in water content and the water collection capacity was strong, so the water pouring was more serious when the tunnel passes through the area. Besides fissure water, karst water and Quaternary loose rock void water were encountered in this area.

2.3. Ground Stress Characteristics. According to previous studies [17–19], hydraulic fracturing was used to measure the ground stress at two measurement points: AK214 + 738 m and AK219 + 422.8 m, at test depths of 492.00 and 499.00 m, respectively. According to the test results, the stress condition was such that the horizontal maximum principal stress S_H was greater than the horizontal minimum principal stress S_h , which was greater than the straight principal stress S_v . The ground stress was mainly tectonic stress. The ratio of stress size to R_c in the Muzhailing Tunnel area is shown in Table 1.

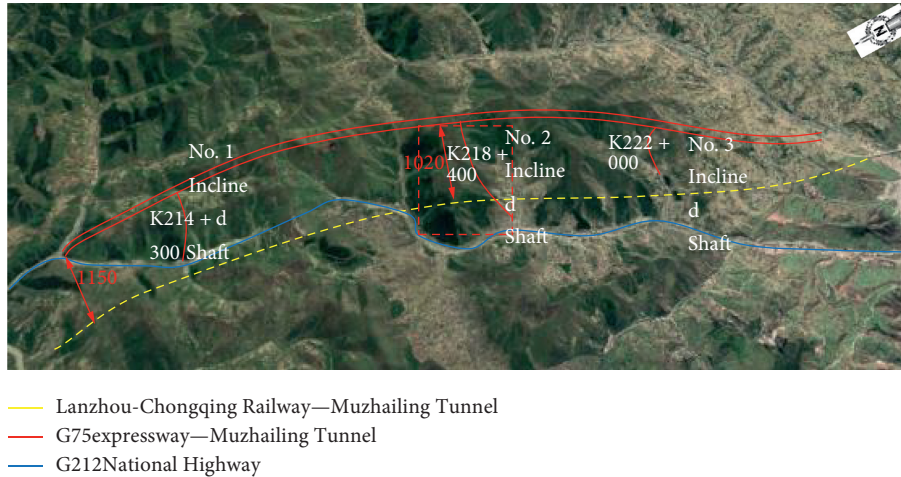


FIGURE 1: Location of the Muzhailing Tunnel and the no. 2 inclined shaft.

TABLE 1: Ratio of crustal stress to R_c in the Muzhailing Tunnel area.

No.	Measuring depth	S_H (MPa)	R_c (MPa)	R_c/S_H
1	250	11.37	20–30	1.76–2.64
2	270	12.14	20–30	1.65–2.47
3	300	11.37	20–30	1.76–2.64
4	320	14.93	20–30	1.34–2.01
5	365	14.84	20–30	1.35–2.02
6	370	17.98	20–30	1.11–1.67
7	397	16.28	20–30	1.23–1.84
8	427	18.76	20–30	1.07–1.60

According to the Standard for Engineering Classification of Rock Mass (GB/50218-94), $R_c/S_H < 4$ is extremely high stress, $4 < R_c/S_H < 7$ is high stress, and $7 < R_c/S_H$ is low stress. Table 1 shows that the value of R_c/S_H in the Muzhailing Tunnel is < 4 , which is categorized as extremely high ground stress. Moreover, the stratum rock mass is relatively broken and the possibility of large deformation in the surrounding rock of the tunnel is relatively high.

2.4. Properties of Rock Mass. The surrounding rock inclination angles and surrounding rock integrity of the No. 2 inclined shaft of the Muzhailing Tunnel in the large deformation area vary widely. The dominant joint angle is between 30° and 85° , and the thickness of the slate layer is 5–30 cm. To understand the mineral composition and mechanical properties of the slate, an X-ray diffraction experiment, a point-load experiment, and a uniaxial compression experiment were performed.

2.4.1. Mineral Composition Analysis. Six positions (pile number K1430/K1460/K1490/K1520/K1550/K1570) in the No. 2 inclined shafts of the Muzhailing Tunnel were selected as sampling points, and the selected carbonaceous slate samples were quantitatively analyzed by using a TTR III multifunctional X-ray diffractometer. The mineral composition and relative content of rock and clay were obtained as shown in Tables 2 and 3. A small difference was observed in

the mineral composition among the six groups, particularly in the quartz and clay minerals, which mainly included illite, chlorite, illite mixed layer, and kaolinite. The montmorillonite content was low, and the samples exhibited low water absorption and expansion.

2.4.2. Effect of Water on the Strength of Slate. Because of the fissured joints and severe weathering of the surrounding rock of the No. 2 inclined shaft of the Muzhailing Tunnel, the lithology is mainly carbonaceous slate with scattered sandstones. The rock samples were significantly affected by the disturbance during sample acquisition, and the processing of standard samples was found to be challenging. Therefore, a field point load intensity meter was selected for a rapid experimental analysis. During the selection of specimens, the integrity of the selected rock should be ensured (avoiding rocks with cracks). A total of 82 specimens of carbonaceous slate from K1740 to K1800 in the No. 2 inclined shaft were selected in the field, of which 41 specimens were tested for uniaxial compressive strength in the natural state, and the other 41 specimens were tested for uniaxial compressive strength after 24 hours of water absorption. The experimental results for the 82 specimens are shown in Figure 2.

The uniaxial compressive strength was estimated by the point-load method, and the average uniaxial compressive strength of the carbonaceous slate in the natural state was found to be 29.6 MPa. The average uniaxial compressive strength of the carbonaceous slate after water absorption for 24 hours was 12.7 MPa. The uniaxial compressive strength after water absorption was reduced by 57% when compared with the natural state.

2.4.3. Uniaxial Compressive Strength Test. Slate with visible joints was processed into standard $\Phi 50 \text{ mm} \times 100 \text{ mm}$ specimens. Specimens with 30° , 45° , and 60° bedding inclinations were tested for their uniaxial compressive strength by using a 2000 kN capacity mono-triaxial test system. This test revealed the influence of different joint surface

TABLE 2: Relative content of different minerals in the rock mass.

No.	Mineral content (%)						
	Quartz	Potash feldspar	Plagioclase	Siderite	Pyrite	Dolomite	Clay mineral
1	43.8	1.0	2.2	—	—	—	53.0
2	48.1	—	—	—	—	—	51.9
3	56.5	—	1.5	—	—	—	42.0
4	50.9	0.9	1.8	—	—	—	46.4
5	50.3	1.0	1.8	—	—	—	46.9
6	48.0	0.9	1.6	—	2.1	—	47.4

TABLE 3: Relative content of different minerals in the clay mass.

No.	Relative content of clay minerals (%)							Mixed layer ratio (%S)	
	S	I/S	I	K	C	C/S	Py	I/S	C/S
1	—	16	44	10	25	—	5	10	—
2	3	16	47	9	25	—	—	5	—
3	2	12	46	8	32	—	—	5	—
4	—	22	42	13	18	—	5	10	—
5	—	20	37	11	27	—	5	10	—
6	1	15	50	9	25	—	—	5	—

Note. Ta: talc; Py: pyrophyllite; Se: serpentine; V: vermiculite; I/V: illite/vermiculite mixed layer; S: smectite; I/S: illite mixed layer; I: illite; K: kaolinite; C: chlorite; C/S: chlorite mixed layer.

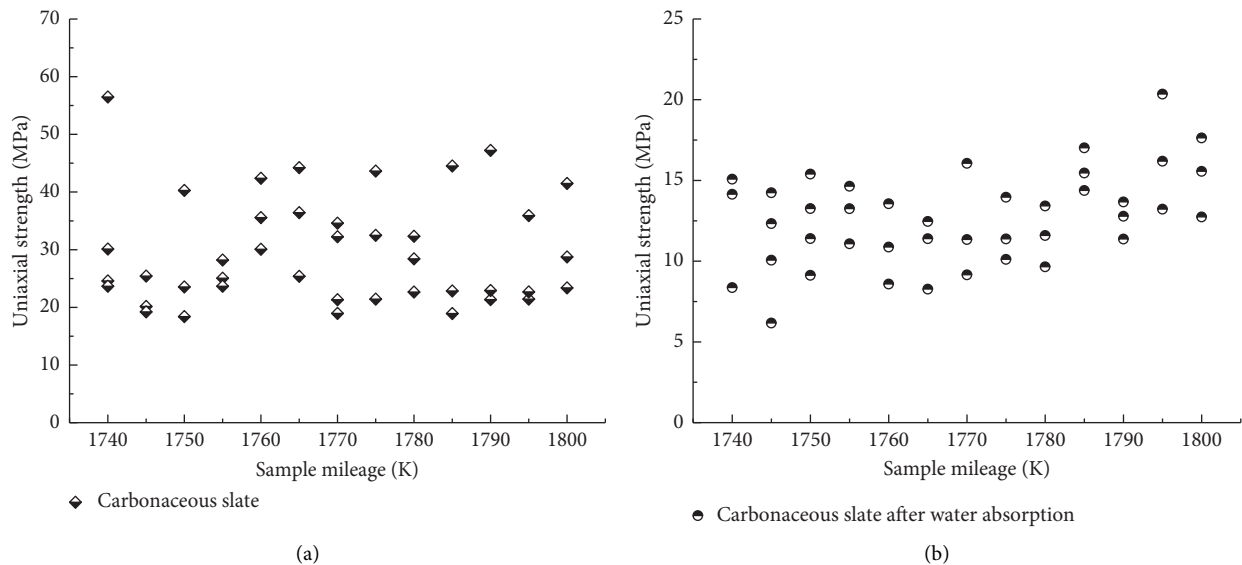


FIGURE 2: Uniaxial compressive strength of carbonaceous slate in the Muzhailing No. 2 inclined shaft: (a) compressive strength of carbonaceous slate in the natural state and (b) compressive strength of carbonaceous slate after water absorption.

inclinations on the strength of slate rock samples, as shown in Table 4.

According to the above results, the uniaxial compressive strength and elastic modulus of the rock specimens were relatively low when the joint surface of the three groups with different joint inclination angles was 45° (that is, the angle between the joint surface and the horizontal plane was 45°). For inclination angles between 30° and 60°, the surrounding rock essentially failed in shear.

3. Analysis of Deformation Characteristics of the Surrounding Rock of the Tunnel

3.1. Failure Characteristics of the Tunnel. To further study the large deformation characteristics of the surrounding rock of the Muzhailing Tunnel, we used a three-dimensional laser scanner and a total station together (Figure 3) to monitor eight sections of the No. 2 inclined shaft of the Muzhailing Tunnel, including XK0 + 060–XK0 + 250, XK0 +

TABLE 4: Uniaxial compressive strength test results.

No.	Compressive strength σ_c (MPa)	Average value (MPa)	Elastic modulus E (GPa)	Average value (GPa)	Poisson's ratio μ	Average value	Type of failure
U30-1	89.1		11.7		0.1		Shear failure
U30-2	82.8	74.3	12.5	11.9	0.1	0.1	Shear failure
U30-3	51.0		11.5		0.02		Shear failure
U45-1	69.7		12.6		0.1		Shear failure
U45-2	30.2	40.5	10.8	10.3	0.54	0.1	Shear failure
U45-3	21.5		7.4		0.003		Shear failure
U60-1	63.0		11.9		0.1		Shear failure
U60-2	65.8	63.0	13.0	12.3	0.03	0.08	Shear failure
U60-3	60.3		12.1		0.1		Shear failure

Note. For U30-1, 30 denotes joint inclination and 1 denotes rock number.

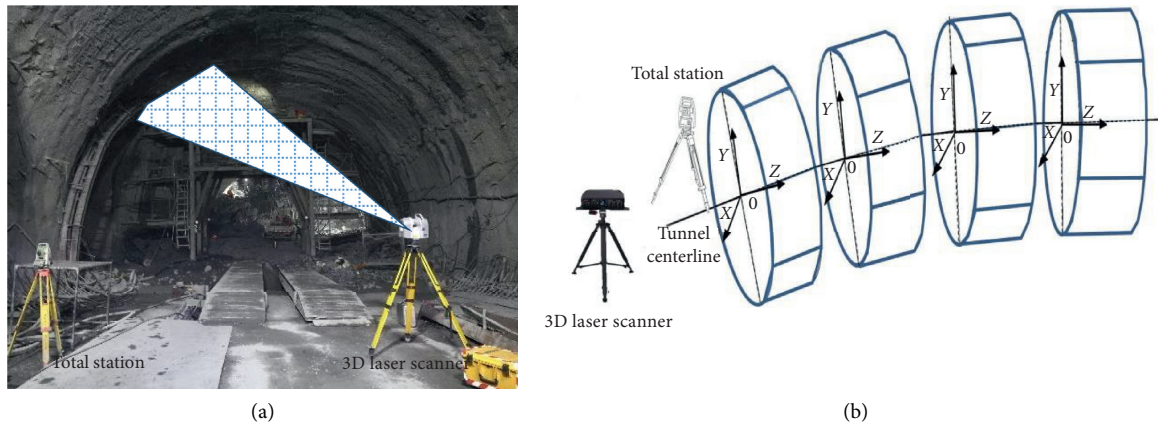


FIGURE 3: (a) Instrument for measuring the displacement of the surrounding rock of the tunnel and (b) monitoring schematic diagram of the displacement of the surrounding rock.

250–XK0 + 410, XK0 + 764–XK0 + 865, XK1 + 010–XK1 + 115, XK1 + 330–XK1 + 380, XK1 + 525–XK1 + 564, XK1 + 564–XK1 + 587, and XK1 + 622–XK1 + 666. The results of the monitoring are shown in Table 2. Figure 4 shows the initial support damage as photographed on-site. According to Table 5 and Figure 4, the initial deformation and cracking of the tunnel support were severe, the steel frame was distorted, the deformation rate was high, and the amount of deformation was large.

3.2. Deformation Characteristics of Surrounding Rock. On the basis of the deformation of the surrounding rock of the No. 2 inclined shaft, the deformation of the surrounding rock of the tunnel was classified according to the standard of tunnel deformation. The length of the tunnel was K1713 m, which is divided into four zones: basic stable zone (maximum deformation of less than 100 mm), slight deformation zone (maximum deformation of 100–250 mm), larger deformation zone (maximum deformation of 250–1000 mm), and severe deformation zone (deformation of more than 1000 mm). Through the above analysis, 41% of the total length of the tunnel was found to be in the large deformation zone and the buried depth of the severe deformation zone was more than 500 m. The length of the basic stable, slight

deformation, larger deformation, and severe deformation zones were 407, 250, 717, and 338 m, respectively.

The deformation of the surrounding rock in the essentially stable area was analyzed in this study. After the initial support of the tunnel was completed, the deformation of the surrounding rock increased sharply and the arch sank by 200–600 mm. Generally, the tunnel reached basic stability within 14 to 18 days, while the deformation continued by 1–2 mm per day. From the displacement distribution along the entire section, the deformation of the tunnel in a given section was asymmetric: the deformation on the left side of the tunnel was significantly larger than that on the right side. Figure 5 shows the typical deformation curve of the surrounding rock.

From the field investigation, the laboratory experiments, and the analysis of the field-monitoring data, we found that the surrounding rock joints of the No. 2 inclined shaft of the Muzhailing Tunnel were developed, the slate layer spacing was 5–30 cm, and the structure largely influenced the strength of the rock mass. The mineral content of the slate clay was approximately 50%, indicating that the rock strength had a certain influence on the damage of the surrounding rock and that water largely influenced the rock strength. The stress distribution of the surrounding rock varied with an increase in buried depth. The area around the

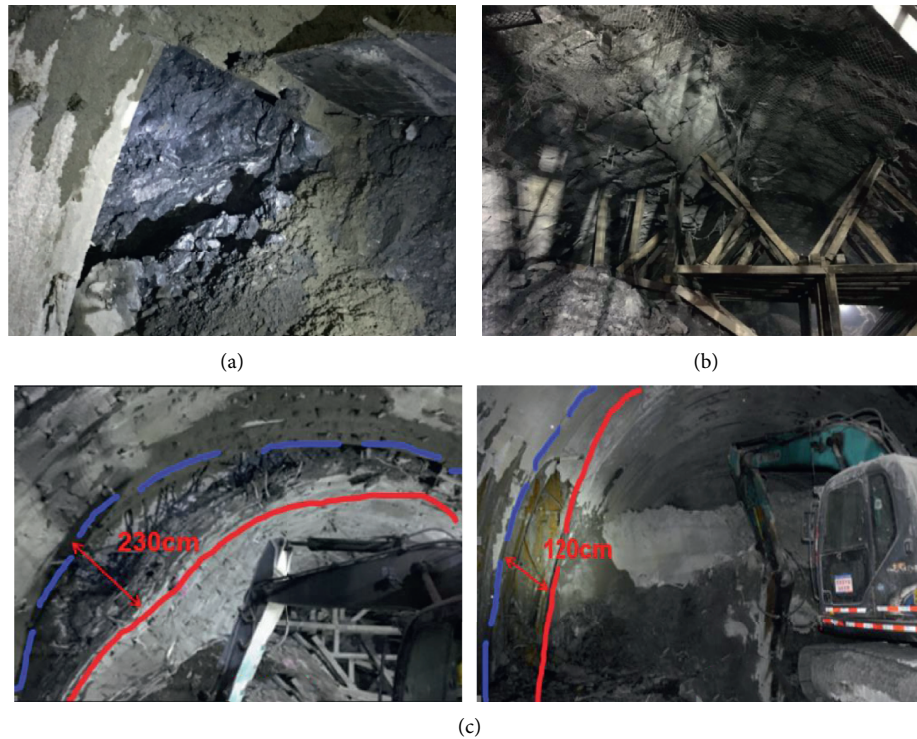


FIGURE 4: Damage characteristics of the surrounding rock of the tunnel: (a) severe drip of water in the middle steps on the left, (b) severe deformation of the arch, and (c) large deformation of the local vault.

TABLE 5: Results of the monitoring of the initial support of the tunnel.

Monitoring section	Buried depth (m)	Surrounding rock lithology	Cumulative sinking (mm)	Cumulative convergence value (mm)	Maximum deformation convergence rate (mm/d)
XK0 + 060–XK0 + 250	35–137	Fault fracture zone, strong compression, and torsion of the surrounding rock	120–180	150–430	—
XK0 + 060–XK0 + 250	137–215	Fault fracture zone, strong compression, and torsion of the surrounding rock	230–327	300–580	—
XK0 + 764–XK0 + 865	280–290	Interlayer of the sandy slate and carbonaceous slate	250–427	320–600	—
XK1 + 010–XK1 + 115	309–352	Carbonaceous slate	500–750	650–1550	560
XK1 + 330–XK1 + 380	447–474	Thin-layer carbonaceous slate	240–513	637–1224	174
XK1 + 525–XK1 + 564	568–597	Thin-layer carbonaceous slate	240–565	637–3145	831
XK1 + 564–XK1 + 587	590–597	Thin-layer slate	291–467	657–1205	57
XK1 + 622–XK1 + 666	548–569	Thin-layer slate with stranded water flowing out	140–458	127–2936	814

Muzhailing Tunnel experienced extremely high ground stress, and the deformation of the surrounding rock was significant.

Therefore, three main factors influencing tunnel deformation were determined from the experimental study: joint inclination angle variation of the surrounding rock, attenuation of the strength of the surrounding rock owing to water absorption, and the buried depth of the tunnel. To further reveal the deformation and failure mechanism of the surrounding rock of the Muzhailing Tunnel, a numerical simulation was performed by considering these three

aspects: joint inclination angle, burial depth, and softening caused by water absorption.

4. Numerical Analysis of the Deformation Mechanism of the Thin-Layer Slate Tunnel

4.1. Modelling Approach. The software 3 Dimension Distinct Element Code (3DEC) is a three-dimensional discrete element program that represents the discontinuous discrete characteristics of a material. It can explain the interaction between rock blocks and structural surfaces in rock masses,

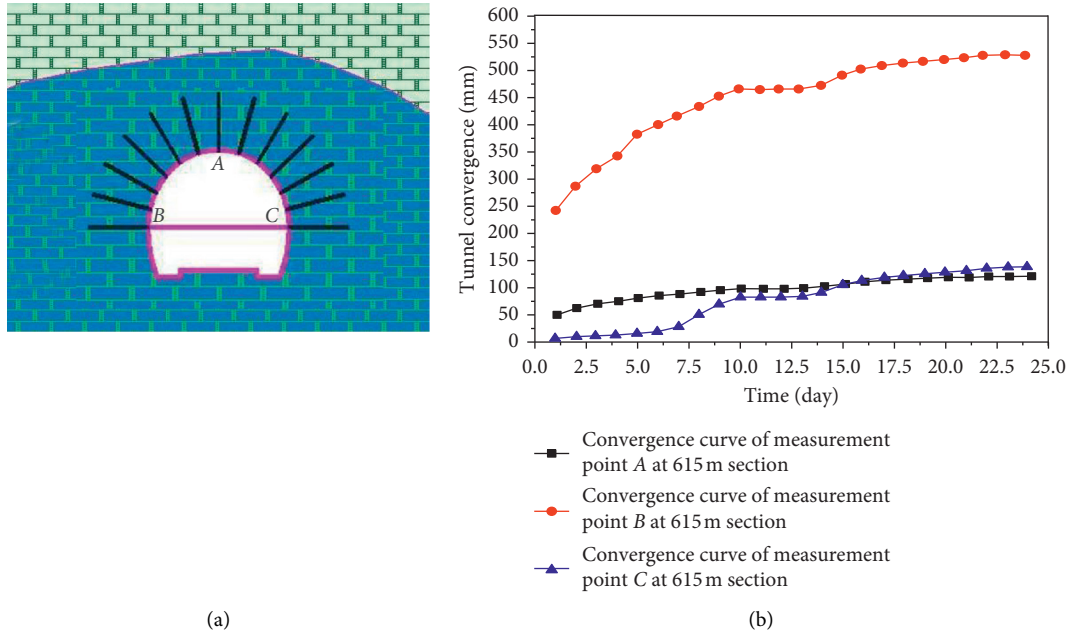


FIGURE 5: (a) Distribution of tunnel-displacement monitoring points and (b) tunnel-displacement monitoring curve.

and it effectively simulates the realistic failure phenomenon of a rock mass. Cui et al. [20] used the discrete element 3DEC software to study the influence of the inclination of layered surrounding rock on the deformation of a tunnel. Their results demonstrated that the deformation of the surrounding rock of the tunnel primarily manifested in the form of block sliding and bending of the layered rock layer. Bahrani and Hadjigeorgiou [21] used the 3DEC joint constitutive model to study the deformation characteristics of layered rock mass in a roadway under the action of the supporting body. Hou [22] used the 3DEC numerical analysis software to analyze the deformation and failure characteristics of a roadway tunnel supported by an anchor mesh and obtained the stress distribution characteristics, displacement characteristics, and plastic zone distribution characteristics of the surrounding rock.

To determine the characteristics of prominent dominant joints and coexistence of multiple joint forms in the No. 2 inclined shaft of the Muzhailing Tunnel, a simulation method using equivalent ubiquitous joints of dominant joint groups was proposed in this study, as shown in Figure 6. Considering the computational cost, we did not individually simulate all joints in the numerical model and we generalized the distribution of surrounding rock joints as shown in Figure 6(b). The joints were grouped into dominant joint groups (Figure 6(c)) and other joints. Locally, other joints (except for superior joints) had anisotropic characteristics, while macroscopically they were regarded as isotropic. Therefore, the 3DEC-Trigon method was used to simulate the rock mass as continuous media equivalence. The simulation considered the representative elementary volume (REV) characteristics of the rock mass and the transformation of rock-to-rock mass parameters in the process of equivalence [23, 24]. Compared with other methods, this

method can better adapt to the actual characteristics of the surrounding rock of the Muzhailing Tunnel.

4.2. Determination of Numerical Simulation Parameters. According to the principle of joint parameter selection [25], joints were modelled as uniformly distributed. The mechanical properties of the rock were obtained from equations (1) to (4), and the edge length of the irregular blocks was selected as $\Delta z_{\min} = 0.8$.

$$K = \frac{E}{3(1-2\mu)}, \quad (1)$$

$$G = \frac{E}{2(1+\mu)}, \quad (2)$$

$$K_n = 10 \left[\frac{K + (3/4)G}{\Delta z_{\min}} \right], \quad (3)$$

$$K_s = 0.4K_n, \quad (4)$$

where K is the bulk modulus, G is the shear modulus, K_n is the normal stiffness of the contact model parameters, and K_s is the shear stiffness.

According to the geological strength index (GSI) rock classification standard [26–30], for the mechanical properties as obtained from equations (1) to (4), the numerical inversion analysis was used during the simulation process. Accordingly, the strengths of carbonaceous slate in the natural state and under the saturated condition were obtained as shown in Tables 6 and 7. On the basis of multiple numerical analyses, the REV with a stable structural plane combination was found to be $8 \times 8 \times 16$ m. The results of the numerical test on the uniaxial compressive strength of the rock mass are shown in Figure 7.

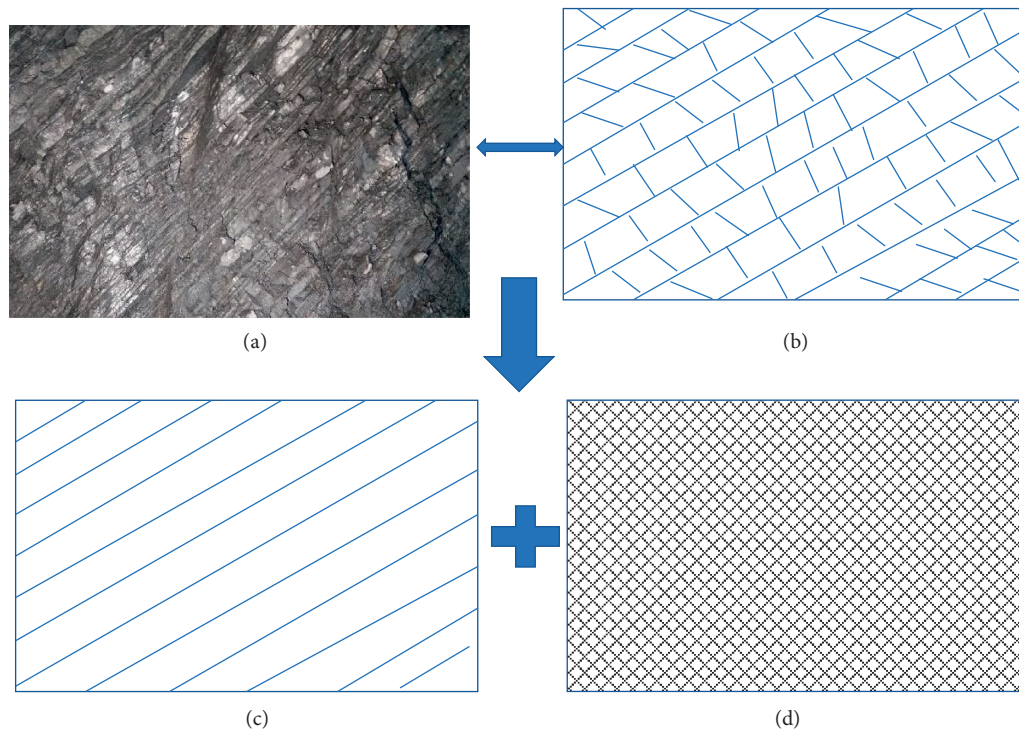


FIGURE 6: Modelling method of equivalent joints with dominant joints: (a) photo of the tunnel face, (b) generalization of the joint distribution, (c) dominant joints, and (d) equivalent joints.

After several inversion analyses combined with field measured deformation data of the surrounding rock, the dominant joint parameters selected were $j_{kn} = 2e9$, $j_{ks} = 1e9$, $j_{coh} = 1e5$, $j_{fr} = 25$, and $j_{ten} = 5e4$.

4.3. Establishment of the Numerical Model. A tunnel excavation model was established as shown in Figure 8. The model includes the tunnel section, uniform joints, and dominant joints. The ground stress was obtained from the field investigation as discussed in Section 2.3. The size of the model was $60\text{ m} \times 30\text{ m} \times 60\text{ m}$ (length \times width \times height). The reverse arch at the bottom of the tunnel was filled with concrete. Fixed constraints were imposed at the bottom of the model, and other boundary conditions were subjected to stress constraints based on the ground stress.

4.4. Effect of Joint Inclination on the Deformation of the Tunnel. Using the numerical model presented in Section 4.3, we estimated the ground stress when the buried depth was 500 m. The vertical stress was 12.5 MPa, the maximum horizontal stress was 21 MPa, and the minimum horizontal stress was 12.5 MPa. This simulation did not consider the tunnel support. By changing the dominant joint angle, we analyzed the deformation characteristics, stress distribution, and plastic zone expansion of the surrounding rock under different joint inclination angles.

4.4.1. Variation in the Surrounding Rock Displacement under Different Joint Inclinations. As shown in Figure 9, bending deformation and block slip deformation were caused by tunnel excavation, with bending deformation being the primary deformation encountered by the tunnel. The maximum bending deformation occurred at the left shoulder socket of the tunnel. The bending deformation was mainly due to an increase in the deflection of the plate-like surrounding rock under the action of the ground stresses, and the slip deformation was mainly the result of the shear slip of the structural surface. The deformation of the tunnel was influenced by the presence of joints and was consequently asymmetric. Among the joint inclination angles of 30° , 45° , and 60° , the most evident asymmetry was observed for a joint inclination angle of 45° . As shown in Figure 9, the displacement distribution is in the form of asymmetric butterfly displacement.

The maximum value of bending deformation corresponding to the 30° joint inclination was 0.7 m, and the displacement and deformation essentially stopped when the calculation reached 8000 steps. A separation layer developed at a depth of approximately 3.5 m in the surrounding rock, and sliding failure occurred in the surrounding rock of the tunnel. The maximum value of bending deformation corresponding to the 45° joint inclination was 1.2 m, and the displacement deformation essentially stopped after 10000 steps. A separation layer developed at a depth of approximately 7 m in the surrounding rock, the mass spalling caused by tunnel slip failure gradually increased, and the deformation of the surrounding rock of the tunnel presented strong

TABLE 6: Strength of the carbonaceous slate rock mass.

Lithology	Rock		GSI	Constant			Rock mass		
	σ_{ci} (MPa)	E_i (GPa)		m_i	m_b	s	a	σ_{cmass} (MPa)	E_{rm} (GPa)
Carbonaceous slate in the natural state	29.5	7.6	40	19	1.091	0.000335	0.511	7.4	0.6
Carbonaceous slate in the saturated state	11.7	2.8	37	5	0.249	0.000225	0.514	3.0	0.1

Note. E_{rm} : rock mass modulus; σ_{cmass} : uniaxial compressive strength of the rock mass; E_i : deformation modulus of the intact rock; σ_{ci} : uniaxial compressive strength of the intact rock.

TABLE 7: Mechanical properties of the carbonaceous slate.

Lithology	Rock mass parameters						Structural plane parameters				
	Density (kg/m ³)	K (GPa)	G (GPa)	C^b (MPa)	ϕ^b	σ_t^b (MPa)	K^n (GPa)	k^s (GPa)	C^j (MPa)	ϕ^j	σ_t^j (MPa)
Carbonaceous slate in the natural state	2500	0.44	0.25	1.7	22	0.6	30.21	12.08	3.75	29	3.45
Carbonaceous slate in the saturated state	2500	0.24	0.092	0.94	20	0.3	11.17	4.45	2.91	20	1.66

Note. ϕ : internal friction angle; σ_t : tensile strength; C : cohesion.

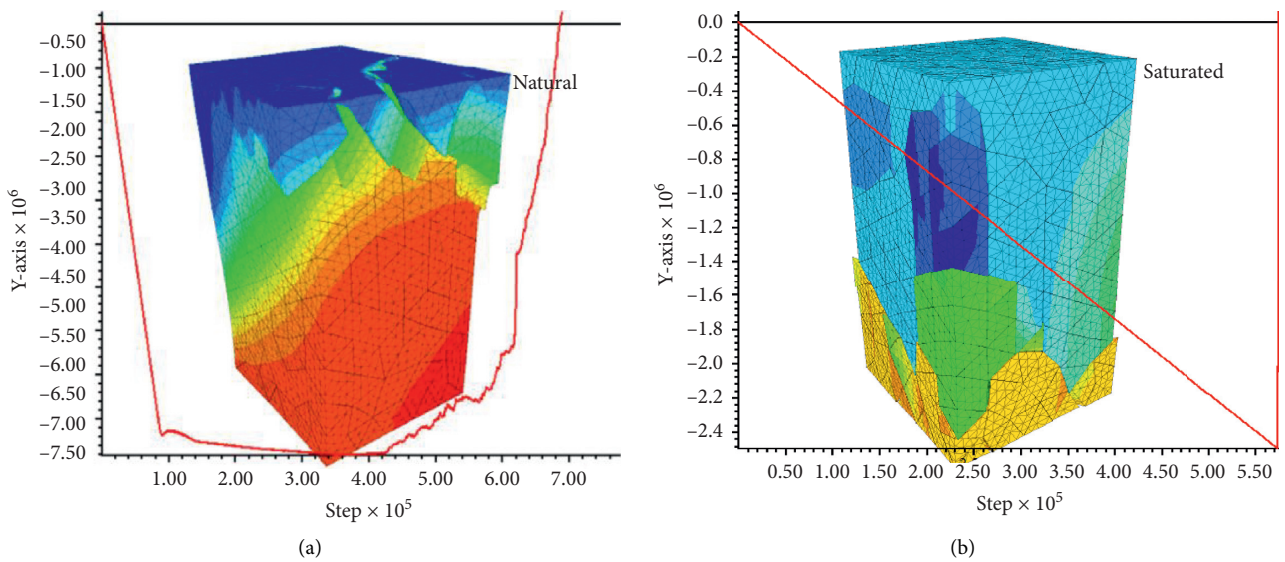


FIGURE 7: Numerical test on the uniaxial compressive strength of the rock mass.

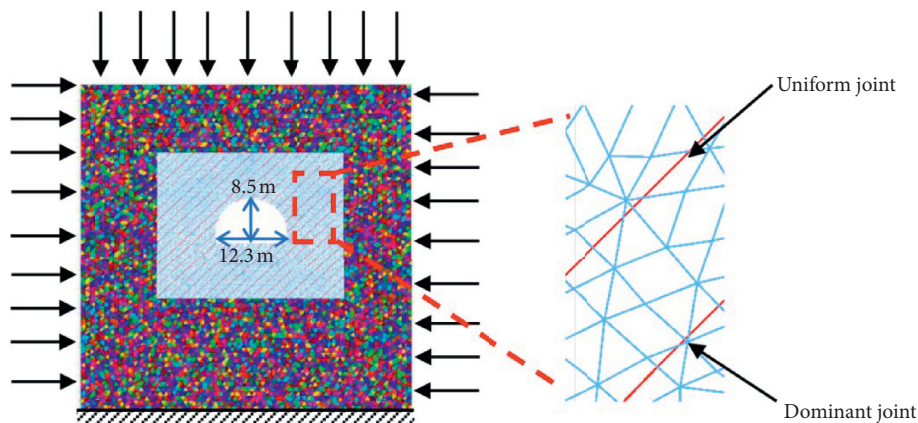


FIGURE 8: Numerical computation model.

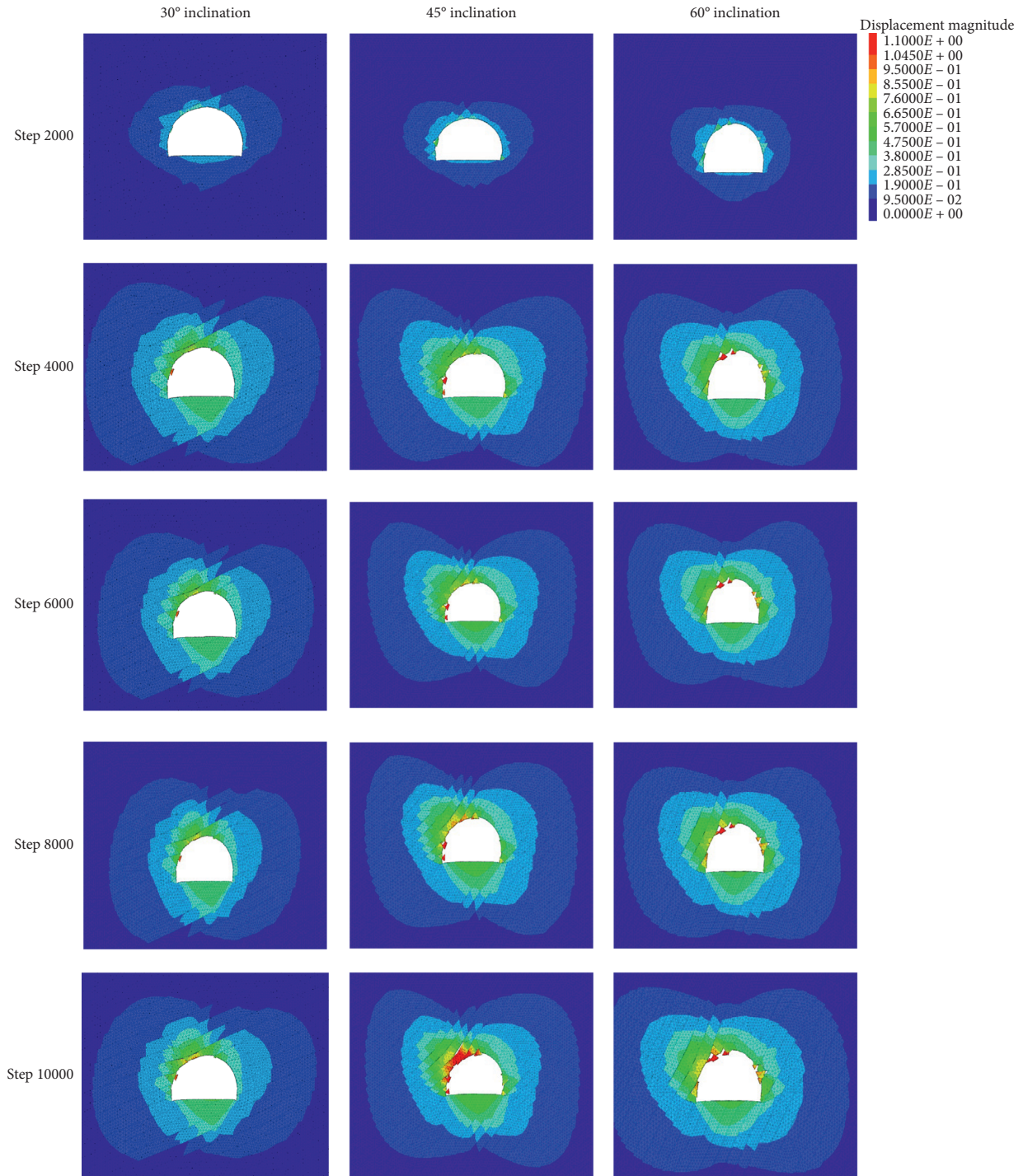


FIGURE 9: Distribution of surrounding rock displacement under different joint inclinations.

asymmetry. The maximum bending deformation corresponding to the 60° joint inclination was 0.8 m, and the displacement deformation essentially stopped when the calculation reached 9000 steps. A separation layer developed at a depth of approximately 4 m in the surrounding rock.

4.4.2. Trend in the Maximum Principal Stress Expansion. The original stress field is rearranged after the excavation of a tunnel. The distribution of the maximum principal stress is

an important basis for judging the stability of the geotechnical engineering, and it is an important index for understanding the range of influence of the excavation. As shown in Figure 10, the maximum principal stress transferred to a greater depth into the surrounding rock with the deformation of the surrounding rock, and the range of influence increased. After the tunnel deformation became stable, the maximum principal stress was concentrated in the vault and the bottom plate of the tunnel, and the maximum principal stress of the vault reached 32 MPa (showing a stress

concentration coefficient of 1.8). The maximum major principal stress of the vault occurred at 11 m from the tunnel wall. At increasing depth of the surrounding rock, the major principal stress decreased. At a distance of 16 m from the tunnel wall, the major principal stress transitioned to the original rock stress state, indicating that the range of influence of tunnel excavation was up to 16 m.

4.5. Impact of Different Buried Depth Conditions on the Surrounding Rock of the Tunnel. The above analysis shows that the deformation of the surrounding rock is most evident when the joint inclination angle is 45° under the same buried depth. Therefore, this section considers the dominant joint with a 45° inclination angle as the structural condition to study the variation in the stress, strain, and plastic zone of the surrounding rock caused by tunnel excavation under different buried depths.

Combined with the site-tunnel buried depth conditions, three tunnel excavation depths H were selected: 250, 330, and 500 m. The displacement distribution of the surrounding rock after tunnel excavation under the three buried depth conditions is shown in Figure 11. The simulation results show that (1) the deformation of the surrounding rock of the tunnel under the influence of the dominant joint is asymmetric under different buried depth conditions, showing that the left side deformation is larger than the right side, the maximum deformation position is located at the left shoulder socket of the tunnel, and the maximum deformation amount and deformation range of the tunnel gradually expand with an increase in buried depth and (2) for $H=250$ m, the tunnel does not have obvious damage, the tunnel section shape is essentially good, and the maximum displacement is 350 mm. When $H=330$ m, the left shoulder socket of the tunnel appears to have a detached layer, the surrounding rock of the tunnel has bending damage, and the maximum displacement is 520 mm. When $H=500$ m, thin-plate bending and damage occurred at the left side and the left shoulder fossa of the tunnel, and the maximum deformation is 1100 mm.

The distribution characteristics of the plastic zone of the surrounding rock excavated by tunnels with different depths are shown in Figure 12. The simulation results show the following. (1) The distribution of the plastic zone is cross-shaped, with vertical dominant joints and parallel dominant joints in the direction of the cross axis. As the burial depth increases, the plastic zone expands gradually and the plastic zone of the surrounding rock mass has shear failure. Primarily, the shear displacement direction is closely related to the direction of the joint surface. (2) When $H=250$ m, the tunnel roof and left shoulder form two shear failure zones and the vertical joints in these zones are in the form of a strip. The width of the shear band gradually decreases with increasing depth in the surrounding rock, and a “V” shear failure zone forms at the bottom of the tunnel, with the boundary of the “V” opening intersecting the bottom corner of the tunnel. (3) When $H=350$ m, the top of the tunnel and the left shoulder failure zone intersect, and the two shear zones gradually combine through the shear action, forming

an “M” plastic zone. The bottom shear zone gradually transitions to the “W” shape under the action of in situ stress. Both ends of the “W” shape intersect the tunnel bottom angle and expand upward along the side, gradually closing up with the upper “M”-type plastic zone. (4) When $H=500$ m, the plastic zone inherits the trend when $H=350$ m, the two plastic zones at the top and the shoulder form a large-scale penetration, and the bottom “W” plastic zone completely closes with the upper “M” model. Eventually, a larger “ π ” plastic zone forms.

The maximum principal stress distribution of the surrounding rock under different buried depths is shown in Figure 13. The simulation results demonstrate the following. (1) The maximum principal stress increases with the increase in buried depth, and the distribution law changes with buried depth. (2) When $H=250$ m, a stress concentration is present at the bottom angle of both sides of the tunnel and the upper and lower parts of the tunnel, and the maximum principal stress is 16 MPa. When $H=350$ m, the maximum principal stress is 19 MPa. (3) When $H=500$ m, the stress of the surrounding rock is concentrated at 1 to 1.5 times the hole diameter from the top and bottom plate, the width of the stress-concentrated area is approximately the same as the hole diameter, and the maximum principal stress is 32 MPa.

4.6. Effect of Softening of the Surrounding Rock on the Deformation of the Tunnel. During the construction of the No. 2 inclined shaft of the Muzhailing Tunnel, water gushing from the fissure was often encountered, and the deformation of the tunnel was found to be more significant in areas where water gushing was large. According to Section 2.4.2, the uniaxial strength of carbonaceous slate after water absorption was 0.4 times the uniaxial strength in the natural state, and the rock strength significantly decreased. Therefore, it is necessary to analyze the influence of water absorption and softening on the deformation of the tunnel. Combined with the difficulty of on-site engineering operations, the influence of water absorption and softening of surrounding rock on the surrounding rock of the tunnel was analyzed under working conditions of a tunnel burial depth of 500 m and a dominant joint angle of 45° .

By reducing the strength of surrounding rock to 40% of the strength before water absorption, we compared the deformation field, plastic zone, and stress field distribution characteristics of the surrounding rock before and after water absorption (Figure 14). (1) The characteristics of the deformation distribution of the surrounding rock before and after water absorption change greatly. The deformation of the tunnel before water absorption is mainly distributed in the left shoulder socket with a maximum deformation of 1200 mm. The left shoulder socket tends to be unstable, while the deformation of other parts is small and there is no instability. After water absorption and softening, the deformation of the surrounding rock at the left shoulder socket is the largest, with a maximum of 1900 mm, while the tunnel floor and the right side also have large deformation, and the deformation range of the surrounding rock extends to a greater depth. The hole has a symmetrical “C” shape, which

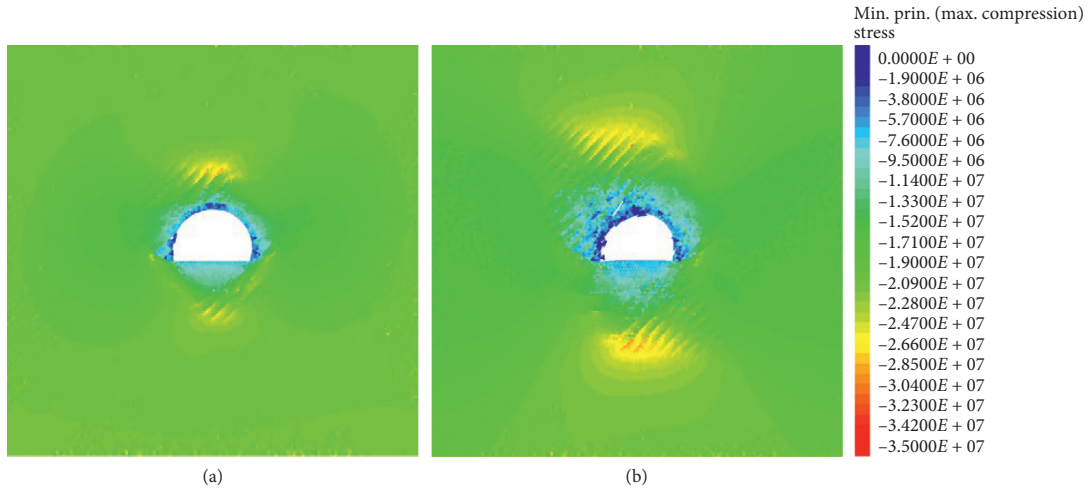


FIGURE 10: Distribution of maximum principal stress corresponding to a 45° inclination of joints: (a) step 2000 and (b) step 6000.

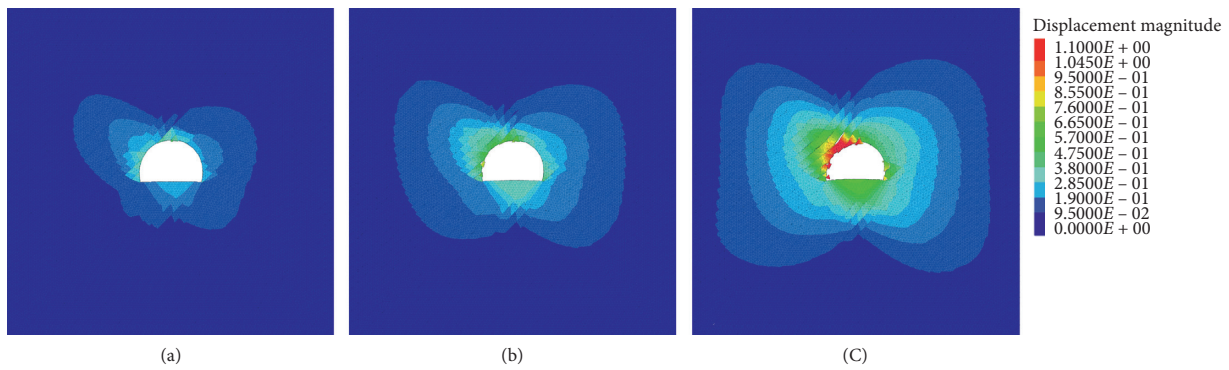


FIGURE 11: Displacement characteristics of the surrounding rock under different buried depths: (a) $H=250$ m, (b) $H=350$ m, and (c) $H=500$ m.

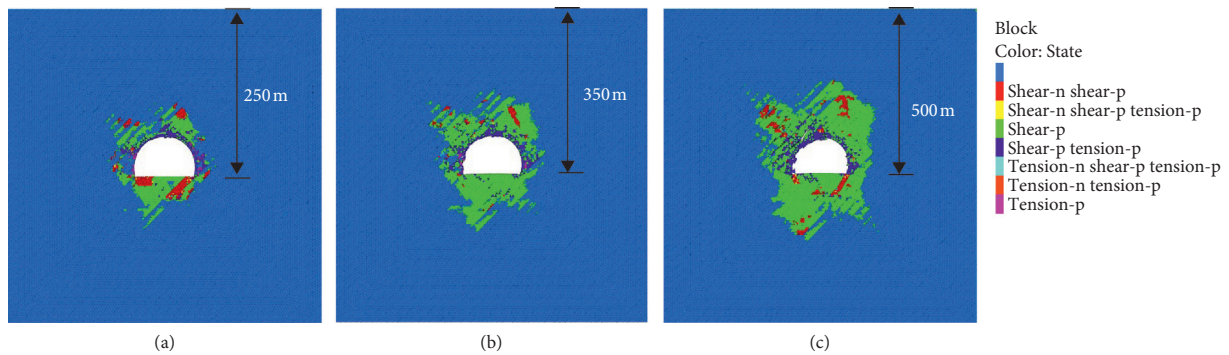


FIGURE 12: Distribution characteristics of the plastic zone at different depths: (a) $H=250$ m, (b) $H=350$ m, and (c) $H=500$ m.

indicates that the decrease of the surrounding rock strength after the water absorption softening helps control the deformation of the tunnel, while the dominant joints have an effect on the deformation direction. (2) The plastic zone of the surrounding rock is also evidently expanded after water absorption softening, which is affected by the decrease in the strength of the surrounding rock. Furthermore, the upper plastic zone completely joins and the dominant joints still affect the distribution characteristics of the plastic zone. The

radius of the plastic zone after water absorption softening can reach 14.5 m, which is approximately 4.2 m more than before water absorption, indicating that the distribution range is mainly controlled by the strength of the surrounding rock. (3) The stress distribution of the surrounding rock also changes greatly before and after water absorption softening. The maximum principal stresses before and after water absorption are concentrated in the deep surrounding rock at the top and bottom of the tunnel, the maximum

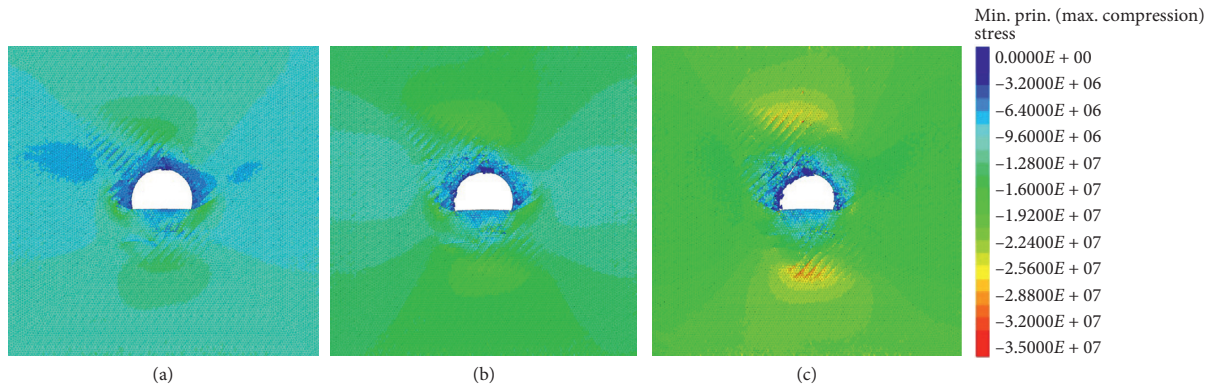


FIGURE 13: Distribution of maximum principal stress under different burial depths: (a) $H = 250$ m, (b) $H = 350$ m, and (c) $H = 500$ m.

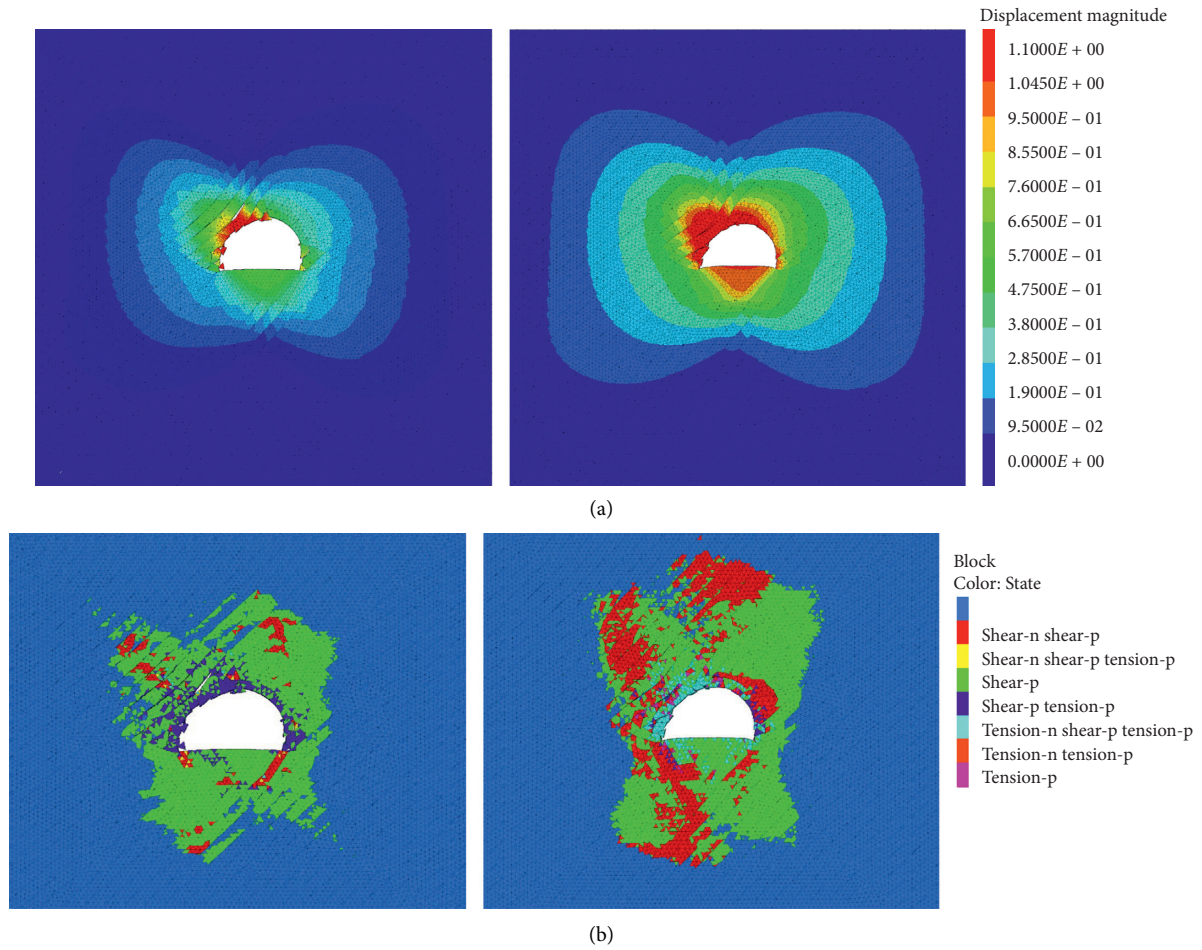


FIGURE 14: Continued.

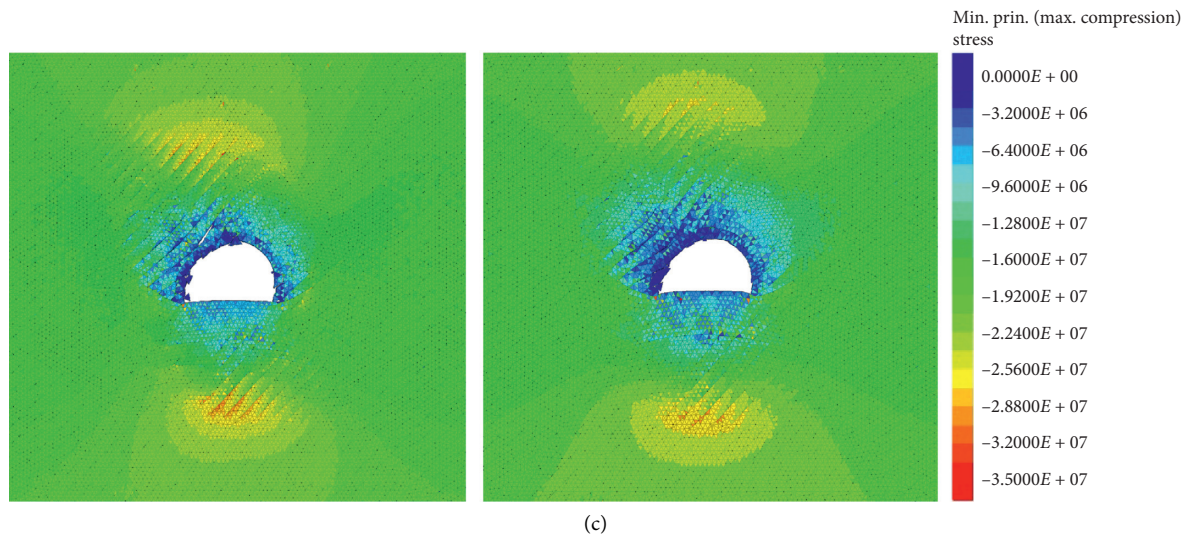


FIGURE 14: Deformation characteristics of the surrounding rock of the tunnel under water absorption and softening: (a) change in the surrounding rock displacement before and after water absorption, (b) changes in the plastic zone of the tunnel before and after water absorption, and (c) changes in the maximum principal stress field of the tunnel before and after water absorption.

principal stress concentration area after water absorption moves to 0.5 times the diameter of the hole to a greater depth, and the maximum principal stress value decreases by approximately 4 MPa after water absorption softening.

5. Conclusions

In view of the large deformation of the surrounding rock during the construction of the No. 2 inclined shaft of the Muzhailing Tunnel, the deformation characteristics and influence of the surrounding rock of the tunnel under the original supporting form were analyzed. The following conclusions are drawn:

- (1) The initial support of the No. 2 inclined shaft of the Muzhailing Tunnel was seriously damaged, and the deformation of the surrounding rock of the tunnel was asymmetric. The deformation on the left side was significantly larger than that on the right side, and the area with a deformation greater than 0.25 m accounted for 41% of the total length of the tunnel. In addition, when the buried depth was more than 500 m, serious deformation of the surrounding rock exceeding 1 m was observed.
- (2) According to the field investigation, the laboratory experiment, and the field-monitoring data analysis, the surrounding rock of the No. 2 inclined shaft of the Muzhailing Tunnel was relatively broken, the lithology was mainly carbonaceous slate, the joints and fractures were well developed, and the area was subjected to extremely high stress. The uniaxial compressive strength after 24 hours of water absorption was markedly lower than that of carbonaceous slate in the natural condition. The uniaxial compressive strength and elastic modulus of the rock with a 45° joint inclination were relatively low when

compared with inclinations of 30° and 60°. Therefore, the main factors affecting the deformation of the thin-layer rock of the Muzhailing Tunnel included the joint inclination angle, buried depth of the tunnel, and softening of the surrounding rock due to water absorption.

- (3) Through the numerical simulation results, it can be concluded that under the same buried depth, the deformation of surrounding rock was maximum for a 45° joint inclination. At the 45° joint inclination, the deformation and failure of the tunnel was intensified with an increase in burial depth. When the burial depth was 500 m, thin-plate bending and damage occurred at the left side and the left shoulder fossa of the tunnel; after the surrounding rock was softened by water absorption, the floor of the tunnel, the left shoulder socket, and the right side of the tunnel deformed greatly and the deformation range of the surrounding rocks extended to a greater depth.

Data Availability

All the data included in this study are available upon request by contact with the corresponding author.

Conflicts of Interest

The authors declare that there are no conflicts of interest regarding the publication of this article.

Acknowledgments

Thanks to the academician He Manchao of the State Key Laboratory for GeoMechanics and Deep Underground Engineering for his valuable comments on the writing and revision of this manuscript. The authors would like to thank

Uni-edit (<http://www.uni-edit.net>) for editing and proof-reading this manuscript. This work was supported by the National Key Research and Development Plan (grant no. 2016YFC0600901) and the Special Fund for Basic Scientific Research Business Expenses of Central Universities (grant no. 2015QB02).

References

- [1] S. Chen, D. Yin, N. Jiang, F. Wang, and Z. Zhao, "Mechanical properties of oil shale-coal composite samples," *International Journal of Rock Mechanics and Mining Sciences*, vol. 123, Article ID 104120, 2019.
- [2] N. Zhang, W. Liu, Y. Zhang, P. F. Shan, and X. L. Shi, "Microscopic pore structure of surrounding rock for underground strategic petroleum reserve (SPR) caverns in bedded rock salt," *Energies*, vol. 13, no. 7, p. 1565, 2020.
- [3] Y. Zhang, S. G. Cao, N. Zhang, and C. Z. Zhao, "The application of short-wall block backfill mining to preserve surface water resources in northwest China," *Journal of Cleaner Production*, vol. 261, Article ID 121232, 2020.
- [4] P. Shan and X. Lai, "An associated evaluation methodology of initial stress level of coal-rock masses in steeply inclined coal seams, Urumchi coal field, China," *Engineering Computations*, vol. 37, no. 6, pp. 2177–2192, 2020.
- [5] C. X. Wang, B. T. Shen, J. T. Chen et al., "Compression characteristics of filling gangue and simulation of mining with gangue backfilling: an experimental investigation," *Geomechanics and Engineering*, vol. 20, no. 6, pp. 485–495, 2020.
- [6] D. Ren, D. Zhou, D. Liu, F. Dong, S. Ma, and H. Huang, "Formation mechanism of the upper Triassic Yanchang Formation tight sandstone reservoir in Ordos Basin-Take Chang 6 reservoir in Jiyuan oil field as an example," *Journal of Petroleum Science and Engineering*, vol. 178, pp. 497–505, 2019.
- [7] N. Jiang, C. Wang, H. Pan, D. Yin, and J. Ma, "Modeling study on the influence of the strip filling mining sequence on mining-induced failure," *Energy Science & Engineering*, vol. 8, no. 6, pp. 2239–2255, 2020.
- [8] H. Huang, T. Babadagli, X. Chen, H. Z. Li, and Y. M. Zhang, "Performance comparison of novel chemical agents for mitigating water-blocking problem in tight gas sandstones," *SPE Reservoir Evaluation & Engineering*, vol. 2020, pp. 1–9, 2020.
- [9] D. Brox and H. Hagedorn, "Extreme deformation and damage during the construction of large tunnels," *Tunnelling and Underground Space Technology*, vol. 14, no. 1, pp. 23–28, 1999.
- [10] E. Hoek and P. Marinos, "Predicting tunnel squeezing problems in weak heterogeneous rock masses," *Tunnels & Tunnelling International*, vol. 32, no. 11, pp. 45–51, 2000.
- [11] G. Liu, F. Y. Zhang, X. Z. Li, and Z.-C. Yang, "Research on large deformation and its mechanism of Muzhailing Tunnel," *Chinese Journal of Rock Mechanics and Engineering*, vol. 24, no. s2, pp. 5521–5526, 2005.
- [12] M. A. Meguid and R. K. Rowe, "Stability of D-shaped tunnels in a Mohr Coulomb material under anisotropic stress conditions," *Canadian Geotechnical Journal*, vol. 43, no. 43, pp. 273–281, 2006.
- [13] X. Guo, Z. Tan, L. Li, and N. Luo, "Deformation and failure mechanism of layered soft rock tunnel under high stress," *China Civil Engineering Journal*, vol. 50, pp. 38–44, 2017.
- [14] T. C. Yu, "Study on large deformation control technology of tunnel in soft rock," *China Civil Engineering Journal*, vol. 50, pp. 112–117, 2017.
- [15] C. Cao, C. Shi, M. Lei, W. Yang, and J. Liu, "Squeezing failure of tunnels: a case study," *Tunnelling and Underground Space Technology*, vol. 77, no. 7, pp. 188–203, 2018.
- [16] X. Sun, B. Zhang, L. Gan, Z. Tao, and C. Zhao, "Application of constant resistance and large deformation anchor cable in soft rock Highway tunnel," *Advances in Civil Engineering*, vol. 2019, Article ID 4347302, 19 pages, 2019.
- [17] Chinese Academy of Geological Sciences, *Test Report on Hydraulic Fracturing Ground Stress of Muzhailing Tunnel on the Highway from Weiyuan (Luyuan) to Wudu (Liangshui) of Gansu Province*, Chinese Academy of Geological Sciences, Beijing, China, 2013.
- [18] G. Feng, Y. Kang, X. Wang, Y. Hu, and X. Li, "Investigation on the failure characteristics and fracture classification of shale under Brazilian test conditions," *Rock Mechanics and Rock Engineering*, vol. 53, no. 7, pp. 3325–3340, 2020.
- [19] G. Feng, X. Wang, M. Wang, and Y. Kang, "Experimental investigation of thermal cycling effect on fracture characteristics of granite in a geothermal-energy reservoir," *Engineering Fracture Mechanics*, vol. 235, Article ID 107180, 2020.
- [20] Z.-D. Cui, D.-A. Liu, and F.-Q. Wu, "Influence of dip directions on the main deformation region of layered rock around tunnels," *Bulletin of Engineering Geology and the Environment*, vol. 73, no. 2, pp. 441–450, 2014.
- [21] N. Bahrani and J. Hadjigeorgiou, "Influence of stope excavation on drift convergence and support behavior: insights from 3D continuum and discontinuum models," *Rock Mechanics and Rock Engineering*, vol. 51, no. 8, pp. 2395–2413, 2018.
- [22] X. B. Hou, "U-shape steel frame and bolt-mesh-anchor coupling support technology in deep soft rock coal roadway by 3DEC," *Safety in Coal Mines*, vol. 49, no. 7, pp. 134–137, 2018.
- [23] X. Sun, G. Li, C. Zhao, Y. Liu, and C. Miao, "Investigation of deep mine shaft stability in alternating hard and soft rock strata using three-dimensional numerical modeling," *Processes*, vol. 7, no. 1, p. 2, 2018.
- [24] W. H. Tan, Z. H. Sun, N. Li, and X. H. Jiang, "Stochastic three-dimensional joint geometry model and the properties of REV for a jointed rock mass," *Advanced Materials Research*, vol. 1079-1080, pp. 266–271, 2014.
- [25] Itasca Consulting Group, Inc. *3DEC User Manual*, Itasca Consulting Group, Inc., Minneapolis, MN, USA, 2016.
- [26] S.-Q. Yang, M. Chen, H.-W. Jing, K.-F. Chen, and B. Meng, "A case study on large deformation failure mechanism of deep soft rock roadway in Xin'an coal mine, China," *Engineering Geology*, vol. 217, pp. 89–101, 2017.
- [27] D. Liu, Z. Gu, R. Liang et al., "Impacts of pore-throat system on fractal characterization of tight sandstones," *Geofluids*, vol. 2020, no. 9, Article ID 4941501, 17 pages, 2020.
- [28] S. Hu, Y. Tan, H. Zhou et al., "Anisotropic modeling of layered rocks incorporating planes of weakness and volumetric stress," *Energy Science & Engineering*, vol. 8, no. 3, pp. 789–803, 2020.
- [29] X. Wang, W. Yuan, Y. T. Yan, and X. Zhang, "Scale effect of mechanical properties of jointed rock mass: a numerical study based on particle flow code," *Geomechanics and Engineering*, vol. 21, no. 3, pp. 259–268, 2020.
- [30] E. Hoek, C. Carranza-Torres, and B. Curkum, "Hoek-Brown failure criterion—2002 edition," in *Proceedings of the Fifth North American Rock Mechanics Symposium*, pp. 267–273, Toronto, Canada, July 2002.

Research Article

Observed Performance of Highway Embankment over Soft Marine Clay: A Case Study in Wenzhou, China

Xia Bian,^{1,2} Jin-Kai Yan ,³ and Wei Zhang²

¹*Institute for Underground Space and Geoenvironment, School of Earth Sciences and Engineering, Nanjing University, Nanjing 210046, China*

²*Key Laboratory of Ministry of Education for Geomechanics and Embankment Engineering, Hohai University, Nanjing 210098, China*

³*Chinese Academy of Geological Sciences, Beijing 100037, China*

Correspondence should be addressed to Jin-Kai Yan; yanjinkaisw@163.com

Received 4 June 2020; Revised 10 July 2020; Accepted 24 July 2020; Published 11 August 2020

Academic Editor: Wen-Chieh Cheng

Copyright © 2020 Xia Bian et al. This is an open access article distributed under the Creative Commons Attribution License, which permits unrestricted use, distribution, and reproduction in any medium, provided the original work is properly cited.

This paper presents a case history of observed performance of highway embankment over soft marine clay in Wenzhou, China. During the embankment construction, the changes of ground settlement, ground displacement, and lateral displacement of subsoil with the construction time were monitored and analyzed. The monitoring results indicate that the ground settlement and lateral displacement of subsoil account for about 75% in the process of embankment construction. The measured maximum values of ground settlement, ground displacement, and lateral displacement of subsoil are 37.88 mm, 21.50 mm, and 23.56 mm, respectively. After the completion of the embankment construction, the settlement gradually tended to be stable. It is suggested that the monitoring data of settlement and displacement of embankment are smaller than the design requirements, and the embankment stability is also ensured.

1. Introduction

Wenzhou is located in the southeastern coastal area of China, and the Feiyun River flows through Wenzhou. Most of the areas near the Feiyun River are alluvial deposits formed in Quaternary [1–4]. The Quaternary alluvial deposits have a high water content, high compressibility, and lower carrying capacity [5–9] and maybe induce many incidents during engineering construction [10]. Normally, this clay alluvial deposit consists of predominated clay mineral such as illite, smectite, and kaolinite [11, 12], resulting in poor engineering characteristics [13]. When highway embankments are constructed on alluvial deposits, the soft soils often bear intolerably large settlements or fail due to insufficient bearing capacity. Therefore, a variety of methods have been used to solve these problems [14–18]. Such reinforcement methods include jet grouting [2, 18–20], deep mixing [21–23], and stiffening method [24, 25]. According to different regional environment and different geological

conditions, each method of foundation treatment has its scope of application.

Recent composite foundation is widely used for the construction of embankments on soft ground [26, 27]. Geosynthetics (such as geotextiles and geogrids) with high tensile strength, low elongation, and high stiffness are laid at the bottom of embankment which form reinforced cushion with gravel to maintain the integrity and continuity of the base [28–30]. Reinforced cushion and concrete pile constitute composite foundation of reinforced pile group. The reinforcement effect of geosynthetics on soft soil is mainly reflected in horizontal reinforcement. The reinforcement principle of geosynthetics reinforced cushion is as follows [31, 32]:

- (1) It can increase the integrality and stiffness of cushion and adjust uneven settlement
- (2) Due to the influence of the increase of cushion stiffness, it enlarges the range of load diffusion and makes the stress uniformly distributed

- (3) The lateral deformation of the underlying soft soil foundation is restrained

In this paper, a case history of observed performance of highway embankment over soft marine clay in Wenzhou, China, was presented. The plain concrete piles were used to support soft soil embankment. The changes of ground settlement, ground displacement, and lateral displacement of subsoil with the construction time were monitored. After the completion of the embankment construction, the settlement gradually tended to be stable. It is suggested that the monitoring data of settlement and displacement of embankment are smaller than the design requirements.

2. Site Conditions

2.1. General Situation of Engineering. The test site was located in the southwest of Zhejiang Province, in the middle and lower reaches of the Feiyun River (Figure 1). The length and width of the selected line were 364 and 17 m. The expressway was constructed on soft soil. The profile of the main soil is shown in Figure 2. There is a 1 m thick coarse grained fill overlying a 4 m thick deposit of silty clay; this deposit overlies mud layer that is approximately 6 m thick. Underneath the mud layer is a mucky clay layer that is about 4 m thick followed by a clay breccia layer. The ground water level is at a depth of 2 m. Based on the Unified Soil Classification System (USCS), the three types of soils can be classified as low plasticity clay (CL; [33]). The available detailed test data are shown in Figure 2, including the water content, the void ratio, and the unit weight to a depth of about 16 m below ground level. The mud layer has the characteristics of low strength, high compressibility, and high water content. Its void ratio is greater than 1.5. And its water content is between 50% and 65%, usually higher than the liquid limit. Compared with the mud layer above, the water content of the mucky clay layer is lower than the liquid limit, and the void ratio is between 1 and 1.5.

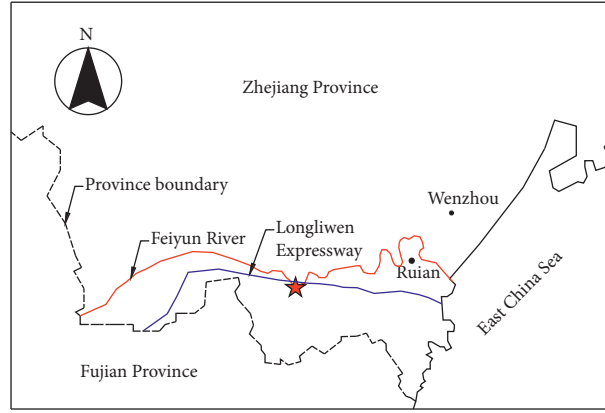
2.2. Embankment Design and Pile Support Reinforcement. The starting point of the route was connected to the 56 provincial highway, and the terminal was connected to the bridgehead approach, with a total length of 364 m. The embankment filling height was about 3.0–5.5 m. The embankment was 5.5 m high. The width of the road was 17 m. The side slope of the embankment was 1 V to 1.5 H (V, vertical; H, horizontal). The embankment was supported by cast-in-place circular plain concrete pile that was formed from a low-slump concrete with a minimum of compressive strength of 15 N/mm^2 . The circular plain concrete piles were 19 m in length and were founded on a relatively harder clay breccia layer (Figure 3(a)). It had a diameter of 0.5 m which was formed with the low-slump concrete. The piles were placed in a square grid with a center-to-center spacing of 2 m. The pile caps had a dimension of $1.2 \text{ m} \times 1.2 \text{ m} \times 0.35 \text{ m}$ (length \times width \times height) that were formed from a minimum of compressive strength of 20 N/mm^2 of concrete and

reinforcement bar with diameter of 12 mm. Soil-rock mixture was used as the fill material for the embankment. According to the Technical Specifications for Construction of Highway Subgrades [34], the ratio of soil and rock by weight is designed as 6:4. Two layers of steel wire mesh were used together with gravels to form a 0.5 m thick load transfer platform as shown in Figure 3(c). The bottom layer of the steel wire mesh was 0.3 m from the base, and the second layer was 0.5 m above the first. The tensile strength of the steel wire mesh was 100 kN/m in both longitudinal and transverse directions. The maximum allowable tensile strain was 3% [35]. The design value of the ultimate pile capacity in this project is about 960 kN, while the allowable pile capacity is about 800 kN. The key construction process of the plain concrete pile is as follows:

- (1) After surface cleaning, the pile rig was placed according to the designed pile position. Pile rig must be level and stable. The immersed pipe was perpendicular to the ground to ensure that the deviation of verticality was not more than 1%.
- (2) The casing pipe was constructed and sunk to the predetermined elevation. During the sinking process of the casing pipe, the current on the ammeter was recorded once per 1 m sinking. The change of soil layer was explained.
- (3) When the immersed pipe reached the design elevation, the material was fed into the pipe immediately until the mixture was level with the inlet. The mixture was formulated according to the design mix ratio and the concrete slump was controlled between 3 and 5 cm.
- (4) The immersed pipe should vibrate while pulling out, each pulling 0.5–0.1 m, retaining vibration for 5–10 s. The upward speed of immersed pipe was not more than 1.0 m/min, and it was evenly pulled up. If there was silt or silty soil, the rate of pipe pulling should be slowed down and controlled within 0.5 m/min. Reverse insertion was not allowed in the process of pulling out the casing pipe. If the supply material was insufficient, concrete should be poured while casing pipe is pulled up. With this method, the top standard of pile can reach the design requirement.
- (5) After the immersed pipe was pulled out of the ground, it was confirmed that the pile reached the design height requirement. The steel reinforcement of pile cap was embedded; then, the casing pipe was moved to carry out the next pile construction.

The piles in this study are friction piles. During the construction of these piles, there exist some problems, such as diameter shrinkage and incline of pile center line. In order to avoid these problems, the casing pipe was used to complete the perfusion of concrete and was pulled out slowly after the completion of the perfusion of concrete; meanwhile, the verticality inspection was also conducted to ensure the verticality of the pile.

Based on the Specifications for Design of Highway Subgrades [34], the factor of safety (FOS) of the



★ The test site

FIGURE 1: Distribution of the planned expressway in Zhejiang Province and location of test site.

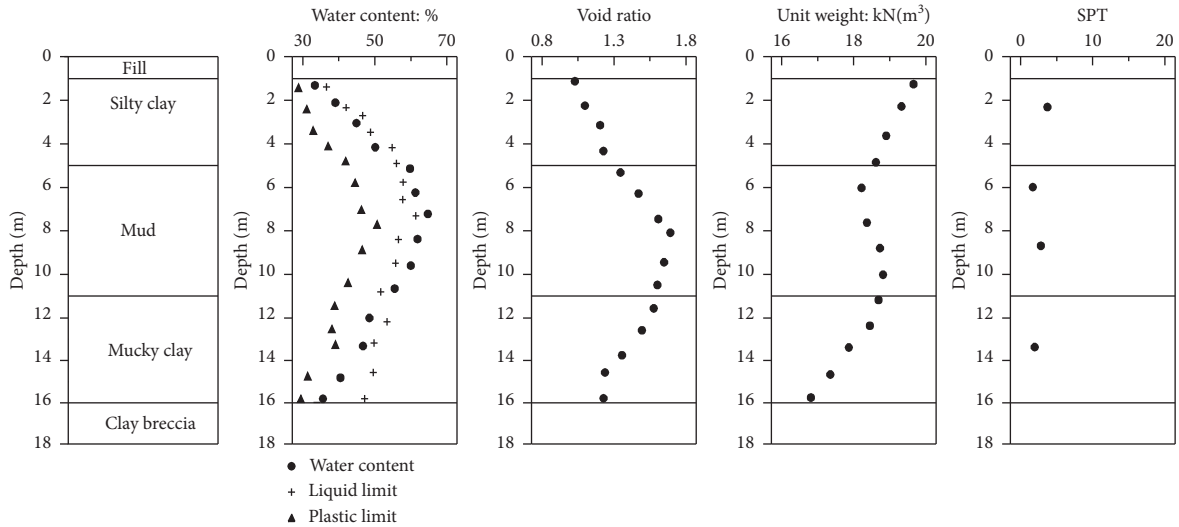


FIGURE 2: Geotechnical profiles and properties on-site.

embankment is evaluated by simplified Bishop method. The FOS can be determined by the following equations:

$$FOS = \frac{\sum K_i}{\sum W_i \sin \alpha_i}, \quad (1)$$

$$K_i = \frac{c_{di}b_i + W_{di} \tan \varphi_{di} + UW_{ti} \tan \varphi_{di}}{m_{ai}} \cdot (\text{soil - slice } i \text{ in ground}), \quad (2)$$

$$K_i = \frac{c_{ti}b_i + W_{ti} \tan \varphi_{ti}}{m_{ai}} (\text{soil - slice } i \text{ in embankment}), \quad (3)$$

$$m_{ai} = \frac{\cos \alpha_i + \sin \alpha_i \tan \varphi_i}{FOS}, \quad (4)$$

where W_i is the gravity of the soil-slice i (as shown in Figure 4); K_i is a factor; α_i is the horizontal angle of the soil-slice i (see Figure 4); c_{di} is the cohesion of the soil-slice i in

ground; φ_{di} is the friction angle of the soil-slice i in ground; W_{di} is the gravity of the soil-slice i in ground; b_i is the width of the soil-slice i (as shown in Figure 4); W_{ti} is the gravity of the soil-slice i in embankment; c_{ti} is the cohesion of the soil-slice i in embankment; φ_{ti} is the friction angle of the soil-slice i in embankment; and φ_i is the friction angle of the soil-slice i . Using the above analytical method, the FOS of this case history can be calculated as 1.8, which is larger than the design requirement, 1.35, and the safety of the embankment construction can also be verified by the measure displacement during the construction.

3. Field Monitoring Program

3.1. Monitoring Methods and Technical Requirements. The settlement of soft foundation was mainly observed by settlement plate. Observation points were laid on the middle line of the subgrade and the edge of the shoulder. Settlement was measured by leveling. Relying on the

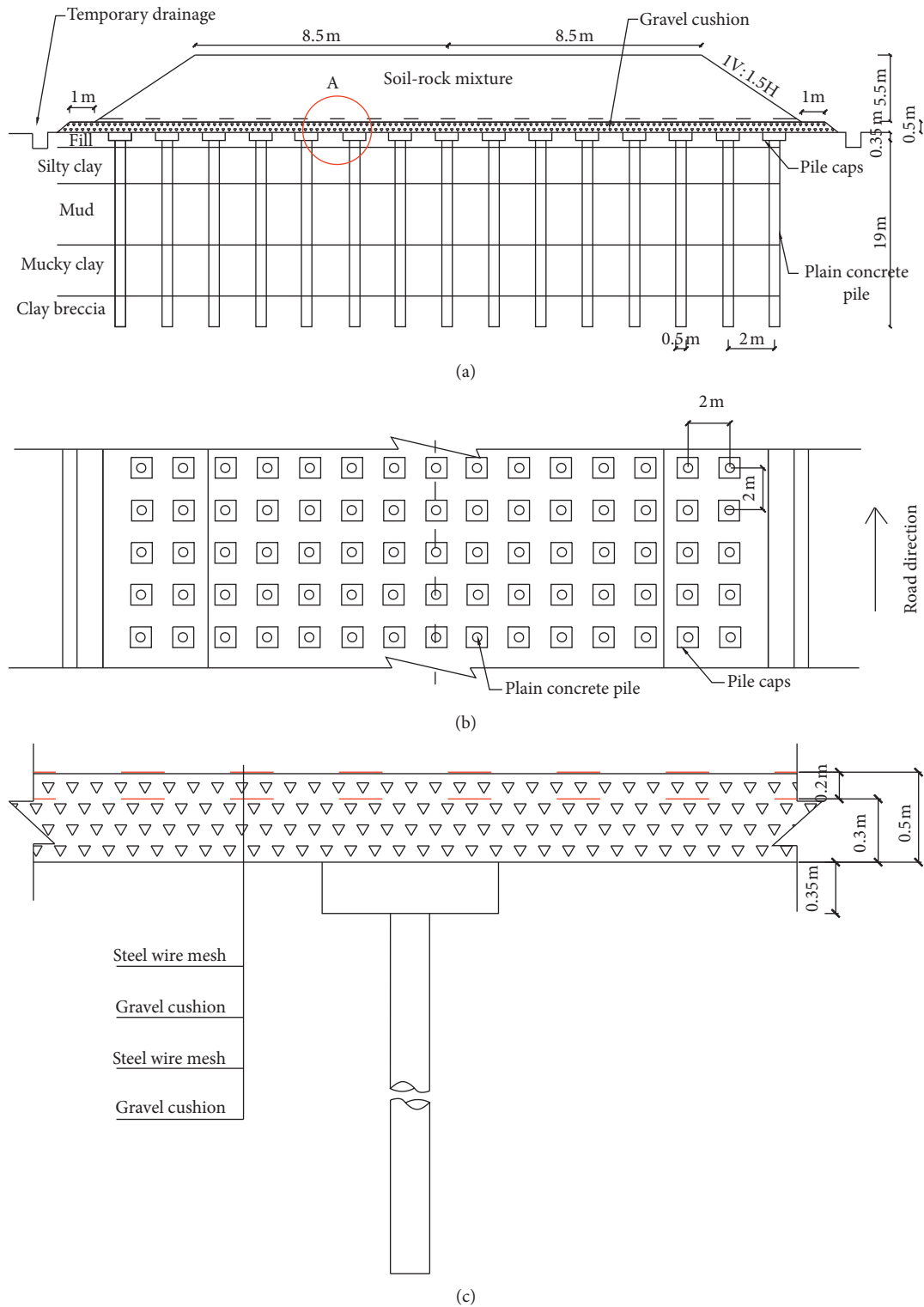


FIGURE 3: Embankment design and pile foundation reinforcement: (a) typical section diagram of soft foundation treated by plain concrete piles, (b) pile foundation plan layout, (c) detailed A section in (a).

construction control network, the monitoring and control network along the route was established. Based on the Code for Engineering Surveying, GB50026-2007 [36], deformation monitoring grade and accuracy requirements are shown in Table 1.

The settlement plate can be laid after soft foundation treatment and before embankment filling. Settlement plate base was made of steel plate of 50 cm × 50 cm × 0.50 cm. The rod should be steel pipe or galvanized pipe, and the bottom rod should be welded with the settlement plate. The casing

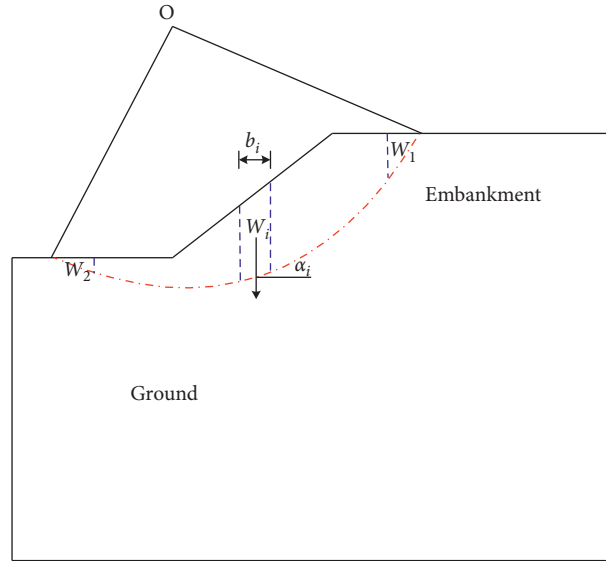


FIGURE 4: Schematic view of calculation of FOS by simplified Bishop method.

TABLE 1: Deformation monitoring grade and accuracy requirements.

Grade	Elevation medium error of deformation observation points (mm)	Median error of height difference between adjacent deformation observation points (mm)	Median error of deformation observation points (mm)
Third class leveling	1.0	0.5	6.0

was plastic pipe. With the increase of filling soil, the measuring rod and casing were connected correspondingly, and the length of each section was generally 50 cm. A small compactor was used to compact the soil around the settlement plate. When placing the settling plate, the bottom groove of the settling plate should be flat. Sand cushion should be laid under the settling plate. The vertical deviation rate of the connecting rod of the settlement plate and the bottom plate should be no more than 1.5%.

Displacement monitoring adopted displacement pile (surface displacement) and inclinometer tube (deep soil displacement) for dynamic monitoring. The displacement piles were mainly used to monitor horizontal and vertical displacements. Horizontal displacement of measuring point can be achieved by polar coordinate method with high precision total station and prism. Vertical displacement can be observed by high precision level or total station with prism. The displacement side piles were laid before soft foundation treatment. They were prefabricated with reinforced concrete. The top of the pile should be pre-embedded with forced alignment facilities. When the displacement piles were placed in excavated soil, the pile body was poured and fixed with concrete from the bottom up to 50 cm.

The inclinometer tube was formed by polyethylene casting. The outer diameter of the tube was 71 mm and the wall thickness is 6 mm. It was buried in the deep section of soft soil and the front of bridge head. The burial depth should be no less than 1 m through the soft soil layer. The accuracy of the inclinometer system was not less than

0.25 mm/m, and the resolution was not less than 0.02 mm/500 mm. The monitoring principle of the inclinometer used in monitoring is shown in Figure 5(b).

The horizontal deviation of the action point of the pulley under the probe relative to the action point of the upper pulley was calculated by the inclination angle θ measured by the instrument. The calculation formula is as follows:

$$(1) \delta_i = L_i \times \sin \theta_i, \quad (5)$$

where δ_i is incremental value of relative horizontal deviation in Section 1 (the bottom of the inclinometer is Section 1); L_i is vertical length of measuring in Section 1; and θ_i is relative increment of inclination in Section 1. Assuming that the horizontal deviation of the section is zero, the total horizontal deviation of the inclinometer at the depth of section n is as follows:

$$(2) \delta = \sum_{i=1}^n \Delta \delta_i = \sum_{i=1}^n L_i * \sin \Delta \theta_i. \quad (6)$$

3.2. Control Standard and Monitoring Frequency. Based on the Chinese Design Code, JTG D30-2015 [34], the filling rate should be strictly controlled during the filling process of embankment in soft foundation section. The control standard was that the land subsidence rate of the embankment center line was not more than 1.0 cm per day and night. The horizontal displacement rate of slope foot was not more than

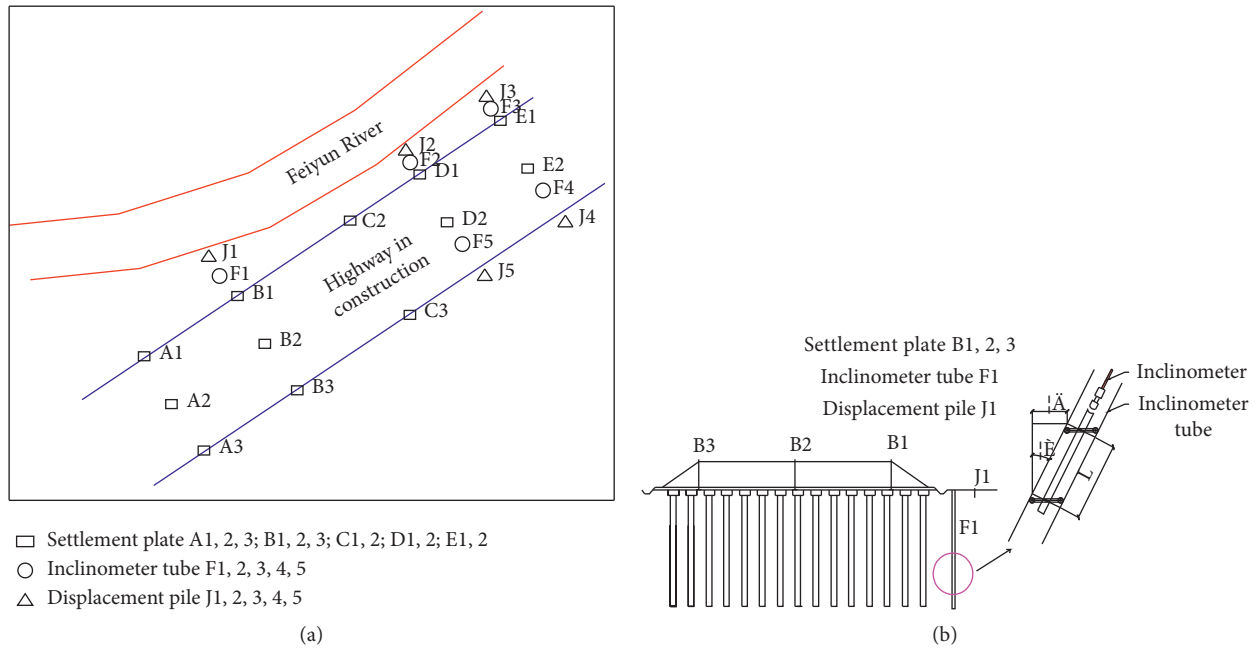


FIGURE 5: Site layout and instrumentation for field test: (a) plan view of the embankment monitoring facilities, (b) diagram of typical section monitoring facilities.

0.5 cm per day and night. Deep lateral displacement rate was 3 mm per day and night. The settlement of the preloaded road section was less than 5 mm for two consecutive months. The monitoring frequency is summarized as follows:

- (1) Construction period: at least one observation per floor was required. If the construction was stopped for any reason, it was observed every three days.
- (2) Preloading period: observation every three days in the first month, observation every seven days from the second month to the third month, and observation every half a month from the fourth month until the pavement is paved.
- (3) Operation period after construction: a small number of typical sections were taken for follow-up observation once every 1-2 months. The frequency of lateral displacement observation was the same as that of settlement observation until the embankment reached the designed construction elevation.

4. Field Observations and Discussion

4.1. Ground Settlement. The settlement observation of embankment section began with embankment filling. Figure 6 illustrates the relationship between the cumulative settlements of section A (A1, A2, A3), section B (B1, B2, B3), section C (C1, C2), section D (D1, D2), and section E (E1, E2) with time. The settlement rate curves of the maximum accumulative settlement measurement points (A1, B1, C1, D1, E1) with time are also described.

The filling height at sections A and B was about 5.5 m. The embankment was filled in layers with a thickness of 50 cm. The filling work was divided into four stages. The first stage consisted of two layers of filling with a filling height of

1 m. It took 25 days to fill and 25 days to consolidate the soil-rock mixture. The filling height of the latter three stages was 1.5 m with 25 days for filling and 30 days for consolidation. In the process of subgrade filling, the settlement of A and B had similar development law with time (Figures 6(a) and 6(b)). Firstly, when the first stage was filled to 1 m, the maximum accumulative settlement of A1 and B1 was 5.53 mm and 6.02 mm, respectively. In the second stage of filling to 2.5 m, the maximum settlement of A1 and B1 was 13.77 mm and 14.85 mm, respectively. When the third stage was filled to 4 m, the maximum accumulated settlement occurred at A1 and B1, which was 23.72 mm and 26.80 mm, respectively. Up to 5.5 m of filling, the maximum accumulative settlement of A1 and B1 was 26.23 mm and 29.78 mm, respectively. This corresponded to 76% and 78% of the ultimate settlement. The filling height at sections C, D, and E was about 3 m. The filling of three sections was constructed in three stages. Each stage was filled in two layers. The filling time was 25 days and the consolidation time was 30 days with 1 m filling height. When the first stage was filled to 1 m, the maximum cumulative settlement of the three sections was 10.54 mm, 6.15 mm, and 10.72 mm at C1, D1, and E1, respectively. When the second stage was filled to 2 m, the accumulative settlement of C1, D1, and E1 was the largest with 18.31 mm, 14.80 mm, and 18.90 mm, respectively. The accumulative settlements of C1, D1, and E1 were 18.96 mm, 17.04 mm, and 16.89 mm, respectively, when filling to 3 m, which were the largest values in each section. These values corresponded to 77%, 73%, and 75% of the ultimate settlement. Finally, the accumulative settlements of A1, B1, C1, D1, and E1 tended to be stable, which were 34.33 mm, 37.88 mm, 24.77 mm, 23.20 mm, and 22.66 mm, respectively. The filling stage was the main consolidation and deformation stage of the embankment [37, 38]. The consolidation of

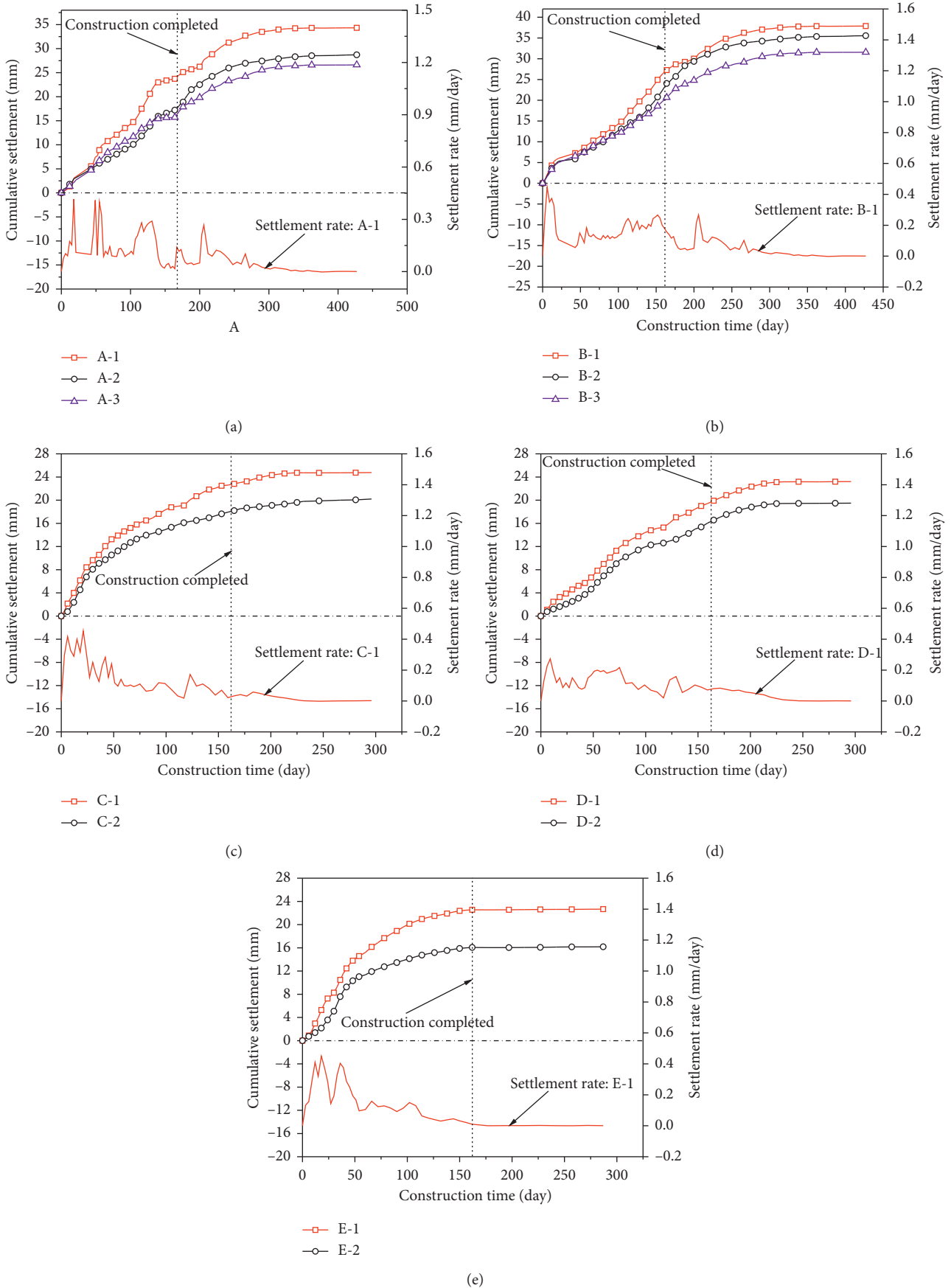
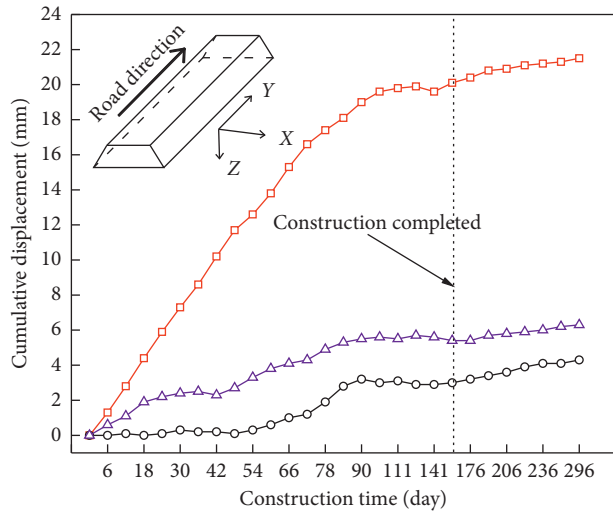
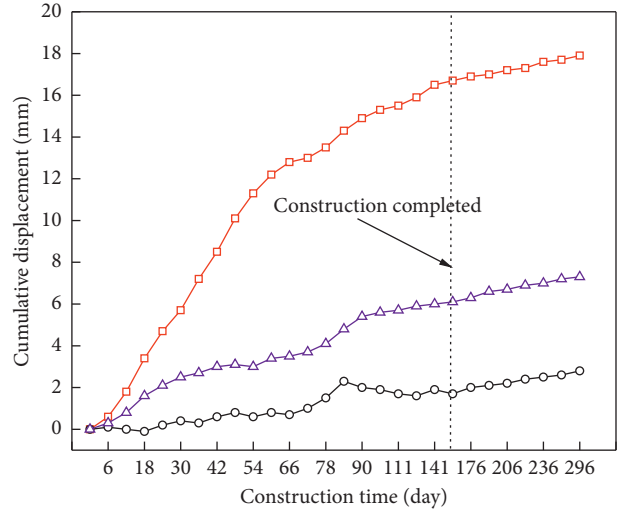


FIGURE 6: Cumulative ground settlement values of each monitoring section and settlement rate corresponding to the maximum cumulative settlement.



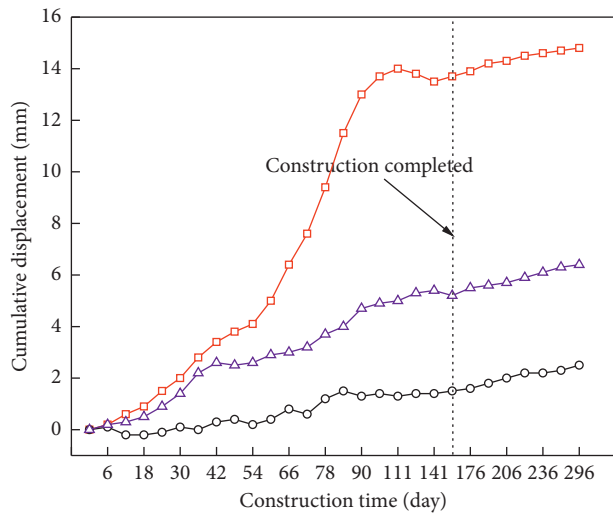
J1
 -□- X
 -○- Y
 -△- Z

(a)



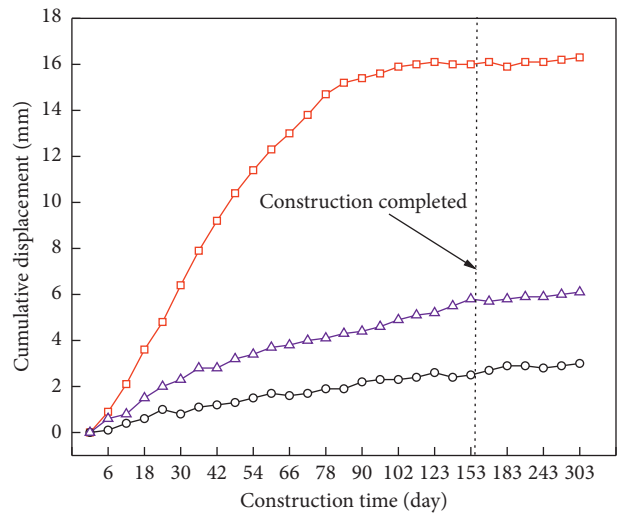
J2
 -□- X
 -○- Y
 -△- Z

(b)



J3
 -□- X
 -○- Y
 -△- Z

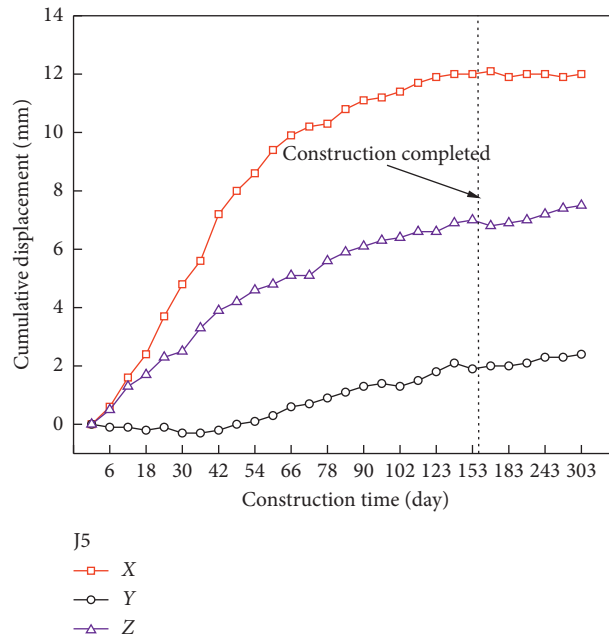
(c)



J4
 -□- X
 -○- Y
 -△- Z

(d)

FIGURE 7: Continued.



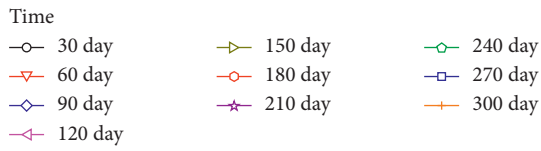
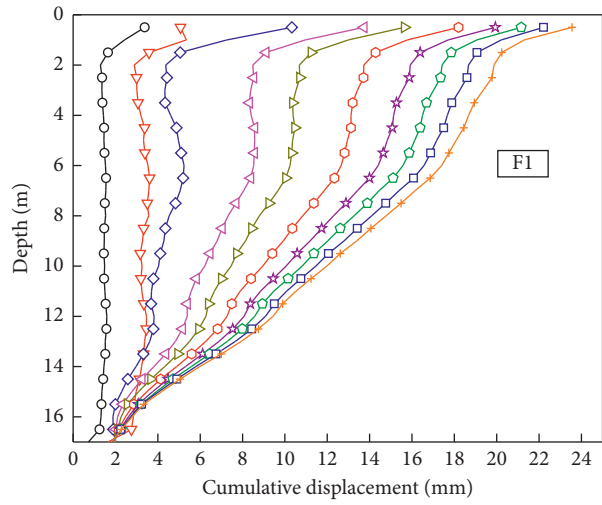
(e)

FIGURE 7: Cumulative ground displacement values of each monitoring point. Notes: X: the positive value is that the measuring point moves away from the central axis of the subgrade, while the negative value is that the measuring point moves towards the central axis of the subgrade. Y: the positive value is that the measuring point moves towards the end of the roadbed, while the negative value is that the measuring point moves towards the beginning of the roadbed. Z: the positive value is sinking and the negative value is uplift.

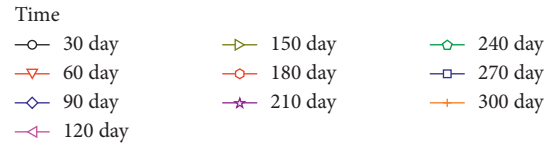
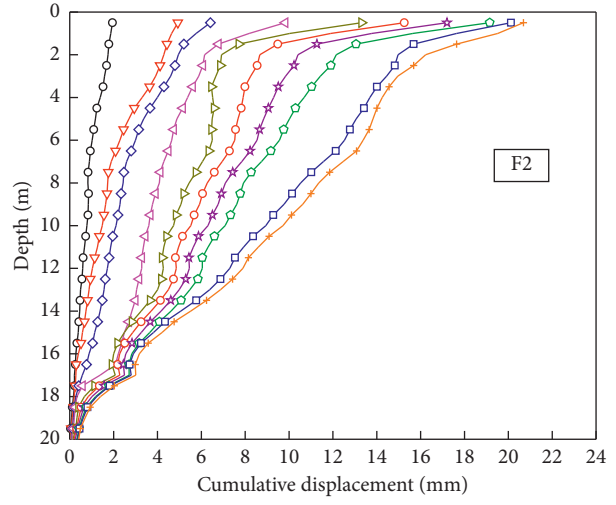
soil is the largest, which accounted for a considerable part of the total settlement. When the filling height was reached, the load gradually became stable. With the drainage consolidation of foundation soil, the strength of soil gradually increased, and the cumulative settlement-time curve of subgrade tended to be flat. At this time, the settlement was mainly secondary consolidation. And the settlement converged to a stable value which was the final settlement. Figure 5 also shows that the settlement rate of A1, B1, C1, D1, and E1 points increased sharply during filling period and tended to be flat during consolidation period. The maximum settlement rates were 0.42 mm/day, 0.37 mm/day, 0.42 mm/day, 0.27 mm/day, and 0.45 mm/day, respectively, which were within the control range.

The maximum cumulative settlement of each section occurred at the location near the riverside on the left side of the subgrade (Figure 4). According to the site geographic environment and geological conditions, the role of the river had a certain impact on the stability of the embankment [39–41]. Based on the Chinese design code, JTG D30-2015 [34], the monitoring results showed that the maximum cumulative settlement and settlement rate did not exceed the control range. It can be seen that the composite foundation composed of plain concrete pile and reinforced cushion plays an important role in improving the stability of embankment. With the increase of filling height of subgrade, the cumulative ground settlement values will become larger, but the settlement rate will be smaller because of the continuous consolidation of soil.

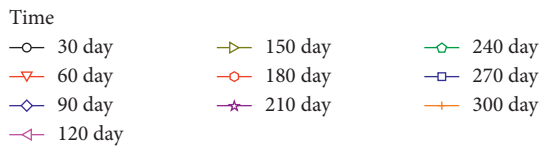
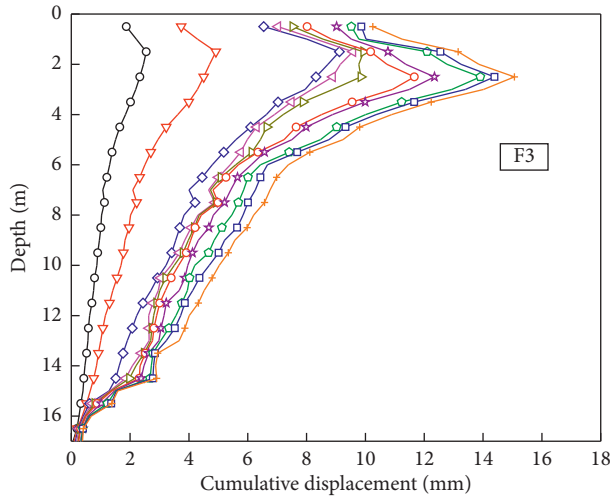
4.2. Ground Displacement. Figure 6 shows the change of accumulated surface displacement of each observation point during the observation period. Displacement piles (J1, J2, J3, J4, J5) were buried outside the treatment scope of soft soil roadbed. Moreover, the cumulative displacement of five displacement piles had similar law with time. With the increase of embankment filling height, the cumulative displacement increased gradually. The displacement tended to be stable after the final filling was completed. The ultimate cumulative displacement of each measuring point in the X direction was relatively large, which was 21.5 mm (J1), 17.9 mm (J2), 15.2 mm (J3), 16.3 mm (J4), and 12.0 mm (J5), respectively. The reason may be that, in the direction perpendicular to the route, the lateral soil body of the embankment was not restrained. The filling increased the load, which resulted in large deformation in this direction. As can be seen, the ultimate cumulative displacement in the Y direction was the smallest, which was 2.5 mm (J1), 2.8 mm (J2), 4.3 mm (J3), 3.0 mm (J4), and 2.4 mm (J5), respectively. Because the filling height of the embankment on the section where the displacement pile (J1) was located is about twice that of other measuring points, and the equivalent load was nearly twice that of other measuring points, the accumulated lateral displacement of the ground surface was relatively large. However, due to the reinforcement effect of the pile, there is not much difference between the maximum displacement and the minimum displacement. Figure 7 also illustrates that the displacement pile (J3) may have a steeper curve change rate due to the rapid filling in the filling process, where the displacement rate was relatively large.



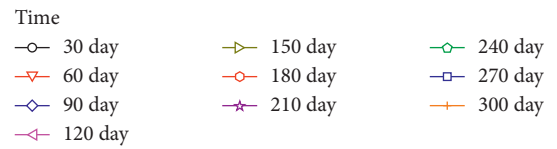
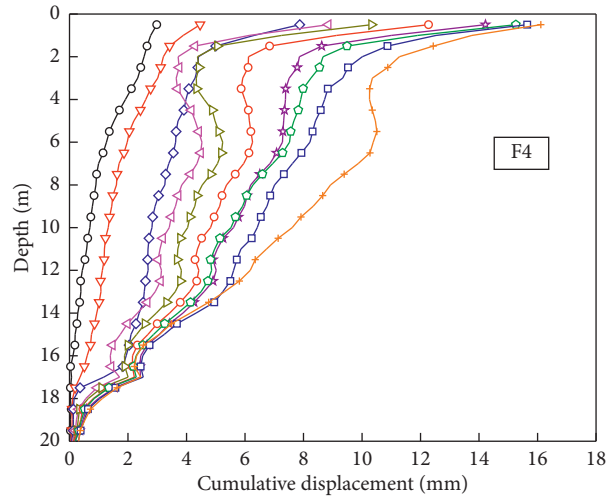
(a)



(b)



(c)



(d)

FIGURE 8: Continued.

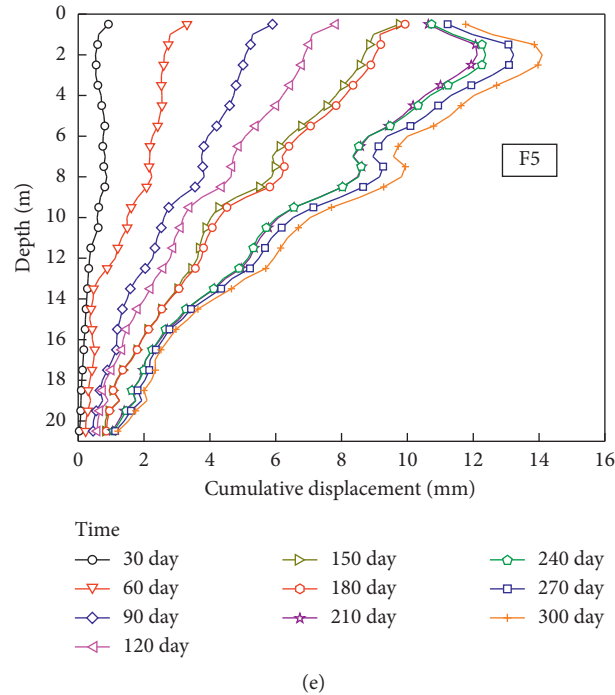


FIGURE 8: Lateral displacement of subsoil of each measuring point.

With the completion of embankment filling, the load gradually stabilized. Lateral surface displacement also decreased gradually, and the displacement curve tended to be flat.

4.3. Lateral Displacement of Subsoil. Figure 8 shows the variation of horizontal displacement in the depth of each survey point. It was measured by an inclinometer at 2 m from the foot of embankment slope. The maximum cumulative lateral displacements of inclinometer tubes (F1, F2, and F4) were 23.56 mm, 20.68 mm, and 16.11 mm, respectively, which all occurred at 0.5 mm below the surface. The maximum cumulative lateral displacement of subsoil of the inclined pipe (F3) was 14.01 mm, which occurred at a depth of 3 m below the surface, while the maximum cumulative lateral displacement of subsoil of the inclined pipe (F5) was 14.10 mm, which occurred at a depth of 2 m below the surface. Among them, the cumulative displacement of the inclinometer tube (F2) was the largest, which was mainly related to the embankment filling height. During embankment filling, the maximum cumulative displacement of each measuring point accounted for 75%, 73%, 78%, 76%, and 64% of the final cumulative displacement, respectively. Therefore, the process of loading caused large displacement of embankment. It can be seen from the data of each monitoring point that the lateral displacement inside the soil was relatively small. From the bottom of the inclinometer tube to the ground, the lateral displacement of soil increases gradually. And the closer the ground, the greater the displacement. It also shows that the treatment of soft soil subgrade played a vital role in the stability of embankment. Embankment construction or excavation process involves a time-dependent problem due to the dissipation of excess

pore water pressure [42, 43]. Due to the fact that the pore water pressure indicators were all destroyed because of the carelessness of construction persons during the construction, the time-dependent behavior of this project was not given more focus.

5. Conclusions

A case study for highway construction over soft marine clay in China is presented in this paper. The obtained results from this study are summarized as follows:

- (1) The settlement on the left side of the embankment was larger than that on the right side. The final cumulative settlement of each section near the river side was the largest, which was 34.33 mm, 37.88 mm, 24.77 mm, 23.20 mm, and 22.66 mm, respectively. During the embankment filling, the settlement accounted for 76%, 78%, 77%, 73%, and 75% of the final settlement. The maximum settlement rate was 0.45 mm/day. With the increase of embankment filling height, the cumulative settlement has an increase. When the embankment construction was completed, the settlement gradually tended to be stable.
- (2) The maximum displacement of the surface at the distance of 2.5 m away from the foot of the embankment was 21.5 mm. The filling height of this section was twice that of other sections, and the load was also nearly twice that of other sections, which makes the lateral displacement of the surface larger. However, due to the reinforcement effect of plain concrete pile and reinforced cushion on roadbed, the observed displacements were not different.

- (3) The maximum cumulative horizontal displacement of each monitoring point was 23.56 mm, which occurred at 0.5 mm below the surface. Moreover, the displacement generated during embankment filling accounted for about 75% of the final displacement. The smallest percentage of other monitoring sites was 64%. It can be seen that the filling had a certain impact on the embankment. The measured settlement and displacement meet the specification requirement, and the monitoring of the process should be strengthened to ensure the safety of the construction.

Data Availability

The data used to support the findings of this study are included within the article.

Conflicts of Interest

The authors declare that they have no conflicts of interest.

Acknowledgments

This research was funded by the China Postdoctoral Science Foundation (Grant nos. 2016M600396 and 2017T100355). Partial financial support from the Fundamental Research Funds for the Central Universities (Grant no. B200204001) is also acknowledged.

References

- [1] S.-L. Shen, Y.-J. Du, and C.-Y. Luo, "Evaluation of the effect of rolling correction of double-o-tunnel shields via one-side loading," *Canadian Geotechnical Journal*, vol. 47, no. 10, pp. 1060–1070, 2010.
- [2] Z.-F. Wang, S.-L. Shen, C.-E. Ho, and Y.-H. Kim, "Investigation of field-installation effects of horizontal twin-jet grouting in Shanghai soft soil deposits," *Canadian Geotechnical Journal*, vol. 50, no. 3, pp. 288–297, 2013.
- [3] X. Bian, L.-L. Zeng, J.-W. Ding, and S. Qian, "Assessment of the effects of initial water contents on the pore pressure response of reconstituted clays," *European Journal of Environmental and Civil Engineering*, vol. 21, no. 4, pp. 454–470, 2017.
- [4] X. Bian, Y.-J. Cui, and X.-Z. Li, "Voids effect on the swelling behaviour of compacted bentonite," *Géotechnique*, vol. 69, no. 7, pp. 593–605, 2019.
- [5] Z. Hong, S. Liu, S. Shen, and T. Negami, "Comparison in undrained shear strength between undisturbed and remolded airake clays," *Journal of Geotechnical and Geoenvironmental Engineering*, vol. 132, no. 2, pp. 272–275, 2006.
- [6] A. M. C. Horbe, I. R. da Trindade, E. L. Dantas, R. V. Santos, and M. Roddaz, "Provenance of quaternary and modern alluvial deposits of the Amazonian floodplain (Brazil) inferred from major and trace elements and Pb-Nd-Sr isotopes," *Palaeogeography, Palaeoclimatology, Palaeoecology*, vol. 411, pp. 144–154, 2014.
- [7] X. Bian, Z.-F. Wang, G.-Q. Ding, and Y.-P. Cao, "Compressibility of cemented dredged clay at high water content with super-absorbent polymer," *Engineering Geology*, vol. 208, pp. 198–205, 2016.
- [8] H. B. Nagaraj, M. V. Sravan, and B. S. Deepa, "Factors influencing undrained strength of fine-grained soils at high water contents," *Geomechanics and Geoengineering*, vol. 13, no. 4, pp. 276–287, 2018.
- [9] X. S. Shi and J. Zhao, "Practical estimation of compression behavior of clayey/silty sands using equivalent void-ratio concept," *Journal of Geotechnical and Geoenvironmental Engineering*, vol. 146, no. 6, Article ID 4020046, 2020.
- [10] W.-C. Cheng, G. Li, N. Liu, J. Xu, and S. Horpibulsuk, "Recent massive incidents for subway construction in soft alluvial deposits of Taiwan: a review," *Tunnelling and Underground Space Technology*, vol. 96, Article ID 103178, 2020.
- [11] X. Bian, Y.-J. Cui, L.-L. Zeng, and X.-Z. Li, "Swelling behavior of compacted bentonite with the presence of rock fracture," *Engineering Geology*, vol. 254, pp. 25–33, 2019.
- [12] X. Bian, Y.-J. Cui, L.-L. Zeng, and X.-Z. Li, "State of compacted bentonite inside a fractured granite cylinder after infiltration," *Applied Clay Science*, vol. 186, Article ID 105438, 2020.
- [13] W.-C. Cheng, J. C. Ni, A. Arulrajah, and H.-W. Huang, "A simple approach for characterising tunnel bore conditions based upon pipe-jacking data," *Tunnelling and Underground Space Technology*, vol. 71, pp. 494–504, 2018.
- [14] H. L. Liu, C. W. W.M. Ng, and K. Fei, "Performance of a geogrid-reinforced and pile-supported highway embankment over soft clay: case study," *Journal of Geotechnical and Geoenvironmental Engineering*, vol. 133, no. 12, pp. 1483–1493, 2007.
- [15] Z. F. Wang, W. C. Cheng, Y. Q. Wang, and J. Q. Du, "Simple method to predict settlement of composite foundation under embankment," *International Journal of Geomechanics*, vol. 18, no. 12, 2018.
- [16] W.-C. Cheng, J. C. Ni, H.-W. Huang, J. S. Shen, and J. S. Shen, "The use of tunnelling parameters and spoil characteristics to assess soil types: a case study from alluvial deposits at a pipejacking project site," *Bulletin of Engineering Geology and the Environment*, vol. 78, no. 4, pp. 2933–2942, 2019.
- [17] W.-C. Cheng, L. Wang, Z.-F. Xue, J. C. Ni, M. M. Rahman, and A. Arulrajah, "Lubrication performance of pipejacking in soft alluvial deposits," *Tunnelling and Underground Space Technology*, vol. 91, Article ID 102991, 2019.
- [18] H. Wang, L. L. Zeng, X. Bian, and Z. S. Hong, "Train moving load-induced vertical superimposed stress at ballasted railway tracks," *Advances in Civil Engineering*, vol. 2020, Article ID 3428395, 11 pages, 2020.
- [19] S. L. Shen, C. Y. Luo, Y. Bai, Y. H. Kim, and S. J. Peng, "Instant solidification of soft ground horizontally using jet-grouting," in *Contemporary Topics in Ground Modification, Problem Soils, and Geo-Support*, pp. 257–264, American Society of Civil Engineers (ASCE) Press, Reston, VA, USA, 2009.
- [20] Z. F. Wang, J. S. Shen, and W. C. Cheng, "Simple method to predict ground displacements caused by installing horizontal jet-grouting columns," *Mathematical Problems in Engineering*, vol. 2018, Article ID 1897394, 11 pages, 2018.
- [21] J.-J. Chen, L. Zhang, J.-F. Zhang, Y.-F. Zhu, and J.-H. Wang, "Field tests, modification, and application of deep soil mixing method in soft clay," *Journal of Geotechnical and Geoenvironmental Engineering*, vol. 139, no. 1, pp. 24–34, 2013.
- [22] A. S. A. Rashid, A. R. Bunawan, and K. N. Mat Said, "The deep mixing method: bearing capacity studies," *Geotechnical and Geological Engineering*, vol. 35, no. 4, pp. 1271–1298, 2017.
- [23] M. Saberian, M. Moradi, R. Vali, and J. Li, "Stabilized marine and desert sands with deep mixing of cement and sodium

- bentonite,” *Geomechanics and Engineering*, vol. 14, no. 6, pp. 553–562, 2018.
- [24] J. L. Briaud, R. Abdelmalak, X. Zhang, and C. Magbo, “Stiffened slab-on-grade on shrink-swell soil: new design method,” *Journal of Geotechnical and Geoenvironmental Engineering*, vol. 142, no. 7, Article ID 4016017, 2016.
- [25] M. A. Shams, M. A. Shahin, and M. A. Ismail, “Simulating the behaviour of reactive soils and slab foundations using hydro-mechanical finite element modelling incorporating soil suction and moisture changes,” *Computers and Geotechnics*, vol. 98, pp. 17–34, 2018.
- [26] Y. Lv, H. Liu, X. Ding, and G. Kong, “Field tests on bearing characteristics of X-section pile composite foundation,” *Journal of Performance of Constructed Facilities*, vol. 26, no. 2, pp. 180–189, 2012.
- [27] A. R. Vosoughi, P. Malekzadeh, and H. Razi, “Response of moderately thick laminated composite plates on elastic foundation subjected to moving load,” *Composite Structures*, vol. 97, pp. 286–295, 2013.
- [28] M. Ehrlich, S. H. Mirmoradi, and R. P. Saramago, “Evaluation of the effect of compaction on the behavior of geosynthetic-reinforced soil walls,” *Geotextiles and Geomembranes*, vol. 34, pp. 108–115, 2012.
- [29] M. Ghazavi and J. Nazari Afshar, “Bearing capacity of geosynthetic encased stone columns,” *Geotextiles and Geomembranes*, vol. 38, pp. 26–36, 2013.
- [30] R. Girout, M. Blanc, L. Thorel, and D. Dias, “Geosynthetic reinforcement of pile-supported embankments,” *Geosynthetics International*, vol. 25, no. 1, pp. 37–49, 2018.
- [31] R. P. Chen, Y. W. Wang, X. W. Ye, X. C. Bian, and X. P. Dong, “Tensile force of geogrids embedded in pile-supported reinforced embankment: a full-scale experimental study,” *Geotextiles and Geomembranes*, vol. 44, no. 2, pp. 157–169, 2016.
- [32] R. Xu and B. Fatahi, “Geosynthetic-reinforced cushioned piles with controlled rocking for seismic safeguarding,” *Geosynthetics International*, vol. 25, no. 6, pp. 561–581, 2018.
- [33] ASTM Standard D2487, *Standard Practice for Classification of Soils for Engineering Purposes (Unified Soil Classification System)*, American Society for Testing and Materials, West Conshohocken, PA, USA, 2011.
- [34] Ministry of Transport of the People’s Republic of China, *Technical Specifications for Construction of Highway Subgrades (JTG/T 3610-2019)*, China Communications Press, Beijing, China, 2019.
- [35] Ministry of Housing and Urban-Rural Development of the People’s Republic of China, *Technical Code for Testing of Building Foundation Piles*, China Architecture & Building Press, Beijing, China, 2014.
- [36] Ministry of Construction of the People’s Republic of China, *Code for Engineering Surveying (GB50021-2007)*, China Architecture and Building Press, Beijing, China, 2008.
- [37] F. Tavenas and S. Leroueil, “The behaviour of embankments on clay foundations,” *Canadian Geotechnical Journal*, vol. 17, no. 2, pp. 236–260, 1980.
- [38] A. S. Al-Homoud and N. Tanash, “Monitoring and analysis of settlement and stability of an embankment dam constructed in stages on soft ground,” *Bulletin of Engineering Geology and the Environment*, vol. 59, no. 4, pp. 259–284, 2001.
- [39] C. Swartenbroekx, S. Soares-Frazaõ, R. Staquet, and Y. Zech, “Two-dimensional operator for bank failures induced by water-level rise in dam-break flows,” *Journal of Hydraulic Research*, vol. 48, no. 3, pp. 302–314, 2010.
- [40] H. Mizutani, H. Nakagawa, T. Yoden, K. Kawaike, and H. Zhang, “Numerical modelling of river embankment failure due to overtopping flow considering infiltration effects,” *Journal of Hydraulic Research*, vol. 51, no. 6, pp. 681–695, 2013.
- [41] Y.-Q. Wang, Z.-F. Wang, and W.-C. Cheng, “A review on land subsidence caused by groundwater withdrawal in Xi’an, China,” *Bulletin of Engineering Geology and the Environment*, vol. 78, no. 4, pp. 2851–2863, 2019.
- [42] D. E. L. Ong, C. F. Leung, Y. K. Chow, and T. G. Ng, “Severe damage of a pile group due to slope failure,” *Journal of Geotechnical and Geoenvironmental Engineering*, vol. 141, no. 5, Article ID 4015014, 2015.
- [43] Z.-F. Wang, S.-L. Shen, G. Modoni, and A. Zhou, “Excess pore water pressure caused by the installation of jet grouting columns in clay,” *Computers and Geotechnics*, vol. 125, Article ID 103667, 2020.

Research Article

The Influence of Complex Subway Station Construction on High Retaining Walls and Appropriate Countermeasures

Kai Wang,¹ Zhaoping Li ,¹ Xuezhao Xu,¹ Leilei Shi,² and Fanbo Zhang¹

¹School of Civil Engineering, Beijing Jiaotong University, Beijing 100044, China

²Beijing No. 4 Municipal Construction Engineering Co., Ltd., Beijing 100176, China

Correspondence should be addressed to Zhaoping Li; zhpli@bjtu.edu.cn

Received 31 May 2020; Revised 7 July 2020; Accepted 13 July 2020; Published 31 July 2020

Academic Editor: Wen-Chieh Cheng

Copyright © 2020 Kai Wang et al. This is an open access article distributed under the Creative Commons Attribution License, which permits unrestricted use, distribution, and reproduction in any medium, provided the original work is properly cited.

Anzhen Bridge Station of Beijing metro line 12, which adopts a separated-island platform constructed by the undermining method, passes along the retaining wall of the North Third Ring Road. A numerical simulation method is adopted to study the deformation laws of the retaining wall under the influence of station construction. The simulation data show that the affected retaining wall will have large settlement and tilt, and countermeasures must be taken. Four countermeasures are formulated, and their control effects are analyzed. The calculation results show that the combination of anchor cables and waist beams can effectively control the tilt of the retaining wall, but the control effect on the absolute settlement is not obvious. The control effect of isolation piles is better than that of foundation grouting. The joint control method of anchor cables combined with waist beams, isolation piles, and deep hole grouting makes the deformation meet the target, and according to this measure, a concept of joint control aiming at the influence of the “source,” “propagation,” and “object” is proposed, which can provide a reference for similar projects with a great difficulty in deformation control.

1. Introduction

In concentrated areas, subway lines are usually laid along a city's main road, so the subway tunnel or station underpasses the road frequently. In overpass sections, retaining walls are often installed, and subway construction will not only affect road safety [1–3], but also threaten the stability and safety of the retaining walls. At present, there have been many studies on the stability of retaining walls, including the stability of retaining walls under static loads [4–6], the dynamic response of retaining walls [7–11], the behavior of retaining walls affected by deep excavation [12, 13], and the time-dependent behavior of piles and retaining walls as a result of excavation-induced soil movement [14]. These studies have made many achievements in terms of the stability of retaining walls. However, the response of a road retaining wall with a shallow foundation under the influence of underground excavation has not been fully studied. According to the in-situ settlement laws of the retaining wall embankment, Ma et al. [15] summarized the experiences on real-time adjustment of shield construction parameters and comprehensive use of grouting. Liu [16] analyzed the settlement laws of the highway

retaining wall under the influence of tunnel construction by numerical simulation. The above research only concerns the settlement of the retaining wall. Sun [17] analyzed the settlement and tilt laws of the road retaining walls affected by shallow buried tunnels. However, the influence of station construction is more complicated than that of tunnel and there is little literature on the response of the road retaining wall under the influence of subway station construction.

According to previous research on the influence of underground construction on soil movement, station construction has the following main effects on retaining walls.

1.1. Absolute Subsidence. Soil excavation causes stratum settlement [18–20]. A retaining wall will settle with the ground if its foundation is in the settlement area. The resulting settlement is absolute subsidence. In this project, the minimum horizontal distance between the main body and the retaining wall foundation is only 1.05 m. Too much absolute settlement will affect the stability of the pavement structure, resulting in a poor connection between the pavement and the bridge deck and endangering traffic safety.

1.2. Differential Settlement. Differential settlement refers to nonuniform settlement along retaining walls, the magnitude of which is the difference in the vertical displacement between two measured points. The reasons for differential settlement are complicated and include the complexity of station construction processes, the inhomogeneity of the strata and the filling, and the construction of connecting channels. Excessive differential settlement will lead to cracks in the retaining wall, which will seriously destabilize the retaining wall and lead to accidents such as soil filling collapse and road damage.

1.3. Tilt Deformation. The closer a retaining wall is to the centerline of the main structure, the greater the surface settlement caused by construction [21–23]. Therefore, a difference in the lateral settlement of the retaining wall foundation will cause the retaining wall to tilt and even collapse in serious cases.

However, the above deformation laws and effective control measures are currently unclear.

The construction of Anzhen Bridge Station of Beijing metro line 12 will affect the retaining walls of the North Third Ring Road. Because the station adopts a separated-island platform constructed by the undermining method, the construction of the main part of the station and the two connecting aisles will have a superimposed impact on the retaining wall, threatening the stability and safety of the retaining wall. Based on this background, this paper analyzed the deformation laws of retaining walls under the influence of station construction and proposed effective control measures and control concepts.

2. Project Overview

Anzhen Bridge Station is at the intersection of An-Ding Road and the North Third Ring Road in an east-west alignment along the North Third Ring Road. It is a double-deck separated-island platform station constructed by the PBA (Pile-Beam-Arc) method. The depth of the standard section is 14.9 m. There are two overpasses named Anzhen East Bridge and Anzhen West Bridge over Andingmenwai Street running from east to west along the North Third Ring Road. There are three sections of retaining walls: one to the east of Anzhen East Bridge, one between the two bridges, and one to the west of Anzhen West Bridge. The retaining wall is a counterfort type with a maximum height of 5.57 m. There are 20 retaining walls between the two bridges, and every five retaining walls share a common foundation. A deformation joint of 20 mm is set between the adjacent retaining walls. The Anzhen East Bridge and the walls are depicted in Figure 1. A plan sketch of the station and the retaining walls is shown in Figure 2. The vertical positions of the connecting aisles and retaining wall and of the main structure of the station and retaining wall are shown in Figures 3 and 4, respectively.

Because the height of the retaining wall between the East and West Anzhen Bridges is large, and it is influenced by the construction of the main structure of the station and the



FIGURE 1: Image of Anzhen East Bridge and the retaining walls.

connection channels, this section of retaining wall is chosen as the research object.

The control indexes of retaining wall deformation were formulated by comprehensively considering the structural features; design calculation results and national standard named the “Code for Monitoring Measurement of Urban Rail Transit Engineering” (GB 50911-2013) are considered comprehensively. The control indexes of retaining wall deformation are as follows:

- (1) Maximum absolute settlement of the retaining wall is 15 mm
- (2) Maximum differential settlement of adjacent retaining walls is 8 mm
- (3) Maximum tilt deformation of the retaining wall is 1%

3. Calculation of the Stability of the Retaining Wall Affected by Station Construction

3.1. Calculation Model. The overall model size should consider the boundary effect. According to the actual relationship between the position of retaining wall and that of the station structure, the calculation model shown in Figure 5 should be established. To better demonstrate the spatial position relationship of each structure, the spatial positions of the station structures and the retaining wall are shown in Figure 6.

The stratum size in the model is $x \times y \times z = 140 \text{ m} \times 50 \text{ m} \times 60 \text{ m}$. There are six layers. From top to bottom, there are miscellaneous fill, silt, silty clay, silty clay and clay, silty-fine sand, and pebbles. The width of a single retaining wall is 2 m, and the width of a deformation joint is 2 cm. There are 19 deformation joints in 20 retaining walls. Therefore, the length of the retaining wall in the model is $y = 40.38 \text{ m}$. The size of the retaining wall fill is $x \times y \times z = 44.1 \text{ m} \times 40.38 \text{ m} \times 5.57 \text{ m}$.

Every five retaining walls share a common foundation, so there are three deformation joints in twenty retaining walls. These deformation joints are designated as #1, #2, and #3 from west to east. Four measurement points are arranged for each deformation joint, which are on both sides of the wall top and on both sides of the wall bottom, so 12 measurement points are arranged for the 3 deformation joints.

Because the north and south retaining walls are symmetrically arranged with the station structure and the deformation laws are similar, only the north retaining wall is selected

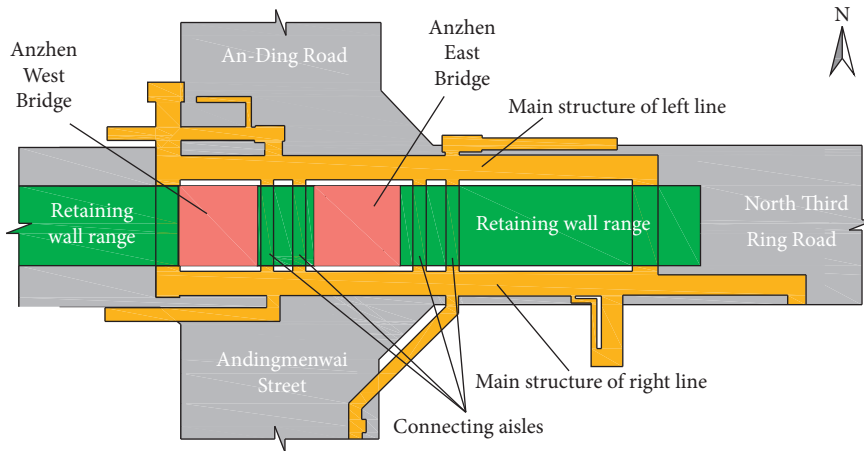


FIGURE 2: Plan sketch of the station and the retaining wall.

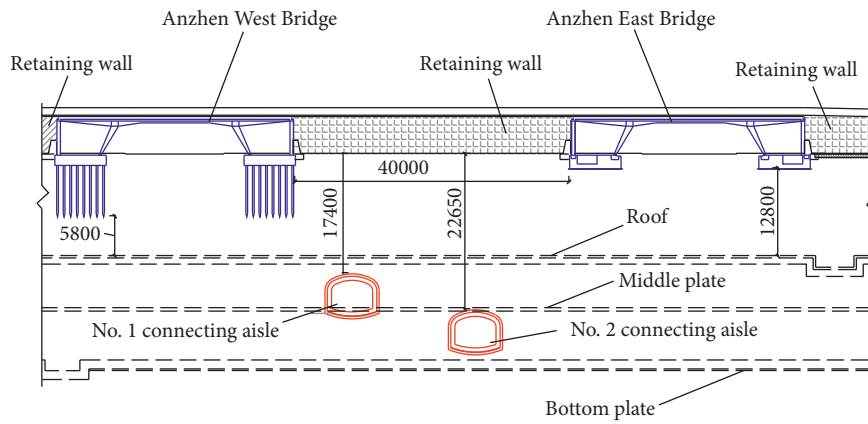


FIGURE 3: Vertical positions of the connecting aisles and the retaining wall (unit: mm).

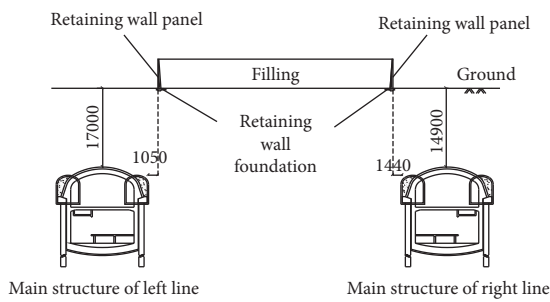


FIGURE 4: Vertical positions of the main structure of the station and the retaining wall (unit: mm).

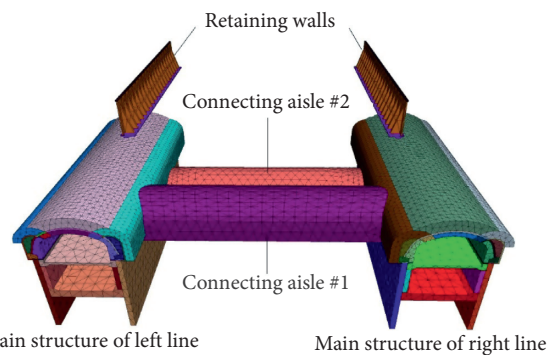


FIGURE 6: Spatial positions of the station structures and the retaining wall.

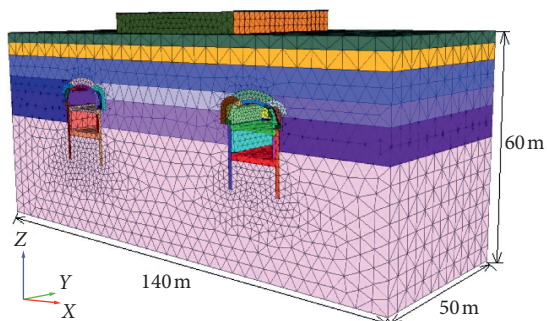


FIGURE 5: Overall model.

as the research object. The number and corresponding location of each measurement point are shown in Figure 7.

3.2. Calculating Parameters. The concrete structures of the station adopt the linear elastic constitutive model, and the soil materials adopt the Mohr-Coulomb constitutive model [24]. To ensure the accuracy of the simulation results, the numerical parameters of the soil layers were obtained from the geological

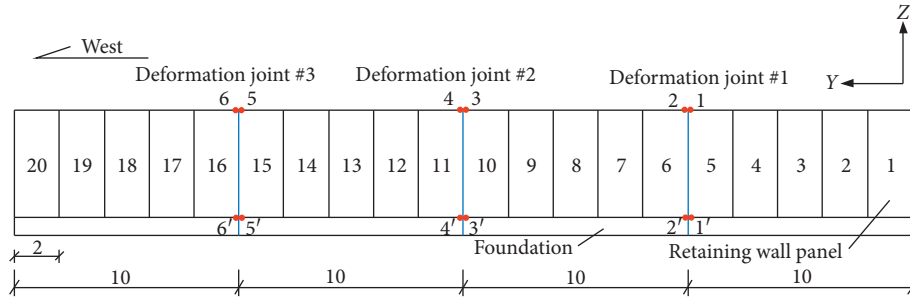


FIGURE 7: Schematic diagram of measurement point arrangement (unit: m).

TABLE 1: Physical and mechanical parameters of the strata.

Layers	Thickness (m)	Unit weight (kN/m ³)	Cohesive force (kPa)	Internal friction angle (°)	Poisson's ratio	Modulus of elasticity (MPa)
Retaining wall fill	3.0	17.0	5	10	0.35	5
Miscellaneous fill	3.0	17.0	5	10	0.35	5
Silt	4.2	19.3	18	25.7	0.30	8
Silty clay	6.8	19.7	28	16	0.30	12
Silty clay and clay	4.8	19.7	32	17	0.30	14
Silty-fine sand	8.2	20.2	15	40	0.25	75
Pebble	33.0	21.2	0	45	0.20	120
Grouting reinforced body	—	22	40	18	0.25	50

TABLE 2: Physical and mechanical parameters of the structures.

Constructions	Materials	Unit weight (kN/m ³)	Cohesive force (GPa)	Poisson's ratio
Retaining wall panel	C35 concrete	24.5	31.5	0.25
Retaining wall foundation	C30 concrete	24.5	30	0.25
Railing base	C40 concrete	25	32.5	0.24
Initial support	C25 concrete	24	28	0.2
Pile	C30 concrete	24.5	30	0.25
Crown beam	C30 concrete	24.5	30	0.25
Pilot tunnel filling	C20 concrete	24	25.5	0.25
Secondary lining	C40 concrete	25	32.5	0.24

investigation report and laboratory tests. To reflect the actual soil-wall interaction behavior, interface elements are used in finite element analysis to simulate sliding between two different materials [25]. The mechanical parameters of the strata and structures are shown in Tables 1 and 2, respectively.

3.3. Calculation Results

3.3.1. Absolute Settlement of the Retaining Wall. The absolute settlement of the top of the wall is affected by the tilt deformation of the retaining wall, so an additional settlement value $h(1 - \cos \theta)$ is added (where h is the height of the wall, and θ is the tilt deformation angle of the retaining wall). Therefore, the displacement data of measurement points 1'–6' in the Z-direction at the bottom of the wall are processed to obtain the settlement curves of the entire construction process, as shown in Figure 8 (the construction sequence of the PBA method is pilot tunnels, side piling, crown beam, arch, middle plate, floor, and side walls. Only the main construction procedures are shown in Figure 8, and the construction of the connecting aisles is added).

Figure 8 shows the following:

- (1) The construction of both the main structure and the connecting aisle will cause the settlement of the retaining wall. The calculated data show that the settlement caused by the construction of the main structure and the construction of the connecting aisle account for approximately 80% and 20% of the final settlement of the retaining wall, respectively
- (2) In the constructions of the pilot tunnels and arch, the curves fall quickly, indicating that these two stages have a great influence on the retaining wall
- (3) Among measurement points 1'–6', the maximum settlement is 56.78 mm at measurement points 1', and the minimum settlement is 44.19 mm at measurement points 5', both of which exceed the settlement index of 15 mm.

According to the settlement value of the midpoint at the bottom of each retaining wall, the final settlement of each retaining wall bottom is shown in Figure 9 (the westernmost

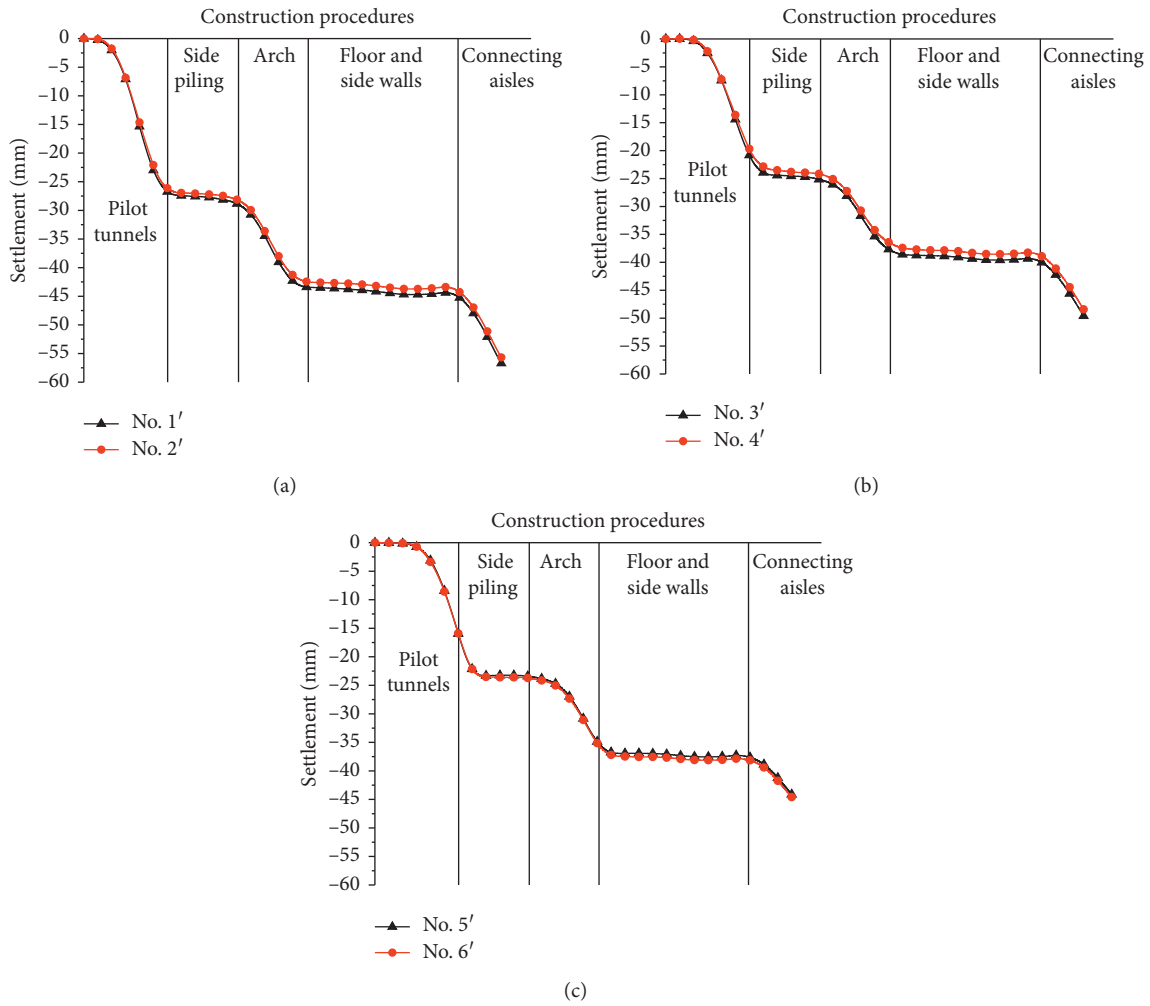


FIGURE 8: (a) Diachronic settlement curves of the measurement points at the wall bottom in the deformation joint #1. (b) Diachronic settlement curves of the measurement points at the wall bottom in the deformation joint #2. (c) Diachronic settlement curves of the measurement points at the wall bottom in the deformation joint #3.

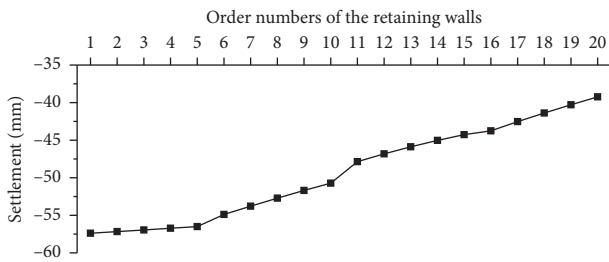


FIGURE 9: Wall bottom final settlement of each retaining wall.

retaining wall is numbered 1, and the numbers increase from west to east).

As shown in Figure 9, under the influence of station construction, the final settlement of the retaining wall presents a trend of “high in the east and low in the west.” The maximum settlement is in retaining wall No. 1 with a settlement value of 57.39 mm, and the minimum settlement is in retaining wall No. 20 with a settlement value of 39.23 mm. The difference between the two is 18.16 mm. The reason why

the retaining wall is high in the east and low in the west is that the west retaining wall is affected by the superposition of the construction of the main structure of the station and the construction of connecting aisle #1. This influence gradually decreases from the centerline of connecting aisle #1 to both sides, so the settlement value decreases gradually from west to east. This phenomenon can be more intuitively illustrated from the settlement cloud map vertically split along the retaining wall, as shown in Figure 10.

3.3.2. *Differential Settlement of the Retaining Wall.* By subtracting the settlement value of measurement point No. 1' from the settlement value of measurement point No. 2', the difference of each time is obtained to form the diachronic differential settlement curve of deformation joint #1, and the differential settlement curves of deformation joints #2 and #3 are also obtained in a similar way, as shown in Figure 11 (the positive and negative signs of the differential settlement value in Figure 11 represent the height difference between the left and right sides of the deformation joint, not the size).

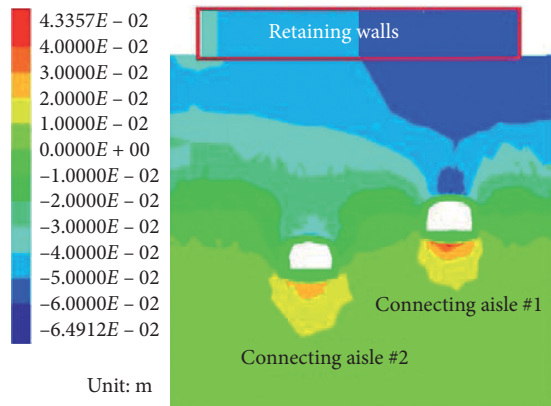


FIGURE 10: Settlement cloud map under the influence of the construction of the connecting aisles.

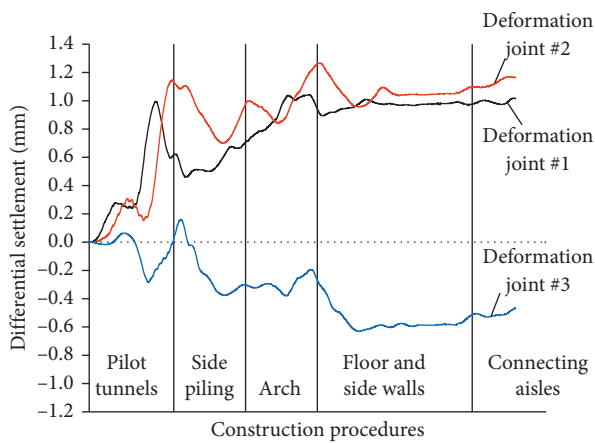


FIGURE 11: Diachronic differential settlement curve of each deformation joint.

As shown in Figure 11, the maximum differential settlement does not occur at the end of construction but rather during construction. The maximum differential settlements of deformation joints #1, #2, and #3 are 1.04 mm, 1.27 mm, and 0.63 mm, respectively, all of which are less than the index value of 8 mm. Therefore, the station construction has little influence on the differential settlement of the retaining wall, so the differential settlement of the retaining wall can be regarded as a nonkey control index when formulating protection measures.

3.3.3. Tilt Rate of the Retaining Wall. The tilt rate of the retaining wall is the ratio of the horizontal displacement difference between the wall top and the wall bottom to the height of the wall—that is,

$$t = \left[\frac{(x - x')}{h} \right] \times 1000\%, \quad (1)$$

where t is the tilt rate of the retaining wall, x is the horizontal displacement of the wall top, x' is the horizontal displacement of the wall bottom, and h is the height of the wall. According to the calculation results of the tilt rate, the

changing curves of the tilt rate with construction progress for the six measurement lines from 1-1' to 6-6' are obtained, as shown in Figure 12 (the positive and negative signs of the tilt rate in the figure represent the tilt direction, not its size).

In the constructions of the pilot tunnels and arch, the curves show obvious peak values, indicating once again that these two stages have a great influence on the retaining wall. The maximum tilt rates of the measurement lines from 1-1' to 6-6' are 4.13‰, 3.62‰, 3.62‰, 3.29‰, 3.16‰, and 3.06‰, respectively, all of which exceed the index value of 1‰.

The simulated data show that the final tilt rate of each retaining wall decreases gradually from west to east. To better reflect this phenomenon, the final tilt rate of each retaining wall is shown in Figure 13 (the westernmost retaining wall is numbered 1, and the numbers increase from west to east).

As shown in Figure 13, due to the construction of connecting aisle #1, the tilt rate of the retaining wall shows a trend of “small in the east and large in the west,” corresponding to the settlement deformation of “high in the east and low in the west,” and the final tilt rates of all 20 retaining walls exceed the index.

The final tilt rate curve of the retaining wall from west to east presents a “step-down” shape comprising four “steps,” and the dividing line between adjacent steps is the position of the deformation joint of the retaining wall foundation. The tilt rate of the five retaining walls sharing one foundation is at the same level, which indicates that the retaining wall foundation features an antitilt ability for the panels.

4. Deformation Control Measures for the Retaining Wall

4.1. Formulation of the Control Measures. After the above analysis, the absolute settlement and the tilt of the affected retaining wall both exceed the index values, so corresponding control measures must be taken to ensure safety. According to the conditions of this project, several countermeasures such as anchor cables with waist beams, foundation grouting, isolation piles, and deep hole grouting inside the tunnel are proposed to control the retaining wall deformation.

4.1.1. Anchor Cables with Waist Beams. The retaining walls are connected by waist beams to form a whole, and the anchor cables penetrate the waist beams and are set inwards. The length of the anchor cable is 11.5 m; the length of the free section is 5 m, the length of the anchorage section is 6.5 m, and the inclination angle is 15° downward. One row of anchor cables is set with 10 cables. To analyze the control effect of the anchor cables with waist beams, two cases are arranged: one row of anchor cables and two rows of anchor cables, as shown in Figure 14.

4.1.2. Foundation Grouting. The grouting position is directly below the retaining wall foundation, and the range is 4.3 m × 42 m × 3 m. When simulating, the stratum parameters after grouting are consistent with those of the advanced

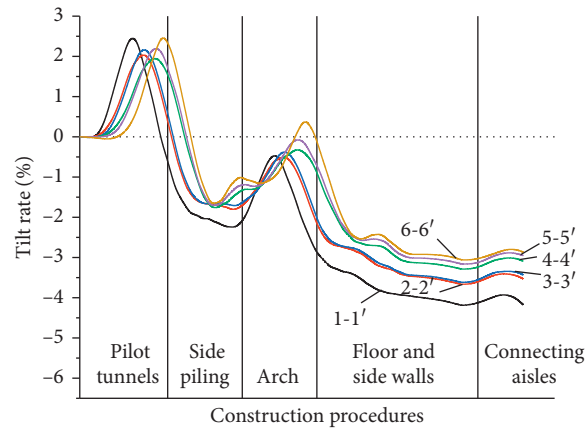


FIGURE 12: Changing curves of the tilt rate.

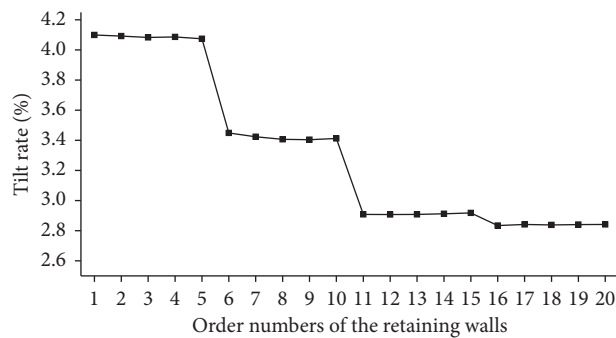


FIGURE 13: Final tilt rate of each retaining wall.

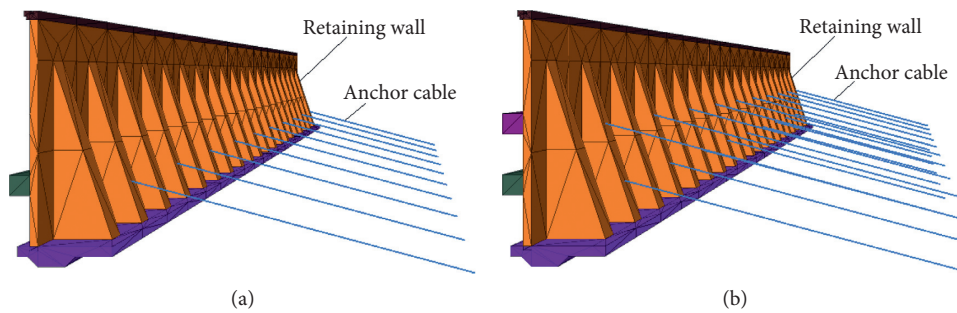


FIGURE 14: Anchor cable + waist beam control measure. (a) A row of anchor cables. (b) Two rows of anchor cables.

small pipe grouting. A sketch of the foundation grouting is shown in Figure 15.

4.1.3. *Isolation Piles.* The isolation pile is in the form of a composite anchor pile, which is designed to bear the bending moment and shear caused by soil movements and is arranged between the main structure of the station and the retaining wall in three rows with a diameter of 0.15 m, an interval of 0.8 m, a row spacing of 1 m, a length of 27 m, and a setting angle of 17°. Based on the principle of equivalent stiffness, the isolated pile is simplified into a continuous structure for simulation. The model diagram is shown in Figure 16.

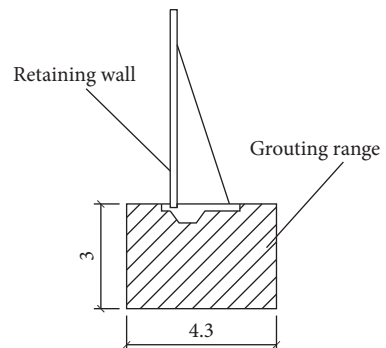


FIGURE 15: Sketch of the foundation grouting (unit: m).

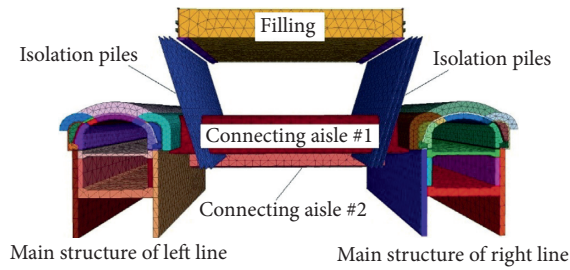


FIGURE 16: Model diagram of the isolation piles.

4.1.4. *Deep Hole Grouting inside the Tunnel.* Before the excavation of the main structure of the station, deep hole grouting should be carried out to reinforce the soil in front of the tunnel face. The grouting range is 1.5 m outside and 0.5 m inside the excavation contour. The grouting section diagram is shown in Figure 17.

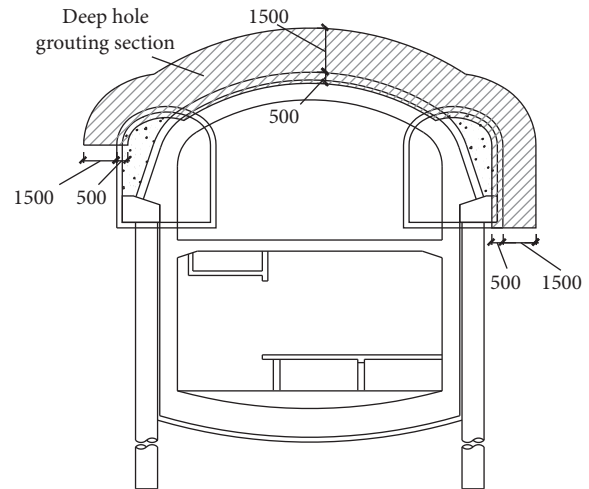


FIGURE 17: Grouting section diagram (unit: mm).

The protective effect of each measure is analyzed below. Because the differential settlement of the retaining wall under the condition of no measures meets the index requirement, analyzing the differential settlement of the retaining wall under various measures is not necessary.

4.2. *Protection Effect of Anchor Cables with Waist Beams*

4.2.1. *Control Effect on the Absolute Settlement.* According to the settlement value of the midpoint at the bottom of each retaining wall, the final settlement curves of 20 retaining walls under the condition of one row of anchor cables and two rows of anchor cables are compared with the settlement curves without measures, as shown in Figure 18.

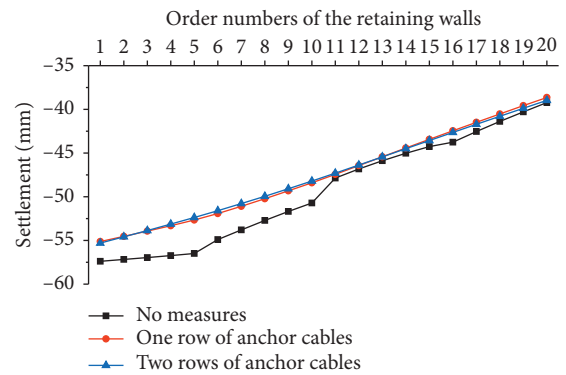
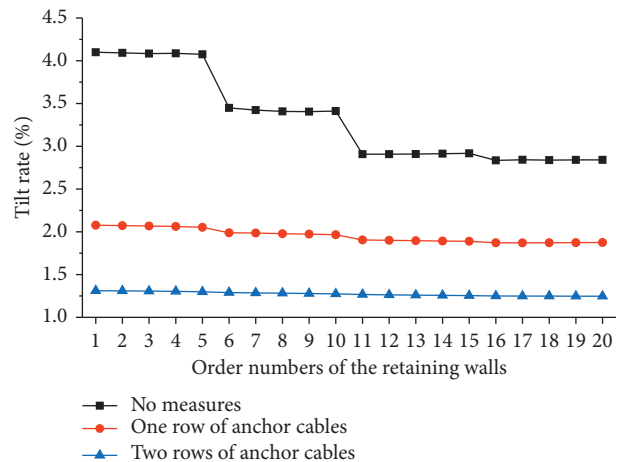


FIGURE 18: Wall bottom final settlement curves in different cases.

Figure 18 shows that the final settlement curves of one row of anchor cables and two rows of anchor cables almost coincide, indicating that there is no significant difference in the control of the absolute settlement between them. The maximum settlement value of one row of anchor cables is 55.34 mm, and the maximum settlement value of two rows of anchor cables is 55.43 mm. Compared with the situation without measures, the settlement value is reduced by 2.04 mm and 1.95 mm, respectively, so the absolute settlement control effect is not obvious.



4.2.2. *Control Effect on Tilt Deformation.* The final tilt rate curves of the retaining wall under the two conditions of one row of anchor cables and two rows of anchor cables are compared with those without measures, as shown in Figure 19.

FIGURE 19: Final tilt rate curves of the retaining wall in different cases.

As shown in Figure 19, the maximum tilt rate of the retaining wall with one row of anchor cables is 2.08%, which is 49.27% lower than that of the retaining wall without measures. The maximum tilt rate of the retaining wall with two rows of anchor cables is 1.31%, which is 68.05% lower than the maximum tilt rate of the retaining wall without measures. Therefore, the use of anchor cables with waist beams has a significant control effect on the tilt of the retaining wall, but the tilt rate still exceeds the requirements of the index.

It is also found that the step height difference of the curve after setting the anchor cables is reduced, which indicates that the use of anchor cables with waist beams reduces the deformation difference among the retaining walls and forms a whole to jointly resist the influence of station construction.

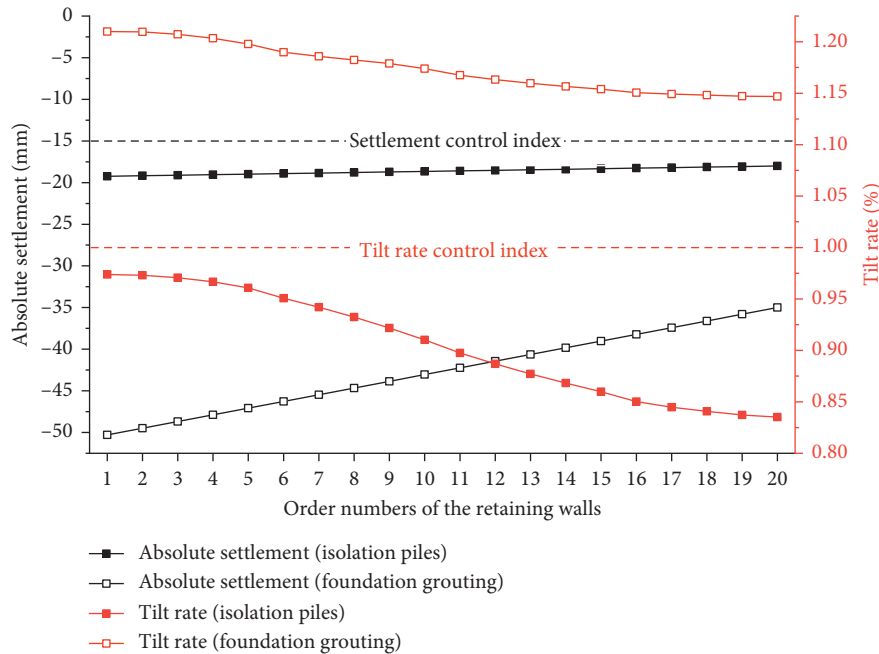


FIGURE 20: Final absolute settlement and final tilt rate of the retaining wall under the conditions of grouting and isolation piles.

4.3. Comparison of the Protection Effect between Foundation Grouting and Isolation Piles. The absolute settlement of the retaining wall cannot be controlled effectively by means of two rows of anchor cables with waist beams, and the tilt rate still exceeds the index value. Therefore, other means should be combined to control the retaining wall deformation. Grouting and isolation piles are two common means to protect adjacent structures in close construction [26–31]. However, in past engineering practices, the selection of grouting and isolation piles was often blind. Thus, scientific protective means were not selected according to the engineering situation, preventing the expected effect from being achieved or causing material waste. This paper compares and evaluates the protection effect of grouting and isolation piles on the premise of applying two rows of anchor cables with waist beams and analyzes the differences of the protection effect between the two measures.

The final absolute settlement and final tilt rate of the retaining wall under the conditions of grouting and isolation piles are shown in Figure 20.

By comparing settlement and tilt rate curves between the two cases, it is indicated that the control effect of the foundation grouting is not ideal. The maximum settlement of the retaining wall is 50.30 mm, and the maximum tilt rate is 1.21‰, exceeding the index value by 235% and 21%, respectively. Relatively speaking, the control effect of the isolation piles is remarkable. The maximum settlement of the retaining wall is 19.24 mm, and the maximum tilt rate of the retaining wall is 0.97‰, which meets the index requirements, but the absolute settlement still exceeds the index value by 28%. Thus, reducing the settlement value of the retaining wall is the most difficult problem in this project, and other means should be combined to control the settlement.

To better explain the reason for the large gap between the protection effects of grouting and those of isolation piles, the stratum settlement cloud maps of the two situations are compared, as shown in Figure 21.

Because the retaining wall foundation is close to the centerline of the main body of the station, the scope of grouting is completely within the scope of the setting tank, and the construction of the station causes the overall settlement of the reinforced soil, which explains why the grouting effect is not significant. In the case of isolation piles, the width of the setting tank decreases obviously, and the impact of the stratum settlement caused by station construction on the retaining wall is weakened. This is because the lower part of the isolation pile goes deep into a stable stratum, and the structure of the isolation pile is stable, which can have an obvious partitioning effect on the transmission of the impacts of construction. In addition, there is no plastic zone in the pile during construction, so the settlement of the retaining wall decreases obviously.

It can be seen from the protection effect of grouting that when grouting reinforcement is carried out around a shallow foundation, if the grouting scope is completely within the construction influence scope, the grouting reinforced body will settle as a whole, and the protection effect on the foundation is not good. A large number of engineering examples have proven that grouting the soils surrounding an excavation space inside a tunnel can effectively control stratum settlement [32–34], so the grouting effect is closely related to the grouting position, and grouting measures are more suitable to solve the settlement problem from the “influence source”; that is, the reasonable grouting range should be the soils around the excavation face.

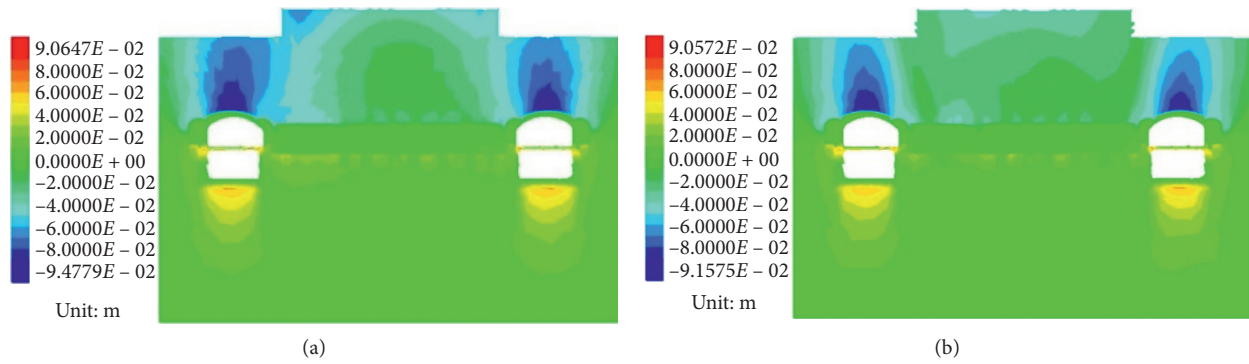


FIGURE 21: Comparison of the two stratum settlement cloud maps. (a) Stratum settlement cloud map under grouting conditions. (b) Stratum settlement cloud map under isolation piles conditions.

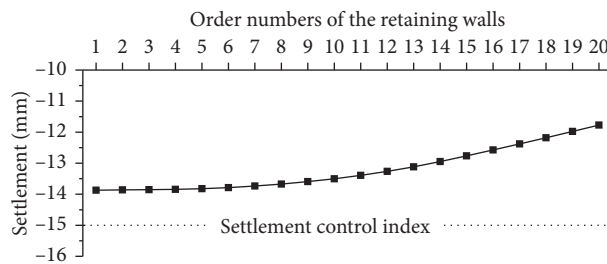


FIGURE 22: Final settlement of each retaining wall.

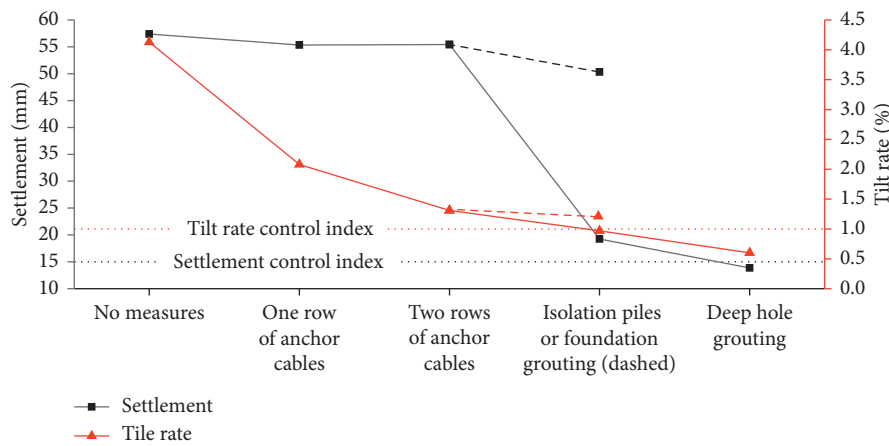


FIGURE 23: Settlement and tilt rate changing curves of the retaining wall.

4.4. *Deep Hole Grouting Protection Effect.* The differential settlement and tilt rate of the retaining wall meet the index requirements based on the combination of two rows of anchor cables and isolation piles, but the absolute settlement still exceeds the index value. To further reduce the settlement value, deep hole grouting is performed in addition to the aforementioned combination of measures, and the final settlement of each retaining wall is obtained, as shown in Figure 22.

According to the calculation results, the maximum settlement of the retaining wall is 13.87 mm, which meets the index requirement, and the maximum tilt rate of the retaining wall is further reduced to 0.60%.

4.5. *Determination of the Final Protection Measure.* After analyzing the effect of each control measure, the final protection measure is determined as a combination of two rows of anchor cables, waist beams, isolation piles, and deep hole grouting. To demonstrate the control effect of each measure on the retaining wall deformation, the settlement and tilt rate changing curves of the retaining wall are drawn according to the final deformation of the retaining wall under each measure, as shown in Figure 23 (the measures are gradually accumulated from left to right, and the settlement value is the absolute value).

The joint measures adopted for retaining wall deformation cover the entire transmission of the impacts of the construction: the deep hole grouting aims at the source of

the influence, the isolation piles aim at the propagation of the influence, and the anchor cables with waist beams aim at the object of the influence. For similar projects with a great difficulty in settlement control, the combination of “source,” “propagation,” and “object” can effectively protect adjacent structures.

5. Conclusions

This paper analyzes the retaining wall deformation under the influence of station construction by a numerical simulation method. Four countermeasures are formulated and their control effects are analyzed. The final protection measures and the protection concept are proposed. The main conclusions are drawn as follows:

- (1) The construction of the station has little influence on the differential settlement of adjacent retaining walls, but the affected retaining walls have large absolute settlement and tilt deformation values, forming a trend of “high in the east and low in the west.”
- (2) Anchor cables with waist beams can effectively control the tilt of the retaining wall, but the tilt rate is still beyond the target in this case. The simulation data show that the control effect of anchor cables on the absolute settlement is not obvious, but this measure has a significant control effect on the tilt of the retaining wall.
- (3) The differences in the protection effect between foundation grouting and isolation piles are analyzed. The calculation results show that the foundation grouting control effect is not ideal because of the oversettlement of the reinforced soil, while the control effect of the isolation piles is significant. The tilt rate meets the index requirements when isolation piles is adopted, but the absolute settlement still exceeds the index.
- (4) After the analysis, a combination of anchor cables, waist beams, isolation piles, and deep hole grouting is adopted to jointly control the retaining wall deformation. The maximum settlement and the maximum tilt rate of the retaining wall in this case are both less than the deformation index. According to this measure, a concept of joint control aiming at the influences of the “source,” “propagation,” and “object” is proposed, which can provide a reference for similar projects with a great difficulty in deformation control.

Data Availability

The data used to support the findings of this study are included within the article.

Conflicts of Interest

The authors declare that there are no conflicts of interest regarding the publication of this paper.

Acknowledgments

This research was supported by the National Natural Science Foundation of China (Grant no. 51678033).

References

- [1] D. H. Hu and J. C. Duan, “Risk source analysis and grade division of subway tunnel undercrossing the existing highway subjected to the complicated geological environment,” in *Proceedings of the International Conference on Power Engineering & Energy, Environment*, pp. 680–684, Shanghai, China, June 2016.
- [2] W. Bai, “Study on the deformation law of super highway roadbed crossed by the metro tunnel,” in *Proceedings of the International Conference on Mechanics and Civil Engineering*, vol. 7, pp. 832–835, Wuhan, China, December 2014.
- [3] C. Cao, C. Shi, M. Lei, L. Peng, and R. Bai, “Deformation characteristics and countermeasures of shallow and large-span tunnel under-crossing the existing highway in soft soil: a case study,” *KSCE Journal of Civil Engineering*, vol. 22, no. 8, pp. 3170–3181, 2018.
- [4] Y. L. Lin and Y. H. Fang, “Settlement behavior of new reinforced earth retaining walls under loading-unloading cycles,” in *Proceedings of the 2nd International Conference on Civil Engineering and Transportation*, vol. 256–259, pp. 215–219, October 2012, Applied Mechanics and Materials.
- [5] Y. T. Liu and X. Huang, “Numerical analysis of deformation and stability of reinforced high retaining wall,” in *Proceedings of the 2nd International Conference on Civil, Architectural and Hydraulic Engineering*, vol. 405–408, pp. 227–232 Applied Mechanics and Materials, Zhuhai, China, July 2013.
- [6] Y. Zhao, G. Q. Yang, B. J. Zhang, and P. Lv, “The horizontal deformation study on the geogrid reinforced earth retaining wall,” in *Proceedings of the 4th Asian Regional Conference on Geosynthetics*, pp. 332–335, Shanghai, China, June 2008.
- [7] T. Akhlaghi and A. Nikkar, “Numerical analyses of dynamic response of geosynthetic-reinforced soil retaining wall,” *Geosystem Engineering*, vol. 17, no. 2, pp. 142–149, 2014.
- [8] K. Y. Jiang, J. Cao, L. Peng, and M. M. Chen, “The deformation character of retaining wall under horizontal earthquake,” in *Proceedings of the International Conference on Mechanical Engineering and Materials*, vol. 152–154, pp. 1443–1447 Applied Mechanics and Materials, Melbourne, Australia, January 2012.
- [9] Y. L. Lin and G. L. Yang, “Dynamic deformation behavior and life analysis of green reinforced gabion retaining wall,” in *Proceedings of the 2nd International Conference on Civil Engineering and Transportation*, vol. 256–259, pp. 251–255, Guilin, China, October 2012.
- [10] S. Nakajima, K. Hong, S. Mulmi, J. Koseki, K. Watanabe, and M. Tateyama, “Study on seismic performance of geogrid reinforced soil retaining walls and deformation characteristics of backfill soil,” in *Proceedings of the 4th Asian Regional Conference on Geosynthetics*, pp. 211–215, Shanghai, China, June 2008.
- [11] H.-w. Zhu, L.-k. Yao, and J. Li, “Influence factors on the seismic behavior and deformation modes of gravity retaining walls,” *Journal of Mountain Science*, vol. 16, no. 1, pp. 168–178, 2019.
- [12] Z. M. Ghazaly, M. A. Rahim, V. K. Hiung, N. F. Isa, and L. A. Sofri, “The effect of construction stage on the development of retaining wall,” in *Proceedings of the International*

- Conference on Advanced Materials Engineering and Technology*, vol. 1835, Taiwan, China, December 2016.
- [13] S. Q. Peng, Q. H. Zhao, and Z. Y. Chen, "The relationship between retaining wall deformation and earth pressure in deep excavation," in *Proceedings of the 2nd International Conference on Structures and Building Materials*, vol. 446–449, pp. 1690–1695, Advanced Materials Research, Changsha, China, July 2012.
- [14] D. E. L. Ong, C. F. Leung, and Y. K. Chow, "Time-dependent pile behavior due to excavation-induced soil movement in clay," in *Proceedings of the 12th Pan-American Conference on Soil Mechanics and Geotechnical Engineering*, vol. 2, pp. 2035–2040, Boston, MA, USA, January 2003.
- [15] W. H. Ma, C. Y. Yang, H. Peng et al., "Settlement control on retaining wall embankment affected by underneath traversing large-diameter slurry shield tunnels," *Journal of Hunan University (Natural Science)*, vol. 47, no. 3, pp. 44–53, 2020, in Chinese.
- [16] X. Y. Liu, "Numerical analysis on construction stability of tunnel crossing underneath existing retaining wall of express highway," *Journal of Water Resources and Architectural Engineering*, vol. 12, no. 3, pp. 31–35, 2014, in Chinese.
- [17] X. Y. Sun, "Analysis and control measures of shallow buried tunnels parallel crossing road retaining wall," Master's thesis, Beijing Municipal Engineering Research Institute, Beijing, China, 2019, in Chinese..
- [18] L. Yu, D. Zhang, Q. Fang, L. Cao, T. Xu, and Q. Li, "Surface settlement of subway station construction using pile-beam-arch approach," *Tunnelling and Underground Space Technology*, vol. 90, pp. 340–356, 2019.
- [19] B. Li and Z. Z. Wang, "Numerical study on the response of ground movements to construction activities of a metro station using the pile-beam-arch method," *Tunnelling and Underground Space Technology*, vol. 88, pp. 209–220, 2019.
- [20] M. S. Pakbaz, S. Imanzadeh, and K. H. Bagherinia, "Characteristics of diaphragm wall lateral deformations and ground surface settlements: case study in Iran-Ahwaz metro," *Tunnelling and Underground Space Technology*, vol. 35, pp. 109–121, 2013.
- [21] X. Liu, Y. Liu, Z. Yang, and C. He, "Numerical Analysis on the mechanical performance of supporting structures and ground settlement characteristics in construction process of subway station built by pile-beam-arch method," *KSCSE Journal of Civil Engineering*, vol. 21, no. 5, pp. 1690–1705, 2017.
- [22] X. Yang and Y. Li, "Research of surface settlement for a single arch long-span subway station using the pipe-roof pre-construction method," *Tunnelling and Underground Space Technology*, vol. 72, pp. 210–217, 2018.
- [23] K. Zhang, J. L. C. Torres, and Z. J. Zang, "Numerical analysis of pipelines settlement induced by tunneling," *Advances in Civil Engineering*, vol. 2019, Article ID 4761904, 10 pages, 2019.
- [24] D. M. Potts, K. Axelsson, L. Grande et al., *Guidelines for the Use of Advanced Numerical Analysis*, Thomas Telford, London, UK, 2002.
- [25] C. S. Desai, M. M. Zaman, J. G. Lightner, and H. J. Siriwardane, "Thin-layer element for interfaces and joints," *International Journal for Numerical and Analytical Methods in Geomechanics*, vol. 8, pp. 9–43, 1984.
- [26] E. Falk, K. Fondazioni, G. Burke, and H. Baker, "Grouting techniques as part of modern urban tunnelling in Europe," in *Proceedings of the 3rd International Conference on Grouting and Ground Treatment*, vol. 120, pp. 1534–1545, New Orleans, LA, USA, February 2003.
- [27] J. Su, Q. Fang, D. L. Zhang, X. Niu, X. Liu, and Y. Jie, "Bridge responses induced by adjacent subway station construction using shallow tunneling method," *Advances in Civil Engineering*, vol. 2018, Article ID 8918749, 16 pages, 2018.
- [28] S. A. Mazek, K. T. Law, and D. T. Lau, "Use of grouting to reduce deformations of an existing tunnel underpass by another tunnel," in *Proceedings of the 3rd International Conference on Grouting and Ground Treatment*, vol. 120, pp. 1570–1581, New Orleans, LA, USA, February 2003.
- [29] J. Lv, X. Li, Z. Li, and H. Fu, "Numerical simulations of construction of shield tunnel with small clearance to adjacent tunnel without and with isolation pile reinforcement," *KSCSE Journal of Civil Engineering*, vol. 24, no. 1, pp. 295–309, 2020.
- [30] J. Tang, J. Y. Liu, and Y. Liu, "Study on the measures of tunnels side-crossing bridge based on sheltering effects of isolation piles," in *Proceedings of the 2nd International Conference on Materials Science, Energy Technology and Environmental Engineering*, vol. 81, Zhuhai, China, April 2017.
- [31] G. Zheng, F. J. Wang, Y. M. Du, Y. Diao, Y. W. Lei, and X. S. Cheng, "The efficiency of the ability of isolation piles to control the deformation of tunnels adjacent to excavations," *International Journal of Civil Engineering*, vol. 16, no. 10, pp. 1475–1490, 2018.
- [32] M. Packer, R. Newman, C. Prangley, and I. Heath, "Permeation grouting and excavation at Victoria station, London," *Proceedings of the Institution of Civil Engineers - Geotechnical Engineering*, vol. 171, no. 3, pp. 267–281, 2018.
- [33] K. Wu and Z. S. Shao, "Effects of pipe roof support and grouting pre-reinforcement on the track settlement," *Advances in Civil Engineering*, vol. 2018, Article ID 6041305, 9 pages, 2018.
- [34] J. J. Li, H. R. Bai, and J. K. Li, "Analysis and control the surface settlement of tunnel excavation," in *Proceedings of the 2nd International Conference on Civil Engineering, Architecture and Sustainable Infrastructure*, vol. 438-439, pp. 939–942, Applied Mechanics and Materials, Zhengzhou, China, July 2013.